Transactions of the ASME®

FLUIDS ENGINEERING DIVISION
Technical Editor
DEMETRI P. TELIONIS (1999)
Executive Secretary
PAT WHITE (1999)
Assistant to the Editor
N. W. SCHAEFFLER
Calendar Editor
M. F. ACKERSON

Associate Technical Editors
S. BANERJEE (1999)
P. W. BEARMAN (2001)
P. BRADSHAW (2000)
M. N. DHAUBHADEL (1999)
J. K. EATON (1999)
G. ERLEBACHER (2000)
U. GHIA (2001)
M. HAJJ (2001)
J. KATZ (2001)
C. L. MERKLE (2000)
P. RAAD (2001)
B. SCHIAVELLO (1999)
M. SOMMERFELD (1999)
F. K. WASDEN (2000)
D. R. WILLIAMS (2000)
K. ZAMAN (2001)

BOARD ON COMMUNICATIONS
Chairman and Vice-President
R. K. SHAH

OFFICERS OF THE ASME
President, **W. M. PHILLIPS**
Exec. Director
D. L. BELDEN
Treasurer
J. A. MASON

PUBLISHING STAFF
Managing Director, Engineering
CHARLES W. BEARDSLEY
Director, Technical Publishing
PHILIP DI VIETRO
Managing Editor, Technical Publishing
CYNTHIA B. CLARK
Managing Editor, Transactions
CORNELIA MONAHAN
Production Assistant
MARISOL ANDINO

Transactions of the ASME, Journal of Fluids Engineering (ISSN 0098-2202) is published quarterly (Mar., June, Sept., Dec.) for $205.00 per year by The American Society of Mechanical Engineers, Three Park Avenue, New York, NY 10016. Periodicals postage paid at New York, NY and additional mailing offices. POSTMASTER: Send address changes to Transactions of the ASME, Journal of Fluids Engineering, c/o THE AMERICAN SOCIETY OF MECHANICAL ENGINEERS, 22 Law Drive, Box 2300, Fairfield, NJ 07007-2300.
CHANGES OF ADDRESS must be received at Society headquarters seven weeks before they are to be effective. Please send old label and new address.
PRICES: To members, $40.00, annually: to nonmembers, $205.00. Add $40.00 for postage to countries outside the United States and Canada.
STATEMENT from By-Laws. The Society shall not be responsible for statements or opinions advanced in papers or . . . printed in its publications (B7.1, Par. 3).

INDEXED by Applied Mechanics Reviews and Engineering Information, Inc. Canadian Goods & Services Tax Registration #126148048.

Journal of Fluids Engineering

Published Quarterly by The American Society of Mechanical Engineers

VOLUME 121 • NUMBER 1 • MARCH 1999

(Contents continued on p. 79)

This journal is printed on acid-free paper, which exceeds the ANSI Z39.48-1992 specification for permanence of paper and library materials. ♾™

♻ 85% recycled content, including 10% post-consumer fibers.

(Contents continued)

Technical Briefs

Announcements and Special Notices

Journal of Fluids Engineering

Editorial

This is the annual report of the Technical Editor, which appears in each March issue of the Journal. We are now completing one year of electronic publishing. Since March of 1998, every issue of this Journal is posted on the Internet in addition to the regular distribution of the printed version to its subscribers. The plan has been to provide this special service only to subscribers after the first year. However, for the first few issues of 1999 it will be still available electronically free of charge.

The on-line version of the *Journal of Fluids Engineering* contains all elements provided in the printed version. Abstracts are fully searchable and full articles are provided in PDF format. Search mechanisms facilitate search by authors' name, title, topic and key words. An index of authors going back to 1992 has also been constructed. Authors are alerted to the fact that abstracts now take even greater significance. Some readers may look only at an abstract in the electronic form before they decide to read the entire paper. Moreover, the search engine that matches key words with papers searches only the abstracts. Authors must therefore make certain that their abstracts contain all of the significant key words that essentially define the content of the paper and that they are free from complex formulas.

The *On-Line Journal of Fluids Engineering* has attracted considerable attention. The first month after the March issue was posted, over 2,000 individuals visited the Journal Web site and the month after the June issue appeared, there were over 10,000 visitors. As of the end of October, i.e., within the first eight months of the availability of this service, the On-Line JFE was accessed 37,108 times.

Apparently the readers are taking full advantage of this service but not the authors. The Editors personally urge authors to include in the On-Line JFE more material pertinent to their publication but few authors have chosen to take advantage of this opportunity, except for depositing data to the JFE Data Bank which has been in operation since December 1992 (see editorial in March, 1992). Many authors argue persistently, and most are willing to pay excess page charges to avoid reducing the printed version of their work by one or two pages. But they are reluctant to include extra material in the electronic version of their paper. As a result, the On-Line JFE has been almost identical with the printed version of the Journal but the advantage is that articles are now fully searchable and more widely available. Notwithstanding, the electronic medium has opened many more opportunities for enhancing the communication of scientific information. Now there is virtually unlimited space for mathematical derivations, computer program listings, or for digital data as well as for figures in color and for video.

We now accept papers submitted electronically and most of the associate editors participate in the experiment of electronic reviewing. If the entire process were to be handled electronically, we estimate that we could reduce the first stage of the review process by four to five weeks. This practice takes place only on a voluntary basis by authors, reviewers, and editors.

Recent increases in the number of pages allotted to the *Journal of Fluids Engineering* have allowed us to virtually eliminate our backlog. We now print 950 pages per year and most papers appear in print three to four months after they are accepted. Many papers are published a little over a year after their submission. Unfortunately, the review process of some papers may take much longer. Although these are the exceptions rather than the norm, it is still embarrassing that we have not succeeded in eliminating such delays. We can attribute most but not all of these delays to negligent reviewers, but some can be attributed to the editors' heavy workload. Quite often the delays are due to the authors themselves. Some authors receiving positive reviews relax their efforts and may take six to nine months to resubmit a revised manuscript.

The March issue always includes a list of the papers published in the previous year, grouped according to their content and the names of all the reviewers who contributed to our efforts the year before. We also acknowledge here the valuable contributions of the associate editors whose tenure expired this year. These are Promode R. Bandyopadhyay, Peter W. Bearman, Mark S. Cramer, Joseph A. C. Humphrey, Fazle Hussain, Joseph Katz, Peter M. Sockol, and Michael S. Triantafyllou. The following associate editors joined the Editorial Board last year but their appointment was not approved by the ASME Board on Communication by the time the March 1998 issue went to print. These are: Peter Bradshaw (Stanford University) and David R. Williams (Illinois Institute of Technology) both in the area of fluid mechanics; Gordon Erlebacher (Florida State University) in the area of computational fluid dynamics; and Frederic K. Wasden (Shell E&P Technology Company) in multiphase flow. The following associate editors were nominated by the corresponding committees and the Executive Committee of the Division of Fluids Engineering and their appointment was confirmed by the ASME Board on Communications: Urmila Ghia (University of Cincinnati) computational fluid dynamics; Muhammad R. Hajj (Virginia Tech) editorial office; Peter E. Raad (Southern Methodist University) and Khairul B. M. Q. Zaman (NASA Lewis Research Center) both fluid mechanics. Peter W. Bearman (Imperial College of Science, Technology and Medicine) and Joseph Katz (The Johns Hopkins University) were reappointed for another three year term.

We should also thank here Philip Di Vietro the Director of Technical Publishing of ASME and Cynthia B. Clark the Managing Editor of Technical Publishing who made the transition to electronic publishing a reality.

Finally, I want to express my sincere thanks to two ladies whose excellent work we all take for granted exactly because it has always been flawless. We are so accustomed to noticing improvements and recognizing unusual contributions that we fail to acknowledge performances that are consistently at the highest possible level. In the order of processing of the editorial work I want to express my sincere thanks to Pat White, the Executive Secretary of the Journal and Connie Monahan, our Copy Editor. Pat has really been the unifying intelligence

of the Journal. In the incredible maze of hundreds of simultaneous communications with authors, editors and reviewers, she has been able to preserve sense and continuity. On many occasions, for example, she would point out that I was contradicting myself by overlooking something I had said many months earlier. She has literally averted numerous small and large disasters. We also owe a lot to Connie Monahan who with firmness and understanding of our constraints consistently kept the highest possible quality in scientific publication. We so often hear the expression "without their efforts we would not have been able to carry out a certain task." I cannot think of any other occasion where this would be more true. Without the efforts of Pat White and Connie Monahan the quality of this publication would have been many grades lower, if it were at all possible.

The Technical Editor

DEDICATION TO LLOYD MACGREGOR TREFETHEN ON THE OCCASION OF HIS 80TH BIRTHDAY

This issue of the *Journal of Fluids Engineering* is dedicated to Lloyd MacGregor Trefethen on the occasion of his 80th birthday. Lloyd was born in Waltham, Massachusetts. In 1940 he received his Bachelor Degree from the Webb Institute, where he acquired a lifelong interest in ships and naval engineering. After Webb, Lloyd attended MIT where he received an MS degree for a thesis on the reversal of ships. In 1944, he entered the U.S. Navy and married Florence Newman also a naval officer. At the end of the war, Lloyd and Florence matriculated at the University of Cambridge where Lloyd received his Ph.D. in 1950 for research on heat transfer in liquid metals. In 1951, they returned to the States and Lloyd assumed the role of Executive Secretary of the NSF under the then Director, Alan Waterman, and served as Secretary of the National Science Board. In 1954 he came to the other Cambridge as an Assistant Professor in the Division of Engineering and Applied Physics at Harvard University. It was during this time that he acquired his abiding interest in the phenomena associated with surface tension and the formation of liquid drops. Indeed, in 1962, as a consultant to the Corporate Research and Development laboratories of General Electric, he formulated a remarkable analogy between the fluid mechanics of candlewicks and capillary pumping in closed cavities, which led to the devices we now know as heat pipes. Lloyd's independent invention of the heat pipe was acknowledged by Chi in the beginning of his book, *Heat Pipes: Theory and Practice,* Hemisphere Publishing, 1976.

In 1958 he came to Tufts University as Professor and Chairman of the Department of Mechanical Engineering. Thus began an association with Tufts, which is now in its 40th year, hardly flagging when he became Professor Emeritus in 1989. During these years Lloyd continued his interest in surface tension and droplets, an interest that was capped by a remarkable educational film, "Surface Tension in Fluid Mechanics," produced first under the auspices of Educational Services, Inc. and later distributed by the Encyclopedia Britannica. This film received many awards, most notably the Golden Eagle award of the CINE society in 1967 and the Le Prix de Physique of the 4th International Scientific Film Festival in 1968. Lloyd was also among the first to see the potential of video cameras, using some of the earliest models to reveal many new phenomena in his much beloved field of small-scale fluid mechanics.

During a sabbatical leave in Australia, Lloyd conducted a series of sensitive experiments that received wide attention in the popular press. In an apparatus especially constructed to magnify the effects of the extremely weak Coriolis force, Lloyd demonstrated that water does, in fact, drain from a bathtub in a vortex that rotates in a clockwise direction in the southern hemisphere. A rigorous account of this work appeared in the September 1965 issue of the journal *Nature.* In that paper, Lloyd and his co-authors raised a concern having to do with the difficulty of the experiment, best illustrated by quoting directly from the paper. "These tests posed for us an unusual problem in experimental work. Normally, one does experiments in which there is some uncertainty in the expected outcome. In these experiments, however, our confidence in the idea that the Earth rotates, and in the applicability of conservation of angular momentum to masses of fluid, was probably so strong that experimental denial would have been almost inadmissible. We should have gone to unusual lengths to get the apparatus to work as expected. Realizing this, we found ourselves reluctant to accept as conclusive the results we were getting, results which apparently confirmed our ideas. One can never prove, for example, that it was not some small air current which persistently maintained a circulation that gave the results we observed, and that a quantitatively comparable, but oppositely directed, air current caused Shapiro's results. There is, in principle, an infinite number of hypotheses that can explain any set of observations. This difficulty in validation of scientific theories is not a new one and, in this instance, as in all instances, it cannot be proved that any one hypothesis is correct."

In his early years at Tufts, Lloyd became an enthusiast for the application of information theory to undergraduate engineering laboratory. His innovative ideas led to a reformulation of laboratory work at Tufts to involve all of the faculty and all of the students in opened-ended, research-based experiments, a trend that not only spread beyond Tufts but marked Tufts as a college that especially fosters undergraduate research. In honor of this, the Mechanical Engineering Department created the Lloyd Trefethen Prize for Undergraduate Research in 1990, a prize that has been awarded annually ever since. In his later years at Tufts, Lloyd conceived the idea of a computer network-based question bank devoted to unanswered questions in fluid mechanics and heat transfer, a database that now contains over 1000 queries. Even after retirement, he continues to pursue his love of research, having invented and patented a unique design for a sailing craft.

A Fellow of the ASME, Lloyd has spearheaded pioneering initiatives for the society. In 1984, at the Winter Annual Meeting of the ASME in New Orleans, he was part of a panel presiding over the first open forum discussion on "Significant Questions in Heat Transfer." The purpose of the forum was to explore ways to move away from the routine cataloging of flow and heat transfer "test" problems to search, instead, for more general "significant questions" which, if properly defined, would spawn in-depth research into matters of more universal and lasting impact. Subsequent to this meeting, Lloyd organized the first ASME session on "Some Unanswered Questions in Fluid Mechanics," for the December 1989 Winter Annual Meeting held in San Francisco, California. In the preface to the paper (89-WA/FE-5) for that session he says: "Questions are not widely used in our literature. The typical paper in fluid mechanics, or in science and engineering generally contains not a single question. . . . Some people are clearly reluctant to pose questions for which they have no answers. But the absence of questions is also in part because they are not part of our profession's tradition. . . . A major hope behind the assembling of the questions in this paper is that they may bring into focus some of the unresolved problems in fluid mechanics." Lloyd went on to organize the 1991, 1993, 1995 and 1997 sessions on "Some Unanswered Questions in Fluid Mechanics" and, eventually, these efforts culminated in the appearance of a "Significant Questions" column in the *Journal of Fluids Engineering.* Both the column and the periodic "significant questions" sessions remain of vital importance to ASME.

Much of Lloyd's early research found its origins in industry, was performed with very simple apparatus, and often became course instruction material. In particular, at General Electric's Corporate Research and Development laboratories he was involved in activities such as diagnosing malfunctioning heavy water plants, developing and applying heat pipes for the cooling of electronic components, and investi-

Lloyd MacGregor Trefethen

gating the effects of rotation on flows through straight pipes. For the last problem he constructed an ingenious device, consisting of a horizontal pipe section, aligned radially through the center of a rotating record player turntable to which it was fixed. A vertical feed mechanism allowed the flow of water and the determination of pressure drop for fixed values of the angular velocity.

Lloyd Trefethen has always possessed an amazing understanding of physical phenomena and has used his understanding to develop new concepts in engineering science and to invent new technologies. He is an exemplar of the creative engineer and educator. His friends among the worldwide readership of this journal wish him well on his 80th birthday and look forward to many more years of his insightful curiosity about fluid mechanics and heat transfer.

Ken Astill, Fred Nelson, and Joseph A. C. Humphrey

The Fluid Mechanics of Microdevices—The Freeman Scholar Lecture

Mohamed Gad-el-Hak
Professor,
Department of Aerospace and Mechanical Engineering,
University of Notre Dame,
Notre Dame, IN 46556.
Fellow ASME
E-mail: Mohamed.Gad-el-Hak.1@nd.edu

Manufacturing processes that can create extremely small machines have been developed in recent years. Microelectromechanical systems (MEMS) refer to devices that have characteristic length of less than 1 mm but more than 1 micron, that combine electrical and mechanical components and that are fabricated using integrated circuit batch-processing techniques. Electrostatic, magnetic, pneumatic and thermal actuators, motors, valves, gears, and tweezers of less than 100-μm size have been fabricated. These have been used as sensors for pressure, temperature, mass flow, velocity and sound, as actuators for linear and angular motions, and as simple components for complex systems such as micro-heat-engines and micro-heat-pumps. The technology is progressing at a rate that far exceeds that of our understanding of the unconventional physics involved in the operation as well as the manufacturing of those minute devices. The primary objective of this article is to critically review the status of our understanding of fluid flow phenomena particular to microdevices. In terms of applications, the paper emphasizes the use of MEMS as sensors and actuators for flow diagnosis and control.

About the Author

Mohamed Gad-el-Hak received his B.Sc. (summa cum laude) in mechanical engineering from Ain Shams University in 1966 and his Ph.D. in fluid mechanics from the Johns Hopkins University in 1973. He has since taught and conducted research at the University of Southern California, University of Virginia, Institut National Polytechnique de Grenoble, and Université de Poitiers, and has lectured extensively at seminars in the United States and overseas. Dr. Gad-el-Hak is currently Professor of Aerospace and Mechanical Engineering at the University of Notre Dame. Prior to that, he was a Senior Research Scientist and Program Manager at Flow Research Company in Seattle, Washington. Dr. Gad-el-Hak has published over 280 articles and presented 170 invited lectures in the basic and applied research areas of isotropic turbulence, boundary layer flows, stratified flows, compliant coatings, unsteady aerodynamics, biological flows, non-Newtonian fluids, hard and soft computing including genetic algorithms, and flow control. He is the author of the book *Flow Control,* and editor of three Springer-Verlag's books *Frontiers in Experimental Fluid Mechanics, Advances in Fluid Mechanics Measurements,* and *Flow Control: Fundamentals and Practices.* Professor Gad-el-Hak is a fellow of The American Society of Mechanical Engineers, a life member of the American Physical Society, and an associate fellow of the American Institute of Aeronautics and Astronautics. He has recently been inducted as an eminent engineer in Tau Beta Pi, an honorary member in Sigma Gamma Tau and Pi Tau Sigma, and a member-at-large in Sigma Xi. From 1988 to 1991, Dr. Gad-el-Hak served as Associate Editor for *AIAA Journal.* He is currently an Associate Editor for *Applied Mechanics Reviews.* In 1998, Professor Gad-el-Hak was named the Fourteenth ASME Freeman Scholar.

1 Introduction

How many times when you are working on something frustratingly tiny, like your wife's wrist watch, have you said to yourself, "If I could only train an ant to do this!" What I would like to suggest is the possibility of training an ant to train a mite to do this. What are the possibilities of small but movable machines? They may or may not be useful, but they surely would be fun to make.

(From the talk "There's Plenty of Room at the Bottom," delivered by Richard P. Feynman at the annual meeting of the American Physical Society, Pasadena, California, 29 December 1959.)

Tool making has always differentiated our species from all others on earth. Aerodynamically correct wooden spears were carved by archaic homosapiens close to 400,000 years ago. Man builds things consistent with his size, typically in the range of two orders of magnitude larger or smaller than himself, as indicated in Fig. 1. (Though the extremes of length-scale are outside the range of this figure, man, at slightly more than 10^0 m, amazingly fits right in the middle of the smallest subatomic particle which is approximately 10^{-26} m and the extent of the observable universe which is $\sim 1.42 \times 10^{26}$ m (15 billion light years). An egocentric universe indeed!) But humans have always striven to explore, build, and control the extremes of length and time scales. In the voyages to Lilliput and Brobdingnag of *Gulliver's Travels,* Jonathan Swift (1727) speculates on the remarkable possibilities which diminution or magnification of physical dimensions provides. The Great Pyramid of Khufu was originally 147 m high when completed around 2600 B.C., while the Empire State Building constructed in 1931 is presently—after the addition of a television antenna mast in 1950—449 m high. At the other end of the spectrum of man-made artifacts, a dime is slightly less than 2 cm in diameter. Watchmakers have practiced the art of miniaturization since the thirteenth century. The invention of the microscope in the seventeenth century opened the way for direct observation of microbes and plant and animal cells. Smaller things were man-made in the latter half of this century. The transistor—invented in 1948—in today integrated circuits has a size of 0.25 micron in production and approaches 50 nanometers in research laboratories. But what about the miniaturization of mechanical parts—machines—envisioned by Feynman (1961) in his legendary speech quoted above?

Manufacturing processes that can create extremely small machines have been developed in recent years (Angell et al., 1983;

Contributed by the Fluids Engineering Division for publication in the JOURNAL OF FLUIDS ENGINEERING. Manuscript received by the Fluids Engineering Division August 31, 1998; revised manuscript received December 14, 1998. Associate Technical Editor: D. P. Telionis.

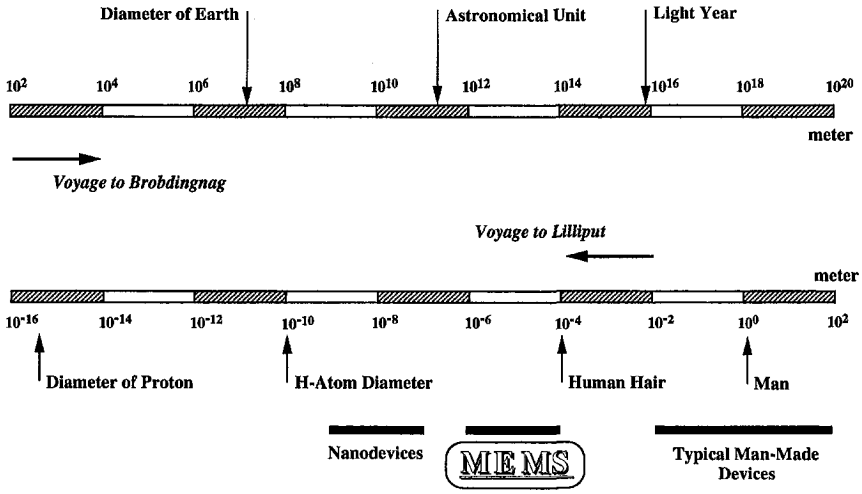

Fig. 1 The scale of things, in meters. Lower scale continues in the upper bar from left to right.

Gabriel et al., 1988; 1992; O'Connor, 1992; Gravesen et al., 1993; Bryzek et al., 1994; Gabriel, 1995; Hogan, 1996; Ho and Tai, 1996; 1998; Tien, 1997; Busch-Vishniac, 1998; Amato, 1998). Electrostatic, magnetic, pneumatic and thermal actuators, motors, valves, gears and tweezers of less than 100 μm size have been fabricated. These have been used as sensors for pressure, temperature, mass flow, velocity and sound, as actuators for linear and angular motions, and as simple components for complex systems such as micro-heat-engines and micro-heat-pumps (Lipkin, 1993; Garcia and Sniegowski, 1993; 1995; Sniegowski and Garcia, 1996; Epstein and Senturia, 1997; Epstein et al., 1997). The technology is progressing at a rate that far exceeds that of our understanding of the unconventional physics involved in the operation as well as the manufacturing of those minute devices. The present paper focuses on one aspect of such physics: fluid flow phenomena associated with micro-scale devices. In terms of applications, the paper will emphasize the use of MEMS as sensors and actuators for flow diagnosis and control.

Microelectromechanical systems (MEMS) refer to devices that have characteristic length of less than 1 mm but more than 1 micron, that combine electrical and mechanical components and that are fabricated using integrated circuit batch-processing technologies. Current manufacturing techniques for MEMS include surface silicon micromachining; bulk silicon micromachining; lithography, electrodeposition and plastic molding (or, in its original German, lithographie galvanoformung abformung, LIGA); and electrodischarge machining (EDM). As indicated in Fig. 1, MEMS are more than four orders of magnitude larger than the diameter of the hydrogen atom, but about four orders of magnitude smaller than the traditional man-made artifacts. Nanodevices (some say NEMS) further push the envelope of electromechanical miniaturization.

Despite Feynman's demurring regarding the usefulness of small machines, MEMS are finding increased applications in a variety of industrial and medical fields, with a potential worldwide market in the billions of dollars. Accelerometers for automobile airbags, keyless entry systems, dense arrays of micromirrors for high-definition optical displays, scanning electron microscope tips to image single atoms, micro-heat-exchangers for cooling of electronic circuits, reactors for separating biological cells, blood analyzers and pressure sensors for catheter tips are but a few of current usage. Microducts are used in infrared detectors, diode lasers, miniature gas chromatographs and high-frequency fluidic control systems. Micropumps are used for ink jet printing, environmental testing and electronic cooling. Potential medical applications for small pumps include controlled delivery and monitoring of minute amount of medication, manufacturing of nanoliters of chemicals and development of artificial pancreas. Several new journals are dedicated to the science and technology of MEMS, for example IEEE/ASME *Journal of Microelectromechanical Systems, Journal of Micromechanics and Microengineering,* and *Microscale Thermophysical Engineering.*

Not all MEMS devices involve fluid flows, but the present review will focus on the ones that do. Microducts, micropumps, microturbines and microvalves are examples of small devices involving the flow of liquids and gases. MEMS can also be related to fluid flows in an indirect way. The availability of inexpensive, batch-processing-produced microsensors and microactuators provides opportunities for targeting small-scale coherent structures in macroscopic turbulent shear flows. Flow control using MEMS promises a quantum leap in control system performance. The present article will cover both the direct and indirect aspects of microdevices and fluid flows. Section 2 addresses the question of modeling fluid flows in microdevices, and Section 3 gives a brief overview of typical applications of MEMS in the field of fluid mechanics. The paper by Löfdahl and Gad-el-Hak (1999) provides more detail on MEMS applications in turbulence and flow control.

The Freeman Scholarship is bestowed biennially, in even-numbered years. The Fourteenth Freeman Lecture presented in 1998 is, therefore, the last of its kind in this millennium, and the topic of micromachines is perhaps a fitting end to a century of spectacular progress in mechanical engineering led in no small part by members of ASME International.

2 Fluid Mechanics Issues

2.1 Prologue. The rapid progress in fabricating and utilizing microelectromechanical systems during the last decade has not been matched by corresponding advances in our understanding of the unconventional physics involved in the operation and manufacture of small devices. Providing such understanding is crucial to designing, optimizing, fabricating and operating improved MEMS devices.

Fluid flows in small devices differ from those in macroscopic machines. The operation of MEMS-based ducts, nozzles, valves, bearings, turbomachines, etc., cannot always be predicted from conventional flow models such as the Navier-Stokes equations with no-slip boundary condition at a fluid-solid interface, as routinely and successfully applied for larger flow devices. Many questions have been raised when the results of experiments with microdevices could not be explained via traditional flow modeling. The pressure gradient in a long microduct was observed to be non-constant and the measured flowrate was

higher than that predicted from the conventional continuum flow model. Load capacities of microbearings were diminished and electric currents needed to move micromotors were extraordinarily high. The dynamic response of micromachined accelerometers operating at atmospheric conditions was observed to be over-damped.

In the early stages of development of this exciting new field, the objective was to build MEMS devices as productively as possible. Microsensors were reading something, but not many researchers seemed to know exactly what. Microactuators were moving, but conventional modeling could not precisely predict their motion. After a decade of unprecedented progress in MEMS technology, perhaps the time is now ripe to take stock, slow down a bit and answer the many questions that arose. The ultimate aim of this long-term exercise is to achieve rational-design capability for useful microdevices and to be able to characterize definitively and with as little empiricism as possible the operations of microsensors and microactuators.

In dealing with fluid flow through microdevices, one is faced with the question of which model to use, which boundary condition to apply and how to proceed to obtain solutions to the problem at hand. Obviously surface effects dominate in small devices. The surface-to-volume ratio for a machine with a characteristic length of 1 m is 1 m^{-1}, while that for a MEMS device having a size of 1 μm is 10^6 m^{-1}. The million-fold increase in surface area relative to the mass of the minute device substantially affects the transport of mass, momentum and energy through the surface. The small length-scale of microdevices may invalidate the continuum approximation altogether. Slip flow, thermal creep, rarefaction, viscous dissipation, compressibility, intermolecular forces and other unconventional effects may have to be taken into account, preferably using only first principles such as conservation of mass, Newton's second law, conservation of energy, etc.

In this section, we discuss continuum as well as molecular-based flow models, and the choices to be made. Computing typical Reynolds, Mach and Knudsen numbers for the flow through a particular device is a good start to characterize the flow. For gases, microfluid mechanics has been studied by incorporating slip boundary conditions, thermal creep, viscous dissipation as well as compressibility effects into the continuum equations of motion. Molecular-based models have also been attempted for certain ranges of the operating parameters. Use is made of the well-developed kinetic theory of gases, embodied in the Boltzmann equation, and direct simulation methods such as Monte Carlo. Microfluid mechanics of liquids is more complicated. The molecules are much more closely packed at normal pressures and temperatures, and the attractive or cohesive potential between the liquid molecules as well as between the liquid and solid ones plays a dominant role if the characteristic length of the flow is sufficiently small. In cases when the traditional continuum model fails to provide accurate predictions or postdictions, expensive molecular dynamics simulations seem to be the only first-principle approach available to rationally characterize liquid flows in microdevices. Such simulations are not yet feasible for realistic flow extent or number of molecules. As a consequence, the microfluid mechanics of liquids is much less developed than that for gases.

2.2 Fluid Modeling. There are basically two ways of modeling a flow field. Either as the fluid really is, a collection of molecules, or as a continuum where the matter is assumed continuous and indefinitely divisible. The former modeling is subdivided into deterministic methods and probabilistic ones, while in the latter approach the velocity, density, pressure, etc., are defined at every point in space and time, and conservation of mass, energy and momentum lead to a set of nonlinear partial differential equations (Euler, Navier-Stokes, Burnett, etc.). Fluid modeling classification is depicted schematically in Fig. 2.

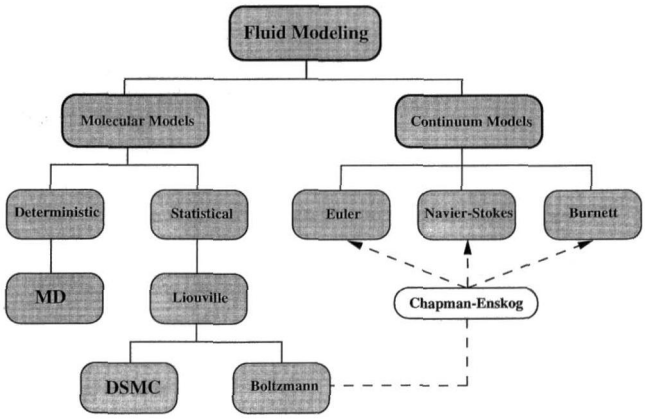

Fig. 2 Molecular and continuum flow models

The continuum model, embodied in the Navier-Stokes equations, is applicable to numerous flow situations. The model ignores the molecular nature of gases and liquids and regards the fluid as a continuous medium describable in terms of the spatial and temporal variations of density, velocity, pressure, temperature and other macroscopic flow quantities. For dilute gas flows near equilibrium, the Navier-Stokes equations are derivable from the molecularly-based Boltzmann equation, but can also be derived independently of that for both liquids and gases. In the case of direct derivation, some empiricism is necessary to close the resulting indeterminate set of equations. The continuum model is easier to handle mathematically (and is also more familiar to most fluid dynamists) than the alternative molecular models. Continuum models should therefore be used as long as they are applicable. Thus, careful considerations of the validity of the Navier-Stokes equations and the like are in order.

Basically, the continuum model leads to fairly accurate predictions as long as local properties such as density and velocity can be defined as averages over elements large compared with the microscopic structure of the fluid but small enough in comparison with the scale of the macroscopic phenomena to permit the use of differential calculus to describe them. Additionally, the flow must not be too far from thermodynamic equilibrium. The former condition is almost always satisfied, but it is the latter which usually restricts the validity of the continuum equations. As will be seen in Section 2.3, the continuum flow equations do not form a determinate set. The shear stress and heat flux must be expressed in terms of lower-order macroscopic quantities such as velocity and temperature, and the simplest (i.e., linear) relations are valid only when the flow is near thermodynamic equilibrium. Worse yet, the traditional no-slip boundary condition at a solid-fluid interface breaks down even before the linear stress-strain relation becomes invalid.

To be more specific, we temporarily restrict the discussion to gases where the concept of mean free path is well defined. Liquids are more problematic and we defer their discussion to Section 2.7. For gases, the mean free path ℓ is the average distance traveled by molecules between collisions. For an ideal gas modeled as rigid spheres, the mean free path is related to temperature T and pressure p as follows

$$\ell = \frac{1}{\sqrt{2}\pi n \sigma^2} = \frac{kT}{\sqrt{2}\pi p \sigma^2} \tag{1}$$

where n is the number density (number of molecules per unit volume), σ is the molecular diameter, and k is the Boltzmann constant.

The continuum model is valid when ℓ is much smaller than a characteristic flow dimension L. As this condition is violated, the flow is no longer near equilibrium and the linear relation

between stress and rate of strain and the no-slip velocity condition are no longer valid. Similarly, the linear relation between heat flux and temperature gradient and the no-jump temperature condition at a solid-fluid interface are no longer accurate when ℓ is not much smaller than L.

The length-scale L can be some overall dimension of the flow, but a more precise choice is the scale of the gradient of a macroscopic quantity, as for example the density ρ,

$$L = \frac{\rho}{\left|\frac{\partial \rho}{\partial y}\right|} \tag{2}$$

The ratio between the mean free path and the characteristic length is known as the Knudsen number

$$\mathrm{Kn} = \frac{\ell}{L} \tag{3}$$

and generally the traditional continuum approach is valid, albeit with modified boundary conditions, as long as $\mathrm{Kn} < 0.1$.

There are two more important dimensionless parameters in fluid mechanics, and the Knudsen number can be expressed in terms of those two. The Reynolds number is the ratio of inertial forces to viscous ones

$$\mathrm{Re} = \frac{v_o L}{\nu} \tag{4}$$

where v_o is a characteristic velocity, and ν is the kinematic viscosity of the fluid. The Mach number is the ratio of flow velocity to the speed of sound

$$\mathrm{Ma} = \frac{v_o}{a_o} \tag{5}$$

The Mach number is a dynamic measure of fluid compressibility and may be considered as the ratio of inertial forces to elastic ones. From the kinetic theory of gases, the mean free path is related to the viscosity as follows

$$\nu = \frac{\mu}{\rho} = \frac{1}{2}\,\ell\,\overline{v}_m \tag{6}$$

where μ is the dynamic viscosity, and $\overline{v}_m$ is the mean molecular speed which is somewhat higher than the sound speed a_o,

$$\overline{v}_m = \sqrt{\frac{8}{\pi\gamma}}\,a_o \tag{7}$$

where γ is the specific heat ratio (i.e. the isentropic exponent). Combining Equations (3)–(7), we reach the required relation

$$\mathrm{Kn} = \sqrt{\frac{\pi\gamma}{2}}\,\frac{\mathrm{Ma}}{\mathrm{Re}} \tag{8}$$

In boundary layers, the relevant length-scale is the shear-layer thickness δ, and for laminar flows

$$\frac{\delta}{L} \sim \frac{1}{\sqrt{\mathrm{Re}}} \tag{9}$$

$$\mathrm{Kn} \sim \frac{\mathrm{Ma}}{\mathrm{Re}_\delta} \sim \frac{\mathrm{Ma}}{\sqrt{\mathrm{Re}}} \tag{10}$$

where Re_δ is the Reynolds number based on the freestream velocity v_o and the boundary layer thickness δ, and Re is based on v_o and the streamwise length-scale L.

Rarefied gas flows are in general encountered in flows in small geometries such as MEMS devices and in low-pressure applications such as high-altitude flying and high-vacuum gadgets. The local value of Knudsen number in a particular flow

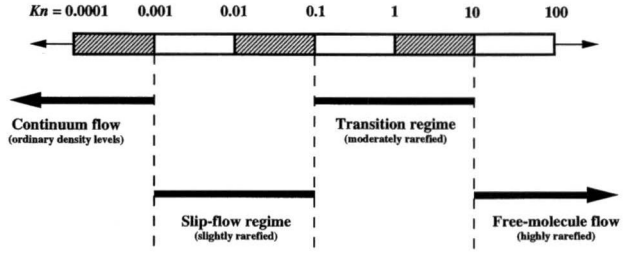

Fig. 3 Knudsen number regimes

determines the degree of rarefaction and the degree of validity of the continuum model. The different Knudsen number regimes are determined empirically and are therefore only approximate for a particular flow geometry. The pioneering experiments in rarefied gas dynamics were conducted by Knudsen in 1909. In the limit of zero Knudsen number, the transport terms in the continuum momentum and energy equations are negligible and the Navier-Stokes equations then reduce to the inviscid Euler equations. Both heat conduction and viscous diffusion and dissipation are negligible, and the flow is then approximately isentropic (i.e., adiabatic and reversible) from the continuum viewpoint while the equivalent molecular viewpoint is that the velocity distribution function is everywhere of the local equilibrium or Maxwellian form. As Kn increases, rarefaction effects become more important, and eventually the continuum approach breaks down altogether. The different Knudsen number regimes are depicted in Fig. 3, and can be summarized as follows

Euler equations (neglect molecular diffusion):

$$\mathrm{Kn} \to 0 \ (\mathrm{Re} \to \infty)$$

Navier-Stokes equations with no-slip boundary conditions:

$$\mathrm{Kn} \lesssim 10^{-3}$$

Navier-Stokes equations with slip boundary conditions:

$$10^{-3} \lesssim \mathrm{Kn} \lesssim 10^{-1}$$

Transition regime: $10^{-1} \lesssim \mathrm{Kn} \lesssim 10$

Free-molecule flow: $\mathrm{Kn} > 10$

We will return to those regimes in the following subsections.

As an example, consider air at standard temperature (T = 288 K) and pressure ($p = 1.01 \times 10^5$ N/m^2). A cube one micron to the side contains 2.54×10^7 molecules separated by an average distance of 0.0034 micron. The gas is considered dilute if the ratio of this distance to the molecular diameter exceeds 7, and in the present example this ratio is 9, barely satisfying the dilute gas assumption. The mean free path computed from Eq. (1) is $\ell = 0.065$ μm. A microdevice with characteristic length of 1 μm would have Kn = 0.065, which is in the slip-flow regime. At lower pressures, the Knudsen number increases. For example, if the pressure is 0.1 atm and the temperature remains the same, Kn = 0.65 for the same 1-μm device, and the flow is then in the transition regime. There would still be over 2 million molecules in the same one-micron cube, and the average distance between them would be 0.0074 μm. The same device at 100 km altitude would have Kn = 3×10^4, well into the free-molecule flow regime. Knudsen number for the flow of a light gas like helium is about 3 times larger than that for air flow at otherwise the same conditions.

Consider a long microchannel where the entrance pressure is atmospheric and the exit conditions are near vacuum. As air goes down the duct, the pressure and density decrease while the velocity, Mach number and Knudsen number increase. The pressure drops to overcome viscous forces in the channel. If isothermal conditions prevail, density also drops and conserva-

tion of mass requires the flow to accelerate down the constant-area tube. (More likely the flow will be somewhere in between isothermal and adiabatic, Fanno flow. In that case both density and temperature decrease downstream, the former not as fast as in the isothermal case. None of that changes the qualitative arguments made in the example.) The fluid acceleration in turn affects the pressure gradient, resulting in a nonlinear pressure drop along the channel. The Mach number increases down the tube, limited only by choked-flow condition (Ma = 1). Additionally, the normal component of velocity is no longer zero. With lower density, the mean free path increases and Kn correspondingly increases. All flow regimes depicted in Fig. 3 may occur in the same tube: continuum with no-slip boundary conditions, slip-flow regime, transition regime and free-molecule flow. The air flow may also change from incompressible to compressible as it moves down the microduct. A similar scenario may take place if the entrance pressure is, say, 5 atm, while the exit is atmospheric. This deceivingly simple duct flow may in fact manifest every single complexity discussed in this section.

In the following six subsections, we discuss in turn the Navier-Stokes equations, compressibility effects, boundary conditions, molecular-based models, liquid flows and surface phenomena.

2.3 Continuum Model. We recall in this subsection the traditional conservation relations in fluid mechanics. No derivation is given here and the reader is referred to any advanced textbook in fluid mechanics, e.g., Batchelor (1967), Landau and Lifshitz (1987), Sherman (1990), Kundu (1990), and Panton (1996). In here, instead, we emphasize the precise assumptions needed to obtain a particular form of those equations. A continuum fluid implies that the derivatives of all the dependent variables exist in some reasonable sense. In other words, local properties such as density and velocity are defined as averages over elements large compared with the microscopic structure of the fluid but small enough in comparison with the scale of the macroscopic phenomena to permit the use of differential calculus to describe them. As mentioned earlier, such conditions are almost always met. For such fluids, and assuming the laws of non-relativistic mechanics hold, the conservation of mass, momentum and energy can be expressed at every point in space and time as a set of partial differential equations as follows

$$\frac{\partial \rho}{\partial t} + \frac{\partial}{\partial x_k}(\rho u_k) = 0 \tag{11}$$

$$\rho\left(\frac{\partial u_i}{\partial t} + u_k \frac{\partial u_i}{\partial x_k}\right) = \frac{\partial \sigma_{ki}}{\partial x_k} + \rho g_i \tag{12}$$

$$\rho\left(\frac{\partial e}{\partial t} + u_k \frac{\partial e}{\partial x_k}\right) = -\frac{\partial q_k}{\partial x_k} + \sigma_{ki}\frac{\partial u_i}{\partial x_k} \tag{13}$$

where ρ is the fluid density, u_k is an instantaneous velocity component (u, v, w), σ_{ki} is the second-order stress tensor (surface force per unit area), and g_i is the body force per unit mass, e is the internal energy, and q_k is the sum of heat flux vectors due to conduction and radiation. The independent variables are time t and the three spatial coordinates x_1, x_2 and x_3 or (x, y, z).

Equations (11), (12), and (13) constitute 5 differential equations for the 17 unknowns ρ, u_i, σ_{ki}, e, and q_k. Absent any body couples, the stress tensor is symmetric having only six independent components, which reduces the number of unknowns to 14. Obviously, the continuum flow equations do not form a determinate set. To close the conservation equations, relation between the stress tensor and deformation rate, relation between the heat flux vector and the temperature field and appropriate equations of state relating the different thermodynamic properties are needed. The stress-rate of strain relation and the heat flux-temperature relation are approximately linear if the flow is not too far from thermodynamic equilibrium. This is a phenomenological result but can be rigorously derived from the Boltzmann equation for a dilute gas assuming the flow is near equilibrium (see Section 2.6). For a Newtonian, isotropic, Fourier, ideal gas, for example, those relations read

$$\sigma_{ki} = -p\delta_{ki} + \mu\left(\frac{\partial u_i}{\partial x_k} + \frac{\partial u_k}{\partial x_i}\right) + \lambda\left(\frac{\partial u_j}{\partial x_j}\right)\delta_{ki} \tag{14}$$

$$q_i = -\kappa\frac{\partial T}{\partial x_i} + \text{Heat flux due to radiation} \tag{15}$$

$$de = c_v dT \quad \text{and} \quad p = \rho \mathcal{R} T \tag{16}$$

where p is the thermodynamic pressure, μ and λ are the first and second coefficients of viscosity, respectively, δ_{ki} is the unit second-order tensor (Kronecker delta), κ is the thermal conductivity, T is the temperature field, c_v is the specific heat at constant volume, and $\mathcal{R}$ is the gas constant which is given by the Boltzmann constant divided by the mass of an individual molecule ($k = m\mathcal{R}$). (Newtonian implies a linear relation between the stress tensor and the symmetric part of the deformation tensor (rate of strain tensor). The isotropy assumption reduces the 81 constants of proportionality in that linear relation to two constants. Fourier fluid is that for which the conduction part of the heat flux vector is linearly related to the temperature gradient, and again isotropy implies that the constant of proportionality in this relation is a single scalar.) The Stokes' hypothesis relates the first and second coefficients of viscosity thus $\lambda + \frac{2}{3}\mu = 0$, although the validity of this assumption for other than dilute, monatomic gases has occasionally been questioned (Gad-el-Hak, 1995). With the above constitutive relations and neglecting radiative heat transfer (a reasonable assumption when dealing with low to moderate temperatures since the radiative heat flux is proportional to T^4), Equations (11), (12), and (13), respectively, read

$$\frac{\partial \rho}{\partial t} + \frac{\partial}{\partial x_k}(\rho u_k) = 0 \tag{17}$$

$$\rho\left(\frac{\partial u_i}{\partial t} + u_k\frac{\partial u_i}{\partial x_k}\right) = -\frac{\partial p}{\partial x_i} + \rho g_i + \frac{\partial}{\partial x_k}\left[\mu\left(\frac{\partial u_i}{\partial x_k} + \frac{\partial u_k}{\partial x_i}\right) + \delta_{ki}\lambda\frac{\partial u_j}{\partial x_j}\right] \tag{18}$$

$$\rho c_v\left(\frac{\partial T}{\partial t} + u_k\frac{\partial T}{\partial x_k}\right) = \frac{\partial}{\partial x_k}\left(\kappa\frac{\partial T}{\partial x_k}\right) - p\frac{\partial u_k}{\partial x_k} + \phi \tag{19}$$

The three components of the vector equation (18) are the Navier-Stokes equations expressing the conservation of momentum for a Newtonian fluid. In the thermal energy equation (19), ϕ is the always positive (as required by the Second Law of thermodynamics) dissipation function expressing the irreversible conversion of mechanical energy to internal energy as a result of the deformation of a fluid element. The second term on the right-hand side of (19) is the reversible work done (per unit time) by the pressure as the volume of a fluid material element changes. For a Newtonian, isotropic fluid, the viscous dissipation rate is given by

$$\phi = \tfrac{1}{2}\mu\left(\frac{\partial u_i}{\partial x_k} + \frac{\partial u_k}{\partial x_i}\right)^2 + \lambda\left(\frac{\partial u_j}{\partial x_j}\right)^2 \tag{20}$$

There are now six unknowns, ρ, u_i, p and T, and the five coupled equations (17), (18), and (19) plus the equation of

state relating pressure, density and temperature. These six equations together with sufficient number of initial and boundary conditions constitute a well-posed, albeit formidable, problem. The system of equations (17)–(19) is an excellent model for the laminar or turbulent flow of most fluids such as air and water under many circumstances, including high-speed gas flows for which the shock waves are thick relative to the mean free path of the molecules. (This condition is met if the shock Mach number is less than 2.)

Considerable simplification is achieved if the flow is assumed incompressible, usually a reasonable assumption provided that the characteristic flow speed is less than 0.3 of the speed of sound. (Although as will be demonstrated in the following subsection, there are circumstances when even a low-Mach-number flow should be treated as compressible.) The incompressibility assumption is readily satisfied for almost all liquid flows and many gas flows. In such cases, the density is assumed either a constant or a given function of temperature (or species concentration). (Within the so-called Boussinesq approximation, density variations have negligible effect on inertia but are retained in the buoyancy terms. The incompressible continuity equation is therefore used.) The governing equations for such flow are

$$\frac{\partial u_k}{\partial x_k} = 0 \tag{21}$$

$$\rho\left(\frac{\partial u_i}{\partial t} + u_k \frac{\partial u_i}{\partial x_k}\right) = -\frac{\partial p}{\partial x_i} + \frac{\partial}{\partial x_k}\left[\mu\left(\frac{\partial u_i}{\partial x_k} + \frac{\partial u_k}{\partial x_i}\right)\right] + \rho g_i \tag{22}$$

$$\rho c_p\left(\frac{\partial T}{\partial t} + u_k \frac{\partial T}{\partial x_k}\right) = \frac{\partial}{\partial x_k}\left(\kappa \frac{\partial T}{\partial x_k}\right) + \phi_{\text{incomp}} \tag{23}$$

where ϕ_{incomp} is the incompressible limit of Eq. (20). These are now five equations for the five dependent variables u_i, p and T. Note that the left-hand side of Eq. (23) has the specific heat at constant pressure c_p and not c_v. It is the convection of enthalpy—and not internal energy—that is balanced by heat conduction and viscous dissipation. This is the correct incompressible-flow limit—of a compressible fluid—as discussed in detail in Section 10.9 of Panton (1996); a subtle point perhaps but one that is frequently misinterpreted in textbooks. The system of equations (21)–(23) is coupled if either the viscosity or density depends on temperature, otherwise the energy equation is uncoupled from the continuity and momentum equations and can therefore be solved *after* the velocity and pressure fields are determined.

For both the compressible and the incompressible equations of motion, the transport terms are neglected away from solid walls in the limit of infinite Reynolds number (Kn $\to$ 0). The fluid is then approximated as inviscid and non-conducting, and the corresponding equations read (for the compressible case)

$$\frac{\partial \rho}{\partial t} + \frac{\partial}{\partial x_k}(\rho u_k) = 0 \tag{24}$$

$$\rho\left(\frac{\partial u_i}{\partial t} + u_k \frac{\partial u_i}{\partial x_k}\right) = -\frac{\partial p}{\partial x_i} + \rho g_i \tag{25}$$

$$\rho c_v\left(\frac{\partial T}{\partial t} + u_k \frac{\partial T}{\partial x_k}\right) = -p \frac{\partial u_k}{\partial x_k} \tag{26}$$

The Euler equation (25) can be integrated along a streamline and the resulting Bernoulli's equation provides a direct relation between the velocity and pressure.

2.4 Compressibility. The issue of whether to consider the continuum flow compressible or incompressible seems to be rather straightforward, but is in fact full of potential pitfalls. If the local Mach number is less than 0.3, then the flow of a compressible fluid like air can—according to the conventional wisdom—be treated as incompressible. But the well-known Ma < 0.3 criterion is only a necessary not a sufficient one to allow treatment of the flow as approximately incompressible. In other words, there are situations where the Mach number can be exceedingly small while the flow is compressible. As is well documented in heat transfer textbooks, strong wall heating or cooling may cause the density to change sufficiently and the incompressible approximation to break down, even at low speeds. Less known is the situation encountered in some microdevices where the pressure may strongly change due to viscous effects even though the speeds may not be high enough for the Mach number to go above the traditional threshold of 0.3. Corresponding to the pressure changes would be strong density changes that must be taken into account when writing the continuum equations of motion. In this section, we systematically explain all situations relevant to MEMS where compressibility effects must be considered. (Two other situations where compressibility effects must also be considered are length-scales comparable to the scale height of the atmosphere and rapidly varying flows as in sound propagation (see Lighthill, 1963). Neither of these situations is likely to be encountered in microdevices.)

Let us rewrite the full continuity equation (11) as follows

$$\frac{D\rho}{Dt} + \rho \frac{\partial u_k}{\partial x_k} = 0 \tag{27}$$

where D/Dt is the substantial derivative $(\partial/\partial t + u_k \partial/\partial x_k)$, expressing changes following a fluid element. The proper criterion for the incompressible approximation to hold is that $(1/\rho)(D\rho/Dt)$ is vanishingly small. In other words, if density changes following a fluid particle are small, the flow is approximately incompressible. Density may change arbitrarily from one particle to another without violating the incompressible flow assumption. This is the case for example in the stratified atmosphere and ocean, where the variable-density/temperature/salinity flow is often treated as incompressible.

From the state principle of thermodynamics, we can express the density changes of a simple system in terms of changes in pressure and temperature,

$$\rho = \rho(p, T) \tag{28}$$

Using the chain rule of calculus,

$$\frac{1}{\rho}\frac{D\rho}{Dt} = \alpha \frac{Dp}{Dt} - \beta \frac{DT}{Dt} \tag{29}$$

where α and β are, respectively, the isothermal compressibility coefficient and the bulk expansion coefficient—two thermodynamic variables that characterize the fluid susceptibility to change of volume—which are defined by the following relations

$$\alpha(p, T) \equiv \frac{1}{\rho}\frac{\partial \rho}{\partial p}\bigg|_T \tag{30}$$

$$\beta(p, T) \equiv -\frac{1}{\rho}\frac{\partial \rho}{\partial T}\bigg|_p \tag{31}$$

For ideal gases, $\alpha = 1/p$, and $\beta = 1/T$. Note, however, that in the following arguments it will not be necessary to invoke the ideal gas assumption.

The flow must be treated as compressible if pressure and/or temperature changes are sufficiently strong. Equation (29) must of course be properly nondimensionalized before deciding whether a term is large or small. In here, we follow closely the procedure detailed in Panton (1996).

Consider first the case of adiabatic walls. Density is normalized with a reference value ρ_o, velocities with a reference speed v_o, spatial coordinates, and time with, respectively, L and L/v_o, the isothermal compressibility coefficient and bulk expansion coefficient with reference values α_o and β_o. The pressure is nondimensionalized with the inertial pressure-scale $\rho_o v_o^2$. This scale is twice the dynamic pressure, i.e., the pressure change as an inviscid fluid moving at the reference speed is brought to rest.

Temperature changes for the case of adiabatic walls result from the irreversible conversion of mechanical energy into internal energy via viscous dissipation. Temperature is therefore nondimensionalized as follows

$$T^* = \frac{T - T_o}{\left(\frac{\mu_o v_o^2}{\kappa_o}\right)} = \frac{T - T_o}{\mathrm{Pr}\left(\frac{v_o^2}{c_{p_o}}\right)} \tag{32}$$

where T_o is a reference temperature, μ_o, κ_o, and c_{p_o} are, respectively, reference viscosity, thermal conductivity and specific heat at constant pressure, and Pr is the reference Prandtl number, $(\mu_o c_{p_o})/\kappa_o$.

In the present formulation, the scaling used for pressure is based on the Bernoulli's equation, and therefore neglects viscous effects. This particular scaling guarantees that the pressure term in the momentum equation will be of the same order as the inertia term. The temperature scaling assumes that the conduction, convection and dissipation terms in the energy equation have the same order of magnitude. The resulting dimensionless form of Eq. (29) reads

$$\frac{1}{\rho^*}\frac{D\rho^*}{Dt^*} = \gamma_o \,\mathrm{Ma}^2\left\{\alpha^* \frac{Dp^*}{Dt^*} - \frac{\mathrm{Pr}\, B\beta^*}{A}\frac{DT^*}{Dt^*}\right\} \tag{33}$$

where the superscript * indicates a nondimensional quantity, Ma is the reference Mach number, and A and B are dimensionless constants defined by $A \equiv \alpha_o \rho_o c_{p_o} T_o$, and $B \equiv \beta_o T_o$. If the scaling is properly chosen, the terms having the * superscript in the right-hand side should be of order one, and the relative importance of such terms in the equations of motion is determined by the magnitude of the dimensionless parameter(s) appearing to their left, e.g. Ma, Pr, etc. Therefore, as $\mathrm{Ma}^2 \to 0$, temperature changes due to viscous dissipation are neglected (unless Pr is very large, as for example in the case of highly viscous polymers and oils). Within the same order of approximation, all thermodynamic properties of the fluid are assumed constant.

Pressure changes are also neglected in the limit of zero Mach number. Hence, for $\mathrm{Ma} < 0.3$ (i.e. $\mathrm{Ma}^2 < 0.09$), density changes following a fluid particle can be neglected and the flow can then be approximated as incompressible. (With an error of about 10% at Ma = 0.3, 4% at Ma = 0.2, 1% at Ma = 0.1, and so on.) However, there is a caveat in this argument. Pressure changes due to inertia can indeed be neglected at small Mach numbers and this is consistent with the way we nondimensionalized the pressure term above. If, on the other hand, pressure changes are mostly due to viscous effects, as is the case for example in a long duct or a gas bearing, pressure changes may be significant even at low speeds (low Ma). In that case the term Dp^*/Dt^* in Eq. (33) is no longer of order one, and may be large regardless of the value of Ma. Density then may change significantly and the flow must be treated as compressible. Had pressure been nondimensionalized using the viscous scale ($\mu_o v_o/L$) instead of the inertial one ($\rho_o v_o^2$), the revised equation (33) would have Re^{-1} appearing explicitly in the first term in the right-hand side, accentuating the importance of this term when viscous forces dominate.

A similar result can be gleaned when the Mach number is interpreted as follows

$$\mathrm{Ma}^2 = \frac{v_o^2}{a_o^2} = v_o^2 \left.\frac{\partial \rho}{\partial p}\right|_s = \frac{\rho_o v_o^2}{\rho_o}\left.\frac{\partial \rho}{\partial p}\right|_s \sim \frac{\Delta p}{\rho_o}\frac{\Delta \rho}{\Delta p} = \frac{\Delta \rho}{\rho_o} \tag{34}$$

where s is the entropy. Again, the above equation assumes that pressure changes are inviscid, and therefore small Mach number means negligible pressure and density changes. In a flow dominated by viscous effects—such as that inside a microduct—density changes may be significant even in the limit of zero Mach number.

Identical arguments can be made in the case of isothermal walls. Here strong temperature changes may be the result of wall heating or cooling, even if viscous dissipation is negligible. The proper temperature scale in this case is given in terms of the wall temperature T_w and the reference temperature T_o as follows

$$\hat{T} = \frac{T - T_o}{T_w - T_o} \tag{35}$$

where $\hat{T}$ is the new dimensionless temperature. The nondimensional form of Eq. (29) now reads

$$\frac{1}{\rho^*}\frac{D\rho^*}{Dt^*} = \gamma_o \,\mathrm{Ma}^2\,\alpha^* \frac{Dp^*}{Dt^*} - \beta^* B\left(\frac{T_w - T_o}{T_o}\right)\frac{D\hat{T}}{Dt^*} \tag{36}$$

Here we notice that the temperature term is different from that in Eq. (33). Ma is no longer appearing in this term, and strong temperature changes, i.e., large $(T_w - T_o)/T_o$, may cause strong density changes regardless of the value of the Mach number. Additionally, the thermodynamic properties of the fluid are not constant but depend on temperature, and as a result, the continuity, momentum and energy equations are all coupled. The pressure term in Eq. (36), on the other hand, is exactly as it was in the adiabatic case and the same arguments made before apply: the flow should be considered compressible if $\mathrm{Ma} > 0.3$, or if pressure changes due to viscous forces are sufficiently large.

Experiments in gaseous microducts confirm the above arguments. For both low- and high-Mach-number flows, pressure gradients in long microchannels are non-constant, consistent with the compressible flow equations. Such experiments were conducted by, among others, Prud'homme et al. (1986), Pfahler et al. (1991), van den Berg et al. (1993), Liu et al. (1993; 1995), Pong et al. (1994), Harley et al. (1995), Piekos and Breuer (1996), Arkilic (1997), and Arkilic et al. (1995; 1997a; 1997b). Sample results will be presented in the following subsection.

There is one last scenario in which significant pressure and density changes may take place without viscous or inertial effects. That is the case of quasi-static compression/expansion of a gas in, for example, a piston-cylinder arrangement. The resulting compressibility effects are, however, compressibility of the fluid and not of the flow.

2.5 Boundary Conditions. The equations of motion described in Section 2.3 require a certain number of initial and boundary conditions for proper mathematical formulation of flow problems. In this subsection, we describe the boundary conditions at a fluid-solid interface. Boundary conditions in the inviscid flow theory pertain only to the velocity component normal to a solid surface. The highest spatial derivative of velocity in the inviscid equations of motion is first-order, and only one velocity boundary condition at the surface is admissible.

The normal velocity component at a fluid-solid interface is specified, and no statement can be made regarding the tangential velocity component. The normal-velocity condition simply states that a fluid-particle path cannot go through an impermeable wall. Real fluids are of course viscous and the corresponding momentum equation has second-order derivatives of velocity, thus requiring an additional boundary condition on the velocity component tangential to a solid surface.

Traditionally, the no-slip condition at a fluid-solid interface is enforced in the momentum equation and an analogous no-temperature-jump condition is applied in the energy equation. The notion underlying the no-slip/no-jump condition is that within the fluid there cannot be any finite discontinuities of velocity/temperature. Those would involve infinite velocity/temperature gradients and so produce infinite viscous stress/heat flux that would destroy the discontinuity in infinitesimal time. The interaction between a fluid particle and a wall is similar to that between neighboring fluid particles, and therefore no discontinuities are allowed at the fluid-solid interface either. In other words, the fluid velocity must be zero relative to the surface and the fluid temperature must equal to that of the surface. But strictly speaking those two boundary conditions are valid only if the fluid flow adjacent to the surface is in thermodynamic equilibrium. This requires an infinitely high frequency of collisions between the fluid and the solid surface. In practice, the no-slip/no-jump condition leads to fairly accurate predictions as long as $\mathrm{Kn} < 0.001$ (for gases). Beyond that, the collision frequency is simply not high enough to ensure equilibrium and a certain degree of tangential-velocity slip and temperature jump must be allowed. This is a case frequently encountered in MEMS flows, and we develop the appropriate relations in this subsection.

For both liquids and gases, the linear Navier boundary condition empirically relates the tangential velocity slip at the wall $\Delta u|_w$ to the local shear

$$\Delta u|_w = u_{\text{fluid}} - u_{\text{wall}} = L_s \left.\frac{\partial u}{\partial y}\right|_w \tag{37}$$

where L_s is the constant slip length, and $\partial u/\partial y|_w$ is the strain rate computed at the wall. In most practical situations, the slip length is so small that the no-slip condition holds. In MEMS applications, however, that may not be the case. Once again we defer the discussion of liquids to Section 2.7, and focus for now on gases.

Assuming isothermal conditions prevail, the above slip relation has been rigorously derived by Maxwell (1879) from considerations of the kinetic theory of dilute, monatomic gases. Gas molecules, modeled as rigid spheres, continuously strike and reflect from a solid surface, just as they continuously collide with each other. For an idealized perfectly smooth (at the molecular scale) wall, the incident angle exactly equals the reflected angle and the molecules conserve their tangential momentum and thus exert no shear on the wall. This is termed specular reflection and results in perfect slip at the wall. For an extremely rough wall, on the other hand, the molecules reflect at some random angle uncorrelated with their entry angle. This perfectly diffuse reflection results in zero tangential-momentum for the reflected fluid molecules to be balanced by a finite slip velocity in order to account for the shear stress transmitted to the wall. A force balance near the wall leads to the following expression for the slip velocity

$$u_{\text{gas}} - u_{\text{wall}} = \mathcal{L} \left.\frac{\partial u}{\partial y}\right|_w \tag{38}$$

where $\mathcal{L}$ is the mean free path. The right-hand side can be considered as the first term in an infinite Taylor series, sufficient if the mean free path is relatively small enough. The equation above states that significant slip occurs only if the mean velocity of the molecules varies appreciably over a distance of one mean free path. This is the case, for example, in vacuum applications and/or flow in microdevices. The number of collisions between the fluid molecules and the solid in those cases is not large enough for even an approximate flow equilibrium to be established. Furthermore, additional (nonlinear) terms in the Taylor series would be needed as $\mathcal{L}$ increases and the flow is further removed from the equilibrium state.

For real walls some molecules reflect diffusively and some reflect specularly. In other words, a portion of the momentum of the incident molecules is lost to the wall and a (typically smaller) portion is retained by the reflected molecules. The tangential-momentum-accommodation coefficient σ_v is defined as the fraction of molecules reflected diffusively. This coefficient depends on the fluid, the solid and the surface finish, and has been determined experimentally to be between 0.2–0.8 (Thomas and Lord, 1974; Seidl and Steiheil, 1974; Porodnov et al., 1974; Arkilic et al., 1997b; Arkilic, 1997), the lower limit being for exceptionally smooth surfaces while the upper limit is typical of most practical surfaces. The final expression derived by Maxwell for an isothermal wall reads

$$u_{\text{gas}} - u_{\text{wall}} = \frac{2 - \sigma_v}{\sigma_v} \mathcal{L} \left.\frac{\partial u}{\partial y}\right|_w \tag{39}$$

For $\sigma_v = 0$, the slip velocity is unbounded, while for $\sigma_v = 1$, Eq. (39) reverts to (38).

Similar arguments were made for the temperature-jump boundary condition by von Smoluchowski (1898). For an ideal gas flow in the presence of wall-normal and tangential temperature gradients, the complete slip-flow and temperature-jump boundary conditions read

$$\begin{aligned} u_{\text{gas}} - u_{\text{wall}} &= \frac{2 - \sigma_v}{\sigma_v} \frac{1}{\rho \sqrt{\dfrac{2\mathcal{R}T_{\text{gas}}}{\pi}}} \tau_w + \frac{3}{4} \frac{\Pr(\gamma - 1)}{\gamma \rho \mathcal{R} T_{\text{gas}}} (-q_x)_w \\ &= \frac{2 - \sigma_v}{\sigma_v} \mathcal{L} \left(\frac{\partial u}{\partial y}\right)_w + \frac{3}{4} \frac{\mu}{\rho T_{\text{gas}}} \left(\frac{\partial T}{\partial x}\right)_w \end{aligned} \tag{40}$$

$$\begin{aligned} T_{\text{gas}} - T_{\text{wall}} &= \frac{2 - \sigma_T}{\sigma_T} \left[\frac{2(\gamma - 1)}{(\gamma + 1)}\right] \frac{1}{\rho \mathcal{R} \sqrt{\dfrac{2\mathcal{R}T_{\text{gas}}}{\pi}}} (-q_y)_w \\ &= \frac{2 - \sigma_T}{\sigma_T} \left[\frac{2\gamma}{(\gamma + 1)}\right] \frac{\mathcal{L}}{\Pr} \left(\frac{\partial T}{\partial y}\right)_w \end{aligned} \tag{41}$$

where x and y are the streamwise and normal coordinates, ρ and μ are respectively the fluid density and viscosity, $\mathcal{R}$ is the gas constant, T_{gas} is the temperature of the gas adjacent to the wall, T_{wall} is the wall temperature, τ_w is the shear stress at the wall, Pr is the Prandtl number, γ is the specific heat ratio, and $(q_x)_w$ and $(q_y)_w$ are, respectively, the tangential and normal heat flux at the wall.

The tangential-momentum-accommodation coefficient σ_v and the thermal-accommodation coefficient σ_T are given by, respectively,

$$\sigma_v = \frac{\tau_i - \tau_r}{\tau_i - \tau_w} \tag{42}$$

$$\sigma_T = \frac{dE_i - dE_r}{dE_i - dE_w} \tag{43}$$

where the subscripts i, r, and w stand for, respectively, incident, reflected and solid wall conditions, τ is a tangential momentum flux, and dE is an energy flux.

The second term in the right-hand side of Eq. (40) is the *thermal creep* which generates slip velocity in the fluid opposite to the direction of the tangential heat flux, i.e., flow in the direction of increasing temperature. At sufficiently high Knudsen numbers, streamwise temperature gradient in a conduit leads to a measurable pressure gradient along the tube. This may be the case in vacuum applications and MEMS devices. Thermal creep is the basis for the so-called Knudsen pump—a device with no moving parts—in which rarefied gas is hauled from one cold chamber to a hot one. (The terminology *Knudsen pump* has been used by, for example, Vargo and Muntz (1996), but according to Loeb (1961), the original experiments demonstrating such pump were carried out by Osborne Reynolds.) Clearly, such pump performs best at high Knudsen numbers, and is typically designed to operate in the free-molecule flow regime.

In dimensionless form, Eqs. (40) and (41), respectively, read

$$u^*_{\text{gas}} - u^*_{\text{wall}} = \frac{2-\sigma_v}{\sigma_v}\,\text{Kn}\left(\frac{\partial u^*}{\partial y^*}\right)_w + \frac{3}{2\pi}\frac{(\gamma-1)}{\gamma}\frac{\text{Kn}^2\,\text{Re}}{\text{Ec}}\left(\frac{\partial T^*}{\partial x^*}\right)_w \quad (44)$$

$$T^*_{\text{gas}} - T^*_{\text{wall}} = \frac{2-\sigma_T}{\sigma_T}\left[\frac{2\gamma}{(\gamma+1)}\right]\frac{\text{Kn}}{\text{Pr}}\left(\frac{\partial T^*}{\partial y^*}\right)_w \quad (45)$$

where the superscript * indicates dimensionless quantity, Kn is the Knudsen number, Re is the Reynolds number, and Ec is the Eckert number defined by

$$\text{Ec} = \frac{v_o^2}{c_p \Delta T} = (\gamma-1)\frac{T_o}{\Delta T}\,\text{Ma}^2 \quad (46)$$

where v_o is a reference velocity, $\Delta T = (T_{\text{gas}} - T_o)$, and T_o is a reference temperature. Note that very low values of σ_v and σ_T lead to substantial velocity slip and temperature jump even for flows with small Knudsen number.

The first term in the right-hand side of Eq. (44) is first-order in Knudsen number, while the thermal creep term is second-order, meaning that the creep phenomenon is potentially significant at large values of the Knudsen number. Equation (45) is first-order in Kn. Using Eqs. (8) and (46), the thermal creep term in Eq. (44) can be rewritten in terms of ΔT and Reynolds number. Thus,

$$u^*_{\text{gas}} - u^*_{\text{wall}} = \frac{2-\sigma_v}{\sigma_v}\,\text{Kn}\left(\frac{\partial u^*}{\partial y^*}\right)_w + \frac{3}{4}\frac{\Delta T}{T_o}\frac{1}{\text{Re}}\left(\frac{\partial T^*}{\partial x^*}\right)_w \quad (47)$$

It is clear that large temperature changes along the surface or low Reynolds numbers lead to significant thermal creep.

The continuum Navier-Stokes equations with no-slip/no-temperature jump boundary conditions are valid as long as the Knudsen number does not exceed 0.001. First-order slip/temperature-jump boundary conditions should be applied to the Navier-Stokes equations in the range of $0.001 < \text{Kn} < 0.1$. The transition regime spans the range of $0.1 < \text{Kn} < 10$, and second-order or higher slip/temperature-jump boundary conditions are applicable there. Note, however, that the Navier-Stokes equations are first-order accurate in Kn as will be shown in Section 2.6, and are themselves not valid in the transition regime. Either higher-order continuum equations, e.g., Burnett equations, should be used there or molecular modeling should be invoked, abandoning the continuum approach altogether.

For isothermal walls, Beskok (1994) derived a higher-order slip-velocity condition as follows

$$u_{\text{gas}} - u_{\text{wall}} = \frac{2-\sigma_v}{\sigma_v}\left[\ell\left(\frac{\partial u}{\partial y}\right)_w + \frac{\ell^2}{2!}\left(\frac{\partial^2 u}{\partial y^2}\right)_w + \frac{\ell^3}{3!}\left(\frac{\partial^3 u}{\partial y^3}\right)_w + \ldots\right] \quad (48)$$

Attempts to implement the above slip condition in numerical simulations are rather difficult. Second-order and higher derivatives of velocity cannot be computed accurately near the wall. Based on asymptotic analysis, Beskok (1996) and Beskok and Karniadakis (1994; 1998) proposed the following alternative higher-order boundary condition for the tangential velocity, including the thermal creep term,

$$u^*_{\text{gas}} - u^*_{\text{wall}} = \frac{2-\sigma_v}{\sigma_v}\frac{\text{Kn}}{1-b\,\text{Kn}}\left(\frac{\partial u^*}{\partial y^*}\right)_w + \frac{3}{2\pi}\frac{(\gamma-1)}{\gamma}\frac{\text{Kn}^2\,\text{Re}}{\text{Ec}}\left(\frac{\partial T^*}{\partial x^*}\right)_w \quad (49)$$

where b is a high-order slip coefficient determined from the presumably known no-slip solution, thus avoiding the computational difficulties mentioned above. If this high-order slip coefficient is chosen as $b = u''_w/2u'_w$, where the prime denotes derivative with respect to y and the velocity is computed from the no-slip Navier-Stokes equations, Eq. (49) becomes second-order accurate in Knudsen number. Beskok's procedure can be extended to third- and higher-orders for both the slip-velocity and thermal creep terms.

Similar arguments can be applied to the temperature-jump boundary condition, and the resulting Taylor series reads in dimensionless form (Beskok, 1996),

$$T^*_{\text{gas}} - T^*_{\text{wall}} = \frac{2-\sigma_T}{\sigma_T}\left[\frac{2\gamma}{(\gamma+1)}\right]\frac{1}{\text{Pr}}\left[\text{Kn}\left(\frac{\partial T^*}{\partial y^*}\right)_w + \frac{\text{Kn}^2}{2!}\left(\frac{\partial^2 T^*}{\partial y^{*2}}\right)_w + \ldots\right] \quad (50)$$

Again, the difficulties associated with computing second- and higher-order derivatives of temperature are alleviated using an identical procedure to that utilized for the tangential velocity boundary condition.

Several experiments in low-pressure macroducts or in microducts confirm the necessity of applying slip boundary condition at sufficiently large Knudsen numbers. Among them are those conducted by Knudsen (1909), Pfahler at al. (1991), Tison (1993), Liu et al. (1993; 1995), Pong et al. (1994), Arkilic et al. (1995), Harley et al. (1995), and Shih et al. (1995; 1996). The experiments are complemented by the numerical simulations carried out by Beskok (1994; 1996), Beskok and Karniadakis (1994; 1998), and Beskok et al. (1996). Here we present selected examples of the experimental and numerical results.

Tison (1993) conducted pipe flow experiments at very low pressures. His pipe has a diameter of 2 mm and a length-to-diameter ratio of 200. Both inlet and outlet pressures were varied to yield Knudsen number in the range of Kn = 0–200. Figure 4 shows the variation of mass flowrate as a function of $(p_i^2 - p_o^2)$, where p_i is the inlet pressure and p_o is the outlet pressure. (The original data in this figure were acquired by S. A. Tison and plotted by Beskok et al. (1996).) The pressure drop in this rarefied pipe flow is nonlinear, characteristic of low-Reynolds-number, compressible flows. Three distinct flow regimes are identified: (1) slip flow regime, $0 < \text{Kn} < 0.6$; (2) transition regime, $0.6 < \text{Kn} < 17$, where the mass flowrate is almost constant as the pressure changes; and (3) free-molecule flow, $\text{Kn} > 17$. Note that the demarkation between these three re-

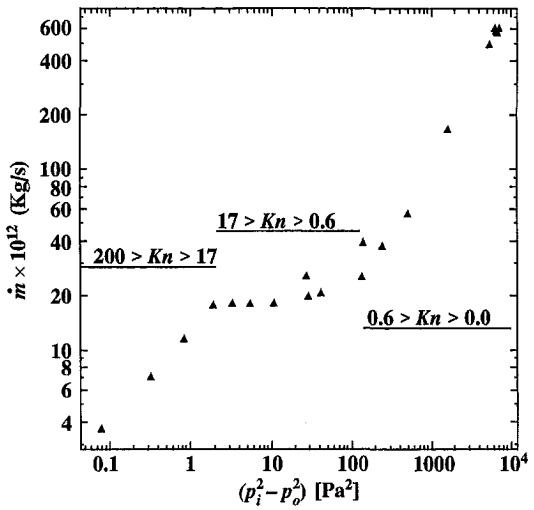

Fig. 4 Variation of mass flowrate as a function of $(p_i^2 - p_o^2)$. Original data acquired by S. A. Tison and plotted by Beskok et al. (1996).

gimes is slightly different from that mentioned in Section 2.2. As stated, the different Knudsen number regimes are determined empirically and are therefore only approximate for a particular flow geometry.

Shih et al. (1995) conducted their experiments in a microchannel using helium as a fluid. The inlet pressure varied but the duct exit was atmospheric. Microsensors where fabricated in-situ along their MEMS channel to measure the pressure. Figure 5 shows their measured mass flowrate versus the inlet pressure. The data are compared to the no-slip solution and the slip solution using three different values of the tangential-momentum-accommodation coefficient, 0.8, 0.9 and 1.0. The agreement is reasonable with the case $\sigma_v = 1.0$, indicating perhaps that the channel used by Shih et al. was quite rough on the molecular scale. In a second experiment (Shih et al., 1996), nitrous oxide was used as the fluid. The square of the pressure distribution along the channel is plotted in Fig. 6 for five different inlet pressures. The experimental data (symbols) compare well with the theoretical predictions (solid lines). Again, the nonlinear pressure drop shown indicates that the gas flow is compressible.

Arkilic (1997) provided an elegant analysis of the compressible, rarefied flow in a microchannel. The results of his theory are compared to the experiments of Pong et al. (1994) in Fig. 7. The dotted line is the incompressible flow solution, where the pressure is predicted to drop linearly with streamwise dis-

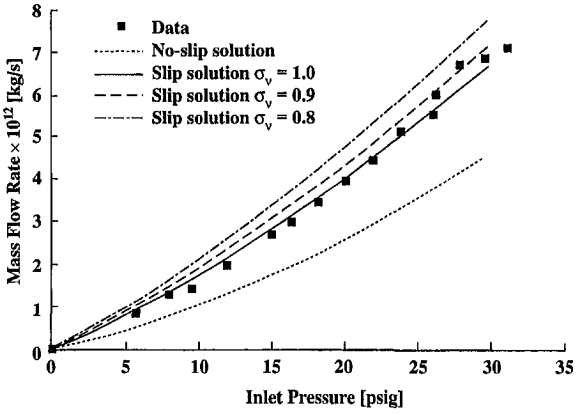

Fig. 5 Mass flowrate versus inlet pressure in a microchannel. From Shih et al. (1995).

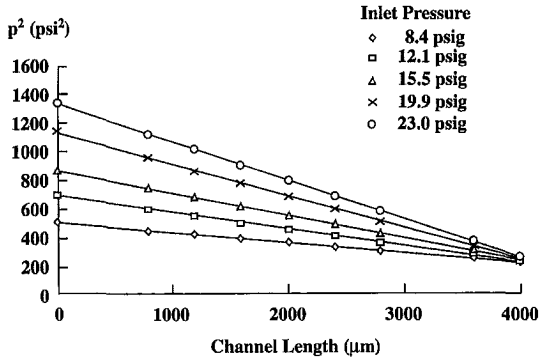

Fig. 6 Pressure distribution of nitrous oxide in a microduct. From Shih et al. (1996).

tance. The dashed line is the compressible flow solution that neglects rarefaction effects (assumes Kn = 0). Finally, the solid line is the theoretical result that takes into account both compressibility and rarefaction via slip-flow boundary condition computed at the exit Knudsen number of Kn = 0.06. That theory compares most favorably with the experimental data. In the compressible flow through the constant-area duct, density decreases and thus velocity increases in the streamwise direction. As a result, the pressure distribution is nonlinear with negative curvature. A moderate Knudsen number (i.e. moderate slip) actually diminishes, albeit rather weakly, this curvature. Thus, compressibility and rarefaction effects lead to opposing trends, as pointed out by Beskok et al. (1996).

2.6 Molecular-Based Models. In the continuum models discussed in Section 2.3, the macroscopic fluid properties are the dependent variables while the independent variables are the three spatial coordinates and time. The molecular models recognize the fluid as a myriad of discrete particles: molecules, atoms, ions and electrons. The goal here is to determine the position, velocity and state of all particles at all times. The molecular approach is either deterministic or probabilistic (refer to Fig. 2). Provided that there is a sufficient number of microscopic particles within the smallest significant volume of a flow, the macroscopic properties at any location in the flow can then be computed from the discrete-particle information by a suitable averaging or weighted averaging process. The present subsection discusses molecular-based models and their relation to the continuum models previously considered.

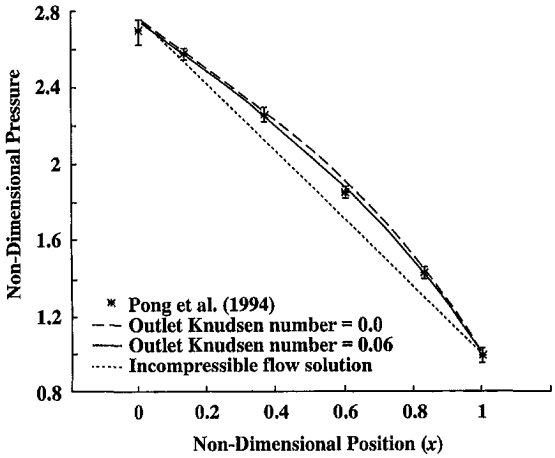

Fig. 7 Pressure distribution in a long microchannel. The symbols are experimental data while the solid lines are different theoretical predictions. From Arkilic (1997).

The most fundamental of the molecular models is a deterministic one. The motion of the molecules are governed by the laws of classical mechanics, although, at the expense of greatly complicating the problem, the laws of quantum mechanics can also be considered in special circumstances. The modern molecular dynamics computer simulations (MD) have been pioneered by Alder and Wainwright (1957; 1958; 1970) and reviewed by Ciccotti and Hoover (1986), Allen and Tildesley (1987), Haile (1993), and Koplik and Banavar (1995). The simulation begins with a set of N molecules in a region of space, each assigned a random velocity corresponding to a Boltzmann distribution at the temperature of interest. The interaction between the particles is prescribed typically in the form of a two-body potential energy and the time evolution of the molecular positions is determined by integrating Newton's equations of motion. Because MD is based on the most basic set of equations, it is valid in principle for any flow extent and any range of parameters. The method is straightforward in principle but there are two hurdles: choosing a proper and convenient potential for particular fluid and solid combinations, and the colossal computer resources required to simulate a reasonable flow field extent.

For purists, the former difficulty is a sticky one. There is no totally rational methodology by which a convenient potential can be chosen. Part of the art of MD is to pick an appropriate potential and validate the simulation results with experiments or other analytical/computational results. A commonly used potential between two molecules is the generalized Lennard-Jones 6-12 potential, to be used in Section 2.7 and further discussed in Section 2.8.

The second difficulty, and by far the most serious limitation of molecular dynamics simulations, is the number of molecules N that can realistically be modeled on a digital computer. Since the computation of an element of trajectory for any particular molecule requires consideration of all other molecules as potential collision partners, the amount of computation required by the MD method is proportional to N^2. Some saving in computer time can be achieved by cutting off the weak tail of the potential (see Fig. 12) at, say, $r_c = 2.5\sigma$, and shifting the potential by a linear term in r so that the force goes smoothly to zero at the cutoff. As a result, only nearby molecules are treated as potential collision partners, and the computation time for N molecules no longer scales with N^2.

The state of the art of molecular dynamics simulations in the 1990s is such that with a few hours of CPU time, general purpose supercomputers can handle around 10,000 molecules. At enormous expense, the fastest parallel machine available can simulate around 1 million particles. Because of the extreme diminution of molecular scales, the above translates into regions of liquid flow of about 0.01 μm (100 Å) in linear size, over time intervals of around 0.001 μs, just enough for continuum behavior to set in, for simple molecules. To simulate 1 s of real time for complex molecular interactions, e.g., including vibration modes, reorientation of polymer molecules, collision of colloidal particles, etc., requires unrealistic CPU time measured in thousands of years.

MD simulations are highly inefficient for dilute gases where the molecular interactions are infrequent. The simulations are more suited for dense gases and liquids. Clearly, molecular dynamics simulations are reserved for situations where the continuum approach or the statistical methods are inadequate to compute from first principles important flow quantities. Slip boundary conditions for liquid flows in extremely small devices is such a case as will be discussed in Section 2.7.

An alternative to the deterministic molecular dynamics is the statistical approach where the goal is to compute the probability of finding a molecule at a particular position and state. If the appropriate conservation equation can be solved for the probability distribution, important statistical properties such as the mean number, momentum or energy of the molecules within an element of volume can be computed from a simple weighted averaging. In a practical problem, it is such average quantities that concern us rather than the detail for every single molecule. Clearly, however, the accuracy of computing average quantities, via the statistical approach, improves as the number of molecules in the sampled volume increases. The kinetic theory of dilute gases is well advanced, but that for dense gases and liquids is much less so due to the extreme complexity of having to include multiple collisions and intermolecular forces in the theoretical formulation. The statistical approach is well covered in books such as those by Kennard (1938), Hirschfelder et al. (1954), Schaaf and Chambré (1961), Vincenti and Kruger (1965), Kogan (1969), Chapman and Cowling (1970), Cercignani (1988), and Bird (1994), and review articles such as those by Kogan (1973), Muntz (1989), and Oran et al. (1998).

In the statistical approach, the fraction of molecules in a given location and state is the sole dependent variable. The independent variables for monatomic molecules are time, the three spatial coordinates and the three components of molecular velocity. Those describe a six-dimensional phase space. (The evolution equation of the probability distribution is considered, hence time is the 7th independent variable.) For diatomic or polyatomic molecules, the dimension of phase space is increased by the number of internal degrees of freedom. Orientation adds an extra dimension for molecules which are not spherically symmetric. Finally, for mixtures of gases, separate probability distribution functions are required for each species. Clearly, the complexity of the approach increases dramatically as the dimension of phase space increases. The simplest problems are, for example, those for steady, one-dimensional flow of a simple monatomic gas.

To simplify the problem we restrict the discussion here to monatomic gases having no internal degrees of freedom. Furthermore, the fluid is restricted to dilute gases and molecular chaos is assumed. The former restriction requires the average distance between molecules δ to be an order of magnitude larger than their diameter σ. That will almost guarantee that all collisions between molecules are binary collisions, avoiding the complexity of modeling multiple encounters. (Dissociation and ionization phenomena involve triple collisions and therefore require separate treatment.) The molecular chaos restriction improves the accuracy of computing the macroscopic quantities from the microscopic information. In essence, the volume over which averages are computed has to have sufficient number of molecules to reduce statistical errors. It can be shown that computing macroscopic flow properties by averaging over a number of molecules will result in statistical fluctuations with a standard deviation of approximately 0.1% if one million molecules are used and around 3% if one thousand molecules are used. The molecular chaos limit requires the length-scale L for the averaging process to be at least 100 times the average distance between molecules (i.e., typical averaging over at least one million molecules).

Figure 8, adapted from Bird (1994), shows the limits of validity of the dilute gas approximation ($\delta/\sigma > 7$), the continuum approach (Kn < 0.1, as discussed previously in Section 2.2), and the neglect of statistical fluctuations ($L/\delta > 100$). Using a molecular diameter of $\sigma = 4 \times 10^{-10}$ m as an example, the three limits are conveniently expressed as functions of the normalized gas density ρ/ρ_o or number density n/n_o, where the reference densities ρ_o and n_o are computed at standard conditions. All three limits are straight lines in the log-log plot of L versus ρ/ρ_o, as depicted in Figure 8. Note the shaded triangular wedge inside which both the Boltzmann and Navier-Stokes equations are valid. Additionally, the lines describing the three limits very nearly intersect at a single point. As a consequence, the continuum breakdown limit always lies between the dilute gas limit and the limit for molecular chaos. As density or characteristic dimension is reduced in a dilute gas, the Navier-Stokes model breaks down before the level of statistical fluctuations becomes significant. In a dense gas, on the other hand, signifi-

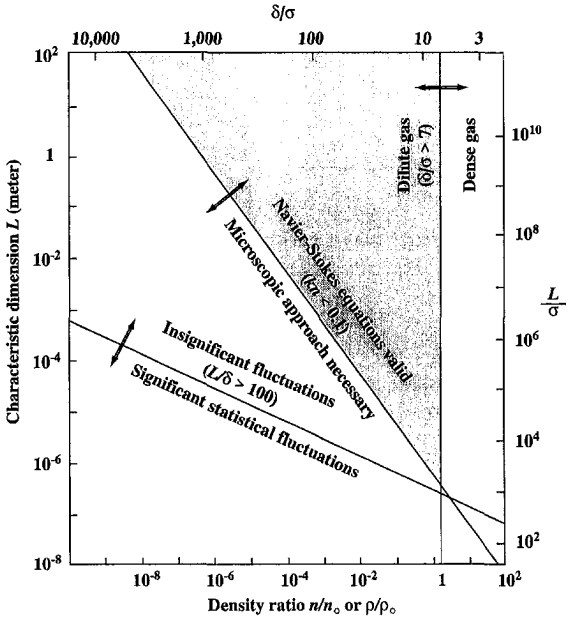

Fig. 8 Effective limits of different flow models. From Bird (1994).

cant fluctuations may be present even when the Navier-Stokes model is still valid.

The starting point in statistical mechanics is the Liouville equation which expresses the conservation of the N-particle distribution function in $6N$-dimensional phase space (three positions and three velocities for each molecule of a monatomic gas with no internal degrees of freedom), where N is the number of particles under consideration. Considering only external forces which do not depend on the velocity of the molecules (this excludes Lorentz forces, for example), the Liouville equation for a system of N mass points reads

$$\frac{\partial \mathcal{F}}{\partial t} + \sum_{k=1}^{N} \boldsymbol{\xi}_k \cdot \frac{\partial \mathcal{F}}{\partial \mathbf{x}_k} + \sum_{k=1}^{N} \mathbf{F}_k \cdot \frac{\partial \mathcal{F}}{\partial \boldsymbol{\xi}_k} = 0 \tag{51}$$

where $\mathcal{F}$ is the probability of finding a molecule at a particular point in phase space, t is time, $\boldsymbol{\xi}_k$ is the three-dimensional velocity vector for the kth molecule, $\mathbf{x}_k$ is the three-dimensional position vector for the kth molecule, and $\mathbf{F}$ is the external force vector. Note that the dot product in the above equation is carried out over each of the three components of the vectors $\boldsymbol{\xi}$, $\mathbf{x}$, and $\mathbf{F}$, and that the summation is over all molecules. Obviously such an equation is not tractable for realistic number of particles.

A hierarchy of reduced distribution functions may be obtained by repeated integration of the Liouville equation above. The final equation in the hierarchy is for the single particle distribution which also involves the two-particle distribution function. Assuming molecular chaos, that final equation becomes a closed one (i.e., one equation in one unknown), and is known as the Boltzmann equation, the fundamental relation of the kinetic theory of gases. That final equation in the hierarchy is the only one which carries any hope of obtaining analytical solutions.

A simpler direct derivation of the Boltzmann equation is provided by Bird (1994). For monatomic gas molecules in binary collisions, the integro-differential Boltzmann equation reads

$$\frac{\partial (nf)}{\partial t} + \xi_j \frac{\partial (nf)}{\partial x_j} + F_j \frac{\partial (nf)}{\partial \xi_j} = J(f, f^*), \qquad j = 1, 2, 3 \tag{52}$$

where nf is the product of the number density and the normalized velocity distribution function ($dn/n = f\,\mathbf{d}\boldsymbol{\xi}$), x_j and ξ_j are, respectively, the coordinates and speeds of a molecule (constituting, together with time, the seven independent variables of the single-dependent-variable equation), F_j is a known external force, and $J(f, f^*)$ is the nonlinear collision integral that describes the net effect of populating and depopulating collisions on the distribution function. The collision integral is the source of difficulty in obtaining analytical solutions to the Boltzmann equation, and is given by

$$J(f, f^*) = \int_{-\infty}^{\infty} \int_{0}^{4\pi} n^2 (f^* f_1^* - f f_1) \boldsymbol{\xi}_r \sigma d\Omega (d\boldsymbol{\xi})_1 \tag{53}$$

where the superscript * indicates post-collision values, f and f_1 represent two different molecules, $\boldsymbol{\xi}_r$ is the relative speed between two molecules, σ is the molecular cross-section, Ω is the solid angle, and $d\boldsymbol{\xi} = d\xi_1 d\xi_2 d\xi_3$.

Once a solution for f is obtained, macroscopic quantities such as density, velocity, temperature, etc., can be computed from the appropriate weighted integral of the distribution function. For example,

$$\rho = mn = m \int (nf) d\boldsymbol{\xi} \tag{54}$$

$$u_i = \int \xi_i f d\boldsymbol{\xi} \tag{55}$$

$$\tfrac{3}{2} kT = \int \frac{1}{2} m \xi_i \xi_i f d\boldsymbol{\xi} \tag{56}$$

If the Boltzmann equation is nondimensionalized with a characteristic length L and characteristic speed $[2(k/m)T]^{1/2}$, where k is the Boltzmann constant, m is the molecular mass, and T is temperature, the inverse Knudsen number appears explicitly in the right-hand side of the equation as follows

$$\frac{\partial \hat{f}}{\partial \hat{t}} + \hat{\xi}_j \frac{\partial \hat{f}}{\partial \hat{x}_j} + \hat{F}_j \frac{\partial \hat{f}}{\partial \hat{\xi}_j} = \frac{1}{\mathrm{Kn}} \hat{J}(\hat{f}, \hat{f}^*), \quad j = 1, 2, 3 \tag{57}$$

where the superscript $\hat{}$ represents a dimensionless variable, and $\hat{f}$ is nondimensionalized using a reference number density n_o.

The five conservation equations for the transport of mass, momentum, and energy can be derived by multiplying the Boltzmann equation above by, respectively, the molecular mass, momentum and energy, then integrating over all possible molecular velocities. Subject to the restrictions of dilute gas and molecular chaos stated earlier, the Boltzmann equation is valid for all ranges of Knudsen number from 0 to ∞. Analytical solutions to this equation for arbitrary geometries are difficult mostly because of the nonlinearity of the collision integral. Simple models of this integral have been proposed to facilitate analytical solutions; see, for example, Bhatnagar et al. (1954).

There are two important asymptotes to Eq. (57). First, as $\mathrm{Kn} \to \infty$, molecular collisions become unimportant. This is the free-molecule flow regime depicted in Fig. 3 for $\mathrm{Kn} > 10$, where the only important collision is that between a gas molecule and the solid surface of an obstacle or a conduit. Analytical solutions are then possible for simple geometries, and numerical simulations for complicated geometries are straightforward once the surface-reflection characteristics are accurately modeled. Second, as $\mathrm{Kn} \to 0$, collisions become important and the flow approaches the continuum regime of conventional fluid dynamics. The Second Law specifies a tendency for thermodynamic systems to revert to equilibrium state, smoothing out any discontinuities in macroscopic flow quantities. The number of molecular collisions in the limit $\mathrm{Kn} \to 0$ is so large that the flow approaches the equilibrium state in a time short compared to the macroscopic time-scale. For example, for air at standard conditions ($T = 288$ K; $p = 1$ atm), each molecule experiences, on the average, 10 collisions per nanosecond and travels

1 micron in the same time period. Such a molecule has already *forgotten* its previous state after 1 ns. In a particular flow field, if the macroscopic quantities vary little over a distance of 1 μm or over a time interval of 1 ns, the flow of STP air is near equilibrium.

At Kn = 0, the velocity distribution function is everywhere of the local equilibrium or Maxwellian form:

$$\hat{f}^{(0)} = \frac{n}{n_o}\,\pi^{-3/2}\exp[-(\hat{\xi} - \hat{u})^2] \tag{58}$$

where $\hat{\xi}$ and $\hat{u}$ are, respectively, the dimensionless speeds of a molecule and of the flow. In this Knudsen number limit, the velocity distribution of each element of the fluid instantaneously adjusts to the equilibrium thermodynamic state appropriate to the local macroscopic properties as this molecule moves through the flow field. From the continuum viewpoint, the flow is isentropic and heat conduction and viscous diffusion and dissipation vanish from the continuum conservation relations.

The Chapman-Enskog theory attempts to solve the Boltzmann equation by considering a small perturbation of $\hat{f}$ from the equilibrium Maxwellian form. For small Knudsen numbers, the distribution function can be expanded in terms of Kn in the form of a power series

$$\hat{f} = \hat{f}^{(0)} + \mathrm{Kn}\,\hat{f}^{(1)} + \mathrm{Kn}^2\hat{f}^{(2)} + \ldots \tag{59}$$

By substituting the above series in the Boltzmann equation (57) and equating terms of equal order, the following recurrent set of integral equations result:

$$\hat{J}(\hat{f}^{(0)}, \hat{f}^{(0)}) = 0,$$

$$\hat{J}(\hat{f}^{(0)}, \hat{f}^{(1)}) = \frac{\partial \hat{f}^{(0)}}{\partial \hat{t}} + \hat{\xi}_j\frac{\partial \hat{f}^{(0)}}{\partial \hat{x}_j} + \hat{F}_j\frac{\partial \hat{f}^{(0)}}{\partial \hat{\xi}_j}, \ldots \tag{60}$$

The first integral is nonlinear and its solution is the local Maxwellian distribution, Eq. (58). The distribution functions $\hat{f}^{(1)}$, $\hat{f}^{(2)}$, etc., each satisfies an inhomogeneous linear equation whose solution leads to the transport terms needed to close the continuum equations appropriate to the particular level of approximation. The continuum stress tensor and heat flux vector can be written in terms of the distribution function, which in turn can be specified in terms of the macroscopic velocity and temperature and their derivatives (Kogan, 1973). The zeroth-order equation yields the Euler equations, the first-order equation results in the linear transport terms of the Navier-Stokes equations, the second-order equation gives the nonlinear transport terms of the Burnett equations, and so on. Keep in mind, however, that the Boltzmann equation as developed in this subsection is for a monatomic gas. This excludes the all important air which is composed largely of diatomic nitrogen and oxygen.

As discussed in Sections 2.2, 2.3, and 2.5, the Navier-Stokes equations can and should be used up to a Knudsen number of 0.1. Beyond that, the transition flow regime commences ($0.1 < \mathrm{Kn} < 10$). In this flow regime, the molecular mean free path for a gas becomes significant relative to a characteristic distance for important flow-property changes to take place. The Burnett equations can be used to obtain analytical/numerical solutions for at least a portion of the transition regime for a monatomic gas, although their complexity have precluded much results for realistic geometries. There is also a certain degree of uncertainty about the proper boundary conditions to use with the continuum Burnett equations, and experimental validation of the results have been very scarce. Additionally, as the gas flow further departs from equilibrium, the bulk viscosity ($=\lambda + \frac{2}{3}\mu$, where λ is the second coefficient of viscosity) is no longer zero, and the Stokes' hypothesis no longer holds (see Gad-el-Hak, 1995, for an interesting summary of the issue of bulk viscosity).

In the transition regime, the molecularly-based Boltzmann equation cannot easily be solved either, unless the nonlinear collision integral is simplified. So, clearly the transition regime is one of dire need of alternative methods of solution. MD simulations as mentioned earlier are not suited for dilute gases. The best approach for the transition regime right now is the direct simulation Monte Carlo (DSMC) method developed by Bird (1963; 1965; 1976; 1978; 1994) and briefly described below. Some recent reviews of DSMC include those by Muntz (1989), Cheng (1993), Cheng and Emmanuel (1995), and Oran et al. (1998). The mechanics as well as the history of the DSMC approach and its ancestors are well described in the book by Bird (1994).

Unlike molecular dynamics simulations, DSMC is a statistical computational approach to solving rarefied gas problems. Both approaches treat the gas as discrete particles. Subject to the dilute gas and molecular chaos assumptions, the direct simulation Monte Carlo method is valid for all ranges of Knudsen number, although it becomes quite expensive for $\mathrm{Kn} < 0.1$. Fortunately, this is the continuum regime where the Navier-Stokes equations can be used analytically or computationally. DSMC is therefore ideal for the transition regime ($0.1 < \mathrm{Kn} < 10$), where the Boltzmann equation is difficult to solve. The Monte Carlo method is, like its name sake, a random number strategy based directly on the physics of the individual molecular interactions. The idea is to track a large number of randomly selected, statistically representative particles, and to use their motions and interactions to modify their positions and states. The primary approximation of the direct simulation Monte Carlo method is to uncouple the molecular motions and the intermolecular collisions over small time intervals. A significant advantage of this approximation is that the amount of computation required is proportional to N, in contrast to N^2 for molecular dynamics simulations. In essence, particle motions are modeled deterministically while collisions are treated probabilistically, each simulated molecule representing a large number of actual molecules. Typical computer runs of DSMC in the 1990s involve tens of millions of intermolecular collisions and fluid-solid interactions.

The DSMC computation is started from some initial condition and followed in small time steps that can be related to physical time. Colliding pairs of molecules in a small geometric cell in physical space are randomly selected after each computational time step. Complex physics such as radiation, chemical reactions and species concentrations can be included in the simulations without the necessity of nonequilibrium thermodynamic assumptions that commonly afflict nonequilibrium continuum-flow calculations. DSMC is more computationally intensive than classical continuum simulations, and should therefore be used only when the continuum approach is not feasible.

The DSMC technique is explicit and time marching, and therefore always produces unsteady flow simulations. For macroscopically steady flows, Monte Carlo simulation proceeds until a steady flow is established, within a desired accuracy, at sufficiently large time. The macroscopic flow quantities are then the time average of all values calculated after reaching the steady state. For macroscopically unsteady flows, ensemble averaging of many independent Monte Carlo simulations is carried out to obtain the final results within a prescribed statistical accuracy.

2.7 Liquid Flows. From the continuum point of view, liquids and gases are both fluids obeying the same equations of motion. For incompressible flows, for example, the Reynolds number is the primary dimensionless parameter that determines the nature of the flow field. True, water, for example, has density and viscosity that are, respectively, three and two orders of magnitude higher than those for air, but if the Reynolds number and geometry are matched, liquid and gas flows should be identical. (Barring phenomena unique to liquids such as cavitation, free surface flows, etc.) For MEMS applications, however, we anticipate the possibility of non-equilibrium flow conditions and

the consequent invalidity of the Navier-Stokes equations and the no-slip boundary conditions. Such circumstances can best be researched using the molecular approach. This was discussed for gases in Section 2.6, and the corresponding arguments for liquids will be given in the present subsection. The literature on non-Newtonian fluids in general and polymers in particular is vast (for example, the bibliographic survey by Nadolink and Haigh, 1995, cites over 4,900 references on polymer drag reduction alone) and provides a rich source of information on the molecular approach for liquid flows.

Solids, liquids and gases are distinguished merely by the degree of proximity and the intensity of motions of their constituent molecules. In solids, the molecules are packed closely and confined, each hemmed in by its neighbors (Chapman and Cowling, 1970). Only rarely would one solid molecule slip from its neighbors to join a new set. As the solid is heated, molecular motion becomes more violent and a slight thermal expansion takes place. At a certain temperature that depends on ambient pressure, sufficiently intense motion of the molecules enables them to pass freely from one set of neighbors to another. The molecules are no longer confined but are nevertheless still closely packed, and the substance is now considered a liquid. Further heating of the matter eventually releases the molecules altogether, allowing them to break the bonds of their mutual attractions. Unlike solids and liquids, the resulting gas expands to fill any volume available to it.

Unlike solids, both liquids and gases cannot resist finite shear force without continuous deformation; that is the definition of a fluid medium. In contrast to the reversible, elastic, static deformation of a solid, the continuous deformation of a fluid resulting from the application of a shear stress results in an irreversible work that eventually becomes random thermal motion of the molecules; that is viscous dissipation. There are around 25-million molecules of STP air in a one-micron cube. The same cube would contain around 34-billion molecules of water. So, liquid flows are continuum even in extremely small devices through which gas flows would not. The average distance between molecules in the gas example is one order of magnitude higher than the diameter of its molecules, while that for the liquid phase approaches the molecular diameter. As a result, liquids are almost incompressible. Their isothermal compressibility coefficient α and bulk expansion coefficient β are much smaller compared to those for gases. For water, for example, a hundred-fold increase in pressure leads to less than 0.5% decrease in volume. Sound speeds through liquids are also high relative to those for gases, and as a result most liquid flows are incompressible. The exception being propagation of ultra-high-frequency sound waves and cavitation phenomena. (Note that we distinguish between a fluid and a flow being compressible/incompressible. For example, the flow of the highly compressible air can be either compressible or incompressible.)

The mechanism by which liquids transport mass, momentum and energy must be very different from that for gases. In dilute gases, intermolecular forces play no role and the molecules spend most of their time in free flight between brief collisions at which instances the molecules' direction and speed abruptly change. The random molecular motions are responsible for gaseous transport processes. In liquids, on the other hand, the molecules are closely packed though not fixed in one position. In essence, the liquid molecules are always in a *collision* state. Applying a shear force must create a velocity gradient so that the molecules move relative to one another, *ad infinitum* as long as the stress is applied. For liquids, momentum transport due to the random molecular motion is negligible compared to that due to the intermolecular forces. The straining between liquid molecules causes some to separate from their original neighbors, bringing them into the force field of new molecules. Across the plane of the shear stress, the sum of all intermolecular forces must, on the average, balance the imposed shear. Liquids at rest transmit only normal force, but when a velocity gradient occurs, the net intermolecular force would have a tangential component.

The incompressible Navier-Stokes equations describe liquid flows under most circumstances. Liquids, however, do not have a well advanced molecular-based theory as that for dilute gases. The concept of mean free path is not very useful for liquids and the conditions under which a liquid flow fails to be in quasi-equilibrium state are not well defined. There is no Knudsen number for liquid flows to guide us through the maze. We do not know, from first principles, the conditions under which the no-slip boundary condition becomes inaccurate, or the point at which the (stress)-(rate of strain) relation or the (heat flux)-(temperature gradient) relation fails to be linear. Certain empirical observations indicate that those simple relations that we take for granted occasionally fail to accurately model liquid flows. For example, it has been shown in rheological studies (Loose and Hess, 1989) that non-Newtonian behavior commences when the strain rate approximately exceeds twice the molecular frequency-scale

$$\dot{\gamma} = \frac{\partial u}{\partial y} \geq 2\tau^{-1} \tag{61}$$

where the molecular time-scale τ is given by

$$\tau = \left[\frac{m\sigma^2}{\epsilon}\right]^{1/2} \tag{62}$$

where m is the molecular mass, and σ and ϵ are respectively the characteristic length- and energy-scale for the molecules. For ordinary liquids such as water, this time-scale is extremely small and the threshold shear rate for the onset of non-Newtonian behavior is therefore extraordinarily high. For high-molecular-weight polymers, on the other hand, m and σ are both many orders of magnitude higher than their respective values for water, and the linear stress-strain relation breaks down at realistic values of the shear rate.

The moving contact line when a liquid spreads on a solid substrate is an example where slip flow must be allowed to avoid singular or unrealistic behavior in the Navier-Stokes solutions (Dussan and Davis, 1974; Dussan, 1976; 1979; Thompson and Robbins, 1989). Other examples where slip-flow must be admitted include corner flows (Moffatt, 1964; Koplik and Banavar, 1995) and extrusion of polymer melts from capillary tubes (Pearson and Petrie, 1968; Richardson, 1973; Den, 1990).

Existing experimental results of liquid flow in microdevices are contradictory. This is not surprising given the difficulty of such experiments and the lack of a guiding rational theory. Pfahler et al. (1990; 1991), Pfahler (1992), and Bau (1994) summarize the relevant literature. For small-length-scale flows, a phenomenological approach for analyzing the data is to define an apparent viscosity μ_a calculated so that if it were used in the traditional no-slip Navier-Stokes equations instead of the fluid viscosity μ, the results would be in agreement with experimental observations. Israelachvili (1986) and Gee et al. (1990) found that $\mu_a = \mu$ for thin-film flows as long as the film thickness exceeds 10 molecular layers ($\approx$5 nm). For thinner films, μ_a depends on the number of molecular layers and can be as much as 10^5 times larger than μ. Chan and Horn's (1985) results are somewhat different; the apparent viscosity deviates from the fluid viscosity for films thinner than 50 nm.

In polar-liquid flows through capillaries, Migun and Prokhorenko (1987) report that μ_a increases for tubes smaller than 1 micron in diameter. In contrast, Debye and Cleland (1959) report μ_a smaller than μ for paraffin flow in porous glass with average pore size several times larger than the molecular length-scale. Experimenting with microchannels ranging in depths from 0.5 micron to 50 microns, Pfahler et al. (1991) found that μ_a is consistently smaller than μ for both liquid (isopropyl alcohol; silicone oil) and gas (nitrogen; helium) flows in micro-

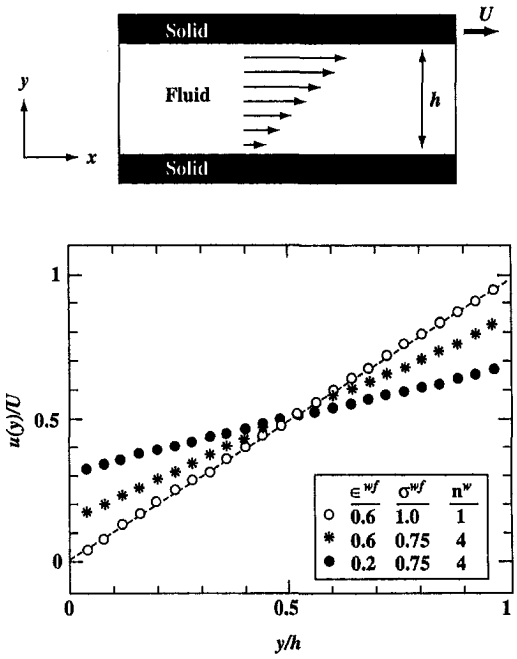

Fig. 9 Velocity profiles in a Couette flow geometry at different interfacial parameters. All three profiles are for $U = \sigma\tau^{-1}$, and $h = 24.57\sigma$. The dashed line is the no-slip Couette-flow solution. From Thompson and Troian (1997).

channels. For liquids, the apparent viscosity decreases with decreasing channel depth. Other researchers using small capillaries report that μ_a is about the same as μ (Anderson and Quinn, 1972; Tukermann and Pease, 1981; 1982; Tuckermann, 1984; Guvenc, 1985; Nakagawa et al., 1990).

The above contradictory results point to the need for replacing phenomenological models by first-principles ones. The lack of molecular-based theory of liquids—despite extensive research by the rheology and polymer communities—leaves molecular dynamics simulations as the nearest weapon to first-principles arsenal. MD simulations offer a unique approach to checking the validity of the traditional continuum assumptions. However, as was pointed out in Section 2.6, such simulations are limited to exceedingly minute flow extent.

Thompson and Troian (1997) provide molecular dynamics simulations to quantify the slip-flow boundary condition dependence on shear rate. Recall the linear Navier boundary condition introduced in Section 2.5,

$$\Delta u|_w = u_{\text{fluid}} - u_{\text{wall}} = L_s \left.\frac{\partial u}{\partial y}\right|_w \tag{63}$$

where L_s is the constant slip length, and $\partial u/\partial y|_w$ is the strain rate computed at the wall. The goal of Thompson and Troian's simulations was to determine the degree of slip at a solid-liquid interface as the interfacial parameters and the shear rate change. In their simulations, a simple liquid underwent planar shear in a Couette cell as shown in Fig. 9. The typical cell measured $12.51 \times 7.22 \times h$, in units of molecular length-scale σ, where the channel depth h varied in the range of $16.71\sigma - 24.57\sigma$, and the corresponding number of molecules simulated ranged from 1,152 to 1,728. The liquid is treated as an isothermal ensemble of spherical molecules. A shifted Lennart-Jones 6-12 potential is used to model intermolecular interactions, with energy- and length-scales ϵ and σ, and cut-off distance $r_c = 2.2\sigma$:

$$V(r) = 4\epsilon\left[\left(\frac{r}{\sigma}\right)^{-12} - \left(\frac{r}{\sigma}\right)^{-6} - \left(\frac{r_c}{\sigma}\right)^{-12} + \left(\frac{r_c}{\sigma}\right)^{-6}\right] \tag{64}$$

The truncated potential is set to zero for $r > r_c$.

The fluid-solid interaction is also modeled with a truncated Lennard-Jones potential, with energy- and length-scales ϵ^{wf} and σ^{wf}, and cut-off distance r_c. The equilibrium state of the fluid is a well-defined liquid phase characterized by number density $n = 0.81\sigma^{-3}$ and temperature $T = 1.1\epsilon/k$, where k is the Boltzmann constant.

The steady-state velocity profiles resulting from Thompson and Troian's (1997) MD simulations are depicted in Fig. 9 for different values of the interfacial parameters ϵ^{wf}, σ^{wf} and n^w. Those parameters, shown in units of the corresponding fluid parameters ϵ, σ and n, characterize, respectively, the strength of the liquid-solid coupling, the thermal roughness of the interface and the commensurability of wall and liquid densities. The macroscopic velocity profiles recover the expected flow behavior from continuum hydrodynamics with boundary conditions involving varying degrees of slip. Note that when slip exists, the shear rate $\dot{\gamma}$ no longer equals U/h. The degree of slip increases (i.e. the amount of momentum transfer at the wall-fluid interface decreases) as the relative wall density n^w increases or the strength of the wall-fluid coupling σ^{wf} decreases; in other words when the relative surface energy corrugation of the wall decreases. Conversely, the corrugation is maximized when the wall and fluid densities are commensurate and the strength of the wall-fluid coupling is large. In this case, the liquid feels the corrugations in the surface energy of the solid owing to the atomic close-packing. Consequently, there is efficient momentum transfer and the no-slip condition applies, or in extreme cases, a 'stick' boundary condition takes hold.

Variations of the slip length L_s and viscosity μ as functions of shear rate $\dot{\gamma}$ are shown in parts (a) and (b) of Fig. 10, for five different sets of interfacial parameters. For Couette flow, the slip length is computed from its definition, $L_s = \Delta u|_w/\dot{\gamma} = (U/\dot{\gamma} - h)/2$. The slip length, viscosity and shear rate are normalized in the figure using the respective molecular scales for length σ, viscosity $\epsilon\tau\sigma^{-3}$, and inverse time τ^{-1}. The viscosity of the fluid is constant over the entire range of shear rates (Fig. 10(b)), indicating Newtonian behavior. As indicated earlier, non-Newtonian behavior is expected for $\dot{\gamma} \geq 2\tau^{-1}$, well above the shear rates used in Thompson and Troian's simulations.

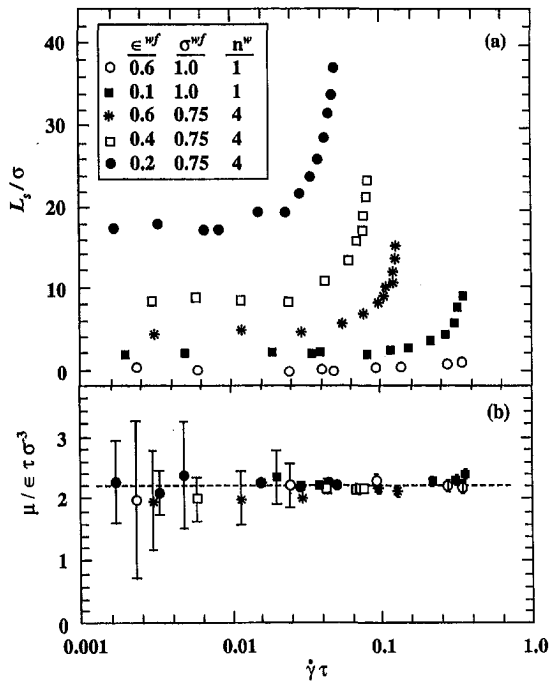

Fig. 10 Variation of slip length and viscosity as functions of shear rate. From Thompson and Troian (1997).

At low shear rates, the slip length behavior is consistent with the Navier model, i.e., is independent of the shear rate. Its limiting value L_s^o ranges from 0 to $\sim 17\sigma$ for the range of interfacial parameters chosen (Fig. 10(*a*)). In general, the amount of slip increases with decreasing surface energy corrugation. Most interestingly, at high shear rates the Navier condition breaks down as the slip length increases rapidly with $\dot{\gamma}$. The critical shear-rate value for the slip length to diverge, $\dot{\gamma}_c$, decreases as the surface energy corrugation decreases. Surprisingly, the boundary condition is nonlinear even though the liquid is still Newtonian. In dilute gases, as discussed in Section 2.6, the linear slip condition and the Navier-Stokes equations, with their linear stress-strain relation, are both valid to the same order of approximation in Knudsen number. In other words, deviation from linearity is expected to take place at the same value of Kn = 0.1. In liquids, in contrast, the slip length appears to become nonlinear and to diverge at a critical value of shear rate well below the shear rate at which the linear stress-strain relation fails. Moreover, the boundary condition deviation from linearity is not gradual but is rather catastrophic. The critical value of shear rate $\dot{\gamma}_c$ signals the point at which the solid can no longer impart momentum to the liquid. This means that the same liquid molecules sheared against different substrates will experience varying amounts of slip and vice versa.

Based on the above results, Thompson and Troian (1997) suggest a universal boundary condition at a solid-liquid interface. Scaling the slip length L_s by its asymptotic limiting value L_s^o and the shear rate $\dot{\gamma}$ by its critical value $\dot{\gamma}_c$, collapses the data in the single curve shown in Figure 11. The data points are well described by the relation

$$L_s = L_s^o \left[1 - \frac{\dot{\gamma}}{\dot{\gamma}_c} \right]^{-1/2} \tag{65}$$

The nonlinear behavior close to a critical shear rate suggests that the boundary condition can significantly affect flow behavior at macroscopic distances from the wall. Experiments with polymers confirm this observation (Atwood and Schwalter, 1989). The rapid change in the slip length suggests that for flows in the vicinity of $\dot{\gamma}_c$, small changes in surface properties can lead to large fluctuations in the apparent boundary condition. Thompson and Troian (1997) conclude that the Navier slip condition is but the low-shear-rate limit of a more generalized universal relationship which is nonlinear and divergent. Their relation provides a mechanism for relieving the stress singularity in spreading contact lines and corner flows, as it naturally allows for varying degrees of slip on approach to regions of higher rate of strain.

To place the above results in physical terms, consider water at a temperature of $T = 288$ K. (Water molecules are complex ones, forming directional, short-range covalent bonds. Thus requiring a more complex potential than the Lennard-Jones to describe the intermolecular interactions. For the purpose of the qualitative example described here, however, we use the computational results of Thompson and Troian (1997) who employed the L-J potential.) The energy-scale in the Lennard-Jones potential is then $\epsilon = 3.62 \times 10^{-21}$ J. For water, $m = 2.99 \times 10^{-26}$ kg, $\sigma = 2.89 \times 10^{-10}$ m, and at standard temperature $n = 3.35 \times 10^{28}$ molecules/m^3. The molecular time-scale can thus be computed, $\tau = [m\sigma^2/\epsilon]^{1/2} = 8.31 \times 10^{-13}$ s. For the third case depicted in Fig. 11 (the open squares), $\dot{\gamma}_c\tau = 0.1$, and the critical shear rate at which the slip condition diverges is thus $\dot{\gamma}_c = 1.2 \times 10^{11}$ s^{-1}. Such an enormous rate of strain may be found in extremely small devices having extremely high speeds. (Note however that $\dot{\gamma}_c$ for high-molecular-weight polymers would be many orders of magnitude smaller than the value developed here for water.) On the other hand, the conditions to achieve a measurable slip of 17σ (the solid circles in Fig. 10) are not difficult to encounter in microdevices: density of solid

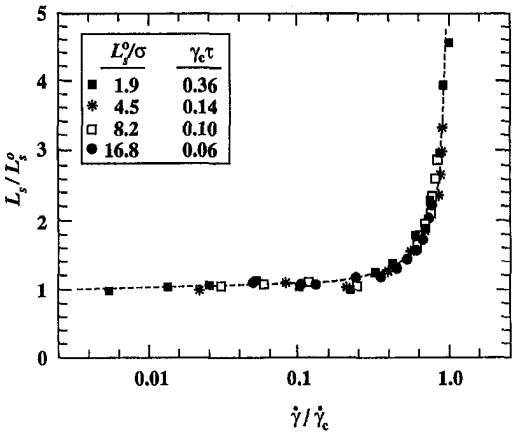

Fig. 11 Universal relation of slip length as a function of shear rate. From Thompson and Troian (1997).

four times that of liquid, and energy-scale for wall-fluid interaction that is one fifth of energy-scale for liquid.

The limiting value of slip length is independent of the shear rate and can be computed for water as $L_s^o = 17\sigma = 4.91 \times 10^{-9}$ m. Consider a water microbearing having a shaft diameter of 100 μm and rotation rate of 20,000 rpm and a minimum gap of $h = 1$ μm. In this case, $U = 0.1$ m/s and the no-slip shear rate is $U/h = 10^5$ s^{-1}. When slip occurs at the limiting value just computed, the shear rate and the wall slip-velocity are computed as follows

$$\dot{\gamma} = \frac{U}{h + 2L_s^o} = 9.90 \times 10^4 \text{ s}^{-1} \tag{66}$$

$$\Delta u|_w = \dot{\gamma} L_s = 4.87 \times 10^{-4} \text{ m/s} \tag{67}$$

As a result of the Navier slip, the shear rate is reduced by 1% from its no-slip value, and the slip velocity at the wall is about 0.5% of U, small but not insignificant.

2.8 Surface Phenomena. As mentioned in Section 2.1, the surface-to-volume ratio for a machine with a characteristic length of 1 m is 1 m^{-1}, while that for a MEMS device having a size of 1 μm is 10^6 m^{-1}. The million-fold increase in surface area relative to the mass of the minute device substantially affects the transport of mass, momentum and energy through the surface. Obviously surface effects dominate in small devices. The surface boundary conditions in MEMS flows have already been discussed in Sections 2.5 and 2.7. In microdevices, it has been shown that it is possible to have measurable slip-velocity and temperature jump at a solid-fluid interface. In this subsection, we illustrate other ramifications of the large surface-to-volume ratio unique to MEMS, and provide a molecular viewpoint to surface forces.

In microdevices, both radiative and convective heat loss/gain are enhanced by the huge surface-to-volume ratio. Consider a device having a characteristic length L_s. Use of the lumped capacitance method to compute the rate of convective heat transfer, for example, is justified if the Biot number ($\equiv hL_s/\kappa_s$, where h is the convective heat transfer coefficient of the fluid and κ_s is the thermal conductivity of the solid) is less than 0.1. Small L_s implies small Biot number, and a nearly uniform temperature within the solid. Within this approximation, the rate at which heat is lost to the surrounding fluid is given by

$$\rho_s L_s^3 c_s \frac{dT_s}{dt} = -hL_s^2(T_s - T_\infty) \tag{68}$$

where ρ_s and c_s are respectively the density and specific heat of the solid, T_s is its (uniform) temperature, and T_∞ is the ambient fluid temperature. Solution of the above equation is trivial,

and the temperature of a hot surface drops exponentially with time from an initial temperature T_i,

$$\frac{T_s(t) - T_\infty}{T_i - T_\infty} = \exp\left[-\frac{t}{\mathcal{T}}\right] \tag{69}$$

where the time constant $\mathcal{T}$ is given by

$$\mathcal{T} = \frac{\rho_s L_s^3 c_s}{h L_s^2} \tag{70}$$

For small devices, the time it takes the solid to cool down is proportionally small. Clearly, the million-fold increase in surface-to-volume ratio implies a proportional increase in the rate at which heat escapes. Identical scaling arguments can be made regarding mass transfer.

Another effect of the diminished scale is the increased importance of surface forces and the waning importance of body forces. Based on biological studies, Went (1968) concludes that the demarkation length-scale is around 1 mm. Below that, surface forces dominate over gravitational forces. A 10-mm piece of paper will fall down when gently placed on a smooth, vertical wall, while a 0.1-mm piece will stick. Try it! *Stiction* is a major problem in MEMS applications. Certain structures such as long, thin polysilicon beams and large, thin comb drives have a propensity to stick to their substrates and thus fail to perform as designed (Mastrangelo and Hsu, 1992; Tang et al., 1989).

Conventional dry friction between two solids in relative motion is proportional to the normal force which is usually a component of the moving device weight. The friction is independent of the contact-surface area because the van der Waals cohesive forces are negligible relative to the weight of the macroscopic device. In MEMS applications, the cohesive intermolecular forces between two surfaces are significant and the stiction is independent of the device mass but is proportional to its surface area. The first micromotor did not move—despite large electric current through it—until the contact area between the 100-micron rotor and the substrate was reduced significantly by placing dimples on the rotor's surface (Fan et al., 1988; 1989; Tai and Muller, 1989).

One last example of surface effects that to my knowledge has not been investigated for microflows is the adsorbed layer in gaseous wall-bounded flows. It is well known (see, for example, Brunauer, 1944; Lighthill, 1963) that when a gas flows in a duct, the gas molecules are attracted to the solid surface by the van der Waals and other forces of cohesion. The potential energy of the gas molecules drops on reaching the surface. The adsorbed layer partakes the thermal vibrations of the solid, and the gas molecules can only escape when their energy exceeds the potential energy minimum. In equilibrium, at least part of the solid would be covered by a monomolecular layer of adsorbed gas molecules. Molecular species with significant partial pressure—relative to their vapor pressure—may locally form layers two or more molecules thick. Consider, for example, the flow of a mixture of dry air and water vapor at STP. The energy of adsorption of water is much larger than that for nitrogen and oxygen, making it more difficult for water molecules to escape the potential energy trap. It follows that the life time of water molecules in the adsorbed layer significantly exceeds that for the air molecules (by 60,000 folds, in fact) and, as a result, the thin surface layer would be mostly water. For example, if the proportion of water vapor in the ambient air is 1:1,000 (i.e., very low humidity level), the ratio of water to air in the adsorbed layer would be 60:1. Microscopic roughness of the solid surface causes partial condensation of the water along portions having sufficiently strong concave curvature. So, surfaces exposed to non-dry air flows are mainly liquid water surfaces. In most applications, this thin adsorbed layer has little effect on the flow dynamics, despite the fact that the density and viscosity of liquid water are far greater than those for air. In MEMS applications, however, the layer thickness may not be an insignificant portion of the characteristic flow dimension and the water layer may have a measurable effect on the gas flow. A hybrid approach of molecular dynamics and continuum flow simulations or MD-Monte Carlo simulations may be used to investigate this issue.

It should be noted that quite recently, Majumdar and Mezic (1998; 1999) have studied the stability and rupture into droplets of thin liquid films on solid surfaces. They point out that the free energy of a liquid film consists of a surface tension component as well as highly nonlinear volumetric intermolecular forces resulting from van der Waals, electrostatic, hydration and elastic strain interactions. For water films on hydrophilic surfaces such as silica and mica, Majumdar and Mezic (1998) estimate the equilibrium film thickness to be about 0.5 nm (2 monolayers) for a wide range of ambient-air relative humidities. The equilibrium thickness grows very sharply, however, as the relative humidity approaches 100%.

Majumdar and Mezic's (1998; 1999) results open many questions. What are the stability characteristics of their water film in the presence of air flow above it? Would this water film affect the accommodation coefficient for microduct air flow? In a modern Winchester-type hard disk, the drive mechanism has a read/write head that floats 50 nm above the surface of the spinning platter. The head and platter together with the air layer in between form a slider bearing. Would the computer performance be affected adversely by the high relative humidity on a particular day when the adsorbed water film is no longer 'thin'? If a microduct hauls liquid water, would the water film adsorbed by the solid walls influence the effective viscosity of the water flow? Electrostatic forces can extend to almost 1 micron (the Debye length), and that length is known to be highly pH-dependent. Would the water flow be influenced by the surface and liquid chemistry? Would this explain the contradictory experimental results of liquid flows in microducts discussed in Section 2.7?

The few examples above illustrate the importance of surface effects in small devices. From the continuum viewpoint, forces at a solid-fluid interface are the limit of pressure and viscous forces acting on a parallel elementary area displaced into the fluid, when the displacement distance is allowed to tend to zero. From the molecular point of view, all macroscopic surface forces are ultimately traced to intermolecular forces, which subject is extensively covered in the book by Israelachvilli (1991) and references therein. Here we provide a very brief introduction to the molecular viewpoint. The four forces in nature are (1) the strong and (2) weak forces describing the interactions between neutrons, protons, electrons, etc.; (3) the electromagnetic forces between atoms and molecules; and (4) gravitational forces between masses. The range of action of the first two forces is around 10^{-5} nm, and hence neither concerns us overly in MEMS applications. The electromagnetic forces are effective over a much larger though still small distance on the order of the interatomic separations (0.1–0.2 nm). Effects over longer range—several orders of magnitude longer—can and do rise from the short range intermolecular forces. For example, the rise of liquid column in capillaries and the action of detergent molecules in removing oily dirt from fabric are the result of intermolecular interactions. Gravitational forces decay with the distance to second power, while intermolecular forces decay much quicker, typically with the seventh power. Cohesive forces are therefore negligible once the distance between molecules exceeds few molecular diameters, while massive bodies like stars and planets are still strongly interacting, via gravity, over astronomical distances.

Electromagnetic forces are the source of all intermolecular interactions and the cohesive forces holding atoms and molecules together in solids and liquids. They can be classified into (1) purely electrostatic arising from the Coulomb force between

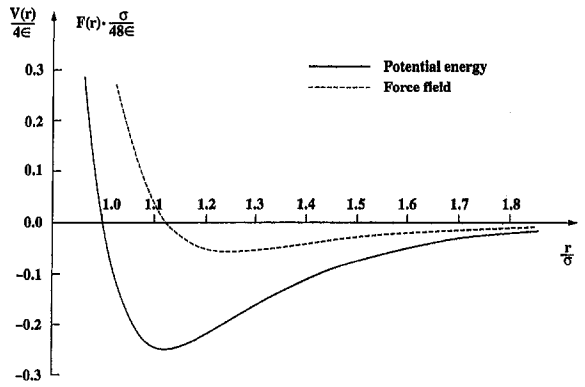

Fig. 12 Typical Lennard-Jones 6–12 potential and the intermolecular force field resulting from it. Only a small portion of the potential function is shown for clarity.

charges, interactions between charges, permanent dipoles, quadrupoles, etc.; (2) polarization forces arising from the dipole moments induced in atoms and molecules by the electric field of nearby charges and permanent dipoles; and (3) quantum mechanical forces that give rise to covalent or chemical bonding and to repulsive steric or exchange interactions that balance the attractive forces at very short distances. The Hellman-Feynman theorem of quantum mechanics states that once the spatial distribution of the electron clouds has been determined by solving the appropriate Schrödinger equation, intermolecular forces may be calculated on the basis of classical electrostatics, in effect reducing all intermolecular forces to Coulombic forces. Note, however, that intermolecular forces exist even when the molecules are totally neutral. Solutions of the Schrödinger equation for general atoms and molecules are not easy of course, and alternative modeling are sought to represent intermolecular forces. The van der Waals attractive forces are usually represented with a potential that varies as the inverse-sixth power of distance, while the repulsive forces are represented with either a power or an exponential potential.

A commonly used potential between two molecules is the generalized Lennard-Jones (L-J 6-12) pair potential given by

$$V_{ij}(r) = 4\epsilon\left[c_{ij}\left(\frac{r}{\sigma}\right)^{-12} - d_{ij}\left(\frac{r}{\sigma}\right)^{-6}\right] \tag{71}$$

where V_{ij} is the potential energy between two particles i and j, r is the distance between the two molecules, ϵ and σ are, respectively, characteristic energy and length-scales, and c_{ij} and d_{ij} are parameters to be chosen for the particular fluid and solid combinations under consideration. The first term in the right-hand side is the strong repulsive force that is felt when two molecules are at extremely close range comparable to the molecular length-scale. That short-range repulsion prevents overlap of the molecules in physical space. The second term is the weaker, van der Waals attractive force that commences when the molecules are sufficiently close (several times σ). That negative part of the potential represents the attractive polarization interaction of neutral, spherically symmetric particles. The power of 6 associated with this term is derivable from quantum mechanics considerations, while the power of the repulsive part of the potential is found empirically. The Lennard-Jones potential is zero at very large distances, has a weak negative peak at r slightly larger than σ, is zero at $r = \sigma$, and is infinite as $r \to 0$.

The force field resulting from this potential is given by

$$F_{ij}(r) = -\frac{\partial V_{ij}}{\partial r} = \frac{48\epsilon}{\sigma}\left[c_{ij}\left(\frac{r}{\sigma}\right)^{-13} - \frac{d_{ij}}{2}\left(\frac{r}{\sigma}\right)^{-7}\right] \tag{72}$$

A typical L-J 6-12 potential and force field are shown in Fig. 12, for $c = d = 1$. The minimum potential $V_{\min} = -\epsilon$, corresponds to the equilibrium position (zero force) and occurs at $r = 1.12\sigma$. The attractive van der Waals contribution to the minimum potential is -2ϵ, while the repulsive energy contribution is $+\epsilon$. Thus the inverse 12th power repulsive force term decreases the strength of the binding energy at equilibrium by 50%.

The L-J potential is commonly used in molecular dynamics simulations to model intermolecular interactions between dense gas or liquid molecules and between fluid and solid molecules. As mentioned in Section 2.7, such potential is not accurate for complex substances such as water whose molecules form directional covalent bonds. As a result, MD simulations for water are much more involved.

3 Typical Fluid Applications

3.1 Prologue. The physics of fluid flows in microdevices was covered in Section 2. In this section, we provide a number of examples of useful applications of MEMS devices in fluid mechanics. The list is by no means exhaustive, but includes the use of MEMS-based sensors and actuators for flow diagnosis and control, a recently developed viscous micropump/microturbine, and analysis of a journal microbearing. The paper by Löfdahl and Gad-el-Hak (1999) offers more detail on some of the topics covered in this section.

3.2 Turbulence Measurements. Microelectromechanical systems offer great opportunities for better flow diagnosis and control, particularly for turbulent flows. The batch processing fabrication of microdevices makes it possible to produce large number of identical transducers within extremely tight tolerance. Microsensors and microactuators are small, inexpensive, combine electronic and mechanical parts, have low energy consumption and can be distributed over a wide area. In this subsection we discuss the advantages of using MEMS-based sensors for turbulence measurements, and in the following subsection the issue of flow control will be addressed.

Turbulence remains largely an enigma, analytically unapproachable yet practically very important. For a turbulent flow, the dependent variables are random functions of space and time, and no straightforward method exists for analytically obtaining stochastic solutions to the governing nonlinear, partial differential equations. The statistical approach to solving the Navier-Stokes equations sets a more modest aim of solving for the average flow quantities rather than the instantaneous ones. But as a result of the nonlinearity of the governing equations, this approach always leads to more unknowns than equations (the closure problem), and solutions based on first principles are again not possible. Turbulence, therefore, is a conundrum that appears to yield its secrets only to physical and numerical experiments, provided that the wide band of relevant scales is fully resolved—a far-from-trivial task particularly at high Reynolds numbers.

A turbulent flow field is composed of a hierarchy of eddies having a broad range of time- and length-scales. The largest eddies have a spatial extension of approximately the same size as the width of the flow field, while the smallest eddies are of the size where viscous effects become dominant and energy is transferred from kinetic into internal. The ratio of the smallest length-scale—the Kolmogorov microscale η—to the largest scale l is related to the turbulence Reynolds number as follows

$$\frac{\eta}{l} \approx \left(\frac{ul}{\nu}\right)^{-3/4} = \mathrm{Re}^{-3/4} \tag{73}$$

Similar expressions can be written for time- and velocity-scales (see, for example, Tennekes and Lumley, 1972). Not only does a sensor have to be sufficiently small to resolve the smallest eddies, but multi-sensors distributed over a large volume are

needed to detect any flow structures at the largest scale. Clearly, the problem worsens as the Reynolds number increases.

In wall-bounded flows, the shear-layer thickness provides a measure of the largest eddies in the flow. The smallest scale is the viscous wall unit. Viscous forces dominate over inertia in the near-wall region. The characteristic scales there are obtained from the magnitude of the mean vorticity in the region and its viscous diffusion away from the wall. Thus, the viscous time-scale, t_ν, is given by the inverse of the mean wall vorticity

$$t_\nu = \left[\left. \frac{\partial \bar{U}}{\partial y} \right|_w \right]^{-1} \tag{74}$$

where $\bar{U}$ is the mean streamwise velocity. The viscous length-scale, l_ν, is determined by the characteristic distance by which the (spanwise) vorticity is diffused from the wall, and is thus given by

$$l_\nu = \sqrt{\nu t_\nu} = \sqrt{\frac{\nu}{\left. \frac{\partial \bar{U}}{\partial y} \right|_w}} \tag{75}$$

where ν is the kinematic viscosity. The wall velocity-scale (so-called friction velocity, u_τ) follows directly from the time and length-scales

$$u_\tau = \frac{l_\nu}{t_\nu} = \sqrt{\nu \left. \frac{\partial \bar{U}}{\partial y} \right|_w} = \sqrt{\frac{\tau_w}{\rho}} \tag{76}$$

where τ_w is the mean shear stress at the wall, and ρ is the fluid density. A wall unit implies scaling with the viscous scales, and the usual $(\ )^+$ notation is used; for example, $y^+ = y/l_\nu = yu_\tau/\nu$. In the wall region, the characteristic length for the large eddies is y itself, while the Kolmogorov scale is related to the distance from the wall y as follows

$$\eta^+ \equiv \frac{\eta u_\tau}{\nu} \approx (\kappa y^+)^{1/4} \tag{77}$$

where κ is the von Kármán constant (≈ 0.41). As y^+ changes in the range of 1–5 (the extent of the viscous sublayer), η changes from 0.8 to 1.2 wall units.

It is clear from the above that the spatial and temporal resolutions for any probe to be used to resolve high-Reynolds-number turbulent flows are extremely tight. For example, both the Kolmogorov scale and the viscous length-scale change from few microns at the typical field Reynolds number—based on the momentum thickness—of 10^6, to a couple of hundred microns at the typical laboratory Reynolds number of 10^3. MEMS sensors for pressure, velocity, temperature and shear stress are at least one order of magnitude smaller than conventional sensors (Ho and Tai, 1996; Löfdahl et al., 1996). Their small size improves both the spatial and temporal resolutions of the measurements, typically few microns and few microseconds, respectively. For example, a micro-hot-wire (called hot point) has very small thermal inertia and the diaphragm of a micro-pressure-transducer has correspondingly fast dynamic response. Moreover, the microsensors' extreme miniaturization and low energy consumption make them ideal for monitoring the flow state without appreciably affecting it. Lastly, literally hundreds of microsensors can be fabricated on the same silicon chip at a reasonable cost, making them well suited for distributed measurements. The UCLA/Caltech team (see, for example, Ho and Tai, 1996; 1998, and references therein) has been very effective in developing many MEMS-based sensors and actuators for turbulence diagnosis and control.

3.3 Flow Control. Due to their small size, fast response, low unit-cost and energy consumption and an ability to combine mechanical and electronic components, MEMS-based sensors and actuators are presently the best candidate for reactive control of turbulent flows where distributed arrays of sensing and actuation elements are required. In this subsection we offer a brief introduction to targeted flow control. More detail are found in the review papers by Gad-el-Hak (1989; 1994; 1996), Wilkinson (1990), and Moin and Bewley (1994).

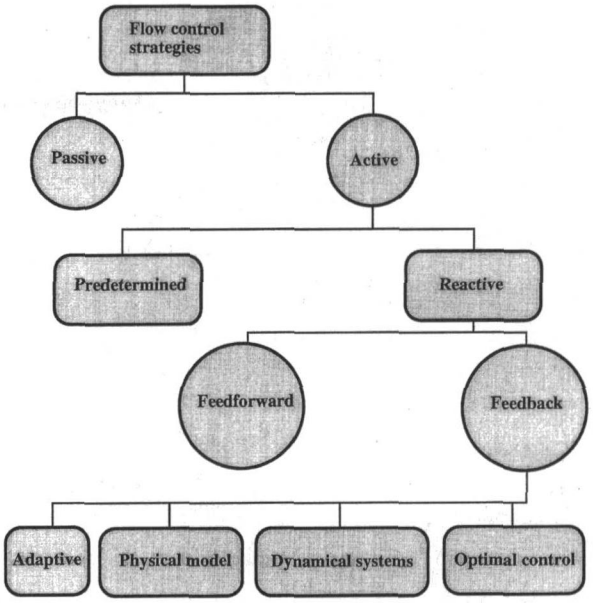

Fig. 13 Classification of flow control strategies

The ability to actively or passively manipulate a flow field to effect a desired change is of immense technological importance, and this undoubtedly accounts for the fact that the subject is more hotly pursued by scientists and engineers than any other topic in fluid mechanics. The potential benefits of realizing efficient flow control systems range from saving billions of dollars in annual fuel cost for land, air and sea vehicles to achieving economically/environmentally more competitive industrial processes involving fluid flows. Flow control can be used to achieve transition delay/advance, separation postponement/provocation, lift enhancement, drag reduction, turbulence augmentation/suppression or noise reduction.

3.3.1 Classification Schemes. There are different classification schemes for flow control methods. One is to consider whether the technique is applied at the wall or away from it. Surface parameters that can influence the flow include roughness, shape, curvature, rigid-wall motion, compliance, temperature and porosity. Heating and cooling of the surface can influence the flow via the resulting viscosity and density gradients. Mass transfer can take place through a porous wall or a wall with slots. Suction and injection of primary fluid can have significant effects on the flow field, influencing particularly the shape of the velocity profile near the wall and thus the boundary layer susceptibility to transition and separation. Different additives, such as polymers, surfactants, micro-bubbles, droplets, particles, dust or fibers, can also be injected through the surface in water or air wall-bounded flows. Control devices located away from the surface can also be beneficial. Large-eddy breakup devices (also called outer-layer devices, or OLDs), acoustic waves bombarding a shear layer from outside, additives introduced in the middle of a shear layer, manipulation of freestream turbulence levels and spectra, gust, and magneto- and electro-hydrodynamic body forces are examples of flow control strategies applied away from the wall.

A second scheme for classifying flow control methods considers energy expenditure and the control loop involved. As shown in the schematic in Fig. 13, a control device can be

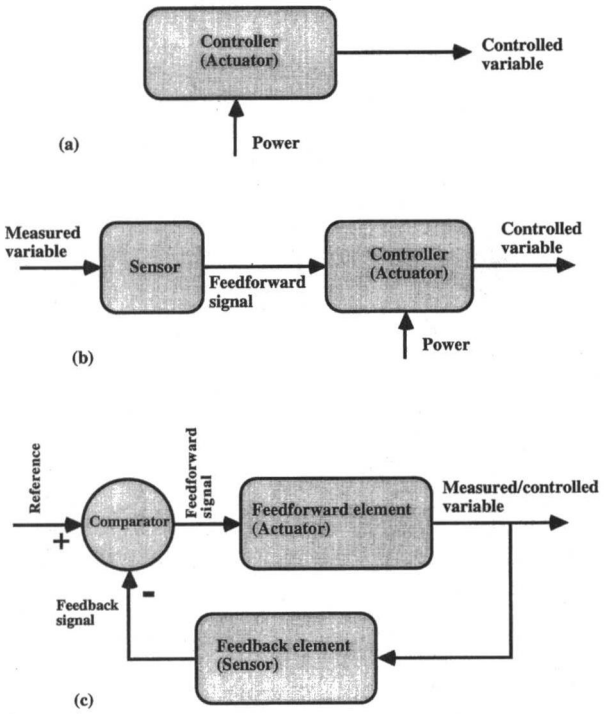

Fig. 14 Different control loops for active flow control. (*a*) Predetermined, open-loop control; (*b*) reactive, feedforward, open-loop control; (*c*) reactive, feedback, closed-loop control.

passive, requiring no auxiliary power, or active, requiring energy expenditure. As for the action of passive devices, some prefer to use the term flow management rather than flow control (Fiedler and Fernholz, 1990), reserving the latter terminology for dynamic processes. Active control—always requiring actuators—is further divided into predetermined or reactive. Predetermined control includes the application of steady or unsteady energy input without regard to the particular state of the flow. The control loop in this case is open as shown in Figure 14(*a*), and no sensors are required. Reactive control is a special class of active control where the control input is continuously adjusted based on measurements of some kind. The control loop in this case can either be an open, feedforward one (Fig. 14(*b*)) or a closed, feedback loop (Fig. 14(*c*)). Classical control theory deals, for the most part, with reactive control.

The distinction between feedforward and feedback is particularly important when dealing with the control of flow structures which convect over stationary sensors and actuators. In feedforward control, the measured variable and the controlled variable differ. For example, the pressure or velocity can be sensed at an upstream location, and the resulting signal is used together with an appropriate control law to trigger an actuator which in turn influences the velocity at a downstream position. Feedback control, on the other hand, necessitates that the controlled variable be measured, fed back and compared with a reference input. Reactive feedback control is further classified into four categories: Adaptive, physical model-based, dynamical systems-based and optimal control (Moin and Bewley, 1994).

A yet another classification scheme is to consider whether the control technique directly modifies the shape of the instantaneous/mean velocity profile or selectively influence the small dissipative eddies. An inspection of the Navier-Stokes equations written at the surface indicates that the spanwise and streamwise vorticity fluxes at the wall can be changed, either instantaneously or in the mean, via wall motion/compliance, suction/injection, streamwise or spanwise pressure-gradient (respectively), or normal viscosity-gradient. (Note that streamwise vorticity exists only if the velocity field is three-dimensional, instantaneously or in the mean.) These vorticity fluxes determine the fullness of the corresponding velocity profiles. For example, suction (or downward wall motion), favorable pressure-gradient or lower wall-viscosity results in vorticity flux away from the wall, making the surface a source of spanwise and streamwise vorticity. The corresponding fuller velocity profiles have negative curvature at the wall and are more resistant to transition and to separation but are associated with higher skin-friction drag. Conversely, an inflectional velocity profile can be produced by injection (or upward wall motion), adverse pressure-gradient or higher wall-viscosity. Such profile is more susceptible to transition and to separation and is associated with lower, even negative, skin friction. Note that many techniques are available to effect a wall viscosity-gradient; for example surface heating/cooling, film boiling, cavitation, sublimation, chemical reaction, wall injection of lower/higher viscosity fluid and the presence of shear thinning/thickening additive.

Flow control devices can alternatively target certain scales of motion rather than globally changing the velocity profile. Polymers, riblets and LEBUs, for example, appear to selectively damp only the small dissipative eddies in turbulent wall-bounded flows. These eddies are responsible for the (instantaneous) inflectional profile and the secondary instability in the buffer zone, and their suppression leads to increased scales, a delay in the reduction of the (mean) velocity-profile slope and consequent thickening of the wall region. In the buffer zone, the scales of the dissipative and energy containing eddies are roughly the same and, hence, the energy containing eddies will also be suppressed resulting in reduced Reynolds stress production, momentum transport and skin friction.

Considering the extreme complexity of the turbulence problem in general and the unattainability of first-principles analytical solutions in particular, it is not surprising that controlling a turbulent flow remains a challenging task, mired in empiricism and unfulfilled promises and aspirations. Brute force suppression, or *taming,* of turbulence via active, energy-consuming control strategies is always possible, but the penalty for doing so often exceeds any potential benefits. The artifice is to achieve a desired effect with minimum energy expenditure. This is where the concept of reactive control and the use of microsensors/microactuators come into the domain of this paper.

3.3.2 Control of Turbulence. Numerous methods of flow control have already been successfully implemented in practical engineering devices. Yet, very few of the classical strategies are effective in controlling free-shear or wall-bounded turbulent flows. Serious limitations exist for some familiar control techniques when applied to certain turbulent flow situations. For example, in attempting to reduce the skin-friction drag of a body having a turbulent boundary layer using global suction, the *penalty* associated with the control device often exceeds the saving derived from its use. What is needed is a way to reduce this penalty to achieve a more efficient control.

Flow control is most effective when applied near the transition or separation points; in other words, near the critical flow regimes where flow instabilities magnify quickly. Therefore, delaying/advancing laminar-to-turbulence transition and preventing/provoking separation are relatively easier tasks to accomplish. To reduce the skin-friction drag in a non-separating turbulent boundary layer, where the mean flow is quite stable, is a more challenging problem. Yet, even a modest reduction in the fluid resistance to the motion of, for example, the worldwide commercial air fleet is translated into fuel savings estimated to be in the billions of dollars. Newer ideas for turbulent flow control focus on the direct onslaught on coherent structures. Spurred by the recent developments in chaos control, microfabrication and soft computing tools, reactive control of turbulent flows is now in the realm of the possible for future practical devices.

Such futuristic systems are envisaged as consisting of a large number of intelligent, interactive, microfabricated wall sensors and actuators arranged in a checkerboard pattern and targeted towards specific organized structures that occur randomly within the boundary layer. Sensors detect oncoming coherent structures, and adaptive controllers process the sensors information and provide control signals to the actuators which in turn attempt to favorably modulate the quasi-periodic events. Finite number of wall sensors perceive only partial information about the entire flow field above. However, a low-dimensional dynamical model of the near-wall region used in a Kalman filter can make the most of the partial information from the sensors. Conceptually all of that is not too difficult, but in practice the complexity of such a control system is daunting and much research and development work still remain.

Targeted control implies sensing and reacting to a particular quasi-periodic structure in the boundary layer. The wall seems to be the logical place for such reactive control, because of the relative ease of placing something in there, the sensitivity of the flow in general to surface perturbations and the proximity and therefore accessibility to the dynamically all important near-wall coherent events.

3.3.3 Targeted Control. As discussed above, successful techniques to reduce the skin friction in a turbulent flow, such as polymers, particles or riblets, appear to act indirectly through local interaction with discrete turbulent structures, particularly small-scale eddies, within the flow. Common characteristics of all these methods are increased losses in the near-wall region, thickening of the buffer layer, and lowered production of Reynolds shear stress (Bandyopadhyay, 1986). Methods that act directly on the mean flow, such as suction or lowering of near-wall viscosity, also lead to inhibition of Reynolds stress. However, skin friction is increased when any of these velocity-profile modifiers is applied globally.

Could these seemingly inefficient techniques, e.g., global suction, be used more sparingly and be optimized to reduce their associated penalty? It appears that the more successful drag-reduction methods, e.g., polymers, act selectively on particular scales of motion and are thought to be associated with stabilization of the secondary instabilities. It is also clear that energy is wasted when suction or heating/cooling is used to suppress the turbulence throughout the boundary layer when the main interest is to affect a near-wall phenomenon. One ponders, what would become of wall turbulence if specific coherent structures are to be targeted, by the operator through a reactive control scheme, for modification? The myriad of organized structures present in all shear flows are instantaneously identifiable, quasi-periodic motions (Cantwell, 1981; Robinson, 1991). Bursting events in wall-bounded flows, for example, are both intermittent and random in space as well as time. The random aspects of these events reduce the effectiveness of a predetermined active control strategy. If such structures are nonintrusively detected and altered, on the other hand, net performance gain might be achieved. It seems clear, however, that temporal phasing as well as spatial selectivity would be required to achieve proper control targeted towards random events.

A nonreactive version of the above idea is the *selective suction technique* which combines suction to achieve an asymptotic turbulent boundary layer and longitudinal riblets to fix the location of low-speed streaks (Gad-el-Hak and Blackwelder, 1989). Although far from indicating net drag reduction, the available results are encouraging and further optimization is needed. When implemented via an array of reactive control loops, the selective suction method is potentially capable of skin-friction reduction that approaches 60%.

3.3.4 Required Characteristics. The randomness of the bursting events necessitates temporal phasing as well as spatial selectivity to effect selective (targeted) control. Practical applications of methods targeted at controlling a particular turbulent structure to achieve a prescibed goal would therefore require implementing a large number of surface sensors/actuators together with appropriate control algorithms. That strategy for controlling wall-bounded turbulent flows has been advocated by, among others and in chronological order, Gad-el-Hak and Blackwelder (1987; 1989), Blackwelder and Gad-el-Hak (1990), Lumley (1991; 1996), Choi et al. (1992; 1994), Reynolds (1993), Jacobson and Reynolds (1993; 1995; 1998), Moin and Bewley (1994), Gad-el-Hak (1994; 1996; 1998), McMichael (1996), Mehregany et al. (1996), and Lumley and Blossey (1998). Special mention should also be made of the UCLA/Caltech team who has been very effective in developing many MEMS-based sensors and actuators for turbulence diagnosis and control. Their list of publications in the field is rather long, but see, for example, Ho and Tai (1996), Tsao et al. (1997), Ho et al. (1997), Ho and Tai (1998), and references therein.

It is instructive to estimate some representative characteristics of the required array of sensors/actuators. Consider a typical commercial aircraft cruising at a speed of $U_\infty = 300$ m/s and at an altitude of 10 km. The density and kinematic viscosity of air and the unit Reynolds number in this case are, respectively, $\rho = 0.4$ kg/m^3, $\nu = 3 \times 10^{-5}$ m^2/s, and Re $= 10^7$/m. Assume further that the portion of fuselage to be controlled has a turbulent boundary layer characteristics which are identical to those for a zero-pressure-gradient flat plate at a distance of 1 m from the leading edge. In this case, the skin-friction coefficient and the friction velocity are, respectively, $C_f = 0.003$ and $u_\tau = 11.62$ m/s. (Note that the skin friction decreases as the distance from the leading edge increases. It is also strongly affected by such things as the externally imposed pressure gradient. Therefore, the estimates provided in here are for illustration purposes only.) At this location, one viscous wall unit is only $\nu/u_\tau = 2.6$ microns. In order for the surface array of sensors/actuators to be hydraulically smooth, it should not protrude beyond the viscous sublayer, or $5\nu/u_\tau = 13$ μm.

Wall-speed streaks are the most visible, reliable and detectable indicators of the preburst turbulence production process. The detection criterion is simply low velocity near the wall, and the actuator response should be to accelerate (or to remove) the low-speed region before it breaks down. Local wall motion, tangential injection, suction or heating triggered on sensed wall-pressure or wall-shear stress could be used to cause local acceleration of near-wall fluid.

The recent numerical experiments of Berkooz et al. (1993) indicate that effective control of bursting pair of rolls may be achieved by using the equivalent of two wall-mounted shear sensors. If the goal is to stabilize or to eliminate all low-speed streaks in the boundary layer, a reasonable estimate for the spanwise and streamwise distances between individual elements of a checkerboard array is, respectively, 100 and 1000 wall units or 260 μm and 2600 μm, for our particular example. (Note that 100 and 1000 wall units are equal to, respectively, the average spanwise wavelength between two adjacent streaks and the average streamwise extent for a typical low-speed region. One can argue that those estimates are too conservative: once a region is relaminarized, it would perhaps stay as such for quite a while as the flow convects downstream. The next row of sensors/actuators may therefore be relegated to a downstream location well beyond 1000 wall units.) A reasonable size for each element is probably one-tenth of the spanwise separation, or 26 μm. A (1 m $\times$ 1 m) portion of the surface would have to be covered with about $n = 1.5$ million elements. This is a colossal number, but the density of sensors/actuators can be considerably reduced if we moderate our goal of targeting every single bursting event (and also if less conservative assumptions are used).

It is well known that not every low-speed streak leads to a burst. On the average, a particular sensor would detect an incipient bursting event every wall-unit interval of $P^+ = Pu_\tau^2/\nu =$

250, or $P = 56\ \mu$s. The corresponding dimensionless and dimensional frequencies are $f^+ = 0.004$ and $f = 18$ kHz, respectively. At different distances from the leading edge and in the presence of nonzero pressure-gradient, the sensors/actuators array would have different characteristics, but the corresponding numbers would still be in the same ballpark as estimated in here.

As a second example, consider an underwater vehicle moving at a speed of $U_\infty = 10$ m/s. Despite the relatively low speed, the unit Reynolds number is still the same as estimated above for the air case, Re $= 10^7$/m, due to the much lower kinematic viscosity of water. At one meter from the leading edge of an imaginary flat plate towed in water at the same speed, the friction velocity is only $u_\tau = 0.39$ m/s, but the wall unit is still the same as in the aircraft example, $\nu/u_\tau = 2.6\ \mu$m. The density of required sensors/actuators array is the same as computed for the aircraft example, $n = 1.5 \times 10^6$ elements/m^2. The anticipated average frequency of sensing a bursting event is, however, much lower at $f = 600$ Hz.

Similar calculations have also been made by Gad-el-Hak (1993; 1994), Reynolds (1993), and Wadsworth et al. (1993). Their results agree closely with the estimates made here for typical field requirements. In either the airplane or the submarine case, the actuator's response need not be too large. As will be shown in Section 3.3.5, wall displacement on the order of 10 wall units (26 μm in both examples), suction coefficient of about 0.0006, or surface cooling/heating on the order of 40°C/2°C (in the first/second example, respectively) should be sufficient to stabilize the turbulent flow.

As computed in the two examples above, both the required size for a sensor/actuator element and the average frequency at which an element would be activated are within the presently known capabilities of microfabrication technology. The number of elements needed per unit area is, however, alarmingly large. The unit cost of manufacturing a programmable sensor/actuator element would have to come down dramatically, perhaps matching the unit cost of a conventional transistor, before the idea advocated in here would become practical.

An additional consideration to the size, amplitude, and frequency response is the energy consumed by each sensor/actuator element. Total energy consumption by the entire control system obviously has to be low enough to achieve net savings. Consider the following calculations for the aircraft example. One meter from the leading edge, the skin-friction drag to be reduced is approximately 54 N/m^2. Engine power needed to overcome this retarding force per unit area is 16 kW/m^2, or $10^4\ \mu$W/sensor. If a 60% drag-reduction is achieved, this energy consumption is reduced to 4320 μW/sensor. This number will increase by the amount of energy consumption of a sensor/actuator unit, but hopefully not back to the uncontrolled levels. The voltage across a sensor is typically in the range of $V = 0.1-1$ V, and its resistance in the range of $R = 0.1-1$ MΩ. This means a power consumption by a typical sensor in the range of $\mathcal{P} = V^2/R = 0.1-10\ \mu$W, well below the anticipated power savings due to reduced drag. For a single actuator in the form of a spring-loaded diaphragm with a spring constant of $k = 100$ N/m, oscillating up and down at the bursting frequency of $f = 18$ kHz, with an amplitude of $y = 26$ microns, the power consumption is $\mathcal{P} = (\frac{1}{2})ky^2f = 600\ \mu$W/actuator. If suction is used instead, $C_q = 0.0006$, and assuming a pressure difference of $\Delta p = 10^4$ N/m^2 across the suction holes/slots, the corresponding power consumption for a single actuator is $\mathcal{P} = C_q U_\infty \Delta p/n = 1200\ \mu$W/actuator. It is clear then that when the power penalty for the sensor/actuator is added to the lower-level drag, a net saving is still achievable. The corresponding actuator power penalties for the submarine example are even smaller ($\mathcal{P} = 20\ \mu$W/actuator, for the wall motion actuator, and $\mathcal{P} = 40\ \mu$W/actuator, for the suction actuator), and larger savings are therefore possible.

3.3.5 Microdevices for Flow Control. MEMS integrates electronics and mechanical components and can therefore execute sense-decision-actuation on a monolithic level. Microsensors/microactuators would be ideal for the reactive flow control concept advocated in the present subsection. Methods of flow control targeted toward specific coherent structures involve nonintrusive detection and subsequent modulation of events that occur randomly in space and time. To achieve proper targeted control of these quasi-periodic vortical events, temporal phasing as well as spatial selectivity are required. Practical implementation of such an idea necessitates the use of a large number of intelligent, communicative wall sensors and actuators arranged in a checkerboard pattern. Section 3.3.4 provided estimates for the number, characteristics and energy consumption of such elements required to modulate the turbulent boundary layer which develops along a typical commercial aircraft or nuclear submarine. An upper-bound number to achieve total turbulence suppression is about one million sensors/actuators per square meter of the surface, although as argued earlier the actual number needed to achieve effective control could perhaps be one or two orders of magnitude below that.

The sensors would be expected to measure the amplitude, location, and phase or frequency of the signals impressed upon the wall by incipient bursting events. Instantaneous wall-pressure or wall-shear stress can be sensed, for example. The normal or in-plane motion of a minute membrane is proportional to the respective point force of primary interest. For measuring wall pressure, microphone-like devices respond to the motion of a vibrating surface membrane or an internal elastomer. Several types are available including variable-capacitance (condenser or electret), ultrasonic, optical (e.g., optical-fiber and diode-laser), and piezoelectric devices (see, for example, Löfdahl et al., 1993; 1994). A potentially useful technique for our purposes has been tried at MIT (Warkentin et al., 1987; Young et al., 1988; Haritonidis et al., 1990a; 1990b). An array of extremely small (0.2 mm in diameter) laser-powered microphones (termed picophones) was machined in silicon using integrated circuit fabrication techniques, and was used for field measurement of the instantaneous surface pressure in a turbulent boundary layer. The wall-shear stress, though smaller and therefore more difficult to measure than pressure, provides a more reliable signature of the near-wall events.

Actuators are expected to produce a desired change in the targeted coherent structures. The local acceleration action needed to stabilize an incipient bursting event can be in the form of adaptive wall, transpiration or wall heat transfer. Traveling surface waves can be used to modify a locally convecting pressure gradient such that the wall motion follows that of the coherent event causing the pressure change. Surface motion in the form of a Gaussian hill with height $y^+ = \mathcal{O}[10]$ should be sufficient to suppress typical incipient bursts (Lumley, 1991; Carlson and Lumley, 1996). Such time-dependent alteration in wall geometry can be generated by driving a flexible skin using an array of piezoelectric devices (dilate or contract depending on the polarity of current passing through them), electromagnetic actuators, magnetoelastic ribbons (made of nonlinear materials that change their stiffness in the presence of varying magnetic fields), or Terfenol-d rods (a novel metal composite, developed at Grumman Corporation, which changes its length when subjected to a magnetic field). Note should also be made of other exotic materials that can be used for actuation. For example, electrorheological fluids (Halsey and Martin, 1993) instantly solidify when exposed to an electric field, and may thus be useful for the present application. Recently constructed microactuators specifically designed for flow control include those by Wiltse and Glezer (1993), James et al. (1994), Jacobson and Reynolds (1993; 1995; 1998), and Vargo and Muntz (1996).

Suction/injection at many discrete points can be achieved by simply connecting a large number of minute streamwise slots,

arranged in a checkerboard pattern, to a low-pressure/high-pressure reservoir located underneath the working surface. The transpiration through each individual slot is turned on and off using a corresponding number of independently controlled microvalves. Alternatively, positive-displacement or rotary micropumps (see, for example, Sen et al., 1996; Sharatchandra et al., 1997) can be used for blowing or sucking fluid through small holes/slits. Based on the results of Gad-el-Hak and Blackwelder (1989), equivalent suction coefficients of about 0.0006 should be sufficient to stabilize the near-wall region. Assuming that the skin-friction coefficient in the uncontrolled boundary layer is $C_f = 0.003$, and assuming further that the suction used is sufficient to establish an asymptotic boundary layer ($d\delta_\theta/dx = 0$, where δ_θ is the momentum thickness), the skin friction in the reactively controlled case is then $C_f = 0 + 2C_q = 0.0012$, or 40% of the original value. The net benefit would, of course, be reduced by the energy expenditure of the suction pump (or micropumps) as well as the array of microsensors and microvalves.

Finally, if the bursting events are to be eliminated by lowering the near-wall viscosity, direct electric-resistance heating can be used in liquid flows and thermoelectric devices based on the Peltier effect can be used for cooling in the case of gaseous boundary layers. The absolute viscosity of water at 20°C decreases by approximately 2% for each 1°C rise in temperature, while for room-temperature air, μ decreases by approximately 0.2% for each 1°C drop in temperature. The streamwise momentum equation written at the wall can be used to show that a suction coefficient of 0.0006 has approximately the same effect on the wall-curvature of the instantaneous velocity profile as a surface heating of 2°C in water or a surface cooling of 40°C in air (Liepmann and Nosenchuck, 1982; Liepmann et al., 1982).

Sensors and actuators of the types discussed in this section can be combined on individual electronic chips using microfabrication technology. The chips can be interconnected in a communication network that is controlled by a massively parallel computer or a self-learning neural network, perhaps each sensor/actuator unit communicating only with its immediate neighbors. In other words, it may not be necessary for one sensor/actuator to exchange signals with another far away unit. Factors to be considered in an eventual field application of chips produced using microfabrication processes include sensitivity of sensors, sufficiency and frequency response of actuators' action, fabrication of large arrays at affordable prices, survivability in the hostile field environment, and energy required to power the sensors/actuators. As argued by Gad-el-Hak (1994), sensor/actuator chips currently produced are small enough for typical field application, and they can be programmed to provide a sufficiently large/fast action in response to a certain sensor output (see also Jacobson and Reynolds, 1995). Present prototypes are, however, still quite expensive as well as delicate. But so was the transistor when first introduced! It is hoped that the unit price of future sensor/actuator elements would follow the same dramatic trends witnessed in case of the simple transistor and even the much more complex integrated circuit. The price anticipated by Texas Instruments for an array of 0.5–2 million, individually actuated mirrors used in high-definition optical displays hints that the technology is well in its way to mass-produce phenomenally inexpensive microsensors and microactuators. Additionally, current automotive applications are a rigorous proving ground for MEMS: under-the-hood sensors can already withstand harsh conditions such as intense heat, shock, continual vibration, corrosive gases and electromagnetic fields.

3.4 Micropumps. There have been several studies of microfabricated pumps. Some of them use non-mechanical effects. The Knudsen pump mentioned in Section 2.5 uses the thermal-creep effect to move rarefied gases from one chamber to another. Ion-drag is used in electrohydrodynamic pumps (Bart et al., 1990; Richter et al., 1991; Fuhr et al., 1992); these rely on the electrical properties of the fluid and are thus not suitable for many applications. Valveless pumping by ultrasound has also been proposed (Moroney et al., 1991), but produces very little pressure difference.

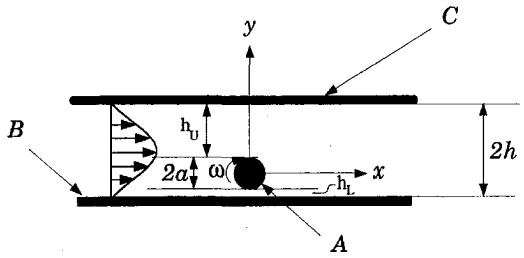

Fig. 15 Schematic of micropump developed by Sen et al. (1996)

Mechanical pumps based on conventional centrifugal or axial turbomachinery will not work at micromachine scales where the Reynolds numbers are typically small, on the order of 1 or less. Centrifugal forces are negligible and, furthermore, the Kutta condition through which lift is normally generated is invalid when inertial forces are vanishingly small. In general there are three ways in which mechanical micropumps can work:

1. Positive-displacement pumps. These are mechanical pumps with a membrane or diaphragm actuated in a reciprocating mode and with unidirectional inlet and outlet valves. They work on the same physical principle as their larger cousins. Micropumps with piezoelectric actuators have been fabricated (Van Lintel et al., 1988; Esashi et al., 1989; Smits, 1990). Other actuators, such as thermopneumatic, electrostatic, electromagnetic or bimetallic, can be used (Pister et al., 1990; Döring et al., 1992; Gabriel et al., 1992). These exceedingly minute positive-displacement pumps require even smaller valves, seals and mechanisms, a not-too-trivial micromanufacturing challenge. In addition there are long-term problems associated with wear or clogging and consequent leaking around valves. The pumping capacity of these pumps is also limited by the small displacement and frequency involved. Gear pumps are a different kind of positive-displacement device.
2. Continuous, parallel-axis rotary pumps. A screw-type, three-dimensional device for low Reynolds numbers was proposed by Taylor (1972) for propulsion purposes and shown in his seminal film. It has an axis of rotation parallel to the flow direction implying that the powering motor must be submerged in the flow, the flow turned through an angle, or that complicated gearing would be needed.
3. Continuous, transverse-axis rotary pumps. This is the class of machines that was recently developed by Sen et al. (1996). They have shown that a rotating body, asymmetrically placed within a duct, will produce a net flow due to viscous action. The axis of rotation can be perpendicular to the flow direction and the cylinder can thus be easily powered from outside a duct. A related viscous-flow pump was designed by Odell and Kovasznay (1971) for a water channel with density stratification. However, their design operates at a much higher Reynolds number and is too complicated for microfabrication.

As evidenced from the third item above, it is possible to generate axial fluid motion in open channels through the rotation of a cylinder in a viscous fluid medium. Odell and Kovasznay (1971) studied a pump based on this principle at high Reynolds numbers. Sen et al. (1996) carried out an experimental study of a different version of such a pump. The novel viscous pump,

shown schematically in Fig. 15, consists simply of a transverse-axis cylindrical rotor eccentrically placed in a channel, so that the differential viscous resistance between the small and large gaps causes a net flow along the duct. The Reynolds numbers involved in Sen et al.'s work were low ($0.01 < \mathrm{Re} \equiv 2\omega a^2/\nu < 10$, where ω is the radian velocity of the rotor, and a is its radius), typical of microscale devices, but achieved using a macroscale rotor and a very viscous fluid. The bulk velocities obtained were as high as 10% of the surface speed of the rotating cylinder. Sen et al. (1996) have also tried cylinders with square and rectangular cross-sections, but the circular cylinder delivered the best pumping performance.

A finite-element solution for low-Reynolds-number, uniform flow past a rotating cylinder near an impermeable plane boundary has already been obtained by Liang and Liou (1995). However, a detailed two-dimensional Navier-Stokes simulations of the pump described above have been carried out by Sharatchandra et al. (1997), who extended the operating range of Re beyond 100. The effects of varying the channel height H and the rotor eccentricity ϵ have been studied. It was demonstrated that an optimum plate spacing exists and that the induced flow increases monotonically with eccentricity; the maximum flowrate being achieved with the rotor in contact with a channel wall. Both the experimental results of Sen et al. (1996) and the 2-D numerical simulations of Sharatchandra et al. (1997) have verified that, at $\mathrm{Re} < 10$, the pump characteristics are linear and therefore kinematically reversible. Sharatchandra et al. (1997; 1998a) also investigated the effects of slip flow on the pump performance as well as the thermal aspects of the viscous device. Wall slip does reduce the traction at the rotor surface and thus lowers the performance of the pump somewhat. However, the slip effects appear to be significant only for Knudsen numbers greater than 0.1, which is encouraging from the point of view of microscale applications.

In an actual implementation of the micropump, several practical obstacles need to be considered. Among those are the larger stiction and seal design associated with rotational motion of microscale devices. Both the rotor and the channel have a finite, in fact rather small, width. DeCourtye et al. (1998) numerically investigated the viscous micropump performance as the width of the channel W becomes exceedingly small. The bulk flow generated by the pump decreased as a result of the additional resistance to the flow caused by the side walls. However, effective pumping was still observed with extremely narrow channels. Finally, Shartchandra et al. (1998b) used a genetic algorithm to determine the optimum wall shape to maximize the micropump performance. Their genetic algorithm uncovered shapes that were nonintuitive but yielded vastly superior pump performance.

Though most of the micropump discussion above is of flow in the steady state, it should be possible to give the eccentric cylinder a finite number of turns or even a portion of a turn to displace a prescribed minute volume of fluid. Numerical computations will easily show the order of magnitude of the volume discharged and the errors induced by acceleration at the beginning of the rotation and deceleration at the end. Such system can be used for microdosage delivery in medical applications.

3.5 Microturbines. DeCourtye et al. (1998) have described the possible utilization of the inverse micropump device (Section 3.4) as a turbine. The most interesting application of such a microturbine would be as a microsensor for measuring exceedingly small flowrates on the order of nanoliter/s (i.e., microflow metering for medical and other applications).

The viscous pump described in Section 3.4 operates best at low Reynolds numbers and should therefore be kinematically reversible in the creeping-flow regime. A microturbine based on the same principle should, therefore, lead to a net torque in the presence of a prescribed bulk velocity. The results of three-dimensional numerical simulations of the envisioned microturbine are summarized in this subsection. The Reynolds number for the turbine problem is defined in terms of the bulk velocity, since the rotor surface speed is unknown in this case,

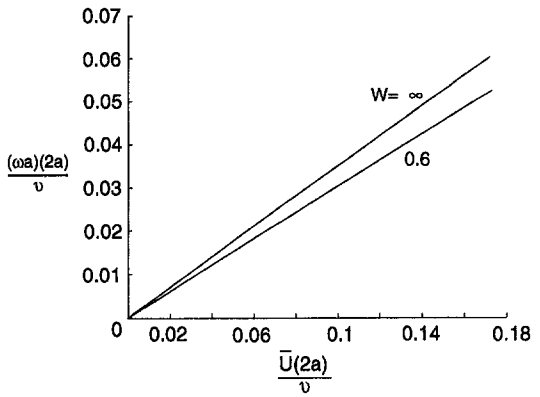

Fig. 16 Turbine rotation as a function of the bulk velocity in the channel. From DeCourtye et al. (1998).

$$\mathrm{Re} = \frac{\bar{U}(2a)}{\nu} \tag{78}$$

where $\bar{U}$ is the prescribed bulk velocity in the channel, a is the rotor radius, and ν is the kinematic viscosity of the fluid.

Figure 16 shows the dimensionless rotor speed as a function of the bulk velocity, for two dimensionless channel widths $W = \infty$ and $W = 0.6$. In these simulations, the dimensionless channel depth is $H = 2.5$ and the rotor eccentricity is $\epsilon/\epsilon_{\max} = 0.9$. The relation is linear as was the case for the pump problem. The slope of the lines is 0.37 for the 2-D turbine and 0.33 for the narrow channel with $W = 0.6$. This means that the induced rotor speed is, respectively, 0.37 and 0.33 of the bulk velocity in the channel. (The rotor speed can never, of course, exceed the fluid velocity even if there is no load on the turbine. Without load, the integral of the viscous shear stress over the entire surface area of the rotor is exactly zero, and the turbine achieves its highest albeit finite rpm.) For the pump, the corresponding numbers were 11.11 for the 2-D case and 100 for the 3-D case. Although it appears that the side walls have bigger influence on the pump performance, it should be noted that in the turbine case a vastly higher pressure drop is required in the 3-D duct to yield the same bulk velocity as that in the 2-D duct (dimensionless pressure drop of $\Delta p^* \equiv \Delta p 4a^2/\rho\nu^2 = -29$ versus $\Delta p^* = -1.5$).

The turbine characteristics are defined by the relation between the shaft speed and the applied load. A turbine load results in a moment on the shaft, which at steady state balances the torque due to viscous stresses. At a fixed bulk velocity, the rotor speed is determined for different loads on the turbine. Again, the turbine characteristics are linear in the Stokes (creeping) flow regime, but the side walls have weaker, though still adverse, effect on the device performance as compared to the pump case. For a given bulk velocity, the rotor speed drops linearly as the external load on the turbine increases. At large enough loads, the rotor will not spin, and maximum rotation is achieved when the turbine is subjected to zero load.

At present it is difficult to measure flowrates on the order of 10^{-12} m^3/s (1 nanoliter/s). One possible way is to directly collect the effluent over time. This is useful for calibration but is not practical for on-line flow measurement. Another is to use heat transfer from a wire or film to determine the local flowrate as in a thermal anemometer. Heat transfer from slowly moving fluids is mainly by conduction so that temperature gradients can be large. This is undesirable for biological and other fluids easily damaged by heat. The viscous mechanism that has been

proposed and verified for pumping may be turned around and used for measuring. As demonstrated in this subsection, a freely rotating cylinder eccentrically placed in a duct will rotate at a rate proportional to the flowrate due to a turbine effect. In fact other geometries such as a freely rotating sphere in a cylindrical tube should also behave similarly. The calibration constant, which depends on system parameters such as geometry and bearing friction, should be determined computationally to ascertain the practical viability of such a microflow meter. Geometries that are simplest to fabricate should be explored and studied in detail.

3.6 Microbearings. Many of the micromachines use rotating shafts and other moving parts which carry a load and need fluid bearings for support, most of them operating with air or water as the lubricating fluid. The fluid mechanics of these bearings are very different compared to that of their larger cousins. Their study falls in the area of microfluid mechanics, an emerging discipline which has been greatly stimulated by its applications to micromachines and which is the subject of this paper.

Macroscale journal bearings develop their load-bearing capacity from large pressure differences which are a consequence of the presence of a viscous fluid, an eccentricity between the shaft and its housing, a large surface speed of the shaft, and a small clearance to diameter ratio. Several closed-form solutions of the no-slip flow in a macrobearing have been developed. Wannier (1950) used modified Cartesian coordinates to find an exact solution to the biharmonic equation governing two-dimensional journal bearings in the no-slip, creeping flow regime. Kamal (1966) and Ashino and Yoshida (1975) worked in bipolar coordinates; they assumed a general form for the streamfunction with several constants which were determined using the boundary conditions. Though all these methods work if there is no slip, they cannot be readily adapted to slip flow. The basic reason is that the flow pattern changes if there is slip at the walls and the assumed form of the solution is no longer valid.

Microbearings are different in the following aspects: (1) being so small, it is difficult to manufacture them with a clearance that is much smaller than the diameter of the shaft; (2) because of the small shaft size, its surface speed, at normal rotational speeds, is also small; and (3) air bearings in particular may be small enough for non-continuum effects to become important. (The microturbomachines being developed presently at MIT operate at shaft rotational speeds on the order of 1 million rpm, and are therefore operating at different flow regime from that considered here.) For these reasons the hydrodynamics of lubrication is very different at microscales. The lubrication approximation that is normally used is no longer directly applicable and other effects come into play. From an analytical point of view there are three consequences of the above: fluid inertia is negligible, slip flow may be important for air and other gases, and relative shaft clearance need not be small.

In a recent study, Maureau et al. (1997) analyzed microbearings represented as an eccentric cylinder rotating in a stationary housing. The flow Reynolds number is assumed small, the clearance between shaft and housing is not small relative to the overall bearing dimensions, and there is slip at the walls due to nonequilibrium effects. The two-dimensional governing equations are written in terms of the streamfunction in bipolar coordinates. Following the method of Jeffery (1920), Maureau et al. (1997) succeeded in obtaining an exact infinite-series solution of the Navier-Stokes equations for the specified geometry and flow conditions. In contrast to macrobearings and due to the large clearance, flow in a microbearing is characterized by the possibility of a recirculation zone which strongly affects the velocity and pressure fields. For high values of the eccentricity and low slip factors the flow develop a recirculation region, as shown in the streamlines plot in Fig. 17.

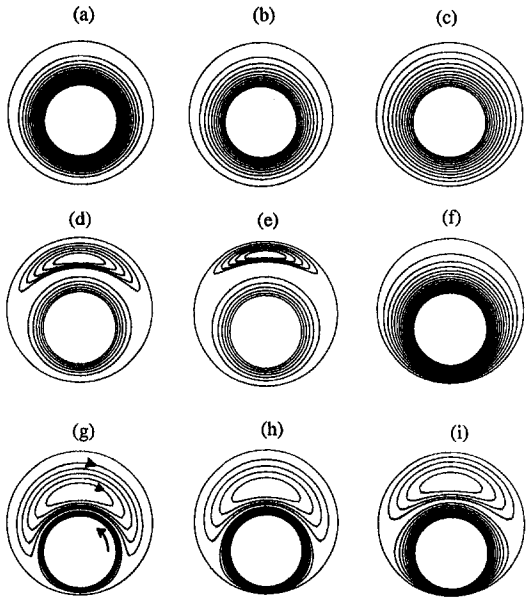

Fig. 17 Effect of slip factor and eccentricity on the microbearing streamlines. From top to bottom, eccentricity changes as $\epsilon = 0.2, 0.5, 0.8$. From left to right, slip factor changes as $S \equiv (2 - \sigma_v/\sigma)Kn = 0, 0.1, 0.5$. From Maureau et al. (1997).

From the infinite-series solution the frictional torque and the load-bearing capacity can be determined. The results show that both are similarly affected by the eccentricity and the slip factor: they increase with the former and decrease with the latter. For a given load, there is a corresponding eccentricity which generates a force sufficient to separate shaft from housing (i.e. sufficient to prevent solid-to-solid contact). As the load changes the rotational center of the shaft shifts a distance necessary for the forces to balance. It is interesting to note that for a weight that is vertically downwards, the equilibrium displacement of the center of the shaft is in the horizontal direction. This can lead to complicated rotor dynamics governed by mechanical inertia, viscous damping and pressure forces. A study of this dynamics may of interest. Real microbearings have finite shaft lengths, and end walls and other three-dimensional effects influence the bearing characteristics. Numerical simulations of the three-dimensional problem can readily be carried out and may also be of interest to the designers of microbearings. Other potential research includes determination of a criterion for onset of cavitation in liquid bearings. From the results of these studies, information related to load, rotational speed and geometry can be generated that would be useful for the designer.

Finally, Piekos et al. (1997) have used full Navier-Stokes computations to study the stability of ultra-high-speed, gas microbearings. They conclude that it is possible—despite significant design constraints—to attain stability for specific bearings to be used with the MIT microturbomachines (Epstein and Senturia, 1997; Epstein et al., 1997), which incidentally operate at much higher Reynolds numbers (and rpm) than the micropumps/microturbines/microbearings considered thus far in this and the previous two subsections. According to Piekos et al. (1997), high-speed bearings are more robust than low-speed ones due to their reduced running eccentricities and the large loads required to maintain them.

4 Concluding Remarks

The forty-year-old vision of Richard Feynman of building minute machines is now a reality. Microelectromechanical systems have witnessed explosive growth during the last decade and are finding increased applications in a variety of industrial and medical fields. The physics of fluid flows in microdevices

and some representative applications have been explored in this paper. While we now know a lot more than we did just few years ago, much physics remains to be explored so that rational tools can be developed for the design, fabrication and operation of MEMS devices.

The traditional Navier-Stokes model of fluid flows with no-slip boundary conditions works only for a certain range of the governing parameters. This model basically demands two conditions. (1) The fluid is a continuum, which is almost always satisfied as there are usually more than 1 million molecules in the smallest volume in which appreciable macroscopic changes take place. This is the molecular chaos restriction. (2) The flow is not too far from thermodynamic equilibrium, which is satisfied if there is sufficient number of molecular encounters during a time period small compared to the smallest time-scale for flow changes. During this time period the average molecule would have moved a distance small compared to the smallest flow length-scale.

For gases, the Knudsen number determines the degree of rarefaction and the applicability of traditional flow models. As $Kn \rightarrow 0$, the time- and length-scales of molecular encounters are vanishingly small compared to those for the flow, and the velocity distribution of each element of the fluid instantaneously adjusts to the equilibrium thermodynamic state appropriate to the local macroscopic properties as this molecule moves through the flow field. From the continuum viewpoint, the flow is isentropic and heat conduction and viscous diffusion and dissipation vanish from the continuum conservation relations, leading to the Euler equations of motion. At small but finite Kn, the Navier-Stokes equations describe near-equilibrium, continuum flows.

Slip flow must be taken into account for $Kn > 0.001$. The slip boundary condition is at first linear in Knudsen number then nonlinear effects take over beyond a Knudsen number of 0.1. At the same transition regime, i.e., $0.1 < Kn < 10$, the linear (stress)-(rate of strain) and (heat flux)-(temperature gradient) relations—needed to close the Navier-Stokes equations—also break down, and alternative continuum equations (e.g., Burnett) or molecular-based models must be invoked. In the transition regime, provided that the dilute gas and molecular chaos assumptions hold, solutions to the difficult Boltzmann equation are sought, but physical simulations such as Monte Carlo methods are more readily executed in this range of Knudsen number. In the free-molecule flow regime, i.e., $Kn > 10$, the nonlinear collision integral is negligible and the Boltzmann equation is drastically simplified. Analytical solutions are possible in this case for simple geometries and numerical integration of the Boltzmann equation is straightforward for arbitrary geometries, provided that the surface-reflection characteristics are accurately modeled.

Gaseous flows are often compressible in microdevices even at low Mach numbers. Viscous effects can cause sufficient pressure drop and density changes for the flow to be treated as compressible. In a long, constant-area microduct, all Knudsen number regimes may be encountered and the degree of rarefaction increases along the tube. The pressure drop is nonlinear and the Mach number increases downstream, limited only by choked-flow condition.

Similar deviation and breakdown of the traditional Navier-Stokes equations occur for liquids as well, but there the situation is more murky. Existing experiments are contradictory. There is no kinetic theory of liquids, and first-principles prediction methods are scarce. Molecular dynamics simulations can be used, but they are limited to extremely small flow extents. Nevertheless, measurable slip is predicted from MD simulations at realistic shear rates in microdevices.

MEMS are finding increased applications in the diagnosis and control of turbulent flows. The use of microsensors and microactuators promises a quantum leap in the performance of reactive flow control systems, and is now in the realm of the possible for future practical devices. Simple, viscous-based micropumps can be utilized for microdosage delivery, and microturbines can be used for measuring flowrates in the nanoliter/s range. Both of these can be of value in several medical applications.

Much nontraditional physics is still to be learned and many exciting applications of microdevices are yet to be discovered. The future is bright for this emerging field of science and technology and members of the American Society of Mechanical Engineers should be in the forefront of this progress. Richard Feynman was right about the possibility of building mite-size machines, but was somewhat cautious in forecasting that such machines, while "would be fun to make," may or may not be useful.

Acknowledgments

My original involvement with microdevices was performed under a contract from the National Science Foundation, under the Small Grants for Exploratory Research initiative (SGER Grant no. CTS-95-21612). The technical monitors were Robert Powell and Roger Arndt. I would like to express my sincere appreciation to the members of the ASME Freeman Scholar committee, Richard Bajura, Clayton Crowe and Michael Billet, for their confidence in my ability to deliver this treatise. I am very grateful to Chih-Ming Ho, Fazle Hussain and George Karniadakis for their continuous support and encouragement through the years. Haim Bau, Ali Beskok, Kenneth Breuer, Stuart Jacobson and Sandra Troian provided invaluable help in preparing this manuscript, including sharing some of their reports and papers. Finally, my sincere gratitude to my friend and colleague Mihir Sen, for all the great times we have had while working together on small devices and big ideas.

References

Alder, B. J., and Wainwright, T. E., 1957, "Studies in Molecular Dynamics," *Journal of Chemical Physics,* Vol. 27, pp. 1208–1209.

Alder, B. J., and Wainwright, T. E., 1958, "Molecular Dynamics by Electronic Computers," *Transport Processes in Statistical Mechanics,* I. Prigogine, ed., pp. 97–131, Interscience, New York.

Alder, B. J., and Wainwright, T. E., 1970, "Decay of the Velocity Auto-Correlation Function," *Physical Review A,* Vol. 1, pp. 18–21.

Allen, M. P., and Tildesley, D. J., 1987, *Computer Simulation of Liquids,* Clarendon Press, Oxford, England.

Amato, I., 1998, "Formenting a Revolution, in Miniature," *Science,* Vol. 282, No. 5388, 16 October, pp. 402–405.

Anderson, J. L., and Quinn, J. A., 1972, "Ionic Mobility in Microcapillaries," *Journal of Chemical Physics,* Vol. 27, pp. 1208–1209.

Angell, J. B., Terry, S. C., and Barth, P. W., 1983, "Silicon Micromechanical Devices," *Faraday Transactions I,* Vol. 68, pp. 744–748.

Arkilic, E. B., 1997, "Measurement of the Mass Flow and Tangential Momentum Accommodation Coefficient in Silicon Micromachined Channels," Ph.D. thesis, Massachusetts Institute of Technology, Cambridge, Massachusetts.

Arkilic, E. B., Schmidt, M. A., and Breuer, K. S., 1995, "Slip Flow in Microchannels," *Rarefied Gas Dynamics 19,* J. Harvey and G. Lord, eds., Oxford University Press, Oxford, United kingdom.

Arkilic, E. B., Schmidt, M. A., and Breuer, K. S., 1997a, "Gaseous Slip Flow in Long Microchannels," *Journal of Microelectromechanical Systems,* Vol. 6, pp. 167–178.

Arkilic, E. B., Schmidt, M. A., and Breuer, K. S., 1997b, "TMAC Measurement in Silicon Micromachined Channels," *Rarefied Gas Dynamics 20,* C. Shen, ed., 6 pp., Beijing University Press, Beijing, China.

Ashino, I., and Yoshida, K., 1975, "Slow Motion between Eccentric Rotating Cylinders," *Bulletin of the JSME,* Vol. 18, No. 117, pp. 280–285.

Atwood, B. T., and Schowalter, W. R., 1989, "Measurements of Slip at the Wall during Flow of High-Density Polyethylene through a Rectangular Conduit," *Rheologica Acta,* Vol. 28, p. 134–146.

Bandyopadhyay, P. R., 1986, "Review—Mean Flow in Turbulent Boundary Layers Disturbed to Alter Skin Friction," ASME JOURNAL OF FLUIDS ENGINEERING, Vol. 108, pp. 127–140.

Bart, S. F., Tavrow, L. S., Mehregany, M., and Lang, J. H., 1990, "Microfabricated Electrohydrodynamic Pumps," *Sensors and Actuators A,* Vol. 21–23, pp. 193–197.

Batchelor, G. K., 1967, *An Introduction to Fluid Dynamics,* Cambridge University Press, London, United Kingdom.

Bau, H. H., 1994, "Transport Processes Associated with Micro-Devices," *Thermal Science and Engineering,* Vol. 2, pp. 172–178.

Berkooz, G., Fisher, M., and Psiaki, M., 1993, "Estimation and Control of Models of the Turbulent Wall Layer," *Bulletin of the American Physical Society,* Vol. 38, p. 2197.

Beskok, A., 1994, "Simulation of Heat and Momentum Transfer in Complex Micro-Geometries," M.Sc. thesis, Princeton University, Princeton, New Jersey.

Beskok, A., 1996, "Simulations and Models of Gas Flows in Microgeometries," Ph.D. thesis, Princeton University, Princeton, New Jersey.

Beskok, A., and Karniadakis, G. E., 1994, "Simulation of Heat and Momentum Transfer in Complex Micro-Geometries," *Journal of Thermophysics and Heat Transfer,* Vol. 8, pp. 355–370.

Beskok, A., and Karniadakis, G. E., 1998, "A Model for Flows in Channels, Pipes and Ducts at Micro- and Nano-Scales," *Microscale Thermophysicsl Engineering,* to appear.

Beskok, A., Karniadakis, G. E., and Trimmer, W., 1996, "Rarefaction and Compressibility Effects in Gas Microflows," ASME JOURNAL OF FLUIDS ENGINEERING, Vol. 118, pp. 448–456.

Bhatnagar, P. L., Gross, E. P., and Krook, M., 1954, "A Model for Collision Processes in Gases. I. Small Amplitude Processes in Charged and Neutral One-Component Systems," *Physical Review,* Vol. 94, pp. 511–524.

Bird, G. A., 1963, "Approach to Translational Equilibrium in a Rigid Sphere Gas," *Physics of Fluids,* Vol. 6, pp. 1518–1519.

Bird, G. A., 1965, "The Velocity Distribution Function within a Shock Wave," *Journal of Fluid Mechanics,* Vol. 30, pp. 479–487.

Bird, G. A., 1976, *Molecular Gas Dynamics,* Clarendon Press, Oxford, United Kingdom.

Bird, G. A., 1978, "Monte Carlo Simulation of Gas Flows," *Annual Review of Fluid Mechanics,* Vol. 10, pp. 11–31.

Bird, G. A., 1994, *Molecular Gas Dynamics and the Direct Simulation of Gas Flows,* Clarendon Press, Oxford, United Kingdom.

Blackwelder, R. F., and Gad-el-Hak M., 1990, "Method and Apparatus for Reducing Turbulent Skin Friction," United States Patent No. 4,932,612.

Bryzek, J., Peterson, K., and McCulley, W., 1994, "Micromachines on the March," *IEEE Spectrum,* Vol. 31, May, pp. 20–31.

Brunauer, S., 1944, *Physical Adsorption of Gases and Vapours,* Oxford University Press, Oxford, United Kingdom.

Busch-Vishniac, I. J., 1998, "Trends in Electromechanical Transduction," *Physics Today,* Vol. 51, July, pp. 28–34.

Cantwell, B. J., 1981, "Organized Motion in Turbulent Flow," *Annual Review of Fluid Mechanics,* Vol. 13, pp. 457–515.

Carlson, H. A., and Lumley, J. L., 1996, "Flow over an Obstacle Emerging from the Wall of a Channel," *AIAA Journal,* Vol. 34, pp. 924–931.

Cercignani, C., 1988, *The Boltzmann Equation and Its Applications,* Springer-Verlag, Berlin.

Chan, D. Y. C., and Horn, R. G., 1985, "Drainage of Thin Liquid Films," *Journal of Chemical Physics,* Vol. 83, pp. 5311–5324.

Chapman, S., and Cowling, T. G., 1970, *The Mathematical Theory of Non-Uniform Gases,* Third Edition, Cambridge University Press, London, United Kingdom.

Cheng, H. K., 1993, "Perspectives on Hypersonic Viscous Flow Research," *Annual Review of Fluid Mechanics,* Vol. 25, pp. 455–484.

Cheng, H. K., and Emmanuel, G., 1995, "Perspectives on Hypersonic Nonequilibrium Flow," *AIAA Journal,* Vol. 33, pp. 385–400.

Choi, H., Moin, P., and Kim, J., 1992, "Turbulent Drag Reduction: Studies of Feedback Control and Flow Over Riblets," Department of Mechanical Engineering Report No. TF-55, Stanford University, Stanford, CA.

Choi, H., Moin, P., and Kim, J., 1994, "Active Turbulence Control for Drag Reduction in Wall-Bounded Flows," *Journal of Fluid Mechanics,* Vol. 262, pp. 75–110.

Ciccotti, G., and Hoover, W. G. (editors), 1986, *Molecular Dynamics Simulation of Statistical Mechanics Systems,* North Holland, Amsterdam, the Netherlands.

Debye, P., and Cleland, R. L., 1959, "Flow of Liquid Hydrocarbons in Porous Vycor," *Journal of Applied Physics,* Vol. 30, pp. 843–849.

DeCourtye, D., Sen, M., and Gad-el-Hak, M., 1998, "Analysis of Viscous Micropumps and Microturbines," *International Journal of Computational Fluid Dynamics,* Vol. 10, pp. 13–25.

Den, L. M., 1990, "Issues in Viscoelastic Fluid Mechanics," *Annual Review of Fluid Mechanics,* Vol. 22, pp. 13–34.

Döring, C., Grauer, T., Marek, J., Mettner, M. S., Trah, H.-P., and Willmann, M., 1992, "Micromachined Thermoelectrically Driven Cantilever Structures for Fluid Jet Deflection," *Proceedings IEEE Micro Electro Mechanical Systems '92,* pp. 12–18, 4–7 February, Travemünde, Germany.

Dussan, E. B., 1976, "The Moving Contact Line: the Slip Boundary Condition," *Journal of Fluid Mechanics,* Vol. 77, pp. 665–684.

Dussan, E. B., 1979, "On the Spreading of Liquids on Solid Surfaces: Static and Dynamic Contact Lines," *Annual Review of Fluid Mechanics,* Vol. 11, pp. 371–400.

Dussan, E. B., and Davis, S. H., 1974, "On the Motion of Fluid-Fluid Interface along a Solid Surface," *Journal of Fluid Mechanics,* Vol. 65, pp. 71–95.

Epstein, A. H., and Senturia, S. D., 1997, "Macro Power from Micro Machinery," *Science,* Vol. 276, 23 May, p. 1211.

Epstein, A. H., Senturia, S. D., Al-Midani, O., Anathasuresh, G., Ayon, A., Breuer, K., Chen, K.-S., Ehrich, F. F., Esteve, E., Frechette, L., Gauba, G., Ghodssi, R., Groshenry, C., Jacobson, S. A., Kerrebrock, J. L., Lang, J. H., Lin, C.-C., London, A., Lopata, J., Mehra, A., Mur Miranda, J. O., Nagle, S., Orr, D. J., Piekos, E., Schmidt, M. A., Shirley, G., Spearing, S. M., Tan, C. S., Tzeng, Y.-S., and Waitz, I. A. (1997), "Micro-Heat Engines, Gas Turbines, and Rocket Engines—The MIT Microengine Project," AIAA paper No. 97-1773, AIAA, Reston, VA.

Esashi, M., Shoji, S., and Nakano, A., 1989, "Normally Closed Microvalve Fabricated on a Silicon Wafer," *Sensors and Actuators,* Vol. 20, pp. 163–169.

Fan, L.-S., Tai, Y.-C., and Muller, R. S., 1988, "Integrated Movable Micromechanical Structures for Sensors and Actuators," *IEEE Transactions on Electronic Devices,* Vol. 35, pp. 724–730.

Fan, L.-S., Tai, Y.-C., and Muller, R. S., 1989, "IC-Processed Electrostatic Micromotors," *Sensors and Actuators,* Vol. 20, pp. 41–47.

Feynman, R. P., 1961, "There's Plenty of Room at the Bottom," *Miniaturization,* H. D. Gilbert, ed., pp. 282–296, Reinhold Publishing, New York.

Fiedler, H. E., and Fernholz, H.-H., 1990, "On Management and Control of Turbulent Shear Flows," *Progress in Aerospace Sciences,* Vol. 27, pp. 305–387.

Fuhr, G., Hagedorn, R., Müller, T., Benecke, W., and Wagner, B., 1992, "Microfabricated Electrohydrodynamic (EHD) Pumps for Liquids of Higher Conductivity," *Journal of Microelectromechanical Systems,* Vol. 1, pp. 141–145.

Gabriel, K. J., 1995, "Engineering Microscopic Machines," *Scientific American,* Vol. 260, Sept., pp. 150–153.

Gabriel, K. J., Jarvis, J., and Trimmer, W. (editors), 1988, *Small Machines, Large Opportunities: A Report on the Emerging Field of Microdynamics,* National Science Foundation, published by AT&T Bell Laboratories, Murray Hill, NJ.

Gabriel, K. J., Tabata, O., Shimaoka, K., Sugiyama, S., and Fujita, H., 1992, "Surface-Normal Electrostatic/Pneumatic Actuator," *Proceedings IEEE Micro Electro Mechanical Systems '92,* pp. 128–131, 4–7 February, Travemünde, Germany.

Gad-el-Hak, M., 1989, "Flow Control," *Applied Mechanics Reviews,* Vol. 42, pp. 261–293.

Gad-el-Hak, M., 1993, "Innovative Control of Turbulent Flows," AIAA Paper No. 93-3268, AIAA, NY.

Gad-el-Hak, M., 1994, "Interactive Control of Turbulent Boundary Layers: A Futuristic Overview," *AIAA Journal,* Vol. 32, pp. 1753–1765.

Gad-el-Hak, M., 1995, "Questions in Fluid Mechanics: Stokes' Hypothesis for a Newtonian, Isotropic Fluid," ASME JOURNAL OF FLUIDS ENGINEERING, Vol. 117, pp. 3–5.

Gad-el-Hak, M., 1996, "Modern Developments in Flow Control," *Applied Mechanics Reviews,* Vol. 49, pp. 365–379.

Gad-el-Hak, M., 1998, "Frontiers of Flow Control," *Flow Control: Fundamentals and Practices,* M. Gad-el-Hak, A. Pollard and J.-P. Bonnet, eds., *Lecture Notes in Physics,* Vol. 53, pp. 109–153, Springer-Verlag, Berlin.

Gad-el-Hak, M., and Blackwelder, R. F., 1987, "A Drag Reduction Method for Turbulent Boundary Layers," AIAA Paper No. 87-0358, AIAA, New York.

Gad-el-Hak, M., and Blackwelder, R. F., 1989, "Selective Suction for Controlling Bursting Events in a Boundary Layer," *AIAA Journal,* Vol. 27, pp. 308–314.

Garcia, E. J., and Sniegowski, J. J., 1993, "The Design and Modelling of a Comb-Drive-Based Microengine for Mechanism Drive Applications," *Proceedings of the Seventh International Conference on Solid-State Sensors and Actuators (Transducers '93),* pp. 763–766, Yokohama, Japan, 7–10 June.

Garcia, E. J., and Sniegowski, J. J., 1995, "Surface Micromachined Microengine," *Sensors and Actuators A,* Vol. 48, pp. 203–214.

Gee, M. L., McGuiggan, P. M., Israelachvili, J. N., and Homola, A. M., 1990, "Liquid to Solidlike Transitions of Molecularly Thin Films under Shear," *Journal of Chemical Physics,* Vol. 93, pp. 1895–1906.

Gravesen, P., Branebjerg, J., and Jensen, O. S., 1993, "Microfluidics—A Review," *Journal of Micromechanics and Microengineering,* Vol. 3, pp. 168–182.

Guvenc, M. G., 1985, "V-Groove Capillary for Low Flow Control and Measurement," *Micromachining and Micropackaging of Transducers,* C. D. Fung, P. W. Cheung, W. H. Ko and D. G. Fleming, eds., pp. 215–223, Elsevier, Amsterdam, The Netherlands.

Haile, J. M., 1993, *Molecular Dynamics Simulation: Elementary Methods,* Wiley, New York.

Halsey, T. C., and Martin, J. E., 1993, "Electrorheological Fluids," *Scientific American,* Vol. 269, Oct., pp. 58–64.

Haritonidis, J. H., Senturia, S. D., Warkentin, D. J., and Mehregany, M., 1990a, "Optical Micropressure Transducer," United States Patent number 4,926,696, 22 May 1990.

Haritonidis, J. H., Senturia, S. D., Warkentin, D. J., and Mehregany, M., 1990b, "Pressure Transducer Apparatus," United States Patent number 4,942,767, 24 July 1990.

Harley, J. C., Huang, Y., Bau, H. H., and Zemel, J. N., 1995, "Gas Flow in Micro-Channels," *Journal of Fluid Mechanics,* Vol. 284, pp. 257–274.

Hirschfelder, J. O., Curtiss, C. F., and Bird, R. B., 1954, *Molecular Theory of Gases and Liquids,* Wiley, New York.

Ho, C.-M., and Tai, Y.-C., 1996, "Review: MEMS and Its Applications for Flow Control," ASME JOURNAL OF FLUIDS ENGINEERING, Vol. 118, pp. 437–447.

Ho, C.-M., and Tai, Y.-C., 1998, "Micro-Elctro-Mechanical Systems (MEMS) and Fluid Flows," *Annual Review of Fluid Mechanics,* Vol. 30, pp. 579–612.

Ho, C.-M., Tung, S., Lee, G. B., Tai, Y.-C., Jiang, F., and Tsao, T., 1997, "MEMS—A Technology for Advancements in Aerospace Engineering," AIAA Paper No. 97-0545, AIAA, Washington, D.C.

Hogan, H., 1996, "Invasion of the micromachines," *New Scientist,* 29 June, pp. 28–33.

Israelachvili, J. N., 1986, "Measurement of the Viscosity of Liquids in Very Thin Films," *Journal of Colloid and Interface Science,* Vol. 110, pp. 263–271.

Israelachvili, J. N., 1991, *Intermolecular and Surface Forces,* second edition, Academic Press, New York.

Jacobson, S. A., and Reynolds, W. C., 1993, "Active Control of Boundary Layer Wall Shear Stress Using Self-Learning Neural Networks," AIAA Paper No. 93-3272, AIAA, Washington, D.C.

Jacobson, S. A., and Reynolds, W. C., 1995, "An Experimental Investigation Towards the Active Control of Turbulent Boundary Layers," Department of Mechanical Engineering Report No. TF-64, Stanford University, Stanford, California.

Jacobson, S. A., and Reynolds, W. C., 1998, "Active Control of Streamwise Vortices and Streaks in Boundary Layers," *Journal of Fluid Mechanics,* Vol. 360, pp. 179–211.

James, R. D., Jacobs, J. W., and Glezer, A., 1994, "Experimental Investigation of a Turbulent Jet Produced by an Oscillating Surface Actuator," *Applied Mechancs Reviews,* Vol. 47, pp. S127–S1131.

Jeffery, G. B., 1920, "Plane Stress and Plane Strain in Bipolar Co-ordinates," *Philosophical Transactions of the Royal Society, Series A,* Vol. 221, pp. 265–289.

Kamal, M. M., 1966, "Separation in the Flow Between Eccentric Rotating Cylinders," ASME *Journal of Basic Engineering,* Vol. 88, pp. 717–724.

Kennard, E. H., 1938, *Kinetic Theory of Gases,* McGraw-Hill, NY.

Knudsen, M., 1909, "Die Gesetze der Molekularströmung und der inneren Reibungsströmung der Gase durch Röhren," *Annalen der Physik,* Vol. 28, pp. 75–130.

Kogan, M. N., 1969, *Rarefied Gas Dynamics,* Nauka, Moscow. Translated from Russian, L. Trilling, ed., Plenum, NY.

Kogan, M. N., 1973, "Molecular Gas Dynamics," *Annual Review of Fluid Mechanics,* Vol. 5, pp. 383–404.

Koplik, J., and Banavar, J. R., 1995, "Continuum Deductions from Molecular Hydrodynamics," *Annual Review of Fluid Mechanics,* Vol. 27, pp. 257–292.

Kundu, P. K., 1990, *Fluid Mechanics,* Academic Press, NY.

Landau, L. D., and Lifshitz, E. M., 1987, *Fluid Mechanics,* Second Edition, Pergamon Press, Oxford, United Kingdom.

Liang, W. J., and Liou, J. A., 1995, "Flow Around a Rotating Cylinder Near a Plane Boundary," *Journal of the Chinese Institute of Engineers,* Vol. 18, pp. 35–50.

Liepmann, H. W., and Nosenchuck, D. M., 1982, "Active Control of Laminar-Turbulent Transition," *Journal of Fluid Mechanics,* Vol. 118, pp. 201–204.

Liepmann, H. W., Brown, G. L., and Nosenchuck, D. M., 1982, "Control of Laminar Instability Waves Using a New Technique," *Journal of Fluid Mechanics,* Vol. 118, pp. 187–200.

Lighthill, M. J., 1963, "Introduction. Real and Ideal Fluids," in *Laminar Boundary Layers,* L. Rosenhead, ed., pp. 1–45, Clarendon Press, Oxford, United Kingdom.

Lipkin, R., 1993, "Micro Steam Engine Makes Forceful Debut," *Science News,* Vol. 144, p. 197.

Liu, J., Tai, Y. C., Lee, J., Pong, K. C., Zohar, Y., and Ho, C. M., 1993, "In-Situ Monitoring and Universal Modeling of Sacrificial PSG Etching Using Hydrofluoric Acid," *Proceedings IEEE Micro Electro Mechanical Systems '93,* pp. 71–76, IEEE, NY.

Liu, J., Tai, Y. C., Pong, K., and Ho, C. M., 1995, "MEMS for Pressure Distribution Studies of Gaseous Flows in Microchannels," *Proceedings IEEE Micro Electro Mechanical Systems '95,* pp. 209–215, IEEE, NY.

Loeb, L. B., 1961, *The Kinetic Theory of Gases,* third edition, Dover, New York.

Löfdahl, L., and Gad-el-Hak, M., 1999, "MEMS Applications in Turbulence and Flow Control," *Progress in Aerospace Sciences,* Vol. 35, pp. 101–203.

Löfdahl, L., Glavmo, M., Johansson, B., and Stemme, G., 1993, "A Silicon Transducer for the Determination of Wall-Pressure Fluctuations in Turbulent Boundary Layers," *Applied Scientific Research,* Vol. 51, pp. 203–207.

Löfdahl, L., Kälvesten, E., and Stemme, G., 1994, "Small Silicon Based Pressure Transducers for Measurements in Turbulent Boundary Layers," *Experiments in Fluids,* Vol. 17, pp. 24–31.

Löfdahl, L., Kälvesten, E., and Stemme, G., 1996, "Small Silicon Pressure Transducers for Space-Time Correlation Measurements in a Flat Plate Boundary Layer," ASME JOURNAL OF FLUIDS ENGINEERING, Vol. 118, pp. 457–463.

Loose, W., and Hess, S., 1989, "Rheology of Dense Fluids via Nonequilibrium Molecular Hydrodynamics: Shear Thinning and Ordering Transition," *Rheologica Acta,* Vol. 28, p. 91–101.

Lumley, J. L., 1991, "Control of the Wall Region of a Turbulent Boundary Layer," *Turbulence: Structure and Control,* J. M. McMichael, ed., pp. 61–62, 1–3 Apr., Ohio State University, Columbus, OH.

Lumley, J. L., 1996, "Control of Turbulence," AIAA paper No. 96-0001, AIAA, Washington, D.C.

Lumley, J., and Blossey, P., 1998, "Control of Turbulence," *Annual Review of Fluid Mechanics,* Vol. 30, pp. 311–327.

Majumdar, A., and Mezic, I., 1998, "Stability Regimes of Thin Liquid Films," *Microscale Thermophysical Engineering,* Vol. 2, pp. 203–213.

Majumdar, A., and Mezic, I., 1999, "Instability of Ultra-Thin Water Films and the Mechanism of Droplet Formation on Hydrophilic Surfaces," *Proceedings of the ASME-JSME Thermal Engineering and Solar Energy Joint Conference,* San Diego, CA, 15–19 March.

Mastrangelo, C., and Hsu, C. H., 1992, "A Simple Experimental Technique for the Measurement of the Work of Adhesion of Microstructures," *Technical Digest IEEE Solid-State Sensors and Actuators Workshop,* pp. 208–212, IEEE, NY.

Maureau, J., Sharatchandra, M. C., Sen, M., and Gad-el-Hak, M., 1997, "Flow and Load Characteristics of Microbearings with Slip," *Journal of Micromechanics and Microengineering,* Vol. 7, pp. 55–64.

Maxwell, J. C., 1879, "On Stresses in Rarefied Gases Arising from Inequalities of Temperature," *Philosophical Transactions of the Royal Society Part 1,* Vol. 170, pp. 231–256.

McMichael, J. M., 1996, "Progress and Prospects for Active Flow Control Using Microfabricated Electromechanical Systems (MEMS)," AIAA Paper No. 96-0306, AIAA, Washington, D.C.

Mehregany, M., DeAnna, R. G., Reshotko, E., 1996, "Microelectromechanical Systems for Aerodynamics Applications," AIAA Paper No. 96-0421, AIAA, Washington, D.C.

Migun, N. P., and Prokhorenko, P. P., 1987, "Measurement of the Viscosity of Polar Liquids in Microcapillaries," *Colloid Journal of the USSR,* Vol. 49, pp. 894–897.

Moffatt, H. K., 1964, "Viscous and Resistive Eddies Near a Sharp Corner," *Journal of Fluid Mechanics,* Vol. 18, pp. 1–18.

Moin, P., and Bewley, T., 1994, "Feedback Control of Turbulence," *Applied Mechanics Reviews,* Vol. 47, pp. S3–S13.

Moroney, R. M., White, R. M., and Howe, R. T., 1991 "Ultrasonically Induced Microtransport," *Proceedings IEEE Micro Electro Mechanical Systems '91,* Nara, Japan, pp. 277–282, IEEE, NY.

Muntz, E. P., 1989, "Rarefied Gas Dynamics," *Annual Review of Fluid Mechanics,* Vol. 21, pp. 387–417.

Nadolink, R. H., and Haigh, W. W., 1995, "Bibliography on Skin Friction Reduction with Polymers and other Boundary-Layer Additives," *Applied Mechanics Reviews,* Vol. 48, pp. 351–459.

Nakagawa, S., Shoji, S., and Esashi, M., 1990, "A Micro-Chemical Analyzing System Integrated on Silicon Chip," *Proceedings IEEE: Micro Electro Mechanical Systems,* IEEE 90CH2832-4, Napa Valley, CA.

O'Connor, L., 1992, "MEMS: Micromechanical Systems," *Mechanical Engineering,* Vol. 114, Feb., pp. 40–47.

Odell, G. M., and Kovasznay, L. S. G., 1971, "A New Type of Water Channel with Density Stratification," *Journal of Fluid Mechanics,* Vol. 50, pp. 535–543.

Oran, E. S., Oh, C. K., and Cybyk, B. Z., 1998, "Direct Simulation Monte Carlo: Recent Advances and Applications," *Annual Review of Fluid Mechanics,* Vol. 30, pp. 403–441.

Panton, R. L., 1996, *Incompressible Flow,* Second Edition, Wiley-Interscience, NY.

Pearson, J. R. A., and Petrie, C. J. S., 1968, "On Melt Flow Instability of Extruded Polymers," *Polymer Systems: Deformation and Flow,* R. E. Wetton and R. W. Whorlow, eds., pp. 163–187, Macmillan, London, United Kingdom.

Pfahler, J., 1992, "Liquid Transport in Micron and Submicron Size Channels," Ph.D. thesis, University of Pennsylvania, Philadelphia, Pennsylvania.

Pfahler, J., Harley, J., Bau, H., and Zemel, J. N., 1990, "Liquid Transport in Micron and Submicron Channels," *Sensors and Actuators,* Vol. A21–A23, pp. 431–434.

Pfahler, J., Harley, J., Bau, H., and Zemel, J. N., 1991, "Gas and Liquid Flow in Small Channels," *Symposium on Micromechanical Sensors, Actuators, and Systems,* D. Cho et al., eds., ASME DSC-Vol. 32, pp. 49–60, ASME, NY.

Piekos, E. S., and Breuer, K. S., 1996, "Numerical Modeling of Micromechanical Devices Using the Direct Simulation Monte Carlo Method," ASME JOURNAL OF FLUIDS ENGINEERING, Vol. 118, pp. 464–469.

Piekos, E. S., Orr, D. J., Jacobson, S. A., Ehrich, F. F., and Breuer, K. S., 1997, "Design and Analysis of Microfabricated High Speed Gas Journal Bearings," AIAA Paper No. 97-1966, AIAA, Reston, VA.

Pister, K. S. J., Fearing, R. S., and Howe, R. T., 1990, "A Planar Air Levitated Electrostatic Actuator System," IEEE Paper No. CH2832-4/90/0000-0067, IEEE, NY.

Pong, K.-C., Ho, C.-M., Liu, J., and Tai, Y.-C., 1994, "Non-Linear Pressure Distribution in Uniform Microchannels," *Application of Microfabrication to Fluid Mechanics 1994,* P. R. Bandyopadhyay, K. S. Breuer and C. J. Belchinger, eds., ASME FED-Vol. 197, pp. 47–52, ASME, NY.

Porodnov, B. T., Suetin, P. E., Borisov, S. F., and Akinshin, V. D., 1974, "Experimental Investigation of Rarefied Gas Flow in Different Channels," *Journal of Fluid Mechanics,* Vol. 64, pp. 417–437.

Prud'homme, R. K., Chapman, T. W., and Bowen, J. R., 1986, "Laminar Compressible Flow in a Tube," *Applied Scientific Research,* Vol. 43, pp. 67–74.

Reynolds, W. C., 1993, "Sensors, Actuators, and Strategies for Turbulent Shear-Flow Control," invited oral presentation at the AIAA Third Flow Control Conference, Orlando, FL, 6–9 July.

Richardson, S., 1973, "On the No-Slip Boundary Condition," *Journal of Fluid Mechanics,* Vol. 59, pp. 707–719.

Richter, A., Plettner, A., Hofmann, K. A., and Sandmaier, H., 1991, "A Micromachined Electrohydrodynamic (EHD) Pump," *Sensors and Actuators A,* Vol. 29, pp. 159–168.

Robinson, S. K., 1991, "Coherent Motions in the Turbulent Boundary Layer," *Annual Review of Fluid Mechanics,* Vol. 23, pp. 601–639.

Schaaf, S. A., and Chambré, P. L., 1961, *Flow of Rarefied Gases,* Princeton University Press, Princeton, NJ.

Seidl, M., and Steinheil, E., 1974, "Measurement of Momentum Accommodation Coefficients on Surfaces Characterized by Auger Spectroscopy, SIMS and LEED," *Rarefied Gas Dynamics 9,* M. Becker and M. Fiebig, eds., pp. E9.1–E9.2, DFVLR-Press, Porz-Wahn, Germany.

Sen, M., Wajerski, D., and Gad-el-Hak, M., 1996, "A Novel Pump for MEMS Applications," ASME JOURNAL OF FLUIDS ENGINEERING, Vol. 118, pp. 624–627.

Sharatchandra, M. C., Sen, M., and Gad-el-Hak, M., 1997, "Navier-Stokes Simulations of a Novel Viscous Pump," ASME JOURNAL OF FLUIDS ENGINEERING, Vol. 119, pp. 372–382.

Sharatchandra, M. C., Sen, M., and Gad-el-Hak, M., 1998a, "Thermal Aspects of a Novel Micropumping Device," ASME *Journal of Heat Transfer,* Vol. 120, pp. 99–107.

Sharatchandra, M. C., Sen, M., and Gad-el-Hak, M., 1998b, "A New Approach to Constrained Shape Optimization Using Genetic Algorithms," *AIAA Journal,* Vol. 36, pp. 51–61.

Sherman, F. S., 1990, *Viscous Flow,* McGraw-Hill, NY.

Shih, J. C., Ho, C.-M., Liu, J., and Tai, Y.-C., 1995, "Non-Linear Pressure Distribution in Uniform Microchannels," ASME AMD-MD-Vol. 238, ASME, NY.

Shih, J. C., Ho, C.-M., Liu, J., and Tai, Y-. C., 1996, "Monatomic and Polyatomic Gas Flow through Uniform Microchannels," *Applications of Microfabrication to Fluid Mechanics,* K. Breuer, P. Bandyopadhyay and M. Gad-el-Hak, eds., ASME DSC-Vol. 59, pp. 197–203, ASME, NY.

Smits, J. G., 1990, "Piezoelectric Micropump with Three Valves Working Peristaltically," *Sensors and Actuators A,* Vol. 21–23, pp. 203–206.

Smoluchowski, von M., 1898, "Ueber Wärmeleitung in verdünnten Gasen," *Annalen der Physik und Chemie,* Vol. 64, pp. 101–130.

Sniegowski, J. J., and Garcia, E. J., 1996, "Surface Micromachined Gear Trains Driven by an On-Chip Electrostatic Microengine," *IEEE Electron Device Letters,* Vol. 17, July, p. 366.

Swift, J., 1727, *Gulliver's Travels,* 1906 reprinting, J. M. Dent and Company, London.

Tai, Y.-C., and Muller, R. S., 1989, "IC-Processed Electrostatic Synchronous Micromotors," *Sensors and Actuators,* Vol. 20, pp. 49–55.

Tang, W. C., Nguyen, T.-C., and Howe, R. T., 1989, "Laterally Driven Polysilicon Resonant Microstructures," *Sensors and Actuators,* Vol. 20, pp. 25–32.

Taylor, G., 1972, "Low-Reynolds-Number Flows," *Illustrated Experiments in Fluid Mechanics,* pp. 47–54, National Committee for Fluid Mechanics Films, MIT Press, Cambridge, MA.

Tennekes, H., and Lumley, J. L., 1972, *A First Course in Turbulence,* MIT Press, Cambridge, MA.

Thomas, L. B., and Lord, R. G., 1974, "Comparative Measurements of Tangential Momentum and Thermal Accommodations on Polished and on Roughened Steel Spheres," *Rarefied Gas Dynamics 8,* K. Karamcheti, ed., Academic Press, NY.

Thompson, P. A., and Robbins, M. O., 1989, "Simulations of Contact Line Motion: Slip and the Dynamic Contact Line," *Nature,* Vol. 389, 25 Sept., pp. 360–362.

Thompson, P. A., and Troian, S. M., 1997, "A General Boundary Condition for Liquid Flow at Solid Surfaces," *Physical Review Letters,* Vol. 63, pp. 766–769.

Tien, N. C., 1997, "Silicon Micromachined Thermal Sensors and Actuators," *Microscale Thermophysical Engineering,* Vol. 1, pp. 275–292.

Tison, S. A., 1993, "Experimental Data and Theoretical Modeling of Gas Flows Through Metal Capillary Leaks," *Vacuum,* Vol. 44, pp. 1171–1175.

Tsao, T., Jiang, F., Miller, R. A., Tai, Y.-C., Gupta, B., Goodman, R., Tung, S., and Ho, C.-M., 1997, "An Integrated MEMS System for Turbulent Boundary Layer Control," *Technical Digest (Transducers '97),* Vol. 1, pp. 315–318.

Tuckermann, D. B., 1984, "Heat Transfer Microstructures for Integrated Circuits," Ph.D. Thesis, Stanford University, Stanford, CA.

Tuckermann, D. B., and Pease, R. F. W., 1981, "High-Performance Heat Sinking for VLSI," *IEEE Electron Device Letters,* Vol. EDL-2, No. 5, May.

Tuckermann, D. B., and Pease, R. F. W., 1982, "Optimized Convective Cooling Using Micromachined Structures," *Journal of Electrochemical Society,* Vol. 129, no. 3, C98, March.

Van den Berg, H. R., Seldam, C. A., and Gulik, P. S., 1993, "Compressible Laminar Flow in a Capillary," *Journal of Fluid Mechanics,* Vol. 246, pp. 1–20.

Van Lintel, H. T. G., Van de Pol, F. C. M., and Bouwstra, S., 1988, "A Piezoelectric Micropump Based on Micromachining of Silicon," *Sensors and Actuators,* Vol. 15, pp. 153–167.

Vargo, S. E., and Muntz, E. P., 1996, "A Simple Micromechanical Compressor and Vacuum Pump for Flow Control and Other Distributed Applications," AIAA Paper No. 96-0310, AIAA, Washington, D.C.

Vincenti, W. G., and Kruger, C. H., Jr., 1965, *Introduction to Physical Gas Dynamics,* Wiley, NY.

Wadsworth, D. C., Muntz, E. P., Blackwelder, R. F., and Shiflett, G. R., 1993, "Transient Energy Release Pressure Driven Microactuators for Control of Wall-Bounded Turbulent Flows," AIAA Paper No. 93-3271, AIAA, Washington, D.C.

Wannier, G. H., 1950, "A Contribution to the Hydrodynamics of Lubrication," *Quarterly of Applied Mathematics,* Vol. 8, pp. 1–32.

Warkentin, D. J., Haritonidis, J. H., Mehregany, M., and Senturia, S. D., 1987, "A Micromachined Microphone with Optical Interference Readout," *Proceedings of the Fourth International Conference on Solid-State Sensors and Actuators (Transducers '87),* Tokyo, Japan, June.

Went, F. W., 1968, "The Size of Man," *American Scientist,* Vol. 56, pp. 400–413.

Wilkinson, S. P., 1990, "Interactive Wall Turbulence Control," in Viscous Drag Reduction in Boundary Layers, D. M. Bushnell and J. N. Hefner, eds., *Progress in Astronautics and Aeronautics,* Vol. 123, 479–509, AIAA, Washington, D.C.

Wiltse, J. M., and Glezer, A., 1993, "Manipulation of Free Shear Flows Using Piezoelectric Actuators," *Journal of Fluid Mechanics,* Vol. 249, pp. 261–285.

Young, A. M., Goldsberry, J. E., Haritonidis, J. H., Smith, R. I., and Senturia, S. D., 1988, "A Twin-Interferometer Fiber-Optic Readout for Diaphragm Pressure Transducers," *IEEE Solid-State Sensor and Actuator Workshop,* June 6–9, Hilton Head, SC.

Concentration Profiles in Shallow Turbulent Wakes

R. Balachandar
Associate Professor.
Department of Civil Engineering.

M. F. Tachie
Research Assistant.
Department of Mechanical Engineering.

University of Saskatchewan,
Saskatoon, Canada, S7N 5A9

V. H. Chu
Professor.
Department of Civil Engineering,
McGill University,
Montreal, Canada, H3A 2K6

The present study deals with the noninvasive measurement of concentration in the intermediate shallow turbulent wake region using a video-imaging technique. The flow depths considered in the present study are small compared to the width of the channel and the generated wakes are categorized as shallow. On the basis of the observed behavior, the wakes are classified as deep-shallow wakes and shallow-shallow wakes. The topology of the dye concentration distribution in the near and intermediate wake region indicates that the vortex structure tends to be preserved when the flow depth is relatively high and the dominant eddy structures are similar to that noticed in conventional two-dimensional wakes. In shallow-shallow wakes, the conventional Karman vortex street appears to be annihilated or intermittent. The lateral concentration distribution at several axial stations covering the first thirty body widths are considered for analysis. The instantaneous concentrations are observed to be several times higher than the corresponding mean values. Attempts are also made to determine the paths traversed by the vortex cores and the vortex core convection velocity. The axial variation of the wake half-width with depth of flow is also examined. A model is developed to predict the spread of the wake with downstream distance from the test body. A friction length scale is introduced in the model to account for the influence of depth and bed friction on the development of the wake.

1 Introduction

General Remarks. A convenient way of disposing industrial and municipal wastes is to discharge them into the natural water bodies. The disposed wastes usually have a detrimental impact on both human and aquatic ecosystem. For example, the downstream water quality in a river would depend on the hydrodynamics of transport and mixing of the wastes. Similarly, an increase in the temperature of a river due to heated water discharge may decrease its assimilative capacities for oxygen demanding wastes like sewage effluents (Fischer et al., 1979). As a result, studies have been carried out to better understand the characteristics of these environmentally important flow fields. In many of the flows reported in literature, the primary focus has been on velocity measurement. However, to better understand the dilution process and aid decision making, changes in instantaneous scalar quantities, such as concentration and temperature, are also required. Interestingly, many of the flow fields encountered in the environment can be classified as shallow. Here, a shallow flow is defined as the situation where the horizontal length scale of a typical eddy is significantly larger than the vertical scale (depth of flow).

Turbulent wakes have been studied in the past using conventional single-point instruments such as the hot wire, the thermistor, and the light absorption probe. The statistics obtained from such measurements have been quite useful (Antonia et al., 1991; Browne et al., 1989; Kiya and Matsumura, 1985 and Matsumura and Antonia, 1993). However, during data acquisition, some part of the instrument generally intrudes into the flow. Furthermore, to obtain information about the turbulent structure of the flow, measurement must be made simultaneously at several stations in the flow. The number of measurement stations is quite often limited by the capacity of the data acquisition system available. Moreover, an increase in the number of measurement locations also increases the overall interference effects. It is thus desirable that these measurements be nonintrusive.

Contributed by the Fluids Engineering Division for publication in the JOURNAL OF FLUIDS ENGINEERING. Manuscript received by the Fluids Engineering Division February 18, 1998; revised manuscript received October 15, 1998. Associate Technical Editor: P. W. Bearman.

Previous Studies

Bluff Body Wakes. Turbulent wakes generated by flow past objects have been the focus of many investigations (Townsend, 1949; Antonia et al., 1991; Bisset et al., 1990; Browne et al., 1989; Kiya and Matsumura, 1985; and Matsumura and Antonia, 1993). The wake generator used in many of the earlier studies has been the circular cylinder placed normal to the flow. The flow under such conditions is subject to severe Reynolds number effects (i.e., points of separation shift as the Reynolds number changes) especially in the critical range. As a consequence, the hydrodynamic characteristics have a strong dependence on the Reynolds number (Ramamurthy and Ng, 1973).

Many of the previous studies have been confined to the far wake (Bisset et al., 1990 and LaRue, 1974a and 1974b) where the flow is dynamically similar and approximately self-preserving. A few studies have also been carried out in the near wake by Antonia (1991) and Cantwell and Coles (1983), and in the immediate wake by Fage (1935), Freymuth (1971), Hayakawa and Hussain (1989), and Matsumura and Antonia (1993). Balachandar et al., (1997) remark that earlier measurements in the near and intermediate wakes indicate a qualitative confirmation of loss of organization with increasing distance from the body.

The velocity field has been studied in detail in the past especially using the hot wire anemometer. Kiya (1988) conducted measurements at an axial station eight-body widths downstream of a normal flat plate to obtain the various frequency components of the incoherent velocity fluctuations. Antonia et al. (1991) address the contribution that near wake structures make to the Reynolds stresses and how this contribution varies with distance from the cylinder. Matsumura and Antonia (1993) also examined the contribution of the coherent motion to the transport of both momentum and heat fluxes in the intermediate wake. Hot-wire measurements in the near and intermediate wake of a circular cylinder by Cantwell and Coles (1983), and Hayakawa and Hussain (1989) reveal that the vortex centers can unexpectedly lie very close to the wake axis. Furthermore, using the hot-wire, Cantwell and Coles (1983), Hayakawa and Hussain (1989), and Matsumura and Antonia (1993) have noted that the vortex core convection velocity is about 80 to 90

percent of the freestream velocity for $6 < X/d < 20$. Here, X is the coordinate along the wake axis and d is the diameter of the cylinder.

Some scalar measurements like temperature have also been carried out in the far wake of a circular cylinder by Antonia et al., (1991) and LaRue (1974) and in the intermediate wake by Fage and Falkner (1935), Freymuth (1971), and Matsumura and Antonia (1993). These structures have been studied with regard to the spectra of temperature fluctuations.

There is experimental evidence (Balachandar et al., 1997; Hinze, 1959; LaRue, 1974b; and Kovasznay, 1949) to suggest that the wake half-width obtained from scalar measurements (δ_{sc}) in two-dimensional wakes is wider than the corresponding values obtained from velocity measurements (δ_v). In the near region, it has been noted that the ratio δ_{sc}/δ_v is between 1.5 and 2.5. In the far wake, however, this ratio varies from 1.3 to 1.6. In the case of an axisymmetric wake generated by a sphere, Freymuth and Uberoi (1971) note that the half-width of the temperature profile is only faintly wider than the corresponding width of the velocity profile. One should note that a two-dimensional wake is more strongly organized than the wake of an axisymmetric bluff body.

Shallow Wakes. Most of the previous experiments were conducted in test sections of large depths compared to the width of the wake. However, many turbulent shear flows exist in shallow environments, where the horizontal length scale is significantly large compared to the depth of the flow field (Burger and Wille, 1972; Ingram and Chu, 1987; and Wolanski et al., 1984). The vortex wakes downstream of islands in Rupert Bay (Figs. 3(a) to 3(f) in Ingram and Chu, 1987) are typical examples. Moreover, effluent discharge into shallow waters is often encountered in engineering practice. A few studies have been conducted to study the characteristics of shallow wakes (Balachandar et al., 1993 and Ingram and Chu, 1987).

The present study deals with the measurement of concentration profiles in intermediate shallow turbulent wakes. The study focuses on the instantaneous dye concentration measurement in a non-invasive fashion using a video-imaging technique. Extensive experiments are conducted to study the influence of flow depth and bed friction on the concentration distribution in shallow wakes generated by a flat plate normal to the flow direction.

2 Theoretical Considerations

Deep Wakes. For the flow under consideration, two distinct turbulence scales can be distinguished. There is a large-scale (vortex) motion generated by the test body and a small-scale motion generated by bed friction. The bed friction, besides generating the small-scale motion, exerts a stabilizing influence on the large-scale motion. The transverse flow is stable if the bed friction influence is sufficiently strong to suppress the development of the large-scale disturbance. As a consequence, the spanwise extent of the wake will be limited once the flow becomes stabilized. Moreover, the free water surface and the channel bed impose a restriction on the vertical length scale of the turbulent motion.

The model formulation considered here is based on a Lagrangian averaging procedure and the concept of a dominant eddy. Here, "dominant eddy" refers to a large-scale coherent structure of the turbulent motion that extends across the width of the wake. An obstruction (e.g., the test body) will generate large-scale dominant eddies, which move with a slower velocity relative to the external flow and produce a velocity defect (u) and a momentum defect (M). The following assumptions are made in the model formulation: (i) The flow is turbulent and quasi-two dimensional; (ii) the mean flow velocity transverse to the main flow is negligible compared to the streamwise flow velocity (U); (iii) the static pressure variation across the wake is negligible; and (iv) the flow is essentially parallel and with the aid of depth averaging, the pressure gradient can be defined as: $dP/dX = \rho C_f U^2/2h$. Here, C_f is the skin friction coefficient and h is the depth of flow.

A material volume consisting of dominant eddies produced over one unit of time will have a length equal to $(U - u)$. Figure 1 shows a definition sketch and the coordinate system adopted. Here, "X" refers to the coordinate measured from the body along the axis of the wake and "Y" is the lateral coordinate measured from the axial plane. The momentum defect in a unit time, M, associated with the material volume is given by: $M = 2\rho bhu[U - u]$. Here, h and b are, respectively, the depth of flow and one half of the wake width and ρ is the fluid density. Newton's second law of motion applied to the material volume will yield:

$$dM/dt = F_f - F_p = \rho C_f b\{[U - u][(U - u)^2 - U^2]\} \quad (1)$$

where F_p and F_f refer to the pressure force and bed frictional force, respectively. Rearranging and simplifying, one obtains:

$$dM/dX = -(MC_f/2h) - \rho C_f b[U^2 - U(U - u)] \quad (2)$$

If one assumes that $u \ll U$, Eq. (2) can be simplified and integrated to yield:

$$M(X) = M_o \exp(-C_f X/2h) \quad (3)$$

In Eq. (3), M_o is the initial momentum defect of the wake. This equation reveals that M decays exponentially with downstream distance due to the presence of bed friction. In very deep flows (i.e., for $h \to \infty$), M essentially stays constant.

An entrainment hypothesis is introduced to complete the formulation. The rate of growth of the wake is assumed to be proportional to the velocity defect, i.e.,

$$db/dX = \alpha^* u/[U - u] \quad (4)$$

In the above equation, α^* is a measure of the entrainment coefficient. Making use of assumption 3, one can write: $C_d dU^2 = 2ub[U - u]$. With $u \ll U$, this can be simplified to:

$$u/[U - u] = C_d d/2b = \theta/2b \quad (5)$$

Here, C_d is the drag coefficient and θ is the momentum thickness. Combining Eqs. (4) and (5) and integrating, one can obtain: $b = [\alpha^* \theta X]^{1/2}$. Theoretical evaluation of b from velocity consideration in the far wake of a circular cylinder (Schlichting, 1979) gives:

$$b = 0.57[C_d X d]^{1/2} = 0.57[\theta X]^{1/2} \quad (6)$$

Moreover, the wake half-width based on velocity measurement (δ_v) is typically equal to $0.441b$. Hence, Eq. (6) can be rewritten as:

$$\delta_v/\theta = 0.25[X/\theta]^{1/2} \quad (7)$$

On studying the limited wake velocity data available in literature for near and intermediate wakes, one notes that a relationship similar to Eq. (7) can be found to exist (Fig. 12(a)). One can now take into consideration some experimental evidence (Balachandar et al., 1997; Hinze, 1959; and LaRue, 1974b) with regard to the relative magnitudes of half-width obtained from scalar measurements (δ_{sc}) and velocity measurements (δ_v) in two-dimensional wakes. If one assumes $\delta_{sc} = 1.8\delta_v$ in the intermediate wake, Eq. (7) would yield:

$$\delta_{sc}/\theta = 0.45[X/\theta]^{1/2} = \alpha[X/\theta]^{1/2} \quad (8)$$

Equation (8) is valid for deep wakes and serves to provide an initial estimate of 0.45 for the value of α at other flow depths.

Shallow Wakes. The development of a wake depends on the extent of entrainment, or specifically on the entrainment coefficient. The transverse spreading rate decreases as the friction influence becomes more important, especially in the far

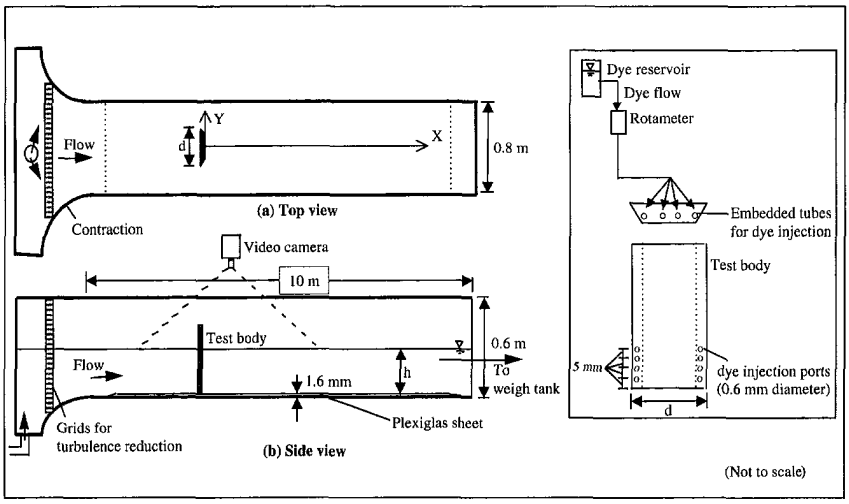

Fig. 1 Experimental setup (inset: schematic of dye injection device)

field. Consistent with Eq. (3), one would expect a deep wake ($h \to \infty$) to grow without bound. On the contrary, the development of shallow wake is limited in extent due to the stabilizing influence of bed friction. In order to account for the effects of depth and bed friction on the entrainment process in quasi-two dimensional shallow wakes, dimensionless bed friction parameters have been proposed by various researchers. In this context, a friction length scale defined as $L_f = h/C_f$, is a useful geometric scale. In the present study, a dimensionless bed friction number is defined as:

$$S = C_f X/h \tag{9}$$

Furthermore, earlier studies (Ingram and Chu, 1987) have shown that while the bed friction tends to stabilize the flow, the transverse shear tends to de-stabilize the flow field. As will be shown later, the Karman vortex street formed behind a two-dimensional bluff body will be annihilated if the flow depth is small. Detailed descriptions of the wake flow field are provided in a subsequent section. However, for the development of the model, one can trace the absence of the Karman vortex street to a bed friction effect. In this context, one can define a wake stability parameter S_w as:

$$S_w = C_f d/h \tag{10}$$

If S_w were less than a certain critical value, one would expect a vortex street to be formed. On the other hand, if S_w is sufficiently large, the shear layers developed along the two sides of the wake would be stabilized and no vortex street would be formed. On studying Eq. (10), the following remarks can be made:

(*i*) For a given depth of flow (h) and size of the wake generator (d), S_w would increase if the skin friction coefficient increases (i.e., if the bed becomes more rough, no vortex street is likely to form).

(*ii*) If h and C_f were held constant, one would expect S_w to increase with increasing size of the wake generator (i.e., a larger wake generator is expected to provide a narrower normalized half-width).

(*iii*) For a given skin friction coefficient and body size, S_w would increase with decreasing depth (i.e., a shallower wake is less likely to have Karman vortex street).

The calculation of the entrainment or spreading rate depends on the entrainment hypothesis adopted. The value of the entrainment coefficient (α) depends on the depth of flow, and at a given depth, it also varies along the wake axis. For the present study, the entrainment coefficient is assumed to be influenced by the bed friction, rather than being constant (as would be the case in very deep flows). One should also note that the assumption of constant entrainment hypothesis would lead to overestimating the entrainment and mixing in shallow flows. Using the friction length scale as the appropriate scaling parameter and following Babarutsi et al. (1989), one can define an entrainment coefficient α as follows:

$$\alpha = \alpha_o[1 - S/S_c] \text{ if } S < S_c \text{ and } \alpha = 0 \text{ for } S \geq S_c \tag{11}$$

Here, S is given by Eq. (9) and α_o is a function of the depth of flow. Further, α_o and S_c (critical bed friction number) are model coefficients to be determined from experimental data. The above equations reveal that the entrainment coefficient (α) decreases as α_o decreases or as S increases (i.e., when the depth becomes more shallow or in the far wake region). In the case of deep flow ($h \to \infty$), $S \to 0$ and α remains constant ($\alpha = \alpha_o$). One would therefore expect very deep wakes to grow indefinitely. In shallow wakes, on the other hand, the spread assumes an asymptotic value once $S = S_c$. In such cases, further growth of the wake is arrested and M continues to decay. From Eqs. (8) and (11), one can write a generalized equation as:

$$\delta_{sc}/\theta = \alpha_o[1 - S/S_c][X/\theta]^{1/2} \tag{12}$$

3 Experimental Arrangement

Video Imaging Technique. Recent advances in flow visualization techniques and the use of video imaging procedures have removed many of the limitations associated with conventional instrumentation. One effective way of studying concentration distribution and the structure of the turbulent motion is to introduce dye into the flow and capture video images of the visual flow field. The color that is recognized at each pixel on a digitized image is a combination of the three primary colors (red (R), green (G), and blue (B)). The R, G, and B values can be used to convert the qualitative images into useful concentration data (Tachie, 1997).

It is known that the absorption of light increases with increasing dye concentration. As a result, if the dye concentration were higher, the digitized images would appear darker and indicate lower values of R, G, and B. At a fixed concentration, the absorption of light would also increase with increasing depth of flow. For all other conditions remaining the same, a certain concentration would indicate lower values of R, G, and B at larger depths when compared with the data obtained at shallower depths. Consequently, these aspects have to be taken into account in the development of a procedure to convert qualitative

flow visualization images into useful quantitative concentration data. With a proper calibration, the qualitative visual images can then be analyzed to obtain very useful quantitative concentration information. Details of the calibration procedure and use of the video camera to measure dye concentration are available in Tachie (1997) and are avoided here for brevity. Comparing results with conventional light absorption probe measurements at similar test conditions has validated the use of video imaging technique to measure concentration. Parameters such as lighting conditions and initial dye injection concentration were chosen such that there would be no saturation of the pixel values at the highest concentration encountered. It should also be remarked that the instantaneous concentration measurement reported herein is effectively an integrated measurement along a line of depth. To ensure that this measurement is meaningful, concentration measurements were obtained using a light absorption probe at one-third, mid, and two-thirds of the depth. The maximum deviation in the three measurements was less than 5 percent.

Comparison of the present video imaging technique to previous nonintrusive concentration measurement techniques such as light-induced fluorescence (LIF) is in order. LIF technique has been proven to be quite useful to measure concentration in a few earlier jet studies (Dahm and Dimotakis, 1987 and Paul et al., 1990). From the reported results, it can be noted that the spatial resolution is higher in the LIF technique. The LIF can also be used to provide an estimate of the instantaneous concentration along the depth of the flow using an array of photodiodes (Koochesfahani and Dimotakis, 1985). However, as remarked earlier, for the present flow configuration, the variation of the instantaneous concentration across the depth is not significant and, the present video-imaging technique is quite useful in estimating concentration over a larger region of the flow field ($0 \leq X/d \leq 30$). The ability to obtain the concentration over a larger area of the flow field is the main advantage of the present method. Besides this, the simplicity and cost of the setup are other major advantages. The image area of 0.8 m $\times$ 2 m in the present study is significantly greater than the image areas of previous LIF studies. Corresponding areas of previous LIF studies were less than 20 cm $\times$ 20-cm even when extremely powerful laser light sources were used for illumination.

Experimental Setup and Procedure. The experiments were conducted in a rectangular cross-section open channel flume (Fig. 1). The flume was 0.6 m deep, 0.8 m wide, and 10 m long. A contraction and several stilling arrangements to reduce any large-scale turbulence in the flow preceded the straight section of the channel. The vertical walls of the channel were made of glass to facilitate visual observation along the depth of flow. The bottom of the channel was made of a white acrylic sheet. This provided a uniform background for the camera looking from above (Fig. 1). Furthermore, four 500 W lamps were strategically placed around the flow field to ensure uniform lighting over the region of interest. In order to eliminate or reduce the dependence of the hydrodynamic characteristics on the flow Reynolds number, a flat plate with sharp edges mounted normal to the flow was used to generate the wake. The flat plate was mounted about 1.5 m downstream of the contraction on the acrylic sheet.

Dye of known concentration (C_o) and flow rate (q_o) was introduced into the wake immediately behind the plate close to the flow separating point. The dye was introduced at $X/d = 0$ in two layers to ensure uniform mixing along the depth (h) of flow. Dye injection was controlled so as not to cause any significant induced velocity. A special type of dye (Triactive-Red, Tri-tex Inc., Quebec) was found to be very suitable in terms of providing measurable concentration levels in the latter part of the intermediate wake and also have a low enough dye injection rate (q_o) so as not to disturb the wake. The value of the diffusion coefficient (D) was evaluated using the experimental molar volume at its boiling point (provided by the dye manufacturer). The effective Schmidt number (ν/D), was of the order of 10^3. The value of the Schmidt number indicates that the diffusion of the dye particles on a molecular scale is extremely low. The dye injection rate was measured using a rotameter. The mass flow rate was measured using a weigh tank. The freestream mean velocity upstream of the test body was evaluated from the mass flow rate measurement.

A summary of the test conditions is shown in Table 1. For the purpose of easy identification, a notation of the form d_ih_j is used to describe the test conditions. In particular, i (=2, 4) and j (= 1, 2, 3, 4, 6 and 8) denote the width of the test body (in cm) and depth of flow (in cm), respectively. At d = 4 cm and h = 4 cm, three tests (test d_4h_4A, d_4h_4B, and d_4h_4C) were conducted. Tests d_4h_4A and d_4h_4B were conducted at similar conditions while Test d_4h_4C was at a higher freestream velocity. Test d_4h_4A was primarily used as a basis for validating the video imaging technique. The initial dye concentration C_o was set at 25 g/l in all the tests except d_4h_4A where C_o was 30 g/l.

The video images of the flow field were obtained using the video camera located directly above the wake region. On reviewing the tape, several images of the flow field were digitized and chosen for analysis. Using an in-house computer program (Dye Concentration Analysis Program—DCAP) developed using Visual Basic, the digitized images of the flow field were converted into concentration contours.

4 Results and Analysis

Visual Observations. In the present series of tests, the depths of flow are small ($10 \leq h$ (mm) ≤ 80) when compared to both the width of the channel (800-mm) and the width of the wake. Consequently, the wake flows can all be considered shallow (Babarutsi et al., 1989). On the basis of the presence or absence of the Karman vortex street, the flows are qualitatively classified as deep-shallow wakes or shallow-shallow wakes. The flow is denoted as a deep-shallow wake when the formation of the Karman vortex street is continuous. This is done, as the flow field based on visual observation is structurally similar to the conventional two-dimensional bluff body wake. On the other hand, the flow is classified as a shallow-shallow wake when there is an absence or intermittent Karman vortex street. Consistent with this observation, in Table 1, $h \geq 3$ cm is classified as deep-shallow wakes and $h < 3$ cm is considered as shallow-shallow wakes.

Typical deep-shallow wake flow patterns are shown in Fig. 2. Images (a), (b), (c), and (d) correspond to tests d_4h_8, d_4h_6, d_4h_4B, and d_4h_4C, respectively. The color contour (concentration variation) in each of the images in Fig. 2 will be discussed in the following section. One can observe from each of these images that the vortices are distinct and fairly well organized. The vortices observed in tests d_2h_3 and d_2h_4 (not shown here) appeared less organized when compared with those shown in Fig. 2. Similar images for shallow-shallow wakes are shown in Fig. 3. At h = 1 cm (i.e., Images (a) and (e)), the wakes are devoid of the Karman vortex street. As is well known, the primary reason for the formation of the vortex street is interaction of the flow separating from the two edges of the test body (Schlichting, 1979). In the very shallow flows, no such interaction was noticeable. The wake regions are also narrow in these tests. In tests d_4h_2 and d_2h_2, intermittent vortex shedding was noted for about 50 to 60 percent of the observation time. As a consequence, the flow patterns vary from time to time, as depicted in Images (b) to (d) and Images (f) to (h), respectively, for tests d_4h_2 and d_2h_2. Image (d) is for a typical instant at which Karman vortex street was observed. However, such vortices are relatively weak and less organized when compared to those observed at deeper depths. The degree of variation from the classical two-dimensional Karman vortex street description increased with increasing downstream distance from the plate. At

Table 1 Summary of test conditions

Test	d (cm)	h (cm)	U (cm/s)	Re = Ud/ν	$S = fd/U$	S_w	Remark
d_4h_4A	4.0	4.0	10.01	3100	0.143	0.0076	KVS*
d_4h_1	4.0	1.0	7.60	2330	—	0.0452	No KVS
d_4h_2	4.0	2.0	10.53	3230	0.149	0.0176	Intermittent#
d_4h_4B	4.0	4.0	9.83	3010	0.156	0.0076	KVS
d_4h_4C	4.0	4.0	15.69	4810	0.151	0.0068	KVS
d_4h_6	4.0	6.0	10.47	3210	0.157	0.0046	KVS
d_4h_8	4.0	8.0	10.16	3110	0.155	0.0033	KVS
d_2h_1	2.0	1.0	10.20	1570	—	0.0210	No KVS
d_2h_2	2.0	2.0	10.30	1590	0.159	0.0088	Intermittent
d_2h_3	2.0	3.0	11.43	1750	0.156	0.0052	KVS
d_2h_4	2.0	4.0	10.52	1620	0.146	0.0038	KVS

* KVS denotes continuous presence of Karman vortex street.
# Intermittent means the presence and absence of the Karman vortex street alternate.

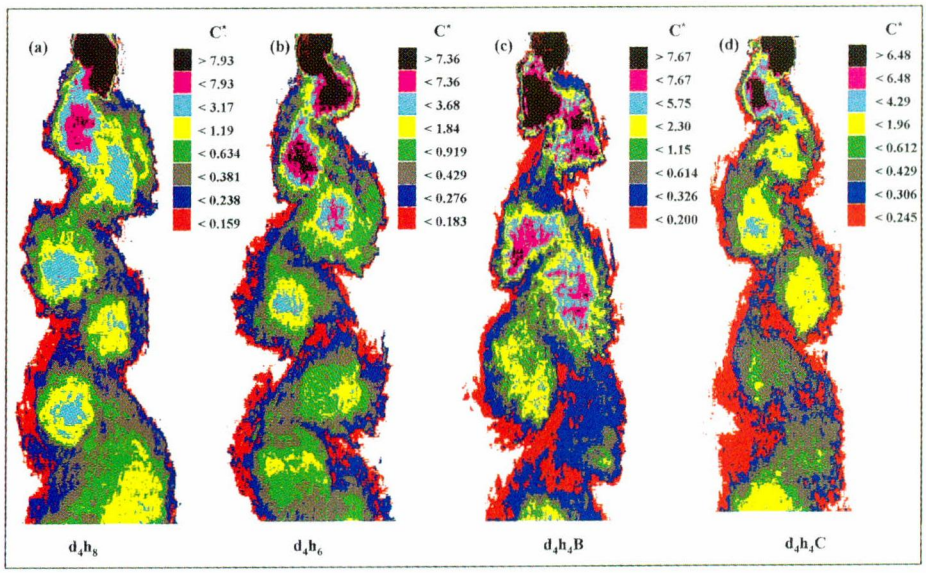

Fig. 2 Concentration contours in deep-shallow flows

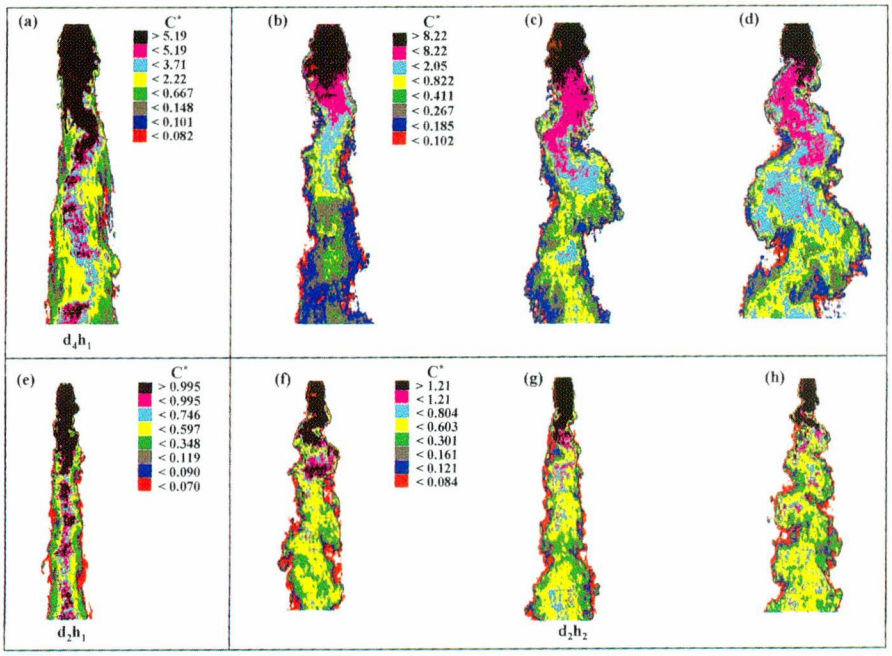

Fig. 3 Concentration contours in shallow-shallow flows

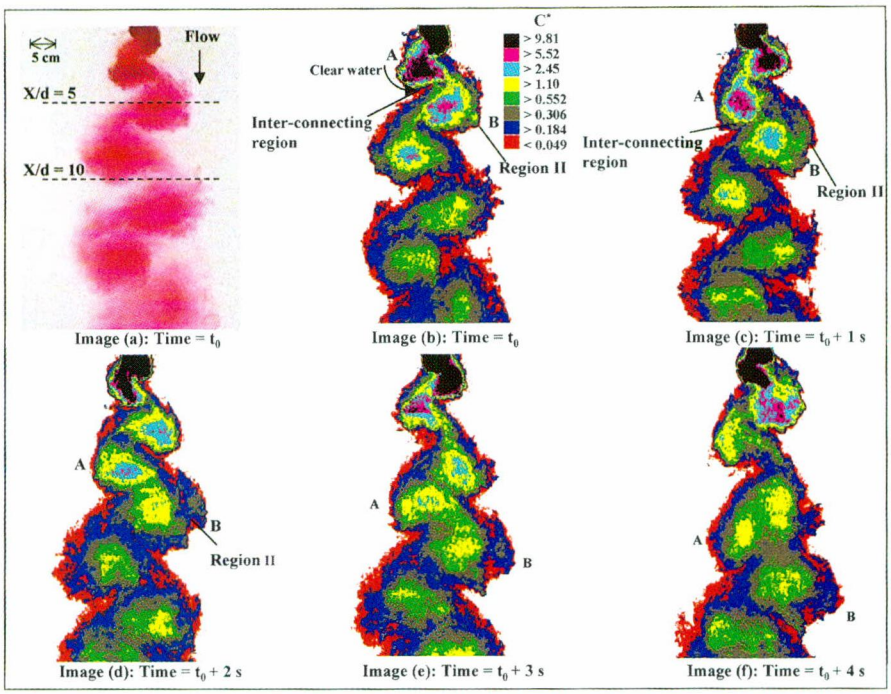

Fig. 4 Original and analyzed video images of the wake (Test d_4h_6)

some instances, the vortex cores were visually found to lie very close to the wake axis. This behavior has also been noted by other researchers (Cantwell and Coles, 1983 and Hayakawa and Hussain, 1989) in the near wake of circular cylinders. As the vortices traveled downstream from the body, they entrained the surrounding fluid and increased in size. As a consequence, the concentration in the core of the vortices appeared to decrease, as visually evidenced from the decrease in the dye color intensity.

Topology of Concentration Field. Figure 4 shows the digitized images of the wake at various instants of time for test d_4h_6. In this figure, Image (a) is the original digitized image, while Image (b) shows the corresponding concentration contour evaluated using DCAP. Images (b) to (f) show the development of the wake over a period of 4 seconds. The color code is indicated adjacent to Image (b). In the color code, $C^* = ChUd/C_oq_o$ is a dimensionless concentration. In each of these images, the flow is from the top to the bottom. It is clear from these images that the dye concentration immediately behind the plate is very high (black color). Following the vortex shedding mechanism, all the injected dye is entrained into the developing vortex on one side of the wake (e.g., right side of the test body in Image (b)). At a later instant, the dye is entrained into the succeeding vortex forming on the other edge of the plate (e.g., left side of the test body in Image (c)).

With the prequalification that the present concentration contours are valid for two-dimensional flows, attempts can be made to understand how the dye is diluted in the wake. Consider two vortices indicated as A and B in Image (b), one on either side of the wake axis. It can be observed from these vortices that the core regions have a very high concentration (black or magenta color). The concentration decreases from the core toward the outer edge of the vortex (Region II). At time t_o, the inter-connecting region between the two vortices also has a low concentration. The color topology indicates that the inter-connecting region is dominated by red and dark blue color. Given the opposite sense of rotation of A and B, one would expect entrainment of the ambient clear water into the inter-connecting region between the two vortices from the left side of the wake axis.

On following these vortices to a latter instant in time (t_o + 1 s), their overall shapes tend to be preserved. The peak concentrations in the cores still maintain values close to that noticed at time t_o and the distribution of concentration within the vortices also appears to be preserved. Thus, in the near and the intermediate wake regions, the images indicate that the preferential mode of transportation of the dye is by the larger scales. However, the local transport of dye out of the vortex may be due to the small scales. The black or magenta areas in the cores of vortices A and B, indicating a larger concentration, are decreased in size in Image (c). The area of the inter-connecting region between vortices A and B is increased in Image (c) when compared to Image (b). Furthermore, the concentration of dye in this area is also increased with a significant presence of green and gray. It is important to note that both A and B lose concentration to the inter-connecting region between the two vortices.

In studying the transport of a scalar in the wake of a circular cylinder using a complex hot-wire probe, Matsumara and Antonia (1993) obtained contours of phase averaged coherent and random heat flux vectors. Using this information, they arrived at a description of the near wake scalar transport similar to the one provided above. However, their results indicate that at $X/d = 10$, the net scalar transport associated with the vortical motion occurs only in the downstream region of the vortex.

As the two vortices travel further (Images (d), (e), and (f)), the concentration topology within the vortices tends to be similar to that noticed in Image (b). The core of the vortices see a gradual decrease in concentration. As a result of entrainment of ambient (clear) water, the inter-connecting region increases significantly in size and thereby decreases the overall concentration. The area indicated as Region II in each of the images shows only a slight change in concentration distribution and no flow is taking place from the core into Region II. These results point to the fact that the scalar transport in the wake (leading to dilution) is taking place from the vortex into the inter-connecting region. The rotational motion within the vortices does not contribute to the transport of dye out of the vortex.

The concentration contours indicated in each of the images in Fig. 2 (deep-shallow wakes) are consistent with the description

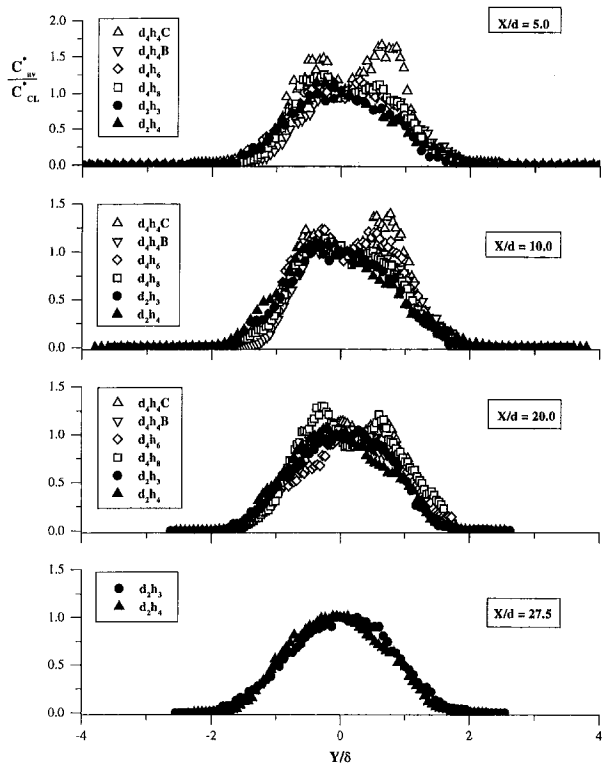

Fig. 5 Normalized concentration across the wake at $h \geq 3$ cm (Uncertainty in $C^* = \pm 8$ percent, in $Y/\delta = \pm 4$ percent)

noted in Fig. 4. In Fig. 3 (shallow-shallow wakes), the dye concentration at larger distances from the plate is still very high and have values close to that found immediately behind the plate (i.e., black color).

Lateral Concentration Profiles

Mean Profiles. Using 50 to 60 images such as those shown in Fig. 4, acquired in time intervals of one-third of a second, one can calculate the average concentration, C^*_{av} at any station in the wake. The fifty images used to compute C^*_{av} correspond to about 12 to 28 vortices passing through the axial stations. The data obtained in the tests with $h \geq 3$ cm at $X/d = 5.0$, 10.0, 20.0 and 27.5 are presented in Fig. 5. In this figure, the concentration values across the axial stations are normalized by the corresponding values on the wake axis, while the lateral locations are normalized by the wake half-width (δ). The characteristic double peaks noted in this figure in the tests with $d = 4$ cm are indication of the presence of a strong and well organized alternating Karman vortex street that prevails at these stations. As a result of dilution, these double peaks become less distinct at larger X/d. This is consistent with the results of Balachandar et al. (1997). No well-defined double peaks are noted in tests d_2h_3 and d_2h_4. This is partly due to the reduced organization of the vortical structures in these tests and partly due to the limitations in the spatial resolution of the technique used. With the exception of the data of test d_4h_4C, at $X/d = 5.0$ and 10.0, all the profiles nearly collapsed onto a single curve. The reason for the deviation in test d_4h_4C may be attributed to the fact that, in obtaining C^*, the freestream velocity (U) has been used. The value of U is higher in test d_4h_4C when compared to the other tests (see Table 1). In fact, a more appropriate choice of the velocity scale would be the local velocity, and not U.

Figure 6 shows the mean concentration distributions at $h \leq 2$ at various axial locations. The absence of the double peaks at $h = 1$ and 2 cm in either set of tests is not unexpected. As noted earlier, the absence of the Karman vortex street (or its intermittent nature at $h = 2$ cm) is responsible for this observation.

In many instances (e.g., mixing of pollutant and fuel), the value of the maximum concentration is the major decision parameter. In order to illustrate the variations in the maximum concentration distribution across the wake, two typical plots are presented in Figs. 7(a) and 7(b). In each of these plots, the corresponding variations of the minimum, time-averaged mean and the r.m.s. concentrations are also shown. Figure 7(a) (Test d_4h_4B, $X/d = 10$) shows that the peak of the maximum concentration distribution is approximately 450 percent greater than the corresponding peak of the mean profile. One also notes from Fig. 7(b) (test d_2h_4) that the peak value of the maximum profile is still about 200 percent greater than the corresponding peak of the mean profile at 27.5 diameters downstream of the plate. The r.m.s. profiles show a variation similar to the mean concentration profiles.

Instantaneous Profiles. The instantaneous concentration distribution is also a useful decision parameter. To gain a better understanding of the concentration distribution in the wake, the instantaneous concentration data at five different instants of time are shown in Fig. 8 for Test d_4h_6 at $X/d = 5$. Due to the nature of the Karman vortex street, the concentration values across the wake vary from one instant to the other. For comparison purposes, the corresponding C^*_{av} values are also indicated in each of these plots. It can be seen that the instantaneous concentrations can be three to four times larger than the C^*_{av} values. This is an aspect of concern in environmentally important flows, especially when one is dealing with pollutant dispersion.

Axial Concentration Profiles. Figure 9 shows the plots of the instantaneous concentration distribution along the wake axis at five instants in time for test d_4h_4A. Also shown in each of these plots are the average values obtained from a set of 50 frames. A rapid decay is noted in the region $X/d \leq 10$. The

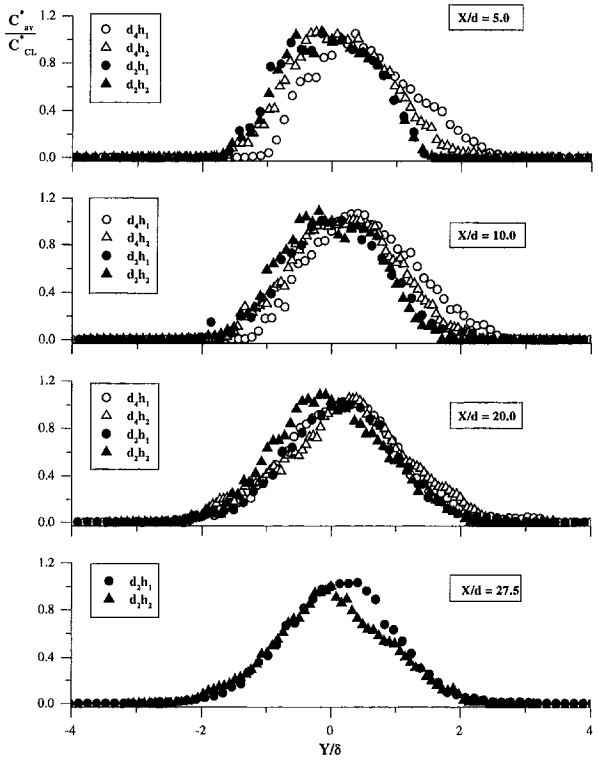

Fig. 6 Normalized concentration across the wake at $h = 1$ and 2 cm (Uncertainty in $C^* = \pm 8$ percent, in $Y/\delta = \pm 4$ percent)

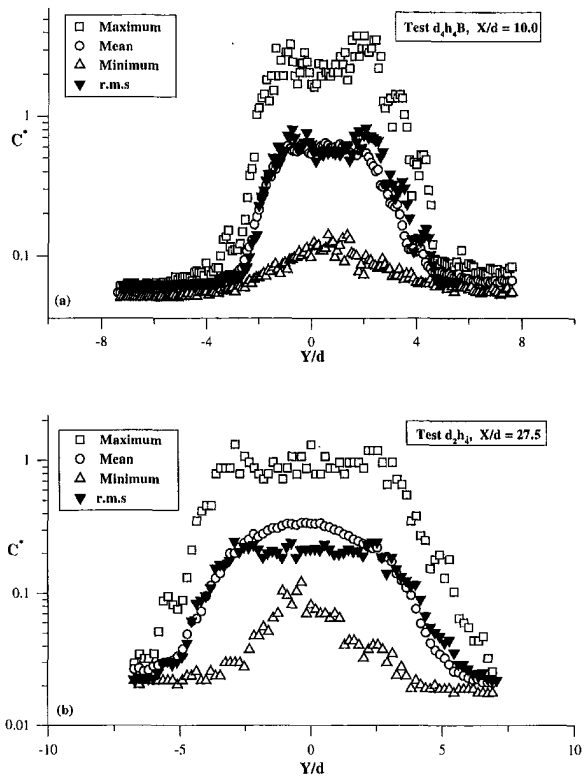

Fig. 7 Lateral variation of typical maximum, minimum and r.m.s concentrations (Uncertainty in C^* = ±8 percent, in Y/d = ±3 percent)

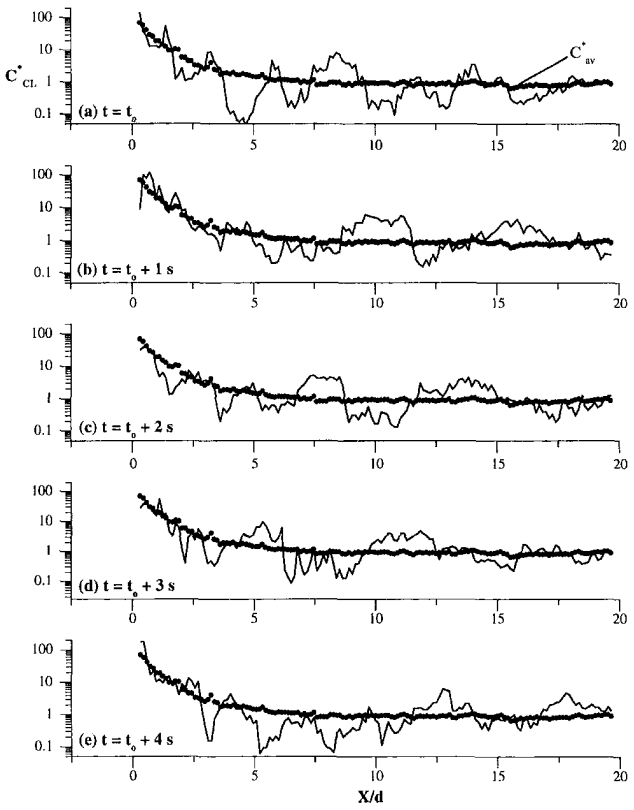

Fig. 9 Variation of instantaneous concentrations along the wake axis (Test d_4h_4A) (Uncertainty in C^* = ±8 percent, in X/d = ±3 percent)

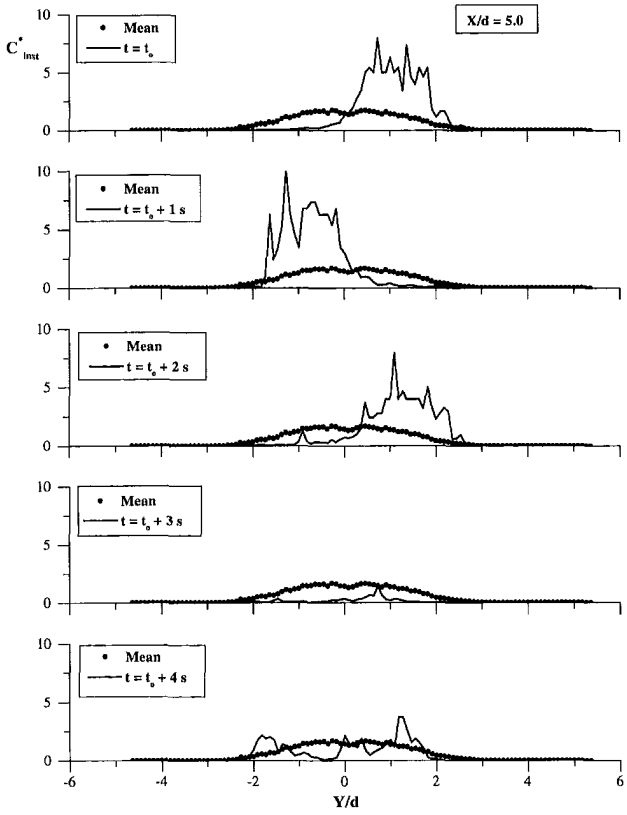

Fig. 8 Lateral variation of instantaneous concentrations (Test d_4h_6) (Uncertainty in C^* = ±8 percent, in Y/d = ±3 percent)

changes in the average concentration along the wake axis beyond X/d = 10 are negligible. These can be attributed to the reduced entrainment of ambient clear water into the wake region. It can also be noted that the instantaneous concentrations vary quite significantly from the average values.

Vortex Centers and Core Velocity. As demonstrated by Matsumura and Antonia (1993), the location of maximum temperature within the vortex corresponds approximately to the location of the extremum in vorticity at all X/d in the intermediate wake. They, however, drew attention to the fact that temperature becomes a less effective marker of the vortices at larger X/d. Zhou and Anontia (1992) identified a similar difficulty. On the basis of this revelation, the video images and DCAP can be used to locate the vortex cores. In this context, a vortex core (Y_c) refers to the point of maximum dye concentration within a vortex. In order to determine the vortex cores most accurately, the ranges of the color codes, as indicated in Image (b) of Fig. 4, can suitably be chosen to minimize the area of maximum concentration within the vortex. Furthermore, by following the locus of a vortex core in succeeding frames, one can also calculate variables such as the vortex core convection velocity.

Figure 10(a) shows the variation of the axial distance, from the test body, of the core locations of two neighboring vortices A and B (similar to Fig. 4), one on each side of the wake axis, (test d_4h_4A) with time. The average longitudinal convection velocity (U_c) for A and B in the axial direction is found to be $0.88U$. This value compares favorably with previous (Cantwell and Coles, 1983; Hayakawa and Hussain, 1989; and Matsumara and Antonia, 1993) hot wire data in the wake of circular cylinder.

In order to gain better insight into the path a vortex takes once it is shed, plots of lateral vortex core locations relative to the wake axis (Y_c) with downstream distance from the test body are shown for some of the tests. A plot depicting three pairs of

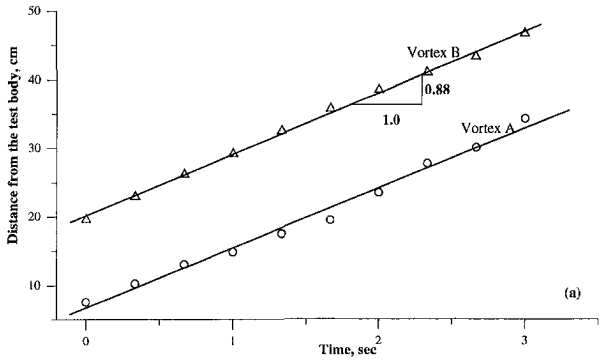

Fig. 10(*a*) Variation of axial location of vortex core centers with time (Test d_4h_4A) (Uncertainty in distance = ±0.5 mm)

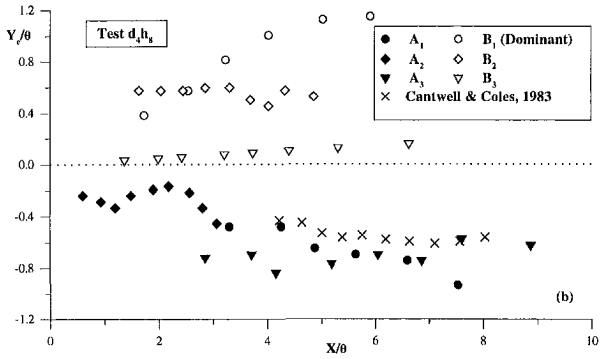

Fig. 10(*b*) Locus of vortex core centers (Uncertainty in Y_c/θ = ±5 percent, in X/θ = ±3 percent)

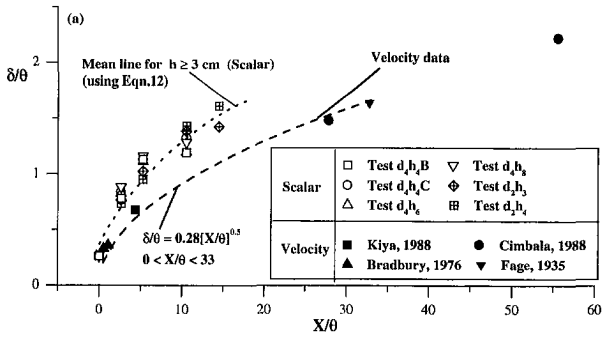

Fig. 12(*a*) Variation of wake half-width with downstream distance from the test body at $h \geq 3$ cm (Uncertainty in δ/θ = ±4 percent, in X/θ = ±3 percent)

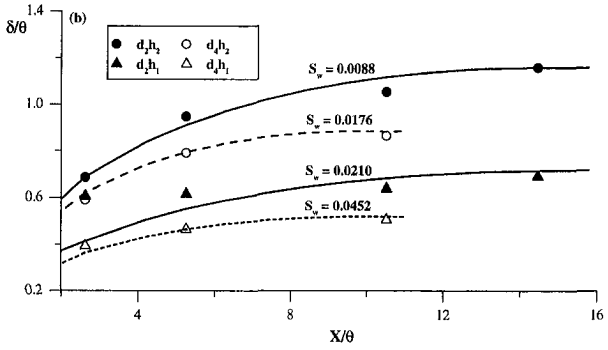

Fig. 12(*b*) Variation of wake half-width with axial distance from the test body in shallow-shallow wakes (Uncertainty in δ/θ = ±4 percent, in X/θ = ±3 percent)

vortices (A_1, B_1; A_2, B_2; A_3, B_3) for test d_4h_8 is shown in Fig. 10(*b*). A pair of vortices consists of two neighboring vortices, one on each side of the wake axis. It is important to note that B_3 is extremely close to the wake axis ($Y_c/\theta \leq 0.15$). This observation was, however, noted for only 8 percent of the observation time while the dominant mode (A_1, B_1) occurs 53 percent of the time. In this plot, the data of Cantwell and Coles (1983) obtained in the two-dimensional wake of circular cylinder using a complicated measuring technique are also shown and compare well with the present data.

The Wake Half-Width. Using Eq. (12) and the appropriate model coefficients, one can predict the variation of δ/θ with axial distance. Figure 11 shows the value of the model coefficients as a function of flow depth. As indicated earlier, a value of 0.45 was used as the first estimate of α_o. The first estimate of S_c was obtained by noting the axial location beyond

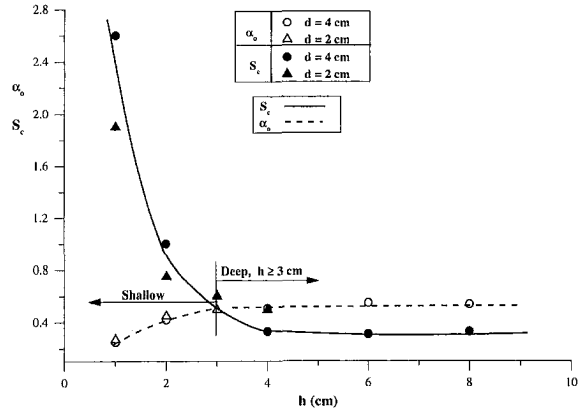

Fig. 11 Variation of model coefficients (α_o and S_c) with depth

which no significant spread was observed. With these initial estimates, Eq. (12) is fitted to each data set. Several iterations were carried out to obtain the values of α_o and S_c that yielded the best fit to a given data set. As expected, α_o increases as the flow depth increases, and at a given depth of flow, it is independent of the plate width. It is significant to note that at shallower flow depths (i.e., $h \leq 2$ cm), both α_o and S_c are a strong function of depth while for $h \geq 3$ cm, the model coefficients are nearly constant. This trend is consistent with the qualitative classification of the flows (on the basis of visual observation). Comparing the present wake characteristics at $h \geq 3$ cm with two-dimensional flows reported in literature, one finds that despite the difference in size and shape of the test body, the two wakes are structurally similar. The structural similarity can be deciphered from the locus of the vortex cores, the concentration distribution and the wake half-widths. As a result, the wakes with $h \geq 3$ cm are classified as deep-shallow wakes.

Figure 12(*a*) shows the variation of δ/θ with X/θ for deep-shallow wakes. The symbols represent the experimental values. Since the model coefficients are nearly independent of flow depth for $h \geq 3$ cm, only a single line is shown in this figure ($S_w < 0.008$). Also shown in this figure is the wake width obtained from previous velocity data. It is noted that at relatively deep depths, the wake half-widths based on scalar measurements (δ_{sc}) are larger than the corresponding half-width obtained from velocity measurements (δ_v). This is consistent with observations reported in an earlier study (Balachandar et al., 1997) and a detailed explanation of this trend is presented therein.

A plot of δ/θ versus X/θ at shallow-shallow wakes are presented in Fig. 12(*b*). Both the experimental data (symbols) and the model (lines) developed in the present study indicate that the depth of flow has a very important effect on the variation of δ/θ with X/θ. The effect of plate width on δ/θ can also be noticed in this figure. Beyond $X/\theta \sim 6$, there is no appreciable increase in δ/θ. It can also be observed from this figure that

for a given body width (say $d = 4$ cm), a smaller value of h will yield a larger value of the wake stability parameter, S_w. This results in a smaller value of δ/θ when compared to a larger depth. Further, at a constant depth of flow, the normalized width at $d = 2$ cm is larger than that noticed at $d = 4$ cm. One can thus associate a smaller value of S_w to an increased δ/θ, and a larger S_w to a reduced δ/θ. A larger value of S_w is an indication of higher bed friction effects or less transverse shear effects. Both of these effects will provide lower rate of entrainment and contribute to less mixing and narrower normalized wake widths. It should be noted that no wake width data based on velocity profiles is presently available for shallow flows.

Uncertainty Estimates. The uncertainty estimates indicated in the figure captions are obtained at an odds of 20:1. To estimate the uncertainty in C/C_o, five known concentrations covering the expected range of measurements were chosen. For each concentration, a set of thirty repeated measurements was carried out and the maximum deviation from the mean determined.

5 Conclusion

On the basis of the observed behavior, the wakes are classified as deep-shallow wakes and shallow-shallow wakes. The deep-shallow wakes are structurally similar to the deep wake wind tunnel studies reported in literature. Visual observations indicate that the Karman vortex street is annihilated at low flow depths. There is a critical value of the wake stability parameter ($S_w < 0.008$) above which only intermittent vortex shedding or complete annihilation of Karman vortex street was noticed. The instantaneous and maximum concentration profiles across the wake are observed to be several times higher than the corresponding mean profiles. Depth has been noted to have a significant effect on the entrainment of the ambient fluid leading to the dilution process. At relatively low depths of flow, the effect of bed friction becomes more significant and the entrainment or spreading rate is reduced. As a consequence, the extent of mixing is reduced and the width of the wake is also limited. At lower depths of flow in the present study, the size of the test body has some effects on the development of the wake. Consistent with earlier discussions, a smaller geometry would give rise to reduced wake stability parameter S_w and a more rapid spread of the wake. The results of the present study, besides supplementing the existing information on bluff body wakes, provide an insight into the mixing of pollutants, fuels and chemicals in the intermediate wake.

References

Antonia, R. A., 1991, "Organization in a Turbulent Near Wake," *Fluid Dynamics Research,* The Japan Society of Fluid Mechanics, North-Holland, Vol. 7, pp. 139–149.

Babarutsi, S., Ganoulis, J., and Chu, V. H., 1989, "Experimental Investigation of Shallow Recirculating Flows," *Journal of Hydraulic Engineering,* Vol. 115, No. 7, pp. 906–924.

Balachandar, R., Zhang, J., and Chu, V. H., 1993, "Quasi-Two Dimensional Turbulence in the Wake of a Normal Flat Plate in Shallow Waters," *Ninth Symposium on Turbulent Shear Flows,* Kyoto, Japan, pp. 16-4-1–16-4-6.

Balachandar, R., Chu, V. H., and Zhang, J., 1997, "Experimental Study of Turbulent Concentration Flow Field in the Wake of a Bluff Body," ASME JOURNAL OF FLUIDS ENGINEERING, Vol. 119, June, pp. 263–270.

Bisset, D. K., Antonia, R. A., and Browne, L. W. B., 1990, "Spatial Organization of Large Structures in The Turbulent Far Wake of a Cylinder," *Journal of Fluids Mechanics,* Vol. 218, pp. 439–461.

Bradbury, L. J. S., 1976, "Measurements with a Pulsed-Wire and Hot-Wire Anemometer in the Highly Turbulent Wake of a Normal Flat Plate," *Journal of Fluid Mechanics,* Vol. 77, Part 3, pp. 473–497.

Browne, L. W., Antonia, R. A., and Shah, D. A., 1989, "On the Origin of the Organized Motion in the Turbulent Far-Wake of a Cylinder," *Experiments in Fluids,* Springer-Verlag, Vol. 7, 475–480.

Cantwell, B., and Coles, D., 1983, "An Experimental Study of Entrainment and Transport in the Turbulent Near Wake of a Circular Cylinder," *Journal of Fluid Mechanics,* Vol. 136, pp. 321–374.

Dahm, W. J. A., and Dimotakis, P. E., 1987, "Measurement of Entrainment and Mixing in Turbulent Jets," *AIAA Journal,* Vol. 25, No. 9, pp. 1216–1223.

Fage, A., and Falkner, V. M., 1935, "Note on Experiments on the Temperature and Velocity in the Wake of a Heated Cylindrical Obstacle," *Proceedings of the Royal Society,* London, Vol. 135A, pp. 702–705.

Fischer, H. B., Imberger, J., List, E. J., Koh, R. C. Y., and Brooks, N. H., 1979, *Mixing in Inland and Coastal Waters,* Academic Press, New York.

Freymuth, P., and Uberoi, M. S., 1971, "Structure of Temperature Fluctuations in the Turbulent Wake Behind a Heated Cylinder," *Physics of Fluids,* Vol. 14, No. 12, pp. 2574–2579.

Freymuth, P., and Uberoi, M. S., 1973, "Temperature Fluctuations in the Turbulent Wake Behind an Optically Heated Sphere," *Physics of Fluids,* Vol. 16, pp. 161–168.

Hayakawa, M., and Hussain, F., 1989, "Three Dimensionality of Organized Structures in a Plane Turbulent Wake," *Journal of Fluid Mechanics,* Vol. 206, pp. 375–404.

Hinze, O., 1959, *Turbulence,* McGraw-Hill, New York.

Ingram, Grant R., and Chu, V. H., 1987, "Flow Around Islands in Rupert Bay: An Investigation of the Bottom Friction Effect," *Journal of Geophysical Research,* Vol. 92, No. C13, pp. 14.521–14.533.

Kiya, M., and Matsumara, M., 1988, "Incoherent Turbulence Structure in the Near Wake of a Normal Plate," *Journal of Fluid Mechanics,* Vol. 190, pp. 343–356.

Koochesfahani, M. M. and Dimotakis, P. E., 1985, "Laser-Induced Fluorescence Measurements of Mixed Fluid Concentration in a Liquid Plane Shear Layer," *AIAA Journal,* Vol. 23, No. 11, pp. 1700–1707.

Kovaszany, 1949, "Hot-Wire Investigation of the Wake Behind Cylinders at Low Reynolds Numbers," *Proceedings of the Royal Society,* London, Vol. A198, pp. 174–189.

LaRue, J. C., and Libby, P. A., 1974a, "Temperature and Intermittency in the Turbulent Wake of a Heated Cylinder," *Physics of Fluids,* Vol. 17, No. 5, May, pp. 873–878.

LaRue, J. C., and Libby, P. A., 1974b, "Temperature Fluctuations in the Plane Turbulent Wake," *The Physics of Fluids,* Vol. 17, No. 11, Nov., pp. 1956–1967.

Matsumara, M., and Antonia, R. A., 1993, "Momentum and Heat Transport in the Turbulent Intermediate Wake of a Circular Cylinder," *Journal of Fluid Mechanics,* Vol. 250, pp. 651–668.

Paul, P. H., Cruyningen, I. V., Hanson, R. K., and Kychakoff, G., 1990, "High Resolution Digital Flowfield Imaging of Jets," *Experiments in Fluids,* Vol. 9, pp. 241–251.

Ramamurthy, A. S., and Ng, C. P., 1973, "Effects of Blockage on Steady Force Coefficient," *Journal of Engineering Mechanics Division,* ASCE, Vol. 99, No. EM4, Aug., pp. 755–772.

Schlichting, H., 1979, *Boundary-Layer Theory,* McGraw-Hill, New York.

Tachie, M. F., 1997, "Scalar Transport in Intermediate Two-dimensional Turbulent Wakes," M. Sc. thesis, University of Saskatchewan.

Townsend, A. A., 1949, "The Fully Developed Turbulent Wake of a Circular Cylinder," *Australian Journal of Science Research,* Vol. 2A, pp. 451–468.

Uberoi, M. S., and Freymuth, P., 1969, "Spectra of Turbulence in the Wake of Circular Cylinders," *Physics of Fluids,* Vol. 12, pp. 1359–1363.

Wolanski, E., Imberger, J., and Heron, M. L., 1984, "Island Wakes in Shallow Coastal Water," *J. Geophys. Res.,* Vol. 89, C6, pp. 10553–10569.

Zhou, Y., and Antonia, R. A., 1992, "Convection Velocity Measurements in a Cylinder Wake," *Experiments in Fluids,* Vol. 13, pp. 63–70.

The Effect of Biofilms on Turbulent Boundary Layers

M. P. Schultz
Research Engineer. Mem. ASME
e-mail: schultz@fit.edu

G. W. Swain
Professor.
e-mail: swain@fit.edu

Ocean Engineering Program,
Florida Institute of Technology,
150 West University Blvd.,
Melbourne, FL 32901

Materials exposed in the marine environment, including those protected by antifouling paints, may rapidly become colonized by microfouling. This may affect frictional resistance and turbulent boundary layer structure. This study compares the mean and turbulent boundary layer velocity characteristics of surfaces covered with a marine biofilm with those of a smooth surface. Measurements were made in a nominally zero pressure gradient, boundary layer flow with a two-component laser Doppler velocimeter at momentum thickness Reynolds numbers of 5600 to 19,000 in a recirculating water tunnel. Profiles of the mean and turbulence velocity components, including the Reynolds shear stress, were measured. An average increase in the skin friction coefficient of 33 to 187 percent was measured on the fouled specimens. The skin friction coefficient was found to be dependent on both biofilm thickness and morphology. The biofilms tested showed varying effect on the Reynolds stresses when those quantities were normalized with the friction velocity.

Introduction

While modern antifouling (AF) systems are effective in controlling most macrofouling (e.g., barnacles, tubeworms, macroalgae, etc.), they do become colonized by microfouling organisms that produce a slime film. In some cases, the growth of this film is stimulated on copper and organo-tin AF paints (Loeb et al., 1984). The effect of biofilms on frictional resistance and turbulent boundary structure is, therefore, of great interest in predicting the hydrodynamic performance of marine vehicles.

A significant body of research has been devoted to studying the effects of marine fouling on frictional resistance. Much of the early work is documented in *Marine Fouling and Its Prevention* (1952). Most of this research addressed the effects of macrofouling. The first anecdotal evidence that slime films increase skin friction was given by Sir Archibald Denny in his discussion of a paper by McEntee (1915). Denny stated that microbial fouling on full-scale ships increased the resistance at a rate of $\frac{1}{2}$ percent per day while at dock. Researchers at Langley Field, in experiments on towed plates, demonstrated that slime films significantly increase skin friction (Benson et al., 1938). An extensive investigation into the effects of microbial slime layers on pipe flow was carried out by Picologlou et al. (1980). They noted that the thickness and morphology of the slime film is affected by the hydrodynamic conditions to which it is exposed. It was also observed that the viscoelastic character of the biofilm combined with its filamentous nature seemed to cause additional energy dissipation mechanisms that led to higher frictional resistance.

Lewkowicz and Das (1981) used uniformly distributed nylon tufts attached to a rough flat plate in order to model a marine slime growth. Detailed profiles of both mean and turbulence quantities were measured. They found that the skin friction in a zero pressure gradient flow was an average of 18 percent higher for the model slime film with a background roughness than for the background roughness alone. Loeb et al. (1984) measured the influence of microbial biofilms on the hydrodynamic drag of rotating discs. Their data showed an increase in frictional resistance of 10 to 20 percent due to slime films. Preroughened disks were also tested both before and after exposure to biofilm formation, since it was hypothesized that a thin slime film might reduce the drag of rough surfaces by effectively smoothing them. This was not the case, as an increase in frictional drag of 10 percent was measured for the fouled, rough disk.

Lewthwaite et al. (1985) conducted an experiment in which velocity profiles were taken on a vessel at sea over a two year period. In this study, a 23 m fleet tender was operated in temperate waters and was subjected to marine biofouling buildup. A pitot-static tube traverse system was outfitted on the ship by means of several through-hull fittings located along the length of the hull. The local skin friction coefficient was found from the mean velocity profile. They measured an increase in c_f from 0.0023 to 0.0042 over the exposure period. A corresponding 15 percent reduction in ship speed was observed. There were no quantitative measurements made on the fouling settlement on the hull. However, it was noted that when the vessel was drydocked, it was virtually free of hard fouling and macroalgae. It was covered with a dense slime film estimated to be 1 mm thick. When the hull was cleaned and returned to the water, measurements confirmed that c_f returned approximately to its clean hull value.

Haslbeck and Bohlander (1992) conducted a full-scale ship trial in order to quantify the effect of microbial biofilms on ship drag. In their investigation, the *USS Brewton,* a Knox class frigate, was instrumented to measure shaft horsepower and ship speed over a mile course. The ship, which was coated with an ablative antifouling paint containing both cuprous oxide and tributyltin oxide, had been subjected to fouling in Pearl Harbor, Hawaii for 22 months. An initial hull inspection by divers indicated the presence of a microbial biofilm but little hard fouling. It was found that there was as much as an 18 percent decrease in the required shaft horsepower to propel the ship at same speed after the microbial biofilm was removed.

While it has been shown that biofilms have the potential to increase ship drag, the authors are unaware of any previous study in which the mean and turbulence structure of boundary layer flows over natural marine biofilms were measured. This information is vital to the understanding and prediction of flows over fouled hulls.

Experimental Facilities and Method

The experimental work was carried out at the Harbor Branch Oceanographic Institution (HBOI) water tunnel (Gangadharan et al., 1996). The tunnel is 2.44 m in height, 8.53 m in length, and 1.22 m in width and is constructed of mild steel coated

Contributed by the Fluids Engineering Division for publication in the JOURNAL OF FLUIDS ENGINEERING. Manuscript received by the Fluids Engineering Division August 17, 1998; revised manuscript received December 8, 1998. Associate Technical Editor: P. Bradshaw.

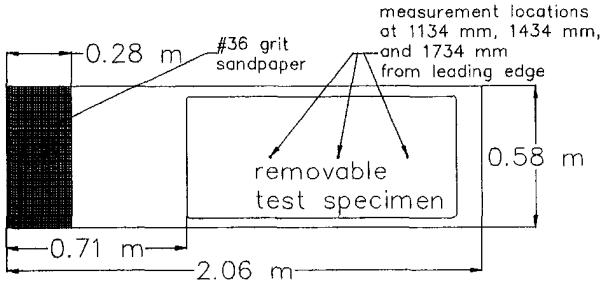

Fig. 1 Boundary layer test fixture

with marine polyamide epoxy. The test section is 0.61 m by 0.61 m and is 2.54 m in length. The contraction ratio in the tunnel is 4 to 1. Flow management devices include turning vanes placed in the tunnel corners and a polycarbonate honeycomb flow straightener in the entrance to the contraction section. The resulting freestream turbulence intensity in the test section ranged from 2.5 to 3.0 percent in the velocity range that was used in the present experiment. The freestream velocities in the test section can be adjusted from 1.2 m/s to 4.0 m/s.

The test matrix consisted of five specimens. Two smooth, unfouled surfaces were used as controls. The remaining three specimens were subjected to biofilm build-up for 6, 14, and 17 days. In order to look at boundary layer development and the effect of varying Reynolds number, velocity profiles were taken at three downstream positions. The profiles were taken at 1.13 m, 1.43 m, and 1.73 m from the leading edge and at three freestream velocities (nominally 1.5 m/s, 2.25 m/s, and 3.0 m/s). Velocity profiles consisted of about 50 logarithmically spaced sampling locations across the boundary layer.

The test specimens were inserted into a flat plate mounted horizontally in the tunnel (Fig. 1). The plate was 0.58 m in width, 2.06 m in length, and 54 mm thick. It was constructed of polyvinylchloride (PVC) and stainless steel and was mounted horizontally in the tunnel's test section. The leading edge of the test plate was shaped to mimic the forward portion of a NACA 0012-64 airfoil. The forward most 280 mm of plate was covered with #36 grit sandpaper to hasten development of a turbulent boundary layer. The use of a strip of roughness to artificially thicken a boundary layer was proposed by Klebanoff and Diehl (1951). The test specimens were fabricated from a cast acrylic sheet. Each specimen measured 558 mm in width, 1168 mm in length, and 12.7 mm in thickness. The forward edge of the specimen was located 710 mm from the leading edge of the plate.

Velocity measurements were made using a TSI two-component, fiber-optic laser Doppler velocimeter (LDV) system. The LDV probe was mounted on an AMPRO System 1618, three-axis traverse unit. The traverse allowed the position of the probe to be maintained to ± 5 μm in all directions. In order to facilitate two-component, near wall measurements, the probe was tilted downwards at an angle of 4 deg to the horizontal and was rotated 45 deg about its axis. This minimized bias error due to introduction of the w' fluctuations into the v' measurements. Using this setup, measurements as close as 40 μm to the wall were made. Velocity measurements were conducted in coincidence mode with 10,000 random samples per location. Doppler bursts for the two channels were required to fall within a set coincidence window or the sample was rejected. This coincidence window was set at 50 μs, 30 μs, and 20 μs for the 1.5 m/s, 2.25 m/s, and 3.0 m/s flows, respectively.

The biofilms on the fouled test specimens were grown at the HBOI Aquaculture facility. Water from the Indian River Lagoon was continuously pumped through a sand filtration system and into three growout tanks. During these experiments, the salinity of the water in the tanks ranged from 20 ppt to 36 ppt. The water temperature ranged from 25°C to 35°C. The thickness of the biofilm on the test specimens was determined using a Gardco comb-type wet film paint thickness (WFT) gauge. It had a thickness measurement range of 25 μm to 2032 μm with a resolution of 25 μm in the 25 μm to 305 μm range. Sixty thickness measurements were made both before and after subjecting each biofilm to hydrodynamic testing in the water tunnel. These were made on the damp biofilm in air. After hydrodynamic testing, a sample of the biofilm was taken and examined under a compound microscope to identify the organisms present. A more detailed description of the experimental setup is provided in Schultz (1998).

In the present investigation, three methods were used to determine c_f for the smooth walls and two methods were used for the fouled walls. For the smooth specimens, c_f was determined using Bradshaw's method. The sublayer slope method and the Reynolds stress method were also used to verify these results. The details of Bradshaw's method, which is based on inner layer similarity, are given in Bradshaw (1959) and Winter (1977). Log-law reference values of $y^+ = 100$ and $U^+ = 16.24$ ($\kappa = 0.41, B = 5.0$) were used in the present study. The sublayer slope method uses the velocity gradient in the linear sublayer to obtain the wall shear stress. Data at $y^+ < 7$ were used. The final method that was used to find c_f on the smooth specimens was the Reynolds stress method, which is detailed by Lee et al. (1993). For the fouled plates, the analysis was a bit more complex. First, before c_f could be found, the location of the

Nomenclature

B = log-law intercept
C_F = frictional resistance coefficient = $(2F_D)/(\rho U_e^2 S)$
c_f = skin friction coefficient = $(2\tau_0)/(\rho U_e^2)$
F_D = drag force
H = shape factor = δ^*/θ
k = some measure of roughness height
k_s = equivalent sand roughness height
Re_x = Reynolds number based on x = xU_e/ν
Re_{δ^*} = displacement thickness Reynolds number = $\delta^* U_e/\nu$
Re_θ = momentum thickness Reynolds number = $\theta U_e/\nu$
S = wetted surface area
t = t-statistic
U, V = mean velocity in the x and y direction
U_e = freestream velocity
ΔU^+ = roughness function
u, v = instantaneous velocity in the x and y direction
u', v' = fluctuating velocity component in the x and y direction
U_τ = friction velocity = $\sqrt{\tau_o/\rho}$
x = streamwise distance from plate leading edge
y = normal distance from the boundary
α = statistical significance level
Δ = Clauser length scale = $\delta^* U_e/U_\tau$
δ = boundary layer thickness (y at $U = 0.99U_e$)
δ^* = displacement thickness
ϵ = wall datum error
κ = von Karman constant (=0.41)
ν = kinematic viscosity of the fluid
θ = momentum thickness
ρ = density of the fluid
τ_o = wall shear stress

Superscript

$+$ = inner variable (normalized with U_τ or U_τ/ν)

virtual origin ($y + \epsilon = 0$) had to be determined. This was accomplished using an adaptation of the method proposed by Perry and Joubert (1963). The log-law slope method, which is detailed in Lewthwaite et al. (1985) and the Reynolds stress method were then used to determine c_f.

Uncertainty Estimates

The precision uncertainties for the velocity measurements were determined using repeatability tests. Ten replicate profiles were taken on both a smooth and a fouled plate. The standard deviation for each of the measurement quantities was then calculated for both samples. In order to estimate the 95 percent confidence limits for a statistic calculated from a single profile, the standard deviation was multiplied by the two-tailed t value ($t = 2.262$) for 9 degrees of freedom and $\alpha = 0.05$, as given by Coleman and Steele (1995). The resulting precision uncertainties in the mean velocities were ±1.0 percent in the outer region of the boundary layer and ±1.9 percent in the near-wall region. For $\overline{u'^2}$ and $\overline{v'^2}$, the precision was ±1.7 percent in the outer region and ±3.4 percent in the near-wall region. The bias errors for the mean velocities were less than 2 percent. A bias error in the v' measurements of ~2 percent was caused by introduction of the w' component due to inclination of the LDV probe. The uncertainties in c_f for the smooth walls using Bradshaw's method, the sublayer slope method, and the Reynolds stress method were ±5, ±7, and ±15 percent, respectively. The uncertainty in c_f for the rough walls using the log-law slope method was ±15 percent and was ±28 percent using the Reynolds stress method. The increased uncertainty resulted mainly from the extra two degrees of freedom (ϵ and ΔU^+) in the analysis of rough walls. The uncertainty in δ was ±12 percent and resulted from the relatively high freestream turbulence and fluctuations in the freestream velocity. In order to test the significance of the differences in the boundary layer parameters that were observed, several analyses of variance (ANOVA) were used (Sokal and Rohfl, 1981).

Results and Discussion

In order to reference each of the test samples, an alphanumeric code is used. The first letter represents the test specimen type. "S" is a smooth plate. "F" is fouled plate. The first number indicates the replicate number. F1, F2, and F3 were exposed for 6, 14, and 17 days, respectively. To further facilitate the reference of individual velocity profiles, an additional letter and number are added to the previous designation. To indicate the downstream distance from the leading edge, x, the letters A–C are used. "A" represents the 1.13 m profiling station, "B" the 1.43 m station, and "C" the 1.73 m station. The nominal freestream velocity is indicated with the numbers 1–3. The number "1" represents 1.5 m/s, "2" represents 2.25 m/s, and "3" represents 3.0 m/s. For example, "S2B3" refers to a profile made on smooth specimen replicate 2 at $x = 1.43$ m and $U_e = 3.0$ m/s.

The biofilm on each of the three fouled plates was characterized by visual assessment both before and after hydrodynamic testing. The results of this evaluation are shown in Table 1. Examination of the biofilm with the aid of a microscope showed that the film on F1 was composed mainly of extracellular polymer substances (EPS), blue-green algae (*Anabaina oscillarioides*), and marine diatoms (dominated by *Melosira spp.*). F2 was fouled with EPS, green algae (*Enteromorpha spp.*), and marine diatoms (dominated by *Melosira spp.* and *Thallasiothrix spp.*). The biofilm on F3 was almost entirely composed of filamentous green algae (*Enteromorpha spp.*). The overall mean thickness (±1 SD) of the biofilms based on 60 individual measurements was found. Before hydrodynamic testing, the thicknesses of F1, F2, and F3 were 350 μm ± 69 μm, 160 μm ± 41 μm, and 310 μm ± 100 μm, respectively. After hydrodynamic testing, the thicknesses of F1, F2, and F3 were 74 μm ± 46 μm, 130 μm ± 27 μm, and 340 μm ± 150 μm, respectively. The reduction in biofilm thickness for F1 and F2 after testing was due in large part to the removal of some portion of these films as a result of the wall shear stress. The thickness of F3 remained the same within measurement uncertainty.

Table 1 Visual assessment of fouled test specimens

Specimen	Total % Fouling Cover	Constituents and Their % Cover
F1 before	97	Slime 97% (light to medium density film)
F1 after	70	Slime 70% (very light density film)
F2 before	98	Slime 94% (medium density film) Filamentous green algae 4%
F2 after	91	Slime 90% (medium density film) Filamentous green algae 1%
F3 before	95	Slime 70% (medium density film) Filamentous green algae 25%
F3 after	82	Slime 70% (medium density film) Filamentous green algae 12%

Figure 2 shows the law of the wall profiles for S1 and the fouled specimens as they develop down the plate. The roughness function, ΔU^+, varied greatly with specimen as well as the downstream position. The profiles for F3, the biofilm dominated by filamentous green algae, generally had the largest roughness function. Biofilms F1 and F2, which consisted of a slime film, had less effect on the mean profile.

The basic boundary layer parameters calculated for the smooth and fouled test plates are shown in Table 2. The boundary layer thickness, δ, is specified for $U = 0.99U_e$. To determine if the differences were significant within the experimental uncertainty, statistical tests were conducted. These consisted of

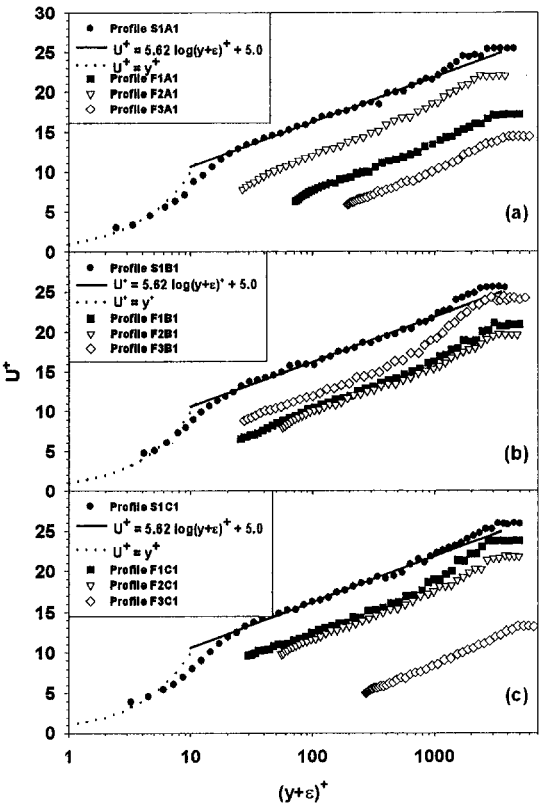

Fig. 2 Law of the wall plots for smooth and fouled specimens: (*a*) x = 1.13 m; (*b*) x = 1.43 m; (*c*) x = 1.73 m (uncertainties in U^+: ±4 percent for smooth profiles; ±11 percent for fouled profiles)

Table 2 Boundary layer parameters

Profile	Re_θ	δ (mm)	δ* (mm)	θ (mm)	Δ (mm)	H
S1A1	6500	33	4.3	3.4	110	1.29
S1B1	6500	33	4.4	3.4	110	1.31
S1C1	8100	43	5.4	4.2	140	1.28
S1A2	8500	33	3.8	3.0	100	1.29
S1B2	13000	38	4.6	3.6	120	1.27
S1C2	10000	36	4.6	3.6	120	1.28
S1A3	11000	32	3.8	2.9	100	1.30
S1B3	12000	33	3.9	3.1	100	1.25
S1C3	14000	43	5.0	4.0	130	1.25
S2A1	5600	30	3.9	3.0	100	1.29
S2B1	6300	35	4.3	3.4	110	1.28
S2C1	7000	37	4.7	3.6	120	1.32
S2A2	8500	28	3.8	3.0	100	1.29
S2B2	10000	35	4.4	3.5	120	1.27
S2C2	9000	37	4.3	3.4	110	1.26
S2A3	12000	30	3.9	3.0	110	1.29
S2B3	13000	36	4.4	3.5	120	1.25
S2C3	15000	36	4.3	3.4	120	1.25
F1A1	6500	29	5.0	3.6	86	1.41
F1B1	7600	37	6.0	4.1	130	1.44
F1C1	9200	38	6.87	5.0	160	1.37
F1A2	9730	30	4.81	3.5	82	1.39
F1B2	10000	35	5.07	3.6	88	1.41
F1C2	12000	37	6.0	4.2	120	1.42
F1A3	14000	39	4.9	3.8	110	1.28
F1B3	13000	32	4.4	3.4	110	1.30
F1C3	15000	37	5.4	4.1	140	1.31
F2A1	5700	27	4.3	3.1	95	1.40
F2B1	7500	35	5.5	4.0	110	1.36
F2C1	8200	40	6.0	4.5	130	1.33
F2A2	9500	30	4.7	3.5	110	1.34
F2B2	11000	34	5.5	4.0	140	1.35
F2C2	12000	39	5.9	4.5	150	1.31
F2A3	9800	26	3.7	2.7	83	1.37
F2B3	15000	36	5.5	4.3	140	1.30
F2C3	13000	35	4.9	3.7	100	1.31
F3A1	6700	28	5.6	3.8	80	1.49
F3B1	7700	35	6.5	4.4	160	1.48
F3C1	9400	38	8.1	5.4	109	1.49
F3A2	10000	34	5.6	3.9	69	1.44
F3B2	12000	35	6.3	4.5	160	1.41
F3C2	14000	43	7.6	5.1	95	1.48
F3A3	14000	33	5.4	3.9	76	1.39
F3B3	19000	38	7.0	5.2	170	1.36
F3C3	19000	38	7.6	5.3	140	1.42

two-way ANOVAs with specimen and Re_x as factors. In cases where the ANOVA indicated significant differences for one of the factors, multiple pairwise comparisons were run using Tukey's test (Sokal and Rohfl, 1981). The significance level for all the tests was set at $\alpha = 0.05$.

The ANOVA on the boundary layer thickness results showed that neither specimen nor Re_x had a significant effect. This may have been due to the high degree of variability in δ. For example, the absolute deviation of δ between the smooth plate replicates ranged from 2.0 to 13 percent of the mean for the 9 profiles and averaged 7.1 percent. This was due in part to the inability to control U_e more precisely in the water tunnel. Thole and Boggart (1996) have also observed that high freestream turbulence levels increase the uncertainty in finding δ. Results from Lewkowicz and Das (1981), on a simulated biofilm roughness, showed that biofilms had a thickening effect on the boundary layer of 25 to 30 percent above that of a background roughness.

Table 3 Skin friction coefficients for the smooth profiles

Profile	Re_θ	c_f (x10^3) Bradshaw Cross Plot	c_f (x10^3) Sublayer Slope	c_f (x10^3) Reynolds Stress
S1A1	6500	3.1	3.0	2.8
S1B1	6500	3.1	2.8	2.9
S1C1	8100	3.0	2.8	2.6
S1A2	8500	2.9	2.9	2.8
S1B2	13000	2.9	2.8	2.5
S1C2	10000	2.9	2.7	2.5
S1A3	11000	2.7	2.7	3.0
S1B3	12000	2.8	-	2.9
S1C3	14000	2.8	2.8	2.6
S2A1	5600	3.2	3.2	2.8
S2B1	6300	3.1	3.1	2.9
S2C1	7000	3.0	3.1	2.7
S2A2	8500	2.8	2.8	2.9
S2B2	10000	2.9	2.7	2.7
S2C2	9000	3.0	3.0	2.7
S2A3	12000	2.7	2.7	2.9
S2B3	13000	2.7	2.6	2.9
S2C3	15000	2.8	-	2.9

- missing data

The presence of the biofilm did have a significant effect on the boundary layer displacement thickness, δ^*. The ANOVA indicated an effect of specimen as well as Re_x. Multiple pairwise comparisons indicated a significant increase in δ^* over that of the smooth specimens for all the fouled specimens tested. Differences between all specimens were found with the exception of S1 versus S2 (the controls) and F1 versus F2. The shape factor, H, was significantly increased for the fouled profiles as well. Multiple pairwise comparisons showed differences for all the specimens with the exception of S1 versus S2 and F1 versus F2. The average increase in H with fouling was 7.0 percent for F1, 4.8 percent for F2, and 13 percent for F3 compared to the smooth plates. The increase in H with the presence of fouling was also seen by Lewkowicz and Das (1981) in flow over a model biofilm and is a typical surface roughness effect. The Clauser length, Δ, was not significantly affected by the presence of the biofilm. There was a higher degree of variability for the fouled specimens, however. It seems that this was related to the fouling extent, as F3, the most heavily fouled specimen, had the largest variability.

The skin friction coefficients for the smooth specimens are shown in Table 3 and Fig. 3. Agreement was found between the replicate smooth plate skin friction results within the uncertainty of the measurements (S1 and S2). There was also agreement between the values obtained using Bradshaw's method, the sublayer slope method, and the Reynolds stress method. Bradshaw's method was chosen to calculate the values of U_τ used in the profile plots. This was because a paucity of linear

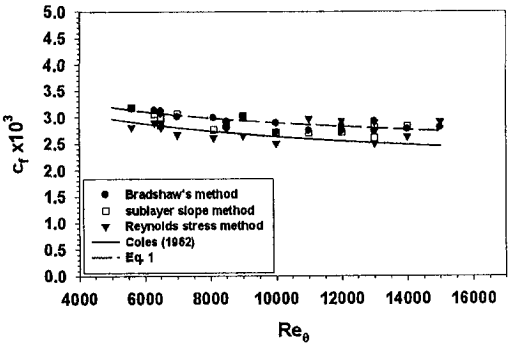

Fig. 3 Skin friction coefficients for the smooth plate profiles (uncertainties in c_f: ±5 percent for Bradshaw's method; ±7 percent for sublayer slope method; ±15 percent for Reynolds stress method)

Table 4 Skin friction coefficients for the fouled specimens

Profile	Re_θ	c_f ($\times 10^3$) Log-law Slope	c_f ($\times 10^3$) Reynolds Stress
F1A1	6500	6.8	4.7
F1B1	7600	4.5	6.4
F1C1	9200	3.5	4.3
F1A2	9730	7.0	4.4
F1B2	10000	6.7	4.4
F1C2	12000	4.7	4.2
F1A3	14000	4.2	4.0
F1B3	13000	3.3	3.5
F1C3	15000	2.9	3.8
F2A1	5700	4.1	4.3
F2B1	7500	5.2	4.5
F2C1	8200	4.2	3.6
F2A2	9500	3.5	4.8
F2B2	11000	3.0	4.8
F2C2	12000	2.9	3.5
F2A3	9800	4.0	4.6
F2B3	15000	3.1	4.0
F2C3	13000	4.7	4.4
F3A1	6700	9.7	8.0
F3B1	7700	3.4	5.2
F3C1	9400	11	10
F3A2	10000	13	5.8
F3B2	12000	3.1	5.2
F3C2	14000	13	8.6
F3A3	14000	10	5.8
F3B3	19000	3.6	5.5
F3C3	19000	6.0	7.8

sublayer data points led to a higher uncertainty in U_τ obtained using the sublayer slope method. It is of note that c_f for the smooth wall case averaged 6–9 percent higher than those given by Coles (1962) (see Fig. 3). This is probably an effect of the high freestream turbulence level. The following is the best-fit, power law of the present smooth plate results using Bradshaw's method:

$$c_f = \frac{0.0105}{\mathrm{Re}_\theta^{0.14}} \tag{1}$$

All the fouled plates had increased c_f values compared to the smooth condition. Fouled specimens F1, F2, and F3 showed increases in c_f of 8 to 130, 3 to 70, and 11 to 370 percent, respectively. The average increase was 70 percent for F1, 30 percent for F2, and 190 percent for F3. However, it should be mentioned that the high freestream turbulence may not affect the smooth and fouled wall c_f values in the same way.

The variation in c_f was greatly increased for the fouled plates. For example, S1 had a mean c_f ($\times 10^3$) (± 1 SD) of 2.9 $\pm$ 0.1, and S2 had a mean c_f ($\times 10^3$) of 2.9 $\pm$ 0.2. Fouled plates F1, F2, and F3 had mean c_f ($\times 10^3$) values of 4.8 $\pm$ 1.6, 3.9 $\pm$ 0.8, and 8.1 $\pm$ 4.2, respectively. A Kruskal-Wallis ANOVA on ranks and Student-Newman-Keuls pairwise comparisons (Sokal and Rohfl, 1981) indicated a significant difference between all of the smooth panels and the fouled panels with the exception of S1 versus S2 (the controls) and F1 versus F2. The c_f results for the fouled specimens show that not only biofilm thickness but also composition and morphology are important determining factors. The average increase in c_f for slime films with a mean thickness before testing of 160 μm and 350 μm was 33 and 68 percent, respectively. The increase in c_f for a surface dominated by filamentous green algae (*Enteromorpha spp.*) with a mean thickness of 310 μm averaged 190 percent. It seems, therefore, that the flapping motions of filamentous algae remove larger amounts of momentum from the mean flow than nonfilamentous films of the same thickness.

The results for the fouled plates indicate an increase in c_f for all the fouled plate profiles (Table 4 and Fig. 4). Both methods indicated increases for the fouled plates, although each method

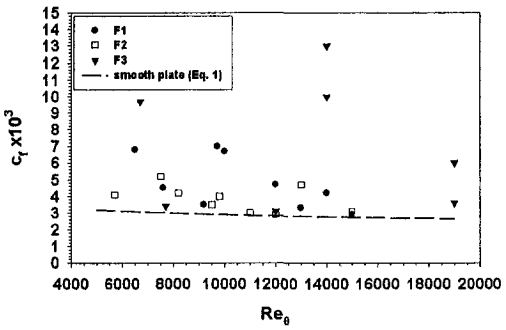

Fig. 4 Skin friction coefficients for the fouled plate profiles using the log-law slope method (uncertainty in c_f $\pm$ 15 percent)

showed high variability. The log-law slope method was used to calculate the values of U_τ used in the fouled plate profile plots because of the smaller uncertainty in this value relative to those obtained using the Reynolds stress method. In order to analyze the change in c_f for the fouled specimens, a comparison with the smooth plate results (Eq. (1)) at the same Re_θ was made.

Much of the variability within c_f results on the same specimen can be attributed to the complex and dynamic nature of the biofilm. First, it is heterogeneous in composition, structure, and distribution. This was especially true for F3. Biofilms may be thought of as a constantly varying streamwise roughness, not only in height but also in morphology. This brings the underlying assumption of boundary layer equilibrium, which is inherent to wall similarity methods, into question. A study by Andreopoulos and Wood (1982), in flows subjected to a short length of surface roughness, has found that boundary layers do not fully recover to a self-preserving state until downstream distances $>55\delta$. Work by Antonia and Luxton (1972) has shown, that on k-type surface roughness, the boundary layer adjusts rather slowly to a step change from rough to smooth surface condition. Antonia and Luxton (1971) have also observed that flows moving from smooth to rough surfaces adjust much more rapidly ($\sim 10\delta$). Further complicating the present situation was that some of the biofilm was removed over the course of the experiment due to the shear stress.

Some of the variation in the c_f results for the fouled plates may also be attributed to the method itself. Using Bradshaw's method for smooth plate flows, there is only a single free parameter, c_f. Additional parameters, ΔU^+ and ϵ, enter the analysis for rough wall flows. While the extra two degrees of freedom can produce a "better" log-law fit in a statistical sense, they can also lead to increased error in c_f. Natural scatter in the inner region data due to the influence of roughness elements may be masked in producing a least-squares fit of the log-law. Archarya and Escudier (1983) report that the use of rough wall analyses with ΔU^+ and ϵ not identically set to zero on smooth wall data produced c_f's with an average error of 12 percent.

Research by Perry et al. (1969), Ligrani and Moffat (1986), Bandyopadhyay (1987), and others has furthered the understanding of boundary layer flows over k-type and d-type roughnesses. Even in these "regular" roughness arrangements, the determination of c_f can be problematic. In general, an independent method for finding c_f is desirable. But, the common methods used on "regular" roughnesses, such as a floating element force balance or pressure taps, are not generally feasible on biofilms and could not be used in the present investigation.

Granville's (1987) method of finding the roughness function, ΔU^+, at the same value of Re_{δ^*} resulted in ΔU^+ ranging from 1.0 to 9.6, 0.54 to 6.5, and 1.8 to 15 for F1, F2, and F3, respectively (see Table 5). F1 had 33 percent of its profiles with k_s^+ values greater than 70, the value given by Schlichting (1979) as the onset of fully rough flow. F2 had no profiles

Table 5 Roughness parameters for the fouled profiles († overall mean biofilm after hydrodynamics testing)

Profile	ΔU^+	k_s^+	k_s (mm)	k (mm)	ε (mm)
F1A1	8.5	140	1.3	0.35	0.68
F1B1	5.0	33	0.38	0.35	0.30
F1C1	2.5	12	0.15	0.35	0.39
F1A2	9.6	220	1.3	0.35	0.53
F1B2	9.4	200	1.2	0.35	0.52
F1C2	6.4	58	0.42	0.35	0.43
F1A3	5.2	35	0.21	0.074†	0.23
F1B3	2.2	10	0.071	0.074†	0.31
F1C3	1.0	6.3	0.046	0.074†	0.32
F2A1	3.3	16	0.19	0.16	0.32
F2B1	6.2	53	0.57	0.16	0.61
F2C1	4.2	24	0.28	0.16	0.66
F2A2	2.7	13	0.11	0.16	0.036
F2B2	0.96	6.2	0.06	0.16	0.25
F2C2	0.54	5.3	0.05	0.16	0.24
F2A3	4.1	23	0.14	0.16	0.087
F2B3	2.2	10	0.073	0.16	0.22
F2C3	6.5	60	0.35	0.16	0.48
F3A1	11	380	3.1	0.31	1.6
F3B1	1.8	8.8	0.12	0.31	0.38
F3C1	13	870	6.7	0.31	2.1
F3A2	15	2000	9.2	0.31	1.9
F3B2	1.7	8.4	0.081	0.31	0.55
F3C2	15	2000	9.3	0.31	3.3
F3A3	13	870	3.4	0.31	1.6
F3B3	4.3	25	0.16	0.31	0.59
F3C3	9.9	240	1.24	0.31	2.0

with k_s^+ greater than 70, while F3 had 66 percent above this value. Plots of ΔU^+ versus k^+ for the three fouled specimens did not show a good collapse to the Nikuradse sand roughness function (see Fig. 5). The scaling length used in Fig. 5 was the mean biofilm height before testing. There was a high degree of scatter in these plots, although there was a significant trend of increasing ΔU^+ with increasing k^+ for all three. The mean roughness height of the biofilm measured with a paint wet film thickness gauge, by itself, does not provide an adequate roughness scaling factor. Picologlou et al. (1980) indicated a better correlation between k_s and the mean biofilm height in their pipe flow experiments. They also had difficulty in finding a functional dependency between the two, however.

Attempts to use the mean biofilm height after testing, the r.m.s. biofilm roughness, and the boundary layer thickness as scaling lengths did not lead to any better collapse of the results than the mean roughness alone. The wall datum error was also employed as a scaling length for the roughness function (Fig. 6). At higher values of ϵ^+, the slope of the roughness function is more closely aligned with the fully rough asymptote for Nikuradse sand, although there is substantial scatter in the data. The inability to adequately scale the roughness effects using a single length scale parameter is not surprising, especially for a surface as complex as a marine biofilm. Patel and Yoon (1995) note that at present there is no theoretical way to predict the roughness function based on roughness geometry alone, and a single length parameter is usually not sufficient to characterize the surface. A profile of the surface might allow a more meaningful parameter to be obtained. Since the biofilm is compliant, changes in the profile will occur with time and flow conditions. Surface topography obtained using a laser interferometer, as was used by Lee et al. (1993) on compliant surfaces, might make a more meaningful surface characterization possible. Other parameters such as the ratio of the wall shear stress to the shear modulus of the biofilm are also likely to be important.

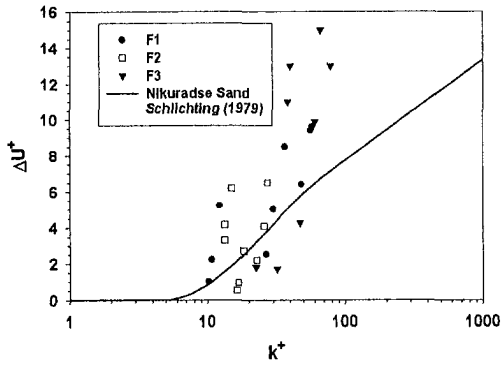

Fig. 5 Roughness functions for the fouled specimens scaled with the mean biofilm height (uncertainty in $\Delta U^+ \pm 15$ percent)

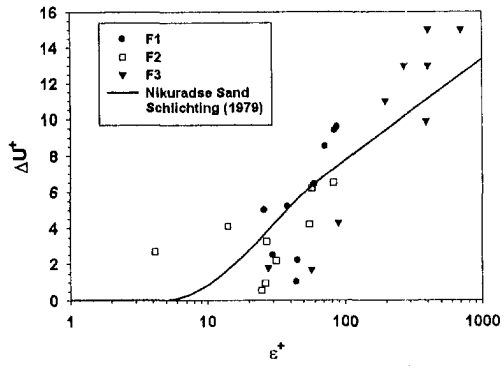

Fig. 6 Roughness functions for the fouled specimens scaled with the wall datum error (uncertainty in $\Delta U^+ \pm 15$ percent)

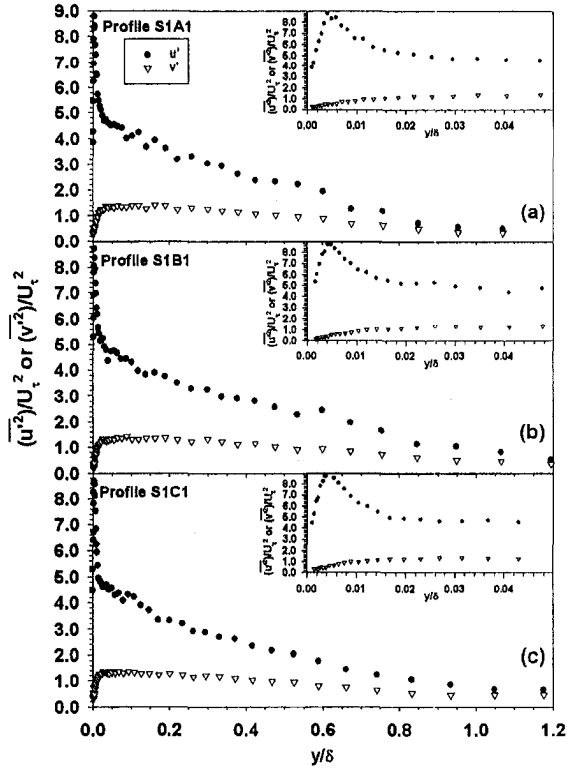

Fig. 7 Reynolds stresses $\overline{u'^2}/U_\tau^2$ and $\overline{v'^2}/U_\tau^2$ for smooth specimen, S1: (a) $x = 1.13$ m; (b) $x = 1.43$ m; (c) $x = 1.73$ m (uncertainty in $\overline{u'^2}/U_\tau^2$ and $\overline{v'^2}/U_\tau^2 \pm 6$ percent)

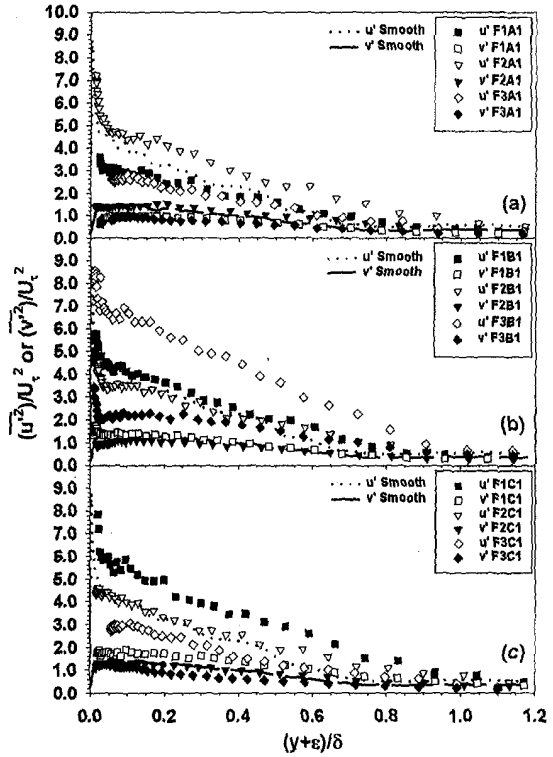

Fig. 8 Reynolds stresses $\overline{u'^2}/U_\tau^2$ and $\overline{v'^2}/U_\tau^2$ for the fouled specimens (uncertainty in $\overline{u'^2}/U_\tau^2$ and $\overline{v'^2}/U_\tau^2$ ± 15 percent)

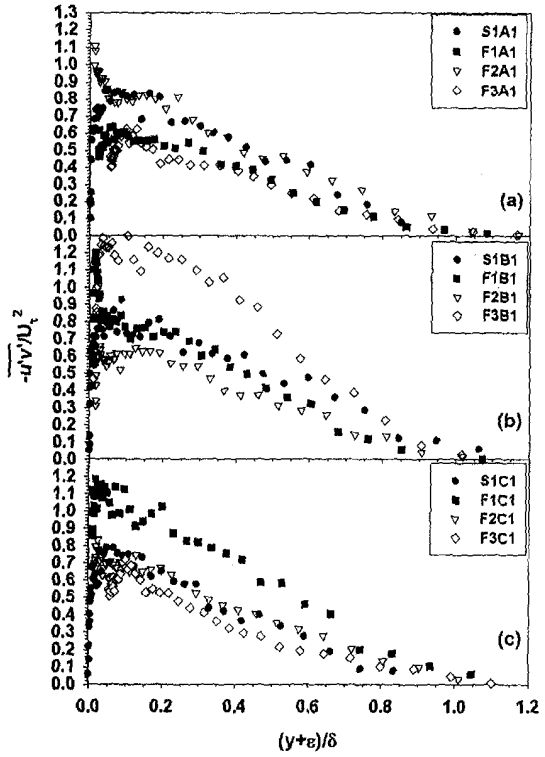

Fig. 9 Reynolds shear stress for the smooth and fouled specimens (uncertainty in normalized Reynolds stress: for smooth profiles ±8 percent; for fouled profiles ±17 percent)

The task of accurately scaling laboratory c_f's to ship scale frictional resistance coefficients (C_F) is a complex one. Even if reliable lab results for a given biofilm are available, fouling on an actual ship hull is likely to be much more heterogeneous. Differences in fouling over a hull can occur for various reasons including light shading effects, larval zonation in the water column, and differences in the flow patterns and stresses along the hull. The complexities in boundary layer flows over biofilms such as surface compliance, deformation, and removal may also increase the error in the prediction of ship scale effects. Given the inability to obtain a suitable length scale parameter to express the roughness function for these biofilms and the aforementioned difficulties, predictions of C_F at ship-scale are not offered here. It seems, however, that there is the potential for significant performance penalties as a result of low-form fouling on marine vehicles.

Normalized Reynolds stresses $\overline{u'^2}/U_\tau^2$ and $\overline{v'^2}/U_\tau^2$ for S1 and the fouled specimens are presented in Figs. 7 and 8, respectively. The profiles for S1 showed little variation with downstream distance, indicating boundary layer equilibrium. Specimen F1 showed greater streamwise variation for both u'^2/U_τ^2 and v'^2/U_τ^2. The differences observed, however, were not significant given the experimental uncertainty. Specimen F2 showed the least variation with downstream distance and collapsed to the smooth plate values within the uncertainty. Specimen F3 had the largest variation in these quantities with streamwise distance. For example, the profile for F3A1 agreed within uncertainty with the smooth results. F3B1 had significant increases in both u'^2/U_τ^2 and v'^2/U_τ^2 that extended over the entire boundary layer. F3C1 had profiles more closely resembling the smooth wall case. This rapid streamwise change in u'^2/U_τ^2 and v'^2/U_τ^2 is probably due to the patchy nature of the fouling coverage on this specimen. It seems that this variation in roughness with streamwise distance may cause production to increase or decrease in the log-law region due to the local surface condition and boundary layer history.

Krogstad and Antonia (1992) observed little change in u'^2/U_τ^2 for mesh-type roughness compared to smooth plate flows. They noted a significant increase in v'^2/U_τ^2, however. Krogstad et al. (1994) concluded that the major effect of the roughness was to tilt the large-scale structures towards the wall-normal direction, leading to a higher degree of isotropy and higher values of v'. In the present study, both u'^2/U_τ^2 and v'^2/U_τ^2 were affected to a similar degree, although there was significant variability in the profiles. Also of note were near-wall peaks in the v'^2/U_τ^2 profiles for F1B1 and F3B1 that are not seen in the smooth wall profiles. This may have resulted from local amplification of the wall-normal fluctuations due to surface compliance and movements of the algae filaments. Such features have also been observed in rough wall flows before the boundary layer reaches equilibrium (e.g., Antonia and Luxton, 1971). In the present study, the profiling stations were located between ~15δ to ~40δ from the start of the fouling. Bandyopadhyay (1987) has shown that sand roughness requires a much greater length to reach equilibrium.

Figure 9 shows the normalized Reynolds shear stress for S1 and the fouled specimens. The smooth plate profiles remained nearly constant down the plate. The F2 profiles agreed most closely with the smooth results. F2A1 did exhibit a large peak in the Reynolds shear stress in the near-wall region. The F1 profiles collapsed to the smooth plate profiles outside of the near-wall region with the exception of F1C1. In this profile, the Reynolds shear stress increased over the entire boundary layer although the uncertainty in the measurements should be noted. F1B1 showed a near-wall peak in the Reynolds shear stress was much like F2A1. Again specimen F3 exhibited the highest downstream variability. F3A1 showed lower Reynolds shear stress compared to the smooth plate, while F3B1 had a significant increase. The profiles followed trends similar to u'^2/U_τ^2 and v'^2/U_τ^2 with respect to boundary layer equilibrium. The peaked nature of some of the profiles indicate a smaller equilibrium or constant stress region than for the smooth plate flows.

Krogstad and Antonia (1992) noted a moderate increase in the Reynolds shear stress for rough wall flows. This was found to be due to both an increase in the magnitude of the burst and sweep events and the frequency of these events. In the present study, it is difficult to make any strong conclusions with regard to the effect of biofilms on the Reynolds shear stress due to the relatively high uncertainty in these measurements.

Conclusion

Comparisons of turbulent boundary layers over natural marine biofilms and a smooth plate have been made. The results have demonstrated the importance of low-form fouling on hydrodynamic drag. An increase in skin friction in these flows that was dependent on biofilm thickness, composition, and morphology was measured. For example, the average increase in c_f for slime films with a mean thickness of 160 μm and 350 μm was 33 and 68 percent, respectively. The average increase in c_f for a surface dominated by filamentous green algae (*Enteromorpha spp.*) with a mean thickness of 310 μm was 190 percent. Waving algae filaments seem to draw a greater amount of momentum from the mean flow than do slime films alone. A statistically significant increase in the displacement thickness (δ^*) and shape factor (H) was found for the biofilms. A standard Nikuradse sand roughness function does not sufficiently collapse the biofilm results to a universal curve using the mean roughness height as a characteristic length scale. A method of better characterizing these complex surfaces under flow may lead to a more appropriate scaling parameter. The biofilms tested showed varying effect on the Reynolds stresses normalized with U_τ.

Acknowledgments

We would like to thank the Office of Naval Research (grant #N00014-91-J-1465) and the Environmental Security and Technology Certification Program for their support of this research and their commitment to the advancement of biofouling control. Thanks go to Dr. Andrew Clark and the engineering staff at Harbor Branch Oceanographic Institution for their assistance and use of their facilities. We are also grateful to Professor Peter Bradshaw, Dr. C. S. Subramanian, and the anonymous referees for reviewing this manuscript and providing many helpful comments.

References

Acharya, M., and Escudier, M. P., 1983, "Measurements of the Wall Shear Stress in Boundary Layers," *Proceedings of the 4th International Symposium on Turbulent Shear Flows,* Karlsruhe, Germany, pp. 277–286.

Andreopoulos, J., and Wood, D. H., 1982, "The Response of a Turbulent Boundary Layer to a Short Length of Surface Roughness," *Journal of Fluid Mechanics,* Vol. 118, pp. 143–164.

Antonia, R. A., and Luxton, R. E., 1972, "The Response of a Turbulent Boundary Layer to a Step Change in Surface Roughness Part 2. Rough to Smooth," *Journal of Fluid Mechanics,* Vol. 53, Part 4, pp. 737–757.

Antonia, R. A., and Luxton, R. E., 1971, "The Response of a Turbulent Boundary Layer to a Step Change in Surface Roughness Part 1. Smooth to Rough," *Journal of Fluid Mechanics,* Vol. 48, Part 4, pp. 721–761.

Bandyopadhyay, P. R., 1987, "Rough-Wall Turbulent Boundary Layers in the Transition Regime," *Journal of Fluid Mechanics,* Vol. 180, pp. 231–266.

Benson, J. M., Ebert, J. W., and Beery, T. D., 1938, "Investigation in the NACA Tank of the Effect of Immersion in Salt Water on the Resistance of Plates Coated with Different Shipbottom Paints," NACA Memorandum Report C&R C-S19-1(3).

Bradshaw, P., 1959, "A Simple Method for Determining Turbulent Skin Friction from Velocity Profiles," *Journal of the Aeronautical Sciences,* Vol. 26, p. 841.

Coleman, H. W., and Steele, W. G., 1995, "Engineering Application of Experimental Uncertainty Analysis," *AIAA Journal,* Vol. 33, No. 10, pp. 1888–1896.

Coles, D., 1962, "The Turbulent Boundary Layer in a Compressible Fluid," The Rand Corp., Rep. R-403-PR.

Gangadharan, S., Wimberly, C. R., Clark, A., and Collino, B., 1996, "Design, Construction and Operation of a Cost Effective Water Tunnel at Harbor Branch Oceanographic Institution," Paper presented at S.N.A.M.E. Southeast Section Meeting, Oct. 11, Fort Pierce, FL.

Granville, P. S., 1987, "Three Indirect Methods for the Drag Characterization of Arbitrarily Rough Surfaces on Flat Plates," *Journal of Ship Research,* Vol. 31, No. 1, pp. 70–77.

Haslbeck, E. G., and Bohlander, G., 1992, "Microbial Biofilm Effects on Drag—Lab and Field," *Proceedings 1992 S.N.A.M.E. Ship Production Symposium.*

Klebanoff, P. S., and Diehl, F. W., 1951, "Some Features of Artificially Thickened Fully Developed Turbulent Boundary Layers with Zero Pressure Gradient," NACA TN 2475.

Krogstad, P. A., and Antonia, R. A., 1992, "Comparison Between Rough- and Smooth-Wall Turbulent Boundary Layers," *Journal of Fluid Mechanics,* Vol. 245, pp. 599–617.

Krogstad, P. A., Antonia, R. A., and Browne, L. W. B., 1994, "Structure of Turbulent Boundary Layers on Smooth and Rough Walls," *Journal of Fluid Mechanics,* Vol. 277, pp. 1–21.

Lee, T., Fisher, M., and Schwarz, W. H., 1993, "Investigation of the Stable Interaction of a Passive Compliant Surface with a Turbulent Boundary Layer," *Journal of Fluid Mechanics,* Vol. 257, pp. 373–401.

Lewkowicz, A. K., and Das, D. K., 1981, "Turbulent Boundary Layers on Rough Surfaces With and Without a Pliable Overlayer: A Simulation of Marine Fouling," *Proceedings of the A.S.M.E/A.S.C.E. Bioengineering, Fluid Engineering, and Applied Mechanics Conference,* pp. 174–186.

Lewthwaite, J. C., Molland, A. F., and Thomas, K. W., 1985, "An Investigation into the Variation of Ship Skin Frictional Resistance with Fouling," *Transactions Royal Institute of Naval Architects,* Vol. 127, pp. 269–284.

Ligrani, P. M., and Moffat, R. J., 1986, "Structure of Transitionally Rough and Fully Rough Turbulent Boundary Layers," *Journal of Fluid Mechanics,* Vol. 162, pp. 69–98.

Loeb, G. I., Laster, D., and Gracik, T., 1984, "The Influence of Microbial Fouling Films on Hydrodynamic Drag of Rotating Discs," *Marine Biodeterioration, An Interdisciplinary Study,* J. D. Costlow and R. Tipper, eds., Naval Institute Press, Annapolis, MD, pp. 88–94.

Marine Fouling and Its Prevention, U.S. Naval Institute Press, Annapolis, MD, 1952.

McEntee, W., 1915, "Variation of Frictional Resistance of Ships with Condition of Wetted Surface," *Transactions Society of Naval Architects and Marine Engineers,* Vol. 24, pp. 37–42.

Patel, V. C., and Yoon, J. Y., 1995, "Application of Turbulence Models to Separated Flow over Rough Surfaces," ASME JOURNAL OF FLUIDS ENGINEERING, Vol. 117, June, pp. 234–241.

Perry, A. E., and Joubert, P. N., 1963, "Rough-Wall Turbulent Boundary Layers," *Journal of Fluid Mechanics,* Vol. 37, pp. 383–413.

Perry, A. E., Schofield, W. H., and Joubert, P. N., 1969, "Rough Wall Turbulent Boundary Layers," *Journal of Fluid Mechanics,* Vol. 37, Part 2, pp. 383–413.

Picologlou, B. F., Zelver, N., and Characklis, W. G., 1980, "Biofilm Growth and Hydraulic Performance," ASCE *Journal of the Hydraulics Division,* HY5, pp. 733–746.

Schlichting, H., 1979, *Boundary-Layer Theory,* Seventh Edition, McGraw-Hill.

Schultz, M. P., 1998, "The Effect of Biofilms on Turbulent Boundary Layer Structure," Florida Institute of Technology, Ph.D. Dissertation, May.

Sokal, R. R., and Rohfl, F. J. Biometry, 1981, *The Principles and Practice of Statistics in Biological Research,* W. H. Freeman, San Francisco.

Thole, K. A., and Bogard, D. G., 1996, "High Freestream Turbulence Effect on Turbulent Boundary Layers," ASME JOURNAL OF FLUIDS ENGINEERING, Vol. 118, pp. 276–284.

Winter, K. G., 1977, "An Outline of the Techniques Available for the Measurement of Skin Friction in Turbulent Boundary Layers," *Progress in the Aerospace Sciences,* Vol. 18, pp. 1–57.

On Pressure-Velocity Correlation of Steady and Oscillating Flows in Regenerators Made of Wire Screens

Chin-Tsau Hsu
Senior Lecturer.

Huili Fu
Graduate Student.

Ping Cheng
Professor. Fellow ASME

Department of Mechanical Engineering,
The Hong Kong University of
Science and Technology,
Clear Water Bay, Kowloon,
Hong Kong

A facility capable of generating steady and oscillating flows was constructed and experiments were conducted to investigate the pressure-drop characteristics of regenerators packed with wire screens. Both the velocity and pressure-drop across the regenerator were measured. To accurately determine the correlation between pressure-drop and velocity, the experiments covered a wide range from very low to very high Reynolds numbers, Re_h. The steady flow results reveal that a three-term correlation with a term proportional to $Re_h^{-1/2}$ in addition to the Darcy-Forchheimer two-term correlation will fit best to the data. This $Re_h^{-1/2}$ term accounts for the boundary layer effect at intermediate Reynolds number. The results also show that the correlation for oscillating flows coincides with that for steady flows in $1 < Re_h < 2000$. This suggests that the oscillating flows in the regenerators behave as quasi-steady at the frequency range of less than 4.0 Hz, which is the maximum operable oscillating flow frequency of the facility.

1 Introduction

An accurate prediction of the pressure drop across a regenerator is crucial to the design of a Stirling engine, a cryocooler, or a catalytic converter. To date, the most popular pressure-drop correlation used for the design of these devices is the one provided by Tong and London (1957), who obtained experimental data for steady flows through a stack of wire screens. Later experiments for the pressure-drop correlation for steady flows through wire screens included those of Walker and Vasishta (1971), Miyabe et al. (1982), and most recently of Sodre and Parise (1997). Since the Stirling-cycle machines are operated under the condition of periodically reversing flow, it becomes questionable if the steady flow correlation remains applicable in predicting the pressure-drop in the regenerator of these machines. Rix (1984), for instance, found that a good agreement between simulated and measured pressure-drops could only be achieved if the pressure-drop coefficient given by Tong and London (1957) was arbitrarily adjusted by a factor of 3 to 5.

Few works were performed on the pressure-drop in a packed column subjected to oscillating flows. Tanaka et al. (1990) experimentally investigated the pressure-drop of oscillating flows in a regenerator and obtained a correlation equation between the coefficient f of maximum pressure-drop and Reynolds number Re_h based on the maximum velocity $u_{\max}$ in the packed column and the hydraulic diameter d_h of wire-screens. Recently, Zhao and Cheng (1996) also performed the experiments for oscillating flows through a column packed with wire-screens and obtained a correlation similar to that of Tanaka et al. (1990). In both experiments, $u_{\max}$ was inferred from the stroke volume of the piston motion in their facilities, rather than from a direct measurement.

To correlate pressure-drop data for oscillating flows through wire screens, the following Darcy-Forchheimer two-term correlation equation has been commonly used:

$$f = \frac{C_S}{\mathrm{Re}_h} + C_I \tag{1}$$

where

$$f = \frac{\Delta p_{\max} d_h}{\rho u_{\max}^2 L_p/2} \quad \text{and} \quad \mathrm{Re}_h = \frac{u_{\max} d_h}{\nu}. \tag{2a, b}$$

Equation (1) indicates that there are two limits: Darcy limit for $\mathrm{Re}_h \ll 1$ and Forchheimer limit for $\mathrm{Re}_h > 2000$, corresponding to the first and second terms on the right-hand side of Eq. (1), respectively. The Darcy limit is contributed from the Stokes viscous drag, while the Forchheimer limit from the form drag due to inertia effect.

To determine the coefficients C_S and C_I accurately, experimental data covering a wide range of $0.1 < \mathrm{Re}_h < 3000$ are required. However, Tanaka et al.'s (1990) data were in $10 < \mathrm{Re}_h < 2000$ while Zhao and Cheng's (1996) in $1 < \mathrm{Re}_h < 60$. Hence, their data were not sufficient for the accurate estimate of C_S and C_I. Furthermore, both Tanaka et al. (1990) and Zhao and Cheng (1996) measured only the oscillating flows. As a result, no direct comparison of the correlations for steady and oscillating flows is possible.

The objective of this investigation is to perform experiments to cover a wide range of very low and very high Reynolds numbers so that the correlations of pressure-drop and velocity for both steady and oscillating flows can be accurately determined and compared. To this end, a facility capable of generating steady and oscillating flows was constructed. To delineate the issue of the inter-applicability of the correlation equation between steady and oscillating flows, experiments were performed for both flows in the same regenerator. In Section 2, we first describe the facility, instrumentation, data acquisition system and the data reduction procedure. The experimental results are then presented and discussed in Section 3. Conclusions based on the present experiments are finally drawn in Section 4.

2 Experiments

2.1 Experimental Facility. Figure 1 shows the schematic of the steady and oscillating flow facility and the experimental

Contributed by the Fluids Engineering Division for publication in the JOURNAL OF FLUIDS ENGINEERING. Manuscript received by the Fluids Engineering Division September 3, 1997; revised manuscript received June 11, 1998. Associate Technical Editor: M. N. Dhaubhadel.

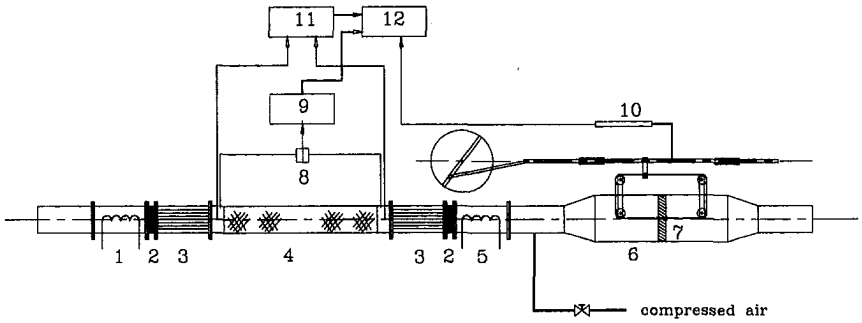

1—heater, 2—mixer, 3—velocity straightner, 4—test section, 5—cooler
6—oscillatory flow generator, 7—piston, 8—pressure transducer
9—CD15 Carrier Demodulator, 10—linear displacement transducer
11—Hot-wire anemometer (TSI-IFA100), 12—A/D converter & computer

Fig. 1 The schematic of the facility and the experimental setup

setup. The facility is basically a circular conduit with one end connected to steady and oscillating flow generating mechanisms and the other end open to the atmosphere. The conduit has a test section (100 mm in diameter) attached to its two ends with two flow-conditioning sections made of steel pipe of the same diameter. The flow conditioning sections were made of a wire-mesh stack for flow mixing and a honeycomb for flow straightening.

The oscillating flow generator consists of a circular cylinder of 220 mm inner diameter, a piston and crank-shaft assembly, and a motor drive mechanism. The piston and crankshaft assembly is connected to a rotation disk driven by a motor through a speed reduction gear box. The speed of the motor is controlled by an AC converter. The stroke of the piston is adjusted by offsetting the center on the rotation disk. By changing the motor speed and the center off-set, oscillating flows with different frequencies and amplitudes were generated. The maximum operable frequency of the oscillating flow generator is 4.0 Hz.

To incorporate the steady flow, a steady flow inlet section was connected between the oscillating flow generator and the flow conditioner as shown in Fig. 1. The steady flow inlet section was fitted with a check valve. In the steady flow operation, compressed air from the laboratory was supplied to the check valve through an adjustable valve to control the air flow rate.

The test section was a column packed with woven screen discs. The mesh sizes of the woven screen were 20, 30 and 40. Three packed column diameters (100, 38.5, 12.8 mm) were used to cover the wide range of Reynolds number needed for the present experiments. The pitch distance p_t (the distance between centers of two consecutive parallel screen wires) and the wire diameter d_w of the wire screens are given in Table 1. For well-packed wire screens, the porosity ϕ and the hydraulic diameter d_h of the column can be determined from the following equations:

$$\phi = 1 - \frac{\pi d_w \sqrt{p_t^2 + d_w^2}}{4p_t^2} \quad \text{and} \quad d_h = \frac{\phi d_w}{1 - \phi}, \quad (3a, b)$$

given by Miyabe et al. (1982) and Tanaka et al. (1990), respectively. The porosity and the hydraulic diameters as determined by Eq. (3) are given in Table 1.

For incompressible oscillating flows as in the present experiment, the fluid-phase volumetric-averaged mean displacement S in the packed column is in phase with the piston motion and the mean velocity u of the fluids is the time derivative of the displacement. Hence, we have

$$S = -S_{\max} \cos \omega t \quad \text{and} \quad u_m = u_{\max} \sin \omega t \quad (4a, b)$$

where $S_{\max} = V_{\text{pis}}/(2A\phi)$ and $u_{\max} = S_{\max}\omega$. The maximum sweep volume V_{pis} of the oscillating flow facility is 4.18×10^{-3} m^3 when the piston was operated at the maximum amplitude of 55 mm. For the maximum frequency of 4.0 Hz, the maximum displacement amplitude is 2.56 m which gives 64.5 m/s as

Nomenclature

d_h = hydraulic diameter of the wire-screen defined in Eq. (3)
d_w = wire diameter of the wire-screen
f = pressure-drop coefficient defined in Eq. (2)
h = arbitrary quantity of interest for performing phase average procedure
i = index for the cycle number in the phase average procedure
p_t = pitch distance of the wire-screen
t = time
u = fluid-phase volumetric averaged mean velocity in the packed column
$u_{\max}$ = maximum mean velocity in the packed column
A = cross-sectional area of the packed column
C_S = constant of the Darcy limit term in correlation Eqs. (1) and (6)
C_B = constant of the skin friction term in correlation Eq. (6)
C_I = constant of the Forchheimer limit term in correlation Eqs. (1) and (6)
L = amplitude of the piston oscillation
L_p = length of the test column packed with wire-screens
N = total number of cycles in the phase average procedure
$\Delta p_{\max}$ = maximum pressure-drop across the packed column
Re_h = hydraulic Reynolds number defined in Eq. (2)
S = mean fluid displacement
$S_{\max}$ = maximum amplitude of mean fluid oscillation in packed column
V_{pis} = sweep volume of the piston motion
ϕ = porosity of the packed column
ν = viscosity of gas
θ_j = phase angle corresponding to the jth data point in a cycle
ρ = density of gas
ω = radian frequency of oscillating flow

Table 1 Properties of the wire-screens and the packed columns

Mesh size	Pitch distance p_t (mm)	Wire diameter d_w (mm)	Porosity ϕ	Hydraulic diameter d_h (mm)
20	1.243	0.32	0.792	1.213
30	0.849	0.22	0.788	0.826
40	0.613	0.224	0.694	0.509

the possible maximum oscillating pore velocity in the packed column of 38.5 mm in diameter.

2.2 Instrumentation. The flow properties measured in the present experiment were the pressure-drop and the velocity across the packed column. The pressure-drop was measured with a differential pressure transducer manufactured by Validyne, Inc. The frequency response of the pressure transducer is higher than 5000 Hz. For the low frequency application of this experiment, a static calibration is adequate. Two transducers with different sensitivities (Models DP15 and DP103) and several diaphragms (#18, #22, #24, #30, #36) were used in order to cover the large range of pressure drop. The velocity was measured at the open end of the packed column using a hot-wire anemometer (IFA100) manufactured by TSI Inc. Because the hot-wire was located immediately outside the packed column, the velocity measured in the present experiment is the Darcy's velocity equal to ϕu. The installation of the hot-wire probe at the open end of the test section ensured that the velocity was measured under the atmospheric pressure, consistent with the calibration condition. For oscillating flow experiments, the displacement of the piston was also measured by a linear displacement transducer. The output signals from the differential pressure transducer, hot-wire anemometer, and linear displacement transducer were connected to a data acquisition system.

2.3 Data Acquisition and Reduction. The data acquisition system used in the present experiment consists of a Concurrent mini-computer, a 12-bit A/D converter, a UNIX operation system, and a Laboratory Workbench software (proprietary of Concurrent Computer Co.). It serves as a data acquisition and analysis tool. The data flow was controlled and processed internally with the Laboratory Workbench software by setting up a virtual data acquisition instruments on a graphic terminal. The burst rate of the A/D converter is up to 10×10^6 Hz. Thus, all channels can be acquired in a nearly real time fashion. The sampling frequency used in the experiment was 500 Hz to ensure enough data points in each oscillation cycle. The data length of each run contains more than 100 cycles of data for different frequencies. Thus, the statistic results of the flow quantities can be obtained.

For steady flow experiments, the straight-forward time average procedure is used. For oscillating flow experiments, a phase-average procedure (averaging per cycle at fixed phase angle of oscillation) and a power spectrum analysis was adapted. The following expression,

$$h(\theta_j) = \frac{1}{N}\sum_{i=1}^{N} h_i(\theta_j), \tag{5}$$

is adapted for the phase-average procedure. It should be noted that the hot-wire anemometer can not distinct the velocity direction of the reversing flow. Therefore, the velocity signal was pre-processed by reversing its sign on every other half cycle. Both phase-averaging and sign-reversing processes used the piston displacement signal as reference.

The power spectral analysis was performed to extract the oscillating frequency from the data. This determines accurately the time period of oscillation for phase-average procedure. The spectral density is obtained by simply taking the discrete Fourier transform (DFT) to the data samples and computing the square of magnitude of the results. Fast Fourier transform technique was used to minimize the DFT execution time.

3 Results and Discussions

3.1 Steady Flows. For steady flows through a packed column, the time-averaged pressure-drop and velocity are taken, respectively, as $\Delta p_{\max}$ and $u_{\max}$, since the steady flow can be regarded as the zero-frequency limit of oscillating flow at maximum. Hence, the pressure-drop coefficient and the Reynolds number defined by Eq. (2) remain applicable for steady flows. Figure 2 shows the correlation of the pressure-drop coefficient with the Reynolds number for steady flows across the column packed with 40 mesh-size wire screens. The experimental data represented by triangular symbols cover the wide range of $0.27 < \mathrm{Re}_h < 2600$. To best fit the experimental data, the following three-term composite correlation equation, proposed by Hsu and Cheng (1990) based on creeping flow for low Reynolds number and boundary layer flow for high Reynolds number, is used:

$$f = \frac{C_S}{\mathrm{Re}_h} + \frac{C_B}{\mathrm{Re}_h^{1/2}} + C_I. \tag{6}$$

The most important feature in Fig. 2 is that the experimental data has covered a wide range to encompass the Darcy limit at low Reynolds number and the Forchheimer limit at high Reynolds number for the accurate determination of the constants C_S and C_I. Therefore, C_B can be determined accurately by the experiment. The values of C_S, C_B, and C_I as obtained from the curve-fitting are 109.3, 5.0, and 1.0, respectively. For comparison, the curve with $C_B = 0$, i.e., Eq. (1), is also plotted in Fig. 2. From the results of Fig. 2, it is seen that the exclusion of the second term on the right hand side of Eq. (6) underestimates the pressure-drop by 20–30 percent in the intermediate Reynolds number range of $40 < \mathrm{Re}_h < 1000$.

The existence of the second term in proportional to $\mathrm{Re}_h^{-1/2}$ in Eq. (6) can be justified from the fact that a flow past a blunt body will experience a boundary layer flow behavior (dominated by viscous skin friction). This boundary layer behavior transits from a creeping flow at very low Reynolds number (dominated by viscous force) to a separated flow at high Reynolds number (dominated by inertia force). This forms the physical base for the closure formulation by Hsu and Cheng (1990). A theoretical closure by Whitaker (1996) also suggested the inclusion of the term of velocity of $\frac{3}{2}$ power as the first correction to Darcy's law. A three-term correlation equation between pressure-drop and velocity for a steady flow in particle beds was also investigated by Molerus and Schweinzer (1989).

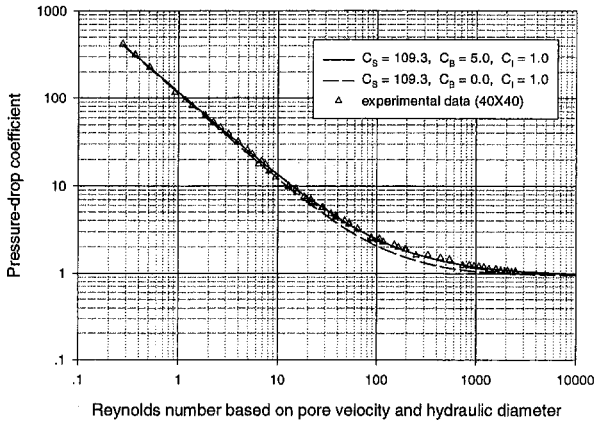

Fig. 2 The pressure-drop coefficient of steady flows through a regenerator packed with wire-screens

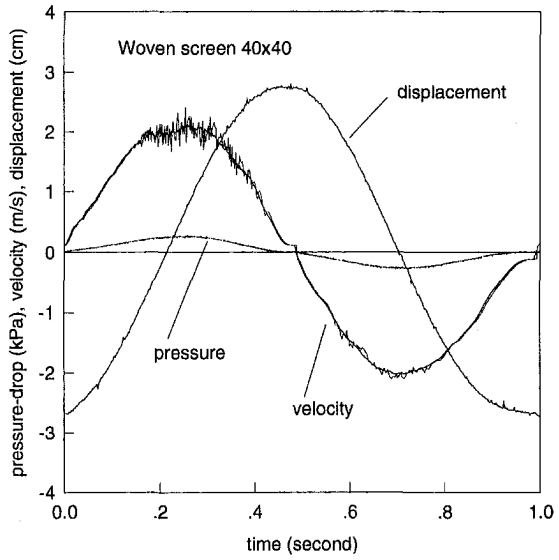

Fig. 3 The phase-averaged results and their comparison to the unaveraged results

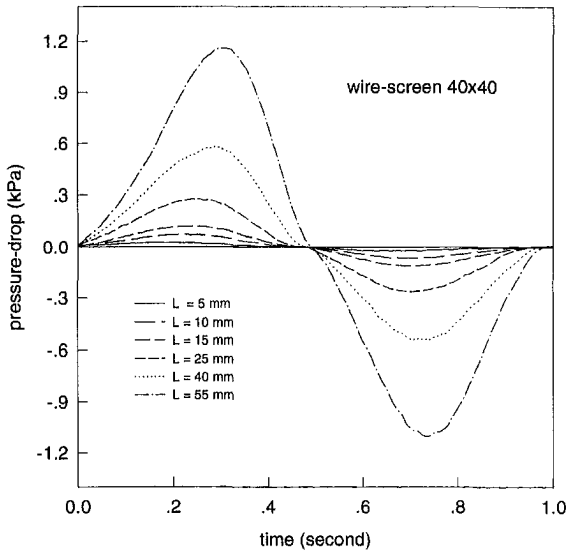

Fig. 5 The phase-averaged results of pressure-drop for different piston amplitudes

3.2 Oscillating Flows. In the following, we shall present first the phase-averaged results for oscillating flows in a regenerator. Only the typical results for the wire-screens of mesh size 40 are presented. Figure 3 shows the phase-averaged pressure-drop and velocity when the oscillatory frequency is 1.0 Hz and the piston amplitude 25 mm. The piston displacement signal used as reference for phase averaging is also shown in Fig. 3. To show the effectiveness and the uncertainty of the phase-average procedure, the raw signals of velocity and pressure-drop of one typical cycle as characterized by distinguishable fluctuations are also plotted in Fig. 3. Figure 3 shows that the maximum velocity occurs when the pressure-drop is maximum and the piston displacement is zero. Zero velocity and zero pressure-drop also occur simultaneously when the displacement is at maximum and minimum. The in-phase relationship suggests that the velocity responses very quickly to the pressure driving force.

The phase-averaged results corresponding to different piston amplitudes are summarized in Figs. 4 for velocity and in Fig. 5 for pressure-drop. Here the frequency is fixed at 1.0 Hz and the location of zero phase is the same as that of Fig. 3. One distinct feature in Figs. 4 and 5 is that the waveform contains more harmonics when the amplitude becomes larger. This leads to the shift of the maximum. The generation of harmonics is usually a sign of nonlinear process. However, we also see that the phases of velocity and pressure-drop are still locked together very well. The results of Figs. 4 and 5 clearly indicate that the correlation between pressure and velocity is linear only when the amplitude is small and the frequency is low.

The correlation of the maximum pressure-drop with the maximum velocity for the oscillating flows in the regenerator of mesh-size 40 wire-screens is shown in Fig. 6. For comparison, the steady flow data are also plotted in Fig. 6. The most fascinating result is that the oscillating flow data collapse into the steady flow data. This implies that the oscillating flows in the regenerator can be regarded as quasi-steady. Hence, the steady flow correlation between pressure-drop and velocity as given by Eq. (6) can be used indiscriminately for oscillating flows, at least up to 4.0 Hz as performed in this experiment.

Figure 7 shows the correlation of the maximum pressure-drop with the maximum velocity for the oscillating flows in the regenerators of the three mesh sizes of 20, 30, and 40. In Fig. 7, the data of Tanaka et al. (1990) for mesh sizes of 50, 100, 200 of wire screens are also plotted. It appears that the results

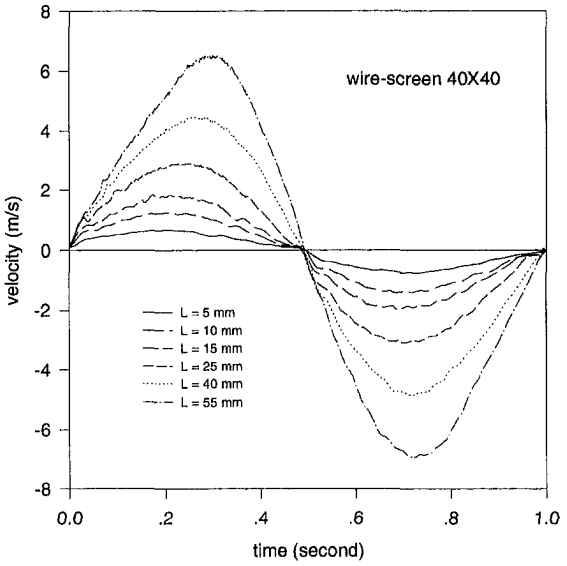

Fig. 4 The phase-averaged results of velocity for different piston amplitudes

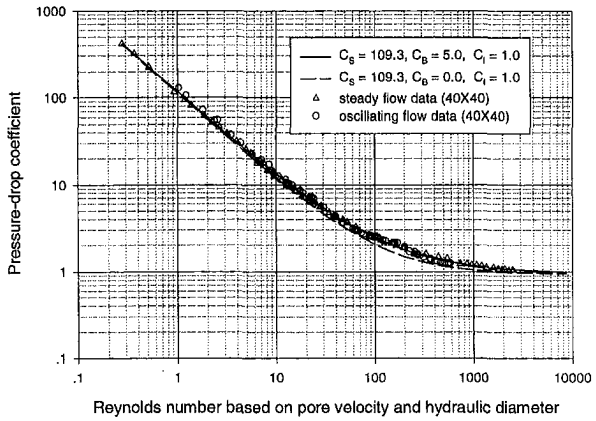

Fig. 6 The comparison of the correlation of pressure-drop with velocity for oscillating flows with the correlation for steady flows

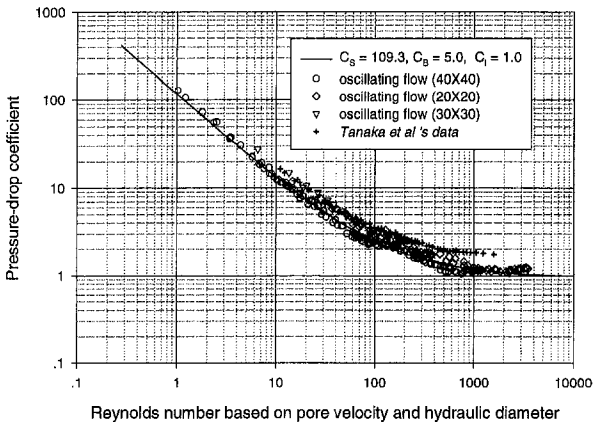

Fig. 7 The correlation of pressure-drop with velocity for oscillating flows in regenerators packed with different mesh-sizes of wire-screens

of Tanaka et al. (1990) are higher than our present results by about 35 percent. The difference may be due to the use of different sizes of wire screens and of different method for obtaining the velocity maximum. Figure 7 also indicates that the C_S, C_B, and C_I seem to depend on the local geometry of the wire-screens.

3.3 Data Uncertainty. Uncertainty analysis based on the method described by Taylor (1982) was performed. The uncertainties of the measured quantities in the present experiments are assumed to be random with normal distribution. These uncertainties are mainly from the measurement accuracy of the pressure drop and the velocity, and the finite data cycles used for phase-average. To minimize the data reduction uncertainty, data with length of 100 cycles was collected in oscillating flow experiments. The uncertainties of velocity and pressure drop are estimated as 2.0 percent. The uncertainty of hydraulic Reynolds number and pressure-drop coefficient is estimated as 3.5 and 6.0 percent, respectively. Therefore, the uncertainty shown in Figs. 2, 6, and 7 are estimated to be seven percent.

4 Conclusions

The correlation between pressure-drop and velocity for steady and unsteady oscillating flows through porous materials packed with wire screens was measured over a wide range of Reynolds number. The maximum frequency imposed in the present experiments was 4.0 Hz. From the experimental results, the following conclusions are drawn:

1. The steady flow experiments show that the three-term Eq. (6), as proposed by Hsu and Cheng (1990) with a term proportional to $\mathrm{Re}_h^{-1/2}$ to account for the boundary layer effect in the intermediate range of Reynolds number, will provide the best correlation between pressure-drop and velocity.
2. For oscillating flows, the velocity responses quite linearly to the pressure gradient when the piston amplitude is small. This suggests that Darcy's law is valid for small amplitude oscillating flows.
3. When the piston amplitude becomes large, the response and therefore the correlation of pressure-drop and velocity in the regenerator become nonlinear.
4. For the same packed column, the correlation between pressure-drop and velocity for oscillating flows is the same as the steady flow correlation. Hence, the oscillating flow in the regenerator can be regarded as quasi-steady, and Eq. (6) can be used to predict pressure drop across a regenerator for both steady and oscillating flows under the present experimental condition.

Acknowledgments

This work is supported by the Hong Kong Government through RGC Grants, Nos. HKUST575/94E, HKUST708/95E, and HKUST815/96E.

References

Hsu, C. T. and Cheng, P., 1990, "Thermal Dispersion in a Porous Medium," *International Journal of Heat and Mass Transfer,* Vol. 33, pp. 1587–1597.

Miyabe, H., Takahashi, S., and Hamaguchi, K., 1982, "An Approach to the Design of Stirling Engine Regenerator matrix Using Packs of Wire Gauges," *Proceedings of 17th IECEC,* pp. 1839–1844.

Molerus, O. and Schweinzer, J., 1989, "Resistance of Particle Beds at Reynolds Number Up to Re $\approx 10^4$," *Chemical Engineering Science,* Vol. 44, pp. 1071–1079.

Rix, D. H., 1984, *Gas Process Asymmetry in Stirling Cycle Machines,* Ph.D. thesis, Engineering Dept., Cambridge University.

Sodre, J. R., and Parise, J. A. R., 1997, "Friction Factor Determination for Flow Through Finite Wire-Mesh Woven-Screen Matrices," ASME JOURNAL OF FLUIDS ENGINEERING, Vol. 119, pp. 847–851.

Tanaka, M., Yamashita, I., and Chisaka, F., 1990, "Flow and Heat Transfer Characteristics of the Stirling Engine Regenerator in an Oscillating Flow," *JSME International Journal,* Vol. 33, pp. 283–298.

Taylor, J. R., 1982, *An Introduction to Error Analysis—Study of Uncertainty in Physical Measurements,* Oxford University Press.

Tong, L. S., and London, A. L., 1957, "Heat Transfer and Flow-Friction Characteristics of Woven-Screen and Cross-Rod Matrices," *Trans. ASME,* pp. 1558–1570.

Walker, G., and Vasishta, V., 1971, "Heat Transfer and Friction Characteristics of Wire-Screen Stirling Engine Regenerators," *Advanced Cryogenic Engineering,* Vol. 16, pp. 324–332.

Whitaker, S., 1996, "The Forchheimer Equation: A Theoretical Development," *Transport in Porous Media,* Vol. 25, pp. 27–61.

Zhao, T. S., and Cheng, P., 1996, "Oscillatory Pressure-Drops Through a Woven-Screen Packed Column Subjected to a Cyclic Flow," *Cryogenics,* Vol. 36, pp. 333–341.

Modeling Turbulent Wall Flows Subjected to Strong Pressure Variations

K. Hanjalić
Professor.

I. Hadžić
Doctoral Candidate.

Faculty of Applied Physics,
Delft University of Technology,
2628 CJ Delft,
The Netherlands

S. Jakirlić
Scientist,
Institute for Fluid Dynamics
and Aerodynamics,
Darmstadt University of Technology,
64287 Darmstadt,
Germany

Mean pressure gradient affects the turbulence mainly through the modulation of the mean rate of strain. Modification of the turbulence structure feeds, in turn, back into the mean flow. Particularly affected is the near wall region (including the viscous sublayer) where the pressure gradient invalidates the conventional boundary-layer "equilibrium" assumptions and inner-wall scaling. Accurate predictions of such flows require application of advanced turbulence closures, preferably at the differential second-moment level with integration up to the wall. This paper aims at demonstrating the potential usefulness of such a model to engineers by revisiting some of the recent experimental and DNS results and by presenting a series of computations relevant to low-speed external aerodynamics. Several attached and separated flows, subjected to strong adverse and favorable pressure gradient, as well as to periodic alternation of the pressure gradient sign, all computed with a low-Re-number second-moment closure, display good agreement with experimental and DNS data. It is argued that models of this kind (in full or a truncated form) may serve both for steady or transient Reynolds-Averaged Navier-Stokes (RANS, TRANS) computations of a variety of industrial and aeronautical flows, particularly if transition phenomena, wall friction, and heat transfer are in focus.

1 Pressure Gradient and Implications on Turbulence Modeling

It is known that in incompressible flow the pressure gradient affects the turbulence properties and their budget only *indirectly,* through the modulation of the mean strain. Experiments and direct numerical simulations (DNS) in attached boundary layers at moderate-to-strong pressure gradients (e.g., Samuel and Joubert, 1974; Simpson et al., 1981; Nagano et al., 1993; Spalart and Watmuff, 1993; Spalart and Coleman, 1997) reveal that the strongest effects are noticed in the wall region, permeating even through the viscous sublayer up to the wall and invalidating the equilibrium inner wall scaling (U_τ, ν/U_τ) for turbulence properties. The free-stream fluctuations remain largely unaffected, except, possibly much further downstream (depending on the imposed pressure gradient) where the turbulent diffusion and lateral convection due to thickening of the boundary layer may modify the rest of the flow away from the wall. Moreover, because of indirect ('chain') effects on the stress production, redistribution, and turbulent transport, different stress components respond at different rates, thus modifying the anisotropy of the stress field and, through a feed-back, the mean flow field. Favorable pressure gradient thickens the viscous sublayer, but also suppresses the wall-normal velocity fluctuations. This leads to an increase in the near-wall stress anisotropy, expanding the extent of the region where the turbulence is closer to the two-component limit, Jakirlić (1997). Adverse pressure gradient acts opposite and shifts the anisotropy maximum away from the wall. The extent of the affected region increases with an increase in the adverse pressure gradient. This is illustrated in Fig. 1, which shows the near-wall distribution of Lumley's two-componentality ("flatness") parameter $A = 1 - 9/8(A_2 - A_3)$ for boundary layers at zero, favorable and adverse pressure gradients where $A_2 = a_{ij}a_{ji}$, $A_3 = a_{ij}a_{jk}a_{ki}$ are the second and third invariants of the turbulent stress anisotropy $a_{ij} = \overline{u_iu_j}/k - 2/3\delta_{ij}$. Of course, the modulation in the turbulence anisotropy is not confined only to the stress-bearing large-scale motion, but extends to the dissipative scales, modulating the anisotropy of the dissipation rate tensor $e_{ij} = \epsilon_{ij}/\epsilon - 2/3\delta_{ij}$ irrespective of the bulk Reynolds number. A plot of the two-componentality parameter for dissipative motion $E = 1 - 9/8(E_2 - E_3)$, where $E_2 = e_{ij}e_{ji}$, $E_3 = e_{ij}e_{jk}e_{ki}$, exhibits a similar effect of pressure gradient, except that the E will approach the isotropic limit ($E = 1$) much closer to the wall (not shown).

These are only some of the facets of the effects of the mean pressure gradient on the turbulence fluctuations in the near-wall region, indicating a necessity for a turbulence model to account for separate contribution of *each* stress components to the momentum balance, as well as to the dynamics of the turbulence scale and of the stress tensor itself. Best prospects for accurate predictions of turbulent flows with strong pressure gradients have the second-moment models which can mimic better the dynamics of the turbulent stress field and evolution of each stress component. Furthermore, the departure from local equilibrium and conventional boundary layer scaling, calls for resolving in full the near-wall layer with all necessary implications on model modifications for the wall-proximity and viscous effects.

This paper presents some results of a systematic testing of a version of the second-moment closure with low-Re-number and wall-vicinity modifications. Some modifications of ϵ-equations are considered, which are applicable also to the high-Re-number models. Arguments in favor of these modifications, as well as the complete low-Re-number model, will be substantiated by presenting some results for a series of attached and separating wall flows. For illustration, some cases obtained with the high-Re-number second-moment and with the standard $k - \epsilon$ closures will also be shown. Considered cases include flows in strong favorable pressure gradient (including laminarization), bypass transition on a finite-thickness plate, flows in adverse pressure gradient (nonseparating and separating) and flows subjected to periodic alternation (in time or space) of positive and negative pressure gradients. Also, some results of computational study of mean flow and turbulence field in flows separating on sharp

Contributed by the Fluids Engineering Division for publication in the JOURNAL OF FLUIDS ENGINEERING. Manuscript received by the Fluids Engineering Division March 19, 1998; revised manuscript received October 12, 1998. Associate Technical Editor: P. Bradshaw.

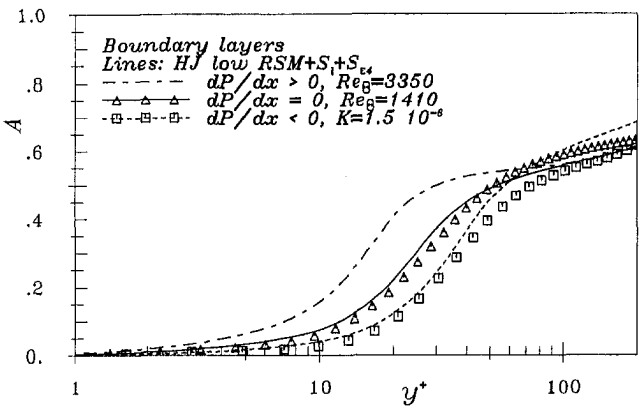

Fig. 1 Lumley's two-componentality ("flatness") parameter $A = 1 - 9/8(A_2 - A_3)$ for boundary layers at zero, favorable and adverse pressure gradients

edges (backstep) and on curved surfaces (airfoil), will be presented.

The presented model serves more as an illustration of a potential, rather than a proposal of a "superior" model to be used for all purposes. The rationale of the model has been published elsewhere (e.g., Hanjalić and Jakirlić, 1998, Hanjalić et al., 1997) and only a brief outline is given in the next chapter. The model demands a fine grid near walls, which may hinder its wider application to very complex three-dimensional flows at high Re-numbers. It is argued, however, that this approach may be unavoidable if transition phenomena and accurate wall friction and heat transfer are in focus, such as in the problem of gas turbine blade cooling. Successful reproduction of the near wall second-moment statistics (in addition to mean flow), even in separation bubbles, around reattachment and in subsequent recovery, qualifies this approach (in full or a truncated form) both for steady or transient Reynolds-Averaged-Navier-Stokes (RANS, TRANS) computations of a variety of industrial and aeronautical flows.

2 The Low-Re-Number Second-Moment Closure

The model is defined by the transport equations for turbulent stress tensor and turbulence energy dissipation:

$$\frac{D\overline{u_iu_j}}{Dt} = \mathscr{D}_{ij} - \left(\overline{u_iu_k}\frac{\partial U_j}{\partial x_k} + \overline{u_ju_k}\frac{\partial U_i}{\partial x_k}\right) + \Phi_{ij} - \epsilon_{ij}$$

$$\frac{D\epsilon}{Dt} = \mathscr{D}_\epsilon - C_{\epsilon_1}\frac{\epsilon}{k}\overline{u_iu_j}\frac{\partial U_i}{\partial x_j} - C_{\epsilon_2}f_\epsilon\frac{\epsilon\tilde{\epsilon}}{k} + C_{\epsilon_3}\nu\frac{k}{\epsilon}\overline{u_ju_k}\frac{\partial^2 U_i}{\partial x_j\partial x_l}\frac{\partial^2 U_i}{\partial x_k\partial x_l} + S_\Omega + S_l$$

where $\mathscr{D}_\Phi = \partial/\partial x_k[(\nu\delta_{kl} + C_\Phi(k/\epsilon)\overline{u_ku_l})\partial\Phi/\partial x_l]$ is the diffusion of property Φ ($\overline{u_iu_j}$ and ϵ).

The model is based on the standard high-Re-number second-moment closure with exception of two additional terms S_Ω and S_l in the ϵ equation:

$$S_\Omega = -C_{\epsilon 4}f_4k\Omega_k\Omega_k$$

$$S_l = \max\left\{\left[\left(\frac{1}{C_l}\frac{\partial l}{\partial x_n}\right)^2 - 1\right]\left(\frac{1}{C_l}\frac{\partial l}{\partial x_n}\right)^2; 0\right\}\frac{\tilde{\epsilon}\epsilon}{k}A$$

The first term (Hanjalić and Launder, 1980), where $\Omega_i = \epsilon_{ijk}\partial U_i/\partial x_j$ is the mean vorticity vector, sensitizes the production of ϵ (in fact, the spectral energy transfer) to both the sign and intensity of the irrotational straining and was found essential for modeling the evolution of ϵ in flows with strong acceleration and deceleration. The above invariant form, with $C_{\epsilon 4} = 0.1$ (and $f_4 = 1$ for high Re numbers) requires $C_{\epsilon 1} = 2.6$ to satisfy the near-wall equilibrium in a constant pressure boundary layer. For two-dimensional flows, a simplified form (used in the present computations) may be derived using near-wall equilibrium conditions, $C^*_{\epsilon 4}(\overline{u_2^2} - \overline{u_1^2})(\partial U_1/\partial x_1)\epsilon/k$, where $C^*_{\epsilon 4} = 1.16$ and $C_{\epsilon 1}$ retains the standard value of 1.44.

The term S_l acts as an extra source of ϵ to suppress an excessive growth of the turbulence length scale. Its origin is empirical, though its expansion (substituting $l = k^{3/2}/\epsilon$) and performing chain differentiation) leads to a cross-diffusion term with mixed derivatives of k and ϵ, which has been earlier proposed by several authors on the basis of more rigorous derivation of ϵ equation from two-point correlation and spectral theories. The term has a local character and was found particularly useful in reproducing the turbulence and flow pattern around separation and reattachment. More details are given in Hanjalić and Jakirlić (1998) and Hanjalić et al. (1997).

A major difference between various high-Re-number models is in the treatment of the pressure strain term Φ_{ij}. In the present work we have adopted the basic linear models both for the slow and rapid terms, with Gibson and Launder (1978) "wall-echo" correction, which ensures a proper level of stress anisotropy in wall-parallel near-equilibrium flows:

$$\Phi_{ij,1} = -C_1\epsilon a_{ij} \quad \Phi_{ij,2} = -C_2\left(P_{ij} - \frac{2}{3}P_k\delta_{ij}\right)$$

$$\Phi^w_{ij,1} = C^w_1 f_w\frac{\epsilon}{k}\left(\overline{u_ku_m}n_kn_m\delta_{ij} - \frac{3}{2}\overline{u_iu_k}n_kn_j - \frac{3}{2}\overline{u_ku_j}n_kn_i\right)$$

$$\Phi^w_{ij,2} = C^w_2 f_w\left(\Phi_{km,2}n_kn_m\delta_{ij} - \frac{3}{2}\Phi_{ik,2}n_kn_j - \frac{3}{2}\Phi_{kj,2}n_kn_i\right).$$

The linear model was adopted because of its simplicity, computational robustness and satisfactory performance in a number of wall bounded flows (except for impinging and rotating flows, which are beyond the scope of present paper). More general tensorial expansion, closed by Caley-Hamilton theorem, leads to nonlinear models with quadratic stresses in the slow term and up to cubic in the rapid term. While the nonlinearity of the return to isotropy seems justified (though the quadratic terms are usually small), the rapid term should be linear in stress tensor, because its exact form is linear in the energy spectrum (Speziale and Gatski (1991)). Cubic models have been proposed which reproduce better DNS for a plane channel, without a need to introduce variable coefficients, nor additional terms for near-wall effects (Craft and Launder), but at the expense of a large number of terms and coefficients. Such a complexity in the model of just a part of a single term in the stress transport equation is disproportionate with the relative simplicity of the rest of the modeled terms both in $\overline{u_iu_j}$- and standard ϵ equation.

In order to enable integration up to the wall, the coefficients in the model need to be modified to account for wall-vicinity and viscous effects, as well as to satisfy the two-componentality and vanishing-Re-number limits. The effect of viscosity, only indirectly related to the wall presence via no-slip conditions (and, hence, independent of the wall distance and its topology), is accounted for by introducing functions of turbulence Re number $\mathrm{Re}_t = k^2/(\nu\epsilon)$ (not only in Φ_{ij}) in a general form to apply both close to a wall and away from it.

Inviscid wall effects are basically dependent on the distance of a solid wall and its orientation, as seen from the surface integral in the Poisson equation for fluctuating pressure ("Stokes term"). This term accounts for the wall blockage and pressure reflection. The DNS data for plane channel flow show that this term decays fast with the wall distance and becomes insignificant outside the viscous layer. However, a notable dif-

ference in the stress anisotropy between a homogeneous shear flow and equilibrium wall boundary layer for comparable shear intensities shows that the effect of wall presence permeates much further away from the wall into the log-layer. This indicates at an indirect wall effect through a strong inhomogeneity of the mean shear rate, the fact which is ignored by all available pressure strain models.

In the present work we have retained Gibson-Launder wall reflection to account predominantly for the wall effects outside the viscous layer. The term contains the nearest wall distance x_n in the function f_w and the unit vector n_i of the normal to the wall projected from the point under consideration. Despite some opposing views in literature, we have retained topology parameters for physical reasons as discussed above. Replacing the wall echo term by nonlinear rapid pressure strain models leads either to very complex expressions (e.g., cubic models), or insufficient effects (e.g., quasi-quadratic models of Speziale, Sarkar and Gatski). Besides, in all flows considered, the use of wall distance and unit normal vector poses no computational problems (both are computed a priori during the process of grid generation).

Wall impermeability imposes a blockage to fluid velocity and its fluctuations in the normal direction causing a strong anisotropy of the turbulence. We exploit this fact by introducing, in addition to Re_t, both the turbulent-stress and dissipation-rate anisotropy invariants A_2, A_3, A, E_2, E_3, and E (defined earlier) as parameters in the coefficients, accounting thus far separately for the wall effect on anisotropy of stress bearing and dissipative scales:

$$C_1 = C + \sqrt{A}E^2 \quad C = 2.5AF^{1/4}f \quad F = \min\{0.6; A_2\}$$

$$f = \min\left\{\left(\frac{\mathrm{Re}_t}{150}\right)^{3/2}; 1\right\} \quad f_w = \min\left[\frac{k^{3/2}}{2.5\epsilon x_n}; 1.4\right]$$

$$C_2 = 0.8A^{1/2} \quad C_1^w = \max(1 - 0.7C; 0.3)$$

$$C_2^w = \min(A; 0.3).$$

For the stress dissipation rate, we use the model of Hanjalić and Jakirlić (1993), which reproduced well the DNS components of ϵ_{ij} both in channel flow and in a backward facing step (Hanjalić and Jakirlić, 1998):

$$\epsilon_{ij} = f_s\epsilon_{ij}^* + (1 - f_s)\frac{2}{3}\delta_{ij}\epsilon$$

$$\epsilon_{ij}^* = \frac{\epsilon}{k}\frac{[\overline{u_iu_j} + (\overline{u_iu_k}n_jn_k + \overline{u_ju_k}n_in_k + \overline{u_ku_l}n_kn_in_j)f_d]}{1 + \frac{3}{2}\frac{\overline{u_pu_q}}{k}n_pn_qf_d}$$

$$f_s = 1 - \sqrt{A}E^2 \quad f_d = (1 + 0.1\ \mathrm{Re}_t)^{-1}$$

$$f_\epsilon = 1 - \frac{C_{\epsilon_2} - 1.4}{C_{\epsilon_2}}\exp\left[-\left(\frac{\mathrm{Re}_t}{6}\right)^2\right]$$

The basic coefficients take the following values:

$$C_s = 0.22 \quad C_\epsilon = 0.18 \quad C_{\epsilon_1} = 1.44$$

$$C_{\epsilon_2} = 1.92 \quad C_{\epsilon_3} = 0.25 \quad C_l = 2.5.$$

3 Illustrations

3.1 Transitional Flows. In addition to reverse transition caused by a strong favorable pressure gradient, the RANS approach can be used also to predict some forms of forward transition. The first category are the laminar-like flows with some background turbulence (''turbulescence''), which is too weak to influence the laminar-like character of the mean flow, but sufficient to be ''revived'' when a flow deformation is imposed, or reaches a sufficient strength to interact with the background turbulence. The second category are the initially laminar flows with a continuous source of turbulence somewhere in the flow or at its edge, from where the turbulence will diffuse (be entrained) into the rest of the nonturbulent flow.

The first example is the oscillating boundary layer around a zero mean, where in a wide range of Reynolds numbers ($\mathrm{Re}_{\delta_S} = U_\infty\delta_S/\nu$ from ≈700 to 3000, where δ_S is the Stokes thickness) both the forward and reverse transitions occur within a single cycle. Once the fully developed conditions are achieved, the flow becomes phase-self-similar and independent of initial conditions, and is very convenient for testing the dynamics of response of turbulence models. Of course, the forward transition in this case has no resemblance with the actual process of development of Tollmien-Schlichting type of instabilities in an originally purely laminar flow. It is merely a switch-over from a ''laminar-like'' regime with slowly decaying turbulence remnants. This transition to fully developed turbulence occurs at the onset of deceleration phase and is characterized by a sudden rise of turbulent stresses, reflected also in a steep increase in the wall shear stress to a value pertaining to fully turbulent wall-boundary layers. Prediction of this phenomenon at an appropriate phase angle, which varies with Reynolds number, is a major challenge to turbulence models, because it reflects the ability of a model to reproduce the full dynamics of a strongly anisotropic turbulence field subjected to periodic perturbations. Because different interactions have their own dynamics (preferential production into the streamwise stress component, subsequent redistribution by pressure-strain, nonhomogeneous decay over the part of the cycle around the flow reversal when the mean flow becomes almost stagnant) each stress component will exhibit a different degree of hysteresis in the response to the mean flow perturbation. The reproduction of the decay process is a major prerequisite for the prediction of sudden transition at the appropriate phase angle. For that reason this flow is a sensitive indicator of the model performances in dealing with low-Re-number phenomena. Figure 2(a) shows a very successful reproduction of DNS by Justesen and Spalart (1990) of the cyclic variation of the wall shear in an oscillating boundary layer with a ''steep'' variation of free-stream velocity with a resting period between the acceleration and deceleration. A sudden revival of turbulence at the phase angle of $\varphi \approx 120$ deg is in excellent agreement with the DNS results. Note the steep variation of the free-stream velocity and the alteration of strong favorable and adverse pressure gradient (inserted figure). The same model gave equally satisfactory results for other Reynolds numbers over a broader range. The model was also applied to predict an oscillating flow in a pipe of finite and infinite length where the pipe-flow Re-number is an additional parameter governing the transition. Figure 2(b) displays the wall shear stress over a cycle in a fully developed oscillating pipe flow with the imposed sinusoidal variation of the pressure gradient (inserted figure) compared with experiments of Akhavan et al. (1991).

Predicting the ''bypass transition'' poses different problems. Here the laminar-to-turbulent transition is promoted by turbulence penetration into the laminar boundary layer from the outer stream with a uniform turbulence field. Unlike preceding cases, the major prerequisite for a successful reproduction of the transition for different levels of free-stream turbulence depends on the model ability to mimic the turbulent diffusion. The review by Savill (1996) of the performances of various models in predicting the bypass transition on a flat plate with different levels of free-stream turbulence revealed that models which do not use the local wall distance in damping functions, perform generally better and that the second-moment closures are generally more powerful than the two-equation models. None of the models was able to reproduce the cases with the free-stream turbulence below 3 percent, what is probably the lower limit tractable by the RANS models.

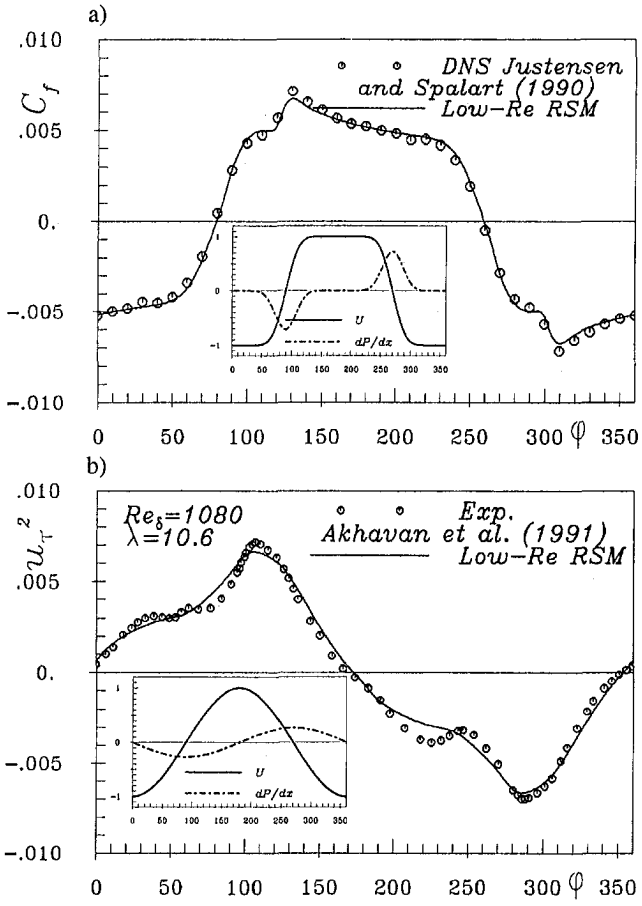

Fig. 2 Cyclic variation of the wall shear stress in: (*a*) an oscillating boundary layer with steep variation of the mean free-stream velocity at $Re_{\delta S}$ = 1000; (*b*) a fully developed oscillating pipe flow with imposed sinusoidal variation of the pressure gradient at $Re_{\delta S}$ = 1080 and $\lambda = R/\delta$ = 10.6

In the case of transition on bodies with finite thickness and in nonuniform pressure field, the inability to reproduce the proper turbulence level and anisotropy in the stagnation region leads usually to very erroneous results. Experiments indicate that a thin laminar separation bubble appears short after the leading edge. The transition to turbulence occurs at the rear end of the separation bubble, very close to the wall, followed by a gradual diffusion of turbulence into the outer flow region. Turbulence generation close to the wall at the end of separation bubble is much more dominant than the entrained free-stream turbulence. Predicting the correct shape and size of the separation region, which is crucial for predicting correctly the transition, requires the application of both an advanced turbulence model and an accurate numerical method (higher order convection schemes) combined with a very fine numerical grid. Computations with the Launder and Sharma low-Re-number $k - \epsilon$ model produces the transition and an excessive turbulence level already in the stagnation region, causing a strong mixing, which prevents the separation. The present low-Re-number second-moment closure reproduced the flow pattern with laminar separation bubble, the location of the transition and the subsequent development of the turbulence field in good agreement with experiments (Hanjalić and Hadžić, 1995).

3.2 Boundary Layers in Adverse Pressure Gradient. The computation of an oscillating boundary layer demonstrated the ability of a model to respond to the imposed alternating favorable and adverse pressure gradient. However, a prolonged action of a strong or increasing adverse pressure gradient, which may lead to flow separation, poses additional challenge since the time lag in response of turbulence field to the pressure variation shows a marked influence only at a later stage downstream. In the 1980/81 AFOSR/HTTM-Stanford Conference on Complex Turbulent Flows one of the test cases was such a flow investigated by Samuel and Joubert (1974). Most participants reproduced well the initial variation of the skin-friction coefficient, but many failed to do so for the later portion of the flow downstream. It should be recalled that over much of the flow length both dP/dx and d^2P/dx^2 are positive (increasingly adverse). Here the turbulence intensities in the outer 80 percent of the flow at all stations retained essentially the same values and similar profile shape irrespective of the imposed pressure gradient. However, at the last measuring station, where the pressure gradient was decreasingly adverse, the turbulence intensity in the outer region showed a sudden increase. Samuel and Joubert (1974) argued that the reason for a sudden change in the turbulence level was caused by the rapid thickening of the layer after imposing a decreasingly adverse pressure gradient. More recent analysis of other data seems to suggest that a prolonged evolution of stress anisotropy due to effects of strong pressure gradient (irrespective whether increasingly or decreasingly adverse) can be a major cause for the downstream modulation of the turbulence field. This would explain the failure of two-equation models to predict the friction factor further downstream. Surprisingly, the standard second-moment closure gave only marginal improvements, indicating at possible inadequacy of the simple form of the standard ϵ equation for reproducing the scale dynamics in strongly evolving flows. Similar deficiencies were discovered later also in other nonequilibrium flows, primarily in separated regions and around reattachment. An indication of the role of scale variable was that somewhat better results were claimed with ω instead of ϵ equation. Because ϵ-equation is more frequently used, various modifications have been proposed in literature to accommodate nonequilibrium and separating flows. An additional term emphasizing the role of irrotational straining in the production of ϵ, proposed in 1980 (Hanjalić and Launder, 1980), produced the desired improvements of flows with a strong pressure variation.

For illustration, we consider in parallel the cases investigated by Samuel and Joubert (1974) and Nagano et al. (1993). Unlike the Samuel and Joubert case, the flow of Nagano et al. was subjected to a more sudden, though moderate (constant) pressure gradient. Experimental data of Nagano et al. seem more consistent and have been obtained closer to the wall, revealing also some other features of the pressure gradient effect. For this reason we present some results of computation of Nagano et al. flow with the low-Re-number second-moment closure. Main features of the two flows are displayed in Fig. 3(a), showing the evolution of the nondimensional pressure gradient (Clauser parameter $\beta = (\delta_1/\tau_w)dP/dx$ and $P^+ = \nu(dP/dx)/\rho U_\tau^3$). Predicted friction factors for the two cases, Fig. 3(b), show good agreement with experiments, illustrating the importance of initial conditions at the start of computations (dotted lines). Figure 3(c) and 3(d) show the production of kinetic energy for the two cases. It should be noted that the chain lines in both figures show the computed results at the last stations, for which data are not available. For the case of Nagano et al. the results were computed by retaining the constant β = 2.2 from the previous station (not correspondent to the experiment) in order to see the effects of prolonged action of the adverse pressure gradient. The profiles at other stations in the outer region collapsed all on one curve indicating no effect of pressure gradient on the absolute level of the kinetic energy (note the normalization with constant reference velocity). However, the last profile shows an increase in the production, fully in accord with the findings of Samuel and Joubert. It should be noted that the pressure gradient in the Nagano et al. case was decreasing already from

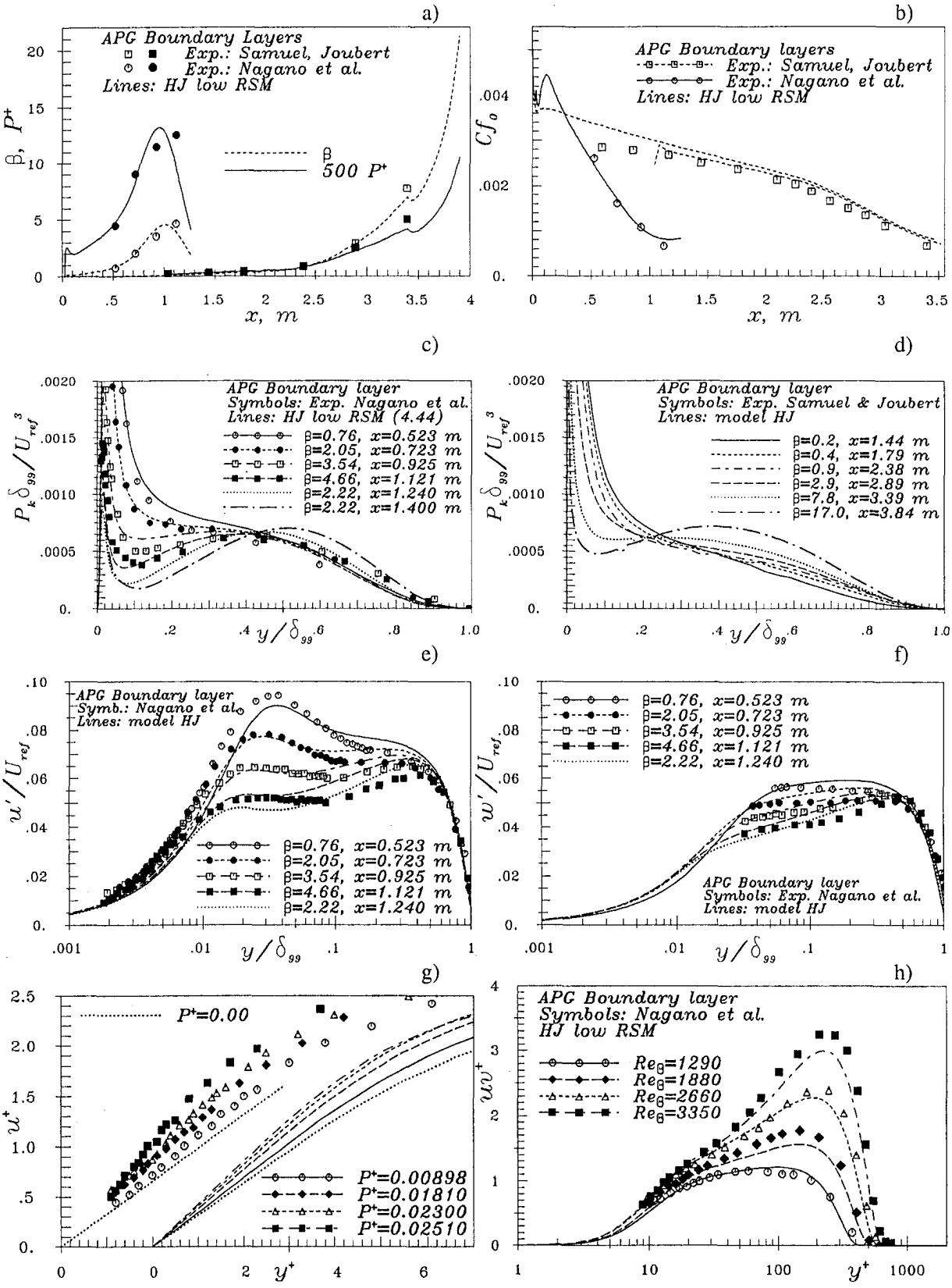

Fig. 3 Boundary layers in increasing adverse pressure gradient; (*a*) - nondimensional pressure gradient parameters and (*b*) - friction factor for Nagano et al. (1993) and Samuel and Joubert (1974); (c) - (d) - Production of turbulent kinetic energy; (*e*) to (*h*) - turbulence intensities and shear stresses at various locations for Nagano et al. flow. Symbols: experiments; Lines: computations

$x \approx 0.6$ and the increase in the kinetic energy production was visible only further downstream due to a cumulative transport.

The same effect is noticeable in the Samuel and Joubert case Fig. 3(*d*) where the chain curve (obtained by extrapolating β further downstream), departs visibly from the rest of the curves. Figures 3(*e*) to 3(*h*) show the results of computations with the low-Re-number second-moment model, with the additional term in the ϵ equation S_Ω, in good agreement with the

measurements along the whole flow length covered by the experiment. An interesting feature of this flow is that the inner wall scaling proved to be inadequate both for the mean and turbulence properties, causing not only a departure from the logarithmic law of the wall, but also the variation of the slope of the normalized turbulent stresses in the limit when the wall is approached, Fig. 3(*g*). It is interesting to note that the model described here can reproduce reasonably well this effect.

3.3 Separation Bubble on a Plane Wall. The next illustration is a "rapid" separation and reattachment of a turbulent flow on a flat wall, for which Direct Numerical Simulations were performed recently by Spalart and Coleman (1997). The pressure gradient was created by imposed suction and blowing along the opposing flow boundary. We have reproduced the flow conditions by adopting the same solution domain and the prescribed transpiration velocity through the upper boundary as in DNS. Due to Reynolds number limitation (Re_δ = 19,000), the incoming boundary layer at $Re_{\theta,in} \approx 300$ was not well developed. This posed uncertainties in reproducing the exact inflow conditions (particularly the dissipation profile, which was not provided by DNS), to which the downstream flow pattern is very sensitive (Spalart and Coleman, 1997).

The present computations were performed with the low-Re-number second-moment closure with and without the term S_l, yielding similar flow patterns in reasonable agreement with the DNS. However, without S_l the dividing streamline shows an anomalous forward bending in the separation point and backward bending at reattachment. This deficiency of the standard second-moment closure was detected earlier in studies of backward facing step flow, particularly at low Re numbers (for discussion, see Hanjalić and Jakirlić, 1998). While the use of wall functions and placing the first grid point at a relatively large distance from the wall concealed the anomaly, it becomes visible when using models which allow the integration up to the wall and the application of finer numerical grids. The introduction of S_l term into the dissipation equation, which compensates for excessive growth of the length scale in the stagnation zones, eliminates the anomaly both when used in conjunction with the standard high-Re-number second-moment model with wall functions, or with low-Re-number models and integration up to the wall.

The computed separation bubbles, Fig. 4, is somewhat thinner than in DNS, what may be a consequence of inadequate inflow conditions. The streamline anomaly without S_l makes the distance between separation and reattachment shorter. The inclusion of S_l rectifies the anomaly (Fig. 4) and extends the bubble length at the wall, though both the separation and reattachment points are predicted somewhat more upstream than in DNS. This is seen in the plot of the friction factor, Fig. 5, which shows also some discrepancy in the recovery zone. The mean velocity profiles, however, agree very well with the DNS, Fig. 6. The computed components of turbulence intensity are similar to DNS (see also the contours of kinetic energy, Fig. 4), though with some discrepancy, which is most noticeable in the profiles of the shear stress.

It should be noted that DNS was performed with 600 × 200 × 256 nodes and the statistical sample contained 429 fields, requiring 800 CRAY 90 hours. Despite such effort, Spalart and Coleman (1997) cautioned at several defects in the results which could not be eliminated because of high costs. In contrast, the present RANS computations were performed with 100 × 100 × 1 grid in a steady mode, requiring 2 CRAY hours.

3.4 Backward-Facing Step and Sudden Expansion. A turbulent flow behind a backward facing step contains several features pertinent to real complex flows: abrupt change of boundary conditions at the step which leads to boundary layer separation, a curved free shear layer and its bifurcation at the reattachment, primary and secondary recirculation, reattachment and subsequent recovery of the wall boundary layer. Flows

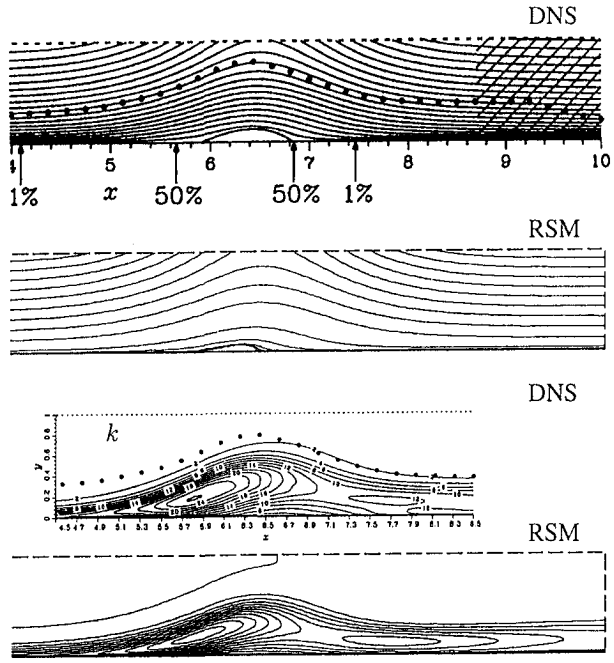

Fig. 4 Streamlines (*a*) and kinetic energy contours (*b*) in a separation bubble. Top figures: DNS (Spalart and Coleman 1997). Bottom figures: computations low-Re-number RSM.

with a smaller expansion ratio R (downstream/upstream flow-width) with a milder effect of pressure gradient seem to be more difficult to reproduce by statistical turbulence models due to a stronger effect of stress field anisotropy (as compared with the pressure gradient) on the flow evolution and recovery.

The standard linear two-equation $k - \epsilon$ model gives a too short recirculation length and a poor reproduction not only of mean velocity and turbulence profiles, but even more of the friction coefficient. Unsatisfactory predictions are not located only around reattachment, but also elsewhere in the recirculating and recovery region. Second moment closures account better for streamline curvature and differentiate the sign of extra strain rate effects through the exact treatment of the stress production term. Indeed, the standard high-Re-number second moment closure produces the desired elongation of the separation bubble and, in the whole, a more realistic flow pattern. However, due to inadequacy of wall functions, near wall region is poorly reproduced leading to a severe underprediction of the friction factor, particularly in the recirculation region. The present model yielded very good agreement with the DNS and experiments for a range of Reynolds numbers and expansion ratios. An illustration of the model performance is given in Fig. 7

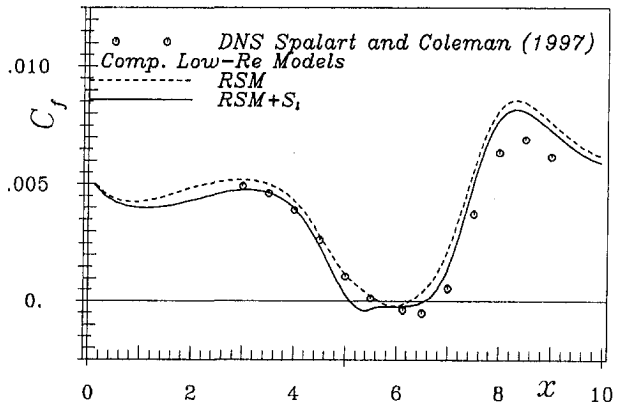

Fig. 5 Friction factor along the wall in the flow with separation bubble

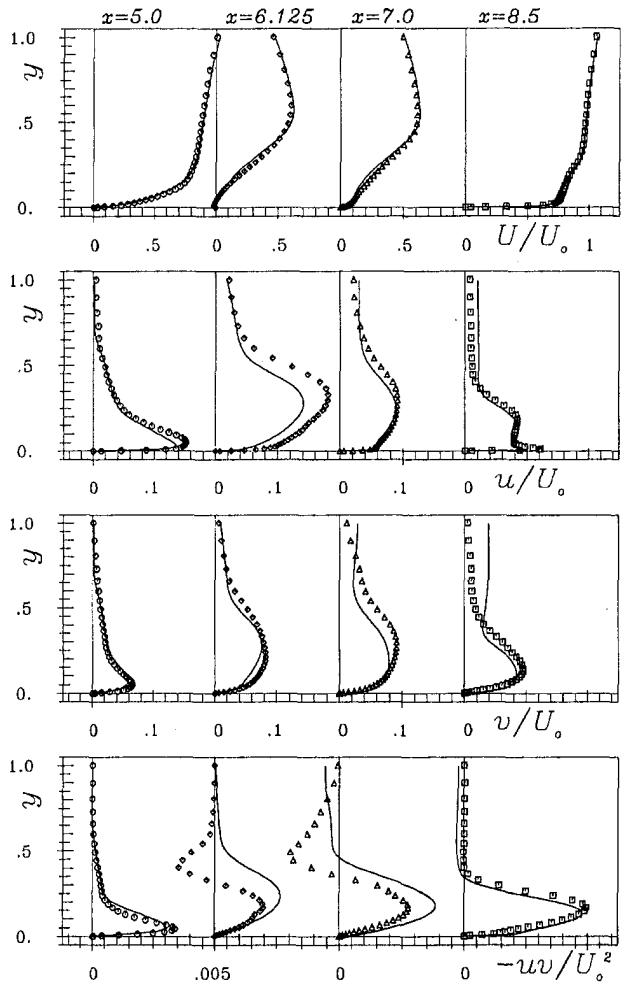

Fig. 6 Mean-velocity and Reynolds-stress tensor components at characteristic positions (x = 5 before separation, x = 6.125 in the middle of separation, x = 7 just beyond separation and x = 8.5 recovery of boundary layer). Symbols: DNS by Spalart and Coleman (1997); Lines: low-Re-number RSM.

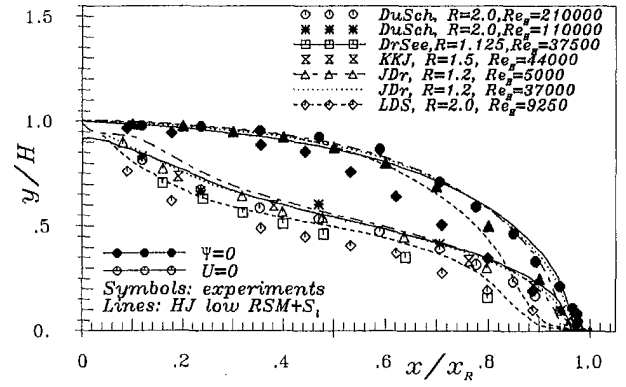

Fig. 7 Dividing and zero streamlines in several backstep flows and sudden plane and axisymmetric expansions. DuSch: Durst and Schmitt (1985); DrSee: Driver and Seegmiller (1985); KKJ: Kim, Kline and Johnston (1980); JDr: Jović and Driver (1995); LDS: Lekakis, Durst and Sender (1995).

showing a comparison of the computed dividing and zero-velocity streamlines (normalized with the step height and reattachment length) with experiments and DNS results for six flows, which include backward-facing steps, sudden plane and axisymmetric expansion, for a range of Re numbers. Note that the reattachment length in the cases considered vary between 6.3 (Re_H = 5000, R = 1.2) to 8.5 (Re_H = 110000, R = 2) for backstep, and up to 11.3 for pipe expansion (Re_H = 9250, R = 2). Predictions for backstep and sudden plane expansion flows show all a remarkable similarity and in good accord with experiments and DNS. Somewhat different behavior in the pipe expansion, particularly close to reattachment, is also well reproduced. More details are given in Hanjalić and Jakirlić (1998).

3.5 Airfoil. The last example is the flow over the NACA 4412 airfoil at maximum lift, with the incidence angle of 13.87 deg (Coles and Wadcock, 1979). Prediction of the leading edge transition (imposed experimentally at $0.023 \le x/c \le 0.1$) and of the trailing edge (oscillatory) separation has posed difficulties to standard one-and two-equation turbulence models used in aeronautics, (e.g., Guilmineau et al., 1997). In most computations reported in literature the transition is imposed artificially at the prescribed location adopted from experiment by switching on the turbulence model (or, alternatively, the production of the kinetic energy). In this case the transition length is very short and the treatment of the transition proved to be of little influence on the overall results. However, predicting the transition location in unknown flows without an empirical input is the major criterion in judging the RANS turbulence model for transitional flows.

Computations were performed with a four-block O-grid with both the high- and low-Re-number second-moment closures (398×88 and 398×128 nodes, respectively), without imposing any artificial transition. The wall nearest grid point was at y^+ between 0.1 and 1.5 for the fine mesh and between 10 and 50 for the coarse mesh. The high-Re-number model gave almost identical results both for 1.5 percent and for 5 percent free-stream turbulence. Because of the high bulk flow Reynolds number (the cord-base $\mathrm{Re} = 1.52 \times 10^6$), the application of the low-Re-number model due to a need for a fine and highly nonuniform numerical grid near walls becomes more demanding (slower convergence), particularly with a low free-stream turbulence. It should be noted that all computations were performed in a steady mode, what may not be fully suitable, particularly for a low free-stream turbulence.

We present here results obtained with 5 percent free-stream turbulence. The pressure coefficient obtained by both models agrees well with the experiments (Fig. 8). A difference between the two sets of results is more visible in the mean velocity and shear stress profiles, and, particularly, in the size of the separation bubble. Unlike the backstep flow, where both models result in a similar streamline pattern in the recirculation zone, here the low-Re-number models yield substantially thinner bubble, though of almost the same length.

Because of insufficient data it is difficult to judge which streamline patter is closer to reality. The mean velocity and shear stress profiles obtained by both models show also close agreement with experiments at most locations along the airfoil and also in the near wake, but the low-Re-number model seems to be slightly superior.

In view of the fact that some simpler models such as the zonal $k - \omega$ model of Menter, see Guilmineau et al. (1997), can give satisfactory reproduction of available experimental mean flow parameters for a two-dimensional high-load airfoils, this example may not be the most appropriate for illustrating arguments in favor of second-moment closures. There is also a doubt that the wind-tunnel walls may have an influence on the results,[1] although it is unlikely that the inner part of the boundary layer (except, perhaps, the location of separation), will be very sensitive to these effects. Nonetheless, we have included this flow in the present discussion mainly to demonstrate that the second-moment closures (including their low-Re-number variants with integration up to the wall) may be successfully used to compute complex flows over curved surfaces at high

[1] As pointed out by one of the referees.

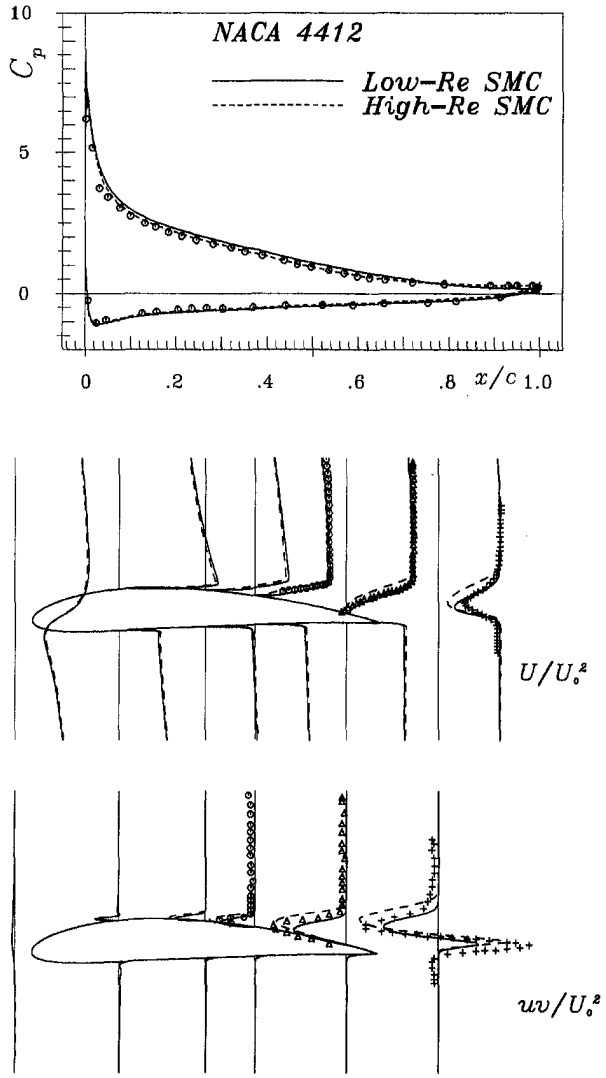

Fig. 8 NACA 4412 flow: (*a*) - pressure coefficient C_p; (*b*) - profiles of chordwise mean velocity U/U_o at x/c = 0.908; (*c*) and (*d*) - profiles of chordwise mean velocity U/U_o and turbulent shear-stress uv/U^2 at x/c = −0.05, 0.25, 0.5, 0.642, 0.908, 1.1747, 1.95146 (full lines low-Re RSM, dashed lines high-Re RSM); (*e*) streamlines obtained with low-Re RSM and (*f*) with high-Re RSM + WF

Re numbers and with strong pressure variations. A comparison of results obtained with high and low-Re-number variants of the same basic model, as well as with results obtained with $k - \epsilon$ and $k - \omega$ models (available in literature) are also believed to provide useful information.

4 Concluding Remarks

There is a view among the Computational Fluid Dynamics (CFD) community that the conventional Reynolds-Averaged Navier-Stokes (RANS) turbulence models will soon be replaced by Large-Eddy Simulation (LES) for a wide industrial applications. While such prospects may sound feasible for specific branches of industry, a wider application of LES for real high-Re-number flows in aeronautics seem still very distant, as argued recently by Spalart et al. (1997). The conventional RANS models have not indeed fulfilled the early expectations, but they remain still the only viable means for complex industrial computations. Of course, improvements are needed and possible, and this article outlines some prospects in that direction.

Some recent advancements in the refinement of second-moment closure models have been presented, which brought improvements in reproducing several types of turbulent flows relevant to external aerodynamics. The illustrations focused on the effect of pressure gradient, but also on some other phenomena (transition, separation, reattachment, recovery), which previously could not be satisfactory resolved, even with the higher order models, casting a shadow over the RANS approach to model turbulence in complex flows. The considered model refinement, as well as others based on different theoretical approaches, but still within the framework of RANS (nonlinear realizable models of pressure-strain based on tensorial expansion, elliptic relaxation method, and others) keep the prospects open and give fresh impetus to further improvement and a wider application of higher-order turbulence models in aerospace industry.

Acknowledgment

We thank P. R. Spalart for providing DNS data for several flows.

References

Akhavan, R., Kamm, R. D., and Shapiro, A. H., 1991, "An Investigation of Transition to Turbulence in Bounded Oscillatory Stokes Flows. Part 1. Experiments," *Journal of Fluid Mechanics,* Vol. 225, pp. 395–422.

Coles, D., and Wadcock, A. J., 1979, "Flying-Hot-Wire Study of Flow Past a NACA 4412 Airfoil at Maximum Lift," *AIAA Journal,* Vol. 17, pp. 321–329.

Guilmineau, E., Piquet, J., and Queutey, P., 1997, "Two-Dimensional Turbulent Viscous Flow Simulation Past Airfoils at Fixed Incidence," *Computers and Fluids,* Vol. 26, pp. 135–162.

Hanjalić, K., and Hadžić, I., 1995, "Modelling the Transition Phenomena with Statistical Turbulence Closure Models," R. A. W. M. Henkes and J. L. van Ingen, eds., *Transitional Boundary Layers in Aeronautics,* pp. 283–294. North-Holland Amsterdam.

Hanjalić, K., and Jakirlić, S., 1993, "A Model of Stress Dissipation in Second-Moment Closures," F. T. M. Nieuwstadt, ed., *Advances in Turbulence IV, Applied Scientific Research 51,* pp. 513–518. Kluwer Academic Publishers.

Hanjalić, K., and Jakirlić, S., 1998, "Contribution Towards the Second-Moment Closure Modelling of Separating Turbulent Flows," *Computers and Fluids,* Vol. 27, No. 2, pp. 437–456.

Hanjalić, K., Jakirlić, S., and Hadžić, I., 1995, "Computation of Oscillating Turbulent Flows at Transitional Re-Numbers," F. Durst et al., ed., *Turbulent Shear Flows,* Vol. 9, pp. 323–342, Springer Berlin.

Hanjalić, K., Jakirlić, S., and Hadžić, I., 1997, "Expanding the Limits of 'Equilibrium' Second-Moment Turbulence Closures," *Fluid Dynamics Research,* Vol. 20, pp. 25–41.

Hanjalić, K., and Launder, B. E., 1980, "Sensitizing the Dissipation Equation to Irrotational Strains," ASME JOURNAL OF FLUIDS ENGINEERING, Vol. 102, pp. 34–40.

Jakirlić, S., 1997, "Reynolds-Spannungs-Modellierung Komplexer Turbulenter Strömungen," Ph.D. thesis, University of Erlangen-Nürnberg.

Jović, S., and Driver, D., 1995, "Reynolds Number Effect on the Skin Friction in Separated Flows Behind a Backward-Facing Step," *Experiments in Fluids,* Vol. 18(6), pp. 464–467.

Justesen, P., and Spalart, P. R., 1990, "Two-Equation Turbulence Modeling of Oscillatory Boundary Layers," AIAA Paper Vol. 41, 90–0496.

Le, H., Moin, P., and Kim, J., 1997, "Direct Numerical Simulation of Turbulent Flow Over a Backward-Facing Step," *Journal of Fluid Mechanics,* Vol. 330, pp. 349–374.

Nagano, Y., Tagawa, M., and Tsuji, T., 1993, "Effects of adverse pressure gradients on mean flows and turbulence statistics in a boundary layer," F. Durst et al., ed., *Turbulent Shear Flows,* Vol. 8, pp. 7–21, Springer, Berlin.

Samuel, A. E., and Joubert, P. N., 1974, "A Boundary Layer Developing in an Increasingly Adverse Pressure Gradient," *Journal of Fluid Mechanics,* Vol. 66, pp. 481–505.

Savill, A. M., 1996, "Transition Predictions with Turbulence Models," R. A. W. M. Henkes and J. L. van Ingen, eds., *Transitional Boundary Layers in Aeronautics,* pp. 311–319. North-Holland Amsterdam.

Simpson, R. L., Chew, Y.-T., and Shivaprasad, B. G., 1981, "The Structure of a Separating Turbulent Boundary Layer. Part 1. Mean Flow and Reynolds Stresses," *Journal of Fluid Mechanics,* Vol. 113, pp. 23–51.

Spalart, P. R., and Coleman, G. N., 1997, "Numerical Study of a Separation Bubble with Heat Transfer," *European Journal of Mechanics,* Vol. 16, pp. 169–189.

Spalart, P. R., Jou, W.-H., Strelets, M., and Allmaras, S. R., 1997, "Comments on the Feasibility of LES for Wings, and on Hybrid RANS/LES Approach," *First AFOSR Int. Conf. on Direct Numerical Simulation and Large Eddy Simulation.*

Spalart, P. R., and Watmuff, J. H., 1993, "Experimental and Numerical Study of a Turbulent Boundary Layer with Pressure Gradient," *Journal of Fluid Mechanics,* Vol. 249, pp. 337–371.

Speziale, C. G., and Gatski, S. S. T. B., 1991, "Modeling the Pressure-Strain Correlation of Turbulence: an Invariant Dynamical Systems Approach," *Journal of Fluid Mechanics,* Vol. 227, pp. 245–272.

N. Raud[1]
Ph.D.

Y. Bury
Ph.D. Student.

R. Bazile
Assistant Professor.

J. Borée
Research Scientist.

G. Charnay
Research Director.

Institut de Mécanique des Fluides de Toulouse, UMR CNRS/INPT-UPS 5502, Avenue Camille Soula, 31400 Toulouse, France

Experimental Study of the Behavior of Confined Variable Density Jets in a Time Varying Crossflow

An experimental work and a physical analysis dedicated to the study of a low density jet subjected to a time varying crossflow with high acceleration/deceleration levels are presented in this paper. Relevant nondimensional numbers are derived and show that unsteady effects associated with the presence of the jet in the acceleration field have noticeable consequences on the flapping of the jet. The Schlieren technique is applied in the test section of a square duct to obtain time resolved images of the jet. Analysis of the results is focused on the influence of the unsteady effects on the global dynamic behaviour of the jet in the near field. The interaction between the jet and the crossflow is analysed in three contrasted situations corresponding to different values of the jet outlet velocity U_0. We predict and observe an increase of the jet deflection during the acceleration phase and a competition between drag and acceleration during the deceleration. This competition is particularly clear for the two lowest ejection velocities of the jet and we have shown that the jet is initially deflected upstream the nozzle. The influence of exit jet injection angle is finally considered. We show that upstream or downstream injections induce a very strong modification of the mixing process of the jet fluid with the pulsed crossflow.

1 Introduction

The flow associated with the turbulent mixing of a jet exhausting at large angles in a crossflow is an example of complex three-dimensional shear flows. This situation is widely used in many technical applications where efficient mixing of the jet fluid with the surrounding is of primary importance (Broadwell and Breidenthal, 1984; Smith and Mungal, 1998). Applications include such contrasted practical problems as discharge of waste gases from chimney stacks, control of missiles or aircraft, gas turbine combustor cooling, or fuel injection. One can refer to the review of Margason (1993) for a complete literature survey concerning jets in crossflow. The crossflow modifies the direction of the initial momentum flux of the jet and three-dimensional effects are important. For nonconfined situations, the structure of the flow is known to range from a free jet like behavior in the near field to a counter-rotating vortex pair in the far field (Kamotani and Greber, 1972; Keffer and Baines, 1963). Typical vortex systems associated with the crossflow interaction are now well-identified (Kelso, Lim, and Perry, 1996). Moreover, the instantaneous structure of the flow bears only a little resemblance to ensemble averaged velocity fields (Smith, Lozano, Mungal, and Hanson, 1993).

In the far field of the jet, Broadwell and Breidenthal (1984) have considered the jet as a point source of normal momentum and have shown that the only global length scale is rD_0. r is the square root of the momentum flux ratio $r = (\rho_0 U_0^2/\rho_1 U_1^2)^{1/2}$. Here, U is velocity, ρ is density, and subscript 0 and 1 refer to jet properties and crossflow properties, respectively. In the near field, Smith and Mungal (1998) have recently shown that the vortex interaction region displays a D_0 scaling which allows for structural effects that depend on the ratio r. Finally, a third length scale $r^2 D_0$ can be used to collapse the data in the first diameter from the jet exit and to locate the branch point of the counter-rotating vortex pair (Smith and Mungal, 1998).

Turbulent jets in confined crossflow are relevant configurations for a lot of engineering situations but have received considerably less attention than turbulent jets in unbounded crossflows (Catalano et al., 1989; Kamotani and Greber, 1974; Stoy and Ben-haim, 1973). Catalano et al. (1989) have shown that the existence of impingement on the opposite wall is strongly dependant on the jet to crossflow velocity ratio r. Stoy and Ben-haim (1973) have used a classical one-dimensional analysis and concluded that the jet trajectory and impingement point can be fairly well predicted using correlations derived in unbounded flows. However, no systematic study of the effect of confinement seems available in the literature.

To the authors' knowledge, no studies are reported concerning the effects of a pulsed crossflow on a jet. Practical applications corresponding to this situation are, however, quite common. For example, the present work is directly linked with the development of natural gas vehicles (NGV) which have a high potential to reduce urban air pollution (Stephenson, 1997). In such spark ignition engines, the gaseous fuel, significantly lighter than the surrounding air ($\rho_0/\rho_1 = 0.5$), is injected in intake ports and submitted to a pulsed air flow where acceleration can reach values of 3000 g (Bates, 1989) – g is the gravity acceleration field. A knowledge of the mixing process of the jet in this particular unsteady situation is clearly useful to optimise the combustion.

In this paper, we will focus on the description of the global behavior of a confined variable density jet in a periodic crosswind. A first physical analysis will show that the unsteady effects associated with the presence of the jet in the acceleration field are expected to have noticeable consequences on the flapping of the jet which are of course enhanced in the case of jets significantly lighter than the ambient fluid. Time resolved images of the near field of a light heated jet ($\rho_0/\rho_1 = 0.5$) have

[1] Present Address: Siemens Automotive SA, Toulouse, France.

Contributed by the Fluids Engineering Division for publication in the JOURNAL OF FLUIDS ENGINEERING. Manuscript received by the Fluids Engineering Division March 6, 1998; revised manuscript received September 21, 1998. Associate Technical Editor: S. Banerjee.

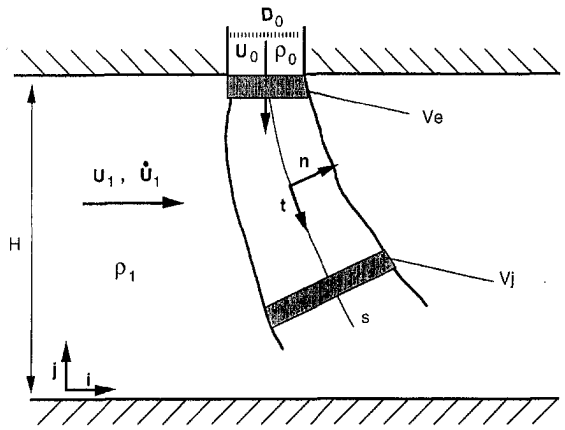

Fig. 1 Jet configuration

been obtained by Schlieren technique in a model experiment setup. In the case of a jet directed normally to the crossflow, contrasted situations corresponding to different values of the ratio of the unsteady effects to the jet initial momentum flux will be presented and discussed. A comparison of the relevant time scales in this situation provides an understanding of the important physical mechanisms.

The behavior of non-normal jets will be described in the last part. We will specifically show that a slight counterflow injection induces dramatic changes and a better dispersion of the injected fluid in the crossflow even during the acceleration phases. Such configurations could have interesting applications in practical situations.

2 Physical Analysis and Derivation of Relevant Nondimensional Numbers

We consider the situation presented in Fig. 1. The jet fluid has an ejection velocity U_0 and an initial density ρ_0 eventually very different from the ambient density ρ_1. In this first part, we assume that the jet flows perpendicularly to the time varying crossflow $U_1(t)$. We will focus on the dynamical behavior of the flow in the first diameters of the jet. The initial momentum flux of the jet can be affected by gravity effects and by the uniform transversal flow of speed U_1 varying with time ($\dot{U}_1 = dU_1/dt$). The time scale of the pulsation classically defined as $\tau_{U_1} \approx \min(U_1/\dot{U}_1)$ is an important quantity that has to be compared with the other relevant time scales. The effect of the gravity field $\mathbf{g}$ is neglected in all the cases presented in this paper. First, it can be easily checked that the jet Froude number defined by $F_j = \rho_0 U_0^2/g|\rho_0 - \rho_1|D_0$ (Chen and Rodi, 1980) is significantly large. The initial development of the jet is therefore inertial and is not affected by gravity (Chassaing et al., 1994; Panchapakesan and Lumley, 1993). Second, we deal with contrasted situations with $|\dot{U}_1| \gg g$ and $\tau_{U_1} \ll \tau_g$ where τ_g is the characteristic time scale of the movement induced by gravity over the channel height H (Tritton, 1988).

A large amplitude pulsation of the crossflow is expected to have a significant effect on the jet behavior. An integral model describing the time and space evolution of the far field of the unsteady jet submitted to a time varying crosswind has been established in (Raud, 1997). A simplified analysis is presented here in order to focus on the flow behavior at the jet outlet and to derive relevant nondimensional numbers. Let us consider the control volume V_e of thickness $\Delta s \ll D_0$ and limited by the jet contour drawn in Fig. 1 at the exit of the fixed jet nozzle of surface S_0. We can easily show (Raud, 1997) that the inertia effects due to the movement of the control volume are negligible. We further assume that the velocity profile is uniform of velocity $\mathbf{V} = U\mathbf{t}$ where the vector $\mathbf{t}$ is the local tangent to the jet axis. Finally, we neglect the entrainment of the external fluid by the early developing annular mixing layers. The modulus of $\mathbf{V}$ is therefore constant and equal to the ejection velocity U_0. The mass flux $\mathbf{Q}$ and the momentum flux $\mathbf{J}$ are respectively $\mathbf{Q} = \rho_0 U_0 S_0 \mathbf{t} = Q_0 \mathbf{t}$ and $\mathbf{J} = \rho_0 U_0^2 S_0 \mathbf{t} = J_0 \mathbf{t}$. The momentum balance writes:

$$\frac{\partial \mathbf{Q}}{\partial t} + \frac{\partial \mathbf{J}}{\partial s} = \frac{J_0}{D_0}\left[\frac{\partial \alpha}{\partial t^*} + \frac{\partial \alpha}{\partial s^*}\right]\mathbf{n} = (\sum F)\mathbf{n} \qquad (1)$$

α is the local angle of the jet axis and $\mathbf{n}$ is the local normal to the jet axis. t^* and s^* are nondimensional time and length based on the jet scales with $t^* = tU_0/D_0$ and $s^* = s/D_0$. ΣF represents the sum of the normal forces by unit length applied on the fluid contained in V_e by the external flow. Near the jet outlet, we have therefore:

$$\left[\frac{\partial \alpha}{\partial t^*} + \frac{\partial \alpha}{\partial s^*}\right] = \sum\left(\frac{D_0 F}{J_0}\right) \qquad (2)$$

In Eq. (2), nondimensional numbers $N = D_0 F/J_0$ represent the spatio-temporal change of α. $N = D_0/L$ compares the steady jet length scale to the characteristic length $L = J_0/F$ associated with the force F. If $N \ll 1$, force F has only a little effect on the exhaust flow. On the contrary, if $N \gg 1$, the exhaust flow is significantly influenced by the external unsteadiness. Neglecting possible history effects, F is classically decomposed into three terms with $\Sigma F = F_D + F_I + F_M$. F_D denotes the quasi-steady drag, F_I represents the pressure force applied by the outer flow to accelerate the equivalent volume V_e of external fluid and F_M is the added mass force due to the presence of the jet in the acceleration field.

The following expressions are easily obtained:

$$F_D = C_d \tfrac{1}{2} D_0 \rho_1 U_1^2; \quad F_I = S_0 \rho_1 \dot{U}_1; \quad F_M = S_0 C_m \rho_1 \dot{U}_1 \qquad (3)$$

F_D is positive as the crossflow is always in the positive direction in the present work.

C_d is the equivalent aerodynamic drag coefficient between crossflow and jet. We assume that the value of C_d is of the same order of magnitude as the value of the drag coefficient of a rigid cylinder (Adler and Baron, 1979; Ooms, 1977). The mean value of the equivalent Reynolds number $R_e = (\bar{U}_1 D_0/\nu)$ is of order $2.\,10^4$, we therefore choose $C_d = 1$. Note that assuming a constant value for C_d removes the effect of the crossflow unsteadiness from the drag force term and that no history forces are considered here. The added mass coefficient C_m is fixed at $C_m = 1$ equal to the coefficient of a rigid cylinder.

The final expressions of N_D (drag effect) and N_{acc} (acceleration effects) are:

$$N_D = \frac{D_0 F_D}{J_0} = \frac{2C_d}{\pi}\frac{\rho_1 U_1^2}{\rho_0 U_0^2}$$

$$N_{acc} = \frac{D_0(F_I + F_M)}{J_0} = (1 + C_m)\frac{\rho_1 D_0 \dot{U}_1}{\rho_0 U_0^2} \qquad (4)$$

The expression of N_D is classical. N_{acc} compares the jet momentum flux to the unsteady pressure effects. Note that these unsteady effects are expected to play a role even if the density ρ_0 is equal to the ambient density ρ_1 because the location of the jet exhaust is fixed in the acceleration field. Both drag and unsteady effects are, however, inversely proportional to the density ratio ρ_0/ρ_1 and are therefore enhanced for light jets.

During an acceleration phase, N_D and N_{acc} have the same sign and the acceleration is expected to increase the jet deflection. On the contrary, during a deceleration phase, unsteady effects are opposed to drag effects and can eventually dominate. To illustrate these statements, the ratio N_{acc}/N_D is computed below

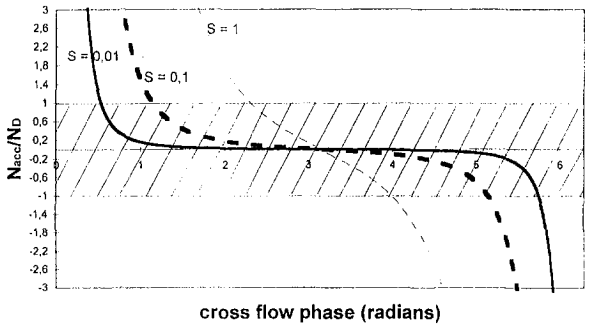

Fig. 2 Evolution of N_{acc}/N_D over a crossflow period for increasing values of parameter $S = D_0 f/U_m$

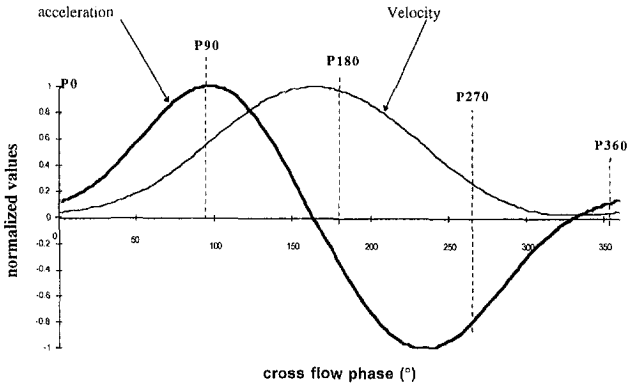

Fig. 4 Evolution of mean velocity and acceleration of the crossflow on the axis of the duct below the jet nozzle (as a function of the phase of the crossflow)

for a periodically time varying crossflow of velocity $U_1(t) = (U_m/2)[1 - \cos(\omega t)]$. One gets:

$$\frac{N_{acc}}{N_D} = \frac{\pi(1 + C_m)}{2C_d}\frac{D_0\dot{U}_1}{U_1^2} = 2\pi^2\frac{1 + C_m}{C_d}\left[\frac{\sin(\omega t)}{1 - \cos(\omega t)}\right]\frac{D_0 f}{U_m} \quad (5)$$

f is the frequency of the pulsation with $f = \omega/2\pi$. N_{acc}/N_D compares the advective time scale D_0/U_1 to τ_{U_1}. The evolution of N_{acc}/N_D is drawn in Fig. 2 for increasing values of the non-dimensional number $S = D_0 f/U_m$. Hatched part of Fig. 2 corresponds to the region of drag effects domination. An increase of S from $S = 0.1$ to $S = 1$ enhances significantly the region of acceleration domination while drag effects are always significant for $\omega t \approx \pi$ corresponding to the maximum crosswind velocity and negligible acceleration. N_{acc}/N_D becomes negative during the deceleration phase. For $N_{acc}/N_D < -1$, the resultant normal force at the jet exhaust is opposed to the flow direction. Corresponding effects will be observed in the following.

Volumes of jet fluid propelled into the pipe flow entrain external air. The resulting mixture experiences the significant velocity and acceleration of the incident flow. Some signatures of the acceleration effects will be observed in the following and a qualitative understanding will be obtained by considering the dynamics of a coherent finite fluid volume in the incident pulsed flow (Hunt, 1987).

3 Experimental Arrangement

3.1 Flows Generation and Main Characteristics

3.1.1 Crossflow. Experiments are performed in a $H = 60$ mm square cross section air tunnel (Fig. 3). The test section is equipped with large windows for the optical access. A fan generates the main crossflow. For the maximum value of the steady crossflow velocity [max $(U_1) \approx 40$ ms^{-1} (± 1 ms^{-1})], the Reynolds number based on the hydraulic diameter is equal to 115,000 and the ratio between the length of the duct L and the half width of the test section is equal to 58. This ensures that the flow is reasonably established at the observation zone (Schlichting, 1979). Velocity measurements have been performed using a hot wire probe (Raud, 1997). Profiles of mean and rms axial velocity are typical of steady fully developed turbulent pipe flow. An integral time scale of the turbulence, τ_t, can be estimated by the ratio h/u^*, where the friction velocity, u^*, is derived from the Blasius relation ($u^* = 0.96$ ms^{-1}). The value of τ_t is approximately 30 ms.

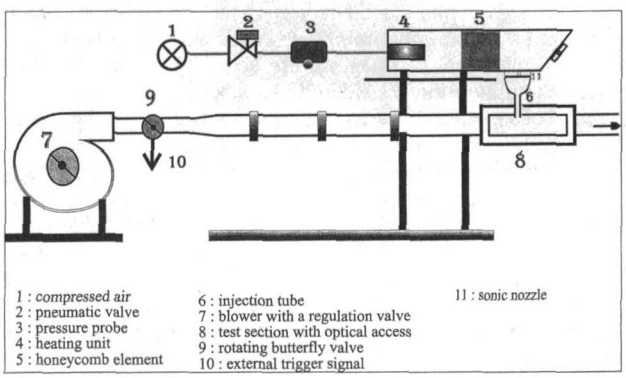

Fig. 3 Experimental setup

A rotating butterfly valve located two meters upstream of the test section produces velocity modulations of the main air flow. Previous studies have shown that rotating butterfly valves can be used to generate quasi-sinusoidal modulations of the velocity in a square duct (Charnay and Mathieu, 1976). A periodic time variation of U_1 is obtained in the present duct for a frequency $f = 66$ Hz (± 0.5 Hz). Figure 4 shows the evolution of the mean velocity on the axis of the test section (averaged from one hundred cycles), as a function of the angle of the rotating value. The velocity amplitude varies from $U_1 = 1.2$ ms^{-1} to a maximum value of $U_1 = 42$ ms^{-1}. The quasi-sinusoidal acceleration curve obtained by time derivation of the measured velocity evolution is superimposed in Fig. 4. The unsteadiness in the duct can lead to strong values of acceleration up to 506 g with $g = 9.81$ ms^{-2}. Four particular phases (P0, P90, P180, and P270) will be studied in this work and have been added on the graph. These observation phases, regularly spaced over a period of pulsation, cover a wide range of acceleration values (see Table 1) where the unsteady effects can be clearly identified and analysed.

The characteristic time, $\tau_{U_1} \approx \min(U_1/\dot{U}_1)$ of the variation of velocity is equal to $\frac{1}{2}\pi f$ for a sinusoidal evolution (i.e., $\tau_{U_1} \approx 2.4$ ms). τ_{U_1} is much smaller than the integral characteristic time of the turbulence ($\tau_t \approx 30$ ms estimated under steady conditions). The turbulence is therefore not established under unsteady conditions.

3.1.2 Jet. The heated air jet [$T_0 = 550$ K (± 2 K), $\rho_0/\rho_1 = 0.5$] is injected through a cylindrical tube ($D_0 = 14$ mm) into the main crossflow with an angle of 90 deg (except in Section 4.3 where the influence of the jet angle is presented). The confinement of the jet is important in this study with $H \approx 4D_0$ (see Fig. 1). Jet impingement can therefore occur during the unsteady flapping of the jet and will be analysed in the following section.

The use of a sonic nozzle ensures a jet of constant mass flux. This sonic nozzle is located just before the convergent section

Table 1 Crossflow velocities and accelerations values at the four selected phases. Expressions of P, N_{acc} and N_D for the three exit jet velocities cases. (Uncertainty of N: 10%.)

		P0		P90		P180		P270	
U_1 (m.s^{-1})		2		22		40.5		9.5	
$\dot{U}_1$ (m.s^{-2})		70 g		500 g		-180 g		-380 g	
	P	N_D	N_{acc}	N_D	N_{acc}	N_D	N_{acc}	N_D	N_{acc}
Case 1 : U_0=56 m s^{-1}	0.4	1.6 10^{-3}	1.2 10^{-2}	0.20	9 10^{-2}	0.66	-3.1 10^{-2}	3.7 10^{-2}	-6.6 10^{-2}
Case 2 : U_0=39 m s^{-1}	0.65	3.3 10^{-3}	2.5 10^{-2}	0.41	0.18	1.4	-6.5 10^{-2}	7.6 10^{-2}	-0.14
Case 3 : U_0=14 m s^{-1}	1.6	2.6 10^{-2}	0.2	3.1	1.4	10.7	-0.50	0.59	-1.1

of the injection device (see Fig. 3). The volume within the convergent and the tube damps any acoustic perturbation induced by the sonic aperture. It has been chosen small enough so that the pressure and related density time variations in the duct, induced by the pulsed crossflow, have no significant influence on the jet exit velocity (small variations less than 1 percent have been estimated (Borée, 1990)).

The exit jet velocity can be set from $U_0 = 10$ ms^{-1} to $U_0 = 60$ ms^{-1} for Reynolds numbers contained between 8900 and 53,500. The uncertainty of the velocity U_0 is 3 percent. Velocity measurements have ensured that the velocity profile at the outlet of the nozzle is nearly uniform for the different operating conditions (Raud, 1997). The maximum turbulence intensity on the axis of the jet is 2 percent.

3.2 Imaging System. In order to observe the jet as it interacts with the main flow, the Schlieren technique was used and adapted to unsteady conditions. The density gradients due to the presence of the heated jet are detected with a gated CCD camera. The integration time of the camera is chosen short enough (40 μs) compared to the period of the crossflow velocity ($2\pi/\omega = 15$ ms) in order to obtain time-resolved images of the heated jet at a given phase ωt. An external signal provided by the rotating butterfly valve (with an accuracy of 1 deg) is used to synchronize the imaging system. The video signal is digitized by a frame grabber board (Magic MATROX, 768 × 572 pixels, 8 bits) connected to a PC. A specific image processing was developed to extract the instantaneous jet boundary in a selected window that corresponds to a field of view of 60 mm height by 85 mm length.

The Schlieren technique is suitable to analyze the location and the global structure of the jet as it interacts with the pulsed crossflow, but no information will be obtained concerning the well known 3D effects and the vortex structures that appear in the present configuration (Kamotani and Greber, 1972).

3.3 Post-Processing. Some Schlieren images dedicated to a pure descriptive approach will be presented in the next section without post-treatment. On the other hand, a more precise and objective analysis of the jet structure for different operating conditions requires a particular post-processing to extract the jet boundary. Images obtained from the Schlieren technique cannot be directly interpreted in terms of pixel value. Moreover, a local pixel value in the jet can be the same than in the background, so that a systematic threshold on the grey levels cannot be easily applied to extract the jet from the background of the image.

The algorithm of the processing is based on the following observation: considering a zoom on a small test window (in the background or in the jet), it appears that the background is locally homogeneous contrary to the heated jet where the density gradients lead to a strong dispersion of the pixel values. The post-processing can be described in two steps. First, over a small test window (11 × 11 pixels) the root mean square of the pixel values is calculated and provides the information concerning the local homogeneity of the image. A small value of this rms, is obtained when the processing window is located in the background whereas high values are expected in the jet.

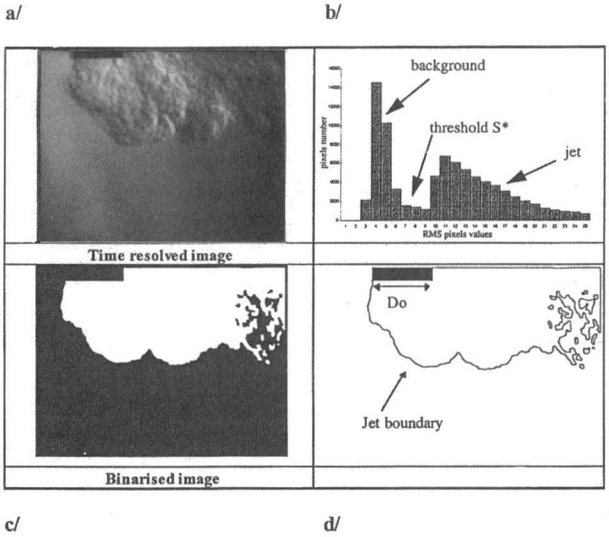

Fig. 5 (*a*) Typical instantaneous Schlieren image of the jet in the pulsed crossflow (*b*) Typical histogram of all the RMS pixels values computed in the test window (11 × 11 pixels) when moving on the whole image. S^* is a threshold between the jet and the background contributions. (*c*) Binarization of the jet image (5.a) after the post-processing. (*d*) Jet boundary extracted after application of a sobel gradient on 5.c.

Figure 5(a) shows a typical histogram of all the rms, pixels values obtained when the test window is moved (pixel by pixel) over the whole image. A cut-off level, S^*, can be objectively determined at the dip between the contribution of the homogeneous background (rms pixel values smaller than S^*) and the contribution of the jet (rms pixel values higher than S^*). When the test window contains jet and background contributions, there is some overlap of the histograms; but the number of calculated values corresponding to this particular case remains negligible and the dip at S^* is still marked. In a second step, when S^* is known, the processing window is moved again over the whole image and its central pixel is replaced by 0 if S^* is not reached (background). Then a simple threshold of the grey levels can extract easily the jet boundary (Fig. 5(b/c/d)).

4 Results and Discussion

Topologic information will be extracted from instantaneous images at a given phase and analysed in terms of global behavior of the jet and mixing between the hot air and the pulsed crossflow. A limited set of images were acquired during the study in each configuration considered. This set is not large enough to perform a precise phase averaging but ensures that the images presented here are fully representative of the periodic evolution of the flow and adapted to the following discussion focused on three points. First, the interaction between the jet and the pulsed flow is analysed for a jet with high ejection velocity corresponding to an important ejection momentum flux and low values of the non-dimensional numbers N. Then the influence of the jet ejection velocity is considered. Lower ejection velocities correspond to a more pronounced interaction with the pulsed crossflow. Finally, results with a variable ejection angle are presented and discussed in terms of influence of the injection concept on the mixing process.

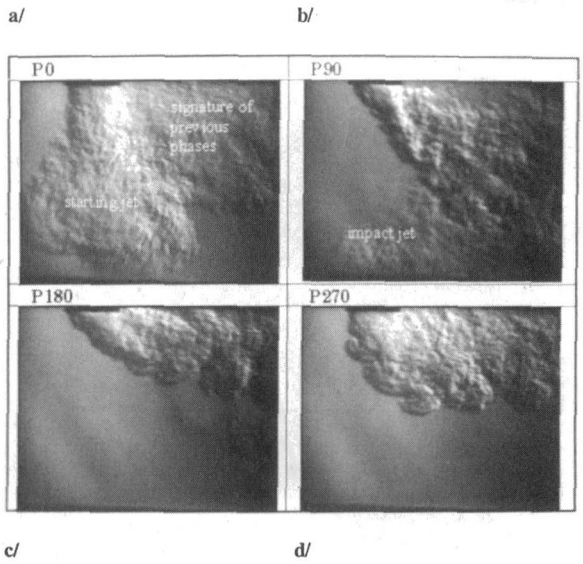

Fig. 6 Time resolved images of the jet (high velocity case: U_0 = 56 m.s^{-1}) at the selected phases of the pulsed crossflow

4.1 Analysis of the Dynamic Behavior of the Jet. Instantaneous images of the heated jet (ejection velocity: 56 ms^{-1}) are presented in Fig. 6 at the different observation phases defined in Section 3. This sequence shows how the acceleration field of the pulsed crossflow perturbs the jet. The jet varies from a straight jet at P0 to a completely deflected jet at P180. The flapping of the jet is a time-continuous periodic phenomenon and the distribution of hot air observed at a given phase inherits the events that occur at the previous phases. These history effects are clearly visible in Figs. 6(a–d). At P0 (Fig. 6(a)), both the crossflow velocity and acceleration are small, the jet penetrates across the main flow and behaves like a starting jet in a quiescent surrounding (Witze, 1980). In particular, the transient vortex region heading the jet is well detected in Fig. 6(a). A hot mixture is also detected at P0 downstream of the starting jet but along the upper half of the channel only. This mixing configuration is the signature of the previous phases. Large pockets of unmixed incident fluid therefore flow downstream of the injection point along the channel lower wall.

The jet impacts on the channel lower wall between phases P0 and P90. To analyze this point, let us introduce a characteristic time defined as: $\tau_j = H/U_0$. τ_j represents the time needed for the jet fluid to cross the height of the duct with velocity U_0. With $H \approx 4D_0$, note that U_0 is a correct velocity scale in the potential core of the jet. Considering τ_{U_1}, the characteristic time of variation of velocity ($\tau_{U_1} = \frac{1}{2}\pi f$), the ratio $P = \tau_j/\tau_{U_1}$ can be used to estimate the relative distance covered by the jet fluid through the duct. In other words a value of $P < 1$ corresponds to a jet that can reach and impact the lower wall. This is consistent with the present case where τ_j = 1 ms, τ_{U_1} = 2.4 ms and P = 0.4. Hot air pockets, witness of this impact, are convected and accelerated downstream along the lower wall at P90 (Fig. 6(b)). At the phase P90, the external velocity U_1 increases and the acceleration is maximal. The core of the jet is strongly deflected. An objective way to isolate the unsteady effects is to compare Fig. 6(b) to the steady situation corresponding to the same velocity of the crossflow. Boundaries of the steady jet (U_1 = 22 ms^{-1}; $\dot{U}_1 = 0g$) and of the unsteady jet (P90: U_1 = 22 ms^{-1}; $\dot{U}_1 = 500g$) are presented respectively in Figs. 7(a) and 7(b). Compared to the steady case, the spreading of the jet is strongly affected by the pulsed crossflow. The non-dimensional numbers N_D and N_{acc} derived in Section 2 are both positive at P90 and are respectively N_D = 0.20 and N_{acc} = 0.09 (see Table 1). Acceleration effects are therefore expected to be significant and to increase the initial deflection of the jet. A zoom of the jet boundary near the nozzle outlet is drawn in Fig. 7(c). The deflection of the unsteady jet is more pronounced and the contribution of the acceleration effects compared to the drag effects is clearly visible on the boundary extractions.

The unsteady jet fluid is strongly deflected and confined near the upper wall at P180 (Fig. 6(c)). With $N_D \approx 0.66$, this strong deflection in the first jet diameter was expected from dimensional analysis. The deceleration is nearly maximum at P270 (Fig. 6(d)). Drag and acceleration effects at the jet outlet are moderate ($N_D \approx 0.04$, $N_{acc} \approx -0.07$) and compete with each other. This may explain why the jet exits perpendicularly in the first diameter and penetrates easier in the flow. One sees that the hot mixture is confined in the upper half of the channel at P270. A precise understanding of the dynamic of the turbulent interface is difficult. Indeed, deceleration induces a strong positive baroclinic torque, which competes with the shear induced by the jet flow. More work is presently dedicated to this aspect which is expected to have a strong influence on mixing.

In the case analyzed in this part, only the penetration of the starting jet type flow at about P0 and the related impact on the lower wall ensures an initial mixing throughout all the channel while large volumes of unmixed incident fluid flow in the channel lower half during the flapping of the jet.

4.2 Influence of the Exit Jet Velocity. The influence of a decrease of the jet ejection velocity is now discussed. Three contrasted cases corresponding respectively to U_0 = 56 ms^{-1}, U_0 = 39 ms^{-1}, and U_0 = 14 ms^{-1} have been studied. The first case has been discussed previously. Images obtained by Schlieren technique at phases P0, P90, P180, and P270 in the two last cases are presented in Figs. 8 and 9. Changing the jet exit velocity is expected to have significant effects on the behavior of the jet. First, existence of a jet impact is dependent of the ratio P, which is inversely proportional to U_0. As the exit jet velocity decreases, the penetration of the jet into the duct becomes less important. One sees that the impact of the jet on the lower wall never occurs for the two lowest ejection velocities. In particular, the jet fluid never crosses the lower part of the duct for U_0 = 14 ms^{-1} which is unfavourable in terms of mixing. Second, the jet initial momentum flux $J_0 = \rho U_0^2 S_0$ decreases strongly with U_0. Drag and acceleration effects are therefore expected to be enhanced.

A comparison of the jet boundaries in steady and unsteady crossflow for U_0 = 39 ms^{-1} (respectively, U_0 = 14 ms^{-1}) at P90 is presented in Fig. 10(a) (respectively, 10(b)). The jet

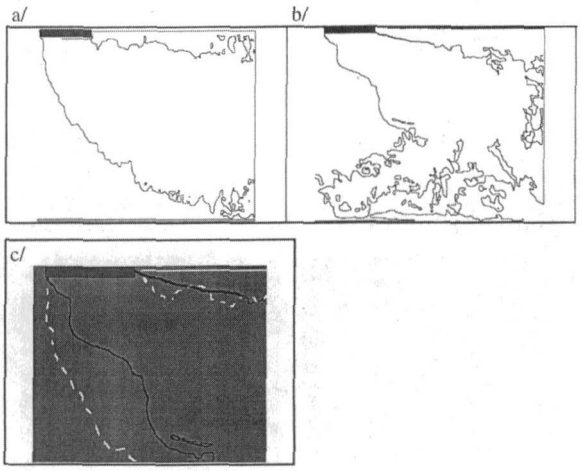

Fig. 7 Jet boundaries (U_0 = 56 m.s^{-1}) extracted respectively for a steady (a) and an unsteady (b) conditions at a phase which corresponds to the same crossflow velocity (U_1 = 22 m.s^{-1}). (c) Comparison of jet boundaries in the first diameters of the jet.

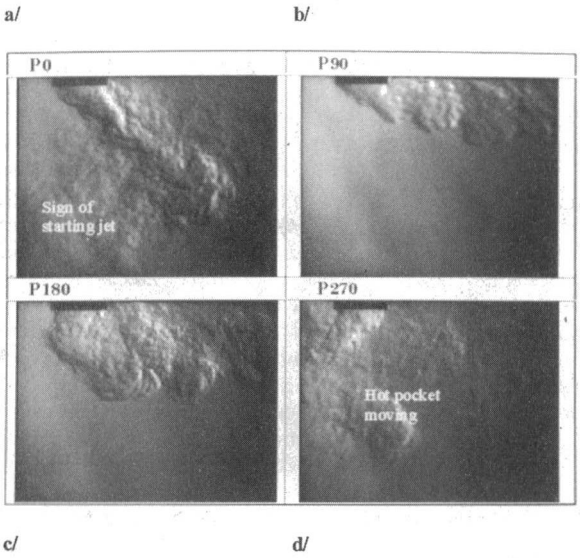

Fig. 8 Time resolved images of the jet (U_0 = 39 ms^{-1}) at the four phases of the pulsed crossflow

is strongly deflected in both cases and the flow of hot mixture develops along the upper wall. The thickness of this layer is, however, significantly reduced in the unsteady situation. This observation is a result of the strong imposed acceleration.

In Figs. 8 and 9, we see that low velocity jets are very sensitive to deceleration. For the sake of clarity, we will focus on phase P270. Table 1 shows that drag and acceleration effects at the jet outlet are significant, opposed and that deceleration effects should dominate. In fact, Figs. 8(d) and 9(d) show that the jet flow is initially deflected upstream the nozzle against the incident flow. One may notice that volumes of jet fluid injected in the channel are moving against the crossflow. This behaviour is believed to be a striking signature of the deceleration effects. A qualitative understanding can be obtained if one considers the dynamics of a coherent finite fluid volume in the incident pulsed flow. Several authors have discussed the motion of such "gas bubbles" in order to investigate either inertia effects in constant density flows (Hunt, 1987) or buoyancy and relative acceleration effects in variable density flows (Chomiak

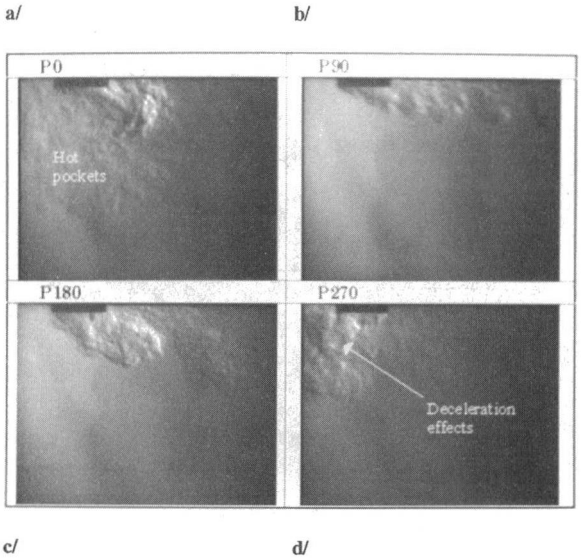

Fig. 9 Time resolved images of the jet (low velocity case: U_0 = 14 ms^{-1}) at the four phases of the pulsed crossflow

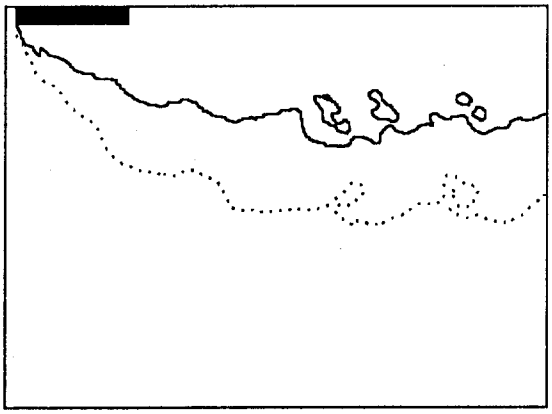

Fig. 10(a)

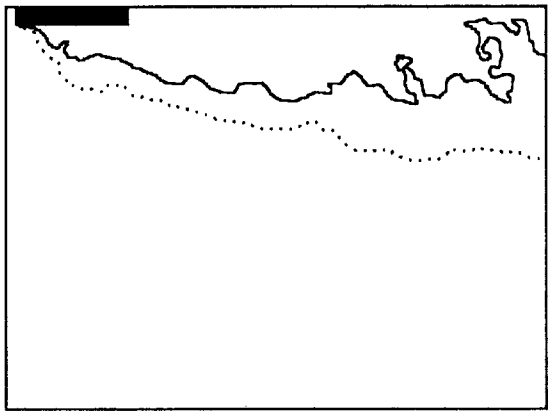

Fig. 10(b)

Fig. 10 Comparison of jet boundaries in steady (---) and unsteady (——) conditions for (a): U_0 = 39 m.s^{-1} and (b): U_0 = 14 m.s^{-1} at P90

and Nisbet, 1995; Veynante and Poinsot, 1997). The simple equations governing the movement of a spherical gas volume submitted to a time varying spatially uniform velocity are recalled in Appendix A and show qualitatively that the unsteady effects due to the external mean pressure gradient and to the added mass force are responsible for such observations. We could proceed in this way by extending the work of (Escudier and Maxworthy, 1973) to take into account entrainment of external air in the gas volume. Any quantitative use of the results would however be very difficult as the particular interaction of the fluid lumps with the time varying external flow depends critically on their unknown initial internal organisations (Chomiak and Nisbet, 1995; Escudier and Maxworthy, 1973).

4.3 Influence of Exit Jet Injection Angle. In this section, we illustrate and compare the behavior of the jet for different injection angles. Varying the jet injection angle can be a sensitive parameter if one wants to optimise the mixing with the crossflow. For example, recent studies (Krothapalli and Shih, 1993; Strykowski et al., 1993) explore the problem of counter current mixing in flows with this goal. Three exit jet angles have been experimented here for an exit jet velocity U_0 = 39 ms^{-1}. Time resolved images at the four phases are presented in Fig. 11 for the downstream injection case (θ = 45 deg) and in Fig. 12 for the upstream injection case (θ = 135 deg). The corresponding phases for a perpendicular jet (θ = 90 deg) were displayed in Fig. 8. For these three cases, the dynamic conditions of the crossflow are similar and equal to the conditions met in the precedent section.

In the downstream injection case (Fig. 11), we again notice a significant deflection of the flow at the jet outlet at phase P90 corresponding to the maximum acceleration. Moreover, the hot

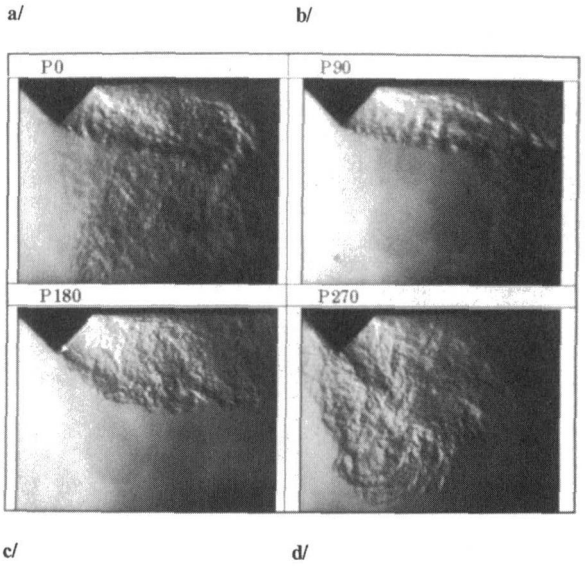

Fig. 11 Instantaneous images of the jet (U_0 = 39 m.s^{-1}) at the four phases of the pulsed crossflow for a jet ejection angle of 45 deg (downstream injection)

mixture is clearly deflected upstream during the deceleration (phase P270). No organized motion is however detected and the turbulent scales involved in this counter-flow are relatively small. By comparing the downstream injection to the perpendicular injection, one may also note that the flapping amplitude of the jet is reduced for the downstream injection.

The structure of the jet is significantly different for upstream injection (Fig. 12). In particular, the jet penetrates completely the duct and impacts on the lower wall about phase P0. As acceleration effects increase, the jet is deflected downstream (phase P90). A large scale turbulent fluid lump of organised nature is clearly seen at phase P180. One sees that this structure flows upstream the jet nozzle during the deceleration phase. In fact, this injection mode is expected to increase the coherence of the large-scale jet fluid lump by increasing the initial vorticity of the structures (Escudier and Maxworthy, 1973). Compared with the two other cases and especially for phases P90 and P180, the major difference is here that the mixture is not confined near the upper wall but expands on the whole height of the duct. This characteristic can be very interesting in terms of homogeneity of the mixing.

Conclusion

An experimental work and a physical analysis dedicated to the study of a low density jet subjected to a time varying crossflow with high acceleration/deceleration levels has been presented in this paper. The crossflow configuration is widely used in many technical applications where efficient mixing of the jet fluid with the surrounding is of primary importance.

A simplified momentum balance was written at the jet exit to derive relevant nondimensional numbers used to estimate the relative importance of the drag and of the acceleration. We have shown that unsteady effects associated with the presence of the jet in the acceleration field are expected to have noticeable consequences on the flapping of the jet which are of course enhanced in the case of jets significantly lighter than the ambient fluid. It was possible to predict an increase of the jet deflection during the acceleration phase and a competition between drag and acceleration during the deceleration; during this phase the unsteady effects can eventually dominate.

The Schlieren technique has been applied in the test section of a square duct to obtain time resolved images of the jet. Analysis of the results was focused on the influence of the unsteady effects on the global dynamic behavior of the jet in the near field and image processing was applied to extract the jet boundary. The modification of the mixing process induced by the unsteadiness was also discussed. The interaction between the jet and the crossflow was analyzed in three contrasted situations corresponding to different values of the jet outlet velocity U_0. The penetration of the hot mixture across the channel is significantly reduced as U_0 decreases. A comparison between jet and pulsation time scales is shown to characterise the possibility of impact of the hot mixture on the lower wall of the channel.

At the phase of maximum acceleration P90 ($\dot{U}_1 = 500\ g$), the influence of the unsteady effects has been isolated by comparing unsteady images to the steady situation corresponding to the same velocity of the crossflow. Compared to the steady case, the spreading of the jet flow submitted to such a strong acceleration is significantly reduced. Conversely, drag and acceleration effects compete with each other at the phase of maximum deceleration P270. This competition is particularly clear for the two lowest ejection velocities of the jet and we have shown that the jet is initially deflected upstream the nozzle as predicted by physical analysis. Moreover, figures display clearly volumes of hot mixture moving against the crossflow in the channel. A qualitative explanation has been proposed.

For the three cases presented here, large volumes of unmixed incident fluid flow in the channel lower half during the flapping of the jet. The influence of exit jet injection angle on the mixing process has been considered. Compared to the perpendicular injection the flapping amplitude is reduced in the downstream injection and the influence of unsteady effects remains quite similar. The most interesting case is the upstream injection where the interaction of the light jet with the crossflow is considerably modified. In particular, over a flapping period, the structure expands on the whole height of the duct and is not confined near the upper wall. Therefore this injection concept provides initial conditions that could be more favourable for the mixing process in terms of spatial homogeneity.

The further evolution of the turbulent mixture carried by the pipe flow should keep a strong memory of the unsteady tridimensional effects observed in the jet near field. Moreover, baroclinic effects and buoyancy driven turbulent scales in the acceleration field are expected to play a significant role in the evolution of this variable density flow.

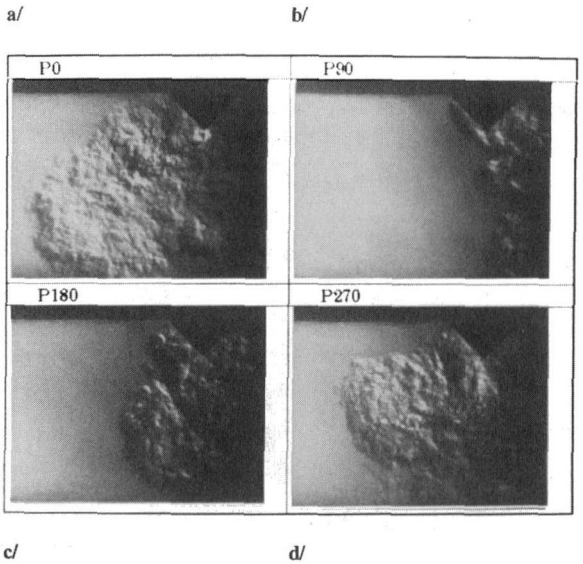

Fig. 12 Instantaneous images of the jet (U_0 = 39 m.s^{-1}) at the four phases of the pulsed crossflow for a jet ejection angle of 135° (upstream injection)

Acknowledgments

This research was supported by the "Conseil Régional de Midi Pyrénées." N. Raud is supported by a grant CIFRE in collaboration with the firm "Energie-Transport-Environnement." We have benefited greatly from discussions with Dr. L. Joly, Dr. H. J. Nuglisch and Dr. P. Labeyrie. The technical support of G. Couteau, J. F. Alquier, and C. Jarnot is acknowledged.

References

Adler, D., and Baron, A., 1979, "Prediction of a Three-Dimensional Circular Turbulent Jet in Crossflow," *AIAA Journal,* Vol. 17, No. 2, pp. 168–174.

Batchelor, G. K., 1967, *An Introduction to Fluid Dynamics,* Cambridge University Press.

Bates, G. J., 1989, "The Effects of Pulsation on Natural Gas Carburation," Thesis University of Auckland.

Borée, J., 1990, "Analyse physique et expérimentale d'un écoulement de jet compressé," Thesis INPT No. 373, Toulouse, France.

Broadwell, J. E., and Breidenthal, R. E., 1984, "Structure and Mixing of a Transverse Jet in Incompressible Flow," *Journal of Fluid Mechanics,* Vol. 148, pp. 405–412.

Catalano, G. D., Chang, K. S., and Mathis, J. A., 1989, "Investigation of Turbulent Jet Impingement in a Confined Crossflow," *AIAA Journal,* Vol. 27, No. 11, pp. 1530–1535.

Charnay, G., and Mathieu, J., 1976, "Periodic Flow in a Wind-Tunnel Produced by Rotating Shutters." ASME JOURNAL OF FLUIDS ENGINEERING, Vol. 98, pp. 1–6.

Chassaing, P., Harran, G., and Joly, L., 1994, "Density Fluctuation Correlations in Free Turbulent Binary Mixing," *Journal of Fluid Mechanics,* Vol. 300, pp. 1–40.

Chen, C. J., and Rodi, W., 1980, "Vertical Turbulent Buoyant Jets—A Review of Experimental Data," HMT-4 Pergamon.

Chomiak, J., and Nisbet, J. R., 1995, "Modeling Variable Density Effects in Turbulent Flames—Some Basic Considerations," *Combustion and Flame,* Vol. 102, pp. 371–386.

Escudier, M. P., and Maxworthy, T., 1973, "On the Motion of Turbulent Thermals," *Journal of Fluid Mechanics,* Vol. 31(3), pp. 541–552.

Hunt, J. C. R., 1987, "Vorticity and Vortex Dynamics in Complex Turbulent Flows," *Transactions of the CSME,* Vol. 11, No. 1, pp. 21–35.

Kamotani, Y., and Greber, I., 1972, "Experiments on a Turbulent Jet in a Cross Flow," *AIAA Journal,* Vol. 10, pp. 1425–1429.

Kamotani, Y., and Greber, I., 1974, "Experiments on Confined Turbulent Jets in a Cross Flow," NASA CR-2392.

Keffer, J. F., and Baines, W. D., 1963, "The Round Turbulent Jet in a Cross-Wind," *Journal of Fluid Mechanics,* Vol. 15, pp. 481–496.

Krothapalli, A., and Shih, C., 1993, "Separated Flow Generated by a Vectored Jet in Crossflow," *AGARD Conference Proceedings 534—Computational and Experimental Assessment of Jets in Crossflow,* pp. 5–1, 5–7.

Margason, R. J., 1993, "Fifty Years of Jet in Crossflow Research," *AGARD Conference Proceedings 534—Computational and Experimental Assessment of Jets in Crossflow,* pp. 1–1, 1–41.

Ooms, G., 1977, "A New Method for the Calculation of the Plume Path of the Gases Emitted by a Stack," *Athmospheric Environment,* Vol. 6, pp. 899–909.

Panchapakesan, N. R., and Lumley, J. L., 1993, "Turbulence Measurements in Axisymmetric Jet of Air and Helium. Part 2. Helium Jet," *Journal of Fluid Mechanics,* Vol. 246, pp. 225–247.

Raud, N., 1997, Mélange Air/Gaz en situation instationnaire. Application à l'emploi du G.N.V. dans les moteurs., Thesis I.N.P. Toulouse N°1316.

Schlichting, H., 1979, *Boundary Layer Theory,* McGraw-Hill, New York.

Smith, S. H., Lozano, A., Mungal, M. G., and Hanson, R. K., 1993, "Scalar Mixing in the Subsonic Jet in Crossflow," *AGARD Conference Proceedings 534—Computational and Experimental Assessment of Jets in Crossflow,* pp. 6–1, 6–13.

Smith, S. H., and Mungal, M. G., 1998, "Mixing, Structure and Scaling of the Jet in Crossflow," *Journal of Fluid Mechanics,* Vol. 357, pp. 83–122.

Stephenson, J., 1997, International Association for Natural Gas Vehicles: A Review of the State of the Art.

Stoy, R. L., and Ben-haim, Y., 1973, "Turbulent Jets in a Confined Crossflow," ASME JOURNAL OF FLUIDS ENGINEERING, Vol. 95, pp. 551–556.

Strykowski, P. J., Krothapalli, A., and Wishart, D., 1993, "Enhancement of Mixing in High-Speed Heated Jets Using a Counterflowing Nozzle," *AIAA Journal,* Vol. 28, No. 12, pp. 2033–2028.

Tritton, D. J., 1988, *Physical Fluid Dynamics,* Oxford Science Publications.

Veynante, D., and Poinsot, T., 1997, "Effects of Pressure Gradients on Turbulent Premixed Flames." *Journal of Fluid Mechanics,* Vol. 353, pp. 83–114.

Witze, P. O., 1980, The Impulsively Started Incompressible Turbulent Jet. Report no SAND80-8617, Sandia Laboratories energy report.

APPENDIX A

We consider here the movement of a spherical fluid lump of density ρ, volume V and velocity $\mathbf{U_b}$ submitted to a spatially uniform incident flow of velocity $\mathbf{U_1}(t)$ periodically varying with time with $0 \leq U_1(t) \leq U_m$. The density of the ambient fluid is ρ_1.

In a viscous flow, the drag force $\mathbf{F_D}$ non-detailed here is due to the diffusion of vorticity away from the gas volume (Hunt, 1987). A second force is caused by the mean pressure gradient $-\nabla \mathbf{p} = \rho_1 \dot{\mathbf{U}}_1(t)$ associated with the acceleration of the external fluid and acting over the volume V. A third force or added mass force is due to the acceleration of the fluid around the spherical body (Batchelor, 1967).

The momentum balance reads:

$$\frac{d\mathbf{U_b}}{dt} = \left[\frac{\rho_1(1 + C_m)}{\rho + C_m\rho_1}\right] \dot{\mathbf{U}}_1(t) + \frac{\mathbf{F_D}}{(\rho + C_m\rho_1)V} \quad \text{(A-1)}$$

In the non-galilean referential linked to the external fluid movement, the evolution of the relative velocity $\mathbf{U_r} = \mathbf{U_b} - \mathbf{U_1}$ is:

$$\frac{d\mathbf{U_r}}{dt} = \left[\frac{\rho_1 - \rho}{\rho + C_m\rho_1}\right] \dot{\mathbf{U}}_1(t) + \frac{\mathbf{F_D}}{(\rho + C_m\rho_1)V} \quad \text{(A-2)}$$

In the jet near field, jet fluid volumes propelled in the pipe are partially mixed with the external air and eventually experience a significant initial negative relative velocity with the external flow. In the constant density case ($\rho = \rho_1$), the unsteady pressure effects tend to keep constant this initial relative velocity and a counterflowing fluid lump can clearly be observed during the deceleration phase. Equation (A-2) shows that these effects are enhanced for light fluid ($\rho < \rho_1$) and reduced for heavy fluid ($\rho > \rho_1$) by buoyancy effects induced by the acceleration.

A pdf Description of Turbulent Axisymmetric Free Jet Flow

Ming-Hua Chen
Ph.D. Candidate.

Zuu-Chang Hong
Professor.

Department of Mechanical Engineering,
National Central University,
Chung-Li, Taiwan 320, R.O.C.

This study presents the application of a turbulence probability density function (pdf) equation to compute an axisymmetric turbulent free jet flow. In view of the difficulty of solving this pdf equation directly by conventional numerical methods, an approximate moment method is applied. The calculated triple velocity correlations appearing in the second-order moments equation are calculated and compared with measured values and with those estimated by moment-closure models. The results reveal that the pdf approach gives consistency in the higher-order moments and radial budget of third moments of velocity, and that the neglect of the mean-strain production, the rapid part of the pressure correlation and the dissipation are responsible for deviations between moment-closure models and experiments. Therefore, pdf methods appear to be more suitable than conventional moment-closure models in terms of revealing turbulence structure.

1 Introduction

Turbulence is not only a ubiquitous phenomenon, but also a recurring problem in engineering applications. The traditional solution is moment-closure approach, where high-order correlations are modeled in terms of the lower-order ones, and model constants are determined with the aid of experimental data and mathematical analysis. This approach has resulted in models including two-equation and Reynolds-stress-equation models (e.g., Launder and Spalding, 1972; Lakshminarayana, 1986; Pollard and Martinuzzi, 1989). An alternative approach is the probability density function (pdf) method. In addition to their utility in modeling turbulence, pdf methods are a promising approach in dealing with turbulent chemically reacting flows. Over the last 20 years, a representive series of documents associated with pdf turbulence models have been published by Pope et al. (e.g., Pope, 1981a, 1983, 1985; Haworth and Pope, 1986; Pope and Chen, 1990).

In practice, pdf turbulence models cannot be solved using conventional grid-based numerical methods because of their high dimensionality. This problem has been overcome using the Monte Carlo method developed by Pope (1981b). Haworth and Pope (1986) reported that every pdf turbulence model corresponds with a Reynolds-stress model (RSM). Furthermore, Pope (1994) performed a detailed examination of the relationship between pdf models and RSMs. Because they are one-point closures, pdf models require external specification of scale information. To remedy this deficiency, Pope and Chen (1990) developed a pdf turbulence model based on the joint pdf of velocity and the instantaneous dissipation rate. Meanwhile, by combining the modeling methods of Chung (1967) and Pope (1981a), Hong et al. (1993) developed the pdf model that is employed in the present study. As compared with Pope's models (e.g., Haworth and Pope, 1986; Pope and Chen, 1990), Hong et al.'s pdf model (1993) is less complicated and includes viscous diffusion to deal with turbulence in the vicinity of a wall. Recently, Dreeben and Pope (1997a, 1997b) also have included wall effects in their pdf models. Hong et al. subsequently used their model (Hong et al., 1993) to compute turbulent Couette flow (Hong et al., 1995) and the two-dimensional mixing layer (Hong and Chen, 1998).

This study is aimed at extending the range of Hong et al.'s pdf model. The configuration studied is an axisymmetric free turbulent jet without swirl. As indicated in some documents (e.g., Launder et al., 1972; Pope, 1978), the spreading rate of a round jet is predicted to be approximately 40 percent higher than the experimental data when using the standard $k - \epsilon$ model and RSMs. Such errors might be due to incorrect modeling of the ϵ-equation, as pointed out by Robinson et al. (1995). This situation has been studied over an extended time by turbulence model researchers, and eventually some modified models have been developed which have provided more satisfactory results (e.g., Launder et al., 1972; Pope, 1978; Hanjalic and Launder, 1980; Fu, 1993; Robinson et al., 1995). It has been suggested that the mechanism of spreading depends greatly on turbulence diffusion. Therefore, a model that addresses the effects of turbulence diffusion caused by velocity and pressure fluctuations is expected to provide better results. In this respect, it has been suggested that the pdf turbulence model can work more accurately on predicting the turbulence structure of round jet flow. This is due to the fact that the triple-moment velocity correlations, which appear in RSMs and require modeling, correspond to the convection term in the pdf model which does not have to be modelled.

This study provides the solution for the axisymmetric free jet flow using the pdf turbulence model developed by Hong et al. (1993, 1995) with the emphasis on the triple-moment velocity correlations. The calculated profiles of mean velocity and Reynolds-stresses and the radial budgets of turbulence kinetic energy and Reynolds-stress have been shown in a previous paper (Chen and Hong, 1998). In the present study, the solution method involves empirical inputs as initial conditions. This specification is for calculation and engineering convenience which will be described in detail in Section 3. Subsequently, a comparison of the calculated results with the measured values and with moment-closure theories is provided.

2 Pdf Equation Model and Mathematical Formulation

In this section, the pdf turbulence model developed by Hong et al. is briefly introduced. The detailed development of this pdf model was provided in the previous papers (Hong et al., 1993, 1995), and it will not be repeated here. For the purpose of solution, the pdf equation model is simplified in this section. Such a simplication is mainly based on the geometric and physical features of the axisymmetric free jet of present interest and the similarity variable introduced.

Contributed by the Fluids Engineering Division for publication in the JOURNAL OF FLUIDS ENGINEERING. Manuscript received by the Fluids Engineering Division June 9, 1998; revised manuscript received December 4, 1998. Associate Technical Editor: P. Bradshaw.

(a) pdf Equation Model. The pdf equation model developed by Hong et al. is shown as follows

$$\frac{\partial f}{\partial t} + U_i \frac{\partial f}{\partial x_i} = \frac{\partial}{\partial u_i}\left[(1 - C_3)\frac{\partial \overline{U_i}}{\partial x_j} u_j f + C_1 \frac{\epsilon}{k} u_i f - \frac{\partial \overline{u_i u_j}}{\partial x_j} f\right] + \nu \frac{\partial^2 f}{\partial x_i \partial x_i} + \left(C_{2\epsilon} + \frac{C_3}{3} P_{kk}\right)\frac{\partial^2 f}{\partial u_i \partial u_i}. \quad (1)$$

where upper and lower cases u's denote the mean and fluctuating components of velocity, respectively. Cartesian tensor notation with the summation convention for repeated indices has been used in Eq. (1). C_1, C_2, and C_3 are three model constants, and k and ϵ are the turbulent kinetic energy and its dissipation rate. $P_{kk} = -\partial \overline{U_i}/\partial x_j \ \overline{u_i u_j}$ is the production term in the turbulence kinetic energy equation. The dependent variable in Eq. (1) is the probability density function $f(\check{u};\ t,\ \check{x})$, where $fd\check{u}$ presents the probability of the fluid element at time t, position $\check{x}$ having a fluctuating velocity between $\check{u}$ and $\check{u} + d\check{u}$. Once f is known, velocity correlations of any order are computed as moments of this pdf f:

$$\overline{Q(u)} = \int Q(u) f d\check{u} \quad (2)$$

The first term on the right-hand side of Eq. (1) is the transport of f in velocity space due to mean velocity gradient, rapid effect of pressure fluctuations, viscous dissipation, and Reynolds-stress gradient. The second term presents the influence of viscous diffusion, and the third term denotes the way the pressure fluctuations work on the transport of f in velocity space. The theoretical basis and modeling of Eq. (1) are detailed in Hong et al.'s papers (1993, 1995). The model constants C_1, C_2, and C_3 need to be specified. A link between C_1 and C_2 can be found by comparing the turbulent kinetic energy equation derived from Eq. (1) with that derived from the Navier-Stokes equation. Furthermore, after the moment equations derived from Eq. (1) are compared with proven Reynolds-stress models (RSM's), one can determine relationships among the model constants C_1, C_2, and C_3 and pressure-strain (PS) term and the dissipation (D) term appearing in RSM's. Different values of C_1, C_2, and C_3 correspond to different models for PS and D. At this point, for simplicity and efficacy, the isotropization of production model (Naot et al., 1970; Launder et al., 1975) is taken as the baseline for the determination of C_1, C_2, and C_3: this yields $C_1 = 0.9$, $C_2 = 0.27$, and $C_3 = 0.6$.

(b) Axisymmetric Free Turbulent Jet. The turbulent flowfield of present interest is the axisymmetric free jet with a statistically steady, isothermal, incompressible fluid issuing into quiescent surroundings. This is a thin-shear-layer flow characterized by remoteness from walls and a single predominant flow direction, the streamwise direction, denoted by x. In addition, this flow has an azimuthal direction of statistical homogeneity, which is denoted by θ. The radial direction is denoted by r. Corresponding velocity components are U_x, U_r, and U_θ, respectively, which are decomposed into their mean and fluctuating parts ($\bar{U}_x$, $\bar{U}_r$, and $\bar{U}_\theta$) and (u, v, and w). It is well known that profiles of any one-point statistic of the Eulerian velocity field in a thin-shear-layer flow are self-similar (implied by an order-of-magnitude analysis). A dimensionless similarity variable η is introduced,

$$\eta = \frac{r}{\delta} \quad (3)$$

where δ denotes the value of r where $\bar{U}_x$ is equal to 1/2 $\bar{U}_m$; the characteristic velocity $\bar{U}_m$ is the centerline mean velocity. Notably, the spreading rate S defined by

$$S = \frac{d\delta}{dx} = \text{constant}. \quad (4)$$

Equation (4) is confirmed by experimental observations.

(c) Mathematical Formulation. First, the similarity equation is obtained by substituting the similarity variable defined by Eq. (3) into Eq. (1), by droping out $\bar{U}_\theta$ and the terms involved in $\partial/\partial t$ and $\partial/\partial\theta$, and by neglecting the viscous diffusion term. The generalized moment equation, subsequently, is obtained by multiplying the similarity equation by an arbitrary function of $\check{u}$, $Q = Q(\check{u})$, and integrating over the entire velocity space. The similarity and generalized moment equations are given by Chen (1998) and are not included here for lack of space. The generalized moment equation then is solved for the distribution function f using the moment method of Liu and Lees (1961). The solution was obtained by approximating the distribution function using two half-Maxwellian functions:

$$f = f_1 = \frac{1}{\left(\frac{2}{3}\pi E_1\right)^{3/2}} \times \exp\left[-\frac{(U_x - U_{o1})^2 + (U_r - V_{o1})^2 + w^2}{2E_1/3}\right] \quad \text{for } v > 0,$$

$$f = f_2 = \frac{1}{\left(\frac{2}{3}\pi E_2\right)^{3/2}} \times \exp\left[-\frac{(U_x - U_{o2})^2 + (U_r - V_{o2})^2 + w^2}{2E_2/3}\right] \quad \text{for } v \le 0. \quad (5)$$

The current moment method of solution involves determining the six unknown functions E_1, E_2, U_{o1}, U_{o2}, V_{o1}, and V_{o2} by substituting the assumed form of the distribution function, Eq. (5), into a set of six particular moment equations to be deduced from the generalized moment equation. With the six function distributions across the jet, any order velocity correlations can be readily evaluated immediately since these correlations are functions of E_1, E_2, U_{o1}, U_{o2}, V_{o1}, and V_{o2}. Some examples are shown in the following:

$$\frac{\overline{U_x}}{\bar{U}_m} = \frac{\alpha_1 + \alpha_2}{2} \quad (6)$$

$$\frac{\overline{u^2}}{\bar{U}_m^2} = \frac{\alpha_5^2 + \alpha_6^2}{6} + \frac{(\alpha_1 - \alpha_2)^2}{4} \quad (7)$$

$$\frac{\overline{uv}}{\bar{U}_m^2} = \frac{(\alpha_1 - \alpha_2)}{2}\left[\frac{\alpha_5 + \alpha_6}{\sqrt{6\pi}} + \frac{\alpha_3 - \alpha_4}{2}\right] \quad (8)$$

$$\frac{\overline{u^3}}{\bar{U}_m^3} = \frac{(\alpha_1 - \alpha_2)(\alpha_5^2 - \alpha_6^2)}{4} \quad (9)$$

where α_i, $i = 1 - 6$, are defined as follows:

$$\alpha_1 = \frac{U_{o1}}{\bar{U}_m}, \quad \alpha_2 = \frac{U_{o2}}{\bar{U}_m}, \quad \alpha_3 = \frac{V_{o1}}{\bar{U}_m}, \quad \alpha_4 = \frac{V_{o2}}{\bar{U}_m}, \quad \alpha_5 = \frac{E_1^{1/2}}{\bar{U}_m}, \quad \alpha_6 = \frac{E_2^{1/2}}{\bar{U}_m}.$$

Table 1 Empirical inputs and initial conditions

$(\bar{U}_x/\bar{U}_m)_{\eta=0}=1$	$(\alpha_1)_{\eta=0}=1.16$
$(\bar{U}_r/\bar{U}_m)_{\eta=0}=0$	$(\alpha_2)_{\eta=0}=0.84$
$(\overline{u^2}/\bar{U}_m^2)_{\eta=0}=0.075^*$	$(\alpha_3)_{\eta=0}=-0.18$
$(\overline{w^2}/\bar{U}_m^2)_{\eta=0}=0.048^*$	$(\alpha_4)_{\eta=0}=0.17$
$(\overline{uv}/\bar{U}_m^2)_{\eta=0}=0$	$(\alpha_5)_{\eta=0}=0.4$
$(\overline{u^3}/\bar{U}_m^3)_{\eta=0}=0.0021^*$	$(\alpha_6)_{\eta=0}=0.36$

(*Hussein, Capp and George 1994)

As we successively allow $Q = 1, u, v, u^2, v^2$ and uv into the generalized moment equation, and make use of Eq. (5), the following six ordinary differential equations are the result:

$$\sum_{j=1}^{6} A_{ij} \cdot \frac{d\alpha_j}{d\eta} = B_i, \quad i = 1 - 6 \tag{10}$$

where A_{ij}, for different i, and B_j are functions of α_j, $j = 1 - 6$.

3 Initial Conditions and Solution Method

The dependent variables α_i, $i = 1 - 6$, in Eq. (10) are functions only of the similarity variable η. The starting positions (or initial conditions) are at the centerline where $r = 0$ and $\eta = 0$. The measured values of some velocity correlations, which are functions of α_i as exemplified in Eqs. (6)–(9), at the centerline can be used to simultaneously determine the initial conditions of α_i, $i = 1 - 6$. Mathematically, the problem at hand needs six initial conditions which can be provided by physical argument. First, $\bar{U}_x/\bar{U}_m = 1$ at $\eta = 0$. Furthermore, the odd functions such as $\bar{U}_r$, $\overline{uv}$, $\overline{v^3}$, $\overline{vu^2}$, and $\overline{vw^2}$ are zero at the centerline. With the above conditions, the initial conditions can be acquired. The manipulation of this task, however, is more troublesome; hence the last three choices are replaced by $\overline{u^2}$, $\overline{w^2}$, and $\overline{u^3}$ for calculation and engineering convenience. Moreover, this replacement gives the closest Reynolds stress distribution across the round jet when compared with the LDA data. Table 1 shows the selected experimental inputs and the initial conditions in which the measured values are adopted from recent Laser-Doppler anemometry (LDA) data (Hussein et al., 1994). The earlier hot-wire (HW) data (Wygnanski and Fiedler, 1969) have not been adopted here due to the inevitably of greater errors in experiments. However, for the sake of comparison, the HW data will be included in the figures discussed in the next section.

The six simultaneous first-order ordinary differential equations, with the given initial conditions tabulated in Table 1, have been solved using a fourth-order Runge-Kutta method. For a convenient comparison with the measured values, the computation domain is $0 \le \eta \le 2$. After checking grid independence, a uniform spacing of 201 mesh points in the η direction arrived at a convergent solution.

For verifying the boundary conditions at the free-stream, the streamwise mean velocity, Reynolds shear-stress and turbulent kinetic energy were calculated with η extending to 10. For $\eta > 3$ the three quantities become less 1 percent of the corresponding maximum, respectively. The calculated results show these physical quantities approach zero with increasing η.

In addition, the values for S (spreading rate) and ϵ/k have to be presumed. Regarding S, the value lies in the conditions of the experiment which varies from 0.086–0.095 (Wilcox 1993). Two sets of recently measured data (Panchapakesan and Lumley, 1993; Hussein et al., 1994) revealed 0.096 and 0.094. Herein, we take the middle ground and adopt $S = 0.095$. The variation for ϵ/k acoss the jet can be determined through solving simultaneously the transport equations for k and ϵ. However, this methodology is a more troublesome task; therefore, they are given directly as done by Haworth and Pope (1987).

$$\frac{\epsilon}{k} = \omega^* \left(\frac{\bar{U}_m}{\delta}\right), \tag{11}$$

where ω^* ranges from 0.146 to 0.234 depending on the different models. In this study the middle value for $\omega^* = 0.21$ is selected along with $S = 0.095$ to give the closest Reynolds-stress distribution when compared with the LDA data.

4 Results and Discussion

This section presents the calculated high-order moments, including the third- and fourth-order velocity correlations. These quantities were evaluated using Eqs. (2), and (5) composed of α_i, $i = 1 - 6$, which were calculated in advance. As mentioned previously, typical corresponding experimental data, respectively, by SHW (stationary hot-wire), FHW (flying hot-wire), and LDA (Laser-Doppler anemometry) are included in the following plots for comparison. These measured values include the works performed by Wygnanski and Fiedler (1969, hereafter referred to as WF), Panchapakesan and Lumley (1993, hereafter referred to as PL), and Hussein et al. (1994, hereafter referred to as HCG). The suffixes SHW, FHW, and LDA indicate the type of measurement system. For comparison, all of the properties in the following figures were normalized using $\bar{U}_m$ and δ.

Figure 1 shows the calculated third moments and the corresponding measured values. The experimental data in these figures exhibit a significant amount of scatter. These results are attributed the differences among these measurements to experimental technique or to any of a number of physical effects. The calculated distribution for $\overline{u^3}$ shown in Fig. 1(a) reveals a closer agreement with the LDA and FHW data as to both profiles shape and magitude. This is an encouraging result, which is usually much underpredicted by simple moment-closure theories which will be discussed later. Figure 1(a) also shows that when away from the central region ($0.5 < \eta$), the SHW data of $\overline{u^3}$ shows a lower value than LDA data by approximately 50 percent.

The calculated profiles for $\overline{v^3}$ show in general a middle value between the LDA and FHW data but are higher near the axis, as shown in Fig. 1(b). The profiles for the SHW measurements of HCG and WF were found to be narrower than the LDA measurements. As pointed out by Panchapakesan and Lumley (1993), this difference may be attributed to the rectifictation and drop-out errors in the SHW measurements. Figure 1(c) shows the $\overline{u^2v}$ profiles. In the central region $0 < \eta < 0.5$ the calculated $\overline{u^2v}$ is found to be negative, a feature also displayed by the LDA and FHW measurements but absent in the SHW measurements of HCG and WF. The sign changes near the centerline may be attributed to the differences in the facilities, such as the SHW measurements made with capacitor-coupled circuits that may pass varying amounts of low-frequency large-scale motions with helical instability which could affect the intensities near the centerline.

Figure 1 above has presented the comparisons between the calculated and measured profiles for triple velocity moments. Moreover, the present calculations for triple velocity moments were compared with those predicted by moment-closure models. Regarding moment-closure models, our attention is confined to relatively simple ones that can be adopted without greatly adding to the computational labour involved in the numerical simulations for axisymmetric free jet flow with second-moment

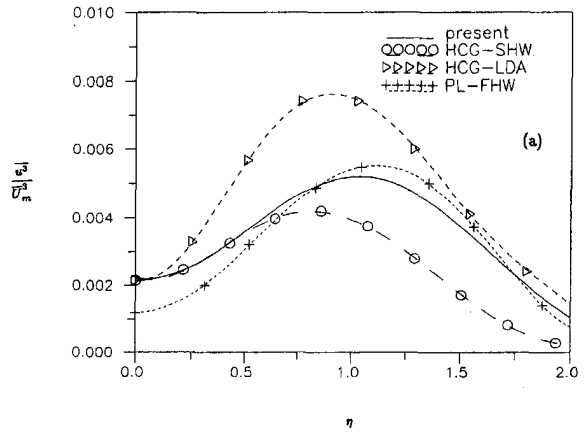

Fig. 1(*a*)

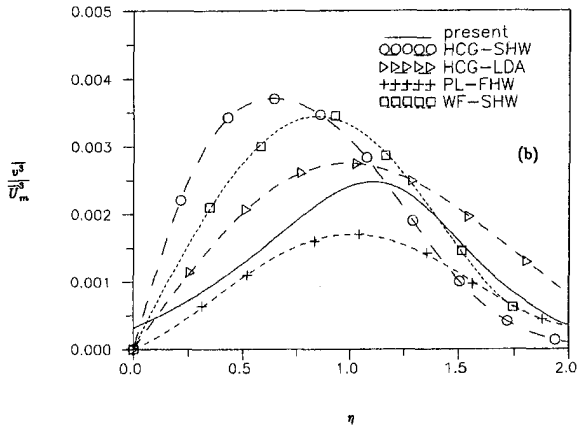

Fig. 1(*b*)

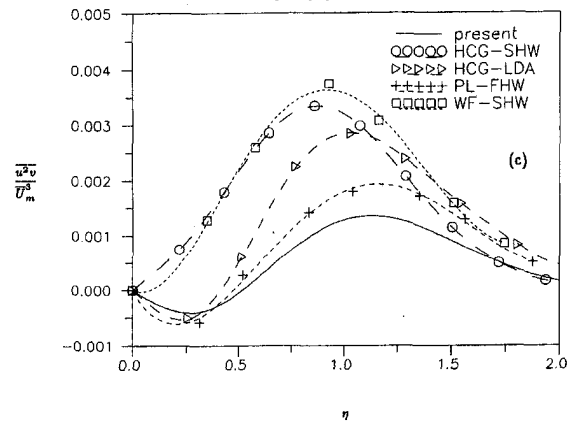

Fig. 1(*c*)

Fig. 1 Variation of third moments across the jet. (*a*) $\overline{u^3}$ (*b*) $\overline{v^3}$ (*c*) $\overline{u^2v}$

closures. There are six models to be chosen for comparison. They can be written in general form as

$$-\overline{u_i u_j u_k} = k^{3/2} \sum_{n=1}^{2} A^{(n)} D_{ijk}^{(n)}, \tag{12}$$

where $A^{(n)}$ are scalar coefficients and $D_{ijk}^{(n)}$ are the nondimensional tensors given as

$$D_{ijk}^{(1)} = \frac{1}{\epsilon k^{1/2}} G_{ijk} \tag{13}$$

$$D_{ijk}^{(2)} = \frac{1}{\epsilon k^{1/2}} (G_{ijk}\delta_{jk} + G_{ijk}\delta_{ik} + G_{ijk}\delta_{ij}) \tag{14}$$

where

$$G_{ijk} = \overline{u_i u_n} \frac{\partial \overline{u_j u_k}}{\partial x_n} + \overline{u_j u_n} \frac{\partial \overline{u_i u_k}}{\partial x_n} + \overline{u_k u_n} \frac{\partial \overline{u_i u_j}}{\partial x_n}, \tag{15}$$

and δ_{ij} is the Kronecker delta. The coefficients $A^{(n)}$ depend on the scalar invariants of the anisotropy tensor,

$$b_{ij} = \frac{\overline{u_i u_j}}{2k} - \frac{1}{3}\delta_{ij}. \tag{16}$$

Table 2 shows the coefficients $A^{(n)}$ corresponding to six models: the Hanjalic and Launder model (1972, hereafter referred to as HL); the Zeman and Lumley model (1976, hereafter referred to as ZL); the Lumley model (1978); the Choi and Lumley model (1984, hereafter referred to as CL); the Shih, Mansour and Chen model (1987, hereafter referred to as SMC) and the Sarkar and Speziale model (1990, hereafter referred to as SS). The scalar functions appearing in the different model coefficients shown in Table 2 are provided in the Appendix. The rational closure techniques and the physical grounds concerning the above models are referred to their original papers and are not repeated here. The basic assumptions under these models are the neglect of advection, mean-strain production, and the rapid part of the pressure correlation in the triple-moment equation and the quasi-Gaussian approximation for the diffusion term.

Using these algebraic models, the velocity triple moments have been calculated using the LDA data (HCG, 1994) of the second-moment quantities. The LDA data of HCG (1994) that can be adopted is because of the set of data satisfying all of the consistency checks imposed by the dynamics equations.

Shown in Fig. 2 are the comparisons for the triple-velocity correlations. Only the LDA measured data of HCG which are the source of the inputs for the evaluation of triple moments by the above six models are included also in Fig. 2 for comparison. The prediction for u^3 by these algebraic models is much lower than experimental data, as shown in Fig. 2(*a*). For u^3 the CL model gives a better agreement profile in the region $0.5 < \eta$, but gives greater negative values in the central region which violates the measured data. For v^3 and u^2v the six models achieve a better than qualitative agreement with the measured data. Of these models, that of Lumley and SMC models present the better approximation to the data, whereas HL and ZL models give the worse prediction. It is noted that the SMC model yields the same predictions as the Lumley model for the triple-velocity correlations. The CL model overpredicts the profiles for v^3 and u^2v. The six models all give profile shapes for u^2v which are consistant with the LDA data being negative near the centerline, as shown in Fig. 2(*c*). When compared with the third-moments profiles calculated by the pdf model, the six models are inferior since the discrepancies between the experiment and prediction by the six models for u^3 are still very serious. In order to further investigate the explanations for this discrepancy, the budget for triple moment u^3 is estimated by HCG data (1994), as shown

Table 2 Coefficients $A^{(n)}$ for different third moment model (see the Appendix for details)

Model	$A^{(1)}$	$A^{(2)}$	Model constants
HL	Cs	0	Cs=0.11
ZL	$1/6C_4$	$(C_4\text{-}1)/[6C_4(4C_4+5)]$	$C_4=[(1\text{-}24\Pi)^{1/2}\text{-}1]/30\Pi$
Lumley	$1/6C_4$	$(C_4\text{-}1)/[6C_4(4C_4+5)]$	$C_4=1+F\beta$
CL	$1/6C_4$	$(C_4\text{-}1)/[6C_4(4C_4+5)]$	$C_4=1+(\rho^*F^{1/2})/(1+G)$
SMC	$1/6C_4$	$(C_4\text{-}1)/[6C_4(4C_4+5)]$	$C_4=1+F^{0.85}\beta\text{-}(1\text{-}F^{0.05})(2\Pi+1/3)$
SS	$1/6C_4$	$(C_4\text{-}1)/[6C_4(4C_4+5)]$	$C_4=1.7$

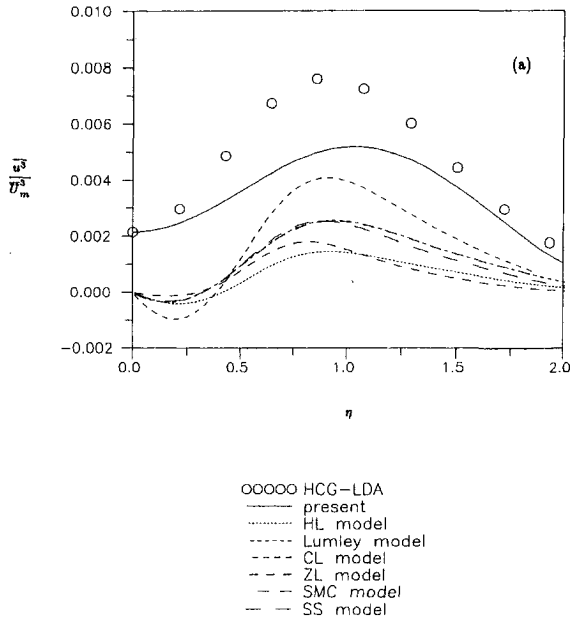

Fig. 2(a)

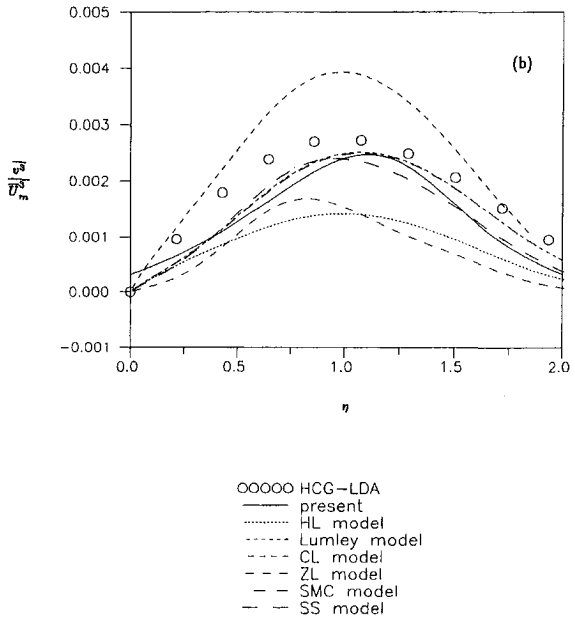

Fig. 2(b)

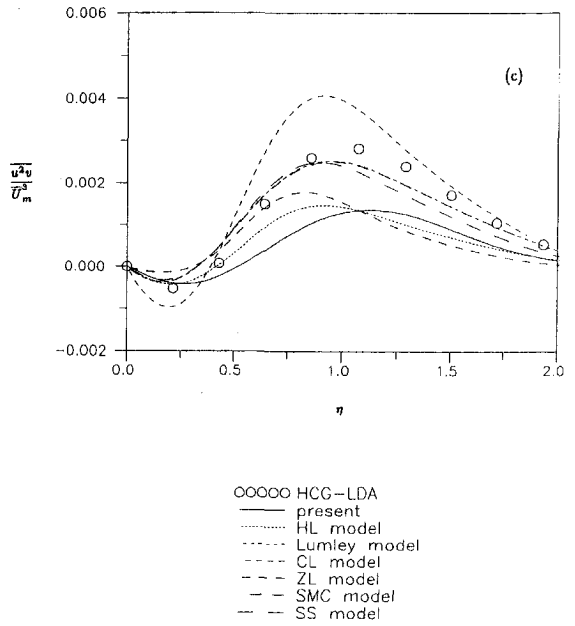

Fig. 2(c)

Fig. 2 Comparison of predictions by the present pdf and the phenomenological models with LDA data for (a) u^3 (b) v^3 (c) u^2v

in Fig. 3. This figure indicates that the advection term is negligible but that away from the central region ($0.5 < \eta$) the mean-strain production term is just as large in magnitude as the turbulent production term. In addition, the pressure and dissipation terms also play important roles in this budget. Therefore, the discrepancy for u^3 can be attributed to the neglect of the mean-strain production, the rapid part of the pressure correlation and the dissipation in the triple-moment equation. Figure 4 reveals whether the quasi-Gaussian approximation is another source of discrepancy or not. From this figure it can be seen that the approximation for the diffusion term is a good hypothesis.

5 Concluding Remarks

The computational results have clearly demonstrated the applicability of both the pdf turbulence model and the moment method adopted in the computation of the axisymmetric free jet flow. The comparisons between the computations of triple velocity moments by the present pdf model and by moment-closure models reveal that the pdf model is more promising than moment-closure models, since a better agreement has been indicated in the former calculation for u^3 which usually has been very much underpredicted by the latter models. From the budget for u^3 it is seen that this discrepancy is to be expected because the assumptions made in deriving these moment-closure models are violated across the jet flow. The disagreement is not due to the inadequency of the quasi-Gaussian approximation for the quadruple moments or due to the neglect of advection. It is the modeling of the pressure correlations and the dissipation term that are unsatisfactory. Therefore, more work is required to further verify closure hypotheses concerning the

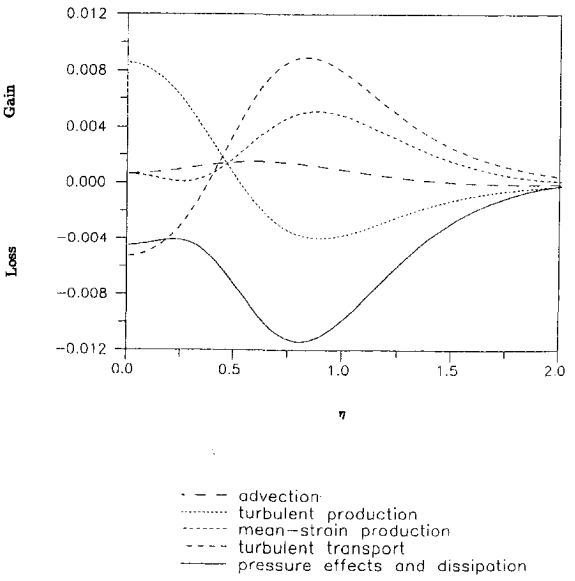

Fig. 3 Budget for the triple moment $\overline{u^3}$ based on the triple-moment equation (see Panchapakesan and Lumley, 1993). All terms have been normalized by U_m^4/δ.

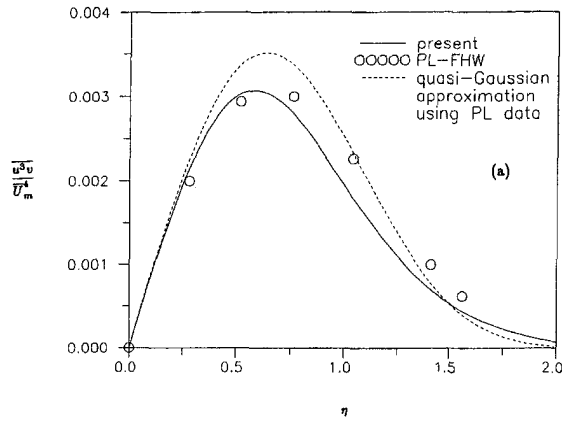

Fig. 4(*a*)

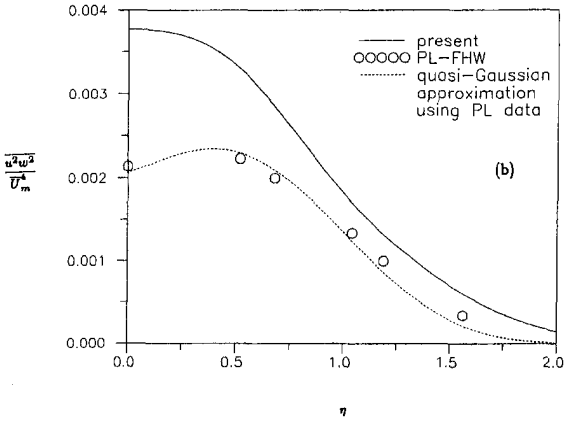

Fig. 4(*b*)

Fig. 4 Variation of the fourth moments across the jet and their quasi-Gaussian approximation according to PL data fit (1993) for (*a*) u^3v (*b*) u^2w^2

third moments that appear in the second-order moment equations.

APPENDIX

Here we list the related scalar functions appearing in the model constants used by different third moment models shown in Table 2. The scalar function β used in the Lumley and SMC models is

$$\beta = \frac{1}{18}\exp\left[\frac{-7.77}{R_e^{1/2}}\right] \times \left\{\frac{72}{R_e^{1/2}} + 80.1\ln[1 + 62.4(-II + 2.3\,III)]\right\}$$

The function F appearing in Lumley, CL, and SMC models is given by

$$F = 1 + 27III + 9II$$

where

$$R_e = \frac{2k}{9\nu\epsilon}, \quad II = \frac{-1}{2}b_{ij}b_{ij}, \quad III = \frac{1}{3}b_{ij}b_{jk}b_{ki}.$$

For the CL model following set of functions were used

$$\rho^* = \frac{1}{2}\exp\left[\frac{-9.29}{R_e^{1/2}}\right] \times \left\{\frac{7.69}{R_e^{1/2}} + \frac{73.7}{R_e} - II[296 - 16.2(\chi + 1)^4]\right\}$$

$$G = -\chi^6 + 0.8\chi^8$$

$$\chi = \frac{(III/2)^{1/3}}{(-II/3)^{1/2}}.$$

References

Chen, M.-H., 1998, "The Probability Density Function Modeling Study of Self-similar Turbulent Free Shear Flows," Ph.D. thesis, Department of Mechanical Engineering, National Central University, Taiwan, R. O. C.

Chen, M.-H., and Hong, Z.-C., 1998, "The Application of the Pdf Equation Model to the Axisymmetric Jet Flow," *Transactions of the Aeronautical and Astronautical Society of the Republic of China,* Vol. 30, No. 2, pp. 161–168.

Choi, K.-S., and Lumley, J. L., 1984, "Return to Isotropy of Homogeneous Turbulence Revisited," *Turbulence and Chaotic Phenomena in Fluids,* T. Tatsumi, ed., Elsevier, North Holland, pp. 267–272.

Chung, P. M., 1967, "A Simplified Statistical Description of Turbulence Chemically Reacting Flows," Aerospace Report TR-1001-S2855-20-5.

Dreeben, T. D., and Pope, S. B., 1997a, "Probability Density Function and Reynolds-stress Modeling of Near-wall Turbulent Flows," *Phys. Fluids,* Vol. 9, No. 1, pp. 154–163.

Dreeben, T. D., and Pope, S. B., 1997b, "Wall-function Treatment in Pdf Methods for Turbulent Flows," *Phys. Fluids,* Vol. 9, No. 9, pp. 2692–2703.

Fu, S., 1993, "Modelling of the Pressure-velocity Correlation in Turbulence Diffusion," *Computers and Fluids,* Vol. 22, No. 2, pp. 199–205.

Hanjalic, K., and Launder, B. E., 1972, "A Reynolds Stress Model and Its Applications to Thin Shear Flow," *Journal of Fluid Mechanics,* Vol. 52, pp. 609–638.

Hanjalic, K., and Launder, B. E., 1980, "Sensitizing the Dissipation Equation to Irrotational Streams," ASME JOURNAL OF FLUIDS ENGINEERING, Vol. 102, pp. 34–39.

Haworth, D. C., and Pope, S. B., 1986, "A Generalized Langevin Model for Turbulent Flows," *Physics of Fluids,* Vol. 29, pp. 387–405.

Haworth, D. C., and Pope, S. B., 1987, "A pdf Modeling Study of Self-similar Turbulent Free Shear Flows," *Physics of Fluids,* Vol. 30, pp. 1026–1044.

Hong, Z.-C., Lin, C., and Chen, M.-H., 1993, "An Eulerian One-point Velocity Probability Density Function Model for Turbulent Flows," *The Chinese Journal of Mechanics,* Vol. 9, No. 3, pp. 167–179.

Hong, Z.-C., Lin, C., and Chen, M.-H., 1995, "A PDF Description of Turbulent Plane Couette Flow," *International Journal of Numerical Methods for Heat and Fluid Flow,* Vol. 5, No. 9, pp. 757–779.

Hong, Z.-C., and Chen, M.-H., 1998, "Statistical Model of a Self-similar Turbulent Plane Shear Layer," ASME JOURNAL OF FLUIDS ENGINEERING, Vol. 120, No. 2, pp. 263–273.

Hussein, H. J., Capp, S. P., and George, W. K., 1994, "Velocity Measurements in a High-Reynolds-number, Moment Conserving, Axisymmetric, Turbulent Jet," *Journal of Fluid Mechanics,* Vol. 258, pp. 31–75.

Lakshminarayana, B., 1986, "Turbulence Modeling for Complex Shear Flows," *AIAA Journal,* Vol. 24, No. 12, pp. 1900–1917.

Launder, B. E., Morse, A., Rodi, W., and Spalding, D. B., 1972, "The Prediction of Free Shear Flows—A Comparison of the Performance of Six Turbulence Models," *Proceedings of NASA Conference on Free Shear Flows,* Langley AFB.

Launder, B. E., and Spalding, D. E., 1972, *Mathematical Models of Turbulence,* Academic, New York.

Liu, C. Y., and Lees, L., 1961, "Kinetic Theory Description of Plane Compressible Couette Flow," *Rarefied Gas Dynamics,* L. Talbot, ed., Academic Press, New York, pp. 391–428.

Lumley, J. L., 1978, "Computational Modeling of Turbulent Flows," *Advances in Applied Mechanics,* Vol. 18, pp. 123–176.

Naot, D., Shavit, A., and Wolfshtein, M., 1970, "Interactions Between Components of the Turbulent Velocity Correlation Tensor due to Pressure Fluctuations," *Israel Journal of Technology,* Vol. 8, pp. 259–265.

Panchapakesan, N. R., and Lumley, J. L., 1993, "Turbulence Measurements in Axisymmetric Jets of Air and Helium. Part 1. Air Jet," *Journal of Fluid Mechanics,* Vol. 246, pp. 197–223.

Pollard, A., and Martinuzzi, R., 1989, "Comparative Study of Turbulence Models in Predicting Turbulent Pipe Flow Part II: Reynolds Stress and $k - \epsilon$ Models," *AIAA Journal,* Vol. 27, No. 12, pp. 1714–1721.

Pope, S. B., 1978, "An Explanation of the Turbulent Round-Jet/Plane-Jet Anormaly," *AIAA Journal,* Vol. 16, No. 3, pp. 279–281.

Pope, S. B., 1981a, "Transport Equation for the Joint Probability Density Function of Velocity and Scalars in Turbulent Flow," *Physics of Fluids,* Vol. 24, pp. 588–596.

Pope, S. B., 1981b, "A Monte Carlo Method for the pdf Equations of Turbulent Reacting Flow," *Combustion Science and Technology,* Vol. 25, pp. 159–174.

Pope, S. B., 1983, "A Lagrangian Two-time Probability Density Function Equation for Inhomogeneous Turbulent Flows," *Physics of Fluids,* Vol. 26, pp. 3448–3450.

Pope, S. B., 1985, "PDF Methods for Turbulent Reactive Flows," *Progress in Energy and Combustion Science,* Vol. 11, pp. 119–192.

Pope, S. B., and Chen, Y.-L., 1990, "The Velocity-dissipation Probability Density Function Model for Turbulent Flows," *Physics of Fluids A,* Vol. 2, pp. 1437–1449.

Pope, S. B., 1994, "On the Relationship Between Stochastic Lagrangian Models of Turbulence and Second-moment Closures," *Physics of Fluids A,* Vol. 6, pp. 973–985.

Robinson, D. F., Harris, J. E., and Hassan, H. A., 1995, "Unified Turbulence Closure Model for Axisymmetric and Planar Free Shear Flows," *AIAA Journal,* Vol. 33, No. 12, pp. 2325–2331.

Sarkar, S., and Speziale, C. G., 1990, "A Simple Nonlinear Model for the Return to Isotropy in Turbulence," *Physics of Fluids A,* Vol. 2, pp. 84–93.

Shih, T. H., Mansour, N. N., and Chen, J.-Y., 1987, "Reynolds Stress Models of Homogeneous Turbulence," *Proceedings of the Summer Program,* Center for Turbulence Research, Stanford University and NASA Ames.

Wilcox, D. C., 1993, *Turbulence Modeling for CFD,* DCW Industries, Inc., La Canada, CA.

Wygnanski, I., and Fiedler, H., 1969, "Some Measurements in the Self-preserving Jet," *Journal of Fluid Mechanics,* Vol. 38, pp. 577–612.

Zeman, O., and Lumley, J. L., 1976, "Modeling Buoyancy Driven Mixed Layers," *Journal of Atmospheric Science,* Vol. 33, pp. 1974–1988.

A Generic Centerline Velocity Decay Curve for Initially Turbulent Axisymmetric Jets[1]

George Papadopoulos[2]

William M. Pitts

Building and Fire Research Laboratory,
National Institute of Standards
and Technology,
Gaithersburg, MD 20899

Recently the authors introduced a length scale which effectively collapsed the near field centerline development of velocity and mass fraction for variable density axisymmetric jets whose initial conditions correspond to those of fully developed turbulent pipe flow. The new length scale incorporated the initial mass, momentum, and turbulence intensity per unit area to capture the Reynolds number dependence of near field development for the velocity and scalar distributions observed in low Reynolds number turbulent jets. The present paper extends the analysis for a constant density jet to the intermediate and self-similar far fields further downstream using a dynamic length scale based on the local centerline turbulence intensity. The normalized mean velocity distributions of an air jet collapse over the entire flow distance investigated when the axial distance is normalized by the proposed length scale, thus scaling the virtual origin shift and effectively incorporating the Reynolds number dependence.

1 Introduction

Axisymmetric turbulent jets are used in a variety of engineering applications because of their ability to provide high mixing rates in simple and safe configurations. To better control such mixing processes accurate prediction of jet dynamics is necessary, especially in the early stages of development where important interacting processes, such as, combustion, recirculation, and entrainment, are initiated.

There is a considerable volume of information on jets available in the literature (Harsha, 1971; Chen and Rodi, 1980; Gouldin et al., 1986) and it is safe to say that a good understanding exists on jet characteristics and development in the far-field, or self-similar region. In this region of flow the mean and fluctuating centerline distribution field of a constant density axisymmetric jet issuing into a still ambient is described by the following equations:

$$\frac{\bar{U}(0,0)}{\bar{U}(z,0)} = K_u\left(\frac{z - z_{o,u}}{r_\epsilon}\right),$$

$$\frac{U'(z,0)}{\bar{U}(z,0)} = \text{constant} \qquad (1)$$

K_u is the centerline decay rate for the velocity distribution, $U(z, r)$. The streamwise distance, z, is measured from the jet exit plane, but to achieve a generic set of equations the introduction of a virtual origin, z_o, is necessary. This latter term is a displacement along the centerline of the jet representing a correction to the actual origin that yields the location where an idealized point jet-source, having the same mass, momentum and far-field development as the actual jet, would be located. It can thus be regarded as a means of incorporating the effects of nonideal initial conditions and flow development.

The effective radius,

$$r_\epsilon = \frac{\dot{m}_o}{(\pi\rho_\infty J_o)^{1/2}}, \qquad (2)$$

introduced in a simpler form first by Thring and Newby (1953) and used in this form by several researchers (Dahm and Dimotakis, 1987; Dowling and Dimotakis, 1990; Pitts, 1991a; Richards and Pitts, 1993) incorporates some initial conditions, such as density ratio $R_\rho = \rho_o/\rho_\infty$ and velocity distribution nonuniformity, through the mass and momentum fluxes at the jet exit plane, $\dot{m}_o$ and J_o, respectively. Dahm and Dimotakis (1990) have shown, using dimensional analysis, that the effective radius as defined in Eq. (2) is the appropriate length scale to nondimensionalize the axial coordinate of the jet fluid concentration in the far-field. After a detailed study of variable density jets, Richards and Pitts (1993) concluded that the final asymptotic state of all momentum-dominated axisymmetric jets depends only on the rate of momentum addition when the streamwise distance is scaled appropriately with r_ϵ. They furthermore showed, regardless of the initial conditions (fully developed pipe and nozzle flow), axisymmetric turbulent free jets decay at the same rate, spread at the same half-angle, and both the mean and rms mass fraction values collapse in a form consistent with full self-preservation. Nevertheless, the problem of the virtual origin still remained, and represented an unknown parameter that needed to be determined specifically for each configuration.

Investigations focusing on the variation of the virtual origin have indicated qualitatively how various initial parameters, such as Reynolds number, profile shape, turbulence intensity, and density ratio, affect its location. Some attempts at quantifying the trends observed, especially with respect to Reynolds number, have yielded empirical relations that are merely best fits to specific experimental data (see discussion by Pitts, 1991b). These correlations indicate a downstream displacement of z_o with increasing Re, reaching an asymptotic value at large Re.

In a recent investigative effort undertaken by the authors (Papadopoulos and Pitts, 1998) the controlling parameter responsible for the variation of centerline velocity and concentration decay characteristics in the near field of jets whose exit characteristics correspond to those of fully developed turbulent pipe flow was identified to be the initial turbulence intensity per unit area. The initial turbulence intensity is a significant source of excitation that feeds into the growing shear layer, thus governing directly the growth of turbulence responsible

[1] Contribution of the National Institute of Standards and Technology and not subject to copyright in the United States.

[2] Current address: Dantec Measurement Technology, Inc., 777 Corporate Drive, Mahwah, NJ 07430.

Contributed by the Fluids Engineering Division for publication in the JOURNAL OF FLUIDS ENGINEERING. Manuscript received by the Fluids Engineering Division March 23, 1996; revised manuscript received November 25, 1998. Associate Technical Editor: F. Hussain.

for breaking up the jet potential core and for transitioning the jet into a fully developed self-similar flow. Combining the initial turbulence intensity per unit area with the definition of the effective radius resulted in a new length scale that captured the near field variation of velocity and scalar centerline decay with Re, and thus collapsed the distributions for these types of turbulent axisymmetric jets. However, the proposed axial scaling was inappropriate when extended to the intermediate and far fields of the jet.

In related work, Faeth and coworkers (Wu et al., 1992; Wu and Faeth, 1993; Wu et al., 1995) investigated the breakup of liquid jets flowing into gas surroundings. Similar to our findings, the degree of jet breakup was shown to depend on the initial turbulence level of the liquid jet. However, the physical processes responsible for the breakup of liquid jets are very different from that proposed for the variation of the initial development rate of a gas jet with initial turbulence intensity level.

The present paper focuses on the centerline velocity field of a constant density jet and extends the aforementioned work by presenting a similar length scale that is more robust, in that not only does it collapse the near-field centerline behavior for variable Re cases, but also the intermediate and far fields as well. Furthermore, it yields a generic centerline mean velocity curve with a single value for the virtual origin. This unique generic curve can be used to predict the velocity virtual origin and centerline development for all axisymmetric jets having fully developed turbulent pipe flow initial conditions.

2 Experimental Setup and Apparatus

Test Configuration. Measurements were performed in a jet produced by a long straight pipe having a sharp-edged exit. The diameter was 6.08 mm ± 0.04 mm.[3] The gas supply to the pipe passed first into a cylindrical settling chamber (120 mm long and 100 mm in diameter) and then through a series of pipe fittings before entering the pipe. The fittings provided the necessary initial artificial disturbance to guarantee fully developed turbulent conditions at the exit of the pipe, 103 diameters downstream, for the flow rates considered in the investigation.

Air was the working fluid supplied from an in-house pressurized distribution system. It was filtered to remove oil, moisture, and particulates. A long supply line with several looped copper sections ensured that the issuing gas was in temperature equilibrium with the ambient air. A 100 L/min mass flow controller, accurate to ±1 percent of full scale and with repeatability of ±0.2 percent of full scale per manufacturer's specifications, was used to meter the gas. Calibration of the mass flow controller was performed using an Optiflow 730 Digital Flowmeter.[4] The uncertainty in the mass flow calibration was less than ±1.5 percent. Ambient conditions, temperature and barometric pressure, were recorded at the beginning and end of each complete test (generally lasting 2 h to 3 h) for determining the average gas properties. Overall, beginning-to-end ambient variations were small, less than ±0.5°C and ±2 Pa. The resulting uncertainty in the bulk flow velocity based on the mass flow controller setting was ±2 percent, which yielded an uncertainty in Re of ±2.2 percent.

Velocity Measurements. A single wire, hot-wire probe was used to measure the velocity at the exit of the pipe and along the centerline of the air jet. The probe was a 2.5-μm-diameter tungsten wire with a sensing length of 0.4 mm. It was controlled by a TSI IFA100 anemometer, interfaced to a Masscomp computer, which incorporated voltage gain and offset capabilities for optimizing the analog output for the voltage range of the 12-bit analog-to-digital converter. Calibration of the hot-wire was performed using a TSI Model 1125 calibrator unit over a velocity range of 2 m/s to 60 m/s. The calibration data was fitted to a general King's law relation, $E^2 = A + BU^n$, where E is the hot-wire voltage output, and A, B, n are calibration constants. The absolute error in an individual velocity measurement was estimated to be no more than 4 percent. The square wave frequency response of the hot-wire was approximately 25 kHz. Data sampling was performed at 500 Hz and 10 kHz, 10,000 and 30,000 samples, respectively, with the high sampling rate used to better evaluate velocity dynamics in the near and intermediate fields ($0 \le z/r_o \le 21$). The uncertainties associated with determining the mean and rms values were less than 0.2 percent of the initial centerline mean velocity at the exit of the jet.

The pipe assembly was fixed horizontally on a lab bench with the jet issuing into the laboratory. Fine meshed screens placed at a standoff distance of about 0.3 m surrounded the jet to limit the effects of cross-currents in the room. A two-dimensional computer-controlled traverse was used to move the hot-wire probe in relation to the jet. For measuring the exit velocity distribution, the wire was centered longitudinally along

[3] Reported expanded uncertainties are at 95 percent confidence (2σ).

[4] Certain commercial equipment, instruments or materials are identified in this paper in order to adequately specify the experimental procedure. Such identification does not imply recommendation or endorsement by the National Institute of Standards and Technology, nor does it imply that the materials or equipment are necessarily the best available for the purpose.

Nomenclature

A = jet cross-sectional area
J_o = initial momentum flux ($= \int_A \rho U(0, r)^2 dA$)
K = centerline decay rate
$\dot{m}_o$ = initial mass flux ($= \int_A \rho U(0, r) dA$)
M_o = initial volume flux for constant density jet ($= \int_A U(0, r) dA$)
N_o = initial momentum flux normalized by density for constant density jet ($= \int_A U(0, r)^2 dA$)
r_o = initial jet radius
r_u = contribution to r_ϵ due to mean velocity profile at jet exit
r_ϵ = effective jet radius
r^* = length scale incorporating mass, momentum and turbulence intensity characteristics
R_ρ = density ratio ($=\rho_o/\rho_\infty$)
Re = Reynolds number ($=2r_o U_b \rho_o/\mu_o$)
t = time
Tu = turbulence intensity ($=U'/\bar{U}$)
U = velocity
z = streamwise distance, measured from jet exit and positive in bulk flow direction
z_o = virtual origin
η = normalized centerline turbulence intensity
μ = dynamic viscosity
ρ = density
τ_o = initial turbulence intensity per unit area ($=1/A \int_A Tu(0, r) dA$)

Subscripts and Other Notation

o = an initial condition
0.5 = streamwise location where the centerline velocity equals half of the maximum jet velocity at the exit
∞ = ambient (surroundings)
b = bulk (average)
l = local field
m = maximum
pc = potential core end location
u = velocity field
$( )'$ = denotes root mean squared (rms) value
$\overline{( )}$ = denotes time averaged mean value

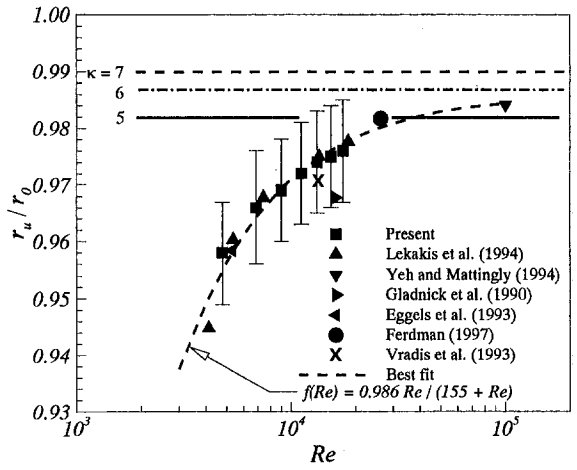

Fig. 1 Normalized effective radii due to the exit velocity distribution dependence on Re

a jet diameter and traversed perpendicular to it with the wire's longitudinal axis normal to the travel and incoming flow directions. The streamwise location of this measurement was z = 0.5 mm. Centerline measurements were performed up to a location of z = 270 mm. The error in initially positioning the probe was less than ±0.05 mm and ±0.1 mm in the radial and streamwise directions, respectively. Subsequent positioning was done at manufacturer's specified accuracy of ±1.6 μm and ±3.2 μm, respectively.

3 Results

Mass, momentum, and turbulence intensity distributions at the exit plane influence flow development in the near field of the jet, the latter being a perturbation mechanism that feeds into the growing shear layer. Initial mass and momentum distributions are already incorporated in the definition of the effective radius, Eq. (2). Since the gas density is constant across the exit of the jet, Eq. (2) may be written as

$$r_\epsilon = r_u; \quad r_u = \frac{M_o}{(\pi N_o)^{1/2}} \tag{3}$$

where $M_o = \int_A U(0, r)dA$ and $N_o = \int_A U(0, r)^2 dA$. The term r_u is the contribution to the effective radius of the mean velocity profile at the exit. For a uniform (top-hat) profile $r_u = r_o$, while for a parabolic profile $r_u = \sqrt{3}r_o/2$. For a turbulent velocity profile r_u is determined by integrating the profile at the pipe exit. Doing so for the present data, as well as for other data found in the literature, gives the results shown in Fig. 1. The horizontal lines in the figure show the expected values if the typical power law profile is assumed,

$$\frac{\bar{U}(0, r)}{\bar{U}(0, 0)} = \left(1 - \frac{r}{r_o}\right)^{1/\kappa}, \tag{4}$$

where κ takes on values from 5 to 7 as Re increases within the range of the experimental data shown (Schlichting, 1979). An obvious difference of a few percent exists between the power law profile and actual experimental measurements for Re < 10,000.

In the authors' previous work (Papadopoulos and Pitts, 1998) a new length scale was defined,

$$r_o^* = r_\epsilon \tau_o^{-1/2} = \frac{R_p^{1/2} M_o}{(\pi N_o \tau_o)^{1/2}} \tag{5}$$

which incorporated the jet's initial mass, momentum, and turbulence intensity, the latter through the turbulence intensity per unit area, τ_o, shown in Fig. 2. Correcting for nonuniform velocity distribution effects had previously involved only the mean characteristics. For turbulent flows, however, the inclusion of fluctuating velocity effects in the definition of a scale was clearly necessary to fully capture the effects of initial conditions on flow development. If the velocity terms in the mass and momentum flux terms of Eq. (3) are separated into mean and fluctuating components, and subsequently time averaged, then an additional term multiplying the mean momentum flux term is apparent. This term is a function of the local turbulence intensity, and although not exactly equivalent to τ_o, it supports the general form of Eq. (5). Normalization of the streamwise distance by r_o^* was shown in this prior investigation to collapse the near field centerline velocity and mass fraction decay curves over a range of Re.

The effectiveness of r_o^* on the present measurements and on those of others found in the literature is shown in Fig. 3 where the mean centerline velocity distribution for several Re is shown. However, since far field self-similarity requires that the flow be dependent only on the total mass and momentum flux, and not on any specific characteristics of the initial flow, the normalization by r_o^* naturally fails to correlate the data when extended to the far field region, as is evident in Fig. 4. Even so, it is an important contribution since it collapses the near field distributions without the introduction of any empirical constants.

To correct the aforementioned shortcoming of r_o^* it is clear that a dynamic term replacing the constant τ_o term is necessary. The effectiveness of r_o^* in the near field implies that this dynamic term be initially equal to τ_o. On the other hand, far field self-similarity requires that the effective radius be the proper length scale for nondimensionalizing the axial coordinate. Thus, in the far field the dynamic term needs to equal unity. These two bounds may be satisfied by introducing a dynamic term of the form $\tau_o^{-\eta/2}$ with $\eta = f(Tu)$ taking on values between one and zero, thus incorporating the expected decreasing effect of initial turbulence intensity on the growth of the shear layer as the jet propagates downstream.

A function for η meeting the aforementioned criteria may be defined in terms of the centerline turbulence intensity distribution, normalized to yield a value of one at the jet exit and zero in the far field. The result is

$$\eta = \frac{Tu(\infty, 0) - Tu(z, 0)}{Tu(\infty, 0) - Tu(0, 0)}, \tag{6}$$

where $Tu(\infty, 0)$ is the centerline turbulence intensity measured in the jet far field, which according to Eq. (1) is a constant throughout the self-similar region. Figure 5 shows distributions of η for several Re versus z/r_o^*, where

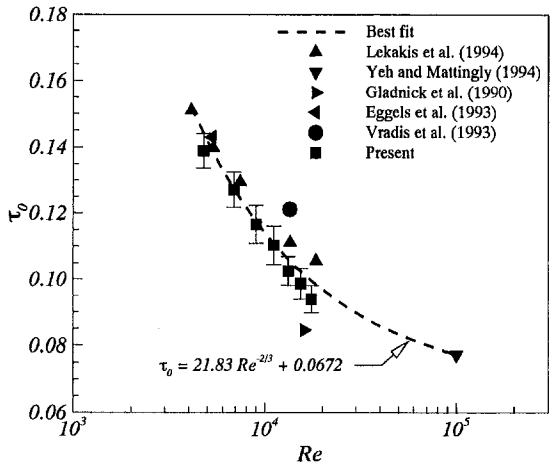

Fig. 2 Initial turbulence intensity per unit area as a function of Re

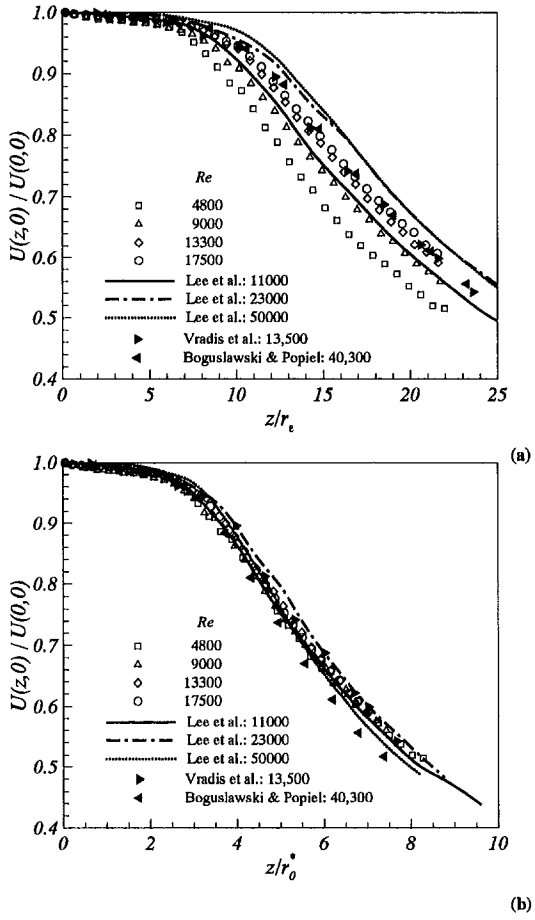

Fig. 3 Normalized mean centerline velocity decay for several Re: (*a*) axial distance normalized by effective radius; (*b*) axial distance normalized by a length scale based on initial mass momentum and turbulence intensity distributions

$$r_j^* = \tau_o^{-\eta/2} r_\epsilon \tag{7}$$

is the new dynamic length scale. Note that when $\eta = 0$ the flow becomes self-similar according to Eq. (1). Figure 5 then indicates that self-similarity is attained over shorter flow distances at lower Re, which agrees with earlier observations (Pitts, 1991b).

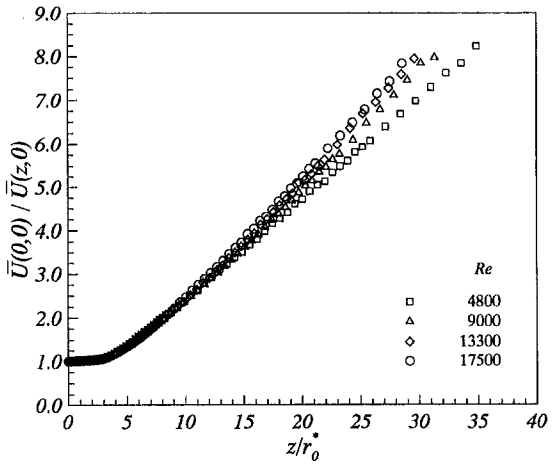

Fig. 4 Inverse decay of mean centerline velocity in near, intermediate and far fields of the air jet; axial distance normalized by r_o^*

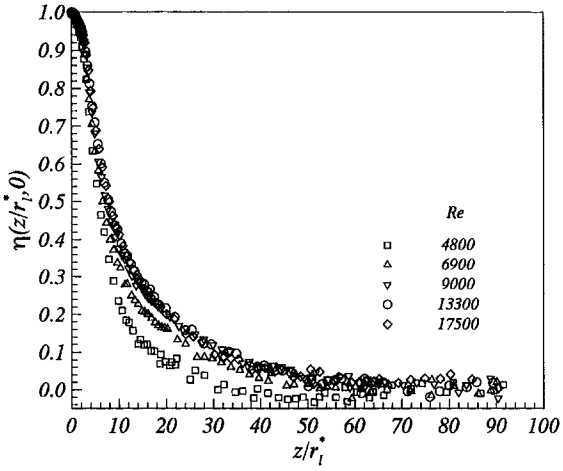

Fig. 5 Normalized centerline turbulence intensity distribution

Recasting the data of Fig. 4 in terms of z/r_j^* yields good results (Fig. 6), implying that a generic curve for the centerline velocity decay of initially turbulent axisymmetric jets can be realized when the streamwise distance variable is normalized using the newly proposed dynamic length scale. Such a generic realization also implies that a single value for the virtual origin exists for data normalized in this way. Its value is obtained by linearly fitting the far field velocity data of Fig. 6 ($z/r_j^* \geq 60$) and extrapolating to $\bar{U}(0, 0)/\bar{U}(z, 0) = 0$, as indicated by the dashed line. The result is $z_o/r_j^* = 6 \pm 1$.

Reverting back to absolute coordinates requires the use of Figs. 1, 2, and 5. By using the proposed dynamic scaling a generic centerline decay curve of the mean velocity is attained, but the second moment (turbulence intensity distribution) still exhibits Re dependence. Thus, it is necessary to construct empirical functions for $\eta(z/r_j^*, 0)$ using the data in Fig. 5. A function which fits the data well is

$$\eta(\zeta) = a_1 e^{-b_1 \zeta^{c_1}} + a_2 e^{-b_2 \zeta^{c_2}};$$

$$\text{with } \zeta = z/r_j^* \quad \text{and} \quad a_1 + a_2 = 1 \tag{8}$$

where $a_{1,2}$, $b_{1,2}$, and $c_{1,2}$ are fit parameters that depend on Re. The resulting curves for $\eta(z/r_j^*, 0)$ are shown in Fig. 7. Figure 8 shows the variation of the constants with Re, in the range investigated. Note that only a_1 is shown in the figure since $a_2 = 1 - a_1$ by the constraint indicated in Eq. (8). Performing

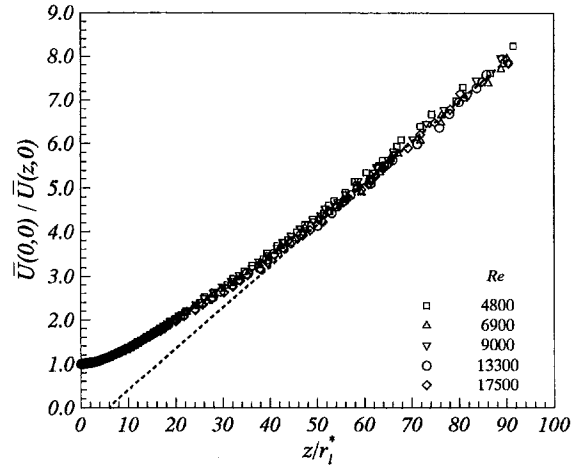

Fig. 6 Inverse decay of mean centerline velocity in near, intermediate and far fields of the air jet; axial distance normalized by the new dynamic length scale

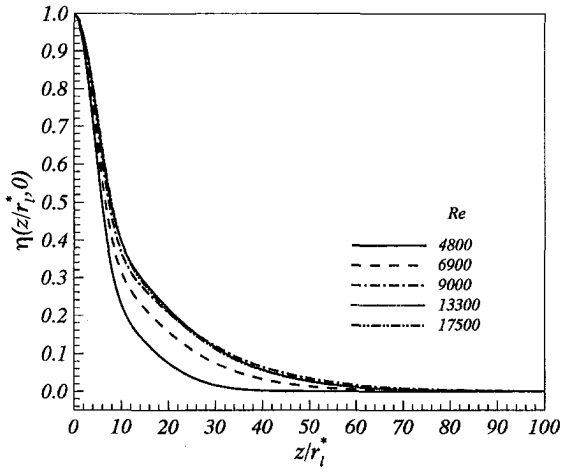

Fig. 7 Empirical curves for the normalized turbulence intensity distribution along the centerline of the jet

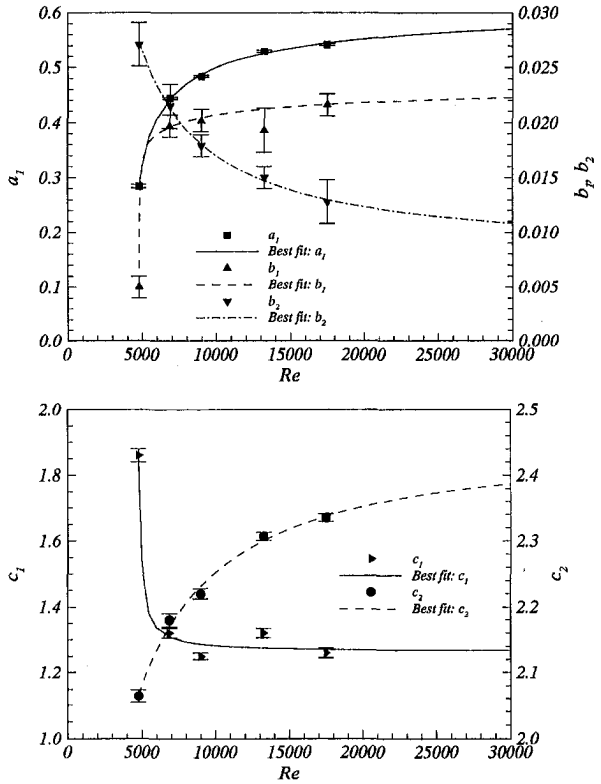

Fig. 8 Empirical fit parameters of Eq. (8) and their variation with Reynolds number

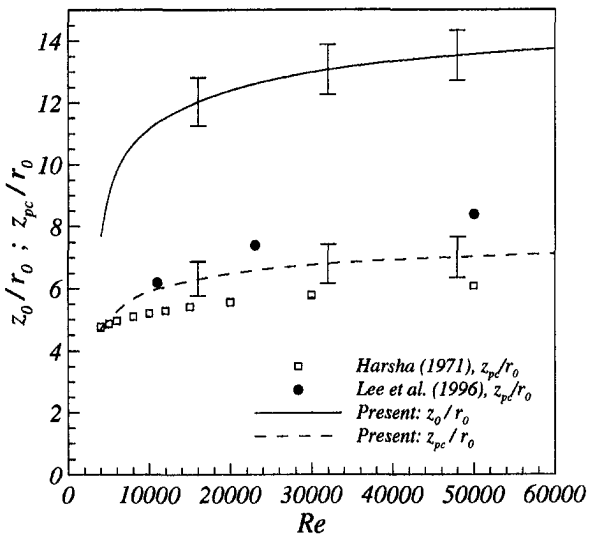

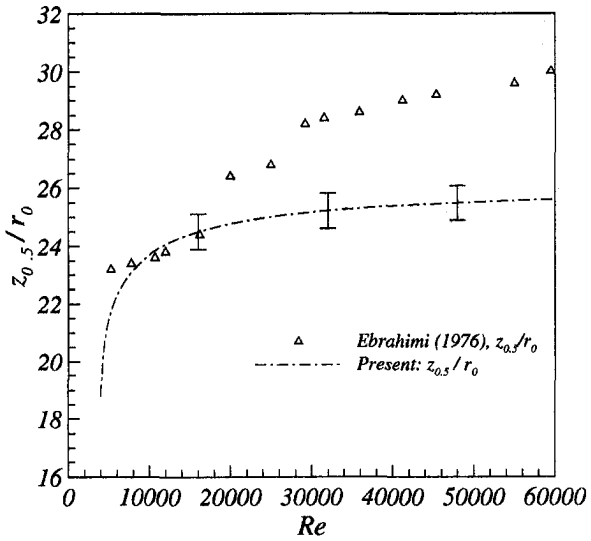

Fig. 9 Virtual origins, z_o, calculated using the generic velocity curve are shown as a function of Reynolds number in the upper panel. Calculated distances to the end of the potential core, z_{pc}, (upper panel) and the distance required for the centerline velocity to drop to half of its initial value, $z_{0.5}$, (lower panel) are also included and compared with appropriate literature measurements.

the necessary calculation for the virtual origin yields the absolute value of the origin, z_o/r_o, for each Reynolds number investigated in the present work, as seen in Fig. 9. Included in the figure are potential core measurements, z_{pc}/r_o, reported by Lee et al. (1996) and Harsha (1971), as well as the length to $\bar{U}(z, 0)/\bar{U}(0, 0) = 0.5$, $z_{0.5}/r_o$, reported by Ebrahimi (1976). These lengths are compared to similar lengths extracted from the generic curve. The agreement is good. It should be noted that the numbers reported by Harsha (1971) and Ebrahimi (1976) are for jets whose initial conditions are unclear and most likely (from their discussion) do not correspond to the type of jets reported here. Even so, the trend of the present data compares well, supporting the conclusions of the present investigation that the mean centerline velocity decay distribution for initially turbulent axisymmetric jets may be dynamically scaled to attain Reynolds number independence using r_j^*.

4 Conclusions

Centerline velocity data were presented for a constant density axisymmetric jet having a nonuniform initial velocity distribution that was fully turbulent. The several Reynolds numbers investigated showed distinctly the effect of Re on the development of the jet, specifically the downstream shift of the virtual origin with increasing Re. This shift of the centerline velocity decay curves was attributed to the initial turbulence intensity distribution, which may be thought of as a natural source of random excitation that disrupts vortex formation and pairing processes responsible for elevated momentum mixing under initial laminar conditions, and hence directly governs the changes in the growth of turbulence within the shear layer of the jet (Papadopoulos and Pitts, 1998). The relative magnitude of the initial turbulence intensity may be used to scale the changes in the growth of the shear layer and by forming an appropriate length scale render Re independence to the center-

line velocity decay distribution when the axial distance is normalized by this length scale. This was achieved in the near field by introducing a new length scale, r_o^*, that incorporated the initial mass, momentum and turbulence intensity distributions.

The effectiveness of r_o^* was, however, limited to the near field of the jet where the influence of initial conditions is greatest. As the jet develops, the effects of initial conditions rapidly diminish. In the self-similar region of the jet development becomes independent of initial conditions, and only the initial mass and momentum fluxes are important. Hence, to extend the near field scaling over the entire jet development region, this diminishing effect of initial conditions (turbulence intensity) was incorporated into the previously proposed near field length scale by using the local normalized centerline turbulence intensity field. The result was a dynamic length scale that effectively captured the virtual origin shift and collapsed the centerline mean velocity distribution curves for initially turbulent axisymmetric jets. From the generic curve a single value for the virtual origin location was obtained, this being $z_o/r_o^* = 6 \pm 1$.

The introduction of a local scale to capture the Reynolds number effect is similar to the approach of Sautet and Stepowski (1995 and 1996) who proposed replacing the ambient density with a local average density to better capture the effects of variable density on the near field decay of mass fraction in variable density jets. Although the present scaling has been shown to work for the velocity distribution of constant density jets, it should be feasible to extend it to the velocity and scalar distributions of variable density jets. Furthermore, by utilizing the idea of a local average density it may be possible to represent the mean dynamic and scalar centerline distributions of constant and variable density initially turbulent jets by a single generic curve. These last two points are presently being investigated.

References

Boguslawsk, L., and Popiel, Cz. O., 1979, "Flow Structure of the Free Round Turbulent Jet in the Initial Region," *Journal of Fluid Mechanics,* Vol. 90, pp. 531–539.

Chen, C. J., and Rodi, W., 1980, *Vertical Turbulent Buoyant Jets—A Review of Experimental Data,* Pergamon Press, New York.

Dahm, W. A., and Dimotakis, P. E., 1987, "Measurements of Entrainment and Mixing in Turbulent Jets," *AIAA Journal,* Vol. 25, pp. 1216–1223.

Dahm, W. A., and Dimotakis, P. E., 1990, "Mixing at Large Schmidt Number in the Self-Similar Far Field of Turbulent Jets," *Journal of Fluid Mechanics,* Vol. 217, pp. 299–330.

Dowling, D. R., and Dimotakis, P. E., 1990, "Similarity of the Concentration Field of Gas-Phase Turbulent Jets," *Journal of Fluid Mechanics,* Vol. 218, pp. 109–141.

Ebrahimi, I., 1976, "Axialer Verlauf der Geschwindigkeit in Luft-Freistrahlen," Forschung Ing.-Wes., Vol. 42, pp. 33–35.

Eggels, J. G. M., Westerweel, J., and Nieuwstadt, F. T. M., 1993, "Direct Numerical Simulation of Turbulent Pipe Flow," *Applied Science Research,* Vol. 51, pp. 319–324.

Ferdman, E., 1997, "An Experimental Investigation of the Initially Asymmetric Turbulent Jets," M.S. thesis, Polytechnic University, New York.

Gladnick, P. G., Enotiadis, A. C., LaRue, J. C., and Samuelsen, G. S., 1990, "Near-Field Characteristics of a Turbulent Coflowing Jet," *AIAA Journal,* Vol. 28, pp. 1405–1414.

Gouldin, F. C., Schefer, R. W., Johnson, S. C., and Kollmann, W., 1986, "Nonreacting Turbulent Mixing Flows," *Progress in Energy Combustion Science,* Vol. 12, pp. 257–303.

Harsha, P. T., 1971, "Free Turbulent Mixing: A Critical Evaluation of Theory and Experiment," *Arnold Engineering Development Center Report,* AED-TR-71-36.

Lee, D. H., Chung, Y. S., and Kim, D. S., 1996, "Surface Curvature Effects on Flow and Heat Transfer from a Round Impinging Jet," *31st ASME National Heat Transfer Conference,* HTD-Vol. 324, pp. 73–83.

Lekakis, I., Durst F., and Sender J., 1994, "LDA Measurements in the Near Wall Region of an Axisymmetric Sudden Expansion," *7th International Symposium on Applications of Laser Tecniques to Fluid Mechanics,* Lisbon, Portugal.

Papadopoulos, G., and Pitts, W. M., 1998, "Scaling the Near-Field Centerline Mixing Behavior of Axisymmetric Turbulent Jets," *AIAA Journal,* Vol. 36, pp. 1635–1642.

Pitts, W. M., 1991a, "Effects of Global Density Ratio on the Centerline Mixing Behavior of Axisymmetric Turbulent Jets," *Experiments in Fluids,* Vol. 11, pp. 125–134.

Pitts, W. M., 1991b, "Reynolds Number Effects on the Mixing Behavior of Axisymmetric Turbulent Jets," *Experiments in Fluids,* Vol. 11, pp. 135–144.

Richards, C. D., and Pitts, W. M., 1993, "Global Density Effects on the Self-Preservation Behaviour of Turbulent Free Jets," *Journal of Fluid Mechanics,* Vol. 254, pp. 417–435.

Sautet, J. C., and Stepowski, D., 1995, "Dynamic Behavior of Variable-Density, Turbulent jets in their Near Development Fields," *Physics of Fluids,* Vol. 7, pp. 2796–2806.

Schlichting, H., 1979, *Boundary-Layer Theory,* 7th Edition, McGraw-Hill, New York, pp. 596–600.

Stepowski, D., and Sautet, J. C., 1996, "Axial Decay of Unmixedness in Round Turbulent Jets with Variable Density," *IUTAM Symposium on Variable Density Low Speed Turbulent Flows,* July 8–10, Marseille, France.

Thring, M. W., and Newby, M. P., 1953, "Combustion Length of Enclosed Turbulent Jet Flames," *Fourth (Intl) Symposium on Combustion,* The Williams & Wilkins Co., pp. 789–796.

Vradis, G. C., Ötügen, M. V., Kim, S. W., and Kim, D. B., 1993, "Round Incompressible Jets with Asymmetric Initial Velocity Distributions," *AIAA Journal,* Vol. 31, pp. 814–815.

Wu, P.-K., Tseng, L.-K., and Faeth, G. M., 1992, "Primary Breakup in Gas/Liquid Mixing Layers for Turbulent Liquids," *Atomization and Sprays,* Vol. 2, pp. 295–317.

Wu, P.-K., and Faeth, G. M., 1993, "Aerodynamic Effects on Primary Breakup of Turbulent Liquids," *Atomization and Sprays,* Vol. 3, pp. 265–289.

Wu, P.-K., Miranda, R. F., and Faeth, G. M., 1995, "Effects of Initial Flow Conditions on Primary Breakup of Nonturbulent and Turbulent Round Liquid Jets," *Atomization and Sprays,* Vol. 5, pp. 175–196.

Yeh, T. T., and Mattingly, G. E., 1994, "Pipeflow Downstream of a Reducer and its Effects on Flowmeters," *Flow Measurement Instrumentation,* Vol. 5, pp. 181–187.

Mehdi N. Naraghi
Research Assistant Professor,
Department of Mechanical Engineering,
Polytechnic University,
Six Metrotech Center,
Brooklyn, NY 11201

M. Karim Moallemi
President,
Benex of NY,
NY, NY 11101

M. H. N. Naraghi
Professor,
Department of Mechanical Engineering,
Manhattan College,
Riverdale, NY 10471

Sunil Kumar
Associate Professor,
Department of Mechanical Engineering,
Polytechnic University,
Six Metrotech Center,
Brooklyn, NY 11201

Experimental Modeling of Circular Hydraulic Jump by the Impingement of a Water Column on a Horizontal Disk

An experimental study is performed to investigate the relationship between an unsubmerged water jet impinging onto a horizontal surface and radius of hydraulic jump. Experiments are undertaken over a wide range of pipe Reynolds numbers for which the pipe flow is laminar. The laminar impinging jet produced a smooth circular hydraulic jump, at which the film thickness experienced a sudden increase in thickness. Effects of various parameters on a stable and stationary hydraulic jump are studied. The impingement point radius r_i is taken as a characteristic length of the film flow, and correlations are obtained for radius of hydraulic jump in terms of various dimensionless parameters.

1 Introduction

In the study of liquid jets impinging onto horizontal surfaces, most investigators focused their attention on high Reynolds number jets due to many applications such as, ice removal (Lipsett and Gilpin, 1978) and jet cooling (Vader et al., 1992). In a number of other processes, such as impingement of molten stream on a spinning disk (Chen et al., 1992), or coating of layers on moving sheets or tubes (Kuiken, 1987), ice making refrigerators (ASHRAE—*Refrigeration Handbook,* 1990), and jet impingement solidification (Moallemi and Naraghi, 1994), surface tension and gravity forces become a significant factor on the characterization of the impingement liquid column and the flow of liquid film over the disk surface. Previous fluid flow studies of liquid jet impingement onto a horizontal disk have been performed over the range of parameters that are not relevant to the above applications (i.e., high pipe/jet Reynolds number). Moreover, the previous investigations have been mainly focused on the phenomena occurring inside of the hydraulic jump region.

When a column of liquid is impinged vertically onto a horizontal disk, it spreads out in a thin liquid film and passes through a hydraulic jump that imposes an abrupt increase in the film thickness. Outside of the hydraulic jump, liquid film thickness is greater than that of inside of the hydraulic jump. The radial flow of the liquid film over the disk is influenced by the tube flow and falling liquid column. Reynolds number and length to diameter ratio of the tube are two parameters which determine the flow regime and the development of the velocity profile. When a column of liquid is discharged from a tube, the radius of the liquid column is reduced due to gravity acceleration and surface tension forces. Tapering effect of liquid column is more pronounced at the exit of the tube. Cullen and Davidson (1957) included a surface tension term into the Bernoulli equation in order to account for capillary forces. A number of researchers have conducted experimental and analytical investigations to evaluate the shape of liquid jet. Among them, Duda and Vrentas (1967) used "Protean" type coordinate system, for which one of the coordinate surface is a stream surface. They used a boundary-layer solution to predict the velocity distribution and the shape of the jet after taking into account the gravitational and surface forces. Lienhard (1968) also developed an approximate boundary layer type solution to predict the velocity profiles and radius of free jets under the influence of both gravity and surface tension. Experimental results of Lienhard (1968) also confirmed the approximate solution of jet radius $r(z)$ when $We_d > 100$. Gonzalez-Mendizabal et al. (1986) conducted experiments on laminar jets of Newtonian liquids issued from long tubes for Reynolds numbers ranging from 300 to 1000. In their experiments jet radii were measured with a photographical method and velocity distribution by laser-doppler anemometry. A Bernoulli based model provided close agreement with measured radius of liquid column by Gonzalez-Mendizabal et al. (1986).

Watson (1964) investigated flow behavior inside of the hydraulic jump in which a liquid jet is impinged onto a horizontal surface. In his work, the characteristic length for the Reynolds number was radius of jet at the impingement point. The spread of liquid film over the surface was divided into several regions. Similarity and approximate solutions were developed for these flow regimes. Watson's solutions were developed based on the assumption that surface tension influence is minimum, Reynolds number is high, and the hydraulic jump width is negligible. An expression was developed for the position of hydraulic jump based on the impingement point Reynolds number $Re_i = Q/r_i\nu$, and liquid film thickness outside of the hydraulic jump. After the pioneering work of Watson (1964), a few other analytical studies of jet impingement on a flat surface were reported. Bouhadef (1978) considered thin film flow both upstream and downstream of the hydraulic jump, and used an approximate integral method, including the effect of gravitational force, to evaluate film thickness variation along the disk. He developed a differential equation to estimate liquid film thickness variations along the plate based on a parabolic velocity profile. In his formulation the hydraulic jump occurred at a

Contributed by the Fluids Engineering Division for publication in the JOURNAL OF FLUIDS ENGINEERING. Manuscript received by the Fluids Engineering Division May 31, 1996; revised manuscript received October 5, 1998. Associate Technical Editor: M. S. Triantafyllou.

critical film Froude number $Fr_c = u^2/g\delta$, where $d\delta/dr$ approaches to infinity. Thomas et al. (1990) used a numerical approach to study one-dimensional characteristics of thin liquid film flow including the hydraulic jump and rotation. They modeled the flow based on the film Froude number from supercritical ($Fr_\delta > Fr_c$) to subcritical ($Fr_\delta < Fr_c$) regimes.

Many researchers performed experiments on the liquid jet impingement problem. Among them, Ishigai et al. (1977) characterized changes in hydraulic jump radius based on the incoming film Froude number with a weir at the edge of a disk. They used a short pipe with length to diameter ratio of 3 to provide a uniform velocity profile at a 30 degree nozzle angle, and reported that vena-contracta occurred (i.e., air was sucked into the pipe). They also compared film thickness for length to diameter ratios of 50 and 3 and reported an increase in the film thickness for a length to diameter ratio of 50. Nakoryakov et al. (1977) used an electrodiffusion method to measure wall shear stresses, flow reversal and recirculation in the vicinity of hydraulic jump. Their results show that the wall shear stress becomes negative at the hydraulic jump region. Azuma and Hoshino (1984a, 1984b, 1984c, 1984d) investigated velocity distribution, film thickness, boundary layer transition, and instability of the film. They used a nozzle that was impinging vertically from either the top or bottom of the plate. Their definition of Reynolds number is based on an equivalent length $\sqrt{CDH}$, $Re = Q/\sqrt{CDH}\nu$, where D is the nozzle diameter, H is the opening distance, and ν is the kinematic viscosity. Discharge coefficient C is evaluated for different nozzle diameter and nozzle spacing.

Craik et al. (1981) conducted experimental work with a low jet Reynolds number, and measured liquid thickness before and after the hydraulic jump via a light absorption technique. They also increased the liquid thickness after the hydraulic jump by using a weir. They demonstrated that as the outer depth of the liquid increases with time, the hydraulic jump radius decreases, and eventually the hydraulic jump become unstable. For a large weir height, the jump radius r_h continues to decrease with violent oscillation, and eventually, closes the jet at the impingement region. They used an absorbent paper to facilitate radial flow of liquid film. Stevens and Webb (1991) conducted measurements of hydraulic jump radius for various high Reynolds numbers and pipe diameters. They have shown that for a fixed Reynolds number, r_h/d decreases as the nozzle becomes larger. Stevens and Webb (1992) have also used laser doppler velocimetry technique to measure free surface velocity, but were not able to scale the data except for a small range of Reynolds numbers. Liu and Lienhard (1993) performed experiments using an orifice for delivering liquid jet when the orifice Reynolds numbers are greater than 4×10^4. They used obstruction (weir) downstream of flow, and observed unsteady hydraulic jump with single or double roller. They explained that the dimensionless jet radius is a function of jet Reynolds number, jet Froude number, jet Weber number, and the dimensionless depth and radius of downstream depth of liquid film.

The intent of this research is to study effects of various jet parameters on the hydraulic jump radius. This is done by both experimental and analytical methods. The experimental efforts focus is on the falling liquid column and its radial spreading after impinging on the disk. The predictions of the analytical models are also presented along with the experimental results. Most of the previous studies of liquid jet impingement were conducted on high inertia liquid jets where surface tension and gravitational influences on liquid column were negligible. This study investigates hydraulic jump location based on variations of three independent parameters, volume flow rate Q, tube diameter d, and plate to tube spacing H. Effects of tube Reynolds number Re_d, tube Froude number Fr_d, tube Weber number We_d, and dimensionless tube to disk spacing H/d are elaborated on hydraulic jump radii. Influence of downstream of hydraulic jump is minimized by using a cotton gauze around the edge of the disk, see also Craick et al. (1997). All tests are performed on three different tube diameters with pipe Reynolds numbers less than 2200, and the dimensionless tube to plate spacing H/d as low as 0.25. Surface tension and gravitational effects on the hydraulic jump radius are included in the present model. Radii of the liquid column at different locations as well as the impingement point are evaluated.

2 Experimental Investigation

The experiments are carried out using a closed-loop water jet system. Deionized water is pumped from a cylindrical reservoir of 2.7 liters volume. The reservoir is connected via a rotameter flowmeter to a long copper tube (12 mm ID, and 12 cm long) to which different sizes of glass tubes can be connected. These glass tubes have length to diameter ratio of 60 to 160 to

Nomenclature

a = radius of tube, m
Bo = Bond number = $We_d/Fr_d = \rho g d^2/\sigma$
c_1 = constant in Eq. (10)
c_2 = constant in Eq. (10)
C = discharge coefficient
d = tube diameter, m
D = nozzle diameter, m
Fr_d = tube Froude number = $\bar{u}^2/gd$
Fr_δ = local film Froude number = $\bar{u}^2/g\delta$
g = gravitational acceleration, m/s^2
H = pipe to plate spacing, m
p = pressure, Pa
Q = volume flow rate, m^3/s
r = radial coordinate/radius of jet, m
r_h = radial position of hydraulic jump, m
r_i = radius of column at the impingement point, m
R = dimensionless radial position = r/r_i
Re_i = impingement point Reynolds number = $Q/\nu r_i$
Re_d = pipe Reynolds number = $4Q/\pi d\nu$
Re_δ = local film Reynolds number = $\bar{u}\delta/\nu$
t = time, s
u_r, u_z = velocity components, m/s
$\bar{u}$ = mean radial velocity or mean column velocity, m/s
$\bar{u}_e$ = mean radial velocity at pipe exit = $Q/\pi a^2$, m/s
We_d = tube Weber number = $\rho d\bar{u}^2/\sigma$
We_δ = local liquid film Weber number = $\rho\delta\bar{u}^2/\sigma$
z = coordinate normal to the surface, m
δ = thickness of liquid film, m
Δ = dimensionless thickness of liquid film = δ/r_i
ζ = dimensionless parameter in Eq. (13) = $z/(d\ Re_d)$
δ_o = thickness of liquid film behind of the hydraulic jump, m
η = dimensionless coordinate for liquid film = z/δ
ν = kinematic viscosity, m^2/s
ρ = density, kg/m^3
σ = surface tension, N/m

Subscripts

c = critical
d = down
e = pipe exit
h = hydraulic jump
i = impingement point
j = jet
l = liquid film
s = surface
o = outer
out = disk edge
u = up

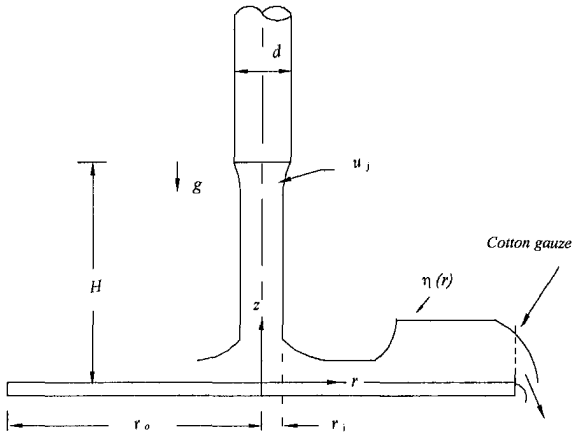

Fig. 1 Schematic of the physical problem and coordinates (disk diameter, 30.5 cm)

ensure a fully developed laminar flow at the exit (tube Reynolds number less than 2200). Turbulent and undeveloped exit flow conditions are not examined. Tube diameters used are 3.95 mm, 4.85 mm, and 7.75 mm. The jet is impinging to the center of a 30.5 cm copper disk. A ribbon of cotton gauze is wrapped flush around the disk to reduce surface tension on the edge of the disk and facilitate radial spread of the liquid film with a smooth and stable hydraulic jump.

All reported uncertainties represent the observation in a single-sample experiment. In the graphical presentations of the raw and processed data, the uncertainties are shown with error bars, unless they are smaller than the symbol. The jet flow rate is measured using a rotameter that is calibrated with an accuracy of ±7 percent. The diameter of the jet at the impingement point, the liquid film profile over the surface is measured using a needle that is attached to an *x-y* traversing system fixed to the enclosure cubical box which has a resolution and repeatability of 0.01 mm in either direction. The needle is connected to an ohm-meter that indicates any contact of the needle with water, and the disk surface. All experiments are conducted at room temperature, and steady-state conditions. These tests are carried out with variation of tube to plate spacing, flow rate, and diameter of tube. Jet radius at the impingement point and hydraulic jump diameter are measured with the traversing system or recorded with camera.

3 Analysis

A schematic drawing of the physical problem considered is shown in Fig. 1. A liquid jet issues downward from a vertical pipe that is positioned at a fixed distance H from a horizontal disk. To simplify the modeling of flow of the liquid film over the disk, the following assumptions are made: the liquid is incompressible and Newtonian, flow is laminar and two-dimensional, viscous dissipation is negligible, the film flow is steady, the boundary layer assumptions are taken to be valid, and surface tension effects are negligible. After applying these assumptions, the governing equations of the problem, the conservation equations for mass, and momentum take the following forms:

$$\frac{\partial u_z}{\partial z} + \frac{1}{r}\frac{\partial (r u_r)}{\partial r} = 0 \tag{1}$$

$$u_r \frac{\partial u_r}{\partial r} + u_z \frac{\partial u_r}{\partial z} = \frac{-1}{\rho}\frac{\partial p}{\partial r} + \nu \frac{\partial^2 u_r}{\partial z^2} \tag{2}$$

$$\frac{\partial p}{\partial z} + \rho g = 0, \tag{3}$$

where $\delta(r)$ is the local thicknesses of the liquid film, $0 \le z \le \delta(r)$. Equations (1)–(3) are used in two regions, inside of the jump $r_i \le r \le r_h$ and outside of the jump $r_h \le r \le r_o$, where r_h is the hydraulic jump radius, and r_o the disk radius. The boundary conditions at the surface of disk is:

$$u_r = u_z = 0, \tag{4}$$

and at the free surface, $z = \delta(r)$, is:

$$\frac{\partial u_r}{\partial z} = 0, \quad p = p_a. \tag{5}$$

Note that the effect of surface tension is neglected. Equation (2) is integrated to yield the following equation

$$\frac{1}{r}\frac{d}{dr}\left[\int_0^\delta r u_r^2 dz\right] = -g\delta\frac{d\delta}{dr} - \nu\left.\frac{\partial u_r}{\partial z}\right|_{z=0}. \tag{6}$$

The velocity profile in Eq. (6) is approximated by polynomials in terms of $\eta = z/\delta$. The consideration is given to the inside of the hydraulic jump where the velocity boundary conditions of Eqs. (4) and (5) are satisfied along with an additional velocity condition at the free surface, specifically,

$$\frac{\partial^2 u_r}{\partial z^2} = 0, \tag{7}$$

The boundary conditions are satisfied by a third order velocity profile,

$$\frac{u_r}{\bar{u}} = 4\eta\left(1 - \eta + \frac{\eta^2}{3}\right). \tag{8}$$

Equation (8) is used inside of the hydraulic jump $r_i \le r \le r_h$, and by substituting in Eq. (6) and integration will results in

$$c_1 \frac{1}{r}\frac{d}{dr}(r\delta\bar{u}^2) = -g\delta\frac{d\delta}{dr} - c_2\nu\frac{\bar{u}}{\delta}, \tag{9}$$

where $c_1 = 6/5$ and $c_2 = 3$ for the quadratic velocity profile, and $c_1 = 8/7$ and $c_2 = 4$ for the cubic velocity profile, and $\bar{u}$ is the mean radial velocity. By simplifying Eq. (9) results in

$$\left(\frac{1}{c_1}\frac{g\delta}{\bar{u}^2} - 1\right)\frac{d\delta}{dr} = \frac{\delta}{r} - \frac{c_1}{c_2}\frac{\nu}{\bar{u}\delta}. \tag{10}$$

The radial variation of the liquid film thickness δ is evaluated by numerical integration of Eq. (10).

In order to integrate Eq. (10) the liquid film thickness δ_i at the impingement point should be known, δ_i is obtained by solving liquid column continuity and Bernoulli equations, with the assumptions that there is no interaction between liquid column and surface of the disk at the impingement region. Liquid column continuity and Bernoulli equations have the following form:

$$\bar{u}r^2 = \bar{u}_e a^2 \tag{11}$$

$$\frac{\bar{u}^2}{2} + \frac{\sigma}{pr} - zg = \frac{\bar{u}_e^2}{2} + \frac{\sigma}{\rho a} \tag{12}$$

where $\bar{u}_e$ is the average velocity of liquid at tube exit, and a is tube radius. Combining Eqs. (11) and (12) results in a dimensionless equation to predict radius of liquid column variations along its fall and is given by

$$\left(\frac{a^4}{r^4} - 1\right) + \frac{4}{\mathrm{We}_d}\left(\frac{a}{r} - 1\right) = \frac{z}{a}\frac{1}{\mathrm{Fr}_d} = \mathrm{Re}_d/\mathrm{Fr}_d\zeta, \tag{13}$$

where ζ is the dimensionless parameter defined by $\zeta = z/(a$

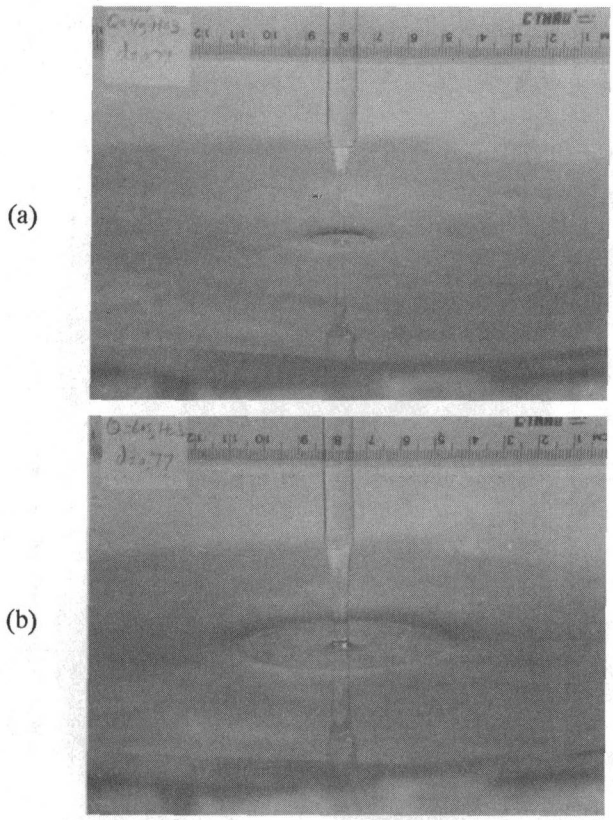

Fig. 2 Photographs of hydraulic jump for d = 7.75 mm, H/d = 3.8 and (a) Re_d = 390 and (b) Re_d = 2150

Re_d), Duda and Vrentas (1967). At the impingement point $r = r_i$ the film thickness δ_i is obtained by solving the Bernoulli equation for the inviscid falling column by Eq. (13), constrained by the conservation of mass, and inviscid flow at impingement region, i.e., at $r = r_i$ and $\delta = \delta_i$:

$$\bar{u}_i|_u = \bar{u}_i|_d = \bar{u}_i, \quad \text{and} \quad Q = \pi r_i^2 \bar{u}_i = 2\pi r_i \delta_i \bar{u}_i. \quad (14)$$

Equation (10) indicates the existence of a singularity ($d\delta/dr \to \infty$) at a radial position at which

$$\delta = \frac{c_1 \bar{u}^2}{g} \quad \text{or} \quad \mathrm{Fr}_c = \frac{\bar{u}^2}{g\delta} = \frac{1}{c_1}, \quad (15)$$

where Fr_c is the critical Froude number. This singularity occurs at the hydraulic jump radius. Numerical integration of Eq. (10) is carried on up to the radial position where the critical Froude number (Fr_c = 0.875 for the cubic profile, and Fr_c = 0.833 for quadratic profile) is reached. A comparison between the predictions of the hydraulic jump positions using the two velocity profiles and the experimental results was performed by Naraghi (1994). The third order velocity profile is employed for inside of the hydraulic jump. Then, the dimensionless forms of Eq. (10) takes the following form

$$\left(\frac{7}{8\,\mathrm{Fr}_\delta} - 1\right)\frac{d\Delta}{dR} = \frac{\Delta}{R} - \frac{3.5}{\mathrm{Re}_\delta} \quad r_i < r < r_h \quad (16)$$

where $\mathrm{Fr}_\delta = \bar{u}^2/g\delta$, $\mathrm{Re}_\delta = \bar{u}\delta/\nu$, $\Delta = \delta/r_i$, and $R = r/r_i$.

4 Results

When a vertical column of liquid strikes a horizontal disk, it spreads out in a thin fast-moving liquid film before experiencing a rather rapid increase in film thickness and reduction of mean speed at certain radial distance. Illustrative examples of this phenomenon are shown in Figs. (2a) and (2b) for H/d = 3.8, and Re_d = 390 and 2150, respectively.

The hydraulic jump divides the flow into two regions, namely, before and after hydraulic jump regions. The hydraulic jump characteristics (i.e., radial position, width and shape, stability, and motion) as well as the flow behavior in two regions are functions of the three independent parameters flow rate Q, jet or tube diameter d, and tube to plate spacing H. They are also influenced by external conditions including outer region boundary condition, gas flow condition above the liquid film, and the exit/discharge conditions of the jet/pipe (Stevens and Webb, 1991). Tube Reynolds number Re_d, tube Froude number Fr_d, tube Weber number We_d, and dimensionless tube to disk spacing H/d are dimensionless parameters which influence hydraulic jump radius. In this study, influences of only a few of these parameters and conditions are examined, and the rest are kept constant. Specifically, the effect of gas flow over the spreading liquid film is not considered and the jet is consistently discharged into the atmospheric air enclosed by the plexiglass cubical box. The effect of disk diameter on hydraulic jump radius was minimum for the considered cases. The same results for the hydraulic jump radius were obtained by using the disk diameters of 25 cm and 42 cm. By changing the disk size the outer depth of hydraulic jump still was shallow. As was mentioned earlier, no weir is used and a cotton gauze is wrapped around the disk to reduce the surface tension at the edge of the disk and to facilitate the liquid film spread. The jet discharges from flat-ended long pipes and pipe flow are kept laminar.

The flow parameters Q, d, and H are changed and dependent parameters such as jet impingement point radius, and hydraulic jump radius are measured. This work focuses on the identification of ranges of the parameters for which the falling column, the hydraulic jump, and the film flow in the inner and outer regions do not exhibit any sign of instability, unsteadiness and/or turbulence.

From the results presented by Naraghi (1994) and Gonzalez-Mendizabal et al. (1986) it may be concluded that for a large enough jet to disk spacing, the radius of the falling column (and impingement point radius) becomes independent of H/d, and thus, r_i is in fact a characteristic length of the spreading film flow. However, it may be argued that the effect of the presence of the disk on the variation of jet radius is not accounted for in the analytical and experimental results of variation of column radius. To address this issue, experiments were conducted in which, jet flow rate and its distance from the disk were altered to measure the impingement point radius. The experimental results are shown in Fig. 3. These results show that for a given Re_d there is an H/d beyond which the r_i/d does not change significantly, and cylindrical shape of liquid column is not al-

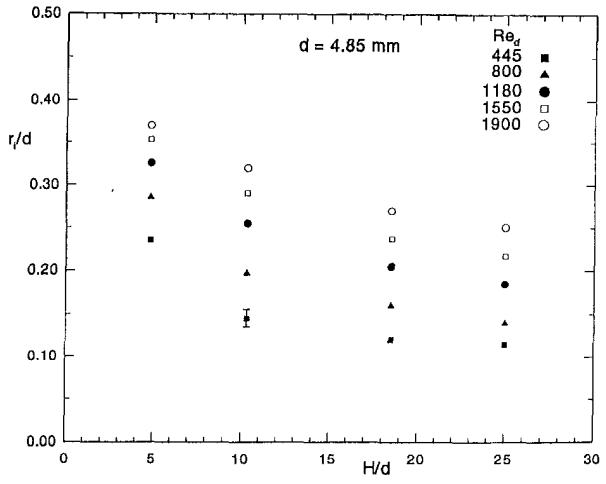

Fig. 3 Variation of jet radius at impingement point r_i with the jet to plate spacing for d = 4.85 mm

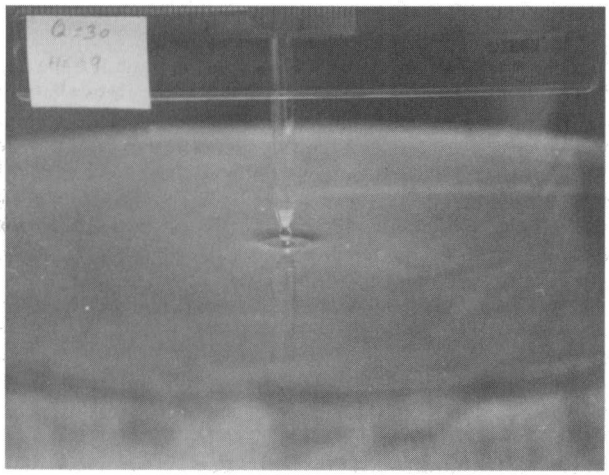

Fig. 4 Photograph of stationary node for d = 3.95 mm, and Re_d = 545 and H/d = 2.3

tered. Figure 3 also reveals that the impingement point radius for a given H/d and Re_d is equal to the jet radius. This finding implies that the effects of jet impingement on the surface are not transmitted upstream to influence the thinning of the jet column for $H/d < 10$. As pipe to plate spacing decreases, liquid column deforms and stationary nodes appear. Formation of stationary nodes on the liquid column, however, does not effect steady film spread over the disk, and the hydraulic jump remains stationary (Naraghi, 1994). An example of this phenomenon is shown in Fig. 4 for Re_d = 545, H/d = 2.3, and d = 3.95 mm.

Figure 5(a) presents the predictions of analytical model for d = 7.75 mm tube and H/d = 10. This figure shows the details of the variations of liquid film thicknesses from the point of impingement and up to the hydraulic jump position for different values of pipe Reynolds numbers. It also shows that the film thickness decreases from the impingement point up to a minimum value, followed by a gradual increase until the hydraulic jump radius is reached. The theoretical predictions of the radial variations of film thickness for d = 7.75 mm, Re_d = 1000 and five different H/d values are shown in Fig. 5(b). The figure shows that twenty times increase in H/d (from 5 to 100) will result in less than 50 percent change in the film thickness, and less than 10% change in the hydraulic jump position (the end point of each curve). Four independent dimensionless parameters control the liquid column radius, the film thickness variations along the surface of plate, and hydraulic jump radius. These parameters are: H/d, Re_d, We_d, and Fr_d. This dependence of liquid column radius on the above parameters can also be seen from Eq. (13). Figure 5(c) shows the effect of tube diameters for Re_d = 800 and H/d = 10 on the thickness of liquid film. Dimensionless liquid film thickness variation along the plate is higher for smaller tube diameters than those of larger tube diameters.

Finally, consideration is given to the hydraulic Jump radius measurements. The position of the hydraulic jump is measured for three different pipe diameters, and over a wide range of H/d and Re_d. The resulting dimensionless hydraulic jump radii are presented in Fig. 6 for d = 4.85 mm. The predictions of the analytical model, calculated by employing a third order velocity profile, are also shown in this figure. The figure indicates that the hydraulic jump radius increases with the pipe Reynolds number, as well as the pipe to plate spacing. The agreement between the measurements and predictions is improved as H/d and Re_d are increased. This is attributed to reduction in the surface tension effects (at the pipe discharge) and its interaction with the plate surface that is not accounted for in the model. Surface tension forces on pipe discharge and at impingement point even alter the cylindrical shape of liquid column in the form of stationary nodes for H/d's less than 6.

A close examination of Fig. 6 reveals a dependency of hydraulic jump radius on the Bond number, $Bo = We_d/Fr_d = \rho g d^2/\sigma$ (i.e., diameter of tube). Diameter dependency of hydraulic jump radius also was observed by Stevens and Webb (1992). Figure 7 presents the result where Bond number is used with r_h/d and H/d's 0.5, 2, and 25. By using the Bond number and H/d to

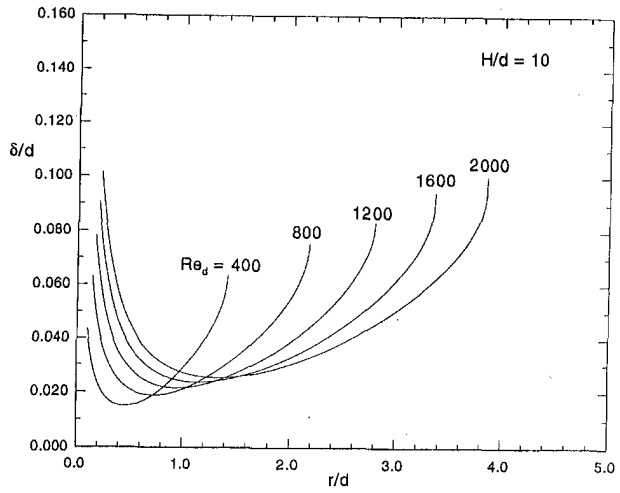

Fig. 5 Variation of dimensionless liquid film thickness over the disk for

Fig. 5(a) influence of Re_d at H/d = 10 and d = 7.75 mm, and

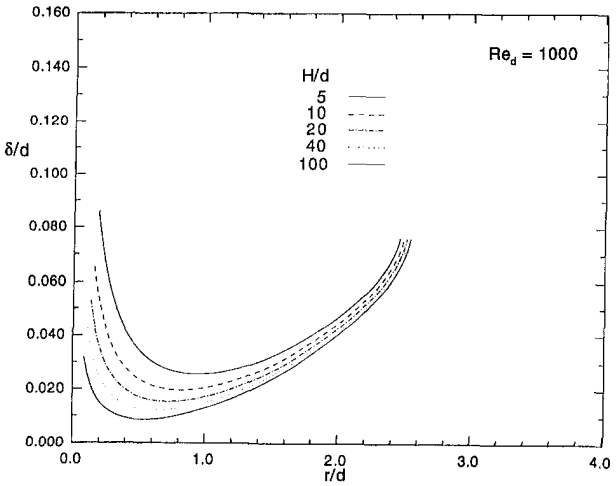

Fig. 5(b) influence of H/d at Re_d = 1000 and d = 7.75 mm, and

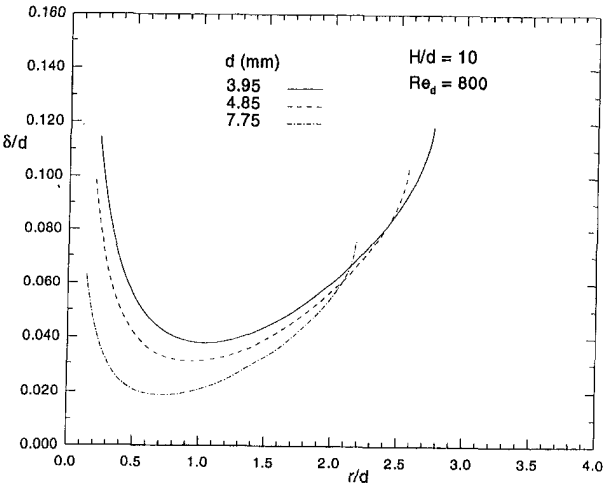

Fig. 5(c) influence of d at Re_d = 800 and H/d = 10.

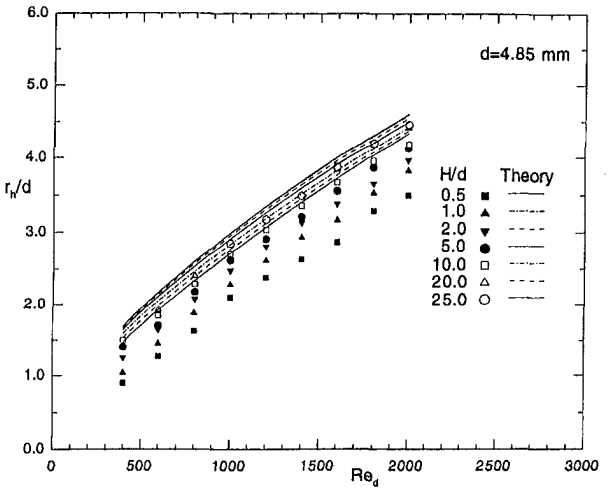

Fig. 6 Variation of hydraulic jump radius with the pipe Reynolds number for d = 4.85 mm

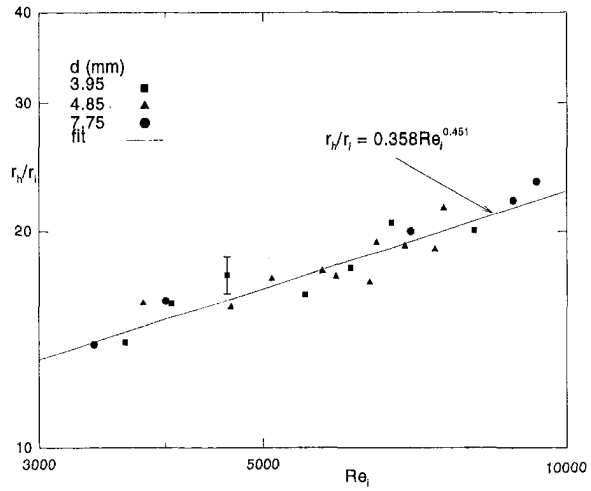

Fig. 8 Hydraulic jump radius variations in terms of jet Reynolds number at impingement point Re_i for three tube diameters

scale dimensionless hydraulic jump the data for all three tube diameters fall into one line. Considering these results a correlation is found for all of the measured data points which is as follows,

$$\frac{r_h}{d} = 0.00843\left(\frac{H}{d}\right)^{0.409} \mathrm{Re}_d^{c3}\ \mathrm{Bo}^{-0.11} \tag{18}$$

where is $c_3 = 0.8162(H/d)^{-0.075}$, and

$$400 \le \mathrm{Re}_d < 2200,$$

$$0.24 \le \mathrm{We}_d \le 12,$$

$$0.028 \le \mathrm{Fr}_d \le 5.5,$$

$$2.1 \le \mathrm{Bo} \le 8.1.$$

The hydraulic jump location is also correlated with impingement point Reynolds number for $H/d > 10$ in Fig. 8 using a least square curve fit to result:

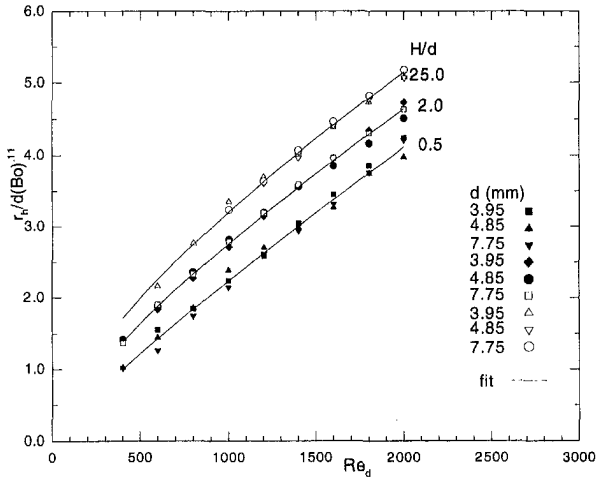

Fig. 7 Variation of dimensionless hydraulic jump radius by Bond number with pipe Reynolds number

$$\frac{r_h}{r_i} = 0.358\ \mathrm{Re}_i^{0.451} \tag{19}$$

5 Conclusions

Hydraulic jump radius variation through a circular jet is studied experimentally and analytically. The film flow of the liquid is generated by issuing a water jet from a vertical pipe, and impinging upon the disk. Experiments are performed over a range of pipe Reynolds number for which the pipe flow is laminar.

The laminar impinging jet produced a smooth circular hydraulic jump, at which the liquid film experiences a rapid increase in thickness. A parametric study of the hydraulic jump variation with the dimensionless parameters of the problem (i.e., Re_d, and H/d) is performed. Comparison between liquid column radius and impingement point radius r_i showed that radius of jet at impingement point will eventually reach almost a constant value for $H/d > 10$. This implies that the effects of jet impingement on the surface are not transmitted upstream to influence the liquid column. It is also found that surface tension forces at pipe discharge and at impingement point influence the hydraulic jump position for $H/d < 10$ and $\mathrm{Re}_d < 1000$, while for higher ranges of H/d a slight variation of hydraulic jump position with H/d is recorded. In the range where the effects of surface tension forces are minimum, radius of hydraulic jump is correlated with Re_i. An analytical model is developed to predict the position of hydraulic jump. The predictions of this model are in good agreement with the experimental results in the range of parameters for which interaction between liquid column and disk, and effect of surface tension forces is minimum. Interactions between falling liquid column with the horizontal disk in the form of stationary nodes are reported when $H/d < 6$.

References

ASHRAE *Refrigeration Systems and Applications Handbook,* 1990, Atlanta.

Azuma, T., and Hoshino, T., 1984a, "The Radial Flow of a Thin Liquid Film, Part 1: Laminar-Turbulent Transition," *Trans. Japan Soc. Mech. Engrs.,* Vol. 50, pp. 974–981.

Azuma, T., and Hoshino, T., 1984b, "The Radial Flow of a Thin Liquid Film, Part 2: Film Thickness," *Trans. Japan Soc. Mech. Engrs.,* Vol. 50, pp. 982–989.

Azuma, T., and Hoshino, T., 1984c, "The Radial Flow of a Thin Liquid Film, Part 2: Velocity Profile," *Trans. Japan Soc. Mech. Engrs.,* Vol. 50, pp. 1126–1133.

Azuma, T., and Hoshino, T., 1984d, "The Radial Flow of a Thin Liquid Film, Part 2: Stability of Liquid Film and Wall Pressure Fluctuation," *Trans. Japan Soc. Mech. Engrs.,* Vol. 50, pp. 1136–1143.

Bouhadef, M., 1978, "Etalment en Couche Mince d'un Jet Liquide Cylindrique Vertical sur un Plan Horizontal," *Z. Angew. Math. Phys.,* Vol. 29, pp. 157–167.

Chen, J-S. J., Praisner, T. J., Fields, L. A., Nornhold, R. T., and Frazier, W. E., 1992, "Rapid Solidification Processing of Titanium by Melt Spinning," *National Heat Transfer Conference Micro/Macro Scale Phenomena in Solidification,* HTD-Vol. 218, pp. 93–100.

Craik, A. D. D., Latham, R. C., Fawkes, M. J., and Gribbon, P. W. F., 1981, "The Circular Hydraulic Jump," *Journal of Fluid Mechanics,* Vol. 112, pp. 347–362.

Cullen, E. J., and Davidson, J. F., 1957, "Absorption of Gases in Liquid Jets," *Trans. Faraday Society,* Vol. 53, pp. 113–120.

Duda, J. L., and Vrentas, J. S., 1967, "Fluid Mechanics of Laminar Liquid Jets," *Chemical Engineering Science,* Vol. 22, pp. 855–869.

Gonzalez-Mendizbal, D., Oliverafuentes, F., and Guzman, J. M., 1987, "Hydrodynamics of Laminar Liquid Jets. Experimental Study and Comparison with Two Models," *Chem. Eng. Comm.,* Vol. 56, pp. 117–137.

Ishigai, S., Nakanishi, S., Mizuno, M., and Imamura, T., 1977, "Heat Transfer of the Impinging Round Water Jet in the Interference Zone of Film Flow Along the Wall," *Bulletin of the JSME,* Vol. 20, No. 139, pp. 85–92.

Kuiken, H. K., 1987, "Solidification of a Liquid on a Moving Sheet," *International Journal of Heat and Mass Transfer,* Vol. 20, pp. 19–314.

Lienhard, J. H., 1968, "Effects of Gravity and Surface Tension Upon Liquid Jets Leaving Poiseuille Tubes," ASME *Journal of Basic Engineering,* pp. 262–268.

Lipsett, A. W., and Gilpin, R. R., 1978, "Laminar Jet Impingement Heat Transfer Including The Effects of Melting," *International Journal of Heat and Mass Transfer,* Vol. 21, pp. 25–33.

Liu, X., and Lienhard, V. J. H., 1993, "The Hydraulic Jump in Circular Jet Impingement and in Other Thin Liquid Films," *Experiments in Fluids,* Vol. 15, pp. 108–116.

Merkosky, N. V., Huk, S., and Ryan, J. T., 1971, "Stationary Nodes on a Liquid Jet," *The Chemical Engineering Journal,* Vol. 2, pp. 133–134.

Moallemi, M. K., Naraghi, M. N., 1994, "Experimental and Analytical Investigation on Ice Formation from a Circular Water Jet Impinging on a Cold Surface," ASME *Journal of Heat Transfer,* Vol. 116, pp. 1016–1027.

Naraghi, M. N., 1994, "An Experimental and Analytical Investigation of Fluid Flow and Heat Transfer Interactions with Solidification of a Liquid Jet Impinging onto a Horizontal Surface," Doctoral thesis, Polytechnic University.

Nakoryakov, V. E., Pokusaev, B. G., and Troyan, E. N., 1978, "Impingement of an Axisymmetric Liquid Jet on a Barrier," *International Journal of Heat and Mass Transfer,* Vol. 21, pp. 1175–1184.

Press, W. H., Flannery, B. P., Teukolsky, S. A., and Vetterling, W. T., 1989, *Numerical Recipes,* Cambridge University Press, Cambridge, pp. 554.

Stevens, J., and Webb, B. W., 1991, "Local Heat Transfer Coefficients Under an Axisymmetric, Single-Phase Liquid Jet," ASME *Journal of Heat Transfer,* Vol. 113, pp. 71–78.

Stevens, J., and Webb, B. W., 1992, "Measurements of the Free Surface Flow Structure Under an Impinging Free Liquid Jet," ASME *Journal of Heat Transfer,* Vol. 114, pp. 79–84.

Thomas, S., Hankey, W., Faghri, A., and Swanson, T., "One-Dimensional Analysis of the Hydrodynamic and Thermal Characteristics of Thin Film Flows Including The Hydraulic Jump and Rotation," ASME *Journal of Heat Transfer,* Vol. 112, pp. 728–735.

Vader, D. T., Incropera, F. P., and Viskanta, R., 1992, "Convective Nucleate Boiling on a Heated Surface Cooled by an Impinging, Planar Jet of Water," ASME *Journal of Heat Transfer,* Vol. 114, pp. 152–160.

Watson, E. J., 1964, "The Radial Spread of a Liquid Jet Over a Horizontal Plane," *Journal of Fluid Mechanics,* Vol. 20, Part 3, pp. 481–499.

Transient Turbulent Gaseous Fuel Jets for Diesel Engines

Philip G. Hill
Professor Emeritus,
Department of Mechanical Engineering,
University of British Columbia,
Vancouver, Canada V6T 1Z4

Patric Ouellette
Chief Scientist,
Westport Research Inc.,
Vancouver, Canada V6T 1X2

Existing data on transient turbulent jet injection into large chambers demonstrates self-similar behavior under a wide range of conditions including compressibility, thermal and species diffusion, and nozzle under expansion. The jet penetration distance well downstream of the virtual origin is proportional to the square root of the time and the fourth root of the ratio of nozzle exit momentum flow rate to chamber density. The constant of proportionality has been evaluated by invoking the concept of Turner that the flow can be modeled as a steady jet headed by a spherical vortex. Using incompressible transient jet observations to determine the asymptotically constant ratio of maximum jet width to penetration distance, and the steady jet entrainment results of Ricou and Spalding, it is shown that the penetration constant is 3 ± 0.1. This value is shown to hold for compressible flows also, with substantial thermal and species diffusion, and even with transient jets from highly under-expanded nozzles. Observations of transient jet injection have been made in a chamber in which, as in diesel engine chambers with gaseous fuel injection, the jet is directed at a small angle to one wall of the chamber. In these tests, with under-expanded nozzles it was found that at high nozzle pressure ratios, depending on the jet injection angle, the jet penetration can be consistent with a penetration constant of 3. At low pressure ratios the presence of the wall noticeably retards the penetration of the jet.

Introduction

The injection of natural gas into the cylinder of a diesel engine is an important practical example of transient turbulent jet behavior. For the injected gas to penetrate the engine cylinder in 1–2 ms after the beginning of injection, high injection pressure is required. The injection duration is much larger than the valve opening time, and of the same order as the penetration time. Usually the nozzle flow is choked and under-expanded. A typical Reynolds number, for nozzle diameter of about 0.5 mm and sonic exit plane velocity, is 500,000 so that the jet is fully turbulent.

Three-dimensional numerical simulation that resolves both the far-field and the near-nozzle velocity profile associated with gas injection into an engine cylinder requires a mesh that can accommodate flow scales differing by a large factor. With, for example, 10 cells within a nozzle of 0.5 mm diameter and a cylinder diameter of 120 mm the factor is 2500. Without the use of a multi-grid method or a fast supercomputer such a mesh could require excessive computing times. There is therefore much practical interest in determining the extent to which the simplifying consideration of self-similarity can be applied even with a highly under-expanded transient jet. Though jet development far from the nozzle is strongly affected by the walls of a typical diesel chamber, self similarity in the near-nozzle region could be used to characterize equivalent starting conditions for a full numerical simulation.

The purposes of the work described in this paper were to determine the conditions under which transient turbulent jets are self-similar, to quantify the appropriate similarity parameter, and to test the assumption of self-similarity even with under expansion and with jet injection near a bounding wall. The underlying question is how much of the detail of the early jet history must be specified to obtain a good description of the downstream transient flow field. The work shows that scaling based on nozzle exit momentum flux and chamber density applies over a wide range of density gradient, compressibility and under expansion.

Much is known about the earliest stage of the impulsively started incompressible jet. Garside (1943) has captured in schlieren photos the beginning of an impulsively started round jet injected into a stationary fluid of the same density (see also Batchelor (1967) and List (1982). Before the jet has moved one diameter into the fluid a head vortex appears, followed initially by symmetrical wave-like disturbances in the transition toward turbulence. Rizk (1958) and Lahbabi et al. (1993) have provided informative flow visualizations of the subsequent transient turbulent jet behavior.

Turner (1959) proposed (for buoyant plumes) that the transient turbulent jet could be considered to be comprised of two simple parts—a quasi-steady-state jet region headed by a traveling vortex. Turner pictured the head vortex as being spherical, as having modest rotational momentum, and as subject to viscous and inertial retarding forces but not as entraining ambient fluid to any significant extent. The vortex ball is continuously supplied with mass and momentum by the jet which displays steady-state behavior within its region as long as the nozzle exit flow is steady. These ideas and associated force estimates have been used successfully in estimating the development of transient jets. Abramovich and Solan (1973) applied this concept to calculate the penetration rate of non-buoyant transient laminar jets and Witze (1980) extended the application to turbulent jets, both using momentum integral methods coupled with steady-state jet growth rate information. Ouellette and Hill (1992) applied the integral method to a turbulent conical jet sheet. However, if the self-similarity assumption is invoked directly, the penetration rate can be found without the need to account explicitly for the relevant forces.

In what follows the similarity parameter for unbounded transient jet injection is developed and tested with respect to incompressible transient jets entering large chambers. Then compressibility and under-expansion effects are considered by examining the relationship between steady and unsteady self-similarity of jets. Next a description is provided of new measurements of transient jet penetration close to a bounding wall. The self-similarity model is then tested with respect to high-speed under-expanded jet propagation near to, or far from, a bounding wall.

Contributed by the Fluids Engineering Division for publication in the JOURNAL OF FLUIDS ENGINEERING. Manuscript received by the Fluids Engineering Division December 26, 1996; revised manuscript received September 23, 1998. Associate Technical Editor: P. W. Bearman.

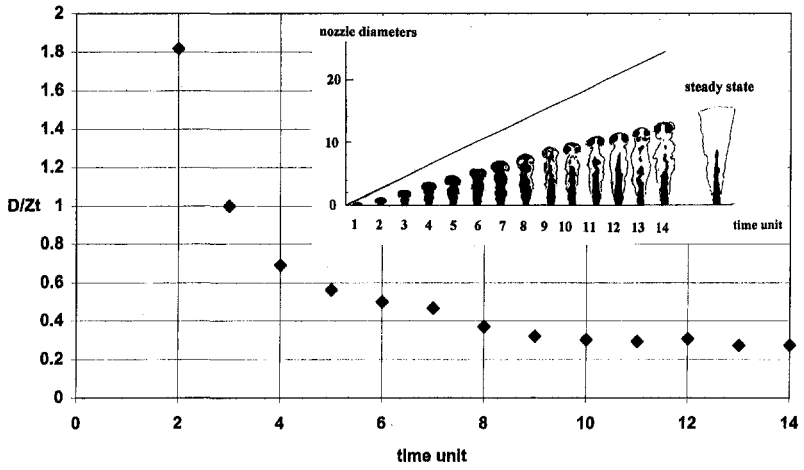

Fig. 1 Approach to self-preserving configuration of Rizk's transient jet; D is maximum width of jet at a given time; Z_t is the penetration (maximum axial length)

Self-Similarity of Transient Turbulent Jets

In this section, chamber wall effects are ignored and we first present the case of incompressible jet transients, for which flow visualizations are available in the literature. Then the reasons why the result can be extended to compressible under-expanded jets are discussed.

(i) Incompressible Transient Jets. The photographic records of Rizk (1958) (inset in Fig. 1) can be used to demonstrate the approach of transient turbulent jets toward self-similarity. Rizk impulsively injected dyed water into a large water chamber. Shown are the jet configurations at equal time intervals after injection. The sloping straight line on the graph indicates hypothetical jet penetration in the absence of inertial and viscous forces. Notable in each of the transient records is the appearance of the head vortex which, dark in its later stages, appears to have suffered little entrainment, and appears almost on the verge of pinching itself off from the preceding flow region. This upstream region meanwhile is close to assuming the character of the steady state jet. Figure 1 shows measurements taken from this photographic record of the maximum width D of the jet plume and its maximum axial length Z_t at each of the times shown. The transient jet apparently approaches a self-similar configuration with an asymptotic D/Z_t ratio of 0.25 ± 0.05. (The significance of the uncertainty estimate will be demonstrated below.) The transition length appears to be 10–15 nozzle diameters, much the same as the transition length for approach to self-similarity for steady-state jets data (as shown, for example, by the round free jet data of Wygnanski and Fiedler, 1969).

This apparent approach to self-similarity is consistent with the following statement of physical dependence:

$$Z_t = f(D, t, \dot{M}, \rho)$$

where t is time, ρ is density, and $\dot{M}$ is the total exit momentum flow rate.

Here for the transient jet in the far field only two length scales are taken to be significant—maximum jet width D and penetration length Z_t, but not nozzle diameter. In the language of Spalding, the jet may be considered to have "forgotten" its original configuration so that the total exit momentum flow rate $\dot{M}$ (assumed constant during the injection period) is considered to be the only significant characteristic of the nozzle flow; likewise the only significant characteristic of the chamber fluid (assumed to be nearly stationary) is its density ρ. This analysis leads, for constant width ratio D/Z_t, to the penetration number

$$\frac{Z_t}{(\dot{M}/\rho)^{1/4} t^{1/2}} = f\left(\frac{D}{Z_t}\right) \rightarrow \text{const}$$

The same kind of argument leads to puff jet penetration (see Appendix A) being proportional to $t^{1/4}$. The difference is that with the puff jet the reference quantity is a fixed amount of momentum M instantaneously discharged from the nozzle, in contrast to the assumed constant momentum discharge rate $\dot{M}$ of the transient jet.

To estimate the transient jet penetration constant from first principles one can invoke the model of Turner, pictured in Fig. 2, in which the transient jet flow is comprised of a steady-state jet region headed by a traveling spherical vortex. In applying the Turner model to the transient jet with uniform density ρ we can directly use the similarity width ratio D/Z_t obtained from the Rizk photographs as 0.25 ± 0.05 to obtain the relative proportions of the steady-state jet region and the spherical vortex. Further, we can use well-established knowledge to estimate the momentum instantaneously contained in the steady-state jet region.

Since, on the assumption of impulsive starting, the transient jet is continuously fed by momentum at a rate $\dot{M}$ during the injection period, the conservation of momentum in this case may be expressed as

$$\dot{M}t = \rho \frac{\pi}{6} D^3 U_m + M_{\text{jet}}$$

where the first term on the right is the approximate mean momentum of the vortex ball and M_{jet} is the instantaneous total

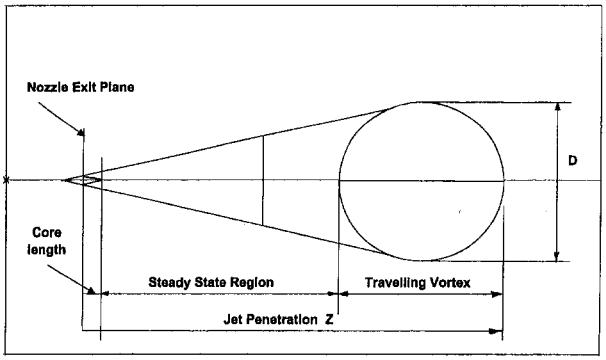

Fig. 2 Representation of transient turbulent jet by the vortex-quasi-steady-jet model of Turner

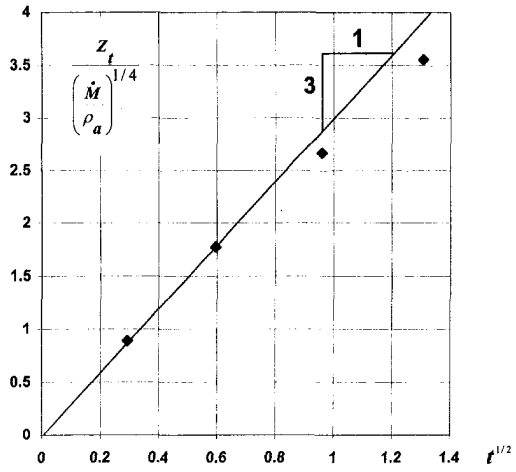

Fig. 3 Transient injection of water into water; data of Lahbabi (1993); time unit (s)$^{1/2}$ on both axes

momentum in the jet region. The mean velocity U_m of the vortex ball may be written

$$U_m = \frac{d}{dt}\left(Z_t - \frac{D}{2}\right)$$

in which Z_t has the definition shown in Fig. 2. Integrating the momentum instantaneously in the volume of the jet region, the local velocity being U, we have

$$\dot{M}t = \rho \frac{\pi}{6} D^3 \frac{d}{dt}\left(Z_t - \frac{D}{2}\right) + \int_0^{Z_t - D}\int_0^{\infty} 2\pi r dr \rho U dx$$

or

$$\dot{M}t = \rho \frac{\pi}{6}\left(\frac{D}{Z_t}\right)^3 Z_t^3 \frac{dZ_t}{dt}\left(1 - \frac{1}{2}\frac{D}{Z_t}\right) + \int_0^{Z_t - D} \dot{m} dx \quad (1)$$

in which r is the radial coordinate and x is the distance from the virtual origin of the jet. Now we utilize the self-similarity derived from the Rizk photographic record and thus assume that $s = D/Z_t$ is constant. We also use the accurate (directly measured) mass entrainment result of Ricou and Spalding (1962) that

$$\frac{\dot{m}}{\dot{m}_0} = K_s \frac{x}{d}, \quad \text{where} \quad K_s = 0.32 \quad (2)$$

where d is the diameter of the nozzle. The approximation of uniform nozzle exit velocity implies

$$\dot{m}_o = \sqrt{\frac{\pi d^2 \rho \dot{M}}{4}}. \quad (3)$$

As shown by the above dimensional analysis,

$$Z_t = \Gamma \left(\frac{\dot{M}}{\rho}\right)^{1/4} t^{1/2}, \quad (4)$$

in which Γ is a pure constant. Now substituting Eqs. (2), (3), and (4) into (1) and integrating, we obtain the following quadratic for Γ^2.

$$\Gamma^4 + \frac{6K_s(1-s)^2}{\sqrt{\pi}(2-s)s^3}\Gamma^2 - \frac{24}{\pi(2-s)s^3} = 0$$

from which the following results are obtained with $K_s = 0.32$ and the previously stated limits on s:

s	Γ
0.30	2.89
0.25	2.99
0.20	3.04

so that $\Gamma = 3.0 \pm 0.1$.

Allowing for an uncertainty of ± 0.01 in K_s does not significantly increase the stated uncertainty of Γ. One indication of the validity of this estimate of Γ is shown in Fig. 3 in the penetration data of Lahbabi (1993) which (for downstream distances greater than 10 diameters) show close agreement with $\Gamma = 3$. Lahbabi reports that the estimated statistical error on the mean penetration distances was less than 5 percent.

With schlieren or other photography, the penetration distance Z_t can be observed directly. With hot wire velocimetry, such as used by Witze (1980, 1983), it is more convenient to think first of the penetration time defined as the time, at a given distance, required for the velocity to rise to, say, 70 percent of the steady state jet value; alternatively we can speak of the distance, say Z_{70}, associated with that same time. We can relate Z_{70} and Z_t as follows:

The fluid velocity U_y at some distance y in the streamwise direction from the center of the vortex ball can be written

$$U_y = \frac{d}{dt}\left[Z_t - \left(\frac{D}{2} - y\right)\right]$$

Setting U_y equal to 70 percent of the steady-state velocity at a location x we have

$$U_y = \frac{0.7U_o}{C_s \frac{x}{d}},$$

in which, as will be shown below, the centerline decay constant C_s for a fully turbulent incompressible jet is close to 0.2. Equating these two expressions for U_y we obtain

$$\frac{0.7U_o d}{C_s} = \left(\frac{0.7}{C_s}\right)\sqrt{\frac{4\dot{M}}{\pi\rho}} = Z_t \frac{dZ_t}{dt}\left[1 - \left(\frac{D}{Z_t}\right)\left(\frac{1}{2} - \frac{y}{D}\right)\right]$$

Then with the use of Eq. (4) to evaluate the time derivative, and again setting $s = D/Z_t$ equal to $\frac{1}{4}$ the result is $y/D = 0.25$ and $Z_t = 1.067\, Z_{70}$.

As one test of these ideas Fig. 4 shows the transient injection data of Witze (1980) for low speed transient air-air injection for nozzle diameters of 1.15 mm (exit velocity 53 m/s) and 1.35 mm (exit velocity 103 m/s). Witze used hot wire anemometry to determine the 70 percent penetration distance Z_{70} so the

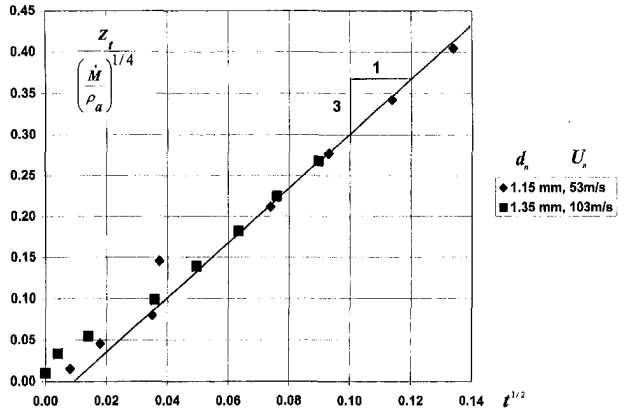

Fig. 4 Transient low-speed air-to-air injection penetration data of Witze (1980) for nozzles without exit screens; time unit (s)$^{1/2}$ on both axes

penetration distance Z_t in Fig. 4 is defined as the measured Z_{70} multiplied by 1.067. The uncertainty in the Witze determinations is high in the early part of the jet development while the jet is approaching the fully developed state. However in the downstream region the uncertainty estimated from the scatter in the data (and assuming negligible systematic error) is of the order of 5 percent. In Fig. 4 the best straight line relating the quantity

$$Z_t \Big/ \left(\frac{\dot{M}}{\rho}\right)^{1/4}$$

to $t^{1/2}$ (with time t in seconds) has a slope of about 3, well within the estimated uncertainty of Γ. Thus the usefulness of the simplifying assumptions of the Turner model appears to be confirmed, even though the Reynolds numbers for these two cases are 4400 and 10,000, well below the lower limit of 30,000 cited by Ricou and Spalding for the fully turbulent jet. The effective opening time of the nozzle appears to be very much shorter than the injection duration.

(ii) Under-Expanded Compressible Jets. As shown above, the value of the constant Γ was estimated on the assumption of uniform density. The dimensional analysis indicates that, for given nozzle exit momentum flow rate, the nozzle exit density has no intrinsic effect on jet penetration. But can this be so for a wide range of density difference between the nozzle exit fluid and the chamber fluid and also for under-expanded jets?

To examine this question we first note that, on the assumption of uniform nozzle exit velocity, and replacing ρ by ρ_a, Eq. (4) can be transformed into its exact equivalent:

$$\left(\frac{Z_t}{d\sqrt{\frac{\rho_n}{\rho_a}}}\right) = \Gamma\sqrt{\frac{\pi}{4}}\left(\frac{U_o t}{d\sqrt{\frac{\rho_n}{\rho_a}}}\right)^{1/2} \qquad (5)$$

in which d, U_n, and ρ_n are the nozzle diameter, exit velocity, and exit flow density, while ρ_a is the chamber density. Since the equivalent diameter $d\sqrt{\rho_n/\rho_a}$ has been widely used as a scaling parameter for steady-state jets of nonuniform density and temperature, and since for the upstream part of a transient jet the flow can be assumed steady, it is relevant to consider the scaling lessons which can be extracted from steady-state jet data, particularly concerning the effects of density, nonuniformity and under expansion.

The Equivalent Diameter for Steady Turbulent Jets With Nonuniform Density. Thring and Newby (1952) concluded that if at the nozzle exit plane the fluid has a density ρ_n different from that, ρ_a, of the ambient fluid (due either to temperature or composition difference), the rate of relative centerline velocity decay and other dimensionless parameters will be essentially unchanged if the distance parameter is changed from

$$\frac{x}{d} \quad \text{to} \quad \frac{x}{d\sqrt{\frac{\rho_n}{\rho_a}}}$$

The argument for this is that though momentum conservation in the absence of a pressure gradient requires

$$\dot{M} = \rho_n \frac{\pi}{4} d^2 U_n^2 = \int \rho 2\pi r u^2 dr$$

and ρ is nonuniform in the jet, yet within 10 diameters or so the average density in the jet has been reduced to nearly ρ_a. Thus, as Dahm and Dimotakis (1990) express it, at axial distances for which the local jet mass flux is sufficiently large compared with its source mass flux the flow is generally presumed to be characterized entirely by the jet source momentum flux and the ambient fluid density.

Therefore the momentum statement could be expressed as

$$\frac{\dot{M}}{\rho_a} = \frac{\pi}{4}\left(d\sqrt{\frac{\rho_n}{\rho_a}}\right)^2 U_n^2 = \int 2\pi r u^2 dr = \text{const}$$

and the effective diameter is thus defined as the actual one multiplied by the square root of the density ratio. One can test this idea by considering whether the same linear relationship (well established for uniform density turbulent round free jets) holds between the distance coordinate $x/d\sqrt{\rho_n/\rho_a}$ and the centerline decay functions U_o/U_m, $(T_o - T_a)/(T_m - T_a)$, and $1/C_m$, in which the subscripts o, a, and m refer to nozzle exit, ambient, and local centerline, respectively, and U and C are temperature and mass concentration.

Another test would be to examine whether the entrainment has the same proportionality to the modified distance coordinate for both uniform and nonuniform density flows. However the determination of local jet mass flow from velocity measurement is inherently inaccurate due to velocity uncertainty at large radius. Thus while the entrainment comparison of Sforza (1978) for heated, cold and CO_2 jets injected into air shows that this is the proper distance coordinate well downstream of the nozzle, the proportionality constant is inconsistent with the accurately and directly measured entrainment results of Ricou and Spalding for cold flow. Thus comparison of centerline jet quantities affords a better method of comparison. Alternatively, Chen and Rodi (1980) have shown that the jet half-velocity width also scales well with respect to the equivalent diameter.

Table 1 shows the downstream proportionality constants K reported by various authors. The table is concerned with the downstream behavior, recognizing that the virtual origins for these jet flows are somewhat apparatus dependent.

As a base case, the results of Wygnanski and Fiedler, for which the Reynolds number was 10^5, show that there is an appreciable transition zone, of the order of 20 diameters, before the cold jet takes up full self-similarity of the mean velocity field. The results of Witze, which are of interest here principally because of Fig. 4, pertain to appreciably lower Reynolds number and are associated with somewhat lower downstream centerline velocity decay rate than the Wygnanski and Fiedler result. The results of Birch, Brown, Dodson, and Thomas for centerline velocity decay, conforming to the Thring and Newby assumption, are in closer agreement with Wygnanski and Fiedler than those of Witze, seemingly because of being at higher Reynolds number.

The results shown in Table 1 are roughly in accord with common observations that in a turbulent jet energy and mass diffuse at about the same rate, and more rapidly than momentum does. The determination of List shows that these proportionality constants must be somewhat uncertain; the range of x/d over which one seeks the best linear fit can have an appreciable effect.

The special feature about the next two data sets referred to in Table 1 is that they pertain to highly under-expanded jets leaving converging nozzles. Birch et al. (1984) performed experiments on natural gas injected into atmospheric air with nine stagnation-to-ambient pressure ratios P_o/P_a in the range 2 to 70, and with ethylene injected into air at a stagnation pressure ratio of 8. (The temperature ratio T_o/T_a in each case could be assumed to be 1.)

The diameter and location of the Mach disk in such largely under-expanded jets are described by the data of Ewan and Moodie shown in Fig. 5, in which X_D is the distance from the nozzle exit to the Mach disc and D is the disc diameter and d the nozzle diameter. The uncertainty in the measurements well downstream of the nozzle appears from Fig. 5 to be of the order of 5 per cent for both the Mach disk diameter and its distance

Table 1 Steady-state round free turbulent jet proportionality constants K (in $Y = K\,X$, in which $X = x/d\sqrt{\rho_n/\rho_a}$)

Author(s)	Y	ρ_n/ρ_a	K	
Wygnanski and Fiedler (1969)	U_o/U_m	1	0.188	$0 < x/d < 100$
(low speed, air/air)		1	0.187	$15 < x/d < 60$
		1	0.206	$30 < x/d < 100$
Witze (1980) (low speed, air/air)	U_o/U_m	1	0.18	$15 < x/d$
Birch, Brown, Dodson, Thomas (1978) (low speed, natural gas/air)	U_o/U_m	0.6	0.200	natural gas/air Re 1.6×10^4
Sunavala, Hulse and Thring (1957)	$\frac{T_o - T_a}{T_m - T_a}$	0.5	0.215	air/air, tracer gas 4 nozzle diam.
	$1/C_m$	0.3	0.22	Re $3-6 \times 10^4$
Birch, Brown, Dodson, Thomas (1978)	$1/C_m$	0.6	0.213	natural gas/air
List (1980) using data on Becker et al. (1967) and Birch et al. (1978)	$1/C_m$		0.194	
Birch, Brown, Dodson, Swaffield (1984)	$1/C_m$	1–40	0.230	natural gas/air
	$1/C_m$	4.8	0.228	ethylene/air
Ewan and Moodie (1986)	U_o/U_m	1–20		air, helium/air
	$1/C_m$	1–20	0.217	air, helium/air

from the nozzle exit plane. Ashkenaz and Sherman (1966) have theoretically determined the axial position of the Mach disk downstream of an ideally uniform nozzle exit flow of gas (injected into the same substance) and their result is simply

$$\frac{X_D}{d} = 0.67\sqrt{\frac{P_0}{P_a}},$$

which is consistent with the theoretical result of Young (1975). As Fig. 5 shows, for nozzle pressure ratio in the range of 2 to 10, both the distance between the nozzle exit plane and the Mach disk and the diameter of the Mach disk of the order of one nozzle diameter.

However, the important question here is whether self-similarity considerations apply to a jet which has suffered a strong shock in its early development; does it act downstream as though it has completely forgotten its traumatic origin? The very high pressure ratio data of Birch et al. up to a pressure ratio of 70:1 show that it can, and that the virtual origin of the jet is little removed from the nozzle exit plane. These data show that the concentration ratios $1/C_m$ (in which C_m was expressed in volume fraction) could all be well fitted to

$$\frac{1}{C_m} = K_P \frac{x}{d\sqrt{\frac{P_o}{P_a}}}$$

with K_P being 0.225 for the natural gas (whose ratio of specific heats was 1.35 and whose ratio of molecular weight to that of air was 0.599), and 0.285 for ethylene (whose ratio of specific heats is 1.25 and whose ratio of molecular weight to that of air is 0.974). Converting from volume fraction to mass fraction the constants K_P become 0.376 for natural gas and 0.293 for ethylene.

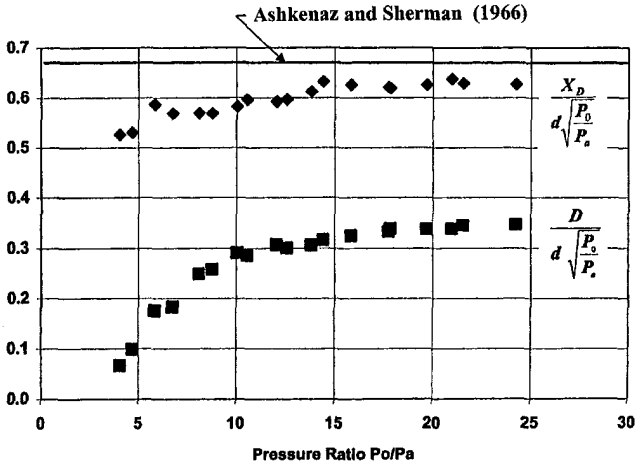

Fig. 5 Location x_D and diameter D of the Mach disk, data of Ewan and Moodie (1986) for air/air injection with pressure ratios 4 to 25

This raises the question as to whether these two empirical K_p values are consistent with the Thring and Newby assumption that the equivalent nozzle diameter is the actual one. We could rewrite the above equation as

$$\frac{1}{C_m} = K_\rho \frac{x}{d\sqrt{\frac{\rho_n}{\rho_a}}} \quad \text{in which} \quad K_\rho = K_p\sqrt{\frac{\rho_n}{\rho_a}\frac{P_a}{P_o}}$$

If the flow in the nozzle is isentropic and the exit Mach number is 1 (and the ambient and upstream stagnation temperatures are the same) then

$$K_\rho = K_p\sqrt{\left(\frac{2}{\gamma+1}\right)^{1/\gamma-1}}\sqrt{\frac{M_g}{M_a}}$$

in which M_g/M_a is the ratio of the molecular weight of the injected gas to that of air. Evaluation for the above data produces K_ρ values of 0.230 for natural gas and 0.228 for ethylene which is a remarkably close indication of similarity. The disagreement between these K_ρ values and the corresponding ones for incompressible flow cited in Table 1 is probably within experimental uncertainty.

In summary, a wide range of experimental data on centerline velocity, temperature and concentration, even including cases with highly under-expanded flows corresponding to methane-air pressure ratios of 70:1, are consistent with the hypothesis that $d\sqrt{\rho_n/\rho_a}$ is a universal scale describing the downstream similarity of jets. The proportionality constant for momentum diffusion is around 0.19 whereas for species and energy diffusion it appears to be around 0.21. Such similarity is valid even for pressure ratio as high as 70:1 with choked compressible flows in a non-diverging nozzle. In this case the expansion immediately downstream of the nozzle is accompanied by strong shock wave effects in the Mach disc located a few diameters downstream of the nozzle. However, despite this shocking experience early in its development, such a jet flow apparently is able in its downstream experience to act as though it had completely forgotten the details of its origin. This leads to the following reasoning:

Given that:

(i) In steady jet flows with nonuniform density the appropriate axial length scale is the nozzle diameter multiplied by the square root of the nozzle-to-ambient density ratio,

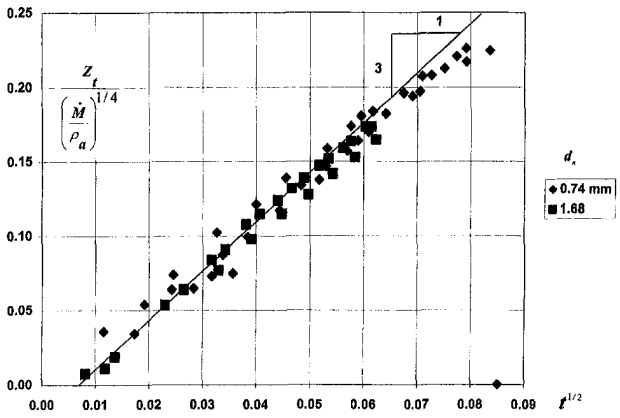

Fig. 6 Transient injection of natural gas into helium-nitrogen mixture; data of Miyake et al. (1983); time unit $(s)^{1/2}$ on both axes

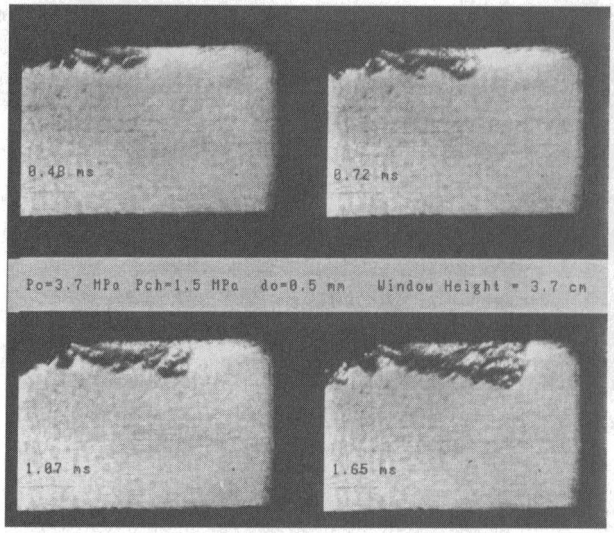

Fig. 7 Typical schlieren photos for nozzle pressure ratio 1.5:1; times after injection ranging from 0.48 to 1.65 ms. The symbol P_{ch} is the chamber pressure.

(ii) The upstream part of the transient jet flow is quasi-steady, and

(iii) The dependence of penetration distance on the square root of time has been well established for uniform density transient jets,

We can expect that for long injection times Eq. (4) should apply not only to jets with large density difference from that of the chamber fluid, but also with highly under-expanded jets, with the same value of Γ as determined from uniform-density transient turbulent jets.

As a further test of Eqs. (4) and (5) we turn now to the long-duration constant-injection-rate data of Miyake et al. (1983) who injected natural gas in to a mixture of nitrogen (13 percent by volume) and helium (87 percent by volume) to provide a nozzle-to-ambient density ratio of 3.2 ands a nozzle exit velocity of 409 m/s. They used two nozzles—one of diameter 0.74 mm, the other of diameter 1.88 mm. The minimum Reynolds number was approximately 2×10^4. Figure 6 shows that on average the experimental penetration constant is close to the expected value of 3.0. The injection time was 4 ms; for the smaller nozzle, data were recorded for as long as 7 ms and in this case some departure is apparent in Fig. 6 from the penetration dependence on the square root of time. The experimental uncertainty for each data set of penetration measurements appears from Fig. 6 to vary from about 20 percent in the upstream region to perhaps 10 percent further downstream. The mean penetration of the tip of the jet from both nozzles appears nearly to obey Eq. (4) as long as the time is less than the injection duration. For larger times the kind of deviation of the mean from the straight line shown in the figure is to be expected. Thus Eqs. (4) and (5) appear to be well confirmed by compressible flow data pertaining to large density differences between jet and surrounding fluid and also for cases in which the nozzle flow is under-expanded.

Measurements of Transient Turbulent Jet Injection Close to a Chamber Wall. Experimental work was performed to test gaseous fuel penetration in a small pressurized chamber in a case where an adjacent wall, simulating the flat cylinder head surface of a diesel engine chamber, could have affected jet penetration. The gaseous fuel was injected through an electronically controlled and hydraulically actuated injection valve of the type used in fueling modern diesel engines.

Optical determinations of transient jet penetration were made with schlieren photography in a rectangular chamber ($123 \times 123 \times 70$ mm) fitted with 2 quartz windows. The diameter of each of the 6 injector holes was 0.5 mm and the length of each injection hole was about 5.6 times the diameter. The fuel jets propagated at an angle of 10° to the upper wall of the chamber.

The penetration was measured from the photographic records; the time uncertainty was 0.02 ms. Jet penetration measurements repeated over several events indicated a standard error of 1 mm in the far field (between 20 and 100 diameters), largely due to turbulent fluctuations of the jet front.

The injected fluid was methane, which at the highest test pressures departed considerably from perfect gas behavior. However, calculations with a real gas equation of state for methane showed that nozzle exit momentum was altered by at most 2 percent by differences between real and perfect gas behavior within the nozzle. Frictional effects within the nozzle were estimated by assuming a surface roughness coefficient of 0.005 and one-dimensional compressible flow within the nozzle. The flow within the nozzle being sonic or nearly so, the calculated stagnation pressure losses were about 10 percent.

Figure 7 shows typical schlieren photos of the injection process with the fuel jet angle 10° for times 0.48, 0.72, 1.07, and 1.65 ms after the start of injection. The time for the gas needle to open was found experimentally to be 0.1 ms. Measurements of the location of the tip of the most prominently seen jet plume are shown in Fig. 8 for various injection times and for 4 ratios of stagnation to chamber pressure. With the estimated uncertainty of 0.02 ms in the time variable, the error in $t^{1/2}$ is about 10 percent at the low end and about four percent at the high

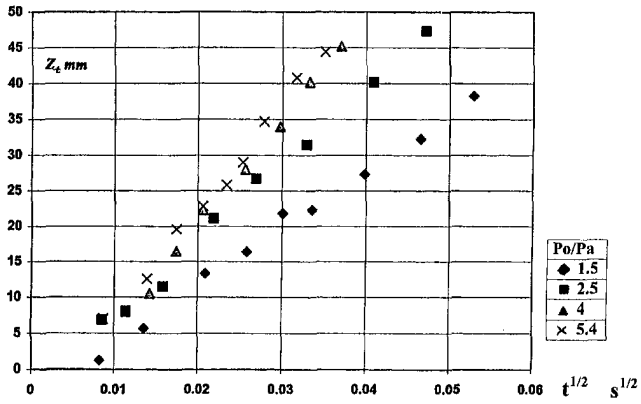

Fig. 8 Data of Ouellette (1996) on transient gas jet mixing in air with various pressure ratios

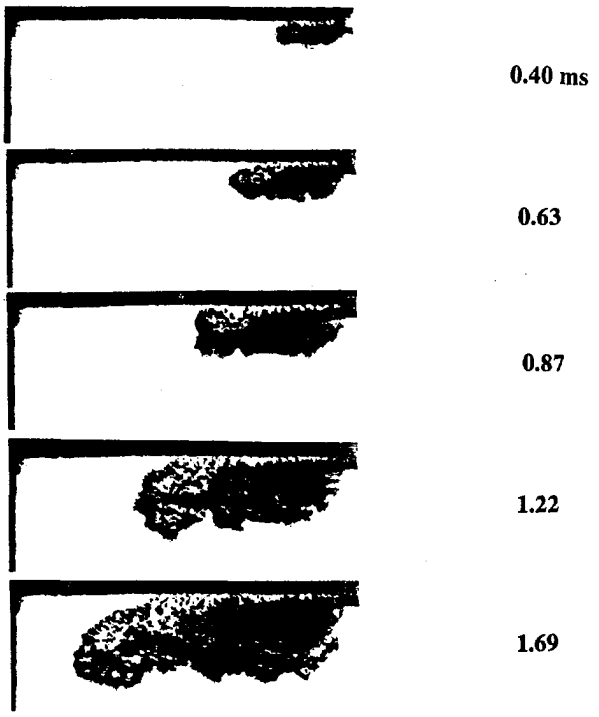

Fig. 9(*a*)

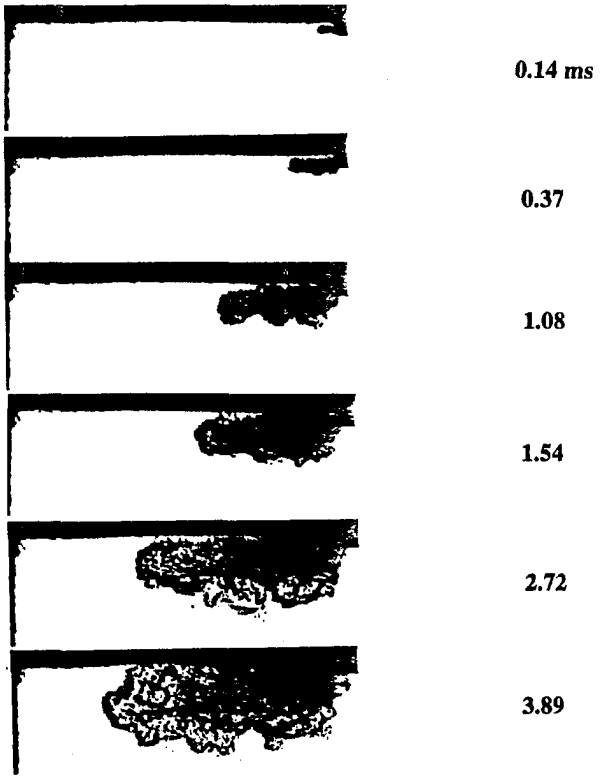

Fig. 9(*b*)

Fig. 9 Typical schlieren photos for two gas injection pressures; chamber pressure 3550 kPa (*a*) Pressure ratio 5:1 (*b*) Pressure ratio 1.5:1

end. The penetration distance error of ±1 mm is ±20 percent at the low end and about three percent at the high end. Thus the size of the symbols shown approximately represents the estimated level of experimental uncertainty. The pressure ratio of 5.4 implies a substantial degree of under-expansion in the nozzle. It is notable, however, that in each case the jet penetration is a linear function of the half power of time after the start of injection. This, as has been shown earlier, is indicative of self-similar behavior, despite the nearby location of the upper wall.

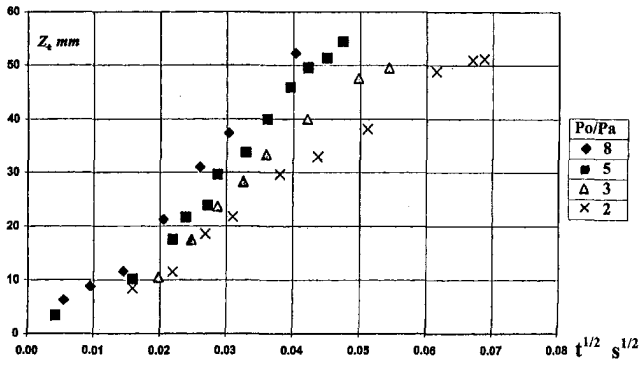

Fig. 10 Data of Chepakovich (1993) on transient gas jet mixing in air with various pressure ratios

Figure 9 shows penetration observations in the same chamber but with a different injector and two pressure ratios. Here as in Fig. 7 more than one jet is in view so that while the tip penetration is shown clearly, the broadening of each jet is not. Figure 10 shows the corresponding penetration data for these and several other pressure ratios. This injector had 9 holes each of 0.38 mm in diameter and directed at 10° downward from the cylinder head surface. It was solenoid-driven with somewhat longer valve opening time than in the first case so the effective valve opening time is, as straight-line fits to the individual data sets of Fig. 10 indicate, given by a value of $t^{1/2}$ of about 0.003 $s^{1/2}$. Nonetheless, the variation of penetration with $t^{1/2}$ is apparently linear over most of the range and with all pressure ratios. Other tests, in which chamber pressure was varied over a wide range with nozzle pressure ratio held constant, showed that jet penetration at a given time is independent of chamber pressure.

To examine the conditions under which self-similarity of transient turbulent jets may be expected we replot the data of Figs. 8 and 10 in similarity coordinates. The results are shown in Figs. 11 and 12, respectively. Figure 11 shows that the Ouellette data are consistent with the estimated penetration constant at the two higher pressure ratios. For pressure ratios 2.5 and 1.5 the data appear to show some effect of retardation of the jet due to wall friction; this is most evident in the downstream region. In these calculations the estimated nozzle exit momentum flow has been reduced by 10 percent (the frictional effect calculated assuming expansion of a perfect gas with specific heat ratio 1.3). As this momentum is raised to the $\frac{1}{4}$ power the effect of the stagnation pressure correction on penetration is not

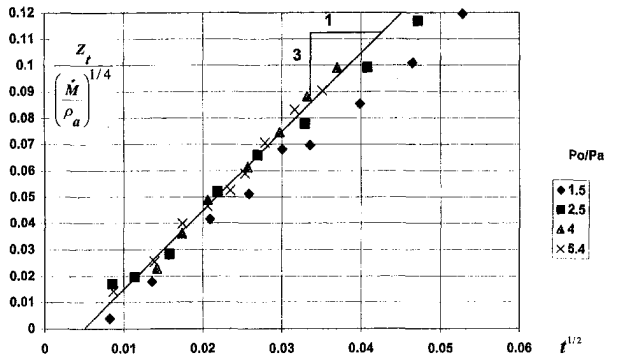

Fig. 11 Data of Ouellette (1996) transformed into the coordinates of self-similarity; time unit $(s)^{1/2}$ on both axes

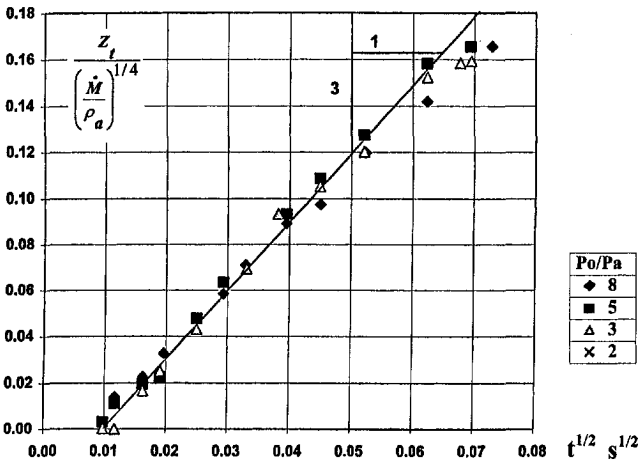

Fig. 12 Data of Chepakovich (1993) on transient injection of natural gas into air; time unit $(s)^{1/2}$ on both axes; pressure ratio 2:1; pressure ratios 8, 5, 3, 2, 1.5

large. In Fig. 12 the data of Chepakovich (1993) also show a divergence from the penetration constant of 3 at lowest pressure ratios. The lesson is that jet penetration is affected by injection within 10° of a flat wall but the effect on penetration is not large in the near field and is least at highest pressure ratio. Self-similarity is a good first approximation though detailed numerical simulation will clearly be needed to fully simulate chamber wall effects as well as the effects of piston motion and mean fluid motion such as swirl. In the data shown in Figs. 11 and 12 there is evidence that the nozzle does not open instantaneously; the virtual time origin is displaced slightly from the signaled opening time of t equal to zero.

Conclusions

1. The round free transient turbulent jet impulsively injected at constant rate into a large quiescent chamber exhibits a self-similar configuration after the tip of the jet has traveled 15–20 nozzle diameters from the nozzle exit plane.

2. Experimental deduction of the self-similar shape ratio of uniform-density transient turbulent jets coupled with use of the Turner structural model, accurate knowledge (due to Ricou and Spalding) of steady-state entrainment rate, and conservation of momentum, provide a simple description of the penetration distance which is accurate within experimental uncertainty, without need for explicit consideration of shear and drag forces.

3. The penetration constant of 3.0 ± 0.1 in Eq. (4) has been shown to be valid not only for uniform density jets but also for cases in which there are large density gradients. The self-similarity criterion for the transient turbulent jet has been shown to be consistent with the equivalent nozzle diameter parameter (geometric diameter multiplied by the square root of nozzle-to-chamber density ratio) which has been well established in scaling steady-state turbulent jets.

4. Highly under-expanded transient turbulent jets conform to the downstream self-similar behavior described by the penetration constant of Eq. (4).

5. Tests with a diesel engine gas injector over a wide range of pressure ratios have shown substantial conformity to the penetration formula of Eq. (4). Nozzle stagnation pressure losses are significant but have a small effect on penetration distance because of the $\frac{1}{4}$ power dependence of the penetration on the nozzle exit momentum flux. The opening transient is typically short compared to the injection duration.

6. In the lowest range of pressure ratios and for injection angles of 10° or less the retarding effect of an adjacent wall on jet penetration can be substantial.

References

Abramovich, S., and Solan, A., 1973, "The Initial Development of a Submerged Laminar Round Jet," *Journal of Fluid Mechanics,* Vol. 59, Part 4, pp. 791–801.

Ashkenaz, H., and Sherman, F.S., 1966, *Rarefied Gas Dynamics,* J.H. de Leeuw, ed., Academic Press, New York, Vol 1, p. 84.

Batchelor, G. K., 1967, *Fluid Mechanics,* Cambridge University Press.

Becker, H.A., Hottel, H.C., and Williams, G.C., 1967, "The Nozzle-Fluid Concentration Field of the Round Turbulent Free Jet," *Journal of Fluid Mechanics,* Vol. 30, pp. 285–303.

Birch, A. D., Brown, D. R., Dodson, M. G., and Thomas, J. R., 1978, "The Turbulent Concentration Field of a Methane Jet," *Journal of Fluid Mechanics,* Vol. 88, pp. 431–3.

Birch, A.D., Brown, D.R., Dodson, M.G., and Swaffield, F., 1984, "The Structure and Concentration Decay of High Pressure Jets of Natural Gas," *Combustion Science and Technology.* Vol. 36, pp. 249–61.

Chepakovich, Alexander C., 1993, "Visualization of Transient Single- and Two-Phase Jets Created by Diesel Engine Injectors," M.A.Sc. thesis, University of British Columbia.

Chen, C. J., and Rodi, W., 1980, *Vertical Turbulent Buovant Jets—A Review of Experimental Data,* Oxford, New York, Pergamon Press.

Dahm, Werner J. A., and Dimotakis, Paul E., 1990, "Mixing at Large Schmidt Number in the Self-Similar Far Field of Turbulent Jets," *Journal of Fluid Mechanics,* Vol. 217, pp. 299–330.

Dedeoglu, Nabi, 1979, "Scavenging Model Solves Problems in Gas Burning Engine," Society of Automotive Engineers Paper SAE 710579.

Ewan, B. C. R., and Moodie, K., 1986, "Structure and Velocity Measurements in Under-Expanded Jets," *Combustion Science and Technology.* Vol. 45, pp. 275–88.

Garside, J.E., Hall, A.R., and D.T.A., Townsend, 1943, *Nature,* Vol. 152, p. 748.

Hinze, J. O., 1987, *Turbulence.* McGraw-Hill, New York.

Keagy, W. R., and Weller, A. E., 1949, "A Study of Freely Expanding Inhomogenous Jets," *Proceedings of the Heat Transfer and Fluid Mechanics Institute,* Vol. 2, Stanford University Press, Stanford, C.A.

Kovasznay, Leslie S. G., Fujita, Hajime, and Lee, Rena, L., 1974, "Unsteady Turbulent Puffs," *Advances in Geophysics,* Vol. 18, pp. 253–263.

Kuo, T.-W., and Bracco, F. V., 1982, "On the Scaling of Transient Laminar, Turbulent, and Spray Jets," Society of Automotive Engineers Paper SAE 820038.

Lahbabi, Fatima Z., Botee, Jacques, Nuglisch, Hans J. and Charnay, Georges, 1993, "Analysis of Starting and Steady Turbulent Jets by Image Processing Techniques," *Experimental and Numerical Flow Visualization,* ASME Fluids Engineering Division, Vol. 172.

List, E. J., 1982, "Turbulent Jets and Plumes," *Annual Review of Fluid Mechanics,* Vol. 14, pp. 189–212.

Miyake, M., Biwa, T., Endoh, Y., Shimotsu, M., Murakami, S., and Komoda, T., 1983, "The Development of High Output, Highly Efficient Gas Burning Diesel Engines," Paper D11.2, CIMAC Conference, Paris, June 13–16.

Ouellette, P., 1996, "Direct Injection of Natural Gas for Diesel Engine Fueling," PhD thesis, University of British Columbia.

Ouellette, P., and Hill, P.G., 1992, "Visualization of Natural Gas Injection for a Compression Ignition Engine," Society of Automotive Engineers Paper SAE 92155.

Richards, J.M., 1965, "Puff Motions in Unstratified Surroundings," *Journal of Fluid Mechanics,* Vol. 21, Part 1, pp. 97–106.

Ricou, F. P., and Spalding, D.B., 1961, "Measurement of Entrainment by Asymmetrical Turbulent Jets," *Journal of Fluid Mechanics,* Vol. 11, Part 1, pp. 21–32.

Rizk, W., 1958, "Experimental Studies of the Mixing Processes and Flow Configurations in Two-Cycle Engine Scavenging," *Proceedings of the Institution of Mechanical Engineers,* Series E, Vol. 172, pp. 417–24.

Sen, M., et al 1989, "Longitudinal and Transverse Dimensions of an Incipient Jet Generated by a Constant Head," *Experiments in Fluids,* Vol. 8, pp. 107–9.

Sforza, P. 1978, "Mass, Momentum and Energy Transport in Turbulent Free Jets", *International Journal of Heat and Mass Transfer,* Vol. 21, pp. 271–384.

Sunavala, P.D. et al., 1957, "Mixing and Combustion in Free and Enclosed Turbulent Jet Diffusion Flames," *Combustion and Flame,* Vol. 1, pp. 179–93.

Thring, M.W., and Newby, M.P., 1952, "Combustion Length of Enclosed Turbulent Jet Flames," *4th Symposium (International) on Combustion,* Baltimore, Williams and Wilkins.

Thring, M. W. 1962, *The Aerodynamics of Hot Systems.* London, Chapman & Hall.

Turner, J. S., 1962, "The 'Starting Plume' in Neutral Surroundings," *Journal of Fluid Mechanics,* Vol. 13, pp. 356–68.

Witze, Peter O., 1980, "The Impulsively Started Incompressible Turbulent Jet," Sandia Laboratories Report SAND80-8617, Livermore, Calfornia.

Witze, Peter O., 1983, "Hot-Film Anemometer Measurements in a Starting Turbulent Jet," *American Institute of Aeronautics and Astronautics Journal,* Vol. 21, No. 2, pp. 308–309.

Wygananski, I., and Fielder, H., 1969, "Some Measurements in the Self-Preserving Jet," *Journal of Fluid Mechanics,* Vol. 38, Part 3, pp. 577–612.

Young, Wen S., 1975, "Derivation of the Free-Jet Mach-Disk Location Using the Entropy-Balance Principle," *Physics of Fluids,* Vol. 18, No. 11, pp. 1421–1425.

APPENDIX A

The Puff Jet

For the puff jet the experiments of Richards (1965) have shown approach to self-similarity with the width ratio D/Z_t becoming about 0.5. For this case the significant momentum quantity is the total momentum of the puff. Again the result is a single penetration number, but in this case the penetration distance is proportional to the fourth root of time. After the injection has ended the transient jet will tend toward a puff jet, but during injection it is the transient jet that is the interesting configuration.

Assuming the density ρ is everywhere uniform within a spherical puff of diameter D, one could write the total axial momentum as, approximately,

$$\rho \frac{\pi D^3}{6} \frac{d(Z_t - D/2)}{dt} = M$$

or, with

$$n = \frac{Z_t}{D},$$

$$\rho \frac{\pi}{6} \frac{Z_t^3}{n^3} \frac{dZ_t}{dt} (1 - 1/2n) = M.$$

With conservation of M and $1/n$ taken to be 0.5, the penetration of the puff can be found by integration to be governed by

$$Z_t = C \left(\frac{Mt}{\rho} \right)^{1/4}$$

where C, equal to $4/\pi^{1/4}$, is very close to 3 and roughly in accord with the observations of Richards for non-buoyant puffs.

For the turbulent puffs experimentally studied by Kovasznay et al. (1974) the value of n was about 0.6 but the puffs were quite nonspherical in configuration and had the configuration of a vortex ring. The total momentum in each puff does not appear to have been measured by these authors but, in conformity with the above penetration constant, the drift velocity of the maximum velocity point in the puff was found to vary with $x^{-1/3}$, where x is the axial location of the maximum velocity point.

Toward a Vortex Breakdown Condition for Swirling Annular Jets

C. F. Stein
Ph. D. Student,
Department of Mathematics,
Chalmers University of Technology,
S-412 96 Göteborg, Sweden

Vortex breakdown is a significant phenomenon in science and technology. In spite of extensive research, the question of the underlying mechanisms for vortex breakdown still lacks a definite answer. The uncertainty of the governing principles for vortex breakdown is revealed by the common use of a variety of different parameters to describe the degree of swirl. In this paper, a theoretical discussion on the suitability of three kinds parameters was conducted, and it was found that one appears to be the natural one if the flow is primarily a swirling channel flow, but if the jet character of the flow is dominant, another one appears to be the most suitable. CFD simulations were performed for a channel with an annular inlet considerably smaller than the channel width. For this case the jet character of the flow should predominate and it was found that the parameter, which theoretically appeared to be best suited for jet flows, indeed was less dependent of the detailed inflow geometry than the others.

1 Introduction

It is a well-known fact that the flow pattern, obtained for a swirling annular jet after vortex breakdown, is very well suited for flow in combustion chambers. This is basically due to two reasons: The large and stable central recirculation zone creates a stable flame and the swirling flow has a high turbulence intensity, which in turn accelerates the vaporization as well as the mixing. Modern CFD (Computational Fluid Dynamics) codes give for a given chamber geometry reasonably accurate predictions of the flow pattern, but such calculations are expensive and very time consuming. In order to optimize the design of combustion chambers, a wide range of different chamber geometries ought to be considered, and consequently, it would be desirable to obtain more general knowledge of swirling jets. For instance, if there were a simple method to calculate the basic shape of the central recirculation zone for any geometry and any degree of swirl, the amount of numerical computation needed in the design process would be greatly reduced.

For the application of swirling jets in combustion chambers it is necessary that the flow has undergone vortex breakdown, and hence a simple criterion determining for which degree of swirl this occurs is needed. Today, no such criterion is available, and this is clearly elucidated by the fact that the quoted critical values in the literature deviate by more than a factor two. The situation is even more complicated, since as many as three different kinds of dimensionless quantities are used to quantify the degree of swirl. In this paper, we discuss the possibility of obtaining a vortex breakdown criterion based on any one of these three commonly used dimensionless quantities. At this point we should stress that by vortex breakdown we will not refer to a sudden change of the flow properties around some point in physical space, but rather to an abrupt change of the entire flow pattern around some value in parameter space. Henceforth, the degree of swirl at which vortex breakdown occurs, is called the critical degree of swirl.

Vortex breakdown theories fall into three categories. In the first, vortex breakdown is considered as a separation phenomenon (Hall, 1972), the second category includes theories where instability is the central issue (Leibovich, 1984), and the third type of theory emphasizes the analogy with hydraulic jumps and the relation to inertial wave propagation. The latter theory, which appears to be the most commonly accepted, is based on the ideas launched in (Benjamin, 1962). In this theory, vortex breakdown is considered as the sudden change from a supercritical state to a subcritical conjugated state. In the subcritical state standing waves can propagate upstream, which is not possible in the supercritical state. This has been confirmed experimentally in Escudier and Keller (1985), and it is this criterion which leads to Benjamin's Critical Equation, which determines whether vortex breakdown has occurred or not. Unfortunately, Benjamin's Critical Equation is very difficult to solve, since it requires explicit knowledge of the critical states, and so far a solution has only been presented for the case of a Rankine vortex with uniform axial velocity. This solution has proven to be rather accurate for prediction of vortex breakdown in a cylindrical channel with no special inlet, but for other flows little quantitative insight has been gained from this theory.

Vortex breakdown has frequently been studied experimentally; see e.g. Sarpkaya (1971), Escudier and Keller (1985) or Sheen et al. (1996a). Quantitative comparison between the different studies is difficult since different dimensionless numbers have been used to characterize swirl. Notwithstanding the practical difficulties the lack of standardization brings, the main problem is that at least two of these dimensionless numbers do not include all the information needed to predict when vortex breakdown occurs. To illustrate how crucial the choice of the correct dimensionless number is, consider an ordinary nonswirling jet emerging from a circular orifice. If we tried to describe the asymptotic angle of expansion of the jet in terms of the mass flow rather than in terms of the axial momentum of the jet, it is easy to see that we would fail.

In this paper our aim is to study how suitable three different dimensionless numbers commonly used to characterize swirl are for describing vortex breakdown. To this end, we will use CFD calculations of a model combustion chamber as depicted in Fig. 1. To try to single out one of the parameters, we will use numerics to see how much the critical degree of swirl, as expressed in the different dimensionless numbers, changes when we alter the inlet geometry or the inlet velocity profiles.

Although the choice of the dimensionless number used to characterize the degree of swirl is of importance, it is a field which appears to have attracted little research. Recently, however, Sheen et al. (1996b) conducted an experimental study to

Contributed by the Fluids Engineering Division for publication in the JOURNAL OF FLUIDS ENGINEERING. Manuscript received by the Fluids Engineering Division June 26, 1998; revised manuscript received October 13, 1998. Associate Technical Editor: F. Hussain.

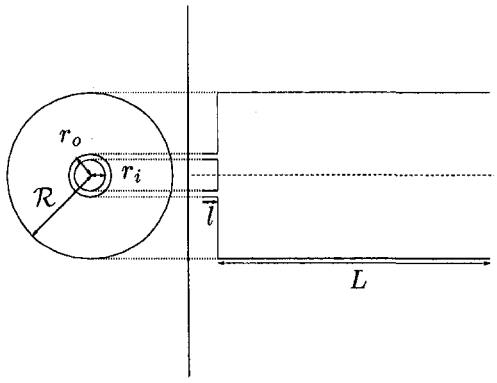

Fig. 1 The principal geometry of a typical combustion chamber

determine the Reynolds number sensitivity of some dimensionless numbers, but they were not concerned with the dynamics of vortex breakdown.

2 The Different Dimensionless Numbers Used to Characterize Swirl

The dimensionless numbers used to characterize the degree of swirl are of three main types. First, it can be a quotient between the flux of angular momentum, L_z, and the flux of axial momentum multiplied by a typical length scale, second, it can be a quotient between the circulation and a typical velocity multiplied by a typical length scale, and finally, it can be a quotient between the flux of axial momentum and the circulation squared, i.e., expressed mathematically the three main types are:

$$S = \frac{\int_{r_i}^{r_o} UWr^2 dr}{r_o \int_{r_i}^{r_o} U^2 r dr}, \tag{1}$$

$$\beta = \frac{K_c}{u_0 r_i} \text{ and} \tag{2}$$

$$M = \frac{J_z}{\rho K_c^2}, \tag{3}$$

where r_o is the outer and r_i the inner radius of the orifice, U the axial and W the azimuthal velocity, K_c a characteristic circulation of the incoming fluid, and ρ the density. Finally, u_0 and J_z are given by:

$$u_0 = \frac{Q}{\rho A} = \frac{2\int_{r_i}^{r_o} Urdr}{r_o^2 - r_i^2} \text{ and} \tag{4}$$

$$J_z = 2\pi\rho \int_0^\infty \left\{ U^2 + \frac{p - p_\infty}{\rho} - 2\nu \frac{\partial U}{\partial z} \right\} rdr. \tag{5}$$

Here, Q is the mass flow, A the surface area of the orifice, p the pressure, p_∞ the atmospheric pressure and ν the viscosity. Note that for intensive flow the the denominator in S is approximately equal to J_z, and in fact in some papers J_z has been used instead of the denominator in S, but the resulting number has been shown to be more sensitive to variations of the Reynolds number (Sheen et al., 1996b) and therefore S seems to be the most commonly used parameter of this type. There are in fact several variations of the dimensionless numbers presented here, but the ones presented here appear to be the most common representatives of the different types.

The parameter S is most often found in experimental (Sheen et al., 1996a) and numerical (Lai, 1996) papers. β is used in Benjamin's vortex breakdown theory and in various related theoretical and experimental articles and M is primarily used in articles which use conically self-similar solutions to describe swirling jets in conical domains.

To summarize, all three of the dimensionless numbers in (1)–(3) measure the ratio between either J_z or Q and either L_z or K_c. The quantities L_z and Q are conserved in a control volume, J_z decays at walls but is conserved in control volumes away from the walls and K_c is conserved on streamsurfaces. One of the main characteristics of Benjamin's theory is that the total head and the circulation is conserved during vortex breakdown. Benjamin found that there was a loss of the axial flow force during vortex breakdown, but in Keller et al. (1985) the theory was modified to allow for vortex breakdown without force loss.

It seems reasonable that a swirl number should be the ratio of the Reynolds numbers in the axial and azimuthal directions. This point of view shows that β is the natural parameter if one treats the flow as essentially a channel flow, and that M is the natural parameter if the flow is essentially a jet flow. Indeed, if we use $\mathrm{Re}_\phi = K_c/\nu$ as the Reynolds number for the azimuthal flow, which we can do since the circulation on a streamsurface is conserved and has the dimension of viscosity, and if we take the axial Reynolds number of a nonswirling jet in unconfined space, $\mathrm{Re}_z^j = (J_z/\rho)^{1/2}/\nu$, we find that $M = (\mathrm{Re}_z^j/\mathrm{Re}_\phi)^2$. Alternatively, if we take the Reynolds number of the flow in an annular channel, $\mathrm{Re}_z^c = Qr_o/\rho A\nu$ we find that $\beta = \mathrm{Re}_\phi r_o/\mathrm{Re}_z^c r_i$. The factor r_o/r_i in β takes into account which proportion of the flow initially swirls. If we similarly view S as a quotient of an azimuthal and axial Reynolds number, we obtain the azimuthal Reynolds number $\mathrm{Re}_\phi^* = (L_z/(\rho r_o))^{1/2}/\nu$, which has the undesirable property that one of the quantities defining it, the characteristic radius of swirl r_o, changes in the process of vortex breakdown.

The quantities involved in the dimensionless number S, J_z, and L_z, are precisely those conserved in the solution for swirling jets developed in, for example, Loitsyanskii (1953). It is, however, known that a Loitsyanskii jet cannot produce a zone of axially reversed flow (Goldshtik, 1979). Consequently, the theoretical support for the use of S to describe vortex breakdown is rather weak. By contrast, both of the dimensionless numbers β and M do have theoretical support. The former from Benjamin's vortex breakdown theory outlined above, and the latter from the conically self-similar solutions, see for example Shtern and Hussain (1996), and both of these methods offer possible predictions for vortex breakdown.

For a given geometry and inlet profile S, β, and M are equivalent, and as we change the axial Reynolds number, the critical values of the different parameters will trace curves which only differ by a constant factor, and such curves have been found experimentally for instance in Sheen et al. (1996a) and Sarpkaya (1971), and they reveal that once the axial Reynolds number is moderately large then the critical value of swirl is rather insensitive to changes in the axial Reynolds number. However, if we change the geometry or the inlet profile these critical values change, and the less relevant the dimensionless number for vortex breakdown, the more sensitive should the parameter be to such changes.

3 Numerical Method

For our CFD calculations, we used a finite volume method for axisymmetric flow with the $k - \epsilon$ turbulence model without wall-functions. The numerical method is an explicit three stage Runge-Kutta time marching method that uses an optimised local time-step. The grid is nonorthogonal, block-structured, and boundary fitted. For the convective terms a third-order accurate cell-centred finite volume scheme is used with upwind biasing based on the characteristic variables and associated velocities. For the k and ϵ equations the third-order scheme is used with a TVD (Total Variation Diminishing) limiter, which makes the

Table 1 Definition of the geometry and the inlet profile of the various cases for which numerical simulations were performed

	Geometry r_i (m)	Geometry l (m)	Velocity profile
Case 1	0.01085	0.05	flat
Case 2	0.01085	0.05	laminar
Case 3	0.01965	0.01	flat

scheme second order accurate. The viscous parts are discretized with a second-order scheme. To avoid the difficulties with k and ϵ becoming negative, the value of k is not allowed to decrease below a certain limit in the early stages of the simulation. This code was developed by Lars-Erik Eriksson at the Volvo Aero Corporation, and is described in more detail in Eriksson (1987), Eriksson (1995) and Larsson (1996).

It must be emphasized that neither the comparison of various turbulence models, nor the quality of the numerical calculations have been of primary interest to us in this study. There may well be turbulence models more suited for swirling flow than the $k - \epsilon$ model without wall functions, but in all our calculations the turbulence model has been the same, and the results of the different calculations were almost exclusively compared to each other.

3.1 Geometry of the Test Cases. In all our numerical calculations we used an axisymmetric channel like the one in Fig. 1. In all our calculations we had $L = 1.2$ m, $\mathscr{R} = 0.13$ m and $r_o = 0.02265$ m.

We simulated swirling jets for two different values of r_i and l, as described in Table 1. The parameter l can appear to have little influence on the flow inside the combustion chamber, however, when obtaining solutions using CFD, a proper choice of the length of the inlet section appeared to be of some importance.

In all our calculation, we assumed the fluid to be air at room temperature.

3.2 Inlet and Outlet Conditions. The difference between Case 1 and Case 2 in Table 1 is that different velocity profiles were given at the inlet boundary. When we used the flat profile we set both the axial and azimuthal velocities to be constant over the entire inlet.

To test the sensitivity of the critical degree of swirl to changes in the inlet profile we wanted an alternative to the flat profile. One such alternative is given by the laminar profile of axial flow in an annular channel when there is no swirl. This profile is given by

$$u(r) = C \frac{r_o^2 \ln \frac{r}{r_i} + r^2 \ln \frac{r_i}{r_o} + r_i^2 \ln \frac{r_o}{r}}{\ln \frac{r_o}{r_i}} \tag{6}$$

where C is an arbitrary number. In Case 2 we set the axial velocity to be of the form (6) at the inlet, with the same value of C for all the calculations performed for this case. From the profiles given in Sheen et al. (1996a), which were measured at the jet exit, it appears that this profile approximates the axial velocity profile well even in the case of moderate swirl.

The choice of the azimuthal velocity profile at the inlet was less evident. The profiles in Sheen et al. (1996a) show that the r-dependence of this profile at the jet exit changes with the amount of swirl present. For our purposes, however, we wanted to keep the same r-dependence of the azimuthal velocity profile at the inlet for all the considered levels of swirl, or else it would have been difficult to tell whether the vortex breakdown was due to a general increase of the amount of swirl present or to the change of the inlet profile. Guided by the profiles in Sheen et al. (1996a) we chose the r-dependence of the azimuthal inlet velocity to be the same as that in (6), but here the value of C was varied. Although this approximation is somewhat less accurate than for the axial velocity, it is considerably more accurate than the flat profiles used in Cases 1 and 3. Besides, the inlet profile is given at the beginning of the inlet section, which is some distance from the jet exit, and hence the flow may adjust itself to the exact level of swirl present. Moreover, as we shall see in the next section even the moderate change of the inlet profile from a flat profile to one with the r-dependence given by (6) has only a weak effect on the critical degree of swirl, and hence there is little to suggest that fine-tuning the azimuthal inlet profile will change the results appreciably.

At the inlet we specified the velocity profiles, the mass flow, the total enthalpy, the turbulent intensity as well as the turbulent dissipation.

The choice of the outflow boundary condition is of major importance for a flow of the kind considered here (Escudier and Keller, 1985). However, the study aimed at investigating the dependence of the inflow geometry, and hence our aim was to neutralize the influence of the outflow boundary condition as much as possible. To this end, a long channel was used, in which the swirl had decayed to a negligible level at the outlet. At the outlet we only specified a constant pressure. This may have caused unphysical reflections, but these should have been small, due to the low level of swirl at the outlet.

At a late stage in the preparation of the manuscript of this paper the author learned of the possibility of using an absorbing outflow condition for the Navier-Stokes equations (Rudy and Strikwerda, 1980; Rudy and Strikwerda, 1981). This condition seems very natural to use in the present case, and it is likely that by using this condition, we could both have improved the rate of convergence of the solutions and shortened the channel length.

4 Results and Discussion

To compare S, β, and M fairly, they should all depend on the axial Reynolds number in the same way. For that reason we do not compare them directly, but form quantities similar to each of them, but on the form $\mathrm{Re}_\phi/\mathrm{Re}_z$. Such quantities are:

$$S^{1/2} = \frac{\mathrm{Re}_\phi^*}{\mathrm{Re}_z^j} \tag{7}$$

$$\beta = \frac{\mathrm{Re}_\phi}{\mathrm{Re}_z^c} \frac{r_o}{r_i} \tag{8}$$

$$M^{-1/2} = \frac{\mathrm{Re}_\phi}{\mathrm{Re}_z^j} \tag{9}$$

and these are the quantities we compared to each other.

In all our cases we started with an almost swirl-free jet, and gradually increased the swirl. For swirl lower than the critical degree the flow pattern typically looked like a nonswirling jet, whereas there appeared a zone of reversed flow along the symmetry axis once the critical degree of swirl had been exceeded.

We measured all quantities in the chamber at a section 0.005 downstream of the orifice. The characteristic circulation posed a difficulty in that it is not clear what circulation to take as the characteristic one, but we selected the maximum circulation at the section 0.005 downstream of the orifice.

From Table 2 it is evident that the geometry dependence of the critical degree of swirl is considerably less for M than for β, and appreciably less than for S. It is known from Sheen et

Table 2 The critical degree of swirl for the different cases as expressed in the different parameters

	Critical degree of swirl			Re numbers	
	$S^{\frac{1}{2}}$	β	$M^{-\frac{1}{2}}$	Re_z^j	Re_z^c
Case 1	0.695 – 0.700	1.266 – 1.286	0.401 – 0.407	20 300	13 500
Case 2	0.701 – 0.717	1.180 – 1.251	0.372 – 0.391	18 500	12 100
Case 3	0.544 – 0.562	0.327 – 0.353	0.330 – 0.355	23 400	27 300

al. (1996a) and Sarpkaya (1971) that the Reynolds number dependence of the critical degree of swirl is weak for Reynolds numbers above 5000. Therefore the high channel Reynolds number for Case 3 can hardly account for the difference in the critical degree of swirl when expressed in β. We also see that the inlet profile dependence of the critical degree of swirl is too weak to support any reasonable conclusion. It must be noted, however, that whereas the inlet profile in Case 1 and Case 2 only varies moderately, the inlet geometry in Case 3 differs considerably from that in Case 1 and Case 2.

The least sensitive of the dimensionless numbers, M, is a natural parameter to use if the jet aspect of the flow is more dominant than the cylinder pipe flow one. This was the parameter used in (Long, 1961), where it was found that vortices close to the symmetry axis could only exist for $M > M_*$, where M_* was some critical value. Since it has been used frequently in studies of conically self-similar solutions to the Navier-Stokes equations (Shtern and Hussain, 1993; Drazin et al., 1995; and Shtern and Hussain, 1996). The study of conically self-similar solutions is not a vortex breakdown theory, but provides illustrations of these. Indeed, this class of solutions to the Navier-Stokes equations contains solutions resembling both those before and after vortex breakdown, and therefore using these solutions, it may be possible to calculate the conjugate states needed to use Benjamin's theory. In fact, by studying the existence of the different kinds of conically self-similar solutions for various values of M and Re_ϕ one may come some way toward a vortex breakdown criterion. A detailed discussion on this and related issues is found in Shtern and Hussain (1996).

In terms of the parameters in Fig. 1 we have for our CFD simulations that $\mathcal{R}/r_0 \approx 6$. In any case, it is clear that if $\mathcal{R}/r_o \gg 1$ the flow should behave like a jet. Moreover, while it is true that the standard jet theories only treat unconfined flow (or flows bounded by conical surfaces), experimental measurements in Sheen et al. (1996a) show that the degree of swirl required to induce the vortex breakdown is approximately the same for an unconfined case as for a confined case with $\mathcal{R}/r_o \approx 3$. This suggests that, at least for moderately confined cases, such as ours, vortex breakdown can be viewed as a jet phenomenon. Hence, we could have expected that the jet character of the flow would be predominant for the flow case we considered, and that the parameter M would be the best performing. Had we, on the other hand, had that $\mathcal{R}/r_o \approx 1$, jet theory would not have been appropriate, since we essentially would have had a swirling channel flow. For such flows we can expect that the parameter β would have performed considerably better, but further research is needed to settle this question.

5 Conclusions

Numerical simulations of swirling annular jets entering into a cylindrical chamber were performed for various inlet geometries and inlet profiles. The amount of swirl required to reach vortex breakdown, expressed in different commonly used dimensionless numbers, were measured for all cases. In order to study the suitability of the various dimensionless numbers, the amounts of change of the critical degree of swirl as expressed in the various dimensionless numbers were compared to each other. It was found that the degree of swirl needed for vortex breakdown, as expressed in the parameter which is the quotient of the circulation and the average inlet velocity multiplied by the outer radius of the inlet, is considerably more sensitive to variations of the inlet geometry than the corresponding values of the other dimensionless numbers in the study. The least sensitive of the dimensionless numbers is formed as quotient of the axial momentum flux and a characteristic circulation squared. This is the dimensionless number, which from a theoretical point of view seems to be the most appropriate for flows which are dominated by jet-like behavior, and indeed in our case we had a fairly wide channel, for which it seems reasonable to assume that, at least in the vicinity of the inlet, the flow is essentially behaving like a jet.

Acknowledgements

The author is grateful to Lars-Erik Eriksson for providing him with the CFD codes used here and for numerical advice. Thanks are also due to Lennart Löfdahl for reading and commenting on the manuscript. The project originated from Volvo Aero Corporation, where part of this research was conducted, and this exchange between university and industry was financed by the Swedish Network for Applied Mathematics (NTM). This research was partially funded by the Swedish Institute for Applied Mathematics (ITM).

References

Benjamin, T. B., 1962, "Theory of the Vortex Breakdown Phenomenon," *Journal of Fluid Mechanics,* Vol. 14, pp. 593–629.

Drazin, P. G., Banks, W. H. H., and Zaturska, M. B., 1995, "The Development of Long's Vortex," *Journal of Fluid Mechanics,* Vol. 286, pp. 359–377.

Eriksson, L.-E., 1987, "Simulation of Transonic Flow in Radial Compressors," *Computer Methods in Applied Mechanics and Engineering,* Vol. 64, pp. 95–111.

Eriksson, L.-E., 1995, "Development and Validation of Highly Modular Flow Solver Versions in g2dFlow and g3dFlow Series for Compressible Viscous Reacting Flow," Report 9970-1162, Volvo Aero Corporation.

Escudier, M. P., and Keller, J. J., 1985, "Recirculation in Swirling Flow: A Manifestation of Vortex Breakdown," *AIAA Journal,* Vol. 23(1), pp. 111–116.

Goldshtik, M. A., 1979, "On Swirling Jets," *Fluid Dynamics,* Vol. 14, pp. 19–26.

Hall, M. G., 1972, "Vortex Breakdown," *Annular Review of Fluid Mechanics,* Vol. 4, pp. 195–218.

Keller, J. J., Egli, W., and Exley, J., 1985, "Force- and Loss-Free Transitions Between Flow States," *Journal of Applied Mathematics and Physics (ZAMP),* Vol. 36, pp. 854–889.

Lai, Y. L., 1996, "Predictive Capabilities of Turbulence Models for a Confined Swirling Flow," *AIAA Journal,* Vol. 34(8), pp. 1743–1745.

Larsson, J., 1996, "Numerical Simulation of Turbine Blade Heat Transfer," Thesis for the Degree of Licenciate of Engineering 96/4, Chalmers University of Technology.

Leibovich, S., 1984, "Vortex Stability and Breakdown: Survey and Extension," *AIAA Journal,* Vol. 22, pp. 1192–1206.

Loitsyanskii, L. G., 1953, "Propagation of a Swirling Jet in Unbounded Space Filled with the Same Fluid," *Prikl. Matem. Mekhan.,* Vol. 17, pp. 3–16.

Long, R. R., 1961, "A Vortex in an Infinite Viscous Fluid," *Journal of Fluid Mechanics,* Vol. 11, pp. 611–624.

Rudy, D. H., and Strikwerda, J. C., 1980, "A Nonreflecting Outflow Boundary Condition for Subsonic Navier-Stokes Calculations," *Journal of Computational Physics,* Vol. 36, pp. 55–70.

Rudy, D. H., and Strikwerda, J. C., 1981, "Boundary Conditions for Subsonic Compressible Navier-Stokes Calculations," *Computers and Fluids,* Vol. 9, pp. 327–338.

Sarpkaya, T., 1971, "Vortex Breakdown in Swirling Conical Flows." *AIAA Journal,* Vol. 9(9), pp. 1792–1799.

Sheen, H. J., Chen, W. J., and Jeng, S. Y., 1996a, "Recirculation Zones of Unconfined and Confined Annular Swirling Jets," *AIAA Journal,* Vol. 34(3), pp. 572–580.

Sheen, H. J., Chen, W. J., Jeng, S. Y., and Huang, T. L., 1996b, "Correlation of Swirl Number for a Radial-Type Swirl Generator," *Experimental Thermal and Fluid Science,* Vol. 12, pp. 444–451.

Shtern, V., and Hussain, F., 1993, "Hysteresis in a Swirling Jet as a Model Tornado," *The Physics of Fluids A,* Vol. 5(9), pp. 2183–2195.

Shtern, V., and Hussain, F., 1996, "Hysteresis in Swirling Jets," *Journal of Fluid Mechanics,* Vol. 309, pp. 1–44.

R. M. S. M. Schulkes
Principal Scientist.

Trygve Rinde
Process Engineer.

Ole Harald Utvik
Process Engineer.

Norsk Hydro ASA,
Research Centre Porsgrunn,
N-3091 Porsgrunn, Norway

Pipe Flow With Radial Inflow: Experimental and Modeling Work

In this paper results are presented from experiments in which the pressure loss in single-phase pipe flow is studied when radial inflow occurs. Experiments have been carried out with pipes which have different perforation geometries so as to be able to investigate the effect of perforation geometry on the pressure loss. Data analysis of these experiments, as well as analysis of experiments carried out by other groups, yields a pressure loss model which accurately describes pressure losses in single-phase pipe flow with radial inflow through perforations in the pipe wall. The experimental data is subsequently used to establish a numerical value of a parameter which is used in a model description. This leads to the formulation of an effective friction factor for pipe flow with radial inflow.

1 Introduction

The pressure loss in perforated pipes where fluid flows into the pipe through the perforations have a number of important engineering applications. One of these applications arises in the oil industry where oil may be extracted from a reservoir by means of a perforated pipe which is inserted into the reservoir. In recent years, it has become common to drill long (>1 km), horizontal wells so as to optimize production from long, flat (thickness 10–15 m) oil reservoirs. Such reservoirs could not be exploited economically until recently. Problems with wells, which have such a long production part, are partly related to the fact that the pressure drop along the length of the well may be of the same order of magnitude as the under-pressure required to get oil out of the reservoir. This is in particular the case when the permeability of the reservoir formation is large. In such situations, the pressure difference between the well and the reservoir increases significantly as one moves from the closed-end to the production-end of the well. A consequence of this may be that the production profile can be severely skewed with significantly more oil being extracted from the reservoir at the production-end than at the closed-end of the well. This, in turn, can lead to the early breakthrough of water or gas with the associated drop in revenues. It is clearly imperative to be able to predict the pressure drop in a production well accurately so as to optimize production from a given reservoir.

The pressure loss in single-phase pipe flow has been studied extensively. The detailed experiments of Schlichting (1936), among many others, lead to the well-known Moody-chart (Moody, 1947). More recent experiments (Perry et al., 1969) have studied effects of the wall roughness on the pressure gradient. These and numerous other experiments have yielded pressure drop correlations where the frictional pressure drop is expressed in terms of the Darcy-Weisbach equation

$$\Delta p = f \frac{L}{D} \frac{1}{2} \rho u^2, \tag{1.1}$$

in which f is the friction factor, L the pipe length, D the pipe diameter, ρ the fluid density, and u the mean fluid velocity. A large number of implicit and explicit expressions exist for the friction factor f (Haaland, 1983).

While the pressure drop in the case of fully-developed pipe flow is well-known, the effect of radially in- or outflowing fluid on the pressure losses is less well understood. The reason for this is that with radial inflow, the axial pipe flow is under continuous development: fully developed turbulent flow does not occur anywhere in the pipe when radial inflow occurs. The development of the velocity profile and the pressure variation in a porous tube with uniform injection of air through the tube wall have been studied by Olsen and Eckert (1966). The measurements of the friction factor showed that the friction factor decreased linearly as a function of the ratio of radial velocity to mean axial velocity. Experiments in the same vein (Aggarwal et al., 1972) showed that radial outflow leads to an increase in the friction factor. More recently, Ouyang et al. (1996) analyzed data from large-scale experiments and found, in accordance with Olsen and Eckert (1966), that the friction factor decreased for increasing radial flow velocities. Ouyang et al. (1996) found that the decrease in the friction factor was only dependent on the Reynolds number of the flow through the perforations. Somewhat surprisingly, the decrease was not found to depend on the axial flow conditions. Recent experiments (Yuan et al., 1996) yielded a number of correlations for pipe flow with radial inflow. These experiments proceed along the lines of the experiments presented in this paper but the data analysis differs on fundamental points. As will be shown in this paper, by properly scaling the results, the data from different experiments show clear patterns which allows very simple and transparent correlations to be obtained. The experiments of Su and Gudmundsson (1995) (see also Su, 1996) are similar to the experiments presented in this paper. However, once again the data analysis obscures some of the patterns which can be obtained from the experimental data. The experiments presented in the present paper are an extension of the results reported by Schulkes and Utvik (1998). Differences between the present experiments and those of Schulkes and Utvik (1998) pertain to the experimental setup and perforation geometry of the pipe.

In this paper, results are presented from experiments of pipe flow with radial inflow. The aim of the experiments was to determine the pressure loss in pipe flow with radial inflow and establish accurate and simple models which can be used to predict the pressure loss in such systems. The paper is organized as follows. We start with theoretical considerations concerning the effect on the pressure profile of radial inflow. A one-dimensional model is derived which takes into account radial inflow effects. This is followed by a discussion of the experimental setup. A detailed data analysis is then presented in which it is

Contributed by the Fluids Engineering Division for publication in the JOURNAL OF FLUIDS ENGINEERING. Manuscript received by the Fluids Engineering Division January 20, 1998; revised manuscript received October 5, 1998. Associate Technical Editor: D. R. Williams.

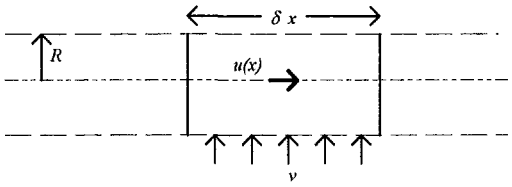

Fig. 1 Schematic diagram of pipe flow with radial inflow

shown that results obtained under widely different experimental conditions have a similar structure. It is also shown that the experimental results agree well with the anticipated theoretical behaviour. Finally, an expression for an effective friction factor is presented which accounts for radial inflow effects in pipe flow.

2 Theoretical Considerations

Consider a pipe with an internal diameter equal to D. Fluid with a density ρ and a viscosity μ flows along the axis of the pipe. It is assumed that the pipe wall is porous and that through the pores fluid with the same physical properties enters the pipe. Details of the flow field near the porous walls are exceedingly complicated and our aim is not to model these local features. Instead, we take a one-dimensional view of the problem, aiming to parameterise the complicating three-dimensional flow structures close to the porous wall. Hence, let $u(x)$ denote the mean velocity in a pipe segment of length δx as shown in Fig. 1. The rate of change of momentum in the segment (that is, the momentum flowing out of the segment minus the momentum flowing into the segment) is equal to

$$\frac{d}{dt}(\delta m \cdot u) = \frac{\partial}{\partial t}(\rho u)\delta x \pi R^2 + \frac{\partial}{\partial x}(\rho u^2)\delta x \pi R^2 + \delta M_{xr}, \quad (2.1)$$

in which δM_{xr} denotes the change in x-momentum due to radially in-flowing fluid. Let Φ denote the fraction of the pipe wall which is perforated. The total area of the perforations in the segment δx is then equal to $\Phi \cdot \delta x \cdot 2\pi R$. If the velocity of the fluid which flows into the pipe through the pores is equal to v, then the mass flow rate through the pores is equal to $\rho v \cdot 2\pi R \Phi \delta x$. This momentum is carried in the x-direction with a velocity which is a fraction of the mean axial velocity u, λu say, where $\lambda \ll 1$. An actual estimate of the parameter λ is difficult to give since it is likely to depend on the local flow structure in/near the wall boundary layer as well as on the ratio of the radial and axial velocities. The above considerations lead to the following expression for the change in x-momentum due to radial inflow of fluid

$$\delta M_{xr} = -2\pi R \lambda \Phi \rho u v \cdot \delta x. \quad (2.2)$$

The reason for the negative sign on the right-hand side of (2.2) is the fact that there is only radial inflow and no radial outflow of momentum. The change in x-momentum in the segment δx is equal to the forces exerted on the segment δx by the fluid, thus

$$\frac{d}{dt}(\delta m \cdot u) = -\frac{\partial p}{\partial x}\pi R^2 \delta x - 2\pi R \tau_w \delta x, \quad (2.3)$$

in which $p(x)$ denotes the pressure and τ_w denotes the wall shear stress. The wall shear stress can be expressed in terms of the mean velocity in the pipe via

$$\tau_w = \tfrac{1}{8}\rho f u^2 \quad (2.4)$$

in which f denotes the friction factor which is a function of the Reynolds number and the wall roughness. Combining (2.1)–(2.4) it follows that a force balance in the segment δx yields the equation

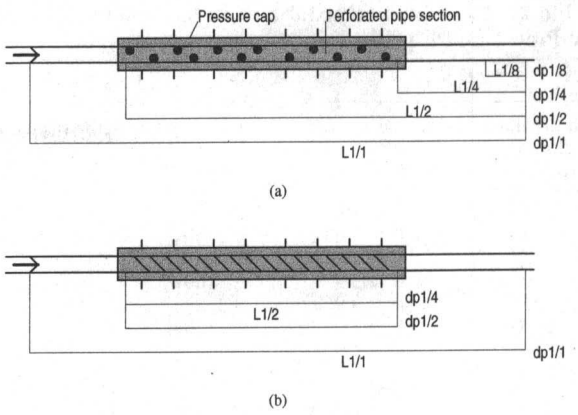

Fig. 2 Schematic diagram of the experimental setup in the cases of experiments with Pipe 1 (*a*) and Pipe 2 (*b*)

$$\frac{\partial}{\partial t}(\rho u) + \frac{\partial}{\partial x}(\rho u^2) - \frac{2\lambda\Phi}{R}\rho u v = -\frac{\partial p}{\partial x} - \frac{f}{2D}\rho u^2, \quad (2.5)$$

in which D denotes the diameter of the pipe. As stated above, the parameter λ is difficult to quantify theoretically. The experiments described below are essentially aimed at determining λ.

3 Experimental Setup

The experiments were performed with two different types of commercially available pipes which are used in actual oil production. Pipe 1 (a HALLIBURTON liner) is a perforated steel pipe (64 perforations per meter, diameter of each perforation is 9.5 mm) with an inner diameter of 0.16 m and a perforated length of 6 m. Pipe 2 (a wire-wrapped CONSLOT screen) is a pipe geometry which is constructed by wrapping a triangular wire around supporting rods which lie in a circular formation along the axis of the pipe. The base of the triangular wire is directed outwards and is typically in the order of 3–4 mm wide. The spacing between the wire-wrappings is 150 μm. The inner diameter of this pipe is 0.15 m while the length of the tested pipe was 8.15 m.

The experimental setup is described elsewhere in some detail (Schulkes and Utvik 1998; Schulkes et al., 1997). The position of the differential pressure transducers differed somewhat between Pipe 1 and Pipe 2. Figure 2 shows the arrangements of the pressure transducers and in Table 1 the distances between the pressure transducers are listed.

In all the experiments, the pressure cells were calibrated to measure in different ranges so as to give the most accurate result. The accuracy of the pressure cells is 0.2 percent of full range. Water flow rates were controlled using manual regulating valves and the accuracy with which the flow rates could be controlled was 0.5 percent of the volume flow rate.

4 Experimental Results

The experimental procedure consists of two parts: a first part without radial inflow to establish the friction factor of the pipe and a second part where radial inflow effects are studied. We begin with a discussion of the experiments in which there was

Table 1 Distances between pressure transducers for the two pipes used in the experiments

Pipe 1	Pipe 2
DP1/8: $L_{1/8}$ = 0.55 m	DP1/4: $L_{1/2}$ = 8.33 m
DP1/4: $L_{1/4}$ = 1.15 m	DP1/2: $L_{1/2}$ = 8.33 m
DP1/2: $L_{1/2}$ = 7.52 m	DP1/1: $L_{1/1}$ = 9.53 m
DP1/1: $L_{1/1}$ = 9.60 m	

Table 2 Experimental axial and radial volume flow rates for Pipe 1 and Pipe 2

Pipe 1		Pipe 2	
Axial volume flow Q (m^3hr^{-1})	Radial volume flow $\hat{q}$ (m^3hr^{-1}/m)	Axial volume flow Q (m^3hr^{-1})	Radial volume flow $\hat{q}$ (m^3hr^{-1}/m)
50	$0 \rightarrow 3.9$	25	$0 \rightarrow 2.8$
75	$0 \rightarrow 3.9$	50	$0 \rightarrow 2.8$
100	$0 \rightarrow 3.9$	75	$0 \rightarrow 3.4$
150	$0 \rightarrow 3.9$	100	$0 \rightarrow 2.5$
175	$0 \rightarrow 3.9$	125	$0 \rightarrow 3.4$
200	$0 \rightarrow 3.9$	150	$0 \rightarrow 2.7$

no radial inflow. The experimental set-up allowed us to determine the pressure drop in the smooth pipe sections upstream and down-stream from the perforated section as well as in the perforated section. The experiments show, as expected, a definite increase in the pressure drop per meter in the perforated section. When the friction factor is calculated we find that the variation with the Reynolds number is as shown in figures 3(a, b) for Pipes 1 and 2, respectively. In the same figure we have plotted the value of the friction factor as calculated using Haaland's equation (Haaland, 1983)

$$f = \left[1.8 \log \left(\frac{6.9}{\mathrm{Re}} + \left(\frac{\epsilon}{3.7D} \right)^{1.11} \right) \right]^{-2}, \qquad (4.1)$$

with a roughness of $\epsilon = 10^{-5}$ m for Pipe 1 and $\epsilon = 1.5 \times 10^{-3}$ m for Pipe 2. In the above equation, Re denotes the Reynolds number of the axial flow, based on the pipe diameter D. We observe that the experimental data follows the Haaland-curve quite well. The calculated roughness for Pipe 1 is surprisingly low given a perforation density of 64 holes per meter. As anticipated, the roughness of Pipe 2 is significantly larger than that of Pipe 1. The error analysis as presented in the appendix shows that the errors in the friction factors were less than 2 percent for both pipes.

We next turn our attention to the experiments with radial inflow. In these experiments a given axial volume flow, Q, is specified and the radial volume flow, q, is increased stepwise. Table 2 lists the axial and radial volume flow rates which were investigated for Pipe 1 and Pipe 2. In Table 2, $\hat{q}$ denotes the radial volume flow per unit length, that is $\hat{q} = q/L$ where L denotes the length of the perforated pipe section.

The essential aim of the experiments presented here is to determine a modification to the friction factor such that radial inflow effects can be taken into account. As the basis of the friction pressure drop computations it is beneficial to be able to use existing friction factors for pipe flow without radial inflow. In this way we naturally build on existing knowledge while extending it to take into account radial inflow effects. Thus, we use Eq. (1.1) as the starting point for the frictional pressure loss computation. The axial velocity u is constant when no radial inflow occurs, so that, given the friction factor f, the pressure drop can be computed using (1.1). When radial inflow occurs, the axial velocity u is not constant so that (1.1) can not be used directly. However, if we know the variation in u as a function of the axial length, one can approximate the frictional pressure drop via

$$\Delta p_f = \frac{\rho}{2D} \int_0^L f(u) u^2 dl. \qquad (4.2)$$

It is, however, important to realize the restrictions of the pressure loss estimate as in (4.2). The friction factor in the integral is the friction factor which is derived from fully developed turbulent flow experiments without radial inflow (as in Fig. 3). However, when radial inflow occurs, the flow field in the pipe is under continuous development and can not be assumed to have a fully developed turbulent structure anywhere in the pipe. Therefore, (4.2) must be regarded as a first approximation to the frictional pressure drop when radial inflow occurs.

As in some previous experiments (Su and Gudmundsson, 1995; Schulkes and Utvik, 1998), the total pressure drop in a pipe with radial inflow is decomposed into three terms: a friction loss term (Δp_f) based on the assumption of fully developed turbulent flow (Eq. (4.2)), a pressure loss term associated with momentum increases (Δp_a) and a term which is essentially a correction to the friction term (Δp_c). Thus,

$$\Delta p = \Delta p_f + \Delta p_a + \Delta p_c. \qquad (4.3)$$

Note that the correction term Δp_c is intimately related to the third term on the left hand side in Eq. (2.5). The exact relation between Δp_c and this term will be established later. The pressure loss associated with accelerating the fluid in the pipe is simply given by

$$\Delta p_a = \rho(u(L)^2 - u(0)^2), \qquad (4.4)$$

in which $u(0)$ and $u(L)$ denote the velocity at the start and end of the perforated section, respectively.

In order to determine the correction term Δp_c, the friction and acceleration pressure losses are subtracted from the measured pressure drop (Δp_m). The results is scaled with the friction pressure loss Δp_f in order to be able to compare the results from different experiments. Plotting now $\Delta p_c/\Delta p_f = (\Delta p_m - \Delta p_f - \Delta p_a)/\Delta p_f$ versus the flux ratio $\hat{q}/Q$, we obtain the results as shown in figures 4(a, b) for Pipe 1 and Pipe 2 respectively. In the figures all the data points from the experiments are used and two things are clear. First of all, we observe that results

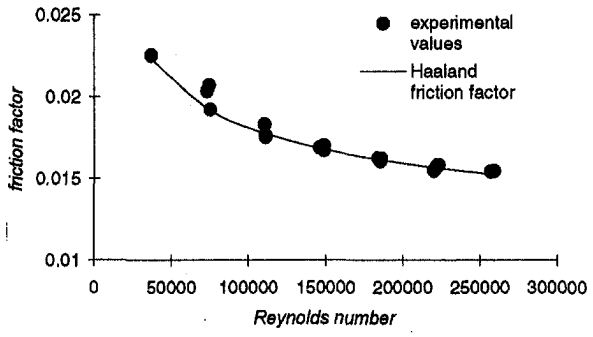

Fig. 3(a)

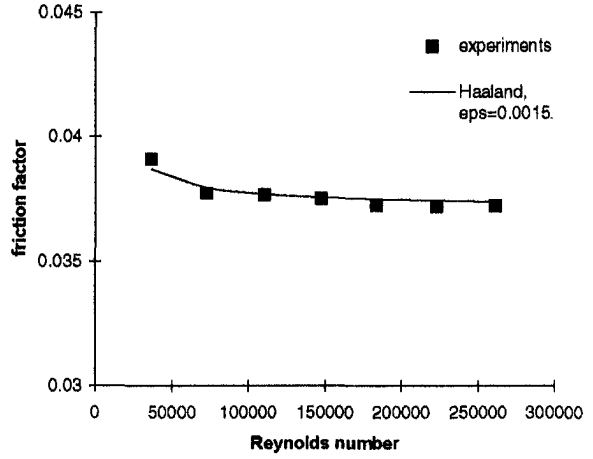

Fig. 3(b)

Fig. 3 A plot of the friction factor as a function of the Reynolds number for Pipe 1 (a) and Pipe 2(b)

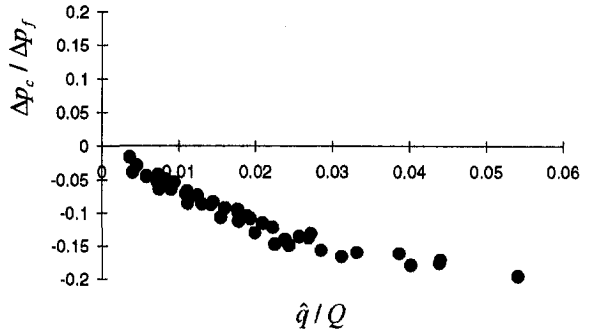

Fig. 4(a)

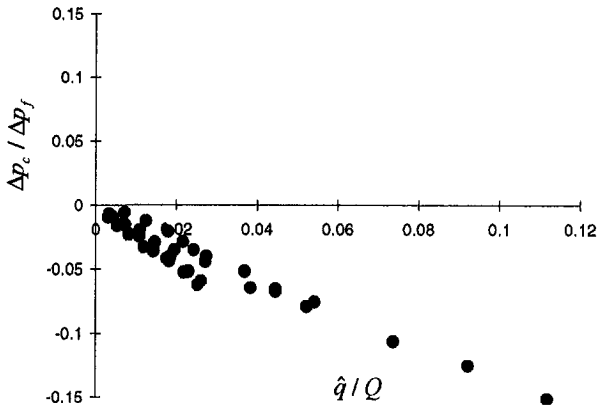

Fig. 4(b)

Fig. 4 A curve of $\Delta p_c / \Delta p_f$ versus the flux ratio $\hat{q}/Q$ for the experiments with Pipe 1 (a) and Pipe 2 (b)

from different experiment collapse onto a well-defined line. Second, we see that the line passes through the origin. The fact that the lines in Fig. 4 passes through the origin is as anticipated: in the limit $\hat{q}/Q \to 0$ we have $\Delta p_a \to 0$ and the total measured pressure loss Δp_m is given by the frictional pressure loss in fully developed turbulent flow, that is Δp_f.

The trends observed in the experiments are qualitatively the same as those from the earlier experiments of Olsen and Eckert (1966), Yuan et al. (1996), and Schulkes and Utvik (1998): for small values of the flux ratio the correction term Δp_c is negative. This implies that computation of the frictional pressure drop on the basis of (4.2) leads to an over-estimate of the actual frictional pressure drop.

5 Comparison Between Different Experiments

It is interesting to see if it is possible to establish a relationship between the present experimental results and similar experiments carried out by Su and Gudmundsson (1995) and Schulkes and Utvik (1998). Additional experimental investigations exist (e.g., Olsen and Eckert, 1966; Ouyang et al., 1996; Yuan et al., 1996) but the data supplied in the papers describing these experiments is insufficient to perform an analysis which is similar to that carried out in the previous section.

In the present experiments as well as those by Su and Gudmundsson (1995) and Schulkes and Utvik (1998) it was found that Δp decreases with increasing values of the flux ratio. A detailed analysis of the data shows that in all the experiments one can approximate the correction term via

$$\Delta p_c = -\alpha D \Delta p_f \times \frac{\hat{q}}{Q}, \qquad (5.1)$$

in which α is an experimentally determined parameter and Δp_f is as calculated in Eq. (4.2). It turns out that the parameter α is fairly constant for a large range of different pipe geometries.

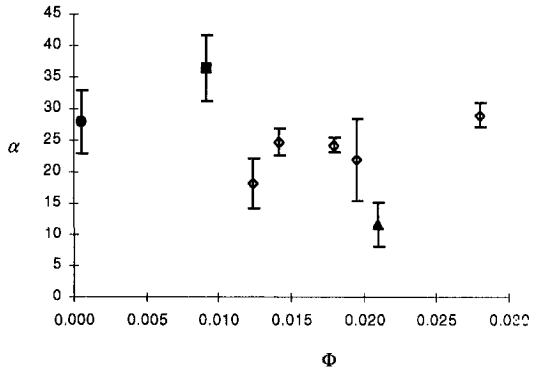

Fig. 5 A plot of the parameter α as defined in Eq. (3.1.1) as a function of perforated area fraction Φ. The different symbols correspond to the experiments of Schulkes and Utvik (1998) (●), the experiments with Pipe 1 (■), the experiments with Pipe 2 (▲), and the experiments of Su and Gudmundsson (1995) (◇). The error bars indicate the experimental uncertainties.

In Fig. 5 we have plotted the value of α as a function of the perforated area fraction Φ for the experiments of Schulkes and Utvik (1998), the present experiments and for the experiments of Su and Gudmundsson (1995). The size of the error bars in Fig. 5 is related to the envelope within which the data points as in Fig. 4 lie.

Figure 5 indicates that the correction term Δp_c is smaller in the case of the pipes with a large wall roughness (like Pipe 2) than with the perforated smooth pipes. In Fig. 5 it is seen that while there is a fair degree of scatter, it is interesting that the quantity α is fairly constant for large ranges in the value of Φ. From the experiments we find that $\alpha = 26.1 \pm 7.6$ for the perforated pipes. For the rather special geometry of Pipe 2, the value of α is significantly lower. We can conclude that with the experiments considered until now, the total pressure drop in a perforated pipe with radial inflow can be approximated by

$$\Delta p = \Delta p_f \times \left(1 - \alpha D \frac{\hat{q}}{Q}\right) + \Delta p_a, \qquad (5.2)$$

where Δp_f is as computed in (4.2).

At least some of the scatter in Fig. 5 will be due to the fact that the values of α were obtained from experiments with vastly different geometrical properties as seen in Table 3. In addition, the experimental error in determining Δp_c may be significant, in particular for low values of the volume flux ratio $\hat{q}/Q$. However, the error analysis as given in the appendix shows that for the largest values of the volume flow ratio, the error in Δp is of the order of 10 percent. It is in particular these large volume flow ratios which are used to determine the coefficient α.

6 Discussion

The experiments of pipe flow with radial inflow have lead to the pressure loss Eq. (5.2). In Section 2 we established the

Table 3 Geometrical properties pipes in four different sets of experiments

Experiment	Pipe diameter (m)	Pipe length (m)	Φ
Pipe 1	0.16	6	9.1×10^{-3}
Pipe 2	0.16	8.15	2.1×10^{-2}
Schulkes and Utvik (1998)	0.15	8.3	5.4×10^{-4}
Su and Gudmundsson (1995)	0.022	0.9	1.4×10^{-2}–2.8×10^{-2}

theoretical model given by Eq. (2.5) which contained an unknown parameter λ which was related to the rate at which radial momentum was carried in the axial direction. Now it will be shown what the relation between the parameters α and λ is.

Assuming steady state, it follows that upon integration, Eq. (2.5) becomes

$$\int_0^L -\frac{\partial p}{\partial l}\,dl = \Delta p = \Delta p_f + \Delta p_a - \frac{4\lambda\Phi\rho}{D}\int_0^L vu dl. \quad (6.1)$$

Equating the expressions for Δp in Eqs. (5.2) and (6.1), it follows that

$$\Delta p_f + \Delta p_a - \frac{4\lambda\Phi\rho}{D}\int_0^L vu dl = \Delta p_f \times \left(1 - \alpha D\frac{\hat{q}}{Q}\right) + \Delta p_a, \quad (6.2)$$

from which one finds immediately that

$$\frac{\alpha D\hat{q}}{Q}\Delta p_f = \frac{4\lambda\Phi\rho}{D}\int_0^L vu dl. \quad (6.3)$$

We now note that $Q = \pi R^2 u(0)$ and $\hat{q} = \pi D\Phi v$ where the radial velocity v is assumed to be constant. Substituting this into (6.3) and using the definition of Δp_f as given in (4.2), the following expression for λ is readily found

$$\lambda = \frac{\alpha}{2u(0)}\int_0^L f(u)u^2 dl \Big/ \int_0^L u dl. \quad (6.4)$$

Table 2 shows that the axial volume flow changes at most 10% due to radial inflow in the case for the experiments with the lowest axial flow rates. For experiments with higher axial flow rates the relative change of the axial flow rate is significantly less than 10 percent. This observation allows us to simplify expression (6.4) by taking the velocity u to be constant as a first approximation, that is $u = u(0)$. It follows immediately that

$$\lambda = \frac{\alpha}{2} f, \quad (6.5)$$

showing that the parameter λ is directly proportional to the friction factor. While this was hard to anticipate without experimental knowledge, the relation (6.4) is in line with physical expectations. Namely, that the rate at which radial momentum is carried in the axial direction should be proportional to the friction factor, which in turn is related to the flow structure near the porous pipe wall, is no real surprise.

For perforated pipe walls it was shown in the previous section that $\alpha \approx 26.1$. Together with variations in the friction factor as shown in Fig. 3, it follows that λ lies in the range $0.2 \leq \lambda \leq 0.25$ for Reynolds numbers exceeding 5×10^4. For very rough pipe walls, like in the case of Pipe 2, it is found that $\lambda \approx 0.2$. This suggests that the rate at which radial momentum is carried in the axial direction is fairly constant over a large range of Reynolds numbers and for vastly different pipe geometries. It is also important to note that $\lambda < 1$ which is in agreement with the arguments leading to the introduction of λ (see Section 2).

Using (6.5) and (2.5) it is now possible to define an effective friction factor for the case of pipe flow with radial inflow. Namely, Eq. (2.5) can be written as

$$\frac{\partial}{\partial t}(\rho u) + \frac{\partial}{\partial x}(\rho u^2) = -\frac{\partial p}{\partial x} - \frac{\tilde{f}}{2D}\rho u^2, \quad (6.6)$$

in which

$$\tilde{f} = f \times \left[1 - 4\alpha\Phi\frac{v}{u}\right] \quad (6.7)$$

denotes the effective friction factor for the case of pipe flow with radial inflow. Equation (6.7) shows that radial inflow leads to a reduction in the friction factor. It should be stressed that Eq. (6.7) is valid, provided the velocity ratio $v/u \ll 1$. Schulkes and Utvik (1998) showed experimentally that a rather abrupt change from "lubrication" to "obstruction" occurs when $v/u \approx 1$.

It is instructive to estimate the volume flux ratio for which the correction term Δp_c is significant. Using Eq. (5.2), it is immediately clear that the correction term can not be neglected when

$$\frac{\alpha D\hat{q}}{Q} \approx 1. \quad (6.8)$$

For a perforated section of length L in which a significant fraction of the liquid enters the pipe through the perforations, we have $\hat{q} = q/L \approx Q/L$. Using this approximation together with (6.8) shows that the correction term cannot be neglected when

$$\frac{\alpha D}{L} \approx 1. \quad (6.9)$$

Equation (6.9) shows that the correction term Δp_c is important only when the length of the perforated section is approximately αD, or less. This implies that only in cases where the axial flow increases significantly over a length of approximately 30 D, the correction term is expected to influence the frictional pressure loss significantly.

7 Conclusions

In this paper, results from experiments have been presented which show how the frictional pressure loss is influenced by radial inflow. Data analysis shows that the radial inflow leads to a reduction in the frictional pressure loss as compared with the case where frictional pressure losses are computed on the basis of fully developed turbulent flow. The same trend in the data was observed in experiments with large differences in perforation geometry and experimental scale. The experimental results lead to a correction term to the frictional pressure loss which takes into account changes due to radial inflow effects.

The experimental results can be adequately explained by a one-dimensional model for pipe flow with radial inflow. The model contains one parameter which is related to the rate at which the radial momentum is transferred in the axial direction. This parameter is subsequently determined experimentally. Finally, a correction to the usual friction factor is established which takes into account radial inflow effects.

Acknowledgment

The work presented in this paper was carried out as part of a co-operative research program on horizontal production wells by Saga, Statoil and Norsk Hydro.

References

Aggarwal, J. K., Hollingsworth, M. A., and Mayhew, Y. R., 1972, "Experimental Friction Factors for Turbulent Flow with Suction in a Porous Tube," *International Journal of Heat and Mass Transfer*, Vol. 15, pp. 1585–1602.

Haaland, S. E., 1983, "Simple and Explicit Formulas for the Friction Factor is Turbulent Pipe Flow," ASME JOURNAL OF FLUIDS ENGINEERING, Vol. 105, pp. 89–90.

Moody, L. M., 1947, "An Approximate Formula for Pipe Friction Factors," *Trans. ASME*, Vol. 69, p. 1005.

Olsen, R. M., and Eckert, E. R. G., 1966, "Experimental Studies of Turbulent Flow in a Porous Circular Tube with Uniform Fluid Injection Through the Tube Wall," ASME *Journal of Applied Mechanics*, pp. 7–17.

Ouyang, L-B., Arbabi, S., and Aziz, K., 1996, "General Wellbore Flow Model for Horizontal, Vertical and Slanted Well Completions," Paper 36608, Society of Petroleum Engineers Conference, CO, Oct., pp. 1–13.

Perry, A. E., Schofield, W. H., and Joubert, P. N., 1969, "Rough Wall Turbulent Boundary Layers," *Journal of Fluid Mechanics* Vol. 37(2).

Schlichting, H., 1936, "Experimental Investigation of the Problem of Surface Roughness," NACA TM-823.

Schulkes, R., and Utvik, O. H., 1998, "Pressure Drop in Perforated Pipe with Radial Inflow: Single-Phase Flow," *Society of Petroleum Eengineers Journal,* Mar., pp. 77–85.

Schulkes, R., Utvik, O. H., and Rinde, T., 1997, "Pressure Drop in Horizontal Wells: Multiphase Flow with Radial Inflow," 8th International Conference Multiphase '97, A. P. Burns, ed., pp. 45–55. Mechanical Engineering Publications Limited, London.

Su, Z., and Gudmundsson, J. S, 1995, "Pressure Drop in Partly Perforated Pipes," *Report of Department of Petroleum Engineering and Applied Geophysics,* University of Trondheim—The Norwegian Institute of Technology (NTH).

Su, Z., 1996, "Pressure Drop in Perforated Pipes for Horizontal Wells," PhD thesis University of Trondheim—The Norwegian Institute of Technology (NTH).

Yuan, H. Sarica, C., and Brill, J. P., 1996, "Effect of Perforation Density on Single Phase Liquid Flow Behaviour in Horizontal Wells," Paper 37109 Society of Petroleum Engineers Conference, Calgary, Nov., pp. 603–612.

APPENDIX

Error Analysis

In the experiments without radial inflow (Figs. 3(a, b)) the friction factors were determined experimentally on the basis of the measured pressure drop. Equation (1.1) was used to evaluate the friction factor, given Δp and u. Standard error analysis methods show that the uncertainty δf in the friction factor f is related to the uncertainties in the measured pressure drop and the volume flow rates via

$$\frac{\delta f}{f} = \frac{\delta \Delta p_m}{\Delta p_m} + 2\,\frac{\delta Q}{Q}\,. \tag{A.1}$$

The accuracy of the pressure transducers and volume flow control is such that $\delta \Delta p_m / \Delta p_m = 0.002$ and $\delta Q/Q = 0.005$. These values, together with (A.1) imply that the uncertainty in the friction factors is equal to $\delta f = 0.012 f$.

For the experiments with radial inflow (Figs. 4(a, b)) the relative error in the correction pressure term Δp_c is given by

$$\frac{\delta \Delta p_c}{\Delta p_c} = \frac{\delta \Delta p_m + \delta \Delta p_f + \delta \Delta p_a}{\Delta p_c}\,. \tag{A.2}$$

Defining the flux ratio $\phi = q/Q$, we find that the error in volume flow control implies $\delta\phi/\phi = 0.005$. In Schulkes and Utvik (1998) it was shown that $\delta \Delta p_a$, $\delta \Delta p_f \propto \rho u^2 \cdot \delta\phi/\phi$ so that the magnitude of the numerator in (A.2) is approximately equal to $0.002\ \Delta p_m + 2 \times 0.005 \rho u^2 \approx 0.01 \rho u^2$. Using this result in (A.2) and using the expression for Δp_c as given in Eq. (5.1), it follows that

$$\frac{\delta \Delta p_c}{\Delta p_c} \approx \frac{0.02}{\alpha L f} \times \frac{Q}{\hat{q}}\,, \tag{A.3}$$

where Δp_f has been estimated using (1.1). Clearly, as the flux ratio $\hat{q}/Q$ decreases, the realtive error in Δp_c increases. For example, at $\hat{q}/Q = 0.05$ we have $\delta \Delta p_c = 0.1\ \Delta p_c$ while at $\hat{q}/Q = 0.01$ the relative error has increased to $\delta \Delta p_c = 0.5\ \Delta p_c$.

On the Suitability of the Low Mach Number Assumption in the Modeling of the Damage Induced by Pressure Transients in Piping Systems

Felipe B. Freitas Rachid
Department Head.

Heraldo S. Costa Mattos
Professor.

Laboratory of Theoretical and Applied Mechanics,
Department of Mechanical Engineering,
Universidade Federal Fluminense,
24.210-240 Niterói RJ, Brazil

One-dimensional models for predicting the damage induced by pressure transients in piping systems conveying liquids have been proposed and analysed recently. However, such works have been concerned mainly with the adequacy of the constitutive equations adopted for different pipe materials and with the numerical techniques used for approximating the solution of the resulting mathematical problems. In the present paper the suitability of the simplifying low Mach number assumption adopted in the modeling is investigated. The analysis is carried out based on the eigenvalue problem associated to the governing equations, without appealing to any specific mechanical behavior of the pipe material. Numerical results obtained for the most used pipe materials show that this simplifying assumption is adequate for metallic tubes, but may fail when plastic tubes are considered.

1 Introduction

Piping systems used for liquid transmission are present in several important installations ranging from simple water supply lines to complex cooling systems of thermo-hydraulic power plants. Whatever the application is, accurate predictions of transient pressures and flow the system might be subjected to is of great concern when one wishes to ensure a proper design and consequently an adequate and safe operation.

On the way to accurately model the pressure pulse propagation in liquid-filled compliant piping systems, considerable progress has been achieved in the past few years. The traditional uncoupled waterhammer model with linear-elastic pipewall behavior (Streeter and Wylie, 1993) has given rise to sophisticated models. These models account for complex phenomena such as the anelastic behavior of the pipewalls and the fluid-structure interaction (fsi) between fluid and pipe motions (A-Monein and Chang, 1978 and 1979; Wiggert, 1986, Wiggert et al., 1987; and Freitas Rachid et al., 1990 and 1991).

Recently, however, a more realistic description of the physical problem, which accounts for the pipe material degradation phenomenon (damage), has been considered by Freitas Rachid and Costa Mattos (1994) and Freitas Rachid et al. (1994). With the incorporation of the damageable behavior of the pipewall into the pressure transient model, the primary concern of the analysis becomes the lifetime and structural failure prediction of the piping. Thus, the main objective of these works was to present a mechanical model, together with a numerical method, to predict the structural failure of the pipelines induced by severe pressure transients. This goal was achieved by incorporating the progressive failure of the pipewalls (induced by anelastic strains) in the analysis by means of a continuum damage theory. An example of application is reported in Freitas Rachid et al. (1994) which illustrates the capability of the theory in predicting piping structural failure generated by accidental pressure transients in stainless steel tubes of nuclear power plants. To reduce the complexity of the governing equations, the axial fluid-structure interaction was not taken into account in that work.

The incorporation of coupled fsi mechanisms along with the damageable anelastic behavior of the pipewalls into a pressure transient model leads to a more complex and also nonlinear set of equations. To allow the use of feasible numerical solutions of the model while retaining its main features, it is essential that simplifying assumptions be investigated.

This paper presents a theoretical analysis about the applicability of the well-known low Mach number assumption (LMN) to a coupled fsi model which accounts for the damage of the pipewalls. Since this failure approach leads to local wavespeeds that can assume values as small as the liquid flow velocity (due to damage evolution), a question arises as to the suitability of the LMN assumption as a simplifying hypothesis.

The quantitative analysis presented herein, based on the eigenvalues associated with the governing equations of the model, is conducted within a very general context, which encompasses a great number of pipe wall mechanical behaviors (such as viscoelastic and elasto-viscoplastic) without appealling to any specific form of these mechanical responses. Hence, it can be applied to the most used pipe materials: mild steel, cast iron, copper, polyethylene, etc. Numerical results show that the LMN assumption is adequate for metallic tubes, but may fail whether plastic tubes are considered.

2 Modeling

In the next paragraphs a pressure transient model will be presented which accounts for the damage of the pipe material without appealing to any specific representation of the pipe material behavior. First, the basic equations are presented and then a set of constitutive relations for the pipe material. Finally, the model is obtained by combining these two set of equations.

2.1 Basic Equations. Because piping systems used for liquid transmission are composed of slender members, pressure transients in fluid-filled compliant pipes are commonly described by means of longitudinal wave theories (Lighthill, 1978; Streeter and Wylie, 1993). So, consider an inviscid transient

Contributed by the Fluids Engineering Division for publication in the JOURNAL OF FLUIDS ENGINEERING. Manuscript received by the Fluids Engineering Division February 24, 1997; revised manuscript received August 10, 1998. Associate Technical Editor: M. S. Cramer.

one-dimensional compressible flow confined into a thin-walled pipe (inside radius R and wall thickness e) for which both fluid and pipewall motions are relevant. Under these assumptions, the equations of conservation of mass and momentum for fluid flow in Eulerian coordinates and in the absence of gravitational effects are:

$$\frac{\partial}{\partial t}(\varrho A) + \frac{\partial}{\partial x}(\varrho A v) = 0;$$

$$\frac{\partial}{\partial t}(\varrho A) + \frac{\partial}{\partial x}(\varrho A v^2) + A\frac{\partial P}{\partial x} = 0 \qquad (1a, b)$$

In the above equations, P, v, ϱ, and A are functions of the spatial position x along the pipe and the time t. They represent, respectively, the fluid pressure, the axial fluid velocity, the fluid density and the cross-sectional area of the fluid inside the pipe.

The underlying assumptions of small deformations and axisymmetrical plane-stress distribution in the pipewall are assumed to hold for the pipe, so that its motion is described by the following momentum equations (in the axial and radial directions),

$$\varrho_t \frac{\partial \dot{u}}{\partial t} - \frac{\partial \sigma_x}{\partial x} = 0; \quad \varrho_t \,\mathrm{Re}\,\frac{\partial \dot{w}}{\partial t} - RP + \sigma_\theta e = 0 \qquad (2a, b)$$

together with the strain-displacement relationships $\epsilon_x = \partial u/\partial x$ and $\epsilon_\theta = w/R$. In these equations, the nonvanishing stress components (σ_x and σ_θ) and the pipewall displacements (u and w), in the axial and circumferential directions, are functions of x and t while ϱ_t designates the pipe density. The superimposed dot stands for partial derivative with respect to time.

To fully couple the fluid and pipe problems, the kinematic relationship between cross-sectional area variation and pipewall deformation, $A = A_f(1 + \epsilon_\theta)^2$, and the equation of state for the liquid, $\varrho = \varrho_f \exp(P/K)$, are considered. Here, K stands for the isoentropic bulk modulus of the liquid (assumed to be constant) and the subscript f is used to designate the undisturbed state from which variations in A and ϱ are measured.

If besides the small deformation assumption ($\epsilon_\theta \ll 1$) we only admit slightly compressible fluid flows ($P/K \ll 1$), the expressions for A and ϱ can be linearized and the term ϱA approximated by:

$$\varrho A = \varrho_f A_f(1 + P/K + 2\epsilon_\theta) \qquad (3)$$

Equations (1-2-3) are the basic equations for the problem. To these, one must add the constitutive equations which will describe the behavior of the pipe material.

2.2 Constitutive Relations. The set of constitutive relations considered in this work encompasses a great number of constitutive models for damageable anelastic solids found in the literature. It also allows the description of different mechanical responses (elastic, plastic, viscoplastic, viscoelastic . . .) presented by metallic and polymeric materials, at high and room temperatures (Lemaitre and Chaboche, 1990). In these theories auxiliary variables are introduced to account for the different dissipative mechanisms involved in the deformation process. Since it is not the goal of this paper to perform a detailed discussion of the different possible approaches in continuum damage mechanics, only the basic features of the theory are presented.

Continuum damage mechanics uses a phenomenological approach to model the effect of geometric discontinuities induced by the deformation process on the macroscopic behavior of a structure. In these theories, an auxiliary variable D related to the damage process (the definition and physical interpretation of such variable may vary from one model to the other) is taken into account in the constitutive description of the material in order to characterize its mechanical failure. Generally, no matter what physical interpretation the damage variable assumes, the following convention is adopted: D is such that $D \in [0, 1]$; if $D = 0$, the material is locally undamaged and, if $D = 1$, the material locally looses its mechanical strength. In practice, for the sake of security, the local failure is considered when the variable D reaches a critical value D_{cr} such that $0 < D_{cr} < 1$. This approach has been used with success in several problems of mechanics to describe the failure induced by creep as well as low and high cycle fatigue (Lemaitre, 1984).

The isothermal evolution of an anelastic damageable solid under small deformations is supposed to be completely characterized by the strain tensor $\boldsymbol{\epsilon}$, the anelastic strain tensor $\boldsymbol{\epsilon}^a$, a damage variable D, and a set of auxiliary variables used to describe other possible dissipative mechanisms (such as hardening phenomena, viscous effect and ageing, for example). The choice of these auxiliary variables will depend upon the degree of detail desired in the modelling and so they can vary from problem to problem. Particular sets of viscoelastic and elasto-viscoplastic constitutive equations taking into account these auxiliary variables can be found in Freitas Rachid et al. (1992 and 1994) for polyethylene and AISI 316L stainless steel materials. For the sake of simplicity, only one abstract scalar auxiliary variable denoted as β will be considered to describe the other dissipative mechanisms.

A general set of constitutive equations for damageable materials is then given by:

$$\boldsymbol{\sigma} = (1 - D)\mathbf{C}(\boldsymbol{\epsilon} - \boldsymbol{\epsilon}^a); \quad \dot{\boldsymbol{\epsilon}}^a = \mathbf{g};$$
$$\dot{D} = h; \quad \dot{\beta} = l \qquad (4a, b, c, d)$$

In the above equations, $\boldsymbol{\sigma}$ is the stress tensor and $\mathbf{C}$ represents the tensor of elasticity,

$$\mathbf{C} = \frac{\nu E}{(1 - 2\nu)(1 + \nu)}\mathbf{1}_2 \otimes \mathbf{1}_2 + \frac{E}{(1 + \nu)}\mathbf{1}_4$$

in which E and ν stand for the Young's modulus and Poisson's ratio whereas $\mathbf{1}_2$ and $\mathbf{1}_4$ represent, respectively, the rank two and rank four identity tensors. Equations ($4b$, c, d) represent the evolution equations for the internal variables $\boldsymbol{\epsilon}^a$, D and β and are expressed here by generic functions $\mathbf{g}$, h, and l of the arguments ($\boldsymbol{\sigma}$, $\boldsymbol{\epsilon}^a$, D, β). These functions may assume different forms according to the type of material behavior considered.

In using the constitutive equations (4) the following assumptions are considered:

1) the total deformation $\boldsymbol{\epsilon}$ of the material response is made up of two additive parcels, one elastic ($\boldsymbol{\epsilon} - \boldsymbol{\epsilon}^a$) and the other anelastic $\boldsymbol{\epsilon}^a$;

2) the elastic response is isotropic and is only affected by the damage through an apparent reduction of the Young's modulus;

3) h is a nonnegative function ($h \geq 0$) to give the damage evolution an irreversible character.

Damage models which are encompassed by this abstract constitutive theory are generally called local damage models. For a comprehensive bibliography and review about these theories the reader is referred to the works of Kachanov (1986), Burr et al. (1995), and de Vree et al. (1995). Particular forms of the functions $\mathbf{g}$, h and l for typical pipewall materials can be found in Lemaitre (1990).

2.3 Mathematical Model. In the particular case of a thin-walled pipe under a plane-stress state, σ_x and σ_θ stand for the principal stresses. Associated to them there will exist only two independent components ϵ_x^a and ϵ_θ^a of the anelastic strain tensor $\boldsymbol{\epsilon}^a$ and the constitutive equations can be reduced to:

$$\sigma_x = \frac{E(1 - D)}{(1 - \nu^2)}\{\epsilon_x + \nu\epsilon_\theta - \epsilon_x^a - \nu\epsilon_\theta^a\};$$

$$\sigma_\theta = \frac{E(1 - D)}{(1 - \nu^2)}\{\epsilon_\theta + \nu\epsilon_x - \epsilon_\theta^a - \nu\epsilon_x^a\} \qquad (5a, b)$$

$$\dot{\epsilon}_x^a = g_x; \quad \dot{\epsilon}_\theta^a = g_\theta; \quad \dot{D} = h; \quad \dot{\beta} = l \quad (6a, b, c, d)$$

where g_x, g_θ, h and l are functions of the arguments (σ_x, σ_θ, ϵ_x^a, ϵ_θ^a, D, β).

Neglecting the radial pipewall inertia term in (2b), it comes out that $\sigma_\theta = (RP)/e$ and the system of equations (1-2-3) along with (5-6) can be reduced to eight equations and eight unknowns (P, v, u, σ_x, ϵ_x^a, ϵ_θ^a, D, β).

After performing some algebraic manipulations in (5) and changing the variables (P, v, σ_x) to (α, η, ϕ) with the transformations,

$$\alpha = 1 + \left(\frac{1}{K} + \frac{2R}{eE(1-D)}\right)P - \frac{2v}{E(1-D)}\sigma_x + 2\epsilon_\theta^a \quad (7a)$$

$$\eta = \alpha v \quad (7b)$$

$$\phi = \frac{R\nu}{eE(1-D)}P - \frac{1}{E(1-D)}\sigma_x \quad (7c)$$

the resulting system of equations can be written in the appropriate form of conservation law:

$$\frac{\partial \mathbf{U}}{\partial t} + \frac{\partial}{\partial x}(\mathbf{F}(\mathbf{U})) - \mathbf{W}(\mathbf{U}) = \mathbf{0} \quad (8)$$

In the above equation $\mathbf{U} \in \mathbb{R}^8$ (the eight dimensional Euclidean vector space), $\mathbf{U} = (\alpha, \eta, u, \phi, \epsilon_x^a, \epsilon_\theta^a, D, \beta)^T$, is the conserved quantity, $\mathbf{F}(\mathbf{U})$, $\mathbf{F} : \mathbb{R}^8 \to \mathbb{R}^8$, and $\mathbf{W}(\mathbf{U})$, $\mathbf{W} : \mathbb{R}^8 \to \mathbb{R}^8$, represent, respectively, the flux and source/sink terms which have the following form:

$$\mathbf{F} = (\eta, \eta^2/\alpha + c_f^2(\alpha - 1 - 2\epsilon_\theta^a - 2\nu\phi),$$
$$c_t^2\phi + c_f^2\xi\nu(2\nu\phi - (\alpha - 1 - 2\epsilon_\theta^a)), u, 0, 0, 0, 0)^T$$
$$\mathbf{W} = (0, 0, 0, g_x, g_x, g_\theta, h, l)^T$$

where $c_f = c_f(D)$, $c_t = c_t(D)$ and ξ are given by:

$$c_f^2 = \frac{K^*}{\varrho_f}; \quad c_t^2 = \frac{E(1-D)}{\varrho_t};$$

$$\xi = \frac{R\varrho_f}{e\varrho_t}; \quad K^* = \frac{K}{1 + \dfrac{2RK(1-\nu^2)}{eE(1-D)}}$$

The pressure transient model characterized by (8) is a coupled fsi model since it accounts for not only the existence but also the interaction of axial pressure waves in fluid flow and axial stress waves in the pipewall. By looking at the $\mathbf{F}$ components, one can see that the main coupling mechanism of these waves is due to the Poisson's ratio ν. Setting artificially $\nu = 0$ in $\mathbf{F}$, the equations that describe the fluid and pipe motions are decoupled. The parameters c_f and c_t are the wavespeeds with which disturbances propagate in the liquid and tube media as if no axial fluid-structure interaction took place.

From the practical viewpoint, the model described by (8), along with appropriate boundary and initial conditions, can be used as a promising tool in predicting piping rupture induced by internal pressure transients. After choosing an adequate time of simulation $t = T$, the piping sections susceptible to failure may be readily identified by the damage distribution $D(x, t = T)$, $x \in [0, L]$, along the pipe length L. If a local failure occurs for $t = t^* \in [0, T]$, then the first sections of the piping to fail will be characterized by the set $\{x^* \in [0, L] \,|\, D\,(x = x^*, t = t^*) \geq D_{cr}\}$.

Because of the highly nonlinear behavior of $\mathbf{F}$, it is not an easy task to construct a numerical solution for (8). Nevertheless, considerable simplification of the $\mathbf{F}$ term (and hence in the method of solution) can be achieved if the additional simplifying LMN assumption is taken into account. The suitability and domain of validity of such a hypothesis is next investigated without appealing to any specific form of the evolution equations or to any particular kind of numerical procedure used to solve (8).

3 Low Mach Number Assumption and Damage Influence on Wavespeeds

The system of nonlinear partial differential equations (8) is of the hyperbolic type since its eigenvalues are all real (although not distinct) and the associated eigenvectors span the eight-dimensional space in which the system is immersed. The eigenvalues related to (8) are defined by (Jeffrey, 1976):

$$\det(\mathbf{H} - \lambda \mathbf{1}_8) = \mathbf{0} \quad (9)$$

where $\mathbf{H} = \mathbf{H}(\mathbf{U}) \equiv \partial\mathbf{F}/\partial\mathbf{U}$ and $\mathbf{1}_8$ are the 8×8 jacobian and identity matrices, respectively. Besides playing an important role in the classification of the system, the knowledge of the eigenvalues is particularly useful when one wishes to get physical information concerning the phenomenon being modelled, such as the speeds of wave propagation.

Since $v = \eta/\alpha$, it results from (9) that the eigenvalues satisfy the following expression:

$$\lambda^4 P(\lambda; D, v) = 0 \Leftrightarrow \lambda^4 = 0 \quad \text{or} \quad P(\lambda; D, v) = 0 \quad (10)$$

where $P(\lambda; D, v)$ is a polynomial of the fourth degree in λ which depends on D (damage variable) and v (liquid velocity):

$$P(\lambda; D, v) = \lambda^4 - 2v\lambda^3 + (v^2 - \zeta^2)\lambda^2 + (\zeta^2 - c_f^2)(2v\lambda - v^2) + c_f^2 c_t^2$$

with

$$c_f = c_f(D), \quad c_t = c_t(D) \quad \text{and} \quad \zeta^2 = c_f^2 + c_t^2 + 2\nu^2\xi c_f^2.$$

The eigenvalues given by $\lambda = 0$ are associated to the stationary wavespeeds whereas those given by $P(\lambda; D, v) = 0$ are related to the nonstationary wavespeeds.

Because the relevant physical information is related to the nonstationary wavespeeds, from now on we shall concentrate on the roots of $P(\lambda; D, v)$. Let us designate $\lambda_i(D, v)$, $i = 1, \ldots, 4$, as being the roots of $P(\lambda; D, v) = 0$. So, $\lambda_i(D, v)$ are the nonstationary relative speeds with which the waves propagate in both the fluid and the pipewalls. Since there are no simple analytical expressions for $\lambda_i(D, v)$, $i = 1, \ldots, 4$, let us assume that $\lambda_{i=1}$ and $\lambda_{i=2}$ correspond, respectively, to the wavespeeds with which pressure pulses propagate backward and forward in relation to the liquid flow and that $\lambda_{i=3}$ and $\lambda_{i=4}$ represent, respectively, the wavespeeds with which axial stress pulses travel backward and forward in the pipewalls.

The dependence of $\lambda_i(D, v)$ with respect to v is due to the presence of the convective terms which appear in the continuity and fluid momentum equations. Depending on the situation, convective terms may or may not play a dominant role on the fluid flow equations. The physical parameter that characterizes the importance of these terms is the Mach number M which, in this context, can be expressed as:

$$M = |2v/(\lambda_{i=1} - \lambda_{i=2})| \quad (11)$$

Convective terms may be neglected under small-Mach-number conditions only. In such situations, it can be shown that the eigenvalues no longer depend on v and are given by very simple expressions $\lambda_{oi}(D) = \lambda_i(D, v = 0)$:

$$\lambda_{oi=1,2} = \mp a_f(D) \quad \text{and} \quad \lambda_{oi=3,4} = \mp a_t(D) \quad (12)$$

where

$$a_f^2 = \{\tfrac{1}{2}(\zeta^2 - (\zeta^4 - 4c_f^2c_t^2)^{1/2})\} \quad \text{and}$$

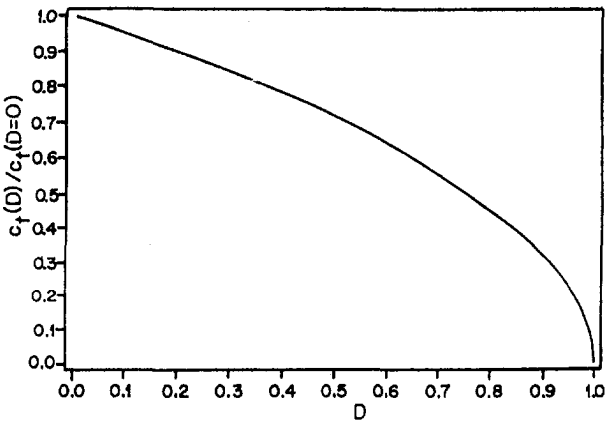

Fig. 1 Damage influence on $c_f(D)$

$$a_i^2 = \{\tfrac{1}{2}(\zeta^2 + (\zeta^4 - 4c_f^2c_i^2)^{1/2})\}.$$

The new feature of the pressure transient models which account for damageable behavior of the pipewalls is that the local wavespeeds depend on the damage variable. As can be seen from (10), the $\lambda_i(D, \upsilon)$ dependence on D is due to $c_f(D)$ and $c_i(D)$. Moreover, due to the damage irreversible character ($\dot{D} \geq 0$), it can be seen that $c_f(D)$ and $c_i(D)$ are nonincreasing functions of the damage (see Figs. 1 and 2). In the limit case, when $D \to 1$, then $c_f \to 0$ and $c_i \to 0$, and consequently $\lambda_i(D, \upsilon) \to 0$. In other words, it means that at the onset of piping rupture disturbances are no longer propagated in either the liquid or the pipe and $M \to \infty$.

This fact has a straightforward implication on the modeling of the problem when one wishes to consider the additional and simplifying LMN assumption. Since during the failure process wavespeeds can assume values near the liquid velocity, a question arises about its suitability. In other words, can convective terms be neglected while considering models which account for the damageable behavior of the pipe material? Before answering precisely this question, it is interesting to note that according to the theoretical model, an initial subsonic fluid flow may become supersonic due to the damage evolution itself. However, as it will be seen later, it seems that this phenomenon is not likely to take place in practice.

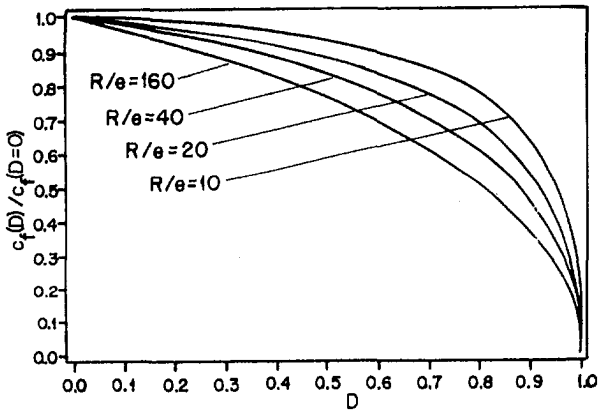

Fig. 2(a)

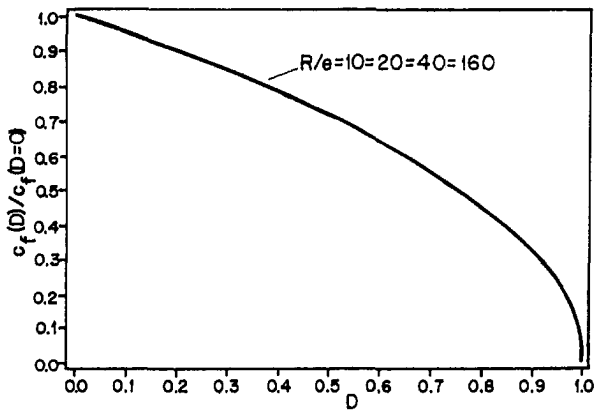

Fig. 2(b)

Fig. 2 Damage influence on $c_f(D)$ for steel (a) and polyethylene (b) water-filled tubes

Table 1 Physical properties of pipe materials

Material	Properties		
	E (GPa)	ν	ϱ_t (kg/m^3)
Steel	210	0.27	7800
Copper	115	0.34	8800
Cast Iron	80	0.25	2700
Polyethylene	0.9	0.46	1000

4 Numerical Results

The qualitative analysis presented in the previous section suggests that the LMN assumption fails whether models with damage are to be considered. However, to properly verify its suitability it is essential to consider practical information concerning the real piping systems used for liquid transmission. To begin with, we shall carry out the forthcoming analysis based on some of the most used pipe materials (mild steel, cast iron, copper and polyethylene). The physical properties used for these materials are presented in Table 1.

Since eigenvalues and hence wavespeeds depend on D through $c_f(D)$ and $c_i(D)$, it is interesting to know first how the damage affects these parameters. The damage influence on $c_i(D)$ can be illustrated for any pipe material by a single curve if we plot $c_i(D)/c_i(D = 0)$, instead of $c_i(D)$, against D. Such a plot is displayed in Fig. 1 where it can be seen that significant reduction of $c_i(D)$, in comparison to this same parameter in an undamaged material, is observed for high values of damage only.

To illustrate the influence of D on $c_f(D)$, we shall suppose pipes are filled with water ($K = 2.2$ GPa and $\varrho_f = 1000$ kg/m^3). In contrast to previous plot, even restricting the analysis to water-filled pipes there is not a single representation of $c_f(D)/c_f(D = 0)$ versus D. In addition to being dependent on the pipe material, this relation is also dependent on the radius-to-thickness ratio R/e. Figure 2 presents the behavior of $c_f(D)/c_f(D = 0)$ against D for steel (Fig. 2(a)) and polyethylene (Fig. 2(b)) tubes, by considering different R/e ratios (R/e = 10, 20, 40, 160). Similar behavior to that observed in Fig. 2(a) is found for materials with high Young modulus such as cast iron and copper. The same is true whether the connection is now made between Fig. 2(b) and materials with low Young modulus. In cases where the behavior of $c_f(D)$ is described by Fig. 2(a), the thinner the tube, the greater is the reduction in c_f for a same damage value. On the other hand, it can be seen in Fig. 2(b) that the $c_f(D)$ behavior is not sensitive to R/e variations for materials which fall within the polyethylene class.

To verify the validity of the LMN assumption for models with damage by means of a quantitative rather than a qualitative analysis, it is still necessary to know the range of values υ may

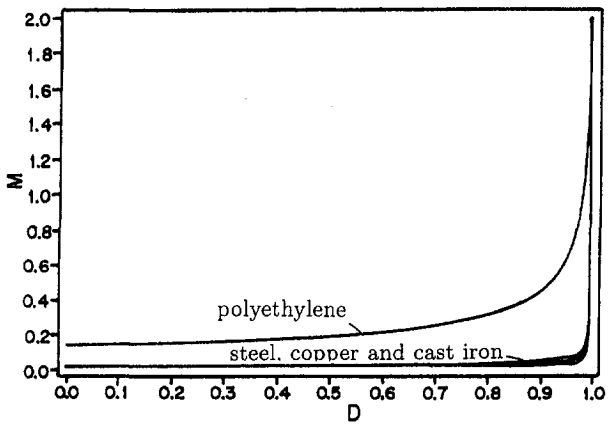

Fig. 3 Mach number versus damage variable for several pipe materials water-filled pipes with $R/e = 40$ and $v = 20$ m/s

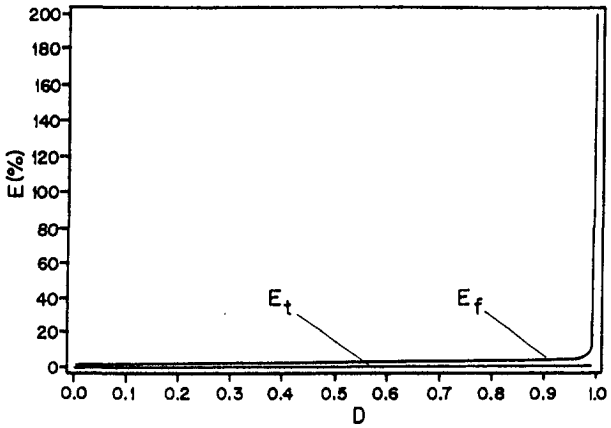

Fig. 4 Relative error of eigenvalues versus damage for steel tubes

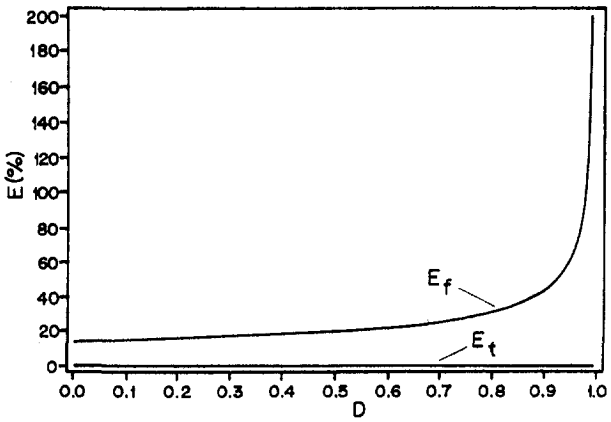

Fig. 5 Relative error of eigenvalues versus damage for polyethylene tubes

assume in practice. In general, piping systems conveying liquids are designed to operate in the range $0.5 < v < 6$ m/s. Under severe transient conditions, however, v may assume values up to three times this upper bound, but rarely exceeds 20 m/s. Since we are interested in the most critical situation, we shall consider $v = 20$ m/s in the subsequent analysis and also assume a radius-to-thickness ratio $R/e = 40$.

The critical damage value D_{cr}, which characterizes the imminent failure (piping rupture in our case), depends on both the history loading and the specific material. Also, it can assume different values in the interval (0, 1). Thus, to investigate the validity of the LMN assumption, it is required that the Mach number dependence on D be analyzed over the whole interval [0, 1).

Based on practical values assumed so far, Fig. 3 shows the Mach number as a function of the damage (Eq. (11)) for several pipe materials. Quite different behavior of M can be identified for the two distinct classes of pipe materials. For steel, copper and cast iron M remains below 0.1 for almost the entire range of D. It allows one to conclude that the LMN approximation is still a good assumption for models with damage, at least for this class of materials.

For polyethylene like tube materials, M does not exceed 0.2 for damage values up to 0.5, but it increases significantly for damage values greater than 0.5. So, for this class of materials, the use of the LMN assumption as a good one is conditioned to the critical damage value of each pipe material. For instance, if D_{cr} were such that $D_{cr} < 0.5$, the LMN approximation could be considered valid. Otherwise, it could not be.

It is important to remark that there exists no physical motivation to associate the violation of the LMN assumption to the imminent failure of the piping. Although it can be used as an ad hoc failure criterion, further investigation is required so that it can be done with confidence.

It is also interesting to note in Fig. 3 that, for both classes of materials, the aforementioned possibility of transition from subsonic to supersonic flow due to damage evolution does not happen in fact. Since $M = 1$ for extremely high values of damage ($D \approx 1$), it is likely that piping rupture occurs before fluid flow becomes supersonic.

Finally, to better quantify the foregoing analysis, we computed the relative error (as a function of damage) that would be committed whether eigenvalues were evaluated with and without the LMN assumption. Defining the relative error E_i between eigenvalues (given by eqs (10) and (12)) as $E_i = |(\lambda_i - \lambda_{oi})/\lambda_{oi}|$, for $i = 1, \ldots, 4$, and noting that $E_1 \cong E_2 = E_f$ and $E_3 \cong E_4 = E_t$, it is possible to speak about relative errors associated to fluid (E_f) and tube (E_t) eigenvalues.

The behavior of the relative errors related to fluid and tube eigenvalues with respect to damage is shown in Figs. 4 and 5, for steel and polyethylene tubes. As expected, E_t is independent of damage and is no greater than 0.1 percent for both pipe materials. On the other hand, E_f is less than 1 percent within the range $0 < D < 0.9$ for steel tubes, but it may reach values up to 40 percent within this same range for polyethylene tubes. So, the results obtained based on the relative error between eigenvalues confirm that the LMN assumption remains valid for models with damage if metallic tubes are considered. However, the same may not be true for plastic tubes made of polyethylene.

5 Concluding Remarks

The validity of the LMN assumption for pressure transients models which account for the damageable behavior of the pipewalls has been investigated by means of an eigenvalue analysis. The results obtained indicate that this simplifying hypothesis is valid for metallic tubes for all range of values the damage may assume. For plastic tubes, however, its domain of validity is conditioned to the critical damage value of each specific pipe material. Since no assumption has been made with regard to the particular forms of the pipewall mechanical behavior, the results obtained herein are valid whatever the expressions adopted for the evolution equations (4b), (4c), and (4d) are.

Acknowledgments

The partial financial support provided by CNPq (Grants 301323/94-1 and 523991/96-7) and FAPERJ (Grant 170279/95) is greatfully acknowledged.

References

A-Moneim, M. T., and Chang, Y. W., 1978, "Comparison of ICEPEL Code Predictions with Straight Flexible Pipe Experiments," *Nuclear Engineering Design,* Vol. 49, pp. 187–196.

A-Moneim, M. T., and Chang, Y. W., 1979, "Comparison of ICEPEL Predictions with Single-Elbow Flexible Piping System Experiments," ASME *Journal of Pressure Vessel Technology,* Vol. 101, pp. 142–148.

Burr, A. F., Hild, F., and Leckie, F. A., 1995, "Micro-mechanics and Continuum Damage Mechanics," *Archives of Applied Mechanics,* Vol. 65, pp. 437–456.

De Vree, J. H. P., Brekelmans, W. A. M., and van Gils, M. A. J., 1995, "Comparison of Nonlocal Approaches in Continuum Damage Mechanics," *Computers & Structures,* Vol. 55, pp. 581–588.

Freitas Rachid, F. B., and Stuckenbruck, S., 1990, "Transients in Liquid and Structure in Viscoelastic Pipes," *BHRA Proc. of the 6th International Conference on Pressure Surges,* pp. 69–84, Cambridge, UK.

Freitas Rachid, F. B., Costa Mattos, H. S., and Stuckenbruck, S., 1991, "Fluid-Structure Interaction in Elasto-Viscoplastic Piping Systems," *Proc. of the 1st ASME/JSME Joint Fluids Engineering Conference,* pp. 65–73, Portland.

Freitas Rachid, F. B., Costa Mattos, H. S., and Stuckenbruck, S., 1992, "Water Hammer in Inelastic Pipes: An Approach via an Internal Variable Constitutive Theory," *Proc. of the International Conference on Unsteady Flow and Fluid Transients,* pp. 63–69, Durham, UK.

Freitas Rachid, F. B., and Costa Mattos, H. S., 1994, "Model for Structural Failure of Elasto-Viscoplastic Pipelines," *Meccanica,* Vol. 29, No. 3, pp. 293–304.

Freitas Rachid, F. B., Costa Mattos, H. S., and Saldanha da Gama, R. M., 1994, "Modelling of Hydraulic Transients in Damageable Elasto-Viscoplastic Piping Systems," *Applied Mathematical Modeling,* Vol. 18, pp. 207–215.

Jeffrey, A., 1976, *Quasilinear Hyperbolic Systems and Waves,* Pitman Publishing, London.

Kachanov, L. M., 1986, *Introduction to Continuum Damage Mechanics,* Martins Nijhoff, Dordecht.

Lemaitre, J., 1984, "How to Use Damage Mechanics," *Nuclear Engineering Design,* Vol. 80, pp. 233–245.

Lemaitre, J., and Chaboche, J. L., 1990, *Mechanics of Solid Materials,* Cambridge University Press, London.

Wiggert, D. C., 1986, "Coupled Transient Flow and Structural Motion in Liquid-Filled Piping Systems: A Survey," ASME Pressure Vessels and Piping Conference, 86-PVP-4, Chicago.

Wiggert, D. C., Hatfield, F. J., and Stuckenbruck, S., 1987, "Analysis of Liquid and Structural Transients in Piping by the Method of Characteristics," ASME JOURNAL OF FLUIDS ENGINEERING, Vol. 109, pp. 161–165.

Wylie, E. B., and Streeter, V. L., 1993, *Fluid Transients in Systems,* Prentice Hall, New Jersey.

Optimization of Trailing Edge Ejection Mixing Losses: A Theoretical and Experimental Study

M. T. Schobeiri
Professor.

K. Pappu
Student.

Turbomachinery Performance Laboratory,
Texas A&M University,
College Station, TX 77843-3123

The aerodynamic effects of trailing edge ejection on mixing losses downstream of cooled gas turbine blades were experimentally investigated and compared with an already existing one-dimensional theory by Schobeiri (1989). The significant parameters determining the mixing losses and, therefore, the efficiency of cooled blades, are the ejection velocity ratio, the cooling mass flow ratio, the temperature ratio, the slot thickness ratio, and the ejection flow angle. To cover a broad range of representative turbine blade geometry and flow deflections, a General Electric power generation gas turbine blade with a high flow deflection and a NASA-turbine blade with intermediate flow deflection and different thickness distributions were experimentally investigated and compared with the existing theory. Comprehensive experimental investigations show that for the ejection velocity ratio $\mu = 1$, the trailing edge ejection reduces the mixing losses downstream of the cooled gas turbine blade to a minimum, which is in agreement with the theory. For the given cooling mass flow ratios that are dictated by the heat transfer requirements, optimum slot thickness to trailing edge thickness ratios are found, which correspond to the minimum mixing loss coefficients. The results allow the turbine aerodynamicist to minimize the mixing losses and to increase the efficiency of cooled gas turbine blades.

Introduction

Increasing the thermal efficiency of aero- and power generation gas turbines requires high turbine inlet temperature. For conventional turbine blade materials, increase of turbine inlet temperature is achieved by cooling the front stages. The required cooling mass flow is injected partially or entirely through the trailing edge slots into the downstream axial gap, where the cooling and main mass flows are mixed. The trailing edge ejection affects the flow regime downstream of the cooled blade, especially the losses associated with the mixing of the cooling mass flow and the main mass flow. The ejection velocity ratio, the cooling mass flow ratio, the slot thickness ratio, the temperature ratio, and the ejection angle affect the mixing losses and therefore the efficiency of cooled blades. Improper selection of these parameters results in higher mixing losses that reduce drastically the efficiency of cooled turbine stage. In this connection, the fundamental question that must be answered is: under which circumstances can the trailing edge ejection reduce the mixing losses and thus improve the efficiency of a cooled gas turbine blade?

There have been several studies dealing with the mechanism of trailing edge mixing. Experimental research work by Prust (1974, 1975) on a two-dimensional turbine stator cascade shows that the trailing edge ejection significantly affects the blade efficiency. Tabakoff and Hamed (1975) investigated the aerodynamic effects of pressure- and suction-surface ejection on the mixing losses and blade efficiency. They varied the location of ejection slots and angles on the suction and pressure surfaces as well as on the trailing edge. Tabakoff and Hamed (1975) found that for the mass flow ratio $\dot{m}_c/\dot{m}_2 > 0.6$ percent, lower total pressure losses are obtained with ejection through the trailing edge slots. In an attempt to better understand the mixing loss phenomenon, Yamamoto et al. (1991) followed the ideas of Tabakoff and Hamed (1975) and performed similar experimental investigations. They varied the location of ejection slots and angles on the suction and pressure surfaces as well as on the trailing edge. Analytical investigations by Schobeiri (1989) identified the significant parameters for determining the criterion for optimization of ejection aerodynamics and mixing losses. A recent study by Bohn et al. (1996) deals with a two-dimensional LDA-experiment and the implementation of its results into a 2-D simulation procedure.

Considering the fundamental question raised above, the purpose of this theoretical and experimental study is to quantify accurately the aerodynamic effects of trailing edge ejection on mixing losses downstream of cooled gas turbine blades. Furthermore, the study exhibits a simple but physically sound aerodynamic tool that enables the turbine designer to take appropriate measures to minimize the trailing edge mixing losses and improve the aerodynamic efficiency of the cooled turbine blade. The present study begins with a theoretical section, where significant parameters determining the mixing losses and, therefore, the efficiency of cooled blades, such as the ejection velocity ratio, the cooling mass flow ratio, the temperature ratio, the slot thickness ratio, and the ejection flow angle, are briefly summarized from Schobeiri (1989). The analytical method exhibits an enhancement of the theory by Schobeiri (1985). To examine the predictive capability of the theory, a comprehensive experimental investigation was conducted and the results are compared with the theory. To cover a broad range of representative turbine blade geometry and flow deflections, a General Electric power generation gas turbine blade with high flow deflection and a NASA-turbine blade with intermediate flow deflection and different thickness distributions were experimentally investigated and compared with the theory.

Theoretical Background

In this section, a brief summary of the final result on calculating the total dissipation due to mixing process is given. The step-

Contributed by the Fluids Engineering Division for publication in the JOURNAL OF FLUIDS ENGINEERING. Manuscript received by the Fluids Engineering Division April 30, 1997; revised manuscript received September 8, 1998. Associate Technical Editor: M. S. Triantafyllou.

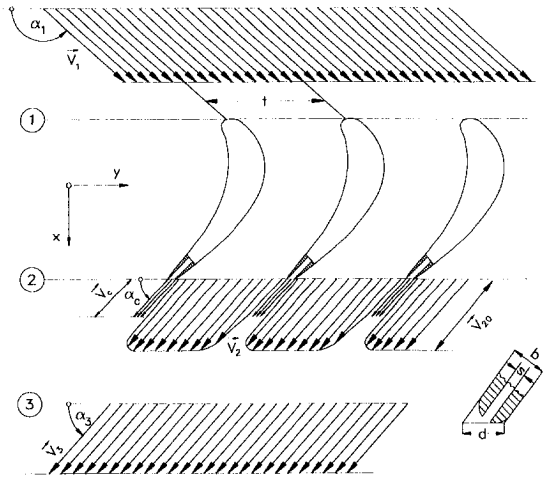

Fig. 1 Trailing edge ejection and mixing downstream of a cooled gas turbine blade

by-step procedure about the derivation is available in Schobeiri (1989). With respect to the exit kinetic energy, the loss coefficient is defined as:

$$\zeta = \frac{\Delta \dot{E}}{\frac{1}{2}\dot{m}_3 V_3^2} \tag{1}$$

where:

$$\Delta \dot{E} = \dot{m}_2\left(\frac{p_{20}}{\rho_2} + \frac{1}{2} V_{20}^2\right) + \dot{m}_c\left(\frac{p_c}{\rho_c} + \frac{1}{2} V_c^2\right) - \dot{m}_3\left(\frac{p_3}{\rho_3} + \frac{1}{2} V_3^2\right) \tag{2}$$

The flow parameters at stations 2 and 3 in the above equation can be calculated using the momentum equations in x- and y-directions and the continuity equation. The details are thoroughly discussed in Schobeiri (1989). Figure 1 shows the flow stations upstream of the blade (station 1), immediately at the trailing edge plane (station 2), and at the mixing plane (station 3). Introducing the mass flow ratios and some auxiliary functions, the loss coefficient is completely described by:

$$\zeta = \frac{G_1^3 - 2RG_1^2G_2 + R^2G_3}{G_1^3} - \cos^2\alpha_3\left[\frac{2G_1^3 - 2RG_2G_1^2 + R^2G_3}{G_1^3} - \frac{G_1G_3}{(G_2 - G_4)^2}\right] \tag{3}$$

where:

$$G_1 = 1 - \Delta^* - D\left(1 - \frac{\sin\alpha_c}{\sin\alpha_2}\mu\tau f\right)$$

$$G_2 = 1 - \Delta^* - \Delta^{**} - D\left[\left(1 - \frac{\sin^2\alpha_c}{\sin^2\alpha_2}\mu^2\tau f\right)\right]$$

$$G_3 = 1 - \Delta^* - D\left[\left(1 - \frac{\sin\alpha_c}{\sin\alpha_2}\mu^3\tau f\right)\right]$$

$$G_4 = \frac{\sin\alpha_c \sin(\alpha_c - \alpha_2)}{\sin^2\alpha_2 \cos\alpha_2}\mu^2\tau f D$$

In Eq. (3) all the significant parameters determining the influence of trailing edge ejection are present. With this relation, it is possible to accurately predict the energy dissipation and mixing losses due to the trailing edge thickness (D), the boundary layer thickness at the trailing edge (Δ^*, Δ^{**}), and the trailing edge ejection (μ, τ, f, R, α_c). To examine the results from Eq. (3), a comprehensive experimental investigation was conducted and the results compared with the theory. As mentioned previously, two representative turbine blades of different geometry and flow deflections were investigated. The first blade was a NASA-turbine blade with intermediate flow deflection. The second one was a General Electric power generation gas turbine blade with high flow deflection. In the following sections, the experimental investigations and the comparison of measurements with theory are presented.

Experimental Investigations

Research Facility. To study the trailing edge ejection aerodynamics, a comprehensive experimental investigation was performed on a large-scale, high-subsonic unsteady turbine cascade research facility at the Turbomachinery Performance Laboratory. Since this facility is described in a recent paper by Schobeiri et al. (1995) in detail, only a brief description of its main components is presented here. The turbine cascade research facility consists of a large centrifugal air supplier, a diffuser, a settling chamber, a nozzle, a turbine cascade test section, and an unsteady wake generator (Fig. 2). For the present steady flow investigations, the wake generator was not in operation. The settling chamber incorporates five equidistantly distributed screens and one honeycomb flow straightener. At the exit of the silence chamber, a nozzle with an area ratio of 6.75:1 is installed that accelerates the flow to the required velocity before entering the test section. With this tunnel configuration, it is possible to achieve a constant mean fluctuation velocity over a wide velocity range. For a nozzle exit velocity of 30 m/s, a

Nomenclature

b = trailing edge thickness (Fig. 1)
$d = b/\sin\alpha_2$ = trailing edge thickness in cascade front (Fig. 1)
D = dimensionless trailing edge thickness, d/t
$f = s/b$ = slot thickness/trailing edge thickness ratio
G_i = auxiliary functions
$\dot{m}$ = mass flow
p = static pressure
$P = p + \rho V^2/2$ = total pressure
$R = \rho_3/\rho_2$ = density ratio
s = slot thickness, surface
t = blade spacing
$\dot{V}$ = velocity vector
$\bar{V}$ = averaged velocity
α = flow angle
δ^*, δ^{**} = displacement, momentum thickness
Δ^*, Δ^{**} = dimensionless displacement (δ^*/t), momentum (δ^{**}/t) thickness
$\mu = \bar{V}_c/V_2$ = velocity ratio
ρ = density
$\tau = T_2/T_c$ = temperature ratio
ζ = loss coefficient
ζ_0 = loss coefficient for no injection ($\mu = 0.0$) case

Indices

c = coolant
P = pressure side
S = suction side
2 = with respect to plane 2 (Fig. 1)
20 = with respect to the potential core
3 = with respect to mixing plane 3 (Fig. 1)
in = inflow
out = outflow

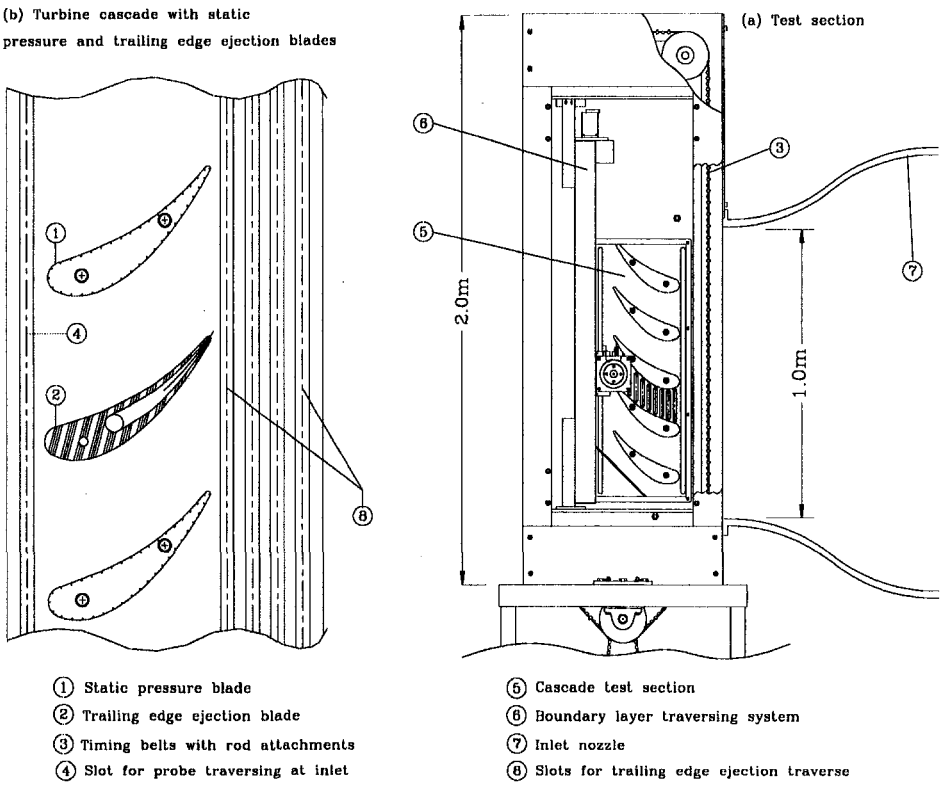

Fig. 2 Turbine cascade flow research facility, test section

turbulent intensity of 0.75 percent was measured (for detailed information see Schobeiri et al. 1995).

The test section has an inlet cross section of 1000×200 mm^2 and can include up to 7 blades with a height of 200 mm and a chord up to 300 mm. The blades are inserted between two vertical plexiglass side walls. One side wall has several slots for the traverse of the probes. For the present investigation, two representative turbine cascade types, each consisting of five blades, were used. This blade number is necessary to establish a full cascade flow periodicity. The first cascade included NASA-turbine blades with intermediate flow deflection (Fig. 3). The geometry of these blades are similar to the SSME (Space Shuttle Main Engine) blades described by Schobeiri et al. (1990). The second turbine cascade incorporated five General Electric blades of high flow deflection. The details about the geometry of these two cascades are shown in Fig. 3. To measure the static pressure distribution for each cascade type, instrumented blades with 40 static pressure ports were manufactured. The ports with a diameter of 0.2 mm are equidistantly distributed on the pressure and suction surfaces

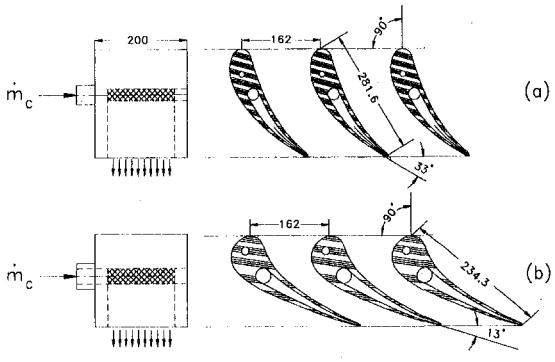

Fig. 3 (a) NASA and (b) GE cascades with internal cavity and ejection slots

along the midsection of the blade. For each cascade type, a special blade with an internal cavity and an external slot is mounted in the middle of the cascade to perform the trailing edge ejection experiments. The internal cavity extends over two-thirds of the blade height and is connected to an external air supplier, whose mass flow can be varied arbitrarily. The cooling air enters the cavity via a pipe perpendicular to the test section side wall. As expected, and confirmed by preliminary measurements, this cooling air inlet configuration with a 90° turn caused a flow non-uniformity inside the cavity and at the exit of the ejection slot. This flow non-uniformity was completely eliminated by inserting a set of three concentric screens inside the cylinder at the cavity inlet (Fig. 3). The velocity traverse at the trailing edge plane in the spanwise direction showed a uniform velocity distribution for a wide range of cooling mass flow ratios $\dot{m}_c/\dot{m}_2$.

A computer-controlled traversing system is used for the traverse of five-hole and X-wire probes. The traversing system is vertically mounted on the test section side wall (Fig. 2). It consists of a slider and lead screw, which is connected to a D.C. stepper motor with an encoder and decoder. The optical encoder provides a continuous feedback to the stepper motor for accurate positioning of the probes. The system is capable of traversing a height of 1200 mm in small steps with a minimum of 2.5 μm.

Instrumentation and Data Acquisition. Filtered air drawn from a medium pressure air line enters a rotameter which is then injected into the blade internal cavity. The measurements were taken for 15 different cooling mass flow ratios ranging from $\dot{m}_c/\dot{m}_2 = 0.0$–$4.0$ percent. The uncertainty in measuring the cooling mass flow was about ± 4.8 percent. Total pressure, static pressure, flow angles, turbulence intensity, Reynolds normal, and shear stresses were measured at the trailing edge plane and at the mixing plane using five-hole and X-wire probes. The x-distance of the trailing edge plane (station 2) and the mixing plane (station 3) are 16 mm and 82 mm, respectively, from the trailing edge. For the pneumatic measurements, a miniature five-hole probe

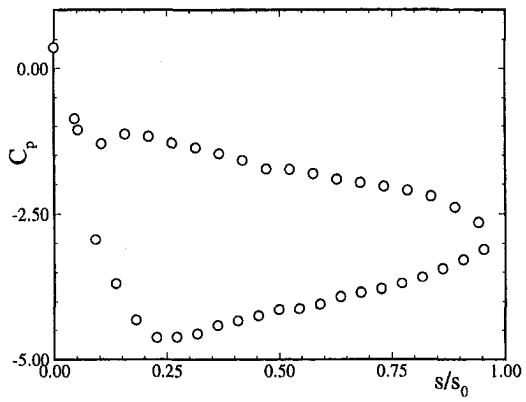

Fig. 4 Pressure distribution at Re_c = 264187

was provided and thoroughly calibrated. For calibration of the five-hole probe, a non-nulling algorithm developed by Wendt and Reichert (1993) was further developed and used that helped in automating the calibration procedure. The pressure from each hole of the five-hole probe was sampled sequentially by a rotary scanner and measured with a high precision differential pressure transducer. The uncertainty in the total pressure measurement was ±1.5 percent. The new method developed by John and Schobeiri (1993) was used for the X-wire calibration. The data acquisition system was controlled by a 486-personal computer that includes a 16 channel, 12-bit analog-digital (A/D) board with 8-channel simultaneous sample and hold.

Results

The discussion of the following results is concentrated on answering the question raised in the Introduction, namely under which circumstances the trailing edge ejection reduces the mixing losses downstream of a cooled turbine blade and, therefore, contributes to the efficiency improvement. As mentioned previously, the trailing edge ejection parameters influencing the mixing pressure loss coefficient ζ are the cooling velocity ratio $\mu = \bar{V}_c/V_2$, the cooling mass flow ratio $\dot{m}_c/\dot{m}_2$, the slot thickness ratio $f = s/b$, and the temperature ratio $\tau = T_c/T_2$. For the NASA cascade, the temperature ratio was $\tau \simeq 1.06$ and the slot thickness ratio was $f = 0.35$, while for the GE cascade $\tau \simeq 1.03$ and $f = 0.33$. For both cascades, the cooling mass flow ratio $\dot{m}_c/\dot{m}_2$ was varied from 0.0 to 0.04, which corresponds to the cooling velocity ratio range of $\mu = \bar{V}_c/V_2 = 0.00-1.40$.

Surface Pressure Distribution. The surface pressure distribution on the NASA blade is presented in this section. The pressure distribution was taken by the above-mentioned 48-port scanivalve. The pressure signals signify the time-averaged pressure because of the internal pneumatic damping effect of the connecting pipes to the transducer. The time-averaged pressure coefficient along the suction and pressure surfaces is shown in Fig. 4. On the suction surface (lower portion), the flow first accelerates sharply, reaches a minimum pressure coefficient at $s/s_0 \approx 0.25$, and then continuously decelerates at a moderate rate until the trailing edge is reached. On the pressure surface, the flow accelerates initially, reaches a minimum pressure coefficient at $s/s_0 \approx 0.1$, and experiences a short deceleration and then accelerates almost continuously at a slower rate. This pressure distribution indicates that the flow on both the surfaces, except for a short distance around $s/s_0 \approx 0.1$, is subjected to a negative pressure gradient until $s/s_0 \approx 0.25$ is reached. Beyond this point, the pressure gradient on the pressure surface remains negative, while on the suction surface, positive pressure gradient prevails.

Total Pressure Distributions. Total pressure, static pressure, and velocity measurements were performed using a five-hole probe. Figure 5 shows that the total pressure distribution traverses in the trailing edge plane, denoted as station 2, for the NASA cascade with an exit flow angle $\alpha_2 = 33°$. In Fig. 5(*a*), the total pressure distribution is plotted for $\mu = 0.0$ and 0.26. For the case of $\mu = 0.0$, a wake is present due to the finite thickness of the trailing edge, which inherently causes total pressure losses. Increasing the cooling velocity ratio to $\mu = 0.26$ resulted in a deeper wake in comparison with the no injection ($\mu = 0.0$) and, consequently, in higher total pressure losses. This phenomenon is explained by the fact that for low velocity ratios, the ejected mass flow (jet) does not have enough momentum to overcome the strong dissipative nature of the wake at the trailing edge. The main mass flow entrains the cooling mass flow resulting in complete dissipation of the energy of the jet and a deeper wake than for the no injection case. This deeper wake results in higher total pressure mixing losses. The cooling velocity ratio $\mu = 0.26$ was chosen for the discussion because it corresponds to the highest mixing loss coefficient, which will be discussed later. A further increase of the velocity ratio causes a continuous reduction of the wake flow zone, resulting in a corresponding reduction of the total pressure losses. Figure 5(*b*) shows the total pressure distribution for velocity ratios of $\mu = 1.01$ and 1.28. As shown for $\mu = 1.01$, the area occupied by the vortical wake flow is distinctively reduced in comparison with the μ-cases presented in Fig. 5(*a*). This indicates that for $\mu > 0.26$, the cooling mass flow with higher momentum is able to sustain and even to compensate the strong dissipative nature of the wake flow. Therefore, the jet is not dissipated completely and accordingly a reduction in total pressure losses can be ob-

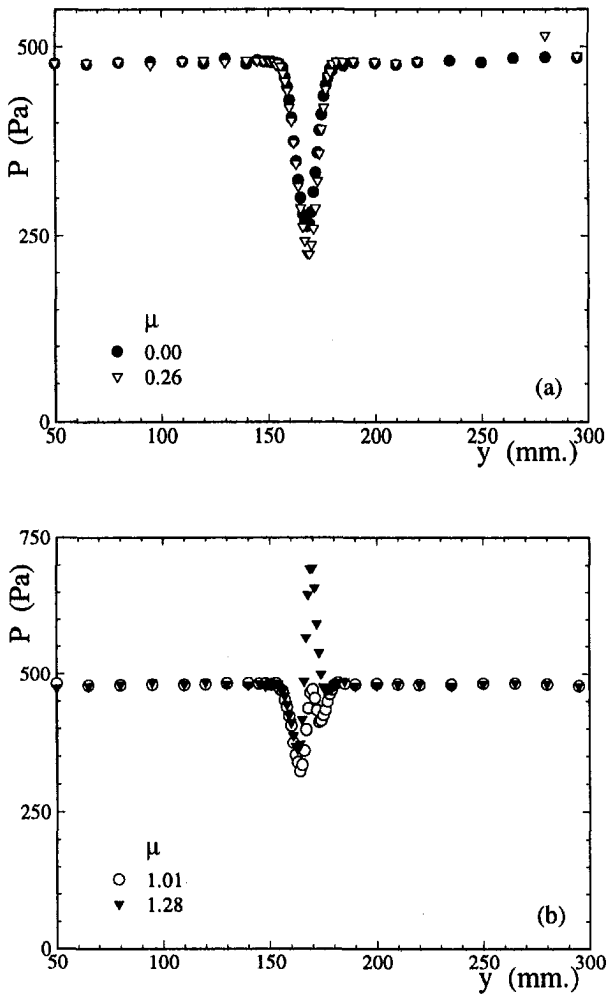

Fig. 5(*a, b*) Total pressure distributions for four representative cooling mass flows for NASA blades

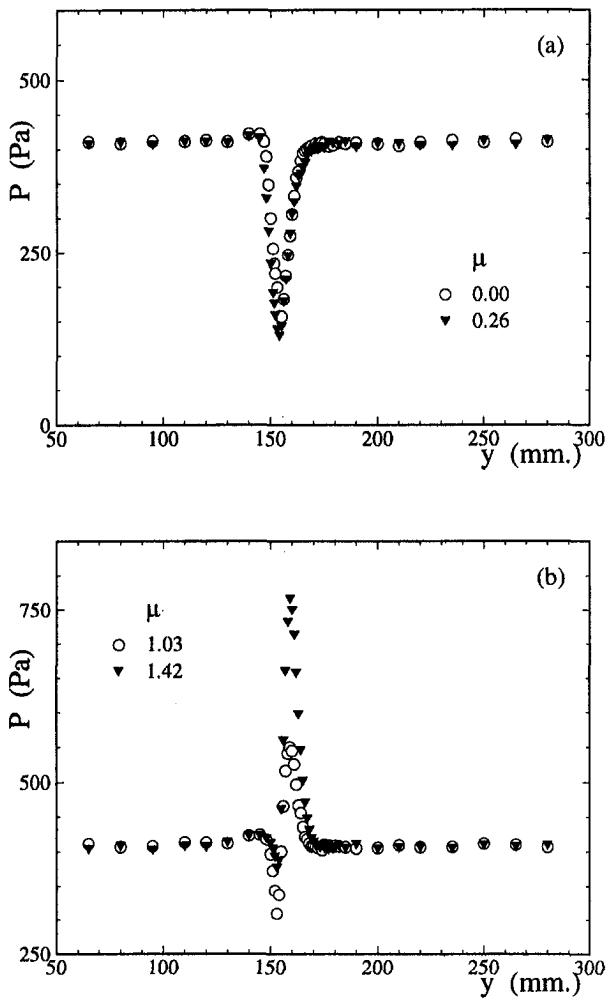

Fig. 6(*a, b*) Total pressure distributions for four representative cooling mass flows for GE blades

served. As will be discussed later, the velocity ratio of μ = 1.01 represents the optimum mixing loss coefficient. It should be pointed out that the presence of the trailing edge ejection with μ = 1.01 would never flatten the total pressure valley. The reason is the existence of the slot walls with their finite thicknesses. The slot walls always generate two shear layers with peaks and valleys as shown in Fig. 5(b). A fully flattened total pressure valley exists only for the hypothetical case of inviscid flow with infinitely thin slot wall thicknesses. A further increase of velocity ratio above $\mu > 1.01$ reverses the improving effect. The physical explanation is the same as above, with reversing the dissipation mechanism. The higher specific momentum of the jet is not able to accelerate the main mass flow. Therefore, despite a higher total pressure peak it is dissipated and further increases the total pressure losses. Figure 6 shows the total pressure distribution traverses at station 2 for the GE cascade with an exit flow angle α_2 = 13°. The same tendencies discussed with respect to Fig. 5 also can be observed here.

Reynolds Normal and Shear Stress Distributions. Figures 7 and 8 show the distribution of the Reynolds stress components $\overline{u'u'}$, $\overline{v'v'}$, and $\overline{u'v'}$ at station 2 for the NASA cascade. These measurements were taken using a X-wire probe. Within the vortical core of the trailing edge region (y = 140–180 mm), the normal components shown in Fig. 7 exhibit for the two distinct values of μ = 0.26 and 1.01 distributions with the highest and lowest integral values. These values correspond to the highest and lowest energy dissipation that occur for the entire range of μ-values. The formation of the normal stress distributions originates from the trailing edge thickness, trailing edge ejection, and boundary layer development along the suction and pressure surfaces. Higher peaks for a lower velocity ratio (μ = 0.26) are due to a higher velocity difference between the jet and the main mass flow. This velocity difference causes a strong shear layer associated with the higher energy dissipation and, as we discuss later, higher mixing losses. In contrast, for μ = 1.01, a substantially smaller region with moderate turbulence activity is observed, which is due to a much lower velocity difference between the jet and the main mass flow. Figure 8 gives a clear idea about the behavior of the turbulent shear stress,for four different values of μ = 0.0, 0.26, 1.01, 1.28. For no injection, the presence of trailing edge thickness and the boundary layer thicknesses on the suction and pressure surfaces are responsible for the typical shear stress distribution shown in Fig. 8(a). Increasing the velocity ratio to μ = 0.26, resulted in a deeper valley on the pressure surface. Again, this is due to the phenomenon discussed previously. Increasing the velocity ratio to μ = 1.01 reduces the area occupied by the shear stress distribution. As seen from Fig. 8(b), the trailing edge flow field is characterized by free turbulent flow, where three jets (left portion of the main mass flow, cooling mass flow, and the right portion of main mass flow) are interacting. For the higher velocity ratios μ = 1.01, 1.28, a double peak is evident, while for the low injection rates of μ = 0.0, 0.26, a single peak is present in the wake region. The additional peak for higher injection rates (Fig. 8(b)) is due to higher momentum of the cooling jet, which is not completely dissipated

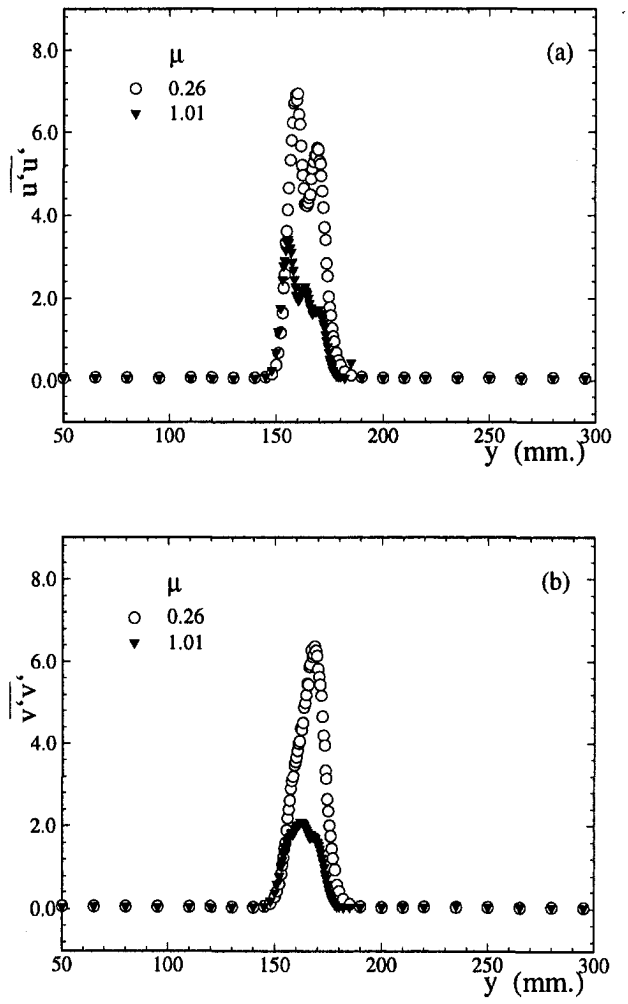

Fig. 7 (*a*) Longitudinal and (*b*) lateral Reynolds normal stresses for NASA blades

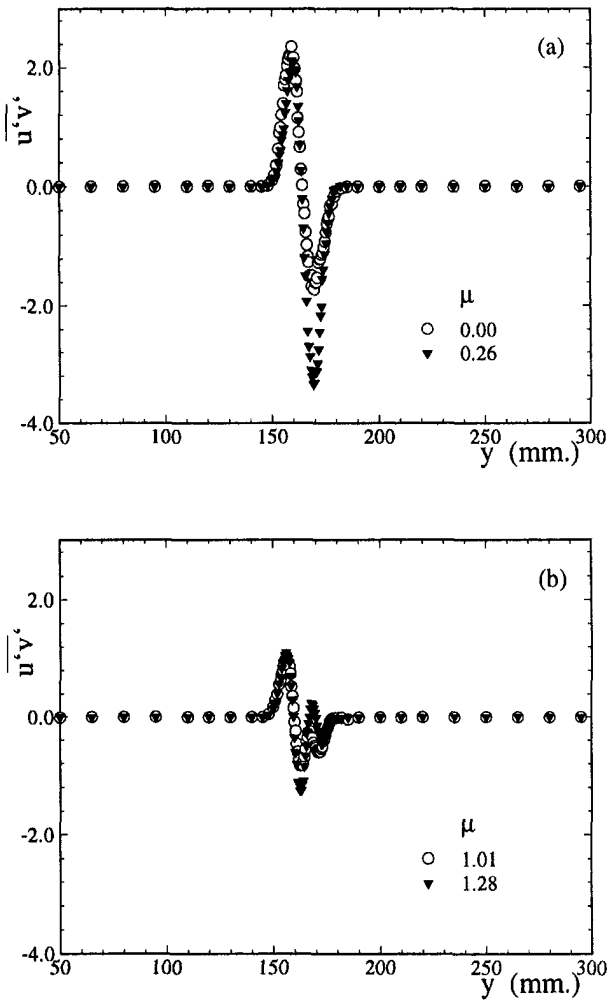

Fig. 8(*a, b*) Reynolds shear stress for four representative cooling mass flows for NASA blades

by the wake. Comparing the shear stress distributions for μ = 1.01 and 1.28, shear stress increased considerably with an increase in the velocity ratio. The jet being at a higher velocity than the main flow for the case of μ = 1.28 results in increased shear stress in comparison with the case of μ = 1.01, where the jet is at almost the same velocity as the main flow. This increase in shear stress is associated with increased mixing losses.

Mixing Losses, Comparison of Experiment and Theory. To compare the experimental results with the theory presented earlier, the experimental data needs to be further analyzed by calculating the average flow properties at the trailing edge plane (station 2) and at the mixing plane (station 3). The total energy dissipation is calculated, using Eq. (2), from the difference of energies at stations 2 and 3. The total energies at stations 2 and 3 for NASA and GE blades are shown in Figs. 9(*a*) and 10(*a*), respectively. In these figures, symbols represent the experimental measurements, solid lines represent the curve fit, and dashed lines represent the uncertainty band due to curve fit. As reported earlier, the uncertainty in the total pressure is ±1.5 percent, while the uncertainty in the mass flows is about ±4.8 percent. These uncertainties resulted in inevitable scatter of data points which necessitated curve fits to bring out the real tendency dictated by the physics of the flow. The total pressure mixing loss coefficient was calculated by using Eq. (3). The boundary layer thicknesses Δ^* and Δ^{**} that are required as input to Eq. (3) were obtained from an earlier boundary layer investigation (Schobeiri et al., 1995) carried out in the cascade under the same flow conditions.

The total pressure mixing loss coefficient is presented in dimensional form (ζ) for NASA blades while it is presented in nondimensional form (ζ/ζ_0) for GE blades where ζ_0 corresponds to the loss coefficient for no injection (μ = 0.0) case. The total pressure mixing loss coefficient as a function of the velocity ratio, $\mu = \bar{V}_c/V_2$, with nondimensional slot thickness ratio f as the parameter is plotted in Figs. 9(*b*) and 10(*b*) for NASA and GE blades, respectively. The symbols represent results from experimental measurements and the solid, dashed lines represent results from theoretical evaluation. For no injection (μ = 0.0), there is pressure loss due to finite thickness of the trailing edge and also from the boundary layer development along the pressure and suction surfaces of the blade. With increasing cooling jet velocities, the losses initially increase until a maximum is reached. Further increase in cooling jet velocities results in the decrease of ζ to a minimum, and then increasing thereafter. For $\mu < 0.7$, the losses due to injection of cooling mass flow are higher than for the no injection case. This was caused by the low momentum of the cooling jet being unable to sustain the strong dissipative nature of the wake flow downstream of the trailing edge. So, the main mass flow entrains the cooling mass flow resulting in complete dissipation of the energy of the jet. Therefore, higher mixing losses occur at low injection velocities until a maximum ζ is reached, which occurs around μ = 0.3 beyond which ζ begins to decrease. For injection velocity ratios $\mu > 0.7$, the momentum of cooling jet is sufficient to overcome the wake flow without being dissipated completely. Owing to this phenomenon, a significant reduction in

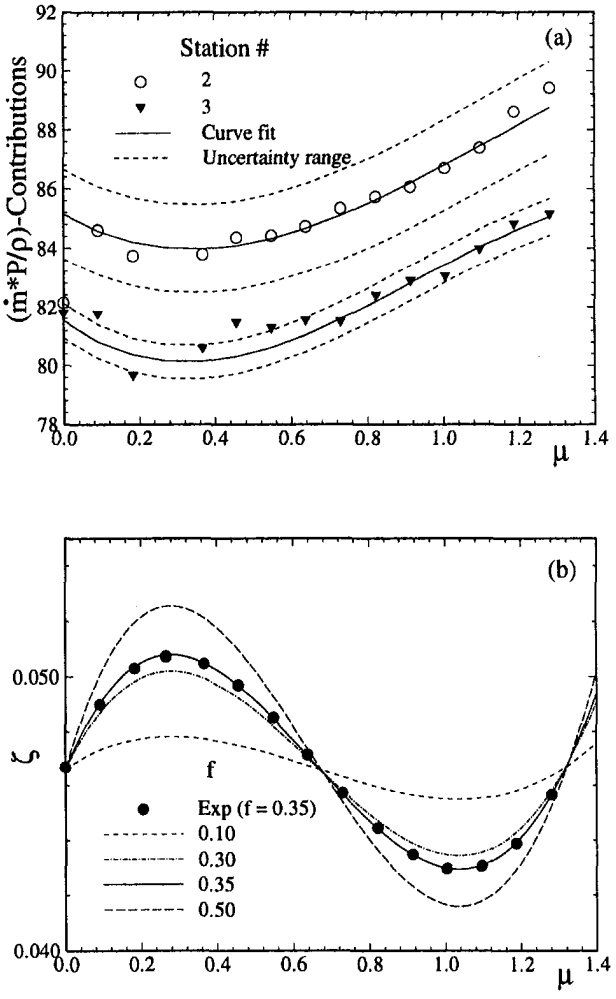

Fig. 9 (*a*) Total energy at stations 2, 3 and (*b*) Loss coefficient as a function of velocity ratio μ for NASA blades

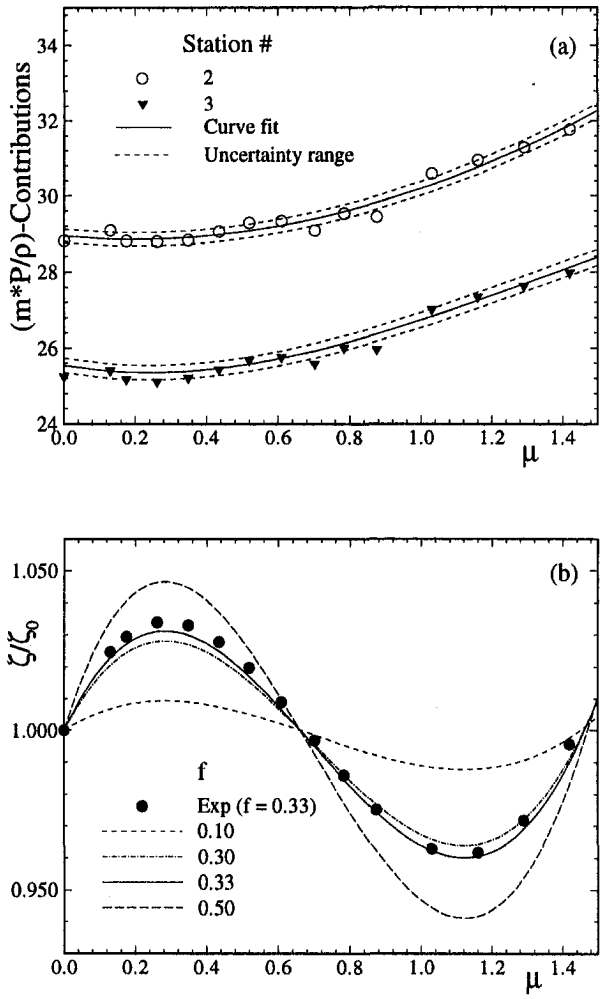

Fig. 10 (*a*) Total energy at stations 2, 3 and (*b*) Loss coefficient as a function of velocity ratio μ for GE blades

mixing losses is evident from Figs. 9(*b*) and 10(*b*). This reduction proceeds until ζ reaches a minimum, which is around $\mu = 1$. Further increase of μ above 1.1 increases the losses again for the reasons explained earlier. As seen from Figs. 9(*b*) and 10(*b*), there is a very good agreement between the theory (lines) and experiment (symbols).

Figures 11(*a*) and 12(*a*) show the mixing loss coefficient as a function of cooling mass flow ratio $\dot{m}_c/\dot{m}_2$ with nondimensional slot thickness ratio f as the parameter for the two types of blades investigated. The loss coefficient follows the same trend described in the previous paragraph. Again, there is excellent agreement between the theory (lines) and experiment (symbols). It is also evident from these figures that for a given f, the mixing loss coefficient has a pronounced optimum. Figures 11(*b*) and 12(*b*) show the mixing loss coefficient as a function of cooling jet momentum $(\dot{m}_c\bar{V}_c)/(\dot{m}_2V_2)$ with slot thickness ratio f as the parameter for the NASA and GE blades. The mixing loss coefficient again shows the same tendencies as discussed above.

Of particular interest to the turbine blade aerodynamicist and designer is how small the slot ratio f should be for a given mass flow, which is dictated by the heat transfer requirements to meet the optimum conditions for ζ. Figures 11(*c*) and 12(*c*) provide this crucial information for both the blades investigated. They show the mixing loss coefficient as a function of nondimensional slot thickness, f, with cooling mass flow ratio, $\dot{m}_c/\dot{m}_2$, as the parameter. The trailing edge thickness loss with no injection is represented by the curve $\dot{m}_c/\dot{m}_2 = 0$. By comparison of dashed lines representing non-zero cooling mass flow rates with solid line representing no injection, it is obvious that improper selection of f can result in losses that are predominantly higher than that due to the trailing edge thickness alone. This is one of the reasons for the cooled gas turbine blades with the trailing edge ejection to not have adequately high efficiency. The solid circle symbol in Fig. 11(*c*) represents the ζ optimum from experimental measurements for NASA blades at $f = 0.35$ and $\dot{m}_c/\dot{m}_2 = 0.033$. For

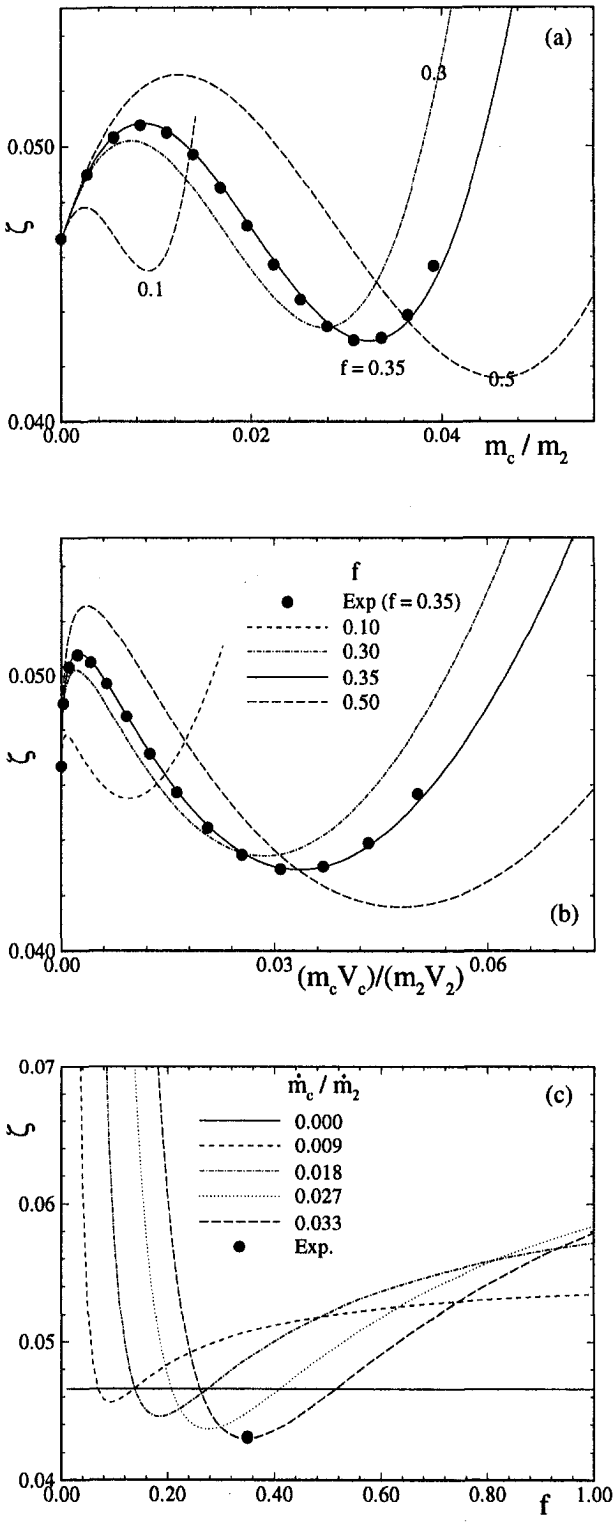

Fig. 11 Loss coefficient as a function of (*a*) mass flow, (*b*) momentum, and (*c*) slot thickness ratios for NASA blades

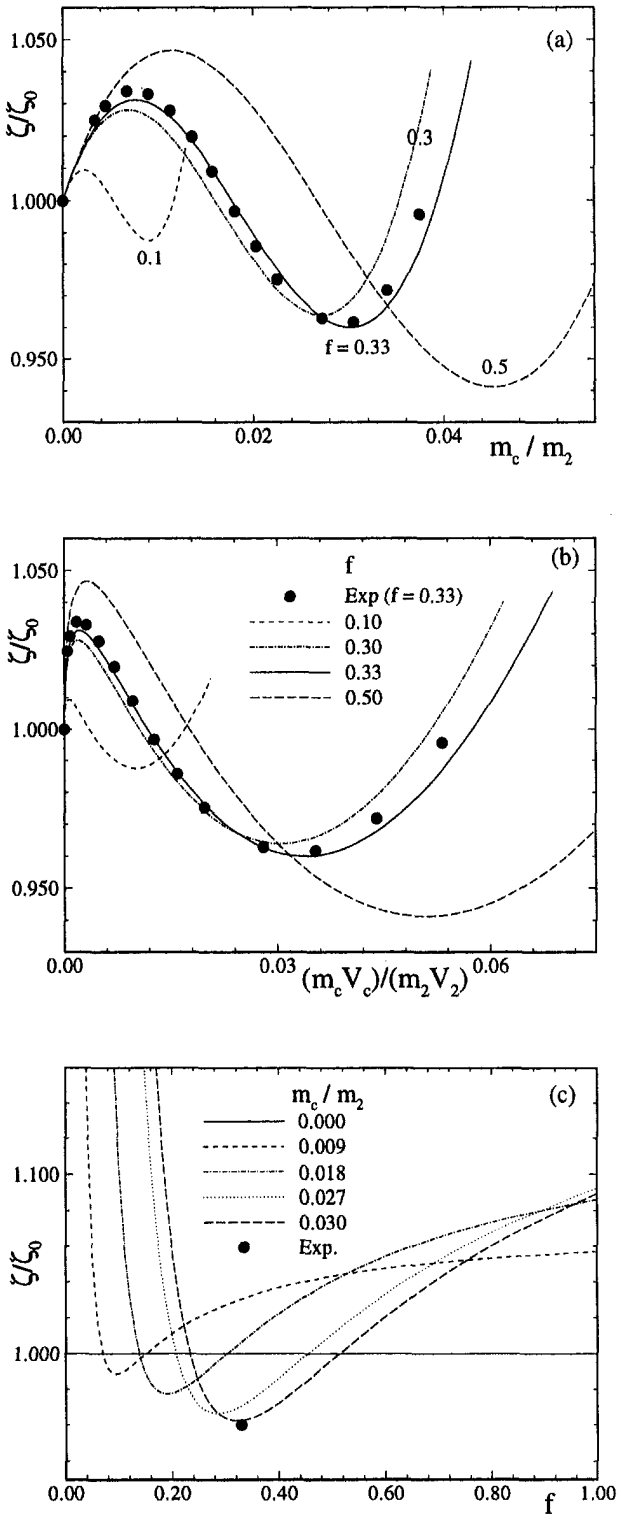

Fig. 12 Loss coefficient as a function of (*a*) mass flow, (*b*) momentum, and (*c*) slot thickness ratios for GE blades

this given mass flow ratio of $\dot{m}_c/\dot{m}_2 = 0.033$, the theory also predicts optimum mixing loss at $f = 0.35$. In Fig. 12(c), the solid circle symbol corresponds to ζ optimum from experimental measurements for GE blades at $f = 0.33$ and $\dot{m}_c/\dot{m}_2 = 0.03$. The data point coincides with the optimum f predicted by theory for the given mass flow ratio of $\dot{m}_c/\dot{m}_2 = 0.03$.

The primary focus of the experimental investigation has been the influence of velocity ratio μ on the mixing loss coefficient ζ. It has been shown that for the ejection velocity ratio of $\mu = 1$, the trailing edge ejection reduces the mixing losses downstream of the cooled blade. However, Eq. (3) reflects the influence of several other significant parameters (τ, R, Δ^*, Δ^{**}, α_c) on the mixing loss coefficient. Investigating the influence of all these parameters requires vast amount of measurement time. The limited time frame available only permitted the experimental investigation of the influence of one parameter μ. To understand how other parameters in Eq. (3) influence ζ, we refer to the analytical predictions presented in Schobeiri (1989).

Conclusions

The effect of trailing edge ejection on the flow downstream of a cooled gas turbine blade was experimentally and theoretically investigated. For the two types of blades investigated, the results show that for ejection velocity ratio $\mu = 1$, the trailing edge ejection reduces the mixing losses downstream of the cooled blade. For the given cooling mass flow ratios, optimum slot thickness to trailing edge thickness ratios are found from the theory, which correspond to the minimum mixing loss coefficients. These predictions are in good agreement with the experimental measurements.

Acknowledgment

This research work was sponsored by the DOE-AGTSR program. The blades were provided by NASA Le.R.C. and by General Electric Power Generation Division in Schnectady. The principal author, M. T. Schobeiri, would like to express his sincere thanks to DOE-AGTSR for sponsoring this project, Dr. R. Simoneau and Mrs. B. Lucci, NASA Le.R.C., and General Electric for the blades. He also would like to thank Professor Gyarmathy, Swiss Federal Institute of Technology, for permitting his student, Mr. L. Ducrest, to perform his Diplomarbeit on this project.

References

Bohn, D., Becker, V., Behnke, K., and Schönenborn, H., 1996, "Combined Experimental and 2-D Computational Study on Trailing Edge Ejection with Different Cooling Gases," *Proceedings of the 6th International Symposium on Transport Phenomena and Dynamics of Rotating Machinery,* Vol. 1, pp. 427–436.

John, J., and Schobeiri, T., 1993, "A Simple and Accurate Method for Calibrating X-Probes," ASME JOURNAL OF FLUIDS ENGINEERING, Vol. 115, pp. 148–152.

Prust, H., 1974, "Cold-Air Study of the Effect on Turbine Stator Blade Aerodynamic Performance of Coolant Ejection from Various Trailing-Edge Slot Geometries," NASA-Reports I: TMX 3000.

Prust, H., 1975, "Cold-Air Study of the Effect on Turbine Stator Blade Aerodynamic Performance of Coolant Ejection from Various Trailing-Edge Slot Geometries," NASA-Reports II: TMX 3190.

Schobeiri, T., 1985, "Einfluss der Hinterkantenausblasung auf die hinter den gekühlten Schaufeln entstehenden Mischungsverluste," *Forschung im Ingenieurwesen,* Vol. 51, No. 1, pp. 25–28.

Schobeiri, T., 1989, "Optimum Trailing Edge Ejection for Cooled Gas Turbine Blades," ASME *Journal of Turbomachinery,* Vol. 111, pp. 510–514.

Schobeiri, M. T., McFarland, E., and Yeh, F., 1990, "Aerodynamic and Heat Transfer Investigations on a High Reynolds Number Turbine Cascade," NASA Technical Memorandum 103260.

Schobeiri, M. T., Pappu, K. R., and Wright, L., 1995, "Experimental Study of the Unsteady Boundary Layer Behavior on a Turbine Cascade," ASME Paper 95-GT-435.

Tabakoff, W., and Hamed, A., 1975, "Theoretical and Experimental Study of Flow through Turbine Cascades with Coolant Flow Injection," AIAA Paper No. 75-843.

Wendt, B., and Reichert, A. B., 1993, "A New Algorithm for Five-Hole Probe Calibration and Data Reduction and Its Application to a Rake-Type Probe," *Fluid Measurement and Instrumentation,* FED-Vol. 161, pp. 29–35.

Yamamoto, A., Kondo, Y., and Murao, R., 1991, "Cooling-Air Injection Into Secondary Flow and Loss Fields Within a Linear Turbine Cascade," ASME *Journal of Turbomachinery,* Vol. 113, pp. 375–383.

A Plexiglas Research Pump With Calibrated Magnetic Bearings/ Load Cells for Radial and Axial Hydraulic Force Measurement

D. O. Baun
Graduate Research Assistant
& ROMAC Lab Engineer.

R. D. Flack
Professor & Department Chair.

Department of Mechanical Aerospace and Nuclear Engineering,
University of Virginia,
Charlottesville, VA 22903-2442

A research pump intended for both flow visualization studies and direct measurement of hydrodynamic radial and axial forces has been developed. The impeller and the volute casing are constructed from Plexiglas which facilitates optical access for laser velocimetry measurements of the flow field both inside the impeller and in the volute casing. The pump housing is designed for flexibility allowing for each interchange of impellers and volute configurations. The pump rotor is supported by three radial magnetic bearings and one double acting magnetic thrust bearing. The magnetic bearings have been calibrated to characterize the force versus coil current and air gap relationship for each bearing type. Linear calibration functions valid for rotor eccentricities of up to $\frac{2}{3}$ of the nominal bearing clearances and force level of ±58 N (13 lb_f) and ±267 N (60 lb_f) for the radial and axial bearings, respectively, were found. A detailed uncertainty analysis of the force calibration functions was conducted such that meaningful uncertainty bounds can be applied to in situ force measurements. Hysteresis and eddy current effects were quantified for each bearing such that their effect on the in situ force measurements could be assessed. By directly measuring the bearing reaction forces it is possible to determine the radial and axial hydraulic loads acting on the pump impeller. To demonstrate the capability of the magnetic bearings as active load cells representative hydraulic force measurements for a centered 4 vane 16 degree log spiral radial flow impeller operating in a single tongue spiral volute casing were made. At shut-off a nondimensional radial thrust of 0.084 was measured. A minimum nondimensional radial thrust of about 0.007 was observed at the nominal design flow. The nondimensional radial thrust increased to about 0.019 at 120 percent of design flow. The nondimensional axial thrust had a maximum at shut-off of 0.265 and decreased steadily to approximately 0.185 at 120 percent of design flow. Two regions of increasing axial thrust, in the flow range 75 to 100 percent of design flow, were observed. The measurements are compared to radial and axial force predictions using classical force models. The direct radial force measurements are compared to a representative set of radial force measurements from the literature. In addition, the directly measured radial force at design flow is compared to a single representative radial force measurement (obtained from the literature) calculated from the combination of static pressure and net momentum flux distribution at the impeller exit.

Introduction

The technique of increasing the total pressure of a fluid by imparting angular momentum to it by means of a centrifugal machine has been used extensively for many centuries. The use of this technology has increased in both numbers and variety of installations to the point today where the centrifugal pump is perhaps one of the most prolific machines in service. The need to produce more efficient and mechanically reliable machines has paralleled this trend in use. One of the many technical challenges that face the modern centrifugal pump designer is the rotordynamic analysis. The primary reason why this aspect of centrifugal pump design poses a challenge is the limited understanding of what the static and dynamic hydraulic forces will be at off design conditions and perhaps, more importantly, for the case of an eccentric or whirling impeller.

Much literature exists on the topic of static radial hydraulic forces in centrifugal pumps. Some early studies were conducted by Binder et al. (1936) and Acosta et al. (1957). Stepanoff (1957) presented a simple model based on impeller geometry, pump operating head and the normalized pump capacity for the calculation of resultant radial forces. Agostinelli et al. (1960) modified Stepanoff's model to account for the effect of specific speed (impeller and volute geometry) on radial forces. Biheller (1965) developed a universal equation to predict static radial pump forces applicable for a wide range of pump types and operating conditions. Today, in the absence of experimental data, a commonly used model for prediction of resultant radial thrust, F_r, in a centrifugal pump, as given by the Hydraulic Institute Standards (1994), is

$$F_r = \rho g H \kappa \left(N_s, \frac{Q}{Q_n} \right) 2 r_2 t \qquad (1)$$

where the thrust factor, κ, is given graphically as a function of specific speed, N_s, and normalized capacity, Q/Q_n.

de Ojeda et al. (1995) and Miner et al. (1989) present detailed laser velocimetry studies of the impeller exit flow field

Contributed by the Fluids Engineering Division for publication in the JOURNAL OF FLUIDS ENGINEERING. Manuscript received by the Fluids Engineering Division August 14, 1997; revised manuscript received October 13, 1998. Associate Technical Editor: B. Schiavello.

for a research radial flow centrifugal pump constructed from Plexiglas operating in a double volute and a single volute configuration, respectively. de Ojeda et al. (1995) combine the measured momentum flux distribution with the integrated static pressure distribution around the impeller to evaluate a total resultant radial thrust for the double volute configuration. Around the design flow rate of the test pump as much as 40 percent of the resultant radial thrust was reported to be from the asymmetric impeller exit momentum flux. Below 40 percent of the design flow the momentum flux contribution to the resultant radial thrust was reported to be insignificant. de Ojeda et al. also report the net radial thrust for the single volute configuration operating at the design flow rate.

Less literature exists on resultant static axial thrust in centrifugal pumps. Stepanoff (1957) presents an equation for calculation of axial thrust, F_a, for a closed impeller end suction centrifugal pump mounted between centers based on the unbalanced area and pressure variations between the front and back impeller shrouds,

$$F_a = (A_r - A_s)\left(H_L - \frac{1}{8}\frac{u_r^2 - u_s^2}{2g}\right)\rho g. \qquad (2)$$

Dynamic forces in centrifugal pumps have received much recent attention, Colding-Jorgensen (1980), Brennen et al. (1980), Chamieh et al. (1982), and Adkins et al. (1988). The primary reason for the recent focus on dynamic forces in centrifugal pumps is due to the realization that these forces can be a rotordynamic instability mechanism.

This paper is primarily intended to present a magnetic bearing supported research centrifugal pump apparatus. The magnetic bearings are to serve two primary functions: 1) for the support and control of the pump rotor 2) for the active measurement of both radial and axial forces. The primary motivation for the development of this apparatus was the investigation of dynamic forces in centrifugal pumps.

Test Apparatus

The pump and flow loop discussed in this paper have been documented by Hamkins and Flack (1987), Miner et al. (1989), and de Ojeda et al. (1995). Figure 1 and Fig. 2 show a schematic representation of the flow loop and pump drive assembly, respectively. The flow loop consists of: a 1.9 m^3 (67 ft^3) reservoir, a 76 mm (3 in) inlet pipe, a 100 mm (4 in.) discharge pipe, an orifice flow meter and a throttle valve for controlling the pump operating point. The pump rotor is connected via a jack shaft and two flexible beam couplings, which

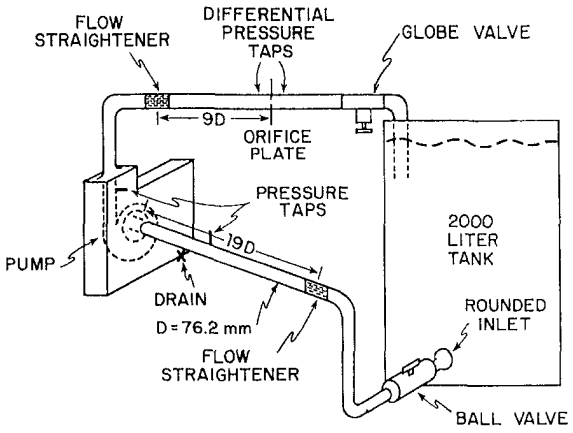

Fig. 1 Test loop

provide a laterally flexible yet torsionally rigid connection to a 0.75 KW (1 hp) drive motor. The motor is mounted on a set of linear bearings to allow free axial float of the entire rotating assembly. The apparatus was initially designed for laser velocimetry studies of the flow field both within the impeller and in the volute casing. Consequently, the volute and the impeller, Figures 3 and 4, respectively, are both constructed from clear optical grade Plexiglas. The four bladed radial flow impeller and the volute casing have logarithmic spiral shapes of 16 and 7 deg angles, respectively. The impeller has a discharge radius, r_2 = 101.6 mm (4 in.), an inlet blade radius, r_1 = 50.8 mm (2 in.) and an exit flow passage width, b_2 = 24.6 mm (0.968 in.). Specially designed mechanical face seals at the impeller eye and at the stuffing box location are used to minimize leakage flow back to the impeller inlet and to provide shaft sealing respectively. The nominal design point of the pump is 6.3 l/s (100 USGPM) at 2.27 m (7.44 ft) total dynamic head at an operating speed of 620 rpm. These parameters give a design specific speed, N_s of 0.504 (1376 US units), a design flow coefficient, ϕ_n of 0.061, and a design head coefficient, ψ_n of 0.511.

Figure 5 shows a nondimensional normalized head versus capacity curve and efficiency versus capacity curve obtained by test. The solid symbols represent data taken for pump loading (operating point going from shut-off to run-out) while the hollow symbols represent data taken for pump unloading (operating point going from run-out to shut-off). The variation between the curves for loading and unloading gives a good

Nomenclature

A_g = actuator pole face area
A_r = area at inlet wear ring
A_s = area at stuffing box shaft seal
b_{exp} = equivalent iron length (experimental)
b_2 = flow passage width at impeller exit
b_3 = flow passage width at volute inlet
c_{m2} = radial velocity at impeller exit ($Q/(2\pi r_2 b_2)$)
D_3 = volute cut water diameter
∂ = partial derivative
F = force (generic)
H = pump total discharge head
H_L = heat at inlet wear ring
g = gravitational constant
g_0 = nominal air gap, 0.762 mm (0.030 in)
$g_{1,2}$ = thrust actuator air gaps
$i_{1,2}$ = thrust actuator coil currents
k_{exp} = proportionality constant (experimental)
L_i = magnetic path in iron
N = number of coil turns
N_s = specific speed
Q = pump capacity
r_1 = impeller inlet blade radius
r_2 = impeller outer radius
u_2 = impeller outer peripheral velocity (Ωr_2)
u_r = peripheral velocity at inlet wear ring
u_s = peripheral velocity at shaft sleeve
t = impeller width at exit including shrouds
X, Y = coordinate directions
x = X direction displacement from center
y = Y direction displacement from center
Δ = uncertainty (generic)
ϕ = flow coefficient (c_{m2}/u_2)
ψ = head coefficient ($H/u_2^2/g$)
Ω = impeller angular velocity
θ_j = angle to jth pole center line
ρ = fluid density
μ_o = permeability of free space
μ_r = relative permeability
η = hydraulic efficiency (ρgHQ/input power)

Subscript

n = nominal design condition

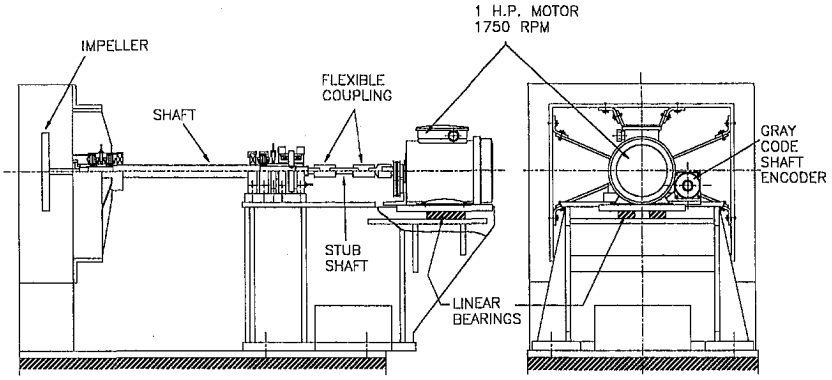

Fig. 2 Drive system

bound on the random uncertainty in the respective measurements and is believed to be due to electrical noise and small variations in operating speed. In addition some of the variation may be due to hysteresis in the pump/system characteristic. The best efficiency point (bep) occurs at approximately 100% of the nominal design flow giving a flow coefficient ratio, ϕ_{bep}/ϕ_n, of 1.0 and a head coefficient ratio, ψ_{bep}/ψ_n, of 1.0. These values give a tested specific speed, N_{sbep} of 0.504 (1306 US units), the same as the design specific speed, N_s.

Recently, the pump rotor has been redesigned and retrofitted with both radial and axial magnetic bearings, Fig. 6. The magnetic bearings are controlled and driven by analogue PID controllers and linear power amplifiers. Position feedback to the controllers is provided by two sets of orthogonally mounted differential proximity probes at each radial bearing location and a pair of differential proximity probes mounted diagonally opposite each other at the thrust bearing. For testing versatility a separate open loop controller is used to provide a rotating perturbation signal to the bearings such that an arbitrary rotor orbit can be imposed. A dedicated data acquisition computer is used for sampling and storing all measured variables. Two modes of data acquisition are used; 1) a free running mode typically used for static or average force measurements and 2) a triggered mode which, for each trigger pulse from an 8 bit absolute shaft encoder, sequentially samples all the magnetic bearing system parameters. The triggered mode provides the capability for discrete force measurements at 256 angular positions of the rotor as it turns.

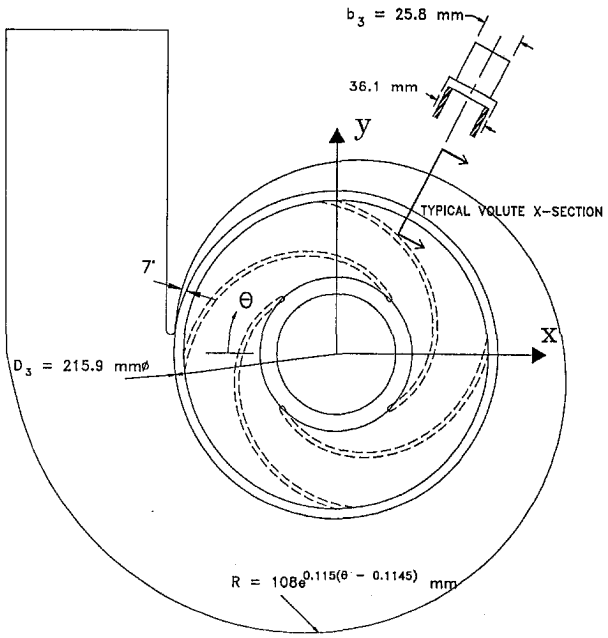

Fig. 3 Plexiglas volute

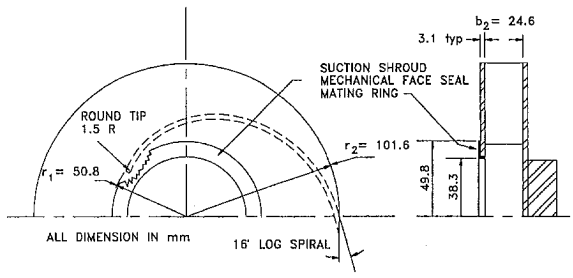

Fig. 4 Plexiglas impeller

Magnetic Bearings as Load Cells

Magnetic bearings provide a versatile diagnostic capability which fundamentally derives from the fact that the magnetic actuator component produces a force acting on the shaft which depends primarily on clearances within the actuator and its electromagnet coil currents. These quantities are all readily measured while the bearing is in operation, thereby providing direct access to the forces applied by the bearing. Many investigators have recognized this capability of magnetic bearings and have developed pump or compressor test rigs fitted with magnetic

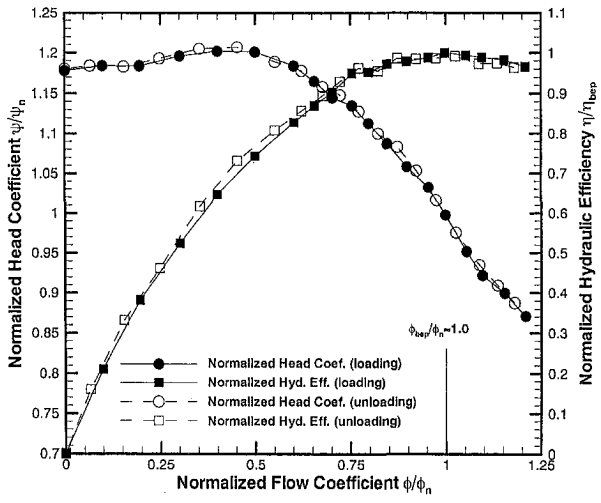

Fig. 5 Head coefficient and normalized efficiency versus flow coefficient (uncertainties: $\phi/\phi_n \approx \pm 0.01$; $\psi/\psi_n \approx \pm 0.007$, $\eta/\eta_{bep} \approx \pm 0.015$)

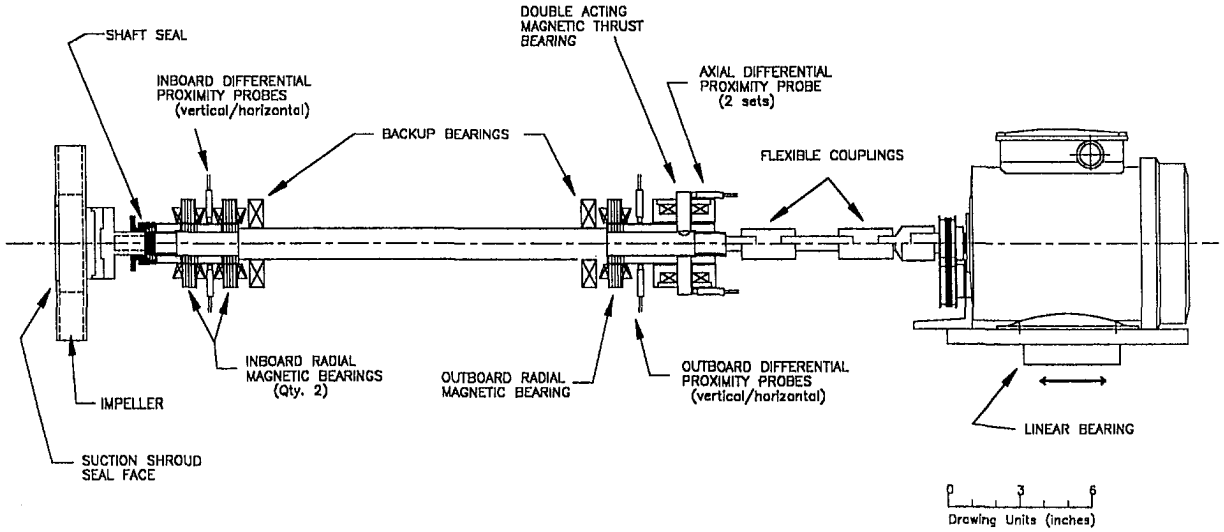

Fig. 6 Pump rotor

bearings for the purpose of measuring hydraulically generated forces. Imlach et al. (1991) examined the application of magnetic bearings to measure force, stiffness and damping in a centrifugal pump. Wagner and Pietruska (1988) constructed a magnetic bearing for measuring hydrodynamic forces in a turbocompressor. Humphris (1992) discussed magnetic bearings as a diagnostic tool for rotating machinery. Guinzburg et al. (1994) measured the static radial and axial reaction forces on a single stage end suction pump rotor through calibrated magnetic bearings. Pottie et al. (1994) used active magnetic bearings for the support and excitation of a boiler feed pump rotor. Bearing reaction force measurements were used to determine on-line frequency response functions from which dynamic fluid/rotor interaction forces were evaluated.

Axial Magnetic Actuator. The double acting thrust actuator installed on the pump test rig was designed for a maximum thrust load of 185 N (42 lb_f). The actuator components (both stators and the thrust disk) were constructed from a powdered metal, Anchor Steel TC-80 chosen for its low core loss properties at high frequencies. The theoretical force relationships for a double acting magnetic thrust actuator based on linear magnetic circuit theory and constant material magnetic properties is given by,

$$F_{th} = k_{th}\left[\frac{i_1^2}{(2g_1 + b_{th})^2} - \frac{i_2^2}{(2g_2 + b_{th})^2}\right] \tag{3}$$

where theoretical values $k_{th} = \mu_0 A_g N^2$ and $b_{th} = L_i/\mu_r$ can be evaluated based on the actuator geometry and material magnetic properties. A detailed development of these force equations is described by Allaire et al. (1994). To establish the actual force relationship for the thrust actuator used on the pump test rig and to assess the nonlinear effects due to material hysteresis, eddy currents, leakage and fringing, a calibration apparatus was used and a systematic calibration performed (Baun et al., 1997).

Static calibration testing was conducted to find optimized values of k_{exp} and b_{exp}. Optimal values of k_{exp} and b_{exp} were those that minimized the root-mean-square error between the experimental actuator force, as measured by a load cell in the calibration apparatus, and the force as calculated from the force calibration equation. The root-mean-squared error was minimized to 2.31 N (0.52 lb_f). A linearized actuator calibration relationship was found which is valid for actuator air gap variations of ±0.38 mm (±0.015 in.) about the nominal, and up to actuator force levels of 291 N (65 lb_f).

A Monte Carlo type perturbation analysis (based on the uncertainty of the measured calibration variables) was performed on the calibration data to determine the uncertainty in k_{exp} and b_{exp}. Using the calculated uncertainties for k_{exp} and b_{exp} and the uncertainties of the independent in situ actuator parameters the uncertainty of an in situ thrust actuator force measurement can be expressed as

$$\Delta F_{th} = \left[\left(\frac{\partial F_{th}}{\partial k}\Delta k\right)^2 + \left(\frac{\partial F_{th}}{\partial g_1}\Delta g_1\right)^2 + \left(\frac{\partial F_{th}}{\partial g_2}\Delta g_2\right)^2 + \left(\frac{\partial F_{th}}{\partial i_1}\Delta i_1\right)^2 + \left(\frac{\partial F_{th}}{\partial i_2}\Delta i_2\right)^2 + \left(\frac{\partial F_{th}}{\partial b}\Delta b\right)^2\right] \tag{4}$$

The uncertainty of a typical in situ thrust actuator force measurement is approximately 2.7 N (0.6 lb_f), about the same magnitude as the RMS error in the actuator static calibration.

Hysteresis in a magnetic material typically produces a variation in the flux density between an increasing and decreasing magnetizing field. Thus in a dynamic environment, such as the support of a centrifugal pump rotor, the minimum uncertainty of in situ actuator force measurements are at least as large as the width of the actuator hysteresis loop that corresponds to the amplitude of the largest actuator force fluctuation encountered during operation. The hysteresis for a force variation of ±35.8 N (8 lb_f) (expected upper bound of in situ axial force variation) was about 3.56 N (0.8 lb_f), or expressed as a coercive force 1.78 N (0.4 lb_f). Thus uncertainty introduced into the in situ axial force measurement due to material hysteresis is within the uncertainty of the static force calibration relationship.

Magnetic actuators are frequency dependent due to the formation of eddy currents. Frequency testing of the thrust actuator confirmed a bandwidth of at least 700 Hz. The current configuration of the pump apparatus will have a vane pass frequency of about 41 Hz so an actuator bandwidth of at least 700 Hz should give adequate frequency response.

Radial Thrust Magnetic Actuator. The radial magnetic actuator used on the pump test rig is a 8-pole planar design constructed from laminated silicon iron. It was designed for an RMS load capacity of 35.6 N (8 lb_f) and a peak load capacity of 89 N (20 lb_f). Using a linear magnetic circuit theory analysis and constant material magnetic properties the theoretical X and Y direction forces developed in a radial magnetic actuator can be expressed by the equations,

$$F_X = \tfrac{1}{2} k_{th} \mathbf{I}^T \mathbf{N}^T \mathbf{R}^{-T} \mathbf{A}_x \mathbf{R}^{-1} \mathbf{N} \mathbf{I}$$

$$F_Y = \tfrac{1}{2} k_{th} \mathbf{I}^T \mathbf{N}^T \mathbf{R}^{-T} \mathbf{A}_y \mathbf{R}^{-1} \mathbf{N} \mathbf{I} \quad (5)$$

Imbedded in the reluctance matrix, $\mathbf{R}$, are expressions for the total effective air gap at each actuator pole. These expressions are of the form

$$g_j = g_0 - x \cos(\theta_j) - y \sin(\theta_j) + b_{th} \quad (6)$$

where the subscript j designates a particular actuator pole. The parameters k_{th} and b_{th} are the same as described above, $\mathbf{I}$ is a current vector, $\mathbf{N}$ is the coil turn matrix and $\mathbf{A}_x$, $\mathbf{A}_y$ are cosine and sine matrices, respectively, that account for the angular orientation of each pole. A detailed development of these force equations is described by Meeker (1996). As with the thrust actuator, it was necessary to assess all nonlinear effects and determine the actual force relationship for the radial actuators. The calibration procedure for the radial actuator parallels the procedure previously described for the thrust actuator. A full account of the calibration can be found in Fittro et al. (1997).

Optimal values of k_{exp} and b_{exp} were found making Eq. (5) suitable for actuator air gap eccentricities of 0.356 mm (0.014 in), and actuator force levels up to 57.8 N (13 lb_f). The root-mean-squared error for the static calibration test was minimized to 0.756 N (0.17 lb_f). The uncertainty of an in situ X or Y direction force developed in the actuator is given by

$$\Delta F = \left[\left(\frac{\partial F}{\partial k} \Delta k \right)^2 + \left(\frac{\partial F}{\partial i_e} \Delta i_e \right)^2 + \left(\frac{\partial F}{\partial i_n} \Delta i_n \right)^2 + \left(\frac{\partial F}{\partial i_w} \Delta i_w \right)^2 + \left(\frac{\partial F}{\partial i_s} \Delta i_s \right)^2 + \left(\frac{\partial F}{\partial \theta} \Delta \theta \right)^2 + \left(\frac{\partial F}{\partial x} \Delta x \right)^2 + \left(\frac{\partial F}{\partial y} \Delta y \right)^2 + \left(\frac{\partial F}{\partial b} \Delta b \right)^2 \right]^{0.5} \quad (7)$$

where the independent measurement parameters i_e, i_n, i_w, i_s are the four quadrature coil currents. A representative in situ actuator force uncertainty at the RMS design load is about 0.74 N (0.165 lb_f). For a force hysteresis loop of ±33.6 N (7.5 lb_f) the net coercive force was found to be about 0.34 N (0.075 lb_f). This coercive force is much less than the uncertainty of the static calibration relationship. Therefore, uncertainty due to hysteresis can be ignored for this magnetic actuator. As with the thrust bearing, actuator frequency response was verified up to 700 Hz.

Impeller Forces

Procedure. A typical static/time averaged impeller force measurement proceeded as follows. First, a set of static bearing reference forces, both radial and axial, were obtained. The radial reference forces were obtained by operating the pump with an impeller blank/disk installed. The impeller blank had a smaller diameter and much larger shroud to casing clearances then the actual impeller while maintaining the same inertial properties as the actual impeller. In addition, the impeller blank had identical seals, both stuffing box and suction shroud, as the actual impeller. By imposing arbitrary differential pressures across the impeller blank it was found that the suction to discharge differential pressure in the pump had no effect on the radial component of the coupling or seal reaction forces. By taking radial reference forces while the pump is operating with an impeller blank installed any biasing effects due to mechanical and/or magnetic run out in the position sensing system can be eliminated. The axial component of the seal forces was found to vary between assemblies of the apparatus. Therefore the axial reference force was taken for the condition of no impeller rotation with the actual impeller and all mechanical seals installed. It was found that by judicious system alignment variations in the axial force due to mechanical run out were small. The radial and axial reference forces were then subtracted from the operating bearing reaction forces at each measurement/test condition. The static bearing reference forces removed any biasing effects due to seal or coupling reactions as well as the rotor weight. Dynamic effects due to mass unbalance in the rotor were removed by applying open loop balancing. This consisted of applying a synchronously rotating magnetic force that canceled the dynamic forces due to mass unbalance of the rotor.

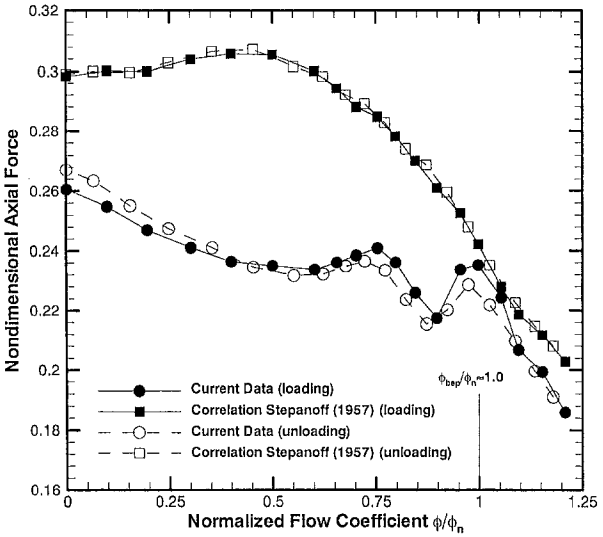

Fig. 7 Nondimensional axial thrust versus flow coefficient (uncertainties: $\phi/\phi_n \approx \pm 0.01$; $F_{\text{axial}} \approx \pm 0.016$; Eq. (2) $\approx \pm 0.001$)

Axial Forces. In Fig. 7 a representative set of measured nondimensional axial thrust versus normalized flow coefficient data are presented. The forces are nondimensionalized by the factor, $\rho \pi \Omega^2 r_2^3 t$. The solid symbols represent data for loading (operating point going from shut-off to run-out) while the hollow symbols represent data for unloading (operating point going from run-out to shut-off). In addition to giving an indication on the magnitude of random uncertainty in the measurements, the variation in the axial thrust between loading and unloading clearly demonstrates the hysteresis in the axial magnetic actuator/bearing as previously discussed. The nondimensional axial thrust steadily decreases from the shut-off value of 0.265 to about 0.185 at 120 percent of the nominal design flow except between the normalized flow coefficients of 0.75 and 1.0 where two regions of increasing force are observed. The region of increasing axial thrust coefficient occurring at the normalized flow coefficient, $\phi_{\text{bep}}/\phi_n = 1.0$, corresponds exactly with the point of minimum radial thrust, Fig. 9. Also included on Fig. 7 is a plot of the axial thrust using the correlation from Stepanoff (1957), Eq. (2). The shape of the pump head capacity characteristic is reflected in the shape of the curve given by Eq. (2). The nondimensional shut-off thrust coefficient as calculated from Eq. (2) is about 0.298, approximately 12 percent higher than the measured shut-off thrust coefficient. For flow coefficients below the nominal design flow coefficient the measured axial thrust is as much as 30 percent less than that given by Eq. (2) and in addition the shape of the measured axial thrust curve does not follow the general shape of the head capacity characteristic. Between the normalized flow coefficients of 0.7 and 0.9 the current data follows the general shape of the head capacity characteristic, but is about 10 percent lower in magnitude than that given by Eq. (2). Above the design flow coefficient the current data begins to follow the prediction given by Eq. (2) both qualitatively and quantitatively. One should note

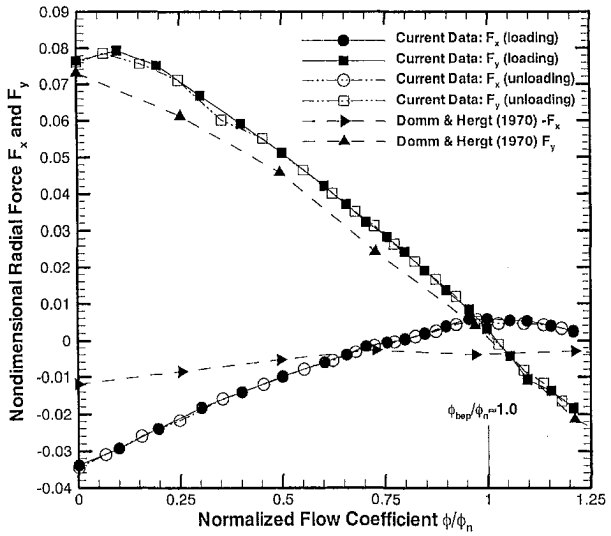

Fig. 8 Nondimensional radial force (X and Y components) versus flow coefficient (uncertainties: $\phi/\phi_n \approx \pm 0.01$; F_x and $F_y \approx \pm 0.008$)

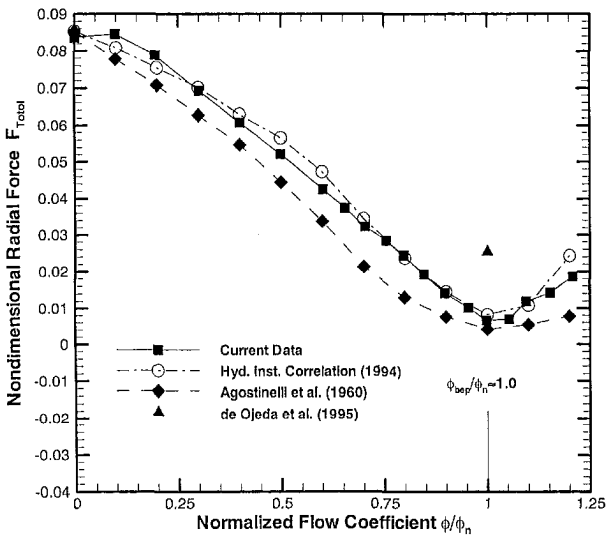

Fig. 9 Nondimensional radial force (resultant) versus flow coefficient (uncertainties: $\phi/\phi_n \approx \pm 0.01$; $F_{resultant} \approx \pm 0.008$; Eq. (1) $\approx \pm 0.001$)

that the correlation given by Eq. (2) is not strictly applicable to the current pump geometry. Equation (2) assumes that the pump shaft extends through the suction eye of the impeller. In addition, Eq. (2) is based on a wear ring (clearance type) seal on the suction shroud, whereas the current pump has a mechanical face (contact type) seal on the suction shroud. A mechanical face seal allows much less leakage back to the impeller inlet thus a more symmetric pressure distribution between the front and back shrouds results and better thrust balancing is achieved. The contribution to the axial force resulting from fluid pressure acting on the unbalanced area of the stuffing box mechanical seal is very small; within the uncertainty of the measurement. The nondimensional uncertainty of the measured data presented in Fig. 7 is approximately ± 0.016.

An investigation was conducted to verify that the observed trends in the measured axial thrust were not a function of the magnetic thrust actuator. Axial forces were obtained by operating the pump with the impeller blank/disk installed. The axial thrust on the impeller disk was measured as a function of externally applied differential pressure. A calculated thrust was obtained based on the unbalanced impeller areas and the applied differential pressure. The measured axial thrust and the calculated thrust showed very good correlation and were linear in the differential pressure. In addition, the trends in the measured axial thrust are not a function of thrust actuator calibration, Baun et al. (1997).

Radial Forces. Figures 8 and 9 are representative plots of measured nondimensional radial thrust plotted against the normalized flow coefficient. For presentation clarity, Fig. 8 shows the X and Y components of the force while Fig. 9 shows the resultant or magnitude of the force. The coordinate system used is defined in Fig. 3. The radial forces are nondimensionalized in the same way as the axial thrust.

The nondimensional X and Y components of the radial thrust are compared to the corresponding components of radial thrust for a test pump as published by Domm and Hergt (1970). The solid symbols represent data for loading (operating point going from shut-off to run-out) while the hollow symbols represent data for unloading (operating point going from run-out to shut-off). The differences between the data for loading and unloading give an indication on the magnitude of the random uncertainty in the measurements as well as confirming that hysteresis is not a significant issue with the radial magnetic actuators. The Y-component of the current data qualitatively follows the Y-component of the data from Domm and Hergt, but is slightly larger in magnitude for normalized flow coefficients below 1.0. Above the nominal design flow the Y-components of the two data sets are both qualitatively and quantitatively the same. A comparison between the X-components of the two data sets shows fair qualitative and quantitative correlation. The X-component of the current data shows a lot more variation in magnitude over the operating range than its counterpart from Domm and Hergt. In addition, the magnitude of the X-component of the data from Domm and Hergt remains negative over the full operating range while the magnitude of the corresponding component of the current data becomes positive between the normalized flow coefficients of 0.8 and approximately 1.25 (data extrapolated). At the nominal design flow rate the Y-component of the current data crosses the zero force axis while the X-component of the current data reaches a local maximum. This point corresponds approximately with the point of measured minimum radial thrust, Fig. 9.

The nondimensional resultant radial thrust, Fig. 9, follows the characteristic trend of a maximum (0.084) at shut-off, decreasing to a minimum (0.007) near the design flow, and increasing again for flows above the design point. The correlation given by Eq. (1) using the thrust coefficient, $\kappa(N_s, Q/Q_n)$, as given by the Hydraulic Institute Standard (1994) and as given by Agostinelli et al. (1960) are both presented for comparison. At the shut-off condition the current data shows a nondimensional radial thrust coefficient of 0.085 which is fully consistent with the shut-off value predicted using Eq. (1) with the thrust coefficient given by either the Hydraulic Institute Standard or Agostinelli et al. The radial thrust as predicted using Eq. (1) and the thrust coefficient given by the Hydraulic Institute Standard compare very well with the current data over the full operating range with the largest variation between the two curves being only 0.005. The curve given by Eq. (1) and the thrust coefficients from Agostinelli et al. shows good comparison with the current data, but is slightly lower in magnitude over the full operating range and more rounded in the vicinity of the design flow coefficient. Uncertainty of the measured data presented in Fig. 9 is approximately ± 0.008.

In addition, a single data point at the design flow coefficient as published by de Ojeda et al. (1995) is also presented. The magnitude of the nondimensional radial thrust at the design point from the current data is significantly smaller than the value given by de Ojeda et al. The authors believe this is due to the uncertainty in the value given by de Ojeda et al. as it

was obtained from the integration of a limited number of discrete pressure and velocity data.

Conclusions

A Plexiglas research pump has been retrofitted with magnetic bearings which act as precision active load cells. The magnetic actuators have been rigorously calibrated to define their respective force relationships and to assess the effect of various inherent nonlinearities on the uncertainty of in situ force measurements. Linear calibration functions valid for rotor eccentricities of up to $\frac{2}{3}$ of the nominal bearing clearances were found. Uncertainty functions for the magnetic actuators were defined such that meaningful uncertainties could be applied to the in situ force measurements. Representative axial and radial force measurements have been made to demonstrate the potential of the magnetic bearing load cells on this research pump apparatus. The measurements were compared to values from the literature and showed very good correlation in both magnitude and trend.

Much future work is planned for the apparatus, including static force measurements with various impeller and volute combinations. In addition dynamic force measurements are planned with the intention of studying impeller rotordynamic coefficients.

Acknowledgments

This research was sponsored by the Rotating Machinery and Controls (ROMAC) Industrial Research Program at the University of Virginia.

References

Acosta, A. J., and Bowerman, R. D., 1957, "An Experimental Study of Centrifugal Pump Impellers," *Trans. ASME,* Vol. 79, Apr., pp. 1821–1831.

Adkins, D. R., and Brennen, C. E., 1988, "Analyses of Hydrodynamic Radial Forces on Centrifugal Pump Impellers," ASME JOURNAL OF FLUIDS ENGINEERING, Vol. 110, Mar., pp. 20–28.

Allaire, P. E., Humphris, R. R., Knospe, C. R., and Lewis, D. W., 1994, "Magnetic Bearings," *Handbook of Lubrication and Tribology,* Vol. III, CRC Press, pp. 577–600.

Agostinelli, A., Nobles D., and Mockridge C. R., 1960, "An Experimental Investigation of Radial Thrust in Centrifugal Pumps," ASME *Journal of Engineering for Power,* Apr., pp. 120–126.

Baun, D. O., Fittro, R. L., and Maslen, E. H., 1997, "Force versus Current and Air Gap Calibration of a Double Acting Magnetic Thrust Bearing," ASME *Journal of Engineering for Gas Turbines and Power,* Oct., pp. 942–948.

Biheller, H. J., 1965, "Radial Forces on the Impeller of Centrifugal Pumps with Volute, Semivolute, and Fully Concentric Casings," ASME *Journal of Engineering for Power,* July, pp. 319–323.

Binder R. C., and Knapp, R. T., 1936, "Experimental Determination of the Flow Characteristics in the Volutes of Centrifugal Pumps," *Transactions ASME HYD-58-4,* pp 649–661.

Brennen, C. E., Acosta, A. J., and Caughey, T. K., 1980, "A Test Program to Measure Fluid Mechanical Whirl-Excitation Forces in Centrifugal Pumps," First Workshop on Rotordynamic Instability Problems in High Performance Turbomachinery, Texas A&M University, NASA Pub. 2133, pp. 229–235.

Brennen, C. E., 1994, *Hydrodynamics of Pumps,* Concepts ETI Inc., & Oxford University Press, Oxford England.

Chamieh, D. S., Acosta, A. J., Brennen, C. E., Caughey, T. K., and Franz, R., 1985, "Experimental Measurements of Hydrodynamic Radial Forces and Stiffness Matrices for a Centrifugal Pump Impeller," ASME JOURNAL OF FLUIDS ENGINEERING, Vol. 107, Sept., pp. 307–315.

Colding-Jørgensen, J., 1980, "Effect of Fluid Forces on Rotor Stability of Centrifugal Compressors and Pumps," First Workshop on Rotordynamic Instability Problems in High Performance Turbomachinery, Texas A&M University, NASA Conf. Pub. 2133, pp. 249–266.

de Ojeda, W., Flack, R. D., and Miner, S. M., 1995, "Laser Velocimetry Measurements in a Double Volute Centrifugal Pump," *International Journal of Rotating Machinery,* Vol. 1, No. 3–4, pp. 199–214.

Domm U., and Hergt P., 1970, "Radial Forces on Impeller of Volute Casing Pumps," *Flow Research on Blading,* Elsevier Publ. Co., pp. 305–321.

Fittro, R. L., Baun, D. O., Maslen, E. H., Allaire, P. E., 1997, "Calibration of an 8-Pole Planar Radial Magnetic Actuator," 97-GT-108, ASME Gas Turbine Conference, Orlando FL, June.

Flack, R. D., and Allaire, P. E., 1984, "Lateral Forces on Pump Impellers: A Literature Review," *Shock and Vibration Digest,* Vol. 16, No. 1, Jan., pp. 5–14.

Guinzburg, A., and Buse, F. W., 1994, "Axial and Radial Forces on a Pump Impeller Obtained with a Magnetic-Bearing Force Measurement Rig," *Proceedings of the Fourth International Symposium on Magnetic Bearings,* Hochschulverlag AG, Zurich, Switzerland, August 23–26, pp. 537–542.

Hamkins, C. P., and Flack, R. D., 1987, "Laser Velocimetry Measurements in Shrouded and Unshrouded Radial Flow Pump Impellers," ASME *Journal of Turbomachinery,* Vol. 109, No. 1, Jan., pp. 70–78.

Humphris, R. R., 1992, "A Device for Generating Diagnostic Information for Rotating Machinery," *Proceedings of MAG '92,* Magnetic Bearings, Magnetic Drives, and Dry Gas Seals Conference & Exhibition, July, Technomics Publication Co., pp. 123–135.

"American National Standard for Centrifugal Pumps For Nomenclature, Definitions, Application and Operation," ANSI/HI Vol. 1.1–1.5-1994, pp. 103–104.

Imlach, J., Blair, B. J., and Allaire, P. E., 1991, "Measured and Predicted Force and Stiffness Characteristics of Industrial Magnetic Bearings," ASME *Journal of Tribology,* Vol. 113, Oct, pp. 784–788.

Meeker, D. C., 1996, "Optimal Solutions to the Inverse Problem Quadratic Magnetic Actuators," Ph.D. dissertation, University of Virginia.

Miner, S. M., Beaudoin, R. J., Flack, R. D., 1989, "Laser Velocimetry Measurements in a Centrifugal Flow Pump," ASME *Journal of Turbomachinery,* Vol. 111, No. 3, July, pp. 205–212.

Pottie, K., Wallays, G., Verhoeven, J., Sperry, R., Gielen, L., De Vis, D., Neumer, T., Matros, M., and Jayawant, R., 1994, "Active Magnetic Bearings used in BW/IP Centrifugal Pump," *Proceedings of the Fourth International Symposium on Magnetic Bearings,* Hochschulverlag AG, Zurich, Switzerland, Aug. 23–26, pp. 463–477.

Stepanoff, A. J., 1957, *Centrifugal and Axial Flow Pumps,* Wiley, New York, NY.

Wagner, N. G., and Pietruszka, W. D., 1988, "Identification of Rotor Dynamic Parameters on a Test Stand with Active Magnetic Bearings," *Proceedings of First International Conference on Magnetic Bearings,* June, Springer-Verlag, pp. 289–302.

Primary/Leakage Flow Interaction in a Pump Stage[1]

E. A. Baskharone
Associate Professor. Mem. ASME

N. J. Wyman
Graduate Research Assistant.

Department of Mechanical Engineering,
Texas A&M University
College Station, TX 77843-3123

The finite-element analysis of the combined primary and leakage flow streams in a centrifugal pump is presented. To date, this computational model provides the most accurate "zeroth-order" flow field for rotordynamic calculations, short of analyzing the entire flow field on a fully three-dimensional basis. In formulating the problem, the shaft work is modeled via the angular momentum it imparts to the primary flow stream across the impeller blade region. In casting the boundary conditions, special attention is paid to the multi-connectivity of the newly-contoured computational domain in such a way to avoid over-specification of the problem. The analysis is applied to a typical pump stage with a face seal being part of the leakage passage. The numerical results are then compared to the outcome of the existing lower-order analysis where the impeller subdomain was totally extracted.

Introduction

The demand for lighter, more efficient pump stages has recently increased the desire in the turbomachinery community to understand each component flow structure and identify the different sources of head losses. Of these, leakage losses in the impeller's secondary passage (Fig. 1) is exclusively a major cause of performance degradation, even in a carefully designed stage, such as those in the Space Shuttle Main Engine turbopumps (e.g., Childs, 1983).

Perhaps the most serious consequence of the shroud-to-housing secondary flow is its destabilizing effect (e.g., Black, 1969; Childs, 1978; and Xi-Xuan et al., 1988). In a whirling-shaft operation mode, the fluid-induced forces due to this flow stream can very well cause the impeller's lateral eccentricity to grow unboundedly, resulting in a catastrophic mechanical failure. In predicting such rotordynamic problems, perturbation methods have been extensively utilized (Childs, 1989; Dietzen and Nordmann, 1987; Tam and Przekwas, 1988). More recently, the lead author and Hensel (1991) devised a non-traditional perturbation model, and applied it to a typical pump stage (Baskharone et al., 1994). Among all of these methods, one feature continues to be in common, namely the lack of the impeller flow stream in defining the fluid/rotor interaction domain.

The current computational model is the first, to the authors' knowledge, to produce a detailed centered-impeller flow field, including that in the primary flow subdomain. This is a major enhancement over the flow region of Baskharone and Hensel (1989), where the vaned portion of the primary passage was totally eliminated (Fig. 1).

Analysis

Referring to the computational domain in Fig. 2, the flow is assumed incompressible, swirling, turbulent, and axisymmetric. Of these, the last condition concerns the primary flow, in particular, and implies a negligible pressure-to-suction flow migration in the blade-to-blade passage. Obviously, such a constraint would be sufficiently accurate under such conditions as a significantly large blade count, for full flow guidedness, and a rather thin well-designed impeller blade.

Flow-Governing Equations. Throughout the primary and secondary impeller passages, the flow equations are partly those of momentum and mass conservation, which can be expressed as follows:

$$2\frac{\partial}{\partial z}\left(\upsilon_e\frac{\partial V_z}{\partial z}\right)+\frac{1}{r}\frac{\partial}{\partial r}\left(r\upsilon_e\frac{\partial V_z}{\partial r}\right)+\frac{1}{r}\frac{\partial}{\partial r}\left(r\upsilon_e\frac{\partial V_r}{\partial z}\right)$$

$$=\frac{1}{\rho}\frac{\partial p}{\partial z}+\hat{V}_z\frac{\partial V_z}{\partial z}+\hat{V}_r\frac{\partial V_z}{\partial r}$$

$$\frac{\partial}{\partial z}\left(\upsilon_e\frac{\partial V_r}{\partial z}\right)+\frac{2}{r}\frac{\partial}{\partial r}\left(r\upsilon_e\frac{\partial V_r}{\partial r}\right)+\frac{\partial}{\partial r}\left(\upsilon_e\frac{\partial V_z}{\partial r}\right)$$

$$=\frac{1}{\rho}\frac{\partial p}{\partial r}+\hat{V}_z\frac{\partial V_r}{\partial z}+\hat{V}_r\frac{V_r}{\partial r}-\hat{V}_\theta\frac{V_\theta}{r}+2\upsilon_e\frac{V_r}{r_2}$$

$$\frac{\partial V_r}{\partial r}+\frac{V_r}{r}+\frac{\partial V_z}{\partial z}=0$$

where

V_z, V_r, and V_θ	refer to the components of the absolute velocity vector,
p	is the static pressure,
ρ	is the fluid density,
υ_e	is the effective kinematic viscosity, and
$\hat{V}_z$, $\hat{V}_r$, and $\hat{V}_\theta$	are the velocity components obtained from the previous iteration or an initial guess.

Of the preceding equations, the tangential momentum equation is replaced by a prespecified tangential velocity distribution only over the impeller blade region (Fig. 2). This distribution is based on the pump total head, which yields a unique value of tangential velocity component "V_θ" at the impeller tip, once the impeller inlet conditions are known. Distribution of the tangential velocity is also guided, as it should, by the streamwise distribution of the blade "yaw" angle. Note that the meridional velocity components, namely V_r and V_z, are not externally imposed anywhere in the computational domain (Fig. 2), but are retained as field variables to be achieved in the numerical solution. Equally important is the fact that the primary/leakage flow interfaces are treated as internal subdomains over which only the governing equations, and not external constraints, apply. It follows that the leakage flow rate is not specified a priori, but is an outcome of the numerical solution process, as it should naturally be.

[1] This research was funded by NASA Marshall Space Flight Center, Huntsville, Alabama, Contract No. NAS8-37821 (Technical Monitor: James Cannon). Partial funding was also provided by Texas A&M Turbomachinery Research Consortium.

Contributed by the Fluids Engineering Division for publication in the JOURNAL OF FLUIDS ENGINEERING. Manuscript received by the Fluids Engineering Division June 31, 1995; revised manuscript received April 27, 1998. Associate Technical Editor: D. P. Telionis.

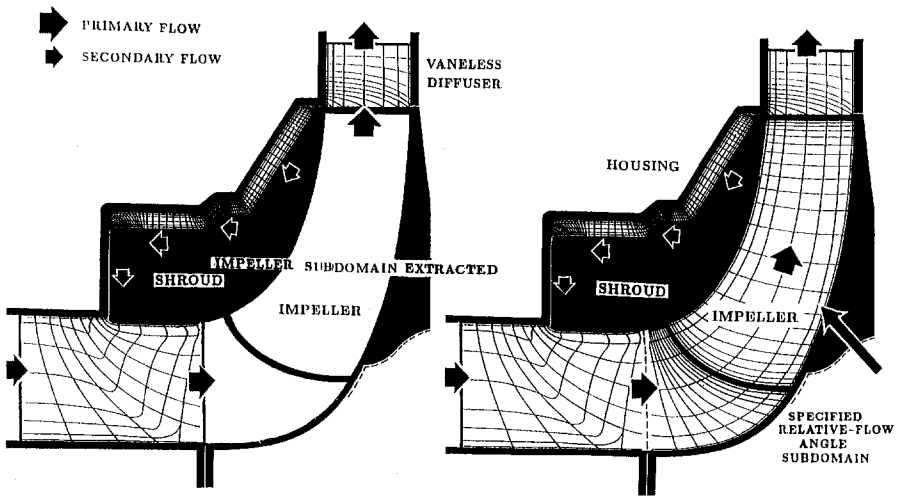

Fig. 1 Finite-element discretization model

Turbulence Closure. In computing the eddy viscosity, a vorticity-based turbulence model was utilized. This is a slightly adapted version of the algebraic model by Baldwin and Lomax (1976), with a near-wall treatment that is similar to that by Benim and Zinser (1985). In applying the model near a rotating wall, i.e., the hub and shroud surfaces, the relative, rather than absolute, fluid motion was considered, giving rise to the following expressions for the vorticity and velocity vector:

$$\Omega_R = \Omega - 2\omega$$

$$\bar{V}_R = V - \omega r \bar{e}_\theta$$

where

ω is the rotational speed,
r is the radius of the rotating solid surface, and
$\bar{e}_\theta$ is the unit vector in the positive tangential direction.

As for the near-wall flow structure, an array of logarithmically-arranged points (Fig. 3), which are independent of the finite-element grid points, was used in computing the turbulence-related variables, as well as the wall shear stress. Among other advantages, this had the effect of enhancing the accuracy of computing the cut-off location between the so-called inner and outer layers in applying Baldwin and Lomax turbulence closure.

Boundary Conditions. Referring to Fig. 2, these are categorized by the boundary segments to which they apply, as follows:

(a) Stage Inlet Station: This is the annulus located sufficiently far upstream of the impeller-blade leading edge (Fig. 2). Over this boundary, known profiles of the velocity components,

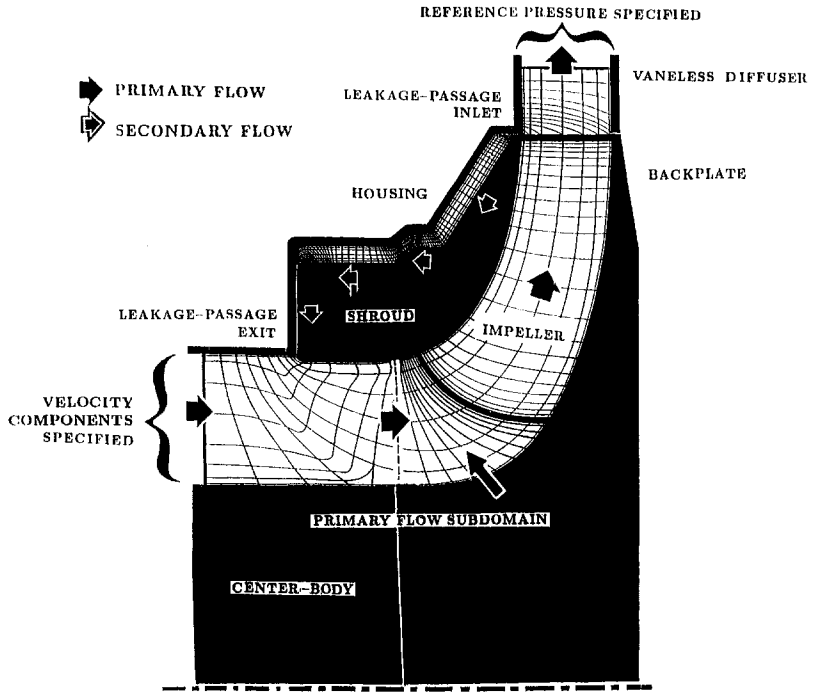

Fig. 2 Finite-element model of the combined axisymmetric flow domain

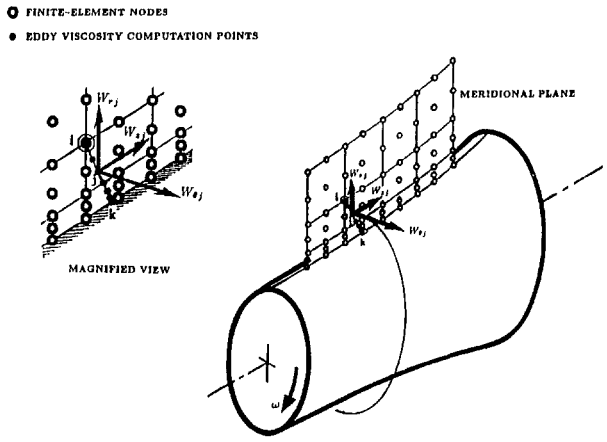

Fig. 3 Mesh refinement in the near-wall region to enhance the prediction of eddy viscosity

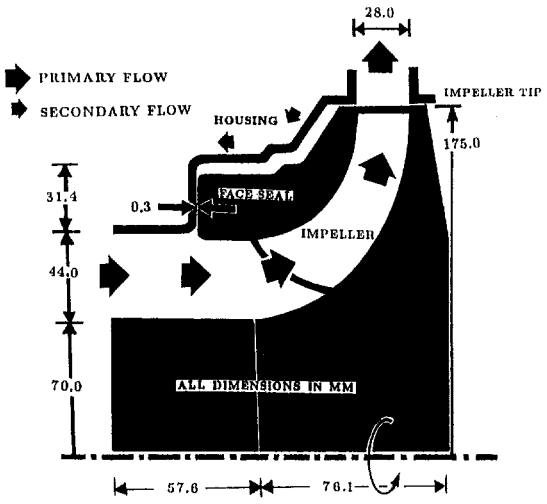

Fig. 5 Sulzer Brothers shrouded impeller pump configuration

which correspond to the pump design point, are specified. Of these, the through-flow velocity distribution sets the volumetric flow rate throughout the pump stage, with no consideration given to the percentage leaking back through the shroud-to-housing secondary passage. As mentioned earlier, the latter is an internal variable, and is controlled by such factors as the static pressure differential across the impeller, the geometry of the secondary flow passage and the manner in which it physically connects with the primary passage.

(b) Stage Discharge Station: This boundary segment is located in the vaneless diffuser region (Fig. 2), at a radial location that is sufficiently far from the impeller tip. Over this exit surface, the flow is confined to satisfying the mass and angular momentum conservation constraints in a global sense. These boundary conditions can be expressed in the following differential form:

$$\frac{\partial V_\theta}{\partial r} = -\frac{V_\theta}{r}$$

$$\frac{\partial V_r}{\partial r} = -\frac{1}{br}\left(b + r\frac{db}{dr}\right) V_r$$

where b is the vaneless diffuser endwall spacing.

Besides, the static pressure is arbitrarily set to a datum value at the middle node on this station.

(c) Solid Boundary Segments: These are primarily the hub and shroud inner and outer surfaces. Here, the no-slip boundary condition is imposed as follows:

$$V_z = V_r = 0$$

$V_\theta = 0$ over a stationary endwall segment

$V_\theta = \omega r$ over a rotating segment

Shown in Fig. 1B, this is physically a fluid/rotor work-exchange subdomain.

(d) Impeller Meridional Projection: This is the cross-hatched area in Fig. 2. Over this entire region, the overall magnitude of shaft work is proportional to the rise in angular momentum across the impeller. Given the total head, rotational speed and magnitude of pre-swirl, if any, the value of exit tangential velocity can be calculated. Next, a streamwise distribution and tangential velocity is established within the impeller region, using a characteristically typical distribution of the blade "yaw" angle, which would ideally be identical to the flow angle. Assuming no blade twist, the swirl velocity distribution is then extended along the cross-flow, hub-to-shroud grid lines in Fig. 2. Once finalized, this swirl velocity distribution is viewed as reflective of the supplied shaft work, and is maintained constant throughout the entire solution process. Worth noting is the fact that there is no need for specifying the pressure differential across the pump, since this amount is implied by the impeller swirl velocity distribution. Indeed, enforcing a streamwise pressure differential as a boundary condition would analytically overspecify the problem.

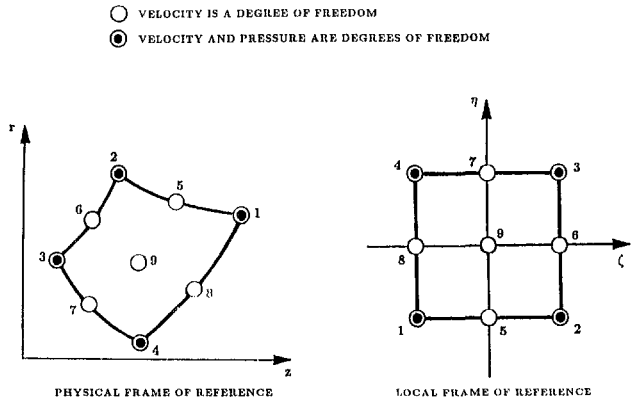

Fig. 4 Typical nine-noded Lagrangian finite-element

Finite-Element Formulation. A Galerkin-Petrov weighted-residual approach was used to arrive at the discrete finite-element version of the flow-governing equations. Using a nine-noded bi-quadratic Lagrangian element (Fig. 4), a mixed linear/quadratic piecewise distribution of the pressure and velocity components was implemented, respectively. As for the weight functions, the element's linear and quadratic shape functions, associated with the four corner nodes and all nine nodes, were used in conjunction with the continuity and momentum equations, respectively. Moreover, a special set of weight functions, giving rise to a piecewise streamline upwinding (Heinrich and Zienkiewicz, 1977), were iteratively constructed and utilized in conjunction with the convective terms in the momentum equations. With all of these considerations, the final set of finite-element equations, written as the typical node "i," in the local frame of reference, is as follows:

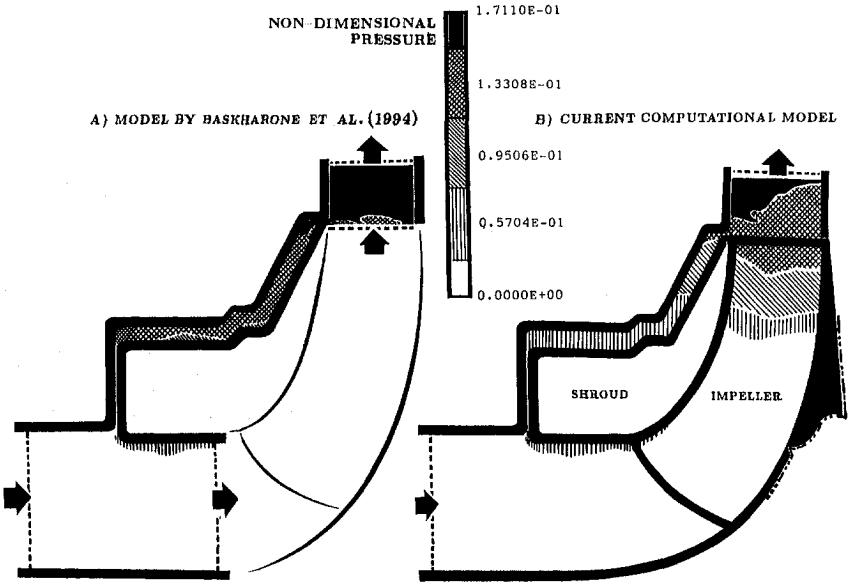

Fig. 6 Comparison of the pressure field

$$\left[\int_A\int_{(e)}\left\{\frac{1}{R_e}\left(\frac{\partial N_i}{\partial z}\frac{\partial N_j}{\partial z}+\frac{\partial N_i}{\partial r}\frac{\partial N_j}{\partial r}\right)+\hat{V}_z W_i\frac{\partial N_j}{\partial z}+\hat{V}_r W_i\frac{\partial N_j}{\partial r}\right\}rdA\right]V_{z-j}+\left[\int_A\int_{(e)}N_j\frac{\partial M_k}{\partial z}rdA\right]p_k=\frac{1}{R_e}\oint_{L(e)}rN_i\frac{\partial V_z}{\partial n}dL$$

$$\left[\int_A\int_{(e)}\left\{\frac{1}{R_e}\left(\frac{\partial N_i}{\partial z}\frac{\partial N_j}{\partial z}+\frac{\partial N_i}{\partial r}\frac{\partial N_j}{\partial r}+\frac{1}{r^2}N_iN_j\right)+\hat{V}_z W_i\frac{\partial N_j}{\partial z}+\hat{V}_r W_i\frac{\partial N_j}{\partial r}\right\}rdA\right]V_{r-j}-\left[\int_A\int_{(e)}\frac{\hat{V}_\theta}{r}N_iN_j\,rdA\right]V_{\theta-j}+\left[\int_A\int_{(e)}N_i\frac{\partial M_k}{\partial r}rdA\right]p_k=\frac{1}{R_e}\oint_{L^{(e)}}rN_i\frac{\partial V_r}{\partial n}dL$$

$$\left[\int\int_{A^{(e)}}\left\{\frac{1}{R_e}\left(\frac{\partial N_i}{\partial z}\frac{\partial N_j}{\partial z}+\frac{\partial N_i}{\partial r}\frac{\partial N_j}{\partial r}+\frac{1}{r^2}N_iN_j\right)+\hat{V}_z W_i\frac{\partial N_j}{\partial r}+\hat{V}_r W_i\frac{\partial N_j}{\partial r}+\frac{\hat{V}_r}{r}W_iN_j\right\}rdA\right]V_{\theta-j}=\frac{1}{R_e}\oint_{L^{(e)}}rN_i\frac{\partial V_\theta}{\partial n}dL$$

$$\left[\int\int_{A^{(e)}}M_i\frac{\partial N_j}{\partial z}rdA\right]V_{z-j}+\left[\int\int_{A^{(e)}}\left(M_i\frac{\partial N_j}{\partial r}+\frac{1}{r}M_iN_j\right)rdA\right]V_{r-j}=0$$

where:

W_i are the upwinding shape functions (Heinrich and Zienkiewicz, 1977),

$\bar{n}$ denotes the unit vector normal to the element boundary; and

$$dA = dzdr = |J|\,d\zeta d\eta$$

J is the Jacobian of local-to-cylindrical coordinate transformation.

$$i = 1, 2, 3, \ldots 9$$

$$j = 1, 2, 3, \ldots 9$$

$$k = 1, 2, 3, 4$$

$$V_z^{(e)} = \sum_{i=1}^{m} N_i(\zeta,\eta)V_{z-i} \quad p^{(e)} = \sum_{i=1}^{n} M_i(\zeta,\eta)P_i$$

$$V_r^{(e)} = \sum_{i=1}^{m} N_i(\zeta,\eta)V_{r-i} \quad z^{(e)} = \sum_{i=1}^{m} N_i(\zeta,\eta)z_i$$

$$V_\theta^{(e)} = \sum_{i=1}^{m} N_i(\zeta,\eta)V_{\theta-i} \quad r^{(e)} = \sum_{i=1}^{m} N_i(\zeta,\eta)r_i$$

In the above equations N_i and M_i are, respectively, quadratic and linear interpolation functions of ζ and η, the spatial coordinates in the local frame of reference, and are often referred to as the element "shape" functions. Note that the "parent" element in the local frame of reference is straight-sided (Fig. 4), and that the variables "m" and "n" are 9 and 4, respectively.

Results and Discussion

Figure 5 shows the pump configuration under investigation in this study. This is a shrouded-impeller hydraulic pump with a conventional face seal in the leakage flow passage. Rotordynamically tested by Bolleter et al. (1989), the pump design point is defined as follows:

Shaft speed = 2000 rpm

Volumetric flow rate = 0.13 m^3/s

Total head = 68 m

Impeller inlet blade angle = 0 deg

Impeller exit blade angle = 67.5 deg

Shown in Fig. 1 is a side-by-side comparison between a previously-devised computational domain, where the primary impeller passage was totally extracted (Baskharone et al., 1994), and the current domain, both for the same pump stage. Note that with the previous double-entry/double-departure domain, no internal mechanism of shaft work simulations existed, a situation which required the specification of a streamwise pressure differential across the leakage passage and fictiteously standard velocity components at the impeller-tip station. With the close proximity of this, as well as the impeller inlet, stations to the secondary/primary flow merging locations, it is seen that the leakage flow rate was, in effect, somewhat implied in the previous numerical model.

Several performance parameters, previously supplied or implied in the input data of the comparatively outdated model (Baskharone and Hensel, 1991) became part of the numerical solution output, and are now examined for validation purposes. Of these, the first and foremost is the stage static-pressure rise. Figure 6 shows a comparison between the pressure fields associated with the full-scale previous and current solution domains. The specific difference here is that the former had a pre-imposed static pressure rise across the impeller. Examination of this figure reveals that the pressure differential deviation associated with the current computational model is approximately 5.5 percent, which is acceptable considering the simplicity of the shaft work absorption mechanism in the current model. The importance of this result stems from the fact that the same pressure rise applies across the secondary passage, controlling the leakage flow rate through it. In the post-processing step, however, a total (static and dynamic) pressure head that is approximately 20% higher than the design-point value was computed. This relatively high over-prediction is due to a significantly high dynamic head at the stage exit station in this case. Despite the closeness of the overall magnitude of the stage static pressure rise, Fig. 6 also suggests a notably smaller differential across the face seal with the current numerical model.

Vector plots of the secondary-passage meridional velocity fields, associated with the former and current models, are shown in Fig. 7. Of interest in this figure is the categorical similarity of the flow structures in both cases, including multiple recirculation zones in the entire passage. This is a result of two opposing effects, namely that of the centrifugal force near the shroud and the unfavorable static pressure gradient entire across the secondary passage. Also similar is the complex flow patterns in the passage axial segment leading to the face seal, with particular reference to the vortex break-down in this flow segment.

In verifying the current numerical model, the distribution of tangential velocity component is equally important, particularly from a rotordynamic stability standpoint (Baskharone et al., 1994). Examination of Fig. 8 reveals similar trends of this velocity component as obtained through the previous and current models. Also clear in this figure is the fact that the secondary-passage inlet stations is the region where the largest difference between the two sets of results occurs. This is understandable since this region is the closest secondary-passage location to the impeller region, where major differences in the domain geometry and boundary conditions exist (Fig. 5).

Concluding Remarks

The topic of fluid-rotor interaction in pumps has recently gained new grounds as a result of applying increasingly rigorous tools of computational fluid dynamics. The improvement, however, has been confined to the shroud-to-housing leakage passage, with the primary impeller passage physically extracted from the computational domain. Short of a fully three-dimensional analysis, the present computational model provides a reasonably accurate, yet simple, means of incorporating this flow field in computing the shroud rotordynamic forces. While maintaining the primary flow axisymmetry, the model is based on simulating the torque transmitted to the impeller via an externally-imposed angular momentum rise over the blade meridional projection. With this and the domain multi-connectivity, some boundary conditions in a previous lower-order flow model, became redundant. Results of the current flow analysis were compared to those of the previous model and various differences were identified and explained from physical and analytical standpoints. The overall picture, nevertheless, is encouraging and provisions for what is rotordynamically termed the "zeroth-order" flow field, are being made to enhance the accuracy of a previously devised perturbation model (Baskharone and Hensel, 1991). Written with the objective of computing the rotordynamic forces on the shroud's outer surface, the latter

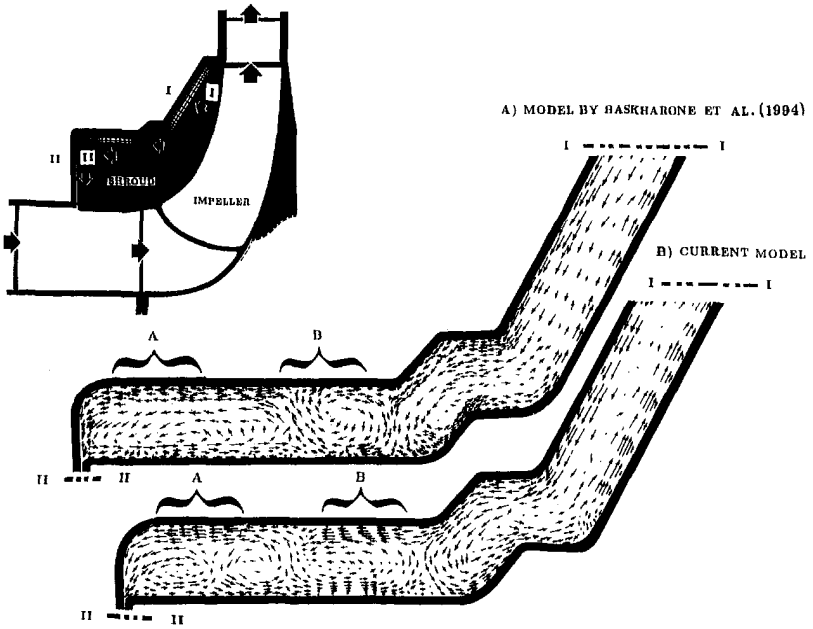

Fig. 7 Comparison of the meridional velocity vector in the leakage passage

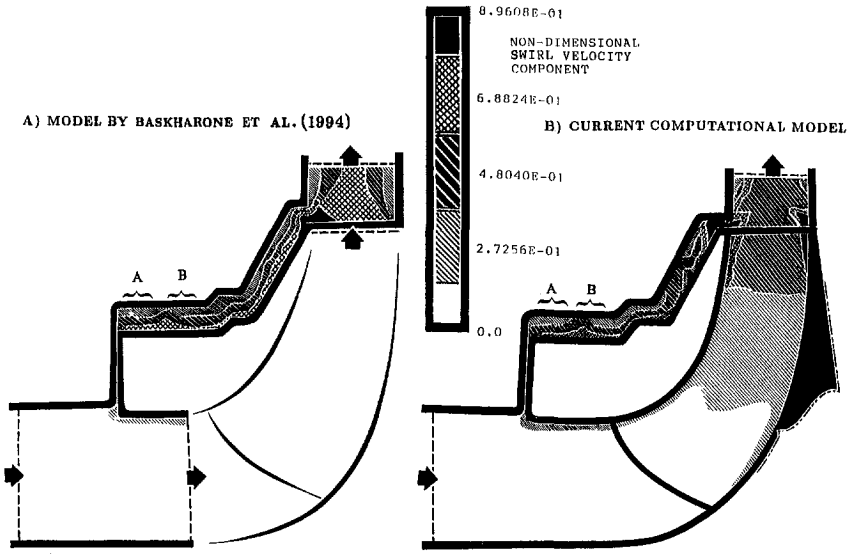

Fig. 8 Comparison of the tangential velocity component

perturbation model can now be upgraded in order to account for the fluid-exerted forces on the shroud/impeller assembly in the primary flow passage. In a shaft excitation of a whirling motion, these reaction forces may be restoring or aggravating to the shaft eccentricity and are, therefore, crucial to the impeller's rotordynamic stability.

References

Baldwin, B. S., and Lomax, H., 1978, "Thin Layer Approximation and Algebraic Model for Separated Turbulent Flows," AIAA Paper No. 78-257.

Baskharone, E. A., and Hensel, S. J., 1989, "A New Model for Leakage Prediction in Shrouded-Impeller Turbopumps," ASME JOURNAL OF FLUIDS ENGINEERING, Vol. III, pp. 111, pp. 118–123.

Baskharone, E. A., and Hensel, S. J., 1991, "A Finite Element Perturbation Approach to Fluid/Rotor Interaction in Turbomachinery Elements: Part 1—Theory," ASME JOURNAL OF FLUIDS ENGINEERING, Vol. 113, No. 3, pp. 362–367.

Baskharone, E. A., Daniel, A. S., and Hensel, S. J., 1994, "Rotordynamic Effects of the Shroud-to-Housing Leakage Flow in Centrifugal Pumps," ASME JOURNAL OF FLUIDS ENGINEERING, Vol. 116, No. 3, pp. 558–563.

Benim, A. C., and Zinser, W., 1985, "Investigation of the Finite Element Analysis of Confined Turbulent Flows Using a k-ϵ Model of Turbulence," *Computer Methods in Applied Mechanics and Engineering,* Vol. 51, pp. 507–523.

Black, H. F., 1969, "Effects of Hydraulic Forces in Annular Pressure Seals on the Vibrations of Centrifugal Pump Rotors," *Mechanical Engineering Science,* Vol. 11, pp. 206–213.

Bolleter, U., Leibundgut, E., and Sturchler, R., 1989, "Hydraulic Interaction and Excitation Forces of High Head Pump Impellers," presented at the Third Joint ASCE/ASME Mechanics Conference, University of California, La Jolla, CA.

Childs, D. W., 1983, "SSME HPFTP Interstage Seals: Analysis and Experiments for Leakage and Reaction Force Coefficients," NASA Contract NASB-33716, Texas A&M University.

Childs, D. W., 1989, "Fluid-Structure Interaction Forces at Pump-Impeller-Shroud Surfaces for Rotordynamic Calculations," ASME *Journal of Vibration, Acoustics, Stress, and Reliability in Design,* Vol. 111, pp. 216–225.

Childs, D. W., 1978, "The Space Shuttle Main Engine High-Pressure Fuel Turbopump Rotordynamic Instability Problem," ASME *Journal of Engineering for Power,* Vol. 100, pp. 48–57.

Dietzen, F. J. and Nordman, R., 1987, "Calculating Rotordynamic Coefficients of Seals by Finite Difference Techniques," ASME *Journal of Tribology,* Vol. 109, pp. 388–394.

Heinrich, J. C., and Zienkiewicz, O. C., 1977, "Quadratic Finite Element Schemes for Two-Dimensional Convective Transport Problems," *International Journal of Numerical Methods in Engineering,* Vol. 11, pp. 1831–1844.

Tam, L. T., and Przekwas, A. J., 1988, "Numerical and Analytical Study of Fluid Dynamic Forces in Seals and Bearings," ASME *Journal of Vibration, Acoustics, Stress, and Reliability in Design,* Vol. 110, pp. 315–325.

Xi-Xuan, Jin-Chu, Qin-Gen, and Lan-Sheng, 1988, "Some Field Experiences with Subsynchronous Vibration in Centrifugal Compressors," *Rotordynamic Instability Problems in High Performance Turbomachinery,* Mechanical Engineering Department, Texas A&M University.

Computation of Unsteady Viscous Marine-Propulsor Blade Flows—Part 2: Parametric Study

Eric G. Paterson
Assistant Research Engineer.
Assoc. Mem. ASME

Fred Stern
Professor.
Mem. ASME

Iowa Institute of Hydraulic Research
and Department of Mechanical Engineering,
The University of Iowa,
Iowa City, Iowa 52242-1585
e-mail: ERIC-PATERSON@UIOWA.EDU

In this two-part paper, time-accurate solutions of the Reynolds-averaged Navier-Stokes equations are presented, which address through model problems, the response of turbulent propeller-blade boundary layers and wakes to external-flow traveling waves. In Part 1, the Massachusetts Institute of Technology flapping-foil experiment was simulated and the results validated through comparisons with data. The response was shown to be significantly more complex than classical unsteady boundary layer and unsteady lifting flows thus motivating further study. In Part 2, the effects of frequency, waveform, and foil geometry are investigated. The results demonstrate that uniquely different response occurs for low and high frequency. High-frequency response agrees with behavior seen in the flapping-foil experiment, whereas low-frequency response displays a temporal behavior which more closely agrees with classical inviscid-flow theories. Study of waveform and geometry show that, for high frequency, the driving mechanism of the response is a viscous-inviscid interaction created by a near-wake peak in the displacement thickness which, in turn, is directly related to unsteady lift and the oscillatory wake sheet. Pressure waves radiate upstream and downstream of the displacement thickness peak for high frequency flows. Secondary effects, which are primarily due to geometry, include gust deformation due to steady-unsteady interaction and trailing-edge counter-rotating vortices which create a two-layered amplitude and phase-angle profile across the boundary layer.

Introduction

In Part 1 of this work (Paterson and Stern, 1997), unsteady viscous-flow computations of the Massachusetts Institute of Technology flapping-foil experiment (FFX) were validated through comparisons with data (Horwich-Lurie, 1993; Lurie, 1996) and analyzed in both time and frequency domains using numerical flow visualization and Fourier analysis. The FFX flow, which is a two-dimensional model of propeller blade and wake flow, was shown to be analogous to both Stokes layers (i.e., unsteady boundary layer flow) and inviscid gust flows (i.e., unsteady lifting flows), but with complexities due to interaction between the mean flow and the external-flow traveling wave (i.e., convection induced steady-unsteady interaction), viscous-inviscid interaction, and trailing-edge geometry. Signatures of these complexities were seen in the distortion of the external-flow waves, upstream- and downstream-traveling pressure-gradient waves radiating from a near-wake displacement-thickness peak, and trailing-edge counter-rotating vortices. Fourier-series analysis combined with back-substitution into the axial Euler equation showed that the pressure response was governed by the interaction between the zeroth and first harmonics. Oscillatory spatial variation of the velocity first-harmonic amplitude was shown to be a necessary condition for the upstream-traveling pressure waves. Overall, viscous-inviscid interaction appears to be an important driving mechanism of the flow.

The conclusions from Part 1 have potentially important implications for marine-propulsor design and, as such, motivate further study. Moreover, the FFX model problem and the directly related classical work on unsteady boundary layers (e.g., Patel, 1977; Choi et al., 1996) and unsteady lifting flows (e.g., Sears, 1941; Horlock, 1968; Naumann and Yeh, 1973; Goldstein and Atassi, 1976; Basu and Hancock, 1978; Ho and Chen, 1981; and Poling and Telionis, 1986) have, as discussed in Part 1, either limited ranges of applicability or are incomplete from the perspective of parameter range. In addition, further study is motivated by the fact that standard Navy design practice is based upon inviscid methods (e.g., Kerwin and Lee, 1978). Although such methods are very capable in the first stages of design, they are unable to resolve boundary layers and wakes and, as such, can not predict the unsteady flow associated with propulsor-hull-appendage interaction or rotor-stator interaction. Given that flow unsteadiness can have a deleterious effect upon cavitation and acoustic performance, development and validation of unsteady RANS methods is critical in meeting future signature requirements.

The objective of this paper is to further investigate viscous unsteady blade flows through a parametric study of the influences of frequency, geometry, and waveform. The justification for studying these parameters is as follows. Blade-section frequency varies with speed of advance, radius, and inflow spatial-harmonic content. Changes in geometry (i.e., thickness, camber, angle-of-attack) influence the mean flow field which affects both the amount of steady-unsteady interaction and the trailing-edge flow. Finally, the external flow waveform represents a model of the spatially-varying (i.e., due to hull and appendage wakes) propulsor inflow. Blade response is directly related to the waveform and its associated time-varying inflow angle of attack. It is of interest to note that the unsteady 3D RANS simulations of Chen and Stern (1994) for a realistic Naval propeller (i.e., DTMB P4132) embedded in a 6th harmonic screen wake (Jessup, 1990), which itself is a model of the spatially-varying inflow, illustrate that 2D models are qualita-

Contributed by the Fluids Engineering Division for publication in the JOURNAL OF FLUIDS ENGINEERING. Manuscript received by the Fluids Engineering Division December 7, 1996; revised manuscript received November 30, 1998. Associate Technical Editor: M. N. Dhaubhadel.

tively accurate. For example, Fig. 1 shows perturbation-velocity particle traces, at 70 percent of the propeller radius, which look very similar, albeit on a much coarser grid, to the low-frequency cases shown subsequently herein.

Since the parametric space for these three variables is very large, a focused set of simulations were designed with the goals of further explaining the physics observed in Part 1 and extending the parameter range, particularly frequency. Initially, it was anticipated, especially given the derivation of an analytical inflow model which could represent the flow created by either co- or counter-rotating flappers, that the FFX configuration could be used for the entire parametric study. However, as the numerical experiments proceeded, it became clear that limitations in the practical frequency range of the FFX necessitated adoption of a second model problem. Sears problem of a foil embedded in a traveling vertical-wave (VW) was selected because of both its simplicity and its use in the ship hydrodynamics community as a "first-order" approximation to unsteady blade flows and forces (e.g., Lewis, 1988). Therefore, effects of frequency are studied using both the FFX tunnel and foil geometry, as in Part 1, and the FFX foil in an unbounded fluid with the incident VW. Effects of geometry are studied through the use of a flat plate in the FFX tunnel. As will be shown, this eliminates both gradients in the mean flow field and, therefore, the steady-unsteady interaction. Effects of waveform are studied through comparisons between the FFX- and Sears-type flows. In addition, the flat plate geometry will be studied in both the co- and counter-rotating flapper-wake inflow. The latter will demonstrate the impact of unsteady lift generation upon high-frequency response.

This paper is organized as follows: the computational method and uncertainty assessment are reviewed; boundary conditions, parameters, and computational grids are described; results are presented; and summary and conclusions are provided. For reference, detailed description of the FFX, the RANS and grid-generation methods, and the uncertainty assessment are provided in Part 1.

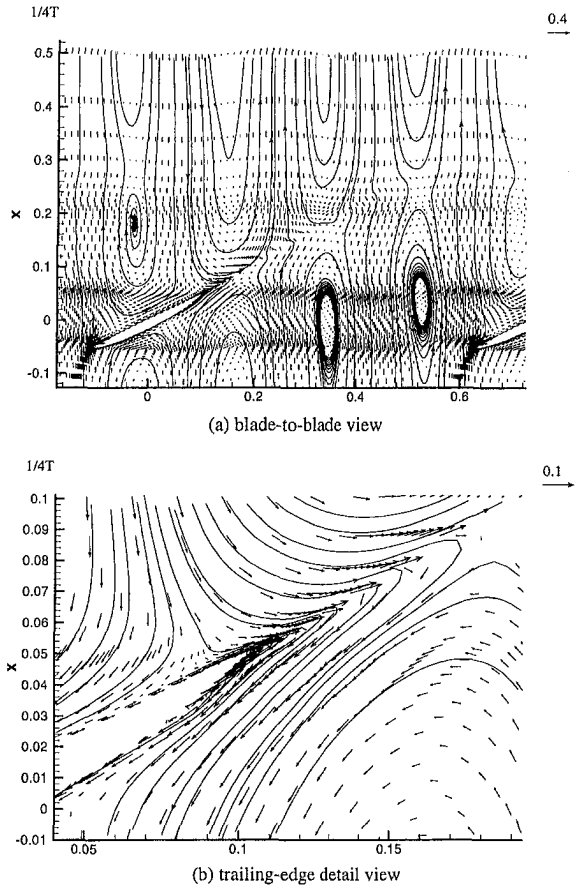

Fig. 1 Perturbation-velocity vectors and particle traces: P4132, r/R = 0.7 (Chen and Stern, 1994)

Computational Method and Uncertainty Assessment

The computational method is based upon time-accurate solution of the two-dimensional incompressible Reynolds-averaged Navier-Stokes (RANS) equations. The PISO algorithm is used as the pressure-velocity coupling scheme and the equations are discretized using finite-analytic and second-order finite-difference discretizations for the spatial and temporal terms, respectively. The algebraic equations are solved using a tri-diagonal algorithm and line ADI. Turbulence closure is attained through quasi-steady application of the Baldwin-Lomax turbulence model with modifications for both wake asymmetry and axial pressure gradients. Further details and references can be found in Part 1. Also, it should be noted that the core solver is essentially the same as that used in the general-purpose three-dimensional RANS CFD code, CFDSHIP-IOWA (Paterson et al., 1998), which has been applied to, and validated for, a wide range of marine-propulsor and surface-ship problems.

Verification analysis, which consists of grid-, iterative-, and time-step-convergence studies was performed. Grid-convergence studies were conducted in Part 1 where, in addition to steady-flow requirements for near-wall spacing and leading- and trailing-edge resolutions, it was determined that approximately 40 grid points per wavelength was required to adequately resolve the traveling waves. This result was used to design the grids for the simulations presented herein. For frequencies at and below the FFX frequency ($\xi = 7.2$), the FFX grid was used. For high frequency, the resolution was increased following the above rule. Iterative convergence was assured through implementation of a convergence criterion of 10^{-4} for the residuals defined as the change between iterates. Time-step-convergence studies were conducted in Part 1 and extrapolated to the work herein, i.e., Δt is 1/64th of the traveling-wave period.

Rigorous CFD validation procedures, as defined by Coleman and Stern (1997), requires benchmark data and both CFD and data uncertainties. Unfortunately, validation data is limited to that which was used in Part 1. As such, no validation is performed herein for the FFX-type flows. For the VW flow cases, comparisons are made to Sears theory. However, as already mentioned, Sears theory has limited range of applicability and, as such, cannot be used as a validation benchmark above $\xi = \pi$.

Boundary Conditions, Parameters, and Computational Grids

Vertical- and Horizontal-Combined Wave Flow. In Part 1, three different domains (i.e., small, tunnel, complete) were used for simulating the FFX. The tunnel domain was chosen for the work here because it is computationally more efficient, i.e., smaller and quicker to converge than the complete domain and more general than the small domain. The tunnel domain boundary conditions remain unchanged from those described in Part 1, except for the inflow conditions. An analytical inflow model for both co-rotating flappers (i.e., vertical-combined wave [VCW]) and counter-rotating flappers (i.e., horizontal-combined wave [HCW]) was derived assuming that the main foil was removed from the tunnel and that the flapper wakes were inviscid, irrotational, and sinusoidal. The wakes were also assumed to travel with wavespeed c, wavelength $\lambda = 2\pi c/\xi$, and amplitude V_1. The tunnel was divided into three regions as shown in Fig. 2 such that the Laplace equation was solved for the velocity potential ϕ in a piecewise fashion across the tunnel. The resulting traveling-wave solution is superimposed with the

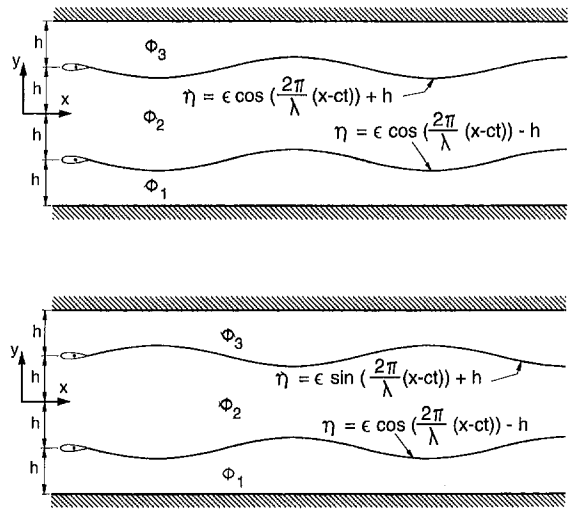

Fig. 2 Schematic of co- and counterrotating flapper wakes. (*a*) VCW external flow; (*b*) HCW external flow.

FFX mean-inflow data (U_0, V_0) to give the following inflow-model equations for the VCW

$$U(x,y,t) = \begin{cases} U_0 + V_1 \dfrac{\cosh[\xi/c(2h+y)]}{\cosh(\xi h/c)} \cos[\xi(t-x/c)] & -2h < y < -h \\ U_0 + V_1 \dfrac{\sinh(\xi y/c)}{\cosh(\xi h/c)} \cos[\xi(t-x/c)] & -h < y < h \\ U_0 - V_1 \dfrac{\cosh[\xi/c(2h-y)]}{\cosh(\xi h/c)} \cos[\xi(t-x/c)] & h < y < 2h \end{cases} \quad (1)$$

$$V(x,y,t) = \begin{cases} V_0 - V_1 \dfrac{\sinh[\xi/c(2h+y)]}{\cosh(\xi h/c)} \sin[\xi(t-x/c)] & -2h < y < -h \\ V_0 - V_1 \dfrac{\cosh(\xi y/c)}{\cosh(\xi h/c)} \sin[\xi(t-x/c)] & -h < y < h \\ V_0 + V_1 \dfrac{\sinh[\xi/c(2h-y)]}{\cosh(\xi h/c)} \sin[\xi(t-x/c)] & h < y < 2h \end{cases} \quad (2)$$

where $4h$ is the tunnel height, x is the inlet location (i.e., -0.26), c is the wavespeed which is assumed to be equal to one, V_1 is the specified amplitude at $y = \pm h$, and t is time. The inflow-model equations for the HCW are very similar to Eqs. (1) and (2) but with small changes to account for the 180 deg phase shift of the flapper wake at $y = h$. In the region between flapper wakes (i.e., $-h < y < h$), the hyperbolic functions in the numerator of the second term in both U and V are switched and in the region between the top flapper wake and the tunnel wall (i.e., $h < y < 2h$), the sign of second term is changed. As will be shown in the discussion section through the use of perturbation-velocity [$U(t) - U_0$, $V(t) - V_0$] particle traces, Eqs. (1) and (2) produce two rows of co- or counter-rotating vortices. Also, note that the terminology VCW and HCW is adopted to signify the dominant flow component along the tunnel centerline.

As observed by Horwich-Lurie (1993), the range of frequencies in the physical FFX was limited and facility/geometry dependent. Similar limitations were found upon application of Eqs. (1) and (2), wherein the practical range was determined to be $4.5 < \xi < 15$. Below this range, the amplitude profiles became unrealistically discontinuous along the wake sheets (i.e., at $y = -h$ and $y = +h$), and above this range, the amplitudes became very small along the tunnel centerline (i.e., $y = 0$). Implementation of Eqs. (1) and (2) requires several other issues to be addressed. First, they contain many dependent parameters. The amplitude profiles across the inlet are determined by hyperbolic sine and cosine functions of ξ, c, h, y. Second, for a parametric study of ξ, it is impossible to hold the inflow-amplitude and angle-of-attack (i.e., $\tan^{-1}(V/U)$) profiles fixed. For the work presented here, the angle of attack on the tunnel centerline was held constant for all frequencies. This results in amplitude profiles that vary with frequency and that become very large at the flapper wake sheets (i.e., $y = \pm h$).

The FFX foil is subject to VCW inflow at three frequencies $\xi = 4.5$, 7.2 (i.e., FFX value), and 15, and amplitude on the tunnel centerline fixed to the FFX value $V_1 = 0.022$ (i.e., ± 1.26 deg angle of attack change). Note that the $\xi = 7.2$ case is nearly the same as the FFX presented in Part 1. The only difference is that herein, the inflow is analytical and purely first harmonic, whereas the FFX was prescribed from data. The corresponding wavelength and time step (λ, Δt) are (1.39, 0.028), (0.87, 0.017), and (0.42, 0.008). Based upon Eqs. (1) and (2), the derived external-flow pressure gradients, $\partial p/\partial x$ and $\partial p/\partial y$, and vorticity ω_z have leading first-order terms of magnitude $\xi V_1(1 - U_0/c)$, $\xi V_1(1 - U_0/c)$, and ξV_1, respectively. For the three selected frequencies, the peak amplitude and frequency-amplitude product ($V_{1-\max}$, $\xi V_{1-\max}$), which are at $y = \pm h$, are (0.045, 0.202), (0.08, 0.576), and (0.60, 4.950). Clearly, it should then be expected that for high frequencies, the response will be extreme and contain higher harmonics due to second-order terms. Also, for regions where $c < U_0$ (e.g., due to gust deformation), the external-flow pressure gradients become nonzero [note: Eqs. (2) and (3) of Part 1 indicate the effect of wavespeed changes upon the pressure gradient]. All remaining parameters are set at the FFX values, i.e., Reynolds number $\mathrm{Re} = U_0 L/\nu = 3{,}780{,}000$, laminar to turbulent transition $x_{tr} = 0.10$, and angle of attack $\alpha = 1.34$ deg. For each of the cases, the calculation was started from a steady-flow solution.

The flat plate, in contrast, is placed in the FFX tunnel and subject to both VCW and HCW inflows at $\xi = 7.2$. The time step is $\Delta t = 0.01745$ and the boundary conditions are the same as those above except the mean inflow is replaced by a uniform freestream (i.e., $U_0 = 1$ and $V_0 = 0$). All other parameters remain unchanged except the angle of attack which is set to $\alpha = 0$. As for the foil, the calculations were started from a steady-flow solution.

To accurately resolve the traveling wave, FFX axial grid-point resolution per wavelength, which was about 40 points per wavelength, is retained. The FFX 180×179 tunnel-domain grid is used for the foil at $\xi = 4.5$ and 7.2 while a high resolution 400×179 grid is used for $\xi = 15$. The flat-plate grid is also 180×179, retains the FFX distributions, and is orthogonal due to the geometry. For all grids, there are approximately 40 points spanning the boundary layer and the near-wall grid spacing was set such that the first grid point was located at $y^+ = \sqrt{\tau_w/\rho}(y/\nu) \approx 0.1$.

Vertical-Wave Flow. For the VW flow, the open-water form of the FFX foil (i.e., the FFX foil was modified by MIT to give same mean pressure distribution in the tunnel as that of the blade section of interest in an infinite fluid) is subject to

a traveling VW. The VW external flow is described by the following

$$U = 1$$

$$V = V_1[\xi(t - x/c)] \tag{3}$$

Based upon this velocity field, the external-flow pressure gradients, $\partial p/\partial x$ and $\partial p/\partial y$, and vorticity ω_z have leading first-order terms of magnitude 0, $\xi V_1(1 - U_0/c)$, and ξV_1, respectively. It is of interest to note that Sears and related analytical theories are based upon the assumption of ideal irrotational flow and therefore assume that ξV_1 is small. Referring to Fig. 3, the boundary conditions are as follows. *On the inlet* S_I, Eq. (3) is used to specify U and V and $\partial p/\partial x = 0$; *on the outer boundaries* S_O, $U = 1$, $\partial V/\partial y = 0$, and $p = 0$; *on the body,* no slip conditions were used; and *on the exit* S_E, zero-diffusion and zero-pressure-gradient conditions were applied.

The magnitude is fixed to $V_1 = 0.022$ and frequencies equal to 0.5, 1.0, π, 7.2, and 10 were studied. The corresponding (λ/L, Δt, ξV_1) are (12.6, 0.1260, 0.011), (2π, 0.0628, 0.022), (2, 0.02, 0.069), (0.87, 0.0145, 0.158), and (0.63, 0.0105, 0.22). The FFX values for Re, α, and x_{tr} are used. The solutions are started from a steady-flow solution.

Again, based upon Part 1 calculations, the grid has a minimum axial distribution of 40 points per wavelength in the near foil region. This requirement is relaxed in the wake for the high frequencies. For $\xi < 7.2$, the grid is 300 × 199 and extends from $-1 < x < 4$ and $-2 < y < 2$. For $\xi = 10$, the same number of points are used but the grid is truncated in the axial direction (i.e., $-1 < x < 2$) such that the grid-point/wavelength ratio is roughly maintained. Both grids have approximately 40 points spanning the boundary-layer and near-wall spacing such that the first grid point is located at $y^+ \approx 0.1$.

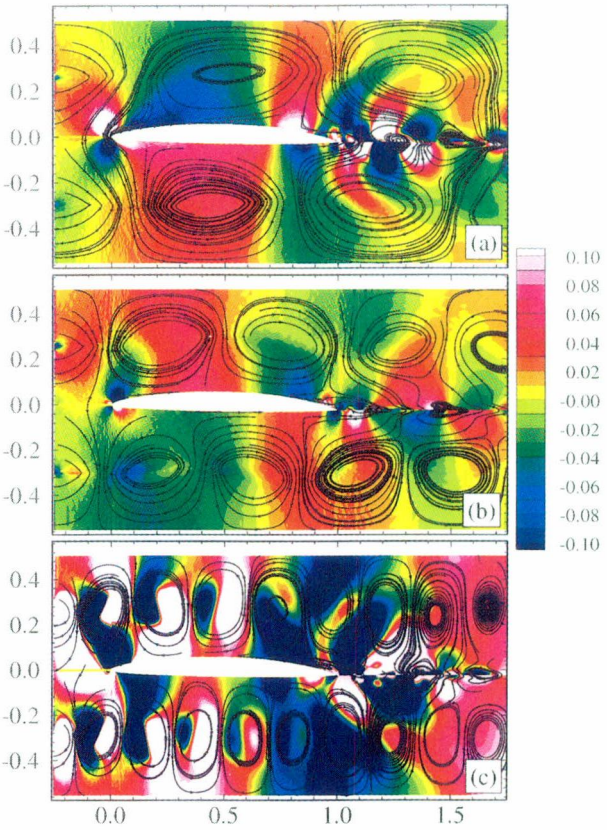

Fig. 4 Perturbation-velocity particle traces and perturbation axial-pressure-gradient contours: VCW study. (*a*) ξ = 4.5; (*b*) ξ = 7.2; (*c*) ξ = 15.

Results

In the following, the results are organized into effects of frequency, effects of geometry, and effects of waveform. For each, discussion is presented in the following order: overall view of flow field, perturbation-velocity particle traces, and contours of perturbation axial pressure gradient field; lift and drag; surface pressure; boundary-layer profiles; and analysis. For brevity, select figures are used to support the discussion. Paterson (1994) provides detailed figures, analysis, and discussion of each simulation. Also, details of the foil steady-flow/zeroth-harmonic flow field can be found in Part 1. Through the work herein, it was found that the zeroth harmonic flow field was not sensitive to frequency, i.e., it can be assumed that second-order streaming effects are negligible or unresolved. For the flat plate, the zeroth-harmonic flow field is a simple turbulent boundary layer and wake.

Effects of Frequency. Figure 4 shows an overall view of the VCW solutions at each of the frequencies. Instantaneous perturbation-velocity particle traces and perturbation axial-pressure-gradient [$p_x(t) - p_{x,0}$] contours are shown for each ξ. The variation in wavelength with frequency is clearly displayed. In addition, the differential distortion, i.e., phase shift between the two flapper wakes, which is measured by $\lambda_p^{-1} - \lambda_s^{-1}$, is shown to increase with frequency. For the three frequencies, (λ_p, λ_s, $\lambda_p^{-1} - \lambda_s^{-1}$) are estimated to be (1.46, 1.75, 0.11), (0.91, 1.10, 0.19), and (0.44, 0.53, 0.38), respectively. Given the higher mean velocity on the suction side, the traveling wave on that side is accelerated in comparison to the pressure side of the foil. Increasing the frequency, which decreases the wavelength, causes the phase shift to increase such that for $\xi = 15$, the wakes are approximately 137 deg out of phase by the time they reach the trailing edge. It is also shown that the foil is shedding vortices from the trailing-edge and that the size of these vortices decrease with frequency. This figure further illustrates the direct comparison between the flow patterns and axial pressure gradient such that the secondary vortices on the foil and in the wake can be directly correlated to alternating regions of favorable and adverse pressure gradient. Furthermore, animations show that $\xi = 4.5$ and 7.2 demonstrate upstream-traveling pressure waves with their origin in the near wake. In comparison, $\xi = 15$ shows an extreme response indicative of the large-amplitude wave.

Figure 5 shows an overall view of the VW solutions over the range of frequencies studied. V-component velocity contours are shown where solid and dashed lines indicate positive and negative values, respectively. Note that a plot similar to Fig. 4 was not very informative since there is neither a horizontal wave nor an unsteady axial pressure gradient in the external flow. The difference in wavelength between the different frequencies is clearly shown as is the numerical dissipation near the exit for the higher frequencies. The effect of steady-unsteady interaction is also shown by the deformation of the gust. A wake structure, which is similar to the FFX flow is displayed.

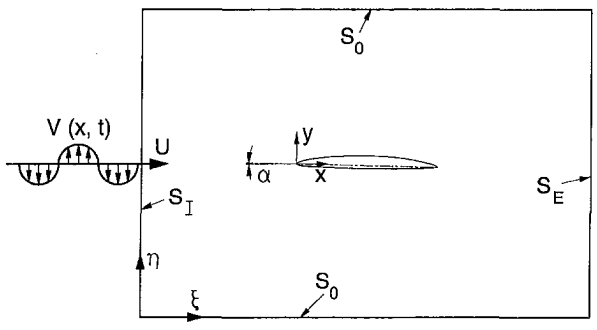

Fig. 3 Calculation domain and boundaries: VW study

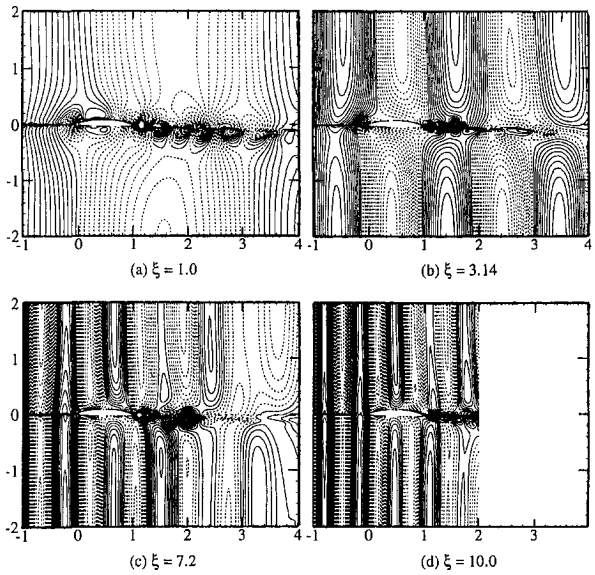

Fig. 5 ***V*-velocity component contours: VW study**

Also, it is shown that the size of the vortices in the wake decrease with increasing frequency.

Figure 6 shows the first harmonics of lift ($C_{L,1}$, $\gamma_{L,1}$) and drag ($C_{D,1}$, $\gamma_{D,1}$) for all of the solutions. It also shows ($C_{L,1}$, $\gamma_{L,1}$) for both the Sears theory and FFX data point of Lurie (1996). It should be noted that the first 10 harmonics were calculated and that, in general, the higher harmonics are at least an order-of-magnitude smaller than $C_{L,1}$ and $C_{D,1}$. For the VCW, $C_{L,1}$ shows decreased amplitude between $\xi = 4.5$ and 7.2 and is less than the Sears values. However, $C_{L,1}$ is quite close to data. For $\xi = 15$, the amplitude increases and is much larger than the Sears value. This is indicative of the large amplitude external flow and the associated vorticity and pressure gradients (i.e., as measured by ξV_1) as previously discussed. The lift phase $\gamma_{CL,1}$ indicates increasing lags with increasing frequency and at $\xi = 7.2$ shows good agreement with data. The drag amplitude $C_{D,1}$ shows trends similar to the lift and $\gamma_{CD,1}$ shows nearly linear decrease with frequency. Also, the lift leads the drag and the difference is shown to increase with frequency, i.e., $\gamma_{CL,1} - \gamma_{CD,1} = 25$, 35, and 141 deg for the three frequencies, respectively. In general, for the VW at the low frequencies (0.5, 1.0, 3.14), $C_{L,1}$ and $\gamma_{CL,1}$ show agreement with the Sears theory. The high frequencies (7.2, 10.0), however, show large deviation from the theory and similar trends to the VCW, i.e., large increase in $C_{L,1}$ and decrease in $\gamma_{CL,1}$ with frequency. Also, the lift leads the drag and the phase difference between them greatly increases with frequency, i.e., ($\gamma_{L,1} - \gamma_{D,1}$) = 1, 5, 10, 148, 150 deg for the five frequencies, respectively. Although not fully understood, reasons for the large departure from Sears theory at high frequencies include an outer flow which is increasingly non-irrotational (i.e., as measured by ω_z and ξV_1), increasing steady-unsteady interaction, and trailing-edge effects which are not resolved by either the inviscid flow approximation or the classical Kutta condition.

Figure 7 shows the surface-pressure first-harmonic amplitude (p_1) and phase (γ_{p1}) for the VCW flows. The $\xi = 4.5$ and 7.2 solutions show amplitudes which decrease with frequency and phases which indicate upstream-traveling waves, i.e., the phase increases with x/L. Moreover, the phase shows the pressure and suction sides of the foil to be nearly 180 deg out of phase. In comparison, $\xi = 15$ shows the largest amplitude, which is consistent with $C_{L,1}$, and the phase indicates complex wave characteristics with the pressure and suction sides showing upstream- and downstream-traveling waves, respectively. Also, the phase difference between sides is closer to 70 than 180 deg, which is due to the differential distortion of the external flow waves. The second harmonic amplitude (not shown) is significant and is due to the large inflow amplitude and aforementioned resultant nonlinearities.

Figure 8 shows p_1 and γ_{p1} for the VW flows at $\xi = 1$ and 7.2. The low frequencies (0.5, 1.0, 3.14), which also agree well with the lift prediction of Sears, show pressure responses which decrease with frequency and shapes which are typical of Sears theory, i.e. strong leading edge peak in amplitude with axial decay to the trailing edge and phase which is essentially constant along the chord (i.e., temporal wave) and with each side of foil 180° out of phase with each other. In contrast, the higher frequencies show an amplitude without the leading edge peak and phases which indicate slowly upstream traveling pressure waves.

Figure 9 shows a typical example (i.e., suction side at $x/L = 0.97$) of the first-harmonic amplitude (U_1) and phase (γ_{U1}) profile for the VCW flows. The amplitude is normalized by the boundary-layer edge value U_{1e}, and phase is plotted relative to the edge value γ_{1e}. In general, $\xi = 4.5$ displays large overshoots and phase lags which increase in amplitude and thickness with x. For $\xi = 7.2$, the response is very similar to the FFX with overshoots and phase lags on the forebody and two-layered U_1 profiles and 180 deg phase shifts near the trailing-edge. For $\xi = 15$, the profiles are more complex with two-layered structures and large phase shifts on both the forebody and afterbody. In the wake, each case shows overshoots and phase lags which are a continuance of the trailing-edge boundary-layer response.

Figure 10 shows a typical example (i.e., suction side at $x/L = 0.97$) of a U_1 and γ_{U1} profile for the VW flows. Overall, the first-harmonic amplitude decreases with increasing frequency. Moreover, there is a general trend that the amplitude shows decreasing overshoots that are increasingly farther from the wall with increasing x. The phase profiles show that for low frequency, there is little phase variation across the boundary layer, whereas for high frequency, there is a much larger variation which is similar to the FFX phase response with large phase shifts across the boundary layer near the trailing edge.

The Euler equation analysis developed in Part 1 was applied to each of the simulations. As explained therein, B indicates the relative spatial harmonic content of U_1 in comparison to the external-flow wavelength and is an indicator of the direction of the pressure-gradient wave: $B > 1$ upstream-traveling wave; $B = 1$ stationary, or temporal, wave; and $B < 1$ downstream-traveling wave. For the VCW, the analysis shows that the first harmonic amplitude U_1 for all three frequencies exhibited significant spatial-harmonic content. In particular, the $\xi = 4.5$ case was second harmonic with very similar response on both sides

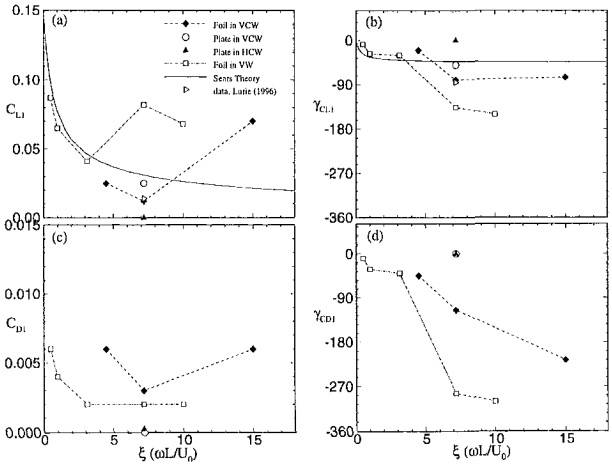

Fig. 6 Lift and drag first-harmonic amplitude and phase. (*a*) Lift amplitude; (*b*) lift phase; (*c*) drag amplitude; (*d*) drag phase.

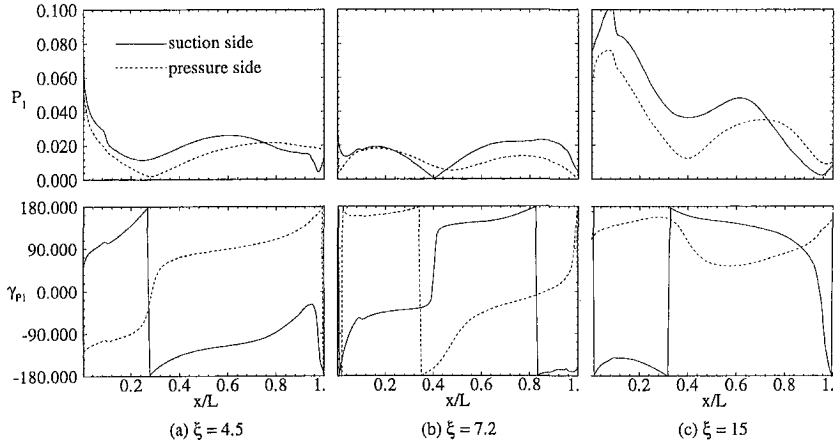

Fig. 7 Surface-pressure first-harmonic amplitude and phase distribution: VCW study

of the foil, i.e., $(B_p, B_s) = (2, 2)$. The $\xi = 7.2$ case showed similar results, except that the differences between the suction and pressure sides increased, i.e., $(B_p, B_s) = (1.95, 1.8)$. The $\xi = 15$ case showed a different response on each side of the foil with downstream-traveling and upstream-traveling pressure waves on the suction and pressure sides, respectively, i.e., $(B_p, B_s) = (1.4, 0.7)$. For each of the cases, the differences between each side of the foil are consistent with the observed phase shift in the outer-flow waves. Upstream-traveling waves over the foil of varying speeds are seen for all three cases. Furthermore, all three demonstrate downstream-traveling waves in the wake. Finally, the displacement-thickness first-harmonic amplitude δ_1^* showed a peak in the wake for all three cases. For $\xi = 4.5$, the peak is very close to the trailing edge and less pronounced whereas for $\xi = 7.2$ and 15, the peaks are more distinct and located further from the trailing edge at about $x = 1.1$.

For the VW flows, the Euler-equation analysis showed that for $\xi = 0.5$, 1, 3.14, the U_1 response was much different from the FFX. This is not surprising since the ambient wavefield, i.e., Eq. (3), has zero horizontal component. As such, U_1 is generated solely due to the localized effect of the near-blade pressure field. This is in contrast to the VCW and HCW flows, i.e., Eqs. (1)–(2), both of which have a dominant horizontal-wave traveling downstream with a phase angle $\gamma_U = -\xi x/c$. For the low frequency VW cases, U_1 shows zero amplitude upstream of the foil and large peaks at the leading and trailing edge. The displacement thickness amplitude δ_1^* for these frequencies shows growth up to the trailing edge and then decays into the wake. In contrast, the high-frequency VW cases, i.e., $\xi = 7.2$, 10, which notably have a wavelength shorter than the foil, look more like the FFX response: the U_1 amplitude contains spatial oscillations (i.e., $B = 1.45$ and 1.5, respectively) which corresponds to upstream-traveling pressure waves. Moreover, δ_1^* shows a peak in the near wake, which, as in the FFX, implies that viscous-inviscid interaction, is the source for the pressure response. Based upon these results, the interaction is shown to be dependent upon the frequency, and moreover, shows distinctly different response for frequencies that correspond to wavelengths that are shorter ($\xi < 2\pi$) and longer ($\xi > 2\pi$) than the foil.

Effects of Geometry. Figure 11(*a*) shows the perturbation-velocity particle traces and perturbation axial-pressure-gradient contours for the flat plate in the VCW. The lack of external flow distortion is evident and the flow shows wake vortices typical of the FFX. Also, consistent with the boundary-layer profiles, which are discussed below, is the lack of trailing-edge vortices which were shown in foil calculations. The pressure-gradient contours further confirm the effect of lift generation and the trailing-edge vortex sheet. The VCW displays the upstream and downstream traveling pressure waves over the foil and in the wake, respectively, with a wake that shows complexity similar to the FFX.

Figure 6 also shows $(C_{L,1}, \gamma_{L,1})$ and $(C_{D,1}, \gamma_{D,1})$ for the flat plate. Lift response to the VCW is first-harmonic with $C_{L,1}$ and $\gamma_{L,1}$ that are close to Sears value. The drag response is second harmonic (i.e., $C_{D,1} \approx 0$) with an amplitude that is an order-of-magnitude smaller than the foil. For the plate, wall-shear stress provides the only contribution to drag. The second-harmonic drag response is due to the symmetry of the plate and the asymmetry of the external flow with respect to each side.

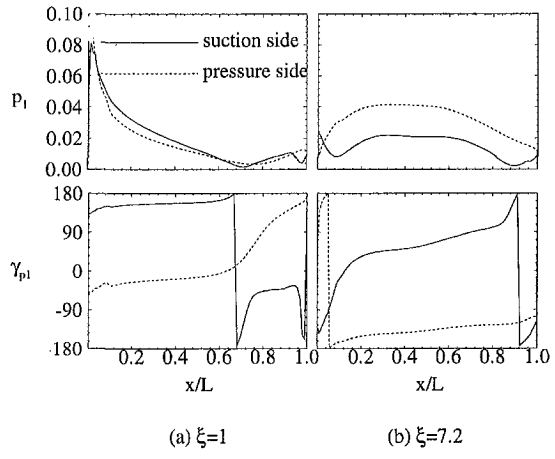

Fig. 8 Surface-pressure first-harmonic amplitude and phase distribution: VW study

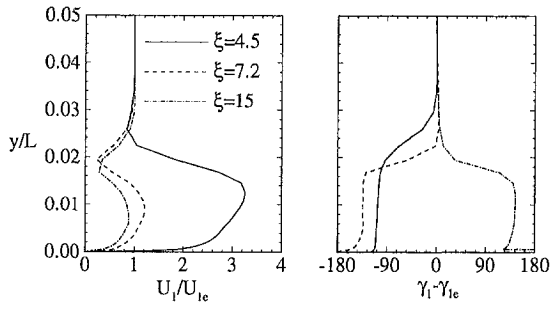

Fig. 9 Velocity first-harmonic amplitude and phase profiles on suction side at $x/L = 0.97$: VCW study

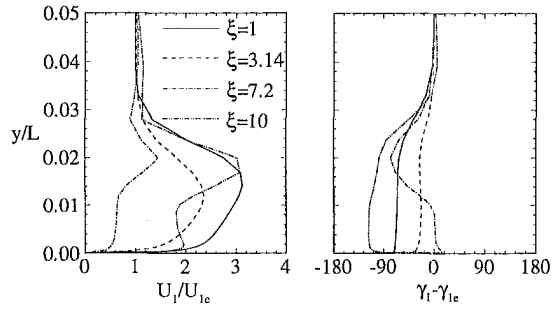

Fig. 10 Velocity first-harmonic amplitude and phase profiles on suction side at x/L = 0.97: VW study

Figure 12(a) shows the pressure first-harmonic amplitude and phase. The VCW shows an amplitude response with a large leading edge peak and decay towards the trailing edge, except that there is a zero amplitude and phase jump at $x/L = 0.58$. In addition, the phase, which shows that each side of the plate is 180 deg out of phase with respect to each other, indicates an upstream-traveling wave.

As a typical example, Fig. 13 shows the first-harmonic amplitude (normalized by the edge value) and phase (with respect to the edge value) profiles at $x/L = 0.5$. The VCW shows a two-layered amplitude response in the outer region of the turbulent boundary layer and a large amplitude response in the sublayer region. The sublayer response can be directly correlated to the pressure amplitude shown in Fig. 12. The phase angle γ_{U1} displays a large lag in the outer region and overall, a complex response of lags in the outer region and lead and lags in the near-wall region. This is caused by the downstream-traveling velocity wave which drives the outer portion of the boundary layer and an upstream-traveling pressure wave which drives the near-wall region. Finally, the flat plate solution does not demonstrates the 180 deg phase shifts at the boundary layer edge which were observed in the FFX and correlated to regions of counter-rotating vortices.

The Euler equation analysis is shown in Fig. 14. The VCW shows U_1 which is second harmonic (i.e., $B \approx 2$). This is consistent with the observations of upstream-traveling waves. Figure 14(b) further shows the tangent behavior $A = \tan(\hat{\gamma}_{p_{x,1}})$ (see Part 1 for definition) for the VCW. Finally, the VCW shows a displacement thickness which is similar, but a factor of 2 smaller, to that shown for the FFX foil flows.

Effects of Waveform. Effects of waveform have, in part, already been discussed. It has been shown that the VCW and VW ambient waveforms and flow-field responses are different

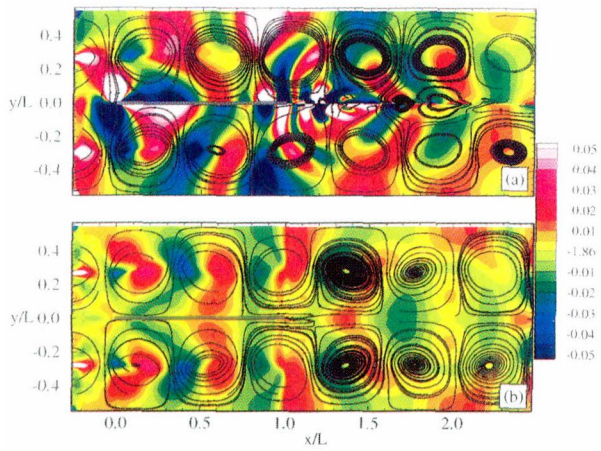

Fig. 11 Perturbation-velocity particle traces and perturbation axial-pressure-gradient contours: flat-plate study. (*a*) VCW; (*b*) HCW.

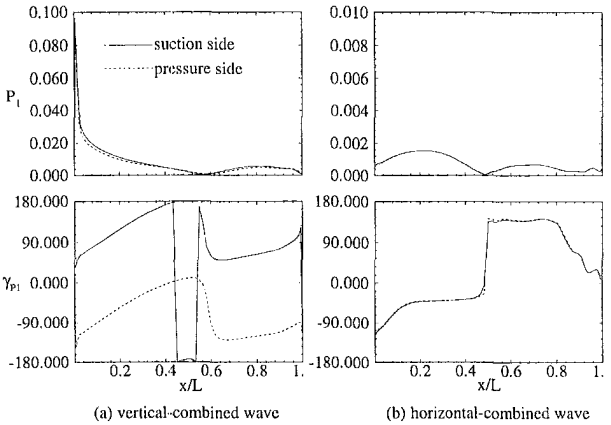

Fig. 12 Surface-pressure first-harmonic amplitude and phase distribution: flat-plate study. (*a*) VCW; (*b*) HCW.

but have similarities particularly for high frequencies. Both waveforms produce a time-varying change in angle of attack and, at high frequency, the responses display many of the FFX flow features. It has also been shown that a flat plate in the VCW shows very similar response. In the following, simulation of the flat plate in the HCW will demonstrate that the source of such response is due to waveform and the generation of unsteady lift.

Figure 11(b) shows the perturbation-velocity particle traces and perturbation axial-pressure-gradient contours for the flat plate in the HCW. The differences between the VCW and HCW are evident. The VCW shows wake vortices typical of the FFX whereas the HCW, which has zero lift, does not display wake vortices. The pressure-gradient contours further confirm the effect of lift generation and its correlation to the wake vortex sheet. In contrast to the VCW, the HCW shows symmetry with respect to both sides of the plate, smaller amplitudes, and no wake sheet.

Figure 12 also shows the pressure first-harmonic amplitude and phase for the HCW. In contrast to the VCW, the HCW shows an amplitude response that is an order of magnitude smaller than the VCW. This is because the pressure field for the HCW is solely due to stagnation versus lift effects for the VCW. In addition, both sides of the foil are in phase and indicate a temporal wave, except over the first and last 20 percent of the plate which are upstream- and downstream-traveling waves, respectively.

Figure 13 also shows the U_1 and γ_{U1} profiles for the HCW at $x/L = 0.5$. In contrast to the VCW, the HCW shows an amplitude which decreases across the boundary layer except with a large sublayer response. The phase increasingly lags the external flow as the wall is approached and is constant across the sublayer. The sublayer phase is consistent with both the pressure and shear-stress. As discussed above for the VCW,

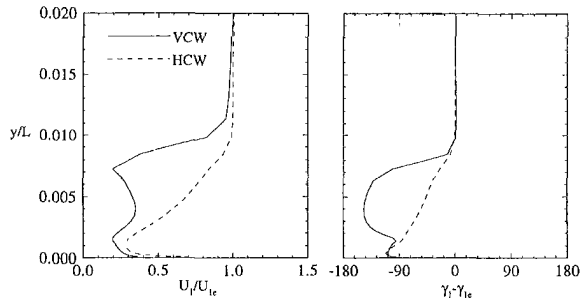

Fig. 13 Velocity first-harmonic amplitude and phase profiles at x/L = 0.5: flat-plate study

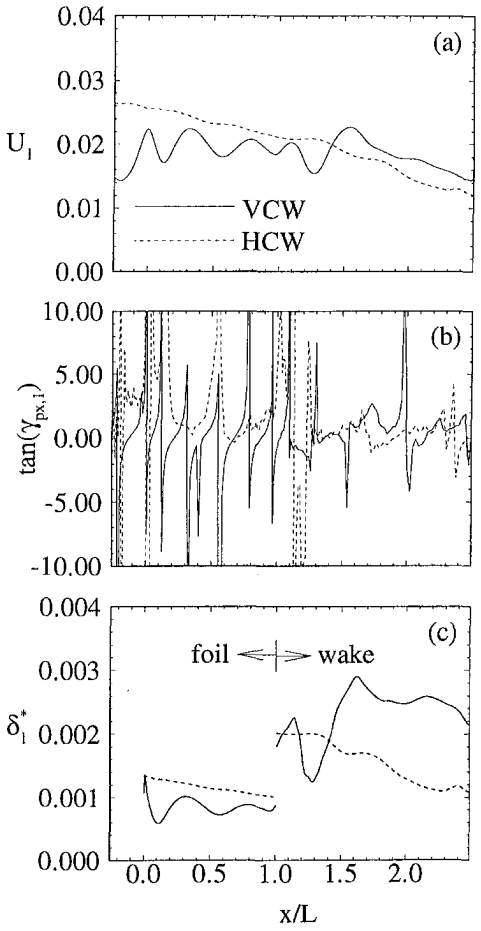

Fig. 14 Euler equation analysis: flat-plate study. (*a*) U_1; (*b*) tan ($\hat{\gamma}_{p_{x,1}}$); (*c*) δ_1^* first-harmonic amplitude

180 deg phase shifts at the boundary layer edge are not observed. Finally, it should be noted that the HCW gives similar results as the high frequency results ($\xi = 1.5$) of Choi et al. (1996). Therein, the authors studied the response of a laminar flat plate boundary layer subject to purely horizontal traveling waves. The most significant difference between HCW and Choi et al. is for the near-wall region where the current calculations, which are for turbulent flow, show rapid amplitude and phase changes at $y^+ \approx 5-10$.

Finally, the Euler-equation analysis shown in Fig. 14 also includes the HCW. The amplitude U_1 shown in Fig. 14(a) decreases in a nearly linear fashion and displays very little spatial harmonic content (i.e., $B \approx 0$) especially in comparison to the VCW. This is consistent with the observation of temporal pressure wave. Figure 14(b) further shows the lack of tangent behavior for the HCW. Finally, Fig. 14(c) shows that the HCW does not have a peak or oscillations in the displacement thickness. This is consistent with the overall response.

Summary and Conclusions

Parts 1 and 2 of this work together have shown that, in comparison to the classical and fundamental boundary layer and potential flow theories, RANS solution to unsteady blade flows gives a consolidated perspective, i.e., both viscous and inviscid effects, and their interactions, are resolved. Furthermore, this perspective has permitted detailed analysis and explanation of the physics of high-frequency flows. High-frequency blade flows display a complex response with significant differences from both the linear inviscid Sears and viscous Stokes theories. The boundary layer displays overshoots and phase lags and in regions of unsteady counter-rotating vortices displays two-layered amplitude and phase profiles. The near-wall response follows the unsteady pressure gradient which is shown to be driven by a near-wake displacement thickness peak for high-frequency flows. Pressure waves radiate upstream and downstream of this peak which indicates that viscous-inviscid interaction is an important mechanism which determines the overall response. Quantitative details of the flow, such as lift and drag, are highly dependent upon frequency, geometry, and waveform.

The results of Part 2 also show that there is a frequency demarcation in the response. For high frequencies (i.e., wavelength shorter than the foil), the FFX-type response is shown and is governed by the viscous-inviscid interaction. Based upon the flat plate HCW calculations, the source of this interaction has been shown to be related to the existence of lift and its associated unsteady trailing-edge wake sheet. This suggests that the oscillating wake sheet significantly excites the displacement thickness which in turn interacts with the inviscid flow. This is in general agreement with the observations made by Poling and Telionis (1986) who observed highly curved streamlines in the near wake and inferred this was the signature of viscous-inviscid interaction and nonzero trailing-edge loading. For low frequencies (i.e., wavelength longer than the foil), the response to the VW displays a temporal behavior which agrees with classical linear potential-flow theories. This implies that as the frequency of oscillation decreases, the displacement thickness is no longer excited in the near wake. This in turn agrees with observations that the classical Kutta condition, and its consequences (e.g., zero trailing-edge loading), is valid at low frequencies.

Based upon the flat plate VCW calculations, it can be seen that geometry also strongly influences the flow. Steady-unsteady interaction causes gust deformation, creates sources of unsteady pressure gradient, and creates a complex wake comprised of vorticity due to lift and the deformed, and out of phase on each side of the wake, gust. This interaction has been shown to increase for increased frequency and is due to the shorter wavelengths having a longer near-foil residence time. Also, the flat plate demonstrates the influence of geometry on the trailing-edge flow. The trailing-edge counter-rotating vortices seen in the foil flows were nonexistent.

Finally, it was shown, as expected, that waveform strongly influences the response. Large differences were shown between the lifting (i.e., VCW and VW) and non-lifting (HCW) external flows. However, the differences between the VCW and VW external flows were more subtle and a function of frequency.

In conclusion, important flow physics have been identified and supported by detailed analysis. High-frequency viscous blade flows display a response with significant differences from both inviscid and boundary layer theories. Furthermore, viscous-inviscid interaction is an important mechanism of the response. Clearly, this has potentially important implications for marine propulsors where current design and analysis methods are based upon potential-flow panel methods and where other physical phenomenon such as cavitation, vibration, and acoustics are sensitive to the unsteady flow details. Finally, given the location and resultant effect of the unsteady displacement thickness peak, it is conceivable that high-frequency blade flows will be receptive to unsteady flow-control schemes, which can mitigate and/or enhance the response.

Acknowledgments

This research was sponsored by ONR under Contracts N00014-92-J-1118 and N00014-91-J-1203 under the administration of Mr. Jim Fein and Dr. Ed Rood whose support is greatly appreciated. Computing resources were provided by the NASA Numerical Aerodynamic Simulation Program and the Naval Oceanographic Office Major Shared Resource Center. This first author is grateful for the support provided by the Iowa Institute of Hydraulic Research Hunter Rouse Fellowship.

References

Basu, B. C., and Hancock, G. J., 1978, "The Unsteady Motion of a Two-Dimensional Aerofoil in Incompressible Inviscid Flow," *Journal of Fluid Mechanics,* Vol. 87.

Chen, B., and Stern, F., 1994, "Computation of Unsteady Viscous Marine Propeller Blade and Wake Flow," *Proceedings of ONR Symposium on Naval Hydrodynamics,* Santa Barbara, CA.

Choi, J. E., Sreedhar, M., and Stern, F., 1996, "Stokes Layers in Horizontal-Wave Outer Flows," ASME JOURNAL OF FLUIDS ENGINEERING, Vol. 118, No. 3.

Goldstein, M. E., and Attasi, H. A., 1976, "A Complete Second-Order Theory for the Unsteady Flow About an Airfoil Due to a Periodic Gust," *Journal of Fluid Mechanics,* Vol. 74.

Horlock, J., 1968, "Fluctuating Lift Forces on Aerofoils Moving Through Transverse and Chordwise Gusts," ASME *Journal of Basic Engineering,* pp. 494–500.

Horwich-Lurie, B., 1993, "Unsteady Response of a Two-Dimensional Hydrofoil Subject to High Reduced Frequency Gust Loading," M.S. thesis, Massachusetts Institute of Technology.

Jessup, S., 1990, "Measurement of Multiple Blade Rate Unsteady Propeller Forces," David Taylor Research Center, Hydromechanics Department, Research and Development Report DTRC-90/015.

Kerwin, J. E., and Lee, C. S., 1978, "Prediction of Steady and Unsteady Marine Propeller Performance by Numerical Lifting-Surface Theory," *Transactions SNAME,* Vol. 86.

Lewis, E. V., editor, 1988, *Principles of Naval Architecture, 2nd Revision, Volume II—Resistance, Propulsion, and Vibration,* The Society of Naval Architects and Marine Engineers, pp. 291–305.

Lurie, E. A., 1996, "Investigation of High Reduced Frequency, Separated Trailing Edge Flows," Sc.D. thesis, Massachusetts Institute of Technology.

Naumann, H., and Yeh, H., 1973, "Lift and Pressure Fluctuations of a Cambered Airfoil Under Periodic Gusts and Applications in Turbomachinery," ASME *Joural of Engineering for Power*, Jan., pp. 1–10.

Patel, M. H., 1977, "On Turbulent Boundary Layers in Oscillatory Flow," *Proceedings of the Royal Society of London A,* Vol. 353, pp. 121–143.

Paterson, E. G., and Stern, F., 1997, "Computation of Unsteady Viscous Marine-Propulsor Blade Flows—Part 1: Validation and Analysis," ASME JOURNAL OF FLUIDS ENGINEERING, Vol. 119, No. 1.

Paterson, E. G., Wilson, R. V., and Stern, F., 1998, "Verification/Validation of Steady Flow RANS Simulation of DTMB Model 5415," *Proceedings 1st Symposium on Marine Applications of CFD,* May 19–21, McLean, VA.

Poling, D. R., and Telionis, D. P., 1986, "The Response of Airfoils to Periodic Disturbances—The Unsteady Kutta Condition," *AIAA Journal,* Vol. 24, No. 2.

Sears, W. R., 1941, "Some Aspects of Non-Stationary Airfoil Theory and Its Practical Application," *Journal of Aeronautical Sciences,* Vol. 8.

M. A. Sima
Doctoral Candidate,
Department of Mechanics,
Royal Institute of Technology (KTH),
S-100 44 Stockholm, Sweden

J. A. Harris
Senior Lecturer,
School of Engineering,
James Cook University,
Townsville Q 4811, Australia

Numerical Modeling of Flow in a Vertical Cooling Crystallizer

Simulations of the flow field and temperature distribution in a low grade vertical continuous cooling sugar crystallizer were carried out by numerically solving the Navier-Stokes equations in a cylindrical coordinate system. The model results indicate highly nonuniform massecuite cooling, primarily due to the massecuite's large Prandtl number, and significant short-circuiting of flow between inlet and outlet. Modifications to the crystallizer design are proposed and demonstrated to be successful in improving the performance of the vessel.

1 Introduction

One of the final stages in the manufacture of raw cane or beet sugar is crystallization of sucrose from concentrated syrup (molasses). Crystallization initially takes place by evaporation of water from the syrup under vacuum to produce a supersaturated solution that drives crystal growth. This process typically takes place in a series of batch vacuum pans, and crystals are separated from the molasses in a centrifuge after each stage of growth. After a number of batch evaporation processes the water and sucrose removed by evaporation and crystal growth, respectively, concentrates existing impurities in the solution to such an extent that further evaporative crystallisation is not practical due to the slow crystal growth rates and high molasses viscosity. At this point the mixture of molasses and crystals, known as massecuite, is transferred to cooling crystallizers where it is cooled (to decrease sucrose solubility and further increase supersaturation) and stored for sufficient time to allow crystal growth (about 10–20 h).

Vertical continuous crystallizers are one type of crystallizer that are popular because of their small footprint and continuous operation. There are various designs available, and the one considered in this study is representative (refer to Fig. 1). It consists of a vertical cylindrical tank, horizontal cooling water pipes connected in two counter-flow circuits (different pipe diameters), and a central rotating shaft and stirrer arms alternatively staggered at 90 deg. The cooled massecuite, which is highly viscous (~2000 Pa·s), is pumped out of the vessel by a positive displacement pump. The main functions of the crystallizer are to provide slow and even cooling of the massecuite to a preset optimum cooling curve (~1°C/h), and to provide sufficient residence time to maximize growth of the sucrose crystals.

The ultimate goal of the present research project is to produce a model that can compute crystal growth throughout the vessel, taking into account crystal size distribution, growth rate variability and other factors. Crystal growth is the integrated value of the growth rate times the residence time, both of which can vary substantially throughout the vessel. The local growth rate is a function of the local temperature, viscosity, shear rate, and level of supersaturation, whereas the residence time can be determined from the flow field. Thus, the calculation of crystal growth requires a knowledge of the flow and temperature fields and vice versa, since the crystal growth is coupled to the flow and temperature fields through the massecuite viscosity. For low grade massecuites in which the change in crystal content throughout the vessel is quite small, Sima (1998) found crystal growth has minimal influence on the flow field. It is therefore reasonable to perform an uncoupled calculation of crystal growth, i.e., first, compute the velocity and temperature distributions, then use these to compute crystal growth using, for example, a population balance approach (Randolph and Larson, 1988).

There have been few previous attempts at modeling the flow and heat transfer in sucrose crystallizers. Bunton (1981) and Brown et al. (1992) studied vacuum pans using simple computational fluid dynamics (CFD) models. Broadfoot and Steindl (1992) developed a one-dimensional model of crystal growth in low grade cooling crystallisers and used it to compute optimum cooling profiles. However, their work implicitly assumed uniform velocity and temperature distributions transverse to the flow direction. Additionally, their model requires the mean shear rate in the vessel as an input, which is difficult to assess a priori. Sima and Harris (1997) demonstrated the calculation of spatial crystal growth rates.

This paper describes the calculation of the velocity and temperature distributions in a low grade crystallizer, similar to that shown in Fig. 1. The aims of the present study are to achieve a better understanding of the flow through the crystallizer, to quantify the extent to which the vessel design meets the stated requirements, and to suggest design improvements.

2 Mathematical Model

2.1 Geometric Simplifications. The crystallizer shown in Fig. 1 is inherently three-dimensional and would be prohibitively expensive to model due to the large number of elements required around each cooling pipe (refer to Section 2.6). To overcome this problem, it was assumed that the crystallizer is rotationally symmetric, as shown in Fig. 2. This assumption greatly reduces the complexity of the problem, but means the results have to be interpreted carefully when applied to the actual three-dimensional geometry. The simplified geometry has symmetry about the z-axis (i.e., all quantities are independent of θ) but has three nonzero velocity components.

2.2 Governing Equations. The flow is assumed to be steady, laminar, and incompressible with a variable viscosity, and the Boussinesq assumption is used to account for the change in density with temperature. The equations governing conservation of mass, momentum and energy in the axisymmetric cylindrical coordinate system are (Hinze, 1975):

$$\frac{1}{r}\frac{\partial}{\partial r}(ru_r) + \frac{\partial u_z}{\partial z} = 0 \tag{1}$$

$$\rho_o\left(\frac{Du_r}{Dt} - \frac{u_\theta^2}{r}\right) = \frac{1}{r}\frac{\partial}{\partial r}(r\sigma_{rr}) - \frac{\sigma_{\theta\theta}}{r} + \frac{\partial \sigma_{rz}}{\partial z} \tag{2}$$

Contributed by the Fluids Engineering Division for publication in the JOURNAL OF FLUIDS ENGINEERING. Manuscript received by the Fluids Engineering Division March 11, 1998; revised manuscript received October 5, 1998. Associate Technical Editor: P. M. Sockol.

$$\rho_o\left(\frac{Du_\theta}{Dt}+\frac{u_r u_\theta}{r}\right)=\frac{1}{r^2}\frac{\partial}{\partial r}(r^2\sigma_{r\theta})+\frac{\partial\sigma_{\theta z}}{\partial z}+\rho_o f_\theta \quad (3)$$

$$\rho_o\frac{Du_z}{Dt}=\frac{1}{r}\frac{\partial}{\partial r}(r\sigma_{rz})+\frac{\partial\sigma_{zz}}{\partial z}+\rho_o f_z \quad (4)$$

$$\rho_o c_p\frac{DT}{Dt}=\frac{k}{r}\frac{\partial}{\partial r}\left(r\frac{\partial T}{\partial r}\right)+k\frac{\partial^2 T}{\partial z^2} \quad (5)$$

For steady, axisymmetric flow the substantial derivative is defined as $D/Dt = u_r\partial/\partial r + u_z\partial/\partial z$. The constitutive relation is

$$\sigma_{ij}=-p\delta_{ij}+2\mu(T,\dot\gamma)d_{ij} \quad (6)$$

where δ_{ij} is the Kroneker delta and the rate of deformation tensor, d_{ij}, for an axisymmetric cylindrical system is given by

$$d_{rr}=\frac{\partial u_r}{\partial r}\quad d_{r\theta}=\frac{1}{2}r\frac{\partial}{\partial r}\left(\frac{u_\theta}{r}\right)$$

$$d_{\theta\theta}=\frac{u_r}{r}\quad d_{rz}=\frac{1}{2}\left(\frac{\partial u_r}{\partial z}+\frac{\partial u_z}{\partial r}\right)$$

$$d_{zz}=\frac{\partial u_z}{\partial z}\quad d_{\theta z}=\frac{1}{2}\frac{\partial u_\theta}{\partial z} \quad (7)$$

The governing equations were solved subject to no-slip boundary conditions on the walls, rotating shaft (0.25 rpm) and cooling pipes, a uniform axial velocity of 0.28 mm/s and temperature of 60°C at the inlet (with natural boundary conditions on the radial and tangential velocity components), adiabatic central shaft, and natural boundary conditions on the outlet (artificially extended). Based on measurements on the unmodified industrial vessel, the cooling pipe temperatures were set between 28°C (inlet) and 35°C (outlet), for both the 100 NB and 150 NB pipe cooling circuits. For one simulation the external wall of the crystalliser was assumed to be insulated (zero heat flux), and for another the effect of cooling the external wall by a combination of convection and radiation was investigated by using a representative heat transfer coefficient of h_w = 30 W/m$^2\cdot$K and an ambient temperature of 30°C.

2.3 Fluid Properties. The mixture of crystals and molasses is treated as a single phase fluid (massecuite). In the above equations the viscosity and other properties are those of massecuite. The massecuite considered in this study has the following properties, which are typical of Australian low grade massecuite: P_{mo} = 47, I/W = 3.7, X_{cr} = 0.35, L = 0.32 mm, CV = 0.30 and I_r/I_a = 0.8. Additional properties are ρ_o = 1488 kg/m^3, k = 0.4 W/m$\cdot$K and c_p = 2200 J/kg$\cdot$K.

Molasses is a non-Newtonian pseudoplastic fluid with an apparent viscosity given by

$$\mu_{mo}=K|\dot\gamma|^{n-1} \quad (8)$$

where the flow behavior index is taken to be n = 0.84 (Broadfoot and Steindl, 1980) and the shear rate is related to the velocity field by

$$\dot\gamma^2=2d_{ij}d_{ij} \quad (9)$$

where d_{ij} is given by Eq. (7). The consistency factor, K, is dependent on the dry substance and purity of the molasses (Broadfoot and Steindl, 1980) and is a strong function of temperature. For the massecuite properties given above, the variation of the consistency factor with temperature is plotted in Fig. 3.

The massecuite viscosity was computed by correcting the molasses viscosity for the presence of sucrose crystals using the correlation determined by Awang and White (1976). For the above massecuite properties (assumed constant throughout the vessel) this correlation yields $\mu = 4.59\mu_{mo}$, independent of temperature. To avoid possible errors associated with the anomalous behavior of the power-law model as the shear rate approaches zero, a cut-off minimum shear rate of 0.001 s^{-1} and a cut off maximum massecuite viscosity of 11500 Pa$\cdot$s were introduced.

2.4 Body Forces. The body force (per unit mass) in the axial momentum equation accounts for the negative buoyancy of the cooled massecuite and is given by

$$f_z=g\beta(T_o-T) \quad (10)$$

where the reference temperature is taken to be the massecuite inlet temperature (T_o = 60°C) and the volume expansion coefficient is $\beta = 4.313\times10^{-4}$ K^{-1}.

The body force term in the tangential momentum equation was introduced to model the tangential drag produced by the stirrer arms over one revolution. The form of the term was deduced from analytical considerations of the drag force produced by a cylinder moving through a power law fluid at low Reynolds number (Re $\ll$ 1), and unknown constants were determined from numerical simulations of an infinite cylinder moving between parallel plates (Sima and Harris, 1996). The resulting expression is

Nomenclature

a_0, a_1, a_2 = constants in tangential body force expression
c_p = massecuite heat capacity
C_{ds} = molasses dry substance (solids content)
CV = coefficient of variation of crystal size distribution
d_{ij} = rate of deformation tensor
f_θ = tangential body force per unit mass
f_z = axial body force per unit mass
g = gravitational acceleration
h = height over which tangential body force is applied
h_w = heat transfer coefficient on outer wall
h_p = heat transfer coefficient on cooling pipes
I/W = mass ratio of impurities to water
I_r/I_a = reducing sugar to ash ratio
k = massecuite thermal conductivity
K = molasses consistency factor
L = mean crystal size
p = pressure (relative to hydrostatic)
Pe = Peclet number
Pr = Prandtl number
P_{mo} = molasses purity
q'' = cooling pipe heat flux
r = radial coordinate
Re = Reynolds number
t^* = dimensionless residence time
T = temperature
T_o = reference temperature
T_p = cooling pipe surface temperature
u_r = radial velocity component
u_θ = tangential velocity component
u_z = axial velocity component
U_{bf} = corrected tangential velocity of the stirrer arm
X_{cr} = crystal content by mass
z = axial coordinate
β = massecuite volume expansion coefficient
$\dot\gamma$ = shear rate
δ_{ij} = Kronecker delta (1 if $i = j$, 0 otherwise)
θ = tangential coordinate
μ = massecuite viscosity
μ_{mo} = molasses viscosity
ρ_o = reference density
σ_{ij} = shear stress tensor

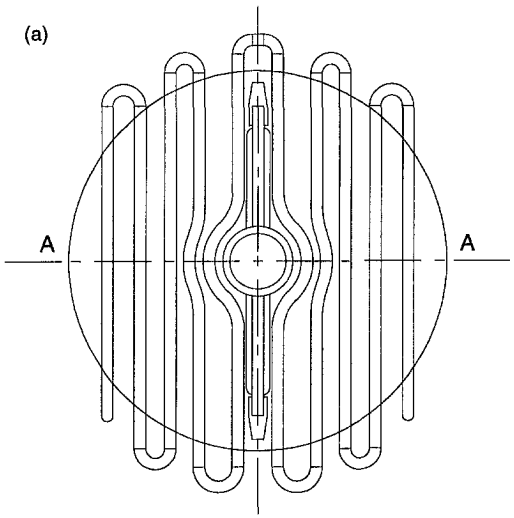

Fig. 1(a)

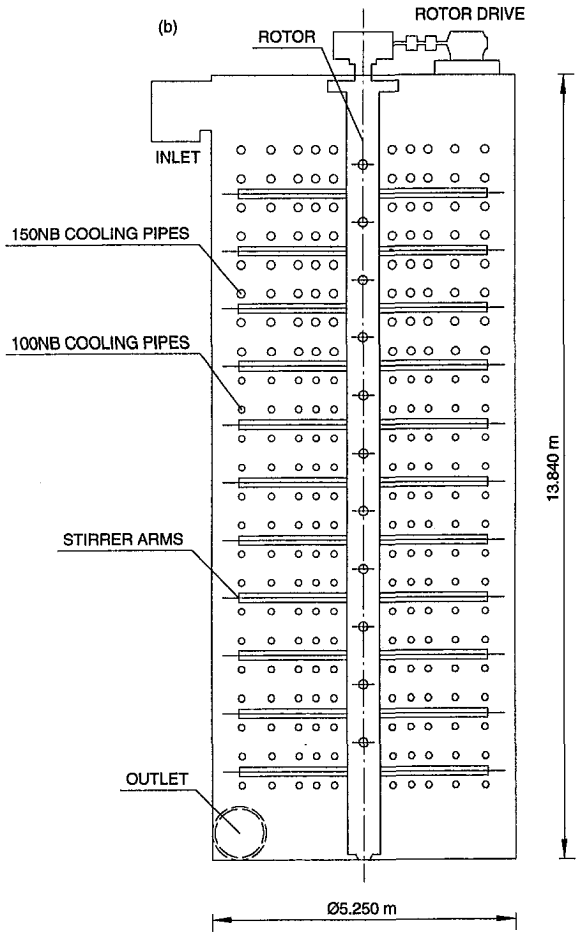

Fig. 1(b)

Fig. 1 Schematic diagram of the crystallizer. (*a*) Plan view showing cooling pipe arrangement; (*b*) Section A-A. Drawing not to scale.

$$f_\theta = \frac{a_0}{\rho_o \pi h r}\left[a_1 + (r - a_2)^{1-n}\right] U_{bf}^n \qquad (11)$$

where the values of the constants are $a_0 = 8921\ \mathrm{Ns}^n/\mathrm{m}^2$, $a_1 = -0.2982\ \mathrm{m}^{1-n}$ and $a_2 = 0.2823$ m, and U_{bf} is the tangential velocity of the stirrer arm ($r\omega$) less a small correction to account for the tangential velocity induced by the rotating central shaft. This body force was only applied in the central region between

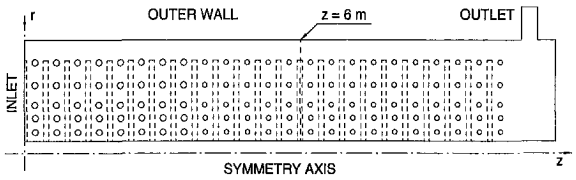

Fig. 2 Simplified axisymmetric geometry. The tangential coordinate (θ) is in the anticlockwise direction about the positive *z*-axis. The dashed lines indicate the area over which tangential body forces are applied.

rows of cooling pipes over a height of $h = 0.13$ m (refer to Fig. 2).

2.5 Solution Method. The governing equations were solved using the finite element CFD code FIDAP. A segregated solution scheme (pressure projection) was used for the discretised equations, with preconditioned conjugate residual and conjugate gradient squared iterative solvers used for the solution of the symmetric and nonsymmetric matrices, respectively (Haroutunian et al., 1993). Streamline upwinding was employed to stabilize the solution of the convection dominated energy equation and a continuous pressure approximation was used with a first-order pressure discretization.

2.6 Meshing and Grid Independence. Assuming a representative massecuite viscosity of 450 Pa·s (e.g., $\dot{\gamma} = 0.09\ \mathrm{s}^{-1}$ and $T = 60°\mathrm{C}$), the Reynolds number of the flow based on the inlet velocity and 150 NB cooling pipe diameter (0.165 m) is $\mathrm{Re} = 1.5 \times 10^{-4}$. Also, the Prandtl number of the massecuite is about $\mathrm{Pr} = 2.5 \times 10^6$, giving a Peclet number of $\mathrm{Pe} = 380$. Since the ratio of the momentum and thermal boundary layer thicknesses scales with $\mathrm{Pr}^{1/3} = 136$, and the momentum boundary layer thickness is about half the width of the gap between the pipes, it is apparent that the thermal boundary layers are confined to extremely narrow regions around each pipe. Additionally, it can be seen that the momentum equations are diffusion dominated (i.e., low Re) whereas the energy equation is convection dominated (i.e., high Pe).

In order to resolve the thin thermal boundary layers it was necessary to use closely spaced elements near the cooling surfaces. Numerical experiments were performed on sub-problems to determine the number of elements required. For the flow around a single 150 NB cooling pipe, mesh refinement tests showed that a graduated mesh with the first node at 1/80th of the pipe diameter (i.e., the mesh used for the full simulations) was able to resolve the pipe heat flux to within less than 1 percent. Additionally, no changes in the test solutions were detected when the relative convergence tolerance was decreased from 10^{-4} to 10^{-6}.

The final mapped mesh consists of 264651 nodal points and 70936 9-noded quadrilateral elements. Within each element the

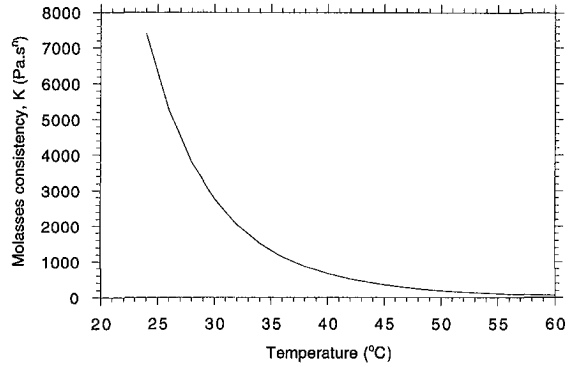

Fig. 3 Molasses consistency factor as a function of temperature. Molasses properties are $P_{mo} = 47$ and $C_{ds} = 87.5\%$.

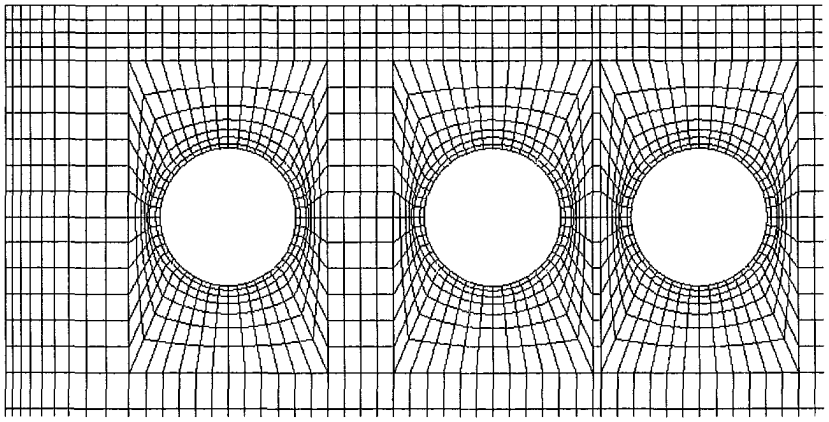

Fig. 4 A portion of the finite element mesh near the inlet of the crystallizer

velocity and temperature fields are approximated by quadratic shape functions so that the numerical method is second order in space. A portion of this mesh is shown in Fig. 4, and illustrates the mesh concentration around each cooling pipe. Elements were also concentrated near the rotating shaft and external walls to resolve the momentum and thermal boundary layers present. The simulations required about 1200–1600 iterations to reach a relative error tolerance of 10^{-5}, taking approximately 150 h of CPU time on a SGI R8000 processor.

3 Results and Discussion

3.1 Velocity and Temperature Fields. The numerical model solves for three velocity components, temperature, and pressure. Additionally, it allows computation of derived variables, such as shear rate and viscosity, related to crystal growth.

Contour plots of vertical and tangential velocity are shown in Fig. 5, and the temperature and viscosity distributions are shown in Fig. 6. These figures are for the case where the external wall is convectively cooled. There are a number of features to note from these results. First, there is a zone of hot, fast moving massecuite in the outer region of the crystalliser and a zone of cool, very slow moving massecuite in the centre region of the vessel. The peak axial velocity in the outer region is nearly three times the average velocity, whereas the velocity in the centre region is about fifteen times less than the average axial velocity. In the immediate vicinity of the outlet there is radial flow of massecuite toward the outlet ''slot''. In the actual vessel the outlet is a pipe rather than a 360 deg slot, which will create three-dimensional movement of massecuite across the diameter of the vessel. However, the large tangential velocities (relative to the axial velocities) expected will lessen the asymmetric movement of the massecuite and, together with the numerical results, suggests that this difference in outlet geometry is only likely to affect the massecuite flow near the bottom of the vessel. Second, cooling of massecuite is confined to narrow boundary layers adjacent to the cooling pipes and outer wall, and there is minimal diffusion of heat to regions away from the cooling surfaces. Cooling surfaces that are placed too far apart (e.g., the outermost cooling pipe and outer wall) can allow the formation of regions through which the hot massecuite can pass freely (termed ''rat holes'' in the local industry). Overall, it can be seen that the massecuite cooling is highly nonuniform; some areas are cooled excessively whereas other areas are essentially uncooled. Third, the mean tangential velocity induced by the stirrer arms is an order of magnitude greater than the mean axial velocity. As expected, there are high tangential velocities near the rotating central shaft and toward the perifery of the arms. However, the tangential velocity between the outer cooling pipes and the wall is virtually zero since the stirrer arms do not extend into this area. In the actual vessel the position of the outlet pipe straight below one area of fast moving massecuite with zero tangential velocity (seen as a segment of a circle in Fig. 1(a)) can be expected to promote flow in that area and, compared with the simulation, have the contrary effect on the flow in the similar segment on the opposite side of the vessel. In this axisymmetric approximation the stirrer arms mainly act to increase the shear rate between the pipe rows (which is important for aiding mass transfer to the crystals) and don't promote cross mixing of the thermal wakes below each cooling

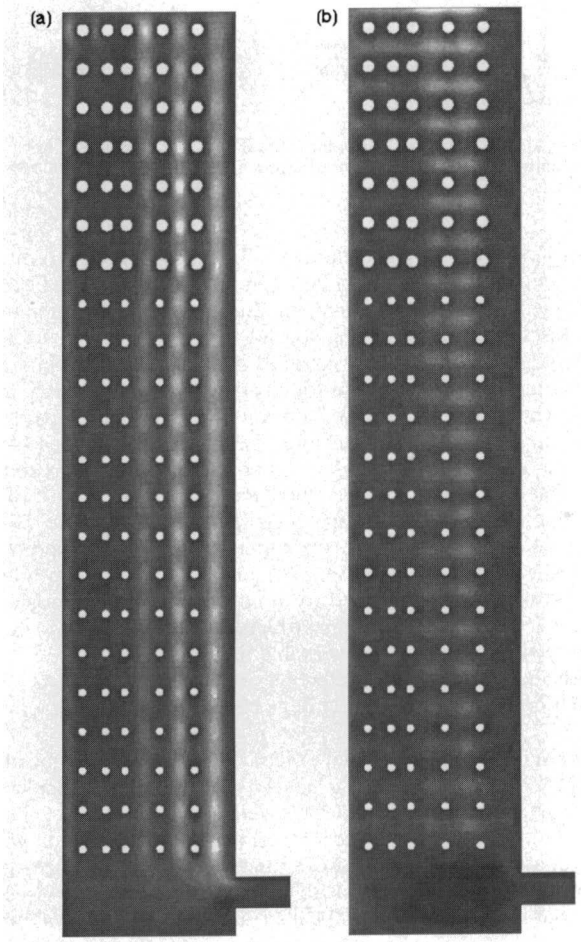

Fig. 5 (a) Axial velocity distribution. (black) $-0.263 \times 10^{-3} \leq u_z \leq 1.000 \times 10^{-3}$ m/s (white); (b) Tangential velocity distribution (black) $-0.485 \times 10^{-2} \leq u_\theta \leq 0.171 \times 10^{-1}$ m/s (white)

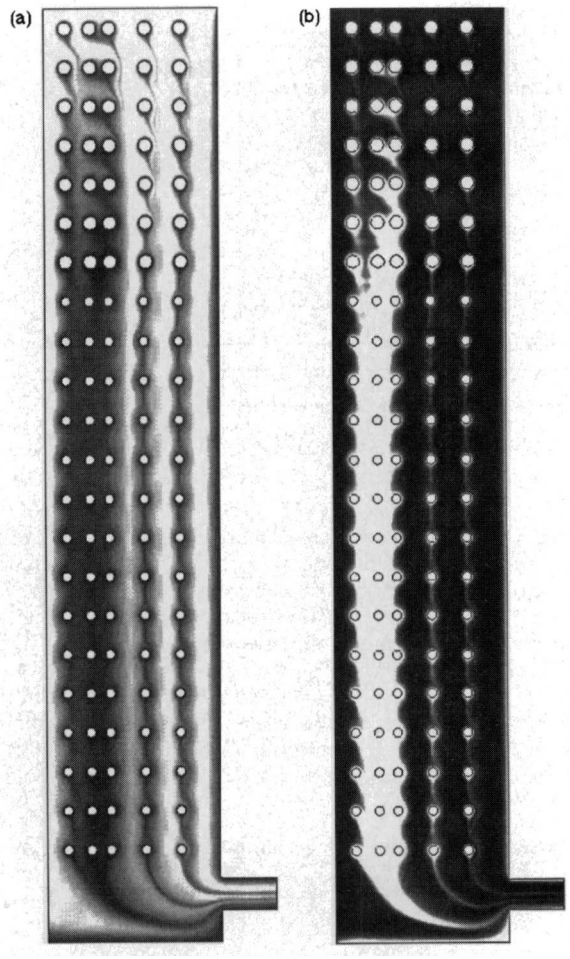

Fig. 6 (*a*) Temperature distribution (Black) 28 ≤ T ≤ 60°C (white); (*b*) Massecuite dynamic viscosity distribution. (black) 410 ≤ μ ≤ 11500 Pa · s (white).

pipes. However, in the actual three-dimensional geometry, it is expected that the interaction between the stirrer arms and cooling pipes would promote cross mixing in the central region of the vessel. Finally, the strong dependence of massecuite viscosity on temperature can be observed in Fig. 6(*b*). The highest viscosities (11500 Pa · s) are found adjacent to the cooling surfaces where the temperatures are lowest. A direct comparison of the mass averaged massecuite viscosity at the outlet (1452 Pa · s or 1205 Pa · s with no wall cooling) with the maximum workable viscosity of about 2000 Pa · s (at a shear rate of 1 s^{-1}) quoted by Broadfoot and Steindl (1992) is of little value since the outlet shape in the axisymmetric model is unrepresentative of the industrial vessel. The alternative approach taken here is to translate the viscosity limit of 2000 Pa · s at a shear rate of 1 s^{-1} into temperature, which, for the conditions simulated, yields 43.3°C as the workable limit on the mass averaged outlet temperature. With reference to §3.3, this suggests that further cooling of the massecuite is both desirable and practicable.

The temperature and axial velocity profiles at a height of z = 6 m are shown in Figs. 7(*a*) and (*b*) for the cases of insulated and convectively cooled external walls. The thermal boundary layer on the outer wall is clearly visible for the simulation with wall cooling. Figure 7(*b*) shows that wall cooling reduces the outer peak axial velocity (due to the increase in apparant viscosity), but increases the inner peaks (due to mass conservation).

3.2 Residence Time Estimation. The mean residence time of the crystalliser under the conditions modeled is approximately 11 h. A simple estimate of the cumulative residence time distribution was computed from the vertical velocity profiles shown in Fig. 7(*b*) and the height over which the massecuite travels (approximately 11.9 m). The estimated cumulative residence time distributions are plotted in Fig. 7(*c*) for each case. The dimensionless residence time is defined as $t^* = t\bar{u}_z/H$, where t is the residence time, H is the height over which the massecuite travels and $\bar{u}_z$ is the mean axial velocity. These estimates suggest that 20 percent of the massecuite exits the crystallizer before 5.8 h (6.0 h with no wall cooling), 20 percent remains in the crystalliser longer than 66 h (47 h with no wall cooling), and the fastest massecuite reaches the outlet in about 4.2 h (3.6 h with no wall cooling). The latter result is consistent with that obtained by computing the travel time of massless particles from the inlet to the outlet (4.0 h and 3.6 h, respectively).

3.3 Overall Heat Transfer. The computed mass averaged temperatures at the crystallizer outlet are 54.3°C and 56.3°C for wall cooling and no wall cooling, respectively. For the overall mass flow rate of 8.89 kg/s (32 t/h), these outlet temperatures correspond to a total heat removal of 112 kW and 73 kW, respectively. For the simulation with wall cooling, 41 percent of the total heat is removed by the 150 NB cooling pipes, 39 percent by the 100 NB cooling pipes and 20 percent through the external wall. Thus, heat loss through the wall is a significant portion of the overall massectuite cooling. With no wall cooling, the 150 NB pipes remove 55 percent with the

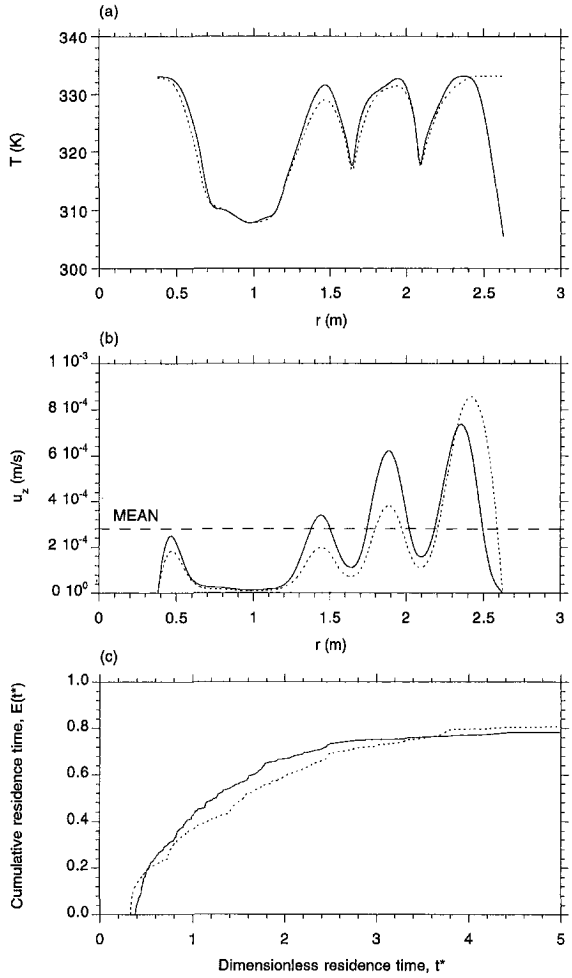

Fig. 7 (*a*) Temperature profile at z = 6 m; (*b*) Axial velocity profile at z = 6 m; (*c*) Estimated cumulative residence time distribution. Solid and dashed lines correspond to simulations with wall cooling and no wall cooling, respectively.

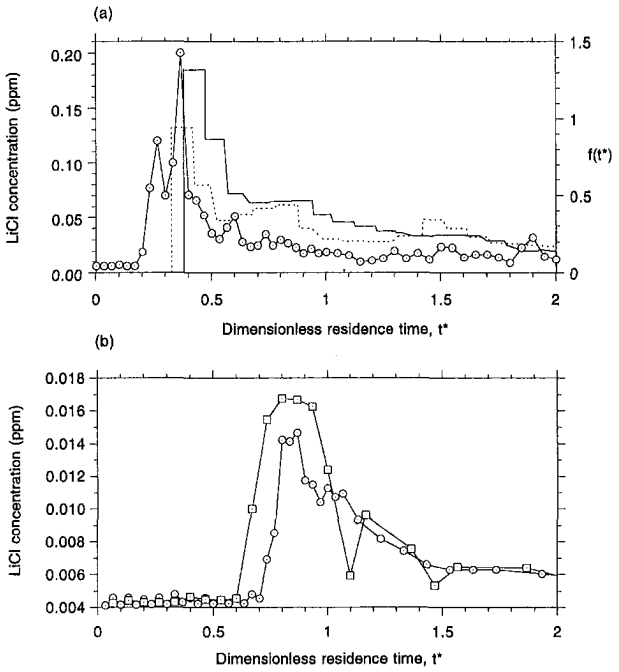

Fig. 8 (*a*) Predicted and measured residence time distributions in the full scale industrial crystalliser prior to modification. Solid and dashed lines correspond to simulations with and without wall cooling, respectively (*right hand ordinate*), *and* ⊙ *symbols correspond to the measured* distribution (left hand ordinate). (*b*) Measured residence time distribution of the modified crystallizer. The two traces correspond to different sample points at the outlet and 90 deg from the outlet.

remainder removed by the 100 NB pipes. The larger cooling pipes take the bulk of the heat load giving faster cooling of the massecuite near the inlet in accordance with the recommendations of Broadfoot and Steindl (1992). In both cases the overall cooling predicted by the model is less than the optimal cooling rate of approximately 1°C/h (Broadfoot and Steindl, 1992) which would imply an overall temperature drop of more than 10 K. The main reason for the lower than expected temperature drop is the short circuiting of virtually uncooled massecuite down the region between the outer cooling pipes and the wall.

For design purposes it is useful to have an estimate of the heat transfer coefficients at the cooling surfaces. Based on a reference temperature of 60°C, the heat transfer coefficient ($h_p = q''/(T_p - T_o)$) of the larger cooling pipes varies between 32.1 $W/m^2 \cdot K$ at the first row to 17.3 $W/m^2 \cdot K$ at the seventh row. The heat transfer coefficient for the 100 NB pipes ranges from 14.1 $W/m^2 \cdot K$ at the top row to 13.7 $W/m^2 \cdot K$ at the bottom row.

3.4 Modifications and Validation Studies. The results of the simulations show that the crystallizer as modeled does not approach its goals of providing slow and even cooling of the massecuite, and sufficient residence time. A significant portion of the massecuite exits the vessel well before the mean residence time having undergone minimal cooling, and a large fraction of the massecuite remains in the vessel for many days and is cooled far too much. However, it is recognized that these results are for an axisymmetric model and must be interpreted carefully when considering the actual three-dimensional vessel.

A tracer study was carried out on the industrial vessel to measure its residence time distribution. The study involved introducing a quantity of LiCl at the inlet of the crystallizer and taking measurements of concentration versus time at the crystallizer outlet. The results of the study are shown in Fig. 8(a), along with the residence time distributions estimated from the simulations with and without wall cooling ($f(t^*) = dE(t^*)/dt^*$). The measurements indicate significant short circuiting between inlet and outlet, with a large fraction of massecuite exiting the vessel between 2.5 and 4.5 h. The measured and predicted residence time distributions show clear similarities. However, the performance of the industrial crystallizer is even worse than the numerical model of the axisymmetric vessel suggests.

It is considered that there are four main design problems with the actual vessel. The first is the relatively large gap between the outermost cooling pipe and the crystalliser wall (seen as the segment of a circle in Fig. 1(a)), the second is that the stirrer arms do not extend close enough to the external walls (the horizontal plates on the ends of the arms have little influence), the third is that the inlet and outlet are aligned vertically with the large gap, and the fourth is that the cooling pipes are too close to each other in the region where they bend around the central shaft. The net result of these problems is that hot massecuite short circuits between inlet and outlet down the gap region. Additionally, massecuite is overcooled in the central region and forms a highly viscous mass which occupies a large volume in the vessel but does little else.

Two modifications were made to the industrial crystallizer to help remedy these problems. First, four horizontal baffle plates shaped like segments of a circle were installed at two vertical locations to force the massecuite out of the gap region and into contact with the cooling pipes and stirrer arms. Second, the inlet pipe was extended to distribute massecuite more evenly at the top of the vessel. Further numerical simulations were performed to assess the impact of these changes and guide the design of the modifications.

Following the modifications, an additional tracer study was performed to quantify the residence time distribution (refer to Fig. 8(b)). This study revealed a marked improvement in the residence time distribution. The peak of the distribution moved from about 4 h to about 9.4 h, much closer to the nominal mean residence time of 11 h. Observations also showed that the cooling circuit of the modified vessel is now loaded normally, whereas it had previously been under loaded. Mill personnel also recorded a significantly larger drop in purity (a measure of sucrose concentration in molasses) through the crystallizer, indicating improved extraction of sucrose in the form of crystals.

4 Conclusions

The numerical model developed provides a considerable amount of detail about the character of the flow and temperature distribution in a vertical crystallizer and the problems associated with cooling a high Prandtl number fluid. The model results show that the vessel as designed did not fulfill its objectives due to highly non-uniform cooling and associated short circuiting of partially cooled massecuite. Using the numerical model as a guide, simple modifications were proposed and installed on the industrial crystalliser. Subsequent tracer tests showed the modifications produced a substantially better residence time distribution resulting in improved sucrose extraction. While the retrofit to the existing crystalliser was very successful, the real power of the CFD model is that it can be used to design improved crystallizers which avoid the design faults of the present vessel.

One of the problems encountered in this study is that the existing expression for molasses viscosity does not span the range of shear rates found in the numerical simulations. There is thus a need for more work in this area to develop an improved correlation for the massecuite viscosity using a model that is valid down to zero shear rate.

Acknowledgments

The authors gratefully acknowledge the financial support of CSR Limited, and would also like to thank Stephen Vigh and James Joyce (CSR Ltd) for their input to this project and for

supplying the data from the residence time tests. The rights to use FIDAP have been acquired by the School of Engineering at James Cook University under license from Fluid Dynamics International.

References

Broadfoot, R., and Steindl, R. J., 1980, "Solubility-Crystallization Characteristics of Queensland Molasses," *Proceedings International Society of Sugar Cane Technologists,* Vol. 17, pp. 2557–2581.

Broadfoot, R., and Steindl, R. J., 1992, "A Model of Cooling Crystallization of Low Grade Massecuites," TR 212, Sugar Research Institute, Mackay.

Brown, D. J., Alexander, K., and Boysan, F., 1992, "Crystal Growth Measurement and Modelling of Fluid Flow in a Crystallizer," *Zuckerind.* Vol. 117, pp. 35–39.

Bunton, J. J., 1981, "Natural Convection, Two-Phase Flow and Crystallization in a Vacuum Pan Sugar Crystallizer," PhD thesis, Louisiana State University Agricultural and Mechanical College.

Haroutunian, V., Engelman, S., and Hasbani, I., 1993, "Segregated Finite Element Algorithms for the Numerical Solution of Large-Scale Incompressible Flow Problems," *International Journal of Numerical Methods in Fluids,* Vol. 17, pp. 323–348.

Hinze, J. O., 1975, *Turbulence,* McGraw-Hill.

Randolph, A. D., and Larson, M. A., 1988, *Theory of Particulate Processes Analysis and Techniques of Continous Crystallization,* Academic Press.

Sima, M. A., and Harris, J. A., 1996, "Simulations of the Flow and Temperature Fields in a Continuous Vertical Cooling Crystallizer," *Proceedings Compumod Tenth Australian Conference,* Melbourne, Australia.

Sima, M. A., and Harris, J. A., 1997, "Modelling of a Low Grade Vertical Cooling Crystalliser Using Computational Fluid Dynamics," *Proceedings Australian Society of Sugar Cane Technologists,* Vol. 19, pp. 448–455.

Sima, M. A., 1998, "CFD Analysis of Sugar Crystallization," Licentiate thesis, Royal Institute of Technology, Stockholm.

Particle Arrestance Modeling Within Fibrous Porous Media

James Giuliani
Graduate Student

Kambiz Vafai
Professor. Fellow ASME
e-mail: vafai.1@osu.edu

Department of Mechanical Engineering,
206 W. 18th Avenue,
Ohio State University,
Columbus, OH 43210

In the present study, particle growth on individual fibers within a fibrous medium is examined as flow conditions transition beyond the Stokes flow regime. Employing a numerical model that solves the viscous, incompressible Navier-Stokes equations, the Stokes flow approximation used in past research to describe the velocity field through the fibrous medium is eliminated. Fibers are modeled in a staggered array to eliminate assumptions regarding the effects of neighboring fibers. Results from the numerical model are compared to the limiting theoretical results obtained for individual cylinders and arrays of cylinders. Particle growth is presented as a function of time, angular position around the fiber, and flow Reynolds number. From the range of conditions examined, particles agglomerate into taller and narrower dendrites as Reynolds number is increased, which increases the probability that they will break off as larger agglomerations and, subsequently, substantially reduce the hydraulic conductivity of the porous medium.

Introduction

The study of particle capture within fibrous porous media has warranted significant interest in past years due to its application in industrial and commercial air filtration where the porous material is a filter medium. In an effort to better predict macroscopic filter performance parameters such as filter efficiency, pressure drop, and most penetrating particle size, researchers have studied the microscopic processes of how individual particles travel through and are captured by fibers within the porous media. Many techniques have been employed to calculate these macroscopic properties directly and to study the microscopic buildup of particles on fiber surfaces to obtain a better understanding of the physical processes. A review of work in this area can be found in Liu and Rubow (1986). This research has permitted fibrous media manufacture's to classify their products into ranges of filtration efficiency based on the airflow velocity that the product will operate at. For new high-efficiency media, the design airflow velocities fall within the Stokes flow regime.

Recent advancements in non-woven microglass media, yielding a higher ratio of efficiency to manufacturing cost, have created many new applications for this medium in the air filtration industry. Designed to achieve high efficiency at low media velocity, research has developed an efficiency rating that is characterized by flow velocity. For high efficiency media these velocities yield Reynolds numbers that fall within the Stokes flow regime, a fact that much past research takes advantage of. With improvements in media performance and reduced material costs, many equipment manufacturers are looking to upgrade existing filtration hardware by retrofitting them with high efficiency filter media. In the past, many aerosol filters moved larger amounts of air through less efficient media to remove a given amount of contaminate. As such, many commercial devices would expose the new high efficiency media to higher velocity flows which extend beyond the Stokes flow regime. In addition, there are new applications that move large volumes of air, such as vacuum cleaners, that are being considered for mating with high efficiency air filters. Designers in both fields are interested in how these high efficiency media, designed for operation at lower airflow velocities, will perform at airflow conditions outside of their design envelope. In related studies, Vafai and Tien (1981 and 1980) discussed the potential of the inertial effects on flow and mass transfer in a porous medium. Their model, or its simplified form, can be applied for obtaining the macroscopic characteristics of the fibrous insulation as discussed by Tien and Vafai (1990), Vafai and Whitaker (1989), and Vafai and Sarkar (1986). Also, an analytical expression for the effective thermal conductivity of fibrous medium was obtained by Tien and Vafai (1979). This study focuses on fibrous media in an unbounded flow.

Flow Model and Numerical Scheme

To compute particle trajectories around the individual fibers, a description of the microscopic flow field within the fibrous medium is required. The particle trajectory and flow field provides the necessary information for the deterministic model that will predict particle capture and dendrite growth. The deterministic model of dendrite growth on a fiber, developed by Payatakes (1976 and 1977) and Payatakes and Gradon (1980), is modified to calculate the height of idealized dendrites at incremental distances along the fiber surface.

To compute the flow field and particle trajectories around individual fibers within the medium, the traditional method of simulating the fiber matrix as a staggered array of parallel, circular cylinders was adopted. Based on knowledge of the flow field and fiber orientation, the computational domain was reduced to the rectangular field shown in Fig. 1. The filter medium considered in this analysis is typical of a non-woven fibrous medium, which is manufactured by a process where fibers are suspended in a liquid slurry and deposited on a mat where the liquid is removed by a combination of suction and evaporative mechanisms. With gravity and the external drying forces acting along the same vertical axis, the majority of fibers lie perpendicular to the air flow direction resulting in tight fiber packing along this axis. This forms the basis for the x coordinate spacing of the fibers in the numerical grid. Combined with concepts formulated by Piekaar and Clarenburg (1967) who developed a distribution model for pores in a fibrous medium, a vertical spacing of three fiber diameters between each fiber was selected.

To solve for the flow field around an individual fiber and include the influence that neighboring cylinders have on the flow field, multiple cylinders around a single target cylinder were modeled. Henry and Ariman (1986) accounted for these forces by modeling two fibers in the flow field. This was based on symmetrical flow conditions that resulted from the Stokes

Contributed by the Fluids Engineering Division for publication in the JOURNAL OF FLUIDS ENGINEERING. Manuscript received by the Fluids Engineering Division September 22, 1997; revised manuscript received October 6, 1998. Associate Technical Editor: M. N. Dhuabhadel.

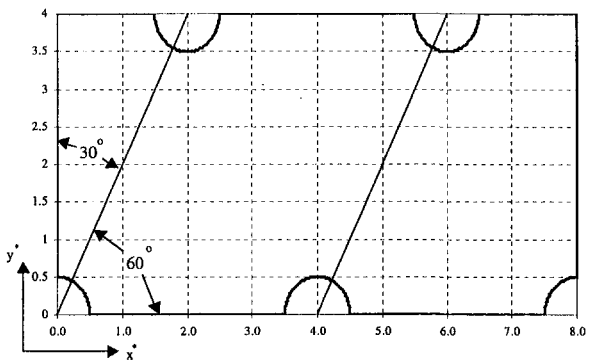

Fig. 1 Staggered array flow field

flow approximation. The asymmetrical flow that is anticipated when the Reynolds number exceeds the Stokes flow regime necessitated that the domain for this study be extended to include the 5 cylinders shown in Fig. 1.

The implicit, finite difference scheme used to solve the incompressible Navier-Stokes equations is described by Kwak and Chakravarthy (1986). In the program methodology, the pressure field solution is based on the pseudocompressibility approach in which a time derivative pressure term is introduced into the mass conservation equation. The solution procedure employs an implicit, approximate factorization scheme. The Navier-Stokes equations for incompressible flow are:

$$\rho\left(\frac{Dv_i}{Dt}\right) + \frac{\partial P}{\partial x_i} = X_i + \frac{\partial}{\partial x_j}\left[\mu\left(\frac{\partial v_i}{\partial x_j} + \frac{\partial v_j}{\partial x_i}\right)\right] \qquad i = 1, 2 \quad (1)$$

where v_i refers to the flow field velocity relative to the fiber. Neglecting gravity forces and assuming a constant viscosity, the Navier-Stokes equations reduce to

$$\rho\left(\frac{\partial v_i}{\partial t} + v_j\frac{\partial v_i}{\partial x_j}\right) = -\frac{\partial P}{\partial x_i} + \mu\frac{\partial^2 v_i}{\partial x_j^2} + \mu\frac{\partial}{\partial x_j}\frac{\partial v_j}{\partial x_i} \qquad i = 1, 2 \quad (2)$$

The numerical scheme is based on an algorithm which iterates on the divergence of the flow field and a solution is obtained when the zero divergence criterion of incompressible flow is met within a specified tolerance.

Initial conditions for the problem were addressed with an iteration scheme. After expanding Eqs. (1) and (2) over the index range and nondimensionalizing all terms, initial conditions for the pressure and velocity were applied at the inlet of the computational domain, $x^* = 0$. Based on the anticipated symmetry and inlet conditions, the profile at the midpoint $x^* = 4$ is obtained.

Initial profile at $x^* = 0.0$ and $t = 0$.

$$u^*(0, y^*) = 1.0$$

$$v^*(0, y^*) = 0.0$$

$$P^*(0, y^*) = 1.0 \qquad (3)$$

Initial profile at $x^* = 0.0$ and $t > 0$.

$$u^*(0, y^*) = u^*(4, y^*)$$

$$v^*(0, y^*) = v^*(4, y^*)$$

$$P^*(0, y^*) = P^*(4, y^*) \qquad (4)$$

Once the solution converged for the given inlet initial condition, the obtained centerline condition was then used as the inlet condition. This process was repeated until the differences between profiles dropped below a specific tolerance. The flow field converged to a solution within three to four iterations.

A symmetry boundary condition was applied at the boundaries of open flow between cylinders on the upper and lower axes. Vertical velocity was set to zero and a second-order extrapolation technique was used to calculate pressure and velocity conditions at these horizontal boundaries. At solid surface boundaries, the usual no-slip condition is applied to the velocity components. The pressure boundary condition on the solid surface is obtained from the normal momentum equation which reduces to the following nondimensional form (Fletcher, 1980):

$$\frac{\partial P}{\partial r} = \frac{1}{\mathrm{Re}}\frac{\partial \omega}{\partial \theta} \qquad (5)$$

where ω denotes the vorticity. In the above equation, the first term is the change in pressure normal to the surface and the last term is the change in vorticity along the boundary surface.

Global conservation of mass and momentum is applied at the outflow boundary. The velocities and pressure are first updated using a second-order extrapolation. The extrapolated velocities are then integrated over the exit boundary to obtain the outlet mass flux. Next, the velocity components are weighted by the mass flux ratio to conserve global mass. If nothing further is done to update the boundary pressure, this procedure can lead to discontinuities in the pressure because momentum is not being conserved. To avoid this, a momentum-weighted pressure was used. This was obtained by integrating the momentum-corrected pressure and the extrapolated pressure across the exit. Using these downstream boundary conditions, global conservation of mass and momentum are ensured and the scheme will not introduce instabilities into the flow field.

Nomenclature

a_p = particle radius [m]
a_f = fiber radius [m]
B = particle mobility, Eq. (9) [m/Ns]
Cs = Cunningham slip correction factor, Eq. (10)
d_p = particle diameter [m]
d_f = fiber diameter [m]
I = interception parameter (a_p/a_f)
l = mean free path of gas molecule [m]
m_k = expected particle number in the kth layer of a dendrite
P = static pressure [N/m^2]
R_k^θ = rate of increase of particles in layer k of a dendrite due to the θ component of velocity
R_k^r = rate of increase of particles in layer k of a dendrite due to the r component of velocity
Re = Reynolds number
s = circumferential cylindrical coordinate
X_i = external body forces [N]
x, y = Cartesian coordinates [m]
y_o = vertical distance above the stagnation line
α = rate of particles approaching a clean fiber per unit length [particles/sm]
μ = dynamic fluid viscosity [kg/ms]
ρ = fluid density [kg/m^3]
r, θ = cylindrical coordinates
ω = vorticity

Superscripts

* = denotes dimensionless quantity

Once a solution for the flow field in Fig. 1 is obtained, particle trajectories are calculated around the cylinder centered at $x^* = 4.0$, $y^* = 0.0$. To obtain the particle trajectories from the flow field solution, the standard trajectory equations given below are used.

$$\frac{4}{3}\pi a_p^3 \rho \frac{du_{\text{particle}}}{dt} = -\frac{(u_{\text{particle}} - u)}{B} \tag{6a}$$

$$\frac{4}{3}\pi a_p^3 \rho \frac{dv_{\text{particle}}}{dt} = -\frac{(v_{\text{particle}} - v)}{B} \tag{6b}$$

Here $(u_{\text{particle}}, v_{\text{particle}})$ are the particle velocity components, and (u, v) remain the fluid velocity components. B is the particle mobility given as

$$B = \frac{Cs}{6\pi\mu d_p} \tag{7}$$

where Cs is the Cunningham slip correction factor given by

$$Cs = 1 + \frac{l}{a_p}\left[1.257 + 0.4 \exp\left(-1.1\,\frac{a_p}{l}\right)\right] \tag{8}$$

Strictly speaking, Eq. (7) has two limitations. First, this equation was derived for creeping flow. While valid with the Stokes flow approximation, its accuracy is expected to decrease somewhat for Re = 1.0 and Re = 2.0 test cases. Additional information is available for flows at Reynolds number greater than 20, but none for Re's which are of the order of 1.0, as indicated by Hidy and Brock (1970). It is therefore assumed for this analysis that the equation given above for the particle mobility is valid. The second limitation is that this equation does not include a correction for the hydrodynamic interaction between the particle and the fiber. However, both Pataykes and Gradon (1980) and Goren (1973) concluded that such hydrodynamic effects are minimal for aerosols. Therefore, this simplification is adopted for the analysis.

Dendrite Growth Model. The original model developed by Payatakes (1976 and 1977) and Payatakes and Gradon (1980) predicts the rate of growth of individual dendrites as a function of their age and angular coordinate on the fiber surface. Payatakes (1977) describes the idealized dendrite structure that is the base for this model and how it compares to actual dendrite structures. In this model, dendrites are modeled as layers of particles. According to this convention, the dendrite structure is described by $m_k(t, \theta)$, the expected number of particles in the kth layer, where t is the time measured from the instant of deposition of the first particle and θ is the angular position of the dendrite foundation around the fiber from the stagnation point. To calculate the size of the dendrites, Payatakes and Tien started with the rate of increase of particles in a given layer k:

$$\frac{dm_k}{dt} = R^{\theta}_{(k-1)} + R^{\theta}_{(k)} + R^{r}_{(k-1)} + R^{r}_{(k)} \tag{9}$$

Here, R is the rate of increase of particles which encompasses four components. When a particle becomes deposited in a given layer (k), it attaches to a particle in the layer below $(k-1)$ or in its current layer (k). Payatakes and Gradon determined the frequency of particles attaching to particles in the layer above $(k+1)$ to be low enough that it can be neglected. With radial and tangential flow components, we have the four components of R, i.e., $R^{\theta}_{(k-1)}$ and $R^{r}_{(k-1)}$, signifying the increase of particles in layer k due to attachment on particles in the $(k-1)$ layer and R^{θ}_{k} and R^{r}_{k} signifying the increase of particles in layer k due to attachment on particles in layer k. Integrating the rate of growth equation gives:

Table 1 Parameters examined in this analysis.

PARAMETER	VALUES
Reynolds number based on fiber diameter	0.2, 1.0, 2.0
Interception parameter	0.05, 0.10

$$m_k = \sum_{i=1}^{k} C_{ki}(\theta) \exp\left[\alpha b_i(\theta) t\right] \tag{10}$$

where

$$C_{11} = 1 \quad C_{2i} = (-1)^i\left(\frac{a_2}{b_2 - b_1}\right) \tag{11}$$

$$C_{ki} = \left(\frac{a_k}{b_i - b_k}\right) C_{(k-1),i}$$

$$i = 2, \ldots, (k-1), \quad k \geq 3, k \neq i \tag{12}$$

$$C_{kk} = \left(\frac{a_k}{b_k - b_1}\right) \prod_{j=2}^{(k-1)} \left(\frac{a_j}{b_k - b_j}\right) \quad k \geq 3 \tag{13}$$

$$C_{kl} = \prod_{j=2}^{k} \left(\frac{a_j}{b_l - b_j}\right) \quad k \geq 3 \tag{14}$$

The parameters a and b are measures of the particle collection efficiency at a particular level and are calculated using the flow field and particle trajectory solution obtained from the previous section. The dendrite layer adjacent to the collector is allowed to contain more than one particle and Payatakes (1977) extended the model to include particle arrestance by interception as well as inertial impaction.

Table 1 lists the parameters varied in this analysis to examine their effect on particle capture and dendrite growth. A Reynolds number of 0.2, based on fiber diameter, was selected so that flow solutions could be compared to those obtained using the Stokes approximation. The inertial effects at this low Reynolds number should be small enough to provide a comparison for the numerical model. Flows at Reynolds numbers of 1.0 and 2.0 were chosen to highlight the changes that occur as operating conditions extend beyond the Stokes flow regime. These conditions also represent the general operating conditions for some of the industrial applications. For each combination of parameters in Table 1, the particle capture model is utilized to predict the time for a fixed volume of particles to deposit on the fiber surface.

Results and Discussion

Flow field solutions were obtained for the three values of Reynolds number listed in Table 1. Numerical calculation of particle trajectories for the high and low Reynolds numbers are presented in Fig. 2. A Stokes flow solution using the single fiber Kuwabara boundary condition was used for comparison. In these figures, the solid line represents the incompressible Navier-Stokes solution and the dashed line represents the single cylinder Kuwabara/Stokes solution. In each case, the particle trajectories are calculated for three entry points of $y_o^* = 0.2$, 0.5 and 0.75, where y_o^* is the dimensionless distance above the stagnation line of the downstream cylinder.

Figure 2(*a*) shows a comparison of the Navier-Stokes solution at a Reynolds number of 0.2 with that of the Kuwabara/Stokes solution. While this case does not satisfy the Stokes assumption of Re $\ll$ 1, it is expected that the inertial effects

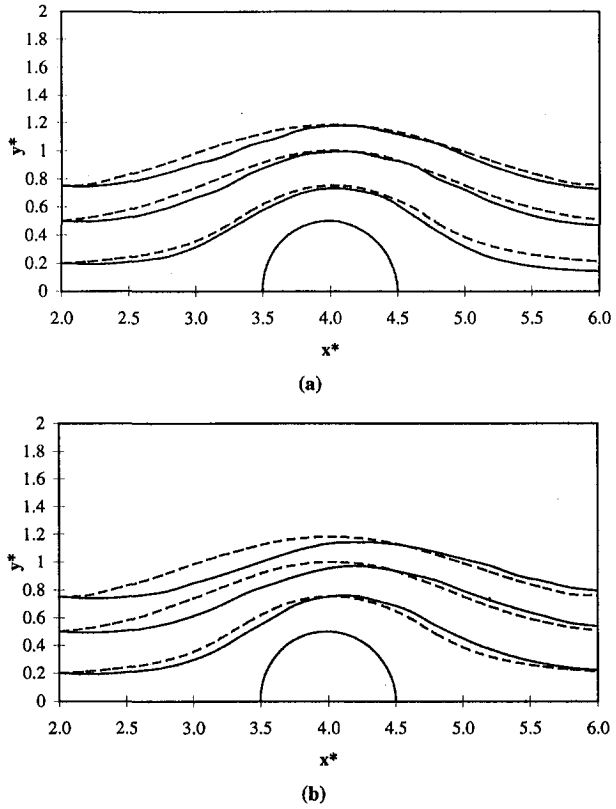

Fig. 2 Particle trajectories with entry points at $y_o^* = 0.2, 0.5, 0.75$. Solid line–Navier-Stokes solution at (a) Re = 0.2, (b) Re = 2.0; dashed line–Stokes flow with Kuwabara single fiber cell model.

at this Reynolds number will be small enough that differences in the results will be primarily due to the implementation of the Kuwabara boundary condition versus physically modeling multiple cylinders. Indeed, the trajectories upstream and downstream of the fiber are only slightly non symmetrical as a result of the inertial effects. Results compare well to calculations made by Henry and Ariman (1983a) who used the Stokes flow assumption and a finite element technique to model two cylinders to eliminate the Kuwabara approximation. Pathlines match at 90 deg from the stagnation point, but more inflection upstream and downstream of this point is predicted from the numerical solution. The solutions show a better agreement at low values of y_o^* where the influence of the downstream cylinder outweighs that of the other cylinders. At larger distances where the effects of neighboring cylinders become more prominent, the Kuwabara solution under-predicts the influence on the flow field. The Navier-Stokes solution presented here also predicts slightly stronger influence from neighboring fibers than that given by Henry and Ariman (1983b).

Figure $2(b)$ shows calculations for the Re = 2.0 case. At this higher Reynolds number, the inertial effects begin to distort the pathlines from those calculated by the Stokes solution. As the flow inertia increases, the pathlines are pushed closer to the cylinder on the upstream side. This causes the flow above the cylinder to have a larger vertical velocity component which causes the downstream separation distance to grow larger.

These trends are similar to those calculated by Fornberg (1987) who studied the flow past a single cylinder in an unbounded flow. In the case of multiple cylinders, the neighboring cylinders add an additional drive that force the velocity field back toward the rear stagnation line within a much shorter distance than the normal recovery length for a single cylinder in an unbounded flow. Of importance to the calculation of particle capture is the angle of attack of the approaching particle relative to the fiber, or collision angle, and the impact parameter, which is the minimal distance between the fiber and particle centroids. As the Reynolds number is increased, the changes in the streamlines cause the collision angle to increase and the impact parameter to decrease. This has the effect that the particle can "see" more fiber surface area and it experiences a corresponding increase in the probability that it will attach. In fact, the velocity profile changes cause an increase in the particle deposition within the 40 to 60 deg range (a point which will be discussed later).

Dendrite Growth Calculations. Payatakes (1977) describes the four stages of aerosol particle deposition in fibrous media. Calculations in this work are presented up to and through the third stage, where individual dendrites grow to the extent that they intermesh with their neighbors and form a coat of usually non-uniform thickness around each fiber. Calculations of this particle layer for each combination of parameters listed in Table 1 are presented in Figs. 3 and 4. The maximum time plot on each graph represents the time required for a fixed volume of particles to be deposited on the fiber surface. The third contour in each figure shows a growth layer at about 60 to 80 percent of the maximum collected volume of the particles for the complete simulation.

Figure $3(a)$ shows the growth calculation at a flow Reynolds number of 0.2 and an interception parameter of 0.1. As time progresses, the particle layer grows to a fairly uniform depth and extends farther back to approximately 90 deg. By the time the target volume of particles deposited on the fiber is reached, the surface is coated from the stagnation point back to approximately 100 deg. The indentation in the layer on the front of the fiber is caused by the flow profile near the stagnation point where the tangential flow component is minimal. The loss of the first two terms in Eq. (11), in addition to the fact that the range of y_o^* that will allow particle capture by impaction at this point is small, requires that a large period of time must pass for the probability to indicate that a particle will attach near the stagnation point. For angles of 20 and 30 deg from the stagnation point, particles begin to be captured by both interception and impaction and an increase in the number of particles captured is seen at each Reynolds number. A similar effect is found towards the downstream end of the growth layer. Here the rate of particles captured by impaction decreases as the flow becomes parallel to the fiber surface, which results in the corresponding reduction in predicted particle growth.

Many trends seen in Fig. $3(a)$ remain for higher Reynolds number flows as seen in Fig. $3(b)$. One important change in the particle layer-profile is the lack of predicted particles near the stagnation point. The reason for this is that the particles collect at a much faster rate and closer to the 50 deg angle at the higher Reynolds numbers. With the higher growth rate, the target volume of aerosol particles is deposited on the fiber before the probability of growth at the zero degree mark becomes large enough to predict a particle capture. Figure $3c$ shows the same characteristics shown in Fig. $3(b)$ that is, initially particles deposit farther back on the fiber surface, more in the 40 to 60 deg range.

Examining Fig. 3, the effects of the higher flow velocities can be seen for an interception parameter of 0.1. In Fig. $3(a)$ the particle growth is more uniform over the front face of the fiber. In Fig. $3(b)$ and Fig. $3(c)$ the loading appears to be less uniform with higher particle concentration in the region of 40 to 60 deg and 300 to 320 deg. This trend can be clearly seen in Fig. $5(a)$. Figure $5(a)$ plots the slope of the particle layer surface at different angles from the stagnation point. The slope for the Re = 0.2 line can be seen to be of a lesser magnitude than either of the 1.0 or 2.0 cases indicating less drastic changes in elevation. The differences between the Re = 1.0 and Re =

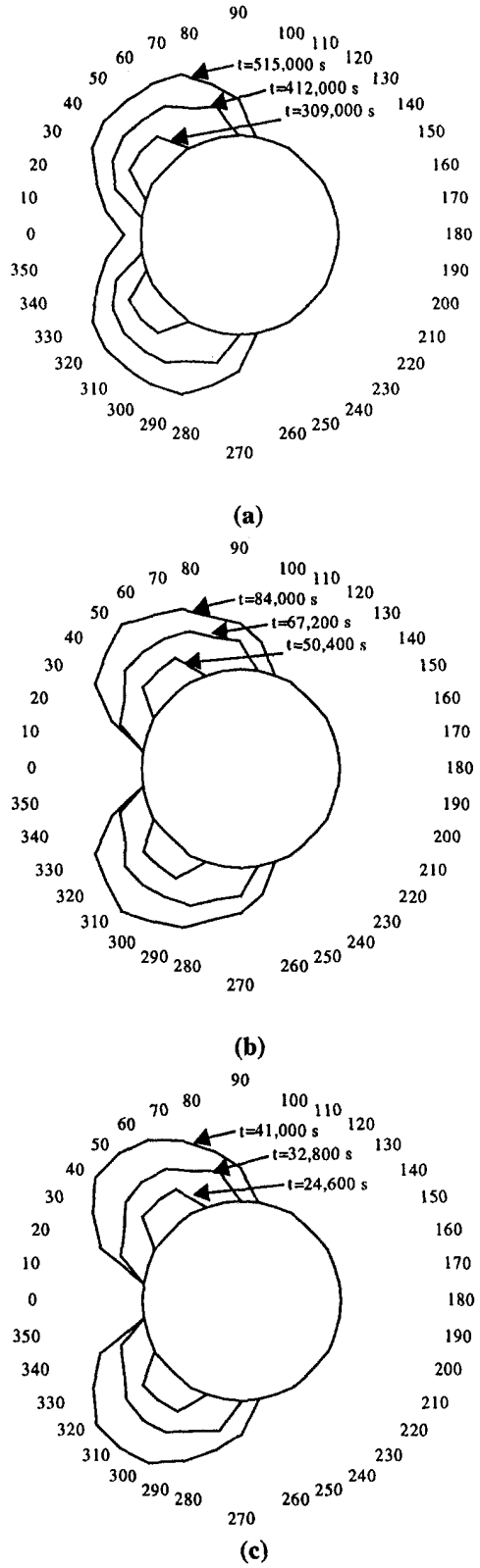

Fig. 3 Particle layer growth as a function of angular position and time. Interception parameter = 0.1. (*a*) Re = 0.2; (*b*) Re = 1.0; (*c*) Re = 2.0.

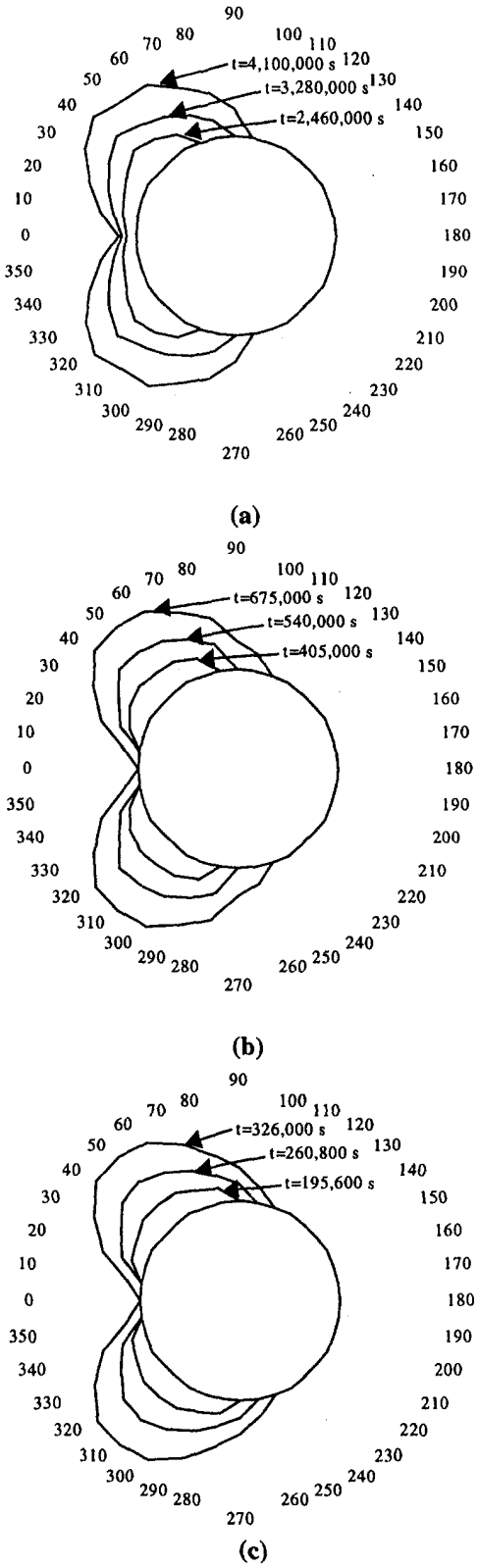

Fig. 4 Particle layer growth as a function of angular position and time. Interception parameter = 0.05. (*a*) Re = 0.2; (*b*) Re = 1.0; (*c*) Re = 2.0.

2.0 are smaller than between 0.2 and 1.0, but it can be seen in Fig. 5 that the Re = 2.0 has a sharper slope. Recalling that results for each case are presented for a fixed volume of particles attached to the surface of the fiber, this result indicates that for larger Reynolds numbers the dendrites form a particle layer that is more narrow and slender in shape than the low Reynolds number case, which has a more uniform coating. An interesting point to note in Fig. 5 is that the point of greatest depth does not change over the range of Reynolds numbers analyzed. The fiber continues to see the deepest particle layer forming around

the 50 and 310 deg points, as indicated from the point where the slope turns negative. This angle was also indicated to be the point of greatest particle growth in the work by Payatakes and Gradon (1980).

Figure 4 gives the particle layer profiles over the Range of Reynolds numbers for an interception parameter of 0.05. Once again, it is seen that a more uniform particle layer is achieved at lower Reynolds numbers. The lower impact parameter does appear to entice a more uniform particle layer. At the 60 percent time mark (the innermost contour), particle coverage is relatively broader for the smaller interception parameter. Figure 8 gives the slope of the particle layer over the surface of the fiber. For the 0.1 interception parameter, the slope reaches a maximum slope of about 2.0. For the 0.05 interception parameter, the slope reaches a maximum of 1.5 indicating a broader coverage with less drastic elevation changes.

Figure 6(a) shows the surface loading trend for the 0.1 interception parameter case for a single fiber. The trends seen in particle growth on the single fiber effect the macroscopic behavior of the filter medium through a condition called "surface loading." At lower flow velocities, particles load throughout the depth of the media. At higher flow velocities, particles attach only to the front of the media and begin to form a cake. This reduces the service life of a filter significantly. It was seen in Fig. 5(a) and Fig. 5(b) that as Reynolds number is increased, the rate of growth increases in the front quarter about 50° as indicated by the slope of the particle layer. This trend along with Fig. 6(a) shows that higher velocities give rise to long slender dendrites on the front of the fiber. Eventually these slender dendrites will be sheared off in the higher velocity flow forming a much larger agglomeration that will clog the next fiber layer downstream. This then forms the foundation for the filter cake that forms. Earlier it was pointed out that as the flow Reynolds number was increased, the particle trajectories were pushed towards the fiber on the upstream surface which resulted in a reduction of the impact parameter and an increase in the collision angle. These changes in the flow field cause an increase in the growth rate of particles at the 50 deg point. Figure 6(b) shows the loading history for an interception parameter of 0.05. The same trends seen in Fig. 6(a) are evident here with the main difference being that the loading now occurs over a much longer time period due to the smaller interception parameter. For the smaller particles present in the 0.05 case, it takes an order of magnitude longer to capture the same volume of particles than it did in the 0.1 interception parameter case.

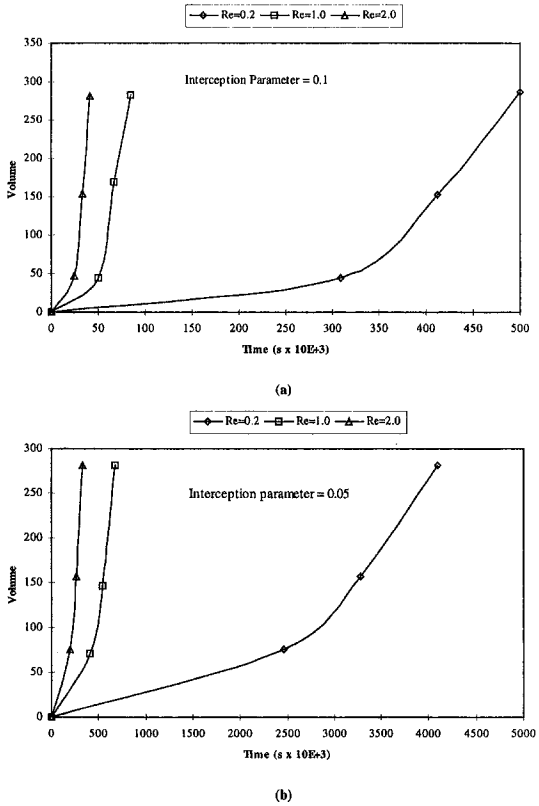

Fig. 6 Surface loading over time. (a) Interception parameter = 0.1; (b) Interception parameter = 0.05.

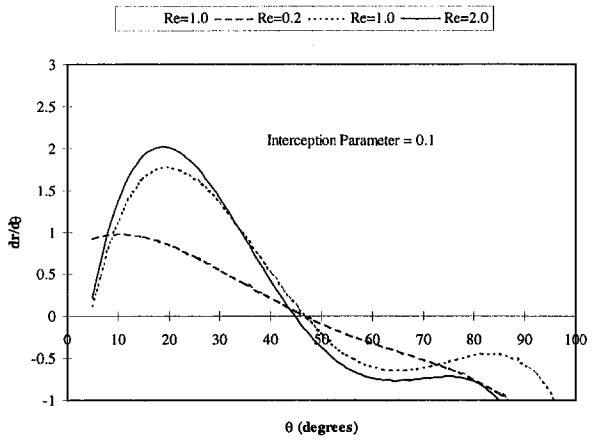

Fig. 5(a) Slope of particle growth layer. Interception parameter = 0.1.

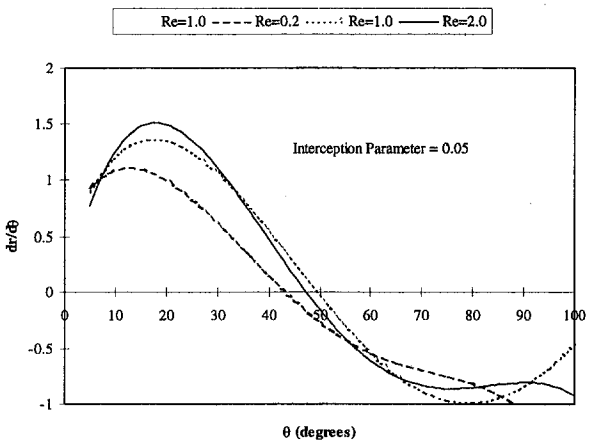

Fig. 5(b) Slope of particle growth layer. Interception parameter = 0.05.

Figures 7 and 8 show the changes in the depth of the particle layer at specific points along the surface of the fiber. Figure 7(a) shows the growth trend of the particle layer at 20 deg from the stagnation point for all three Reynolds number cases. These plots show that at this position on the fiber surface the dendrite growth, both absolute height and growth rate, is greater for lower Reynolds numbers. Examining points farther downstream, the trend is that the growth rate begins to favor larger Reynolds numbers. In Fig. 7(b), the Re = 2.0 case at 40° the growth is consistently shorter than the dendrite seen at Re = 0.2 until when the fiber becomes fully loaded. At this point the dendrite calculated for the Re = 2.0 case grew beyond the one calculated for the Re = 0.2 case. This trend continues in Fig. 7(c) where an angle of 60 deg is considered with the greatest growth for these higher Reynolds numbers occurring around the 50 deg mark. The higher flow velocities are causing more particles to be deposited at a higher rate in cited peak areas and the dendrites outgrow those for lower Reynolds numbers.

The same trends seen for the 0.05 interception parameter case can be seen for the 0.1 interception parameter in Fig. 8. Better growth can be seen towards the stagnation point for the low Reynolds number cases and towards the top of the fiber for the higher Reynolds number cases. This is a result of the particle pathline changes that occur at higher Reynolds numbers. As the flow inertia increases, the particle concentration on the upper portions of the cylinder increases too.

Conclusions

In the present work, the particle level dynamics of a fibrous porous filter at flow conditions above the Stokes flow regime are investigated. Past research has been improved upon by implementing a full Navier Stokes solution of the flow through a fibrous filter to eliminate the Stokes flow assumption. Unlike the Kuwabara cell model, the effect of neighboring cylinders is accounted for by modeling several staggered cylinders. The results of this model can be applied to commercial situations where one is concerned with the effect of using high efficiency media in an application that would expose the media to airflow velocities above the design limit. Results show that lower velocities allow particles to collect on the fiber surface in a more uniform manner. Increasing flow velocity causes the growth in the 40 to 60 deg range to increase significantly resulting in longer, more slender dendrites. These dendrites will be more susceptible to being stripped and re-entrained into the flow as a large agglomeration. These larger agglomerations have the potential of blocking off the flow within the first few fiber diameters, significantly shortening the life of the media. This model provides general insight into the changes in filter performance that could be expected when high efficiency media are employed.

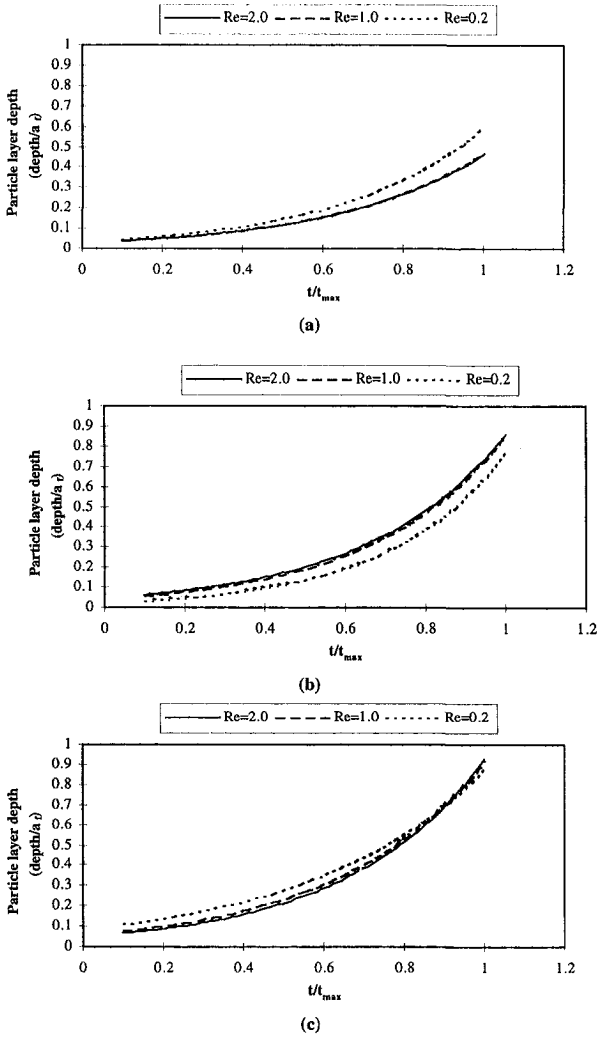

Fig. 7 Depth of particle layer as a function of time. Interception parameter = 0.05. (*a*) θ = 20 deg; (*b*) θ = 40 deg; (*c*) θ = 60 deg.

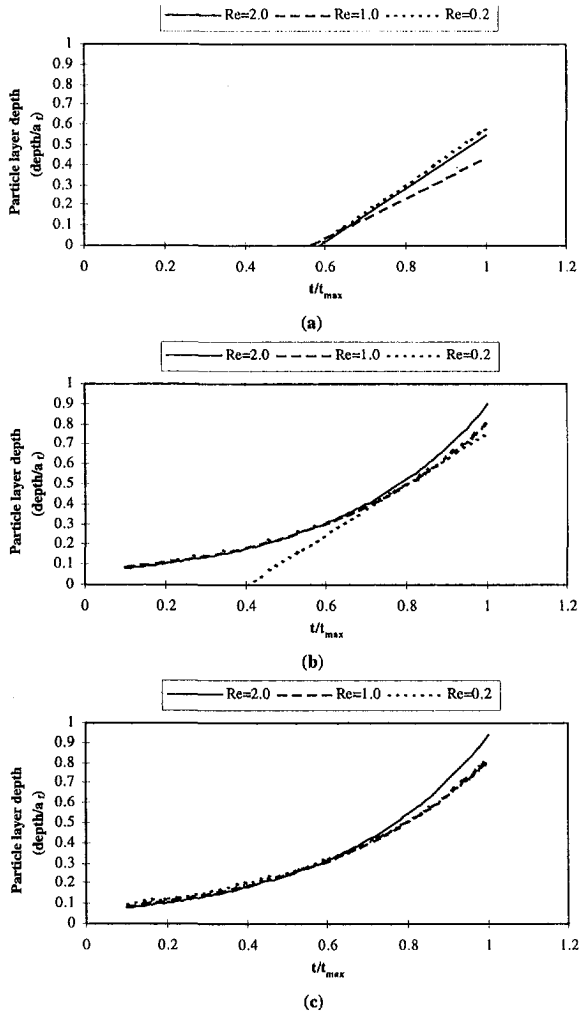

Fig. 8 Depth of particle layer as a function of time. Interception parameter = 0.1. (*a*) θ = 20 deg; (*b*) θ = 40 deg; (*c*) θ = 60 deg.

Acknowledgment

One of the authors (KV) wishes to acknowledge the support from CNR Bilateral Research Project grant # 97-03198-CT07 while working on portions of this project.

References

C. A. J. Fletcher 1980, *Computational Techniques for Fluid Dynamics,* Vol. II.

Fornberg, B., 1987, "A Numerical Study of Steady Viscous Flow Past a Circular Cylinder," Vol. 5, pp. 339–353.

Goren, S. L., 1973, *Journal of Colloidial Interface Science,* Vol. 44, p. 365.

Henry, F. S., and Ariman, T., 1983, "An Evaluation of the Kuwabara Model," *Particulate Science and Technology,* Vol. 1, pp. 1–20.

Henry, F., and Ariman, T., 1987, "A Staggered Array Model of A Fibrous Filter with Electrical Enhancement," *Particulate Science & Technology,* Vol. 1, pp. 139–154.

Henry, F., and Ariman, T., 1986, "Numerical Calculation of Particle Collection In Electrically Enhanced Fibrous Filters," *Particulate Science and Technology,* Vol. 4, pp. 455–477.

Hidy, G. M., and Brock, J. R., 1970, *The Dynamics of Aerocolloidal Systems,* Pergamon Press, Oxford.

Liu, B., and Rubow, K. L., 1986, "Air Filtration By Fibrous Media" *Fluid Filtration: Gas,* Vol. 1, pp. 1–12.

Kwak, D., and Chakravarthy, S. R., 1986, "A Three-Dimensional Incompressible Navier-Stokes Flow Solver Using Primitive Variables," *AIAA Journal,* Vol. 24, No. 3, pp. 390–396.

Payatekes, A. C., 1976, "Model of the Dynamic Behavior of a Fibrous Filter Application to Case of Pure Interception During Period of Unhindered Growth," *Powder Technology,* Vol. 14, pp. 267–278.

Payatekes, A. C., 1977, "Model of Transient Aerosol Particle Deposition in Fibrous Media With Dendritic Pattern," *AIChE Journal,* Vol. 23, pp. 192–202.

Payatekes, A. C., and Gradon, L., 1980, "Dendritic Deposition of Aerosol Particles in Fibrous Media by Inertial Impaction and Interception," *Chemical Engineering Science,* Vol. 35, pp. 1083–1095.

Piekaar, H. W., and Clarenburg, L. A., 1967, "Aerosol Filters—Pore Size Distribution In Fibrous Filters," *Chemical Engineering Science,* Vol. 22, pp. 1399–1403.

Tien, H. C., and Vafai, K., 1990, "A Synthesis of Infiltration Effects on an Isulation Matrix," *International Journal of Heat and Mass Transfer,* Vol. 33, pp. 1263–1280.

Tien, C. L., and Vafai, K., 1979, "Statistical Bounds for the Effective Thermal Conductivity of Microsphere and Fibrous Insulation," *AIAA Progress Series,* Vol. 65, pp. 135–148.

Vafai, K., and Tien, C. L., 1981, "Boundary and Inertia Effects on Flow and Heat Transfer in Porous Media," *International Journal of Heat and Mass Transfer,* Vol. 108, pp. 195–203.

Vafai, K., and Tien, C. L., 1980, "Boundary and Inertia Effects on Convective Mass Transfer in Porous Media," *International Journal of Heat and Mass Transfer,* Vol. 25, No. 8, pp. 1183–1190.

Vafai, K., and Whitaker, S., 1989, "Simultaneous Heat and Mass Transfer Accompanied by Phase Change Effects in Porous Materials," *International Journal of Heat and Mass Transfer,* Vol. 32, pp. 1261–11277.

Vafai, K., and Sarkar, S., 1986, "Condensation Effects in a Fibrous Insulation Slab," ASME *Journal of Heat Transfer,* Vol. 108, pp. 667–675.

G. L. Chahine
President.

K. M. Kalumuck
Principal Research Scientist.

Patrick D. Aley
Laboratory Technician.

G. S. Frederick
Senior Technician.

DYNAFLOW, Inc.,
7210 Pindell School Road,
Fulton, MD 20759
e-mail: info@dynaflow-inc.com
http://dynaflow-inc.com/

High Flux Rate Particle Filtration From Liquids

A method for efficient solid particle removal from liquids using microporous tubes with flow swirl and flow interruption is presented. Experiments were performed using particle laden water obtained from an actual field project of high pressure water jet paint stripping. The flow rate, orientation, flow interruption, and swirl index were varied, and their effect on performance observed and measured as a function of time. Flux rate increases of a factor of 20 over a conventional microporous tube cross flow filtration were generated. Flux rates were found to increase both with increasing swirl and with moderate increases in the shear exerted on the tube wall. Results of independent testing by the US Navy at Port Hueneme of a small field unit demonstrate high flux rate performance with high permeate quality and turbidity removal.

Introduction

Filtration processes can be divided into two general categories: crossflow and through-flow filtration. In through-flow filtration, both feed and filtrate flows are normal to the surface of the filter medium; thus the filtered particles continuously accumulate on and within it. The filtrate flux steadily decreases with time when the pressure drop across the filter is maintained constant, and periodic "back-washing" is necessary to remove the accumulated solids from the filter matrix and continue filtration.

In crossflow filtration, the feed flow is parallel to the filter surface, with the filtrate permeation occurring perpendicular to the flow. A quasi-steady operation is possible, since the continuous build-up of the separated solids on the filter surface is greatly reduced by the hydrodynamic shear exerted by the crossflow (Fig. 1). Crossflow microfiltration removes primarily suspended solids, operates at relatively low pressures (approximately 100 KPa), and employs relatively thick-walled tubes ($\simeq$1 mm). A major advantage of crossflow filtration is its higher filtration rate than through-flow filtration.

In recent years, a number of both passive and active techniques have been proposed and developed for minimizing the cake formation and/or concentration polarization on membranes and filters. These include the inducement of fluid instabilities (Winzeler and Belfort, 1993) including the introduction of Dean vortices by imposing a spiral flow path (e.g., Mullubhotla, et al., 1993; Belfort et al., 1993) and the formation of Taylor vortices by use of a rotating cylinder filter (e.g., Kroner and Nissinen, 1988; Schmidt and Bandiali, 1988). Other techniques include the use of one or more disks that rotate parallel to a flat membrane inducing high shear (Rolchigo, 1992; Fendya, 1997) and spring oscillation of the module (Culkin, 1991).

In this paper, an investigation of novel means of increasing the filtrate flux rate of the conventional crossflow filtration is presented. The new crossflow filtration concept (denoted as DYNAPERM®, Chahine, 1996, Kalumuck et al., 1993, Kalumuck et al., 1994) combines the conventional microfiltration with several major modifying and enhancing mechanisms. These enhancements include:

- A reversal of the filtrate flow direction to flow across the tube from its outside to its inside,
- Addition of swirl to crossflow filtration, and
- Superposition of flow interruption to the filtration process.

The new filtration concept employs conventional microporous tubes with the pore structure and sizes being controlled during the manufacturing process (Sundaram et al., 1978; Baranski et al., 1980; Sundaram and Santo, 1977). This technology has been successfully used in removal of solids in such applications as battery and electroplating wastes. The tubes can be made from a variety of extrudable thermoplastics. The porous tubes allow the small particles to actually penetrate into their wall matrix. The tube pore structure is such that the pore sizes are of the order of several microns, with the pore "length" many times their diameter. When effluents are circulated through the tubular filter, the solid particles are slowly driven, with the permeating flow, toward the wall. Thus, the particle concentration near the wall steadily increases, this tendency being limited by the turbulent diffusion of the particles away from the tube walls from regions of high concentration to those of lower concentration. The turbulent diffusion depends on the shear stress exerted on the walls by the flow, and, hence, on its velocity. The permeation rate increases the particle concentration near the wall and depends on the pressure differential across the filter surface and on the tube pore structure (Darcy's law). A quasi-steady state profile of particle concentration will be established near the wall when these two opposing tendencies balance each other. A fine, dynamic filter cake or "dynamic membrane" forms on the walls. (See, for example, Friedlander and Litz, 1971.) The initially high flux rate across the tube walls rapidly decreases, then attains a "plateau" regime that exhibits little or no change in flux rate due to build up of particles along and within the wall. Theoretically, this regime exhibits constant flux rate and no further filter cake growth. This idealization also requires the filtration to be controlled by the filter cake and that no changes take place in the underlying porous tubes filter medium. In practice, however, this regime often exhibits a very slow decline in flux rate.

The porous tubes utilized in the work reported in this paper were made of nylon with a 1 mm wall thickness and a 6 mm inside diameter. They possess a porosity of approximately 65 percent with a pore size distribution as shown in Fig. 2. Also shown in Fig. 2 is a scanning electron microscope photograph of a tube section showing the open cell reticulated pore structure.

Contributed by the Fluids Engineering Division for publication in the JOURNAL OF FLUIDS ENGINEERING. Manuscript received by the Fluids Engineering Division November 10, 1997; revised manuscript received November 2, 1998. Associate Technical Editor: D. P. Telionis.

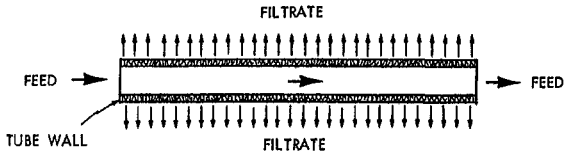

Fig. 1 Crossflow filtration schematic. The filtrate (permeate) flow across the porous tube wall is perpendicular to the main flow direction.

Basic Model

A module of the new filtration concept consists of a bundle of microporous tubes located in the center of a swirl chamber (see Fig. 3). The chamber is constructed of two concentric cylinders. The outer cylinder serves as a manifold. The inner cylinder has a set of tangential slots cut in it such that the flow enters the inner chamber containing the tubes with a tangential velocity that sets up the swirling flow. The filtrate permeates across the porous tube walls and is collected. Part of the particulates remain in the outer flow which is recirculated while the other part become part of the filter cake, referred to as a "dynamic membrane," along the tube walls. The high shears exerted by the swirling flow minimizes the thickness of the filter cake enabling high flux rates. Periodic interruption of the flow causes the filter cake to flake off, rejuvenating the tubes.

Dynamic Membrane. The dynamic membrane is the net result of particle deposition on the tube wall due to flow through the wall, and particle removal due to entrainment by the shear flow parallel to the wall. The permeate flux rate across the tube wall is a function of the pressure drop across the wall/cake porous medium, the resistance of the tube wall and the dynamic membrane thickness and composition. Initially, there is a rapid decline in flux as the membrane forms and grows. This period has been referred to as static filtration (Fordham and Lavda, 1989, Pearson and Sherwood, 1988). There is a net particle mass flux to the wall which arises from the difference between the particle deposition rate and the particle entrainment rate due to turbulent processes.

Following this initial flux decline period, a "plateau" of flux and membrane thickness versus time is achieved due to an approximate equilibrium between particle deposition and entrainment. This period is characterized by a very slow flux decline due to a very slow growth of the particle layer. At this approximate equilibrium, the flux rate is found to be proportional to the friction velocity u^*,

$$u^* = \sqrt{\frac{\tau_w}{\rho}}, \tag{1}$$

with τ_w being the wall shear stress and ρ the density. (See, for example, Fordham and Lavda, 1988 or Kalumuck et al., 1993.)

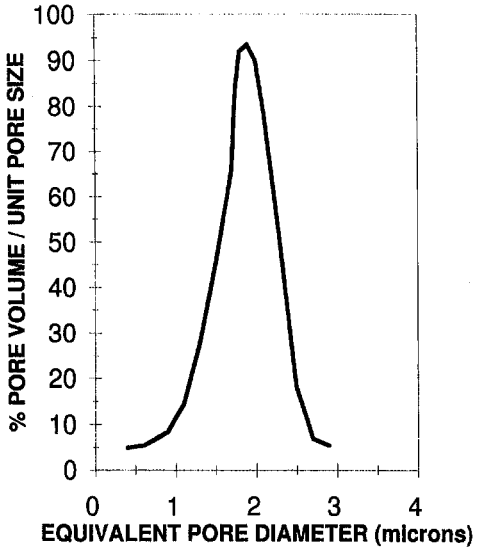

Fig. 2(a)

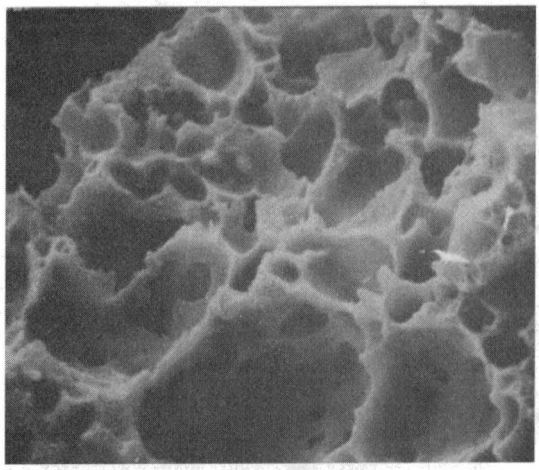

Fig. 2(b)

Fig. 2 Characteristics of microporous tubes utilized. (a) Nylon tube pore size distribution based on mercury intrusion tests. (b) Scanning electron microphotograph of tube pore structure at 1000X.

Swirling Flow Field. Of particular importance to the filtration performance is the flow field within the swirl chamber. To describe this flow, we adopt a cylindrical coordinate system (r, θ, z) with the origin located along the swirl chamber centerline and at its bottom. A sketch of the laboratory test module employing a swirl chamber is provided in Fig. 3. The flow, of tangential velocity V_θ, has an inner core region of solid body rotation of radius a surrounded by an approximately "free vor-

Nomenclature

A_t = total tangential injection slot cross-sectional area
A_z = cross-sectional area for axial flow in swirl chamber
a = core region radius in Rankine vortex model of swirling flow
h = tangential injection slot width
F = permeate flux rate (volumetric flow rate per unit area of filter)
l_t = tangential injection slot length
P = pressure
P_i = ambient pressure outside swirl chamber
$\bar{P}$ = P/P_i
Q = feed volumetric flow rate
Q_P = permeate volumetric flow rate
R = radius of swirl chamber
R_{tb} = radius of tube bundle
r, θ, z = coordinates of cylindrical coordinate system
S^* = swirl index defined in Eq. (9)
V_r, V_θ, V_z = radial, tangential, and axial velocities in swirl chamber
V_{res} = nominal resultant total velocity ($\sqrt{V_t^2 + V_z^2}$)
V_t = average tangential injection velocity
Γ = circulation
ξ = permeate recovery fraction (ratio of permeate to feed flows)

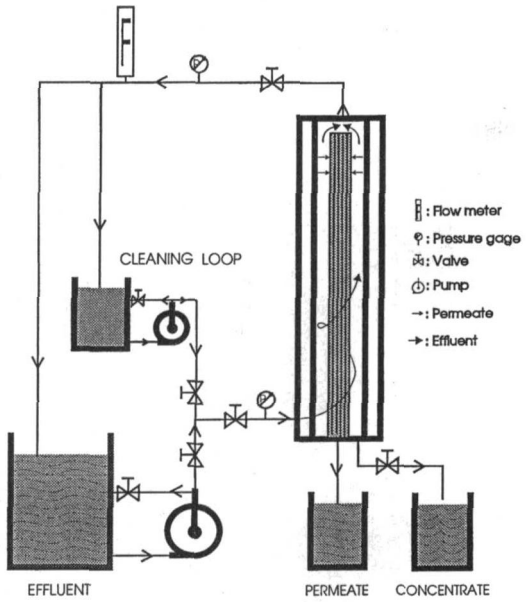

Fig. 3 Test loop

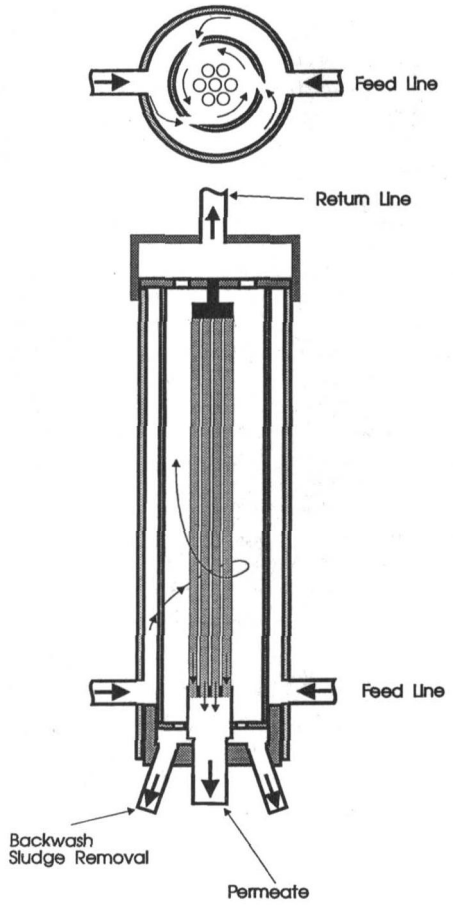

Fig. 3 Module

Fig. 3 Sketch of laboratory test loop (top) and module (bottom). The test loop configuration shown draws off both the permeate and the concentrate. Other configuratins employed included remixing of the concentrate or the concentrate and the permeate into the effluent (feed) reservoir. The module shown here includes a bundle of seven microporous tubes and three sets of tangential injection slots located 120 degrees apart around the circumference.

tex'' region and finally some effects due to wall boundary layers. Concentrating on the region near the tubes and thus neglecting the wall boundary layer effects, the flow is taken to be:

$$V_\theta = \frac{\Gamma r}{2\pi a^2}; \quad r < a, \tag{2}$$

and

$$V_\theta = \frac{\Gamma}{2\pi r}; \quad a < r < R, \tag{3}$$

where R is the swirl chamber radius and Γ is the circulation. This is the classical Rankine vortex (e.g., Milne-Thomson, 1949) for which the pressure field and radial pressure gradients are given in nondimensional form as:

$$\bar{P}(r) = 1 - \frac{\rho}{P_i}\left(\frac{\Gamma}{2\pi a}\right)^2\left[1 - \frac{1}{2}\left(\frac{r}{a}\right)^2\right];$$

$$\frac{\partial \bar{P}}{\partial r}(r) = \frac{\rho}{P_i}\left(\frac{\Gamma}{2\pi a}\right)^2 \frac{r}{a^2}; \quad r \le a, \tag{4}$$

$$\bar{P}(r) = 1 - \frac{\rho}{2P_i}\left(\frac{\Gamma}{2\pi a}\right)^2\left(\frac{a}{r}\right)^2;$$

$$\frac{\partial \bar{P}}{\partial r}(r) = \frac{\rho}{P_i}\left(\frac{\Gamma}{2\pi a}\right)^2 \frac{a^2}{r^3}; \quad r \ge a, \tag{5}$$

where the pressure is normalized with the ambient pressure outside the vortex chamber, P_i.

The tangential injection velocity V_t can be varied and is directly determined by the total tangential flow rate, Q_t and the total tangential slot injection area, A_t by:

$$V_t = V_\theta|_{\text{at } r=R} = \frac{\Gamma}{2\pi R} = Q_t/A_t, \tag{6}$$

where R is the swirl chamber radius, and Γ is the circulation. The average axial velocity, V_z when the flux across the porous tube is neglected is then defined to be

$$V_z = \frac{1}{A_z}\int_0^{z=l_t} V_t h dz = V_t \frac{n_{\text{slot}} h l_t}{A_z} = V_t \frac{A_t}{A_z}, \tag{7}$$

where $z = 0$ is along the slot furthest from the axial outflow, n_{slot} is the number of slots, l_t is the slot length, h is the thickness of the injection slot(s) and V_t and h are taken independent of z. A_z is the cross-sectional area for axial flow which, for a tube bundle radius of R_{tb} is given by:

$$A_z = \pi(R^2 - R_{tb}^2). \tag{8}$$

The relation of the V_θ distribution with V_t and chamber geometry can be found in Escudier et al. (1980) where it is shown that the maximum value of V_θ can be as much as 15 times V_t.

A simple dimensionless ''swirl index,'' S^*, characterizing the overall configuration, can be defined as

$$S^* = \frac{V_t}{V_z} = \frac{A_z}{A_t}. \tag{9}$$

The pressure at the tube wall is equal to the sum of the pressure inside the tube and the pressure drop across the tube wall. That pressure is also determined by the pressure drop due to the swirling flow.

The presence of porous tubes at the center of the swirl chamber leads to a more complicated flow. At $r = R_{tb}$, the radius of the outer tube (or tube bundle) wall/membrane combination, $V_\theta = V_z = 0$ (no slip) and a radial flow, V_r exists that is related to the permeate flux rate, F:

$$V_r|_{r=r_w} = -F\frac{nr_t}{R_{tb}}, \tag{10}$$

for a bundle or n tubes of radius r_t.

A dimensionless parameter, ξ,

$$\xi = \frac{Q_P}{Q} = \frac{2\pi n r_t F}{hV_t}, \tag{11}$$

can be used to measure the relative influence of radial to tangential flow as well as the fraction of permeate recovered, i.e., the permeate flow divided by the feed flow. In our tests, ξ was generally less than 0.2 showing that the radial velocity was only a small fraction of the tangential velocity.

Experimental Setup

Small Scale Laboratory Experiments. Laboratory experiments to investigate the influence of the above parameters were conducted in flow loops schematically depicted in Fig. 3. Particulate laden feed was drawn from a reservoir of between 8 and 20 liter capacity by a circulating centrifugal pump. The feed then entered the filtration module, described below. Part of the flow permeated across the porous tubes leaving the particulates behind, and flowed out of the module as the permeate stream. The remaining flow was circulated back to the reservoir. The pressure drop across the module was controlled by valves at the module inlet and outlet, and pressures at these locations were monitored using gages. A rotameter type flow meter monitored the feed flow. Due to the relatively small flow rates involved, permeate flow was periodically measured. Periodic interruption of the feed flow was achieved by closing the valve at the feed flow entrance to the filtration module. The flow was interrupted for a period of 30 s every 30 min.

Several different test modules were designed and fabricated of clear plastic to afford good observational opportunities. Dye injection was used to visualize the flow pattern. Observations with time showed the relative importance of tangential and axial flow. Strong swirl was apparent near the slots and less dominant away from the slots. The amount of swirl was controlled by varying the open area of the tangential injection slots. The flow which did not permeate across the porous tubes exited via ports at the top of the inner (swirl) chamber. This stream is denoted as the "concentrate" since it will typically contain a higher concentration of particles than the feed due to drawing off of the particle free permeate water. Experiments were conducted with bundles of 1 to 7 tubes along the module axis. The module shown in Fig. 3 includes a bundle of 7 tubes 34 cm long resulting in a total filter area of 0.046 m^2. (The tube characteristics have been described above and in Fig. 2.) The swirl chamber had an inside radius $R = 2.6$ cm while the inside radius of the surrounding plenum chamber was 3.5 cm. Three rows of slots arranged circumferentially at 120 degree intervals were utilized to inject the flow into the swirl chamber as shown in Fig. 3. The pressure of the flow at the inlet to the module was typically 90 kPa above atmospheric.

Waste water from the high pressure water jet stripping of lead based paint from a bridge in the field was used as the feed. This water contained particulate contaminants of lead and rust among others due to the nature of the paint removed. Typical measured particle concentrations after prefiltering out particles larger that 1250 μm were of the order of 600 ppm. Measured particle size distributions are shown in Fig. 4. In some tests this was diluted to a concentration of 200 ppm to enable more experiments to be run with a limited amount of feed. For any given set of comparison experiments, water of the same particle concentration was employed. The filtered permeate was periodically sampled and its quality assessed. Utilizing graded filter paper, the permeate contained no measurable particle concentration down to a size of 2.5 microns indicating removal of all suspended particles of 2.5 microns or larger.

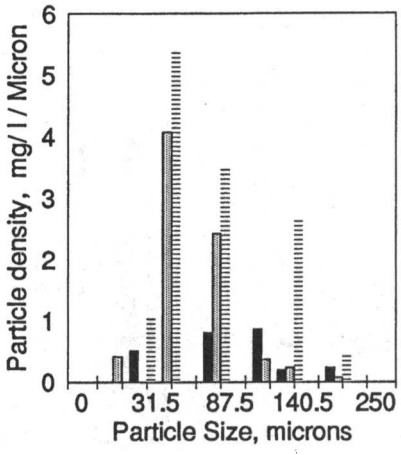

Fig. 4 Measured particle size distribution for feed water used in the filtration tests: weight density distribution per micron for three different batches of feed water denoted by the different shading of the bars

The flow of "clean" water (permeate) produced was monitored as a function of time, and the permeate flux rates per unit area of tube deduced. The flow rates and the slot area were varied. The slot area variation was achieved by blocking a portion of the slots. This enabled variation of the swirl index S^* (and thus average tangential velocity) between the values of 1 and 3 for a given feed flow rate.

Particle concentrations in the feed and filtrate streams were measured both with a series of fine pore sized filter papers (pore size down to 2 μm, weighing the collected particles with a Mettler precision balance) and with a spectrophotometer which uses light transmittance through a sample of the analyzed water to measure particle concentrations. In addition, pH and total dissolved solids content (TDS) were monitored using a pH meter and an electric resistivity meter. Both pH and TDS appeared unaffected by the filtration process remaining at typical values of pH = 7 and TDS = 160 ppm. Visual observations of the flow and particle behavior were also conducted. Base line cases were run with a single conventional microporous tube crossflow system to provide a relative performance yardstick. This conventional configuration utilized the same microporous tubes and involved flow within the tube in the conventional cross flow configuration as depicted in Fig. 1. Feed flows of the same particle size composition, distribution and concentration as those described above were employed.

Two different modes of operation were used. The majority of experiments were conducted in a mode in which the permeate was remixed into the feed reservoir, so that (except for small losses due to evaporation and sampling) the recirculating feed volume remained constant. In the "concentration" mode, a batch wise process is simulated by removing the permeate and collecting it in a separate reservoir so that the circulating feed volume continuously decreased while its suspended solids concentration continuously increased.

Permeate flux rates were measured by timing the filling of a graduated cylinder and are estimated to have an uncertainty of 10 percent. Flow rates were measured with rotameter type flow meters and have an experimental uncertainty of 5 percent.

Field Unit. Figure 5 shows a photograph of a small wheel mounted field unit consisting of 4 modules each having approximately 60 microporous tubes with a total tube surface area of 1.07 m^2 per module. Figure 6 provides a photograph of a tube bundle (left) and an end view of a module with its cap removed (center) exposing the tube bundle and with its cap affixed (right). The four modules were configured to enable operation

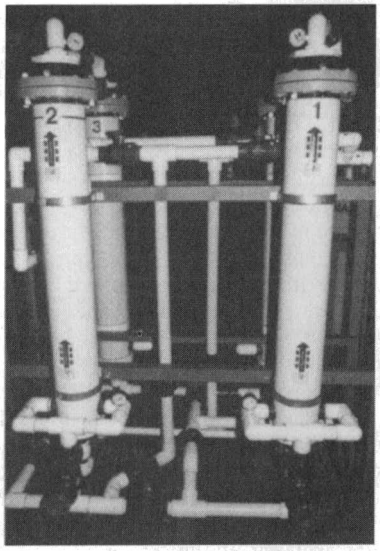

Fig. 5 Photograph of field test unit consisting of four modules of 60 tubes each

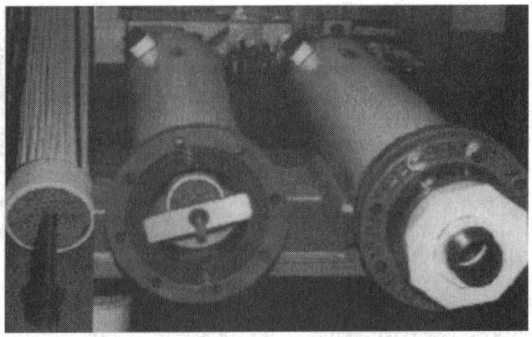

Fig. 6 Photograph of tube bundle and module components. Left: Tube bundle. Center: Vew of top of tube bundle inserted into module shell. Large flange has a diameter of 25 cm. Right: Fully assembled module.

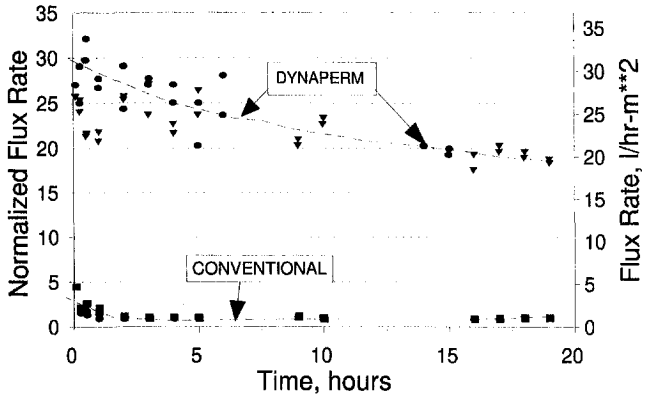

Fig. 7 Comparison of permeate flux rates obtained from long term tests with new and conventional cross flow module configurations

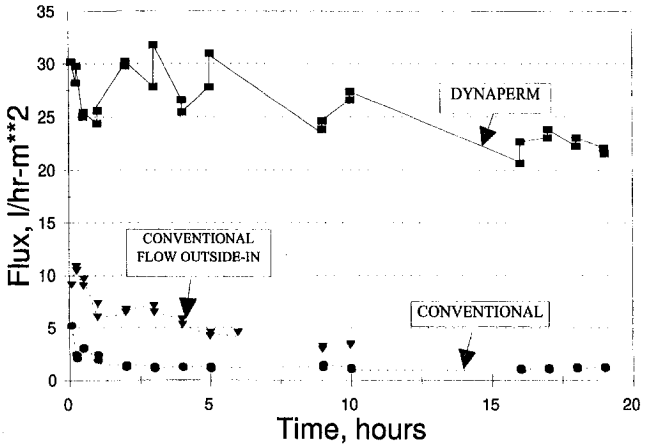

Fig. 8 Comparison of long term tests between new and conventional module configurations. The influence of swirl, flow interruption and inside-out flow are shown. See-saw lines correspond to short duration flow interruptions.

of any combination of the modules in both parallel and series operation. This was done to allow variation in the operating capacity and in the modules used for this experimental unit. The recycle tank and main pump were located on a separate wheeled frame linked to the module unit by hoses. The unit was tested as a possible pretreatment stage for the U.S. military's next generation Reverse Osmosis Water Purification Unit by the Naval Facilities Engineering Service Center (NFESC), Port Hueneme, CA. Tests were conducted with particulate laden sea water with and without the addition of bentonite which increased the feed turbidity. A detailed description of the procedures employed can be found in Miller et al. (1996).

Results and Discussion

Laboratory Scale Flux Rate Improvement. Figure 7 summarizes the data of a large number of tests and compares them with results of conventional cross flow filtration of the same water. Figure 8 isolates one set of tests and compares measured flux rates as a function of time to results without the use of swirl or flow interruption (but with the flow from outside to inside) and with a conventional cross flow filtration configuration in which tubes of the same type are utilized with simple flow from inside to outside as in Fig. 1 (Baranski et al., 1980, Sundaram and Santo, 1977). Figure 8 clearly shows substantially higher flux rates for the new concept with significant but much smaller increases due to changing the flow direction to outside in. Flow interruption continually reestablished the flux rate at near the original high value. As illustrated in Figs. 7 and 8, *the combined swirl and flow interruption resulted in an increase in flux rates of approximately a factor of 20 on average.*

Observations indicated that a particle layer rapidly built up on the outside wall of the tube. Upon flow interruption, the particle layer flaked off and fell to the bottom of the module. A short downtime enables a high frequency of flow interruption such that the flux rate never drops to the plateau level, but rather stays in the higher flux rate region.

Effect of Various Parameters. Experiments were conducted to investigate the influence of three key parameters: the number of tubes, the flow rate, and the swirl parameter. We restricted our test duration to two to three hours per condition in this parametric study. (As discussed above and shown in Figs. 7 and 8, a limited amount of runs were made at longer durations—up to 20 hours.) This is justified by the fact that—as known from previous tests (Sundaram et al., 1978) and as could be seen from Figs. 7 and 8—the first few hours give a very good indication of long term behavior.

Figure 9 considers the case where $S^* = 1$ ($V_t = V_z$) and the flow rate varies. It was found that although the permeate flux rate increases with increasing flow rate, its rate of increase is slower than that of the flow rate. Figure 9 shows that the permeate flow rate is a decreasing fraction of the feed flow rate as the feed flow rate through the module increases.

Figure 10 shows the influence of increasing the ratio of tangential velocity to axial velocity or the swirl parameter, S^*.

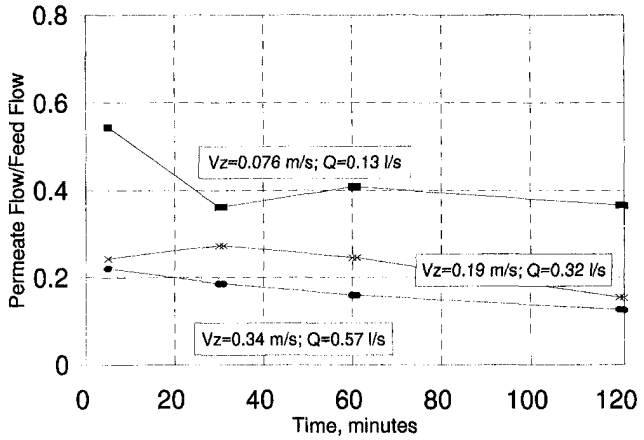

Fig. 9 Influence of feed flow rate on the ratio of permeate to feed flow rates for a constant value of $S^* = 1$. Permeate flux rates increase with feed flow rate but more slowly than the feed flow rate resulting in a decrease in the fraction of the feed flow recovered as permeate with increasing feed flow.

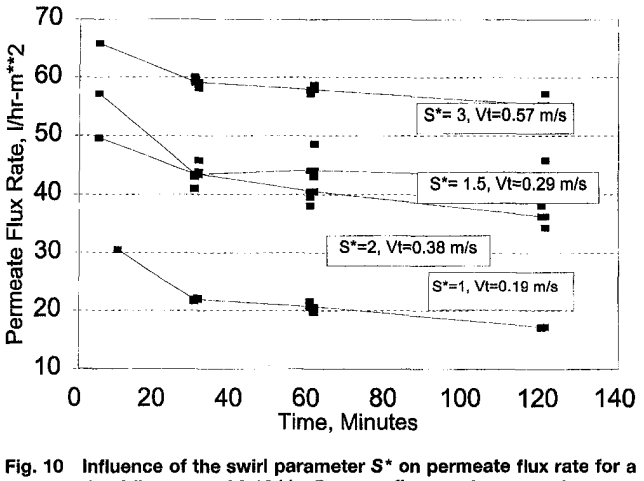

Fig. 10 Influence of the swirl parameter S^* on permeate flux rate for a constant feed flow rate of 0.16 l/s. Permeat flux rate is seen to increase with increasing swirl.

Here S^* takes the values 1, 1.5, 2, and 3 for the same flow rate of 0.16 l/s ($V_z = 0.19$ m/s). The overall tendency is for increased filtration rate with increased tangential velocity. This general tendency was observed at all times during the tests. However, small discrepancies exist in the details of the tests. For example, there are higher fluxes for $S^* = 1.5$ than for $S^* = 2$. A summary of all the data can be found in Kalumuck et al. (1993).

The Reynolds number of the flow around the tubes in our experiments based on the hydraulic diameter of the annular swirl chamber and on the total velocity vector of magnitude

$$V_{res} = \sqrt{V_t^2 + V_z^2}, \qquad (12)$$

ranged from 2000 to 40,000. This suggests the flow field was moderately turbulent which is consistent with observations of dye injection into the flow.

Swirling of the feed flow likely produces several beneficial effects. The liquid has a net flow into the porous tube wall and, without swirl, would carry particles along with it and deposit those onto the wall. The outward centrifugal body force exerted on the particles (particularly, the larger particles) retards their otherwise radially inward flow resulting in "slip" relative to the liquid flow into the wall and less deposition on the wall. This also modifies the concentration of particles in the bulk fluid, decreasing it near the wall. The second beneficial effect is due to the shear set up on the tube wall which tends to limit particle deposition. In tube flow, for a given tube size, the shear is essentially determined by the feed flow rate in the tube. In the swirling system, that shear can be varied over some range *independent* of the feed flow rate by adjusting the tangential injection geometry to vary the amount of swirl which enables higher shears at a given feed flow rate, resulting in deposition of a thinner particle layer.

The filtration process is mainly a balance between two dynamic forces: one moving the particles perpendicular to the wall and the second moving the particles along the microporous tube wall. Since shear forces affect particle layer growth on the wall, then the characteristic velocity to consider in the analysis is the velocity vector along the tube wall of magnitude V_{res}.

The rotating flow field acting on the particle distribution is very particular and is the primary mechanism producing the 20-fold filtration flux rate increase. The combination of tangential injection (swirl) and microfiltration at the center of the module results in a flow field controlled by viscous effects and possessing a maximum tangential velocity located between the tangential injection wall and the microporous tube walls. The induced pressure gradients possess a maximum at that same location (as can be seen from Eqs. (4) and (5)). In the outer region, centrifugal forces are dominant and particles are pushed away from the porous tubes, minimizing the particle concentration near the tubes. In the inner region, the pressure gradient decreases as one approaches the tube bundle. This preferentially drives larger particles to the center faster than smaller particles. This results in a well-segregated stratification of particles on the tube wall with the larger particles closer to the wall. This distribution enhances filtration while minimizing pressure drop and reduces pore clogging. In addition, the presence of larger particles in the filter cake at the wall reduces the contact forces between the particle layer and the wall enabling the layer to more readily fall off when the flow is interrupted.

Figure 11 presents the results using V_{res} for the $S^* = 1$ and $S^* = 1.5$ data. There is a region of maximum flux rate, here $0.46 \text{ m/s} \leq V_{res} \leq 0.76$ m/s. The shear exerted on the tube wall by the flow varies directly with V_{res}. These results of increasing flux rates with increasing shear are consistent with the findings of Fordham and Lavda (1989) for crossflow filtration of bentonite suspensions.

In addition to the beneficial effects described above, increased swirl also reduces the pressure on the outside of the tube wall, as shown in Eqs. (6)–(7), thus reducing the driving pressure across the tube wall and particle layer and potentially reducing the flux rate. Indeed, it has been found by Baranski et al. (1980) that pressure does not affect flux rates once a plateau has been reached, but that there is a mild effect during the initial period while the cake is rapidly growing. However, since we continually interrupt the flow which allows part of the filter cake to

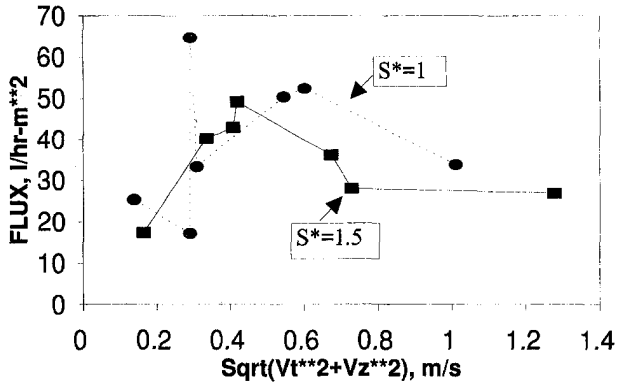

Fig. 11 Filtration rates versus resultant velocity along the tubes for values of $S^* = 1$ and 1.5

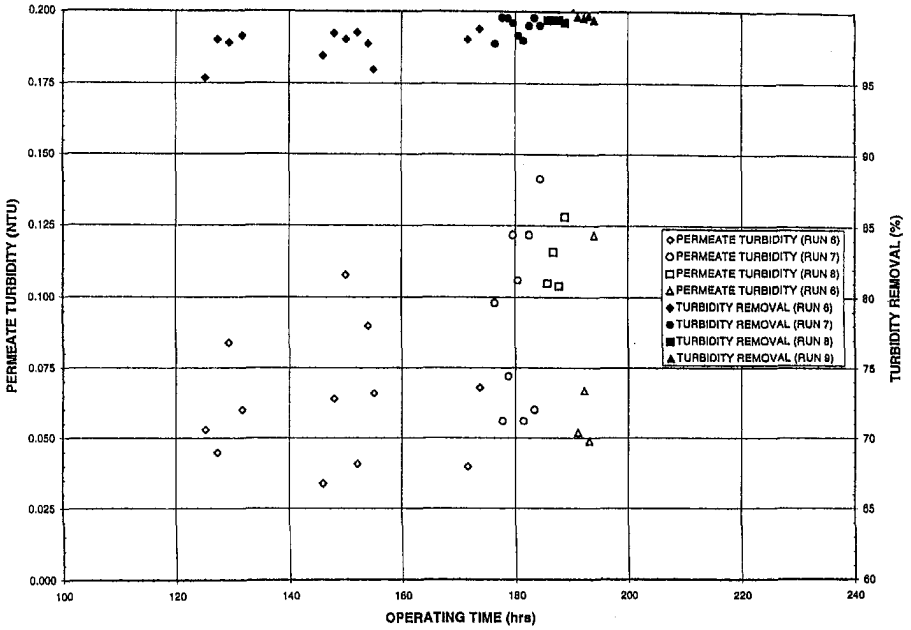

Fig. 12 Turbidity reduction achieved by field test unit filtering mixtures of seawater and bentonite of initial turbidities of 5 and 20 NTU (Miller et al., 1996)

flake off, we may be continually reinitializing the rapid cake growth phase which does have a weak pressure dependence. The weak dependence is also consistent with our observation of decreased flux only at the largest swirls. Thus increasing the swirl too much can be counterproductive.

Field Unit Tests. Results of extended tests with sea water are summarized in Figs. 12 and 13 which are results of tests conducted at Port Hueneme and reported by Miller et al. (1996). The turbidity was reduced from an initial value of 2.1 NTU (Nephelometric Turbidity Units) to a value of less than 0.1 NTU in the permeate with a decrease in silt density index from 38 (feed) to approximately 3 (permeate). Approximately 99 percent of the turbidity was still being removed after 190 hr of operation.

Conclusions

The results presented here demonstrate the capability of the new enhanced crossflow filtration concept (DYNAPERM®) to greatly improve the efficiency of particle removal from liquids. Using particulate laden water obtained from an actual field project of high pressure water jet paint stripping, the new filtration concept was found to result in measured flux rate increases of a factor of 20 over conventional microporous tube crossflow filtration.

Variation of flow rates and swirl index showed that flux rates increased with moderate increases in shear exerted on the tube as controlled by increasing values of the total velocity made up of the axial and tangential components. Flux rates tended generally to increase with the swirl index although there was sometimes a decrease with large amounts of swirl, probably due both to the manner in which this was created and to a decrease in the pressure drop across the tube wall due to the low pressures created at the center of the swirling flow.

Tests of a small field unit on seawater with bentonite addition showed 99 percent turbidity removal after 190 hours of operation.

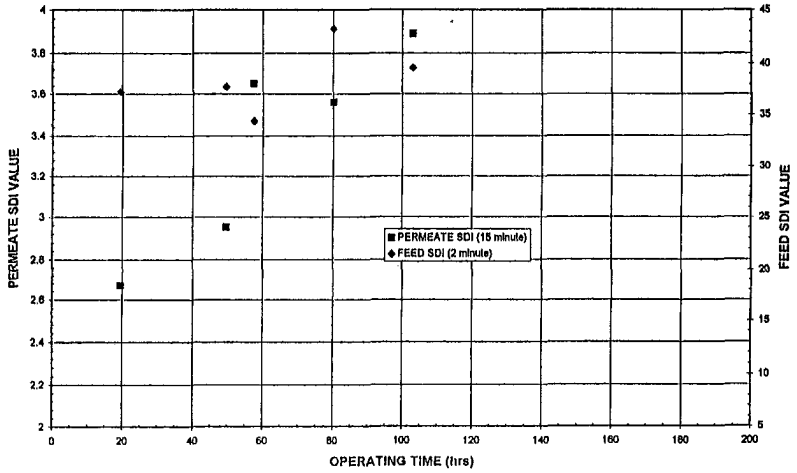

Fig. 13 Silt Density Index (SDI) reduction achieved by field test unit filtering mixtures of seawater and bentonite (Miller et al., 1996)

Acknowledgments

This material is based upon work supported in part by the National Science Foundation under award No. III-9261575.

References

Baranski, J., et al., 1980, "Removal of Heavy Metals by Cross-Flow Microfiltration," *Liquid/Solid Separation,* Spring.

Belfort, G., Brewster, M., and Chung, K.-Y., 1993, "Curved Channel Membrane Filtration," U.S. Patent No. 5,204,002, Apr.

Chahine, G., 1996, "Microfiltration System with Swirling Flow Around Filter Medium," U.S. Patent No. 5,500,134, Mar.

Culkin, B., 1991, "Vibrating Shear Enhanced Processing Applied to Liquid-Solid Separations," Paper 3B, North American Membrane Society Annual Meeting, San Diego, May.

Escudier, M.P., Bornstein, J., and Zehnder, N., 1980, "Observations and LDA Measurements of Confined Turbulent Vortex Flow," *Journal of Fluid Mechanics,* Vol. 98.

Fendya, T., Hurwitz, M., Musto, E., Miller, J. and Ryan, J. E. Jr., 1997, "Dynamic Filter System" U.S. Patent No. 5,679,249, Oct.

Friedlander, H. Z., and Litz, L. M., 1971, "Membranes for Pressure Permeation," *Membrane Processes in Industry and Biomedicine,* M. Bier, ed., Plenum Press, New York.

Fordham, E. J. and Lavda, H. K. J., 1989, "Cross-Flow Filtration of Bentonite Suspensions," *Journal of PhysioChemical Hydrodynamics,* Vol. 11 No. 4.

Kalumuck, K., Chahine, G., Aley, P. and Frederick, G., 1994, "Enhanced Particle Removal from Liquids," *Proceedings, ASME 5th International Symposium on Liquid-Solid Flows,* Lake Tahoe, NV, June.

Kalumuck, K.M., Chahine, G. L., Aley, P. D., and Frederick, G. S., 1993, "Enhanced Particle Removal from Liquids," DYNAFLOW, Inc. *NSF Phase I SBIR Final* Report 93002nsf-1, July. (Available on-line at http://www.dynaflow-inc.com/Reports/93002nsf.PDF.)

Kroner, K. H., and Nissinen, V., 1988, "Dynamic Filtration of Microbial Suspensions Using an Axially Rotating Filter," *Journal of Membrane Science,* Vol. 36.

Miller, M., Silbernagel, M., Kuepper, T., and Varnava, W., 1996, "Testing Prefiltration Systems for the Military ROWPU," *Proceedings of the American Desalting Association Biennial Meeting,* San Diego, Aug.

Mullubhotla, H., Nunes, E., and Belfort, G., 1995, "Microfiltration of Yeast Suspensions with Self-Cleaning Spiral Vortices: Possibilities for a New Membrane Module Design," *Biotechnology and Bioengineering,* Vol. 48.

Milne-Thomson, L. M., 1949, *Theoretical Hydrodynamics,* MacMillan, London.

Pearson, J. R. A., and Sherwood, J. D., 1988, "Continuum Modelling of Cross-Flow Filtration," *Journal of PhysioChemical Hydrodynamics,* Vol. 10 No. 5/6.

Rolchigo, P. M., 1992, "Rotary Disc Filtration Device," U.S. Patent No. 5,143,630, Sept.

Shmidt, I. and Badiali, M., 1988, "Filtration Method and Apparatus," U.S. Patent No. 4,790,942, Dec.

Sundaram, T.R., and Santo, J.E., 1977, "Removal of Suspended and Colloidal Solids from Waste Streams by the Use of Cross-Flow Microfiltration," ASME Publication No. 77-ENAS-51, July.

Sundaram, T.R., Santo, J.E., and Shapira, N.I., 1978, "An In-Depth, Cross-Flow Separation Technique for the Removal of Suspended Solids from Wastewaters," *Industrial Water Engineering,* Jan./Feb.

Winzeler, H., and Belfort, G., 1993, "Enhanced Performance for Pressure-Driven Membrane Processes: The Argument for Fluid Instabilities," *Journal of Membrane Science,* Vol. 80.

Effects of Increasing Particle Loading in an Axisymmetric, Vertical, Liquid-Solid Sudden Expansion Flow

(Data Bank Contribution)*

Maria Founti
Assistant Professor.

Thomas Achimastos
Graduate Student.

Athinodoros Klipfel
Graduate Student.

Mechanical Engineering Department,
Thermal Engineering Section,
National Technical University of Athens,
Athens, Greece

Measurements of particle and fluid velocities are reported for a turbulent, liquid-solid, sudden expansion flow flowing in the direction of gravity and laden with solid particles, at loadings equal to 1, 2, 3, 4, and 5 percent per volume. The measured two-phase flow velocities are compared to the characteristics of the corresponding single phase flow. Forces and flow mechanisms affecting particle dispersion in the various flow regimes are identified and it is indicated that there exist regions where the transverse Saffman lift force attains high values and controls particle dispersion. A consistent correlation between the mean reattachment point and the volumetric particle loading is indicated. All the two phase flows examined reattached upstream the corresponding mean reattachment location measured for the single phase flow. Increasing particle concentration affected locally the flow behaviour, with most obvious consequences within the recirculation zone and the near wall region.

1 Introduction

Sudden expansion flows laden with solid particles occur in a variety of engineering applications and it is known that the behavior of particles can be very important in determining the flow characteristics, especially in near-wall regions and regions of recirculating fluid. Drag and lift forces, viscous dissipation due to particle rotation, concentration gradients and gravity affect the particle motion.

Particle motion and dispersion have been mainly investigated for dilute gas-solid two phase flows, e.g., Fleckhaus et al. (1987), Tsuji et al. (1988), Sommerfeld et al. (1992), Hardalupas et al. (1992), Fessler and Eaton (1994). These results demonstrated the effects of gravity on the particle motion and showed a strong transverse dispersion due to turbulence. Parameters that influence particle dispersion have been postulated to a lesser extent for liquid-solid flows, e.g., Hishida et al. (1989), Nouri et al. (1987), Kenning and Crowe (1994). In general, it has been indicated that small particles disperse in the recirculation zone while large particles tend to pass through when they are injected inside it or, not to disperse at all when they are injected outside it. Kaftori et al. (1995) investigated the effects of particles on the structure of wall turbulence and concluded that some characteristics are altered due to the presence of particles. Berlemont et al. (1994) studied collision effects between particle pairs in isotropic and non-isotropic turbulence fields and showed that their behavior is strongly dependent on particle turbulent dispersion and particle relaxation time.

Previous experiments by Founti and Papaioannides (1992), Achimastos et al. (1993), and Founti and Klipfel (1994, 1998) in the same sudden expansion flow configuration, indicated that for Reynolds numbers higher than 3×10^4, the reattachment length remains independent of the value of expansion ratio (expansion ratios examined 1:2, 1:3, and 1:4), but it is 6–10 percent shorter than the reattachment length of the corresponding single phase flow. For volumetric particle loading of 0.6 and 3 percent, the presence of solid particles resulted in a local increase of the turbulence quantities at the flow inlet. Particles exhibited higher negative velocities inside the recirculation zone and they appeared to reattach upstream the reattachment point of the carrier fluid (water or diesel oil). In this work the volumetric particle loading has been systematically increased from 1 to 5 percent per volume of the working fluid in order to investigate the effects of the shear lift force and of particle to particle collisions on the motion of the particles.

2 Flow Configuration

The experiments have been performed in a closed-loop circuit incorporating a vertically mounted sudden expansion test facility, Fig. 1. The test section consisted of a DURAN-glass pipe, 1 m long and with $D = 51$ mm inner diameter. A second, smaller diameter brass-pipe, with inner diameter, $d = 25.5$ mm, was used to create the sudden expansion geometry. The 25.5 mm diameter brass-pipe was inserted into the 51 mm pipe which resulted to a step height, H, equal to 12.75 mm (expansion ratio 1:2) and provided an inlet to the test-section of ca. 20 D.

The working fluid was a mixture of two diesel oils ($\rho = 830$ kg/m^3, $\nu = 4.3201 \cdot 10^{-3}$ Pa s) with refracting index matching that of the DURAN-glass test section, which was also inserted in a rectangular trough, in order to minimize refraction of the laser beams at the pipe curved walls and to prevent displacement of the measuring volume inside the test-section. The temperature of the diesel mixture was controlled to within 3.5°C throughout the experiments. The DRAGONIT-25 glass particles, used for the dispersed phase, were not exactly matched to the refractive index of the fluid. This allowed measurements at high volumetric particle concentrations. The glass particles were spherical with mean diameter $d_p = 450$ μm, size range 400–520 μm and density equal to 2500 kg/m^3.

The experiments have been performed at Reynolds number equal to 5.6×10^4, based on the large pipe diameter and the

* Data have been deposited in the JFE Data Bank. To access the file for this paper, see instructions on p. 232 of this issue.

Contributed by the Fluids Engineering Division for publication in the JOURNAL OF FLUIDS ENGINEERING. Manuscript received by the Fluids Engineering Division July 18, 1995; revised manuscript received November 2, 1998. The long delay until publication is mostly due to the JFE Editorial Board. Associate Technical Editor: D. Stock.

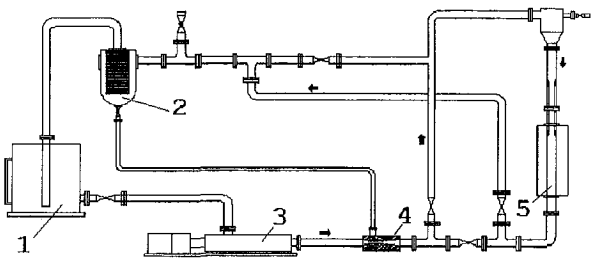

Fig. 1 The experimental setup: 1. Sump tank; 2. Centrifugal filter (particle separator); 3. Mohno-helical pump; 4. Angus-ventouri type fluid inductor; 5. Test section with sudden expansion.

maximum inlet axial mean velocity. Table 1 tabulates average values of the carrier fluid mass flow rates (m_f), of the maximum fluid (U_f) and particle (U_p) axial mean velocities at the inlet of the sudden expansion and of the measured mean reattachment length (x_R) for the various volumetric particle loadings examined.

Mass flow rates have been obtained by integrating the measured axial mean velocity profiles for the single and two-phase flows. The average mass flow rate for the fluid has been calculated equal to 1.736 ± 8 percent Kg/s, Table 1. Variations of the mean density of the fluid and particle mixture with increasing particle loading have not been taken into consideration in the calculation of mass flow rates and corresponding bulk velocities ($U_b = m_f/\rho_f A$, $A = \pi D^2/4$). The bulk velocity calculated for each loading, Table 1, has been used for nondimensionalizing the results.

3 Measuring Technique

An one component laser-Doppler anemometer has been used for the velocity measurements, comprising a 50 mW He-Ne laser, a TSI optical module with double Bragg-cells (frequency shift used 2–5 MHz) and a 150 mm focusing lens resulting to a control volume of 0.918 mm in length (l_m) and 0.15 mm in diameter (d_m). A 350 mm collection lens and an avalanche photo-diode have been used for the collection of the scattered light in the forward scattering light direction. The beams were rotated by 90 deg to allow measurement of the axial, radial, and azimuthal velocity components for the fluid and particles.

The Doppler signals, after being band-pass filtered were processed by a 175 MHz, LeCroy-9400A (LeCroy, Spring Valley, USA) transient recorder interfaced to a 386-SX P.C. The transient recorder was operated in a sequential mode at a digitizing frequency of 12.5 MHz. The amplitude of each filtered Doppler burst was recorded with the help of a burst peak detector, developed by Qiu and Sommerfeld (1992), that evaluated the location of maximum amplitude corresponding to the center of a Doppler burst. Once a burst was detected the transient recorder was triggered only once using a trigger generation logic. The two phases have been distinguished by setting a low and a high amplitude limit whereby bursts with amplitude below the low amplitude limit were classified as the carrier phase and bursts with amplitude above the high amplitude limit were classified as the discrete phase (particles). Bursts in the overlapping amplitude region, especially when they crossed the measuring volume outside its center, may have been included in the measured velocities.

4 Measurement Accuracy

Mean and rms velocities were calculated at each measuring location from approximately 10,000 samples based on a F.F.T. Errors (bias limit) due to the collected sample size were less than 1 percent in the mean velocities for 40 percent turbulence intensity and 95 percent confidence level and less than 2 percent in the turbulence quantities for 99 percent confidence level, Yanta (1973).

Erroneous identification of glass particles as seeding could lead to erroneous choice of the low and high amplitude limits resulting to precision errors up to 3, 5, and 15 percent of the local value of the measured mean, rms velocities and particle data rates, respectively. When the particle concentration was increased, the laser beam intensity attenuated due to multiple scattering from particles outside the control volume or, from particles passing through the edge of the control volume. Hence, in the case of 5 percent volumetric particle loading, combined cross-talk errors originated from erroneous identification of particle size and from attenuation of the maximum burst amplitude due to high particle loading. These errors were partially compensated through appropriate adjustment of the avalanche photo-diode voltage in order to keep always the same maximum burst amplitude for the glass particles and by simultaneous fine adjustment of the low and high amplitude limits.

The error in the measured mass flow rate of the particles was about 30 percent of the value expected from the theoretical volumetric loading of the particles in the flow. This value is similar to other estimates in the literature (Hardalupas et al., 1992 and Saffman, 1987).

Based on the above error estimates an uncertainty analysis has been performed. The 95 percent confidence uncertainty for the mean axial velocity has been calculated as ±3.6 percent, from $U = [B^2 + P^2]^{1/2}$ where B is the bias limit estimated from the above error analysis to be equal to 2 percent and P is the precision limit which has been set equal to 3 percent based on the measured mean values. The 95 percent confidence uncertainty for the local rms velocities was calculated as above equal to $\sigma_{\text{rms}} = \pm 5$, 4 percent by setting $B = 2$ and $P = 5$ percent. The values for B and P were based on the bias and precision errors reported above. The corresponding error for the turbulence kinetic energy, k, was calculated equal to $\sigma_k = \pm 11.4$ percent, considering that $\sigma_k = 1.5\ \sigma_{\text{rms}}{}^2$ assuming turbulence isotropy and setting $\sigma_{\text{rms}}{}^2 = \sqrt{2}\sigma_{\text{rms}}$.

5 Results

A small percentage of the experimental data that was contributed to the ASME databank is presented here. Detailed profiles of the axial, radial and azimuthal mean and fluctuating velocity components have been obtained for the single phase sudden expansion flow and for the two-phase flows (carrier fluid and particles) loaded with 3 and 5 percent particles per volume.

Vector plots and contours of constant axial mean velocity, based on extrapolated values of the measured mean axial and radial velocities of the carrier phase with 3 percent particle volumetric loading, are presented in Figs. 2 and 3 showing the general features of the flow and allowing the identification of four distinct flow regimes. The dividing streamline, the dashed line in Fig. 3 indicates the bending of the shear layer. Four

Table 1 Variation of the mass flow rate of the fluid with increasing particle loading

Particle volumetric concent. (%)	Fluid mass flow rate m_f (kg/s)	Fluid bulk velocity $U_{b,f}$ (m/s)	Maxim. inlet U_f/U_p (m/s)	measured x_R (mm)	% error in m_f
0	1.649	0.973	5.694/-	145	+4.9
1	1.808	1.066	5.543/ 5.556	133	-4.3
2	1.591	0.938	5.511/ 5.518	136	+8.3
3	1.825	1.077	5.543/ 5.473	137	-5.2
4	1.708	1.007	5.402/ 5.405	141	+1.6
5	1.832	1.080	5.586/ 5.616	141	-5.6
Mean value	1.736	1.023			

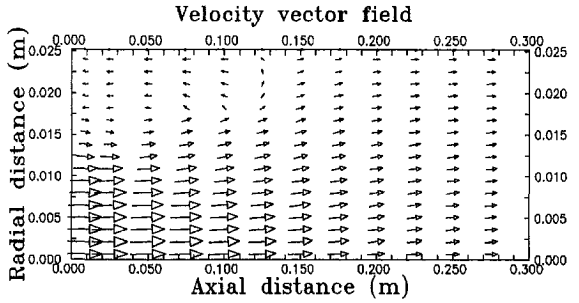

Fig. 2 Vector plots for the carrier phase (particle loading 3 percent per volume)

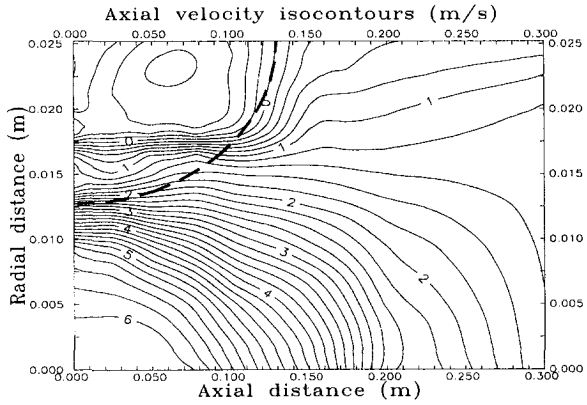

Fig. 3 Isotachs of the carrier phase axial mean velocity (3 percent volumetric particle loading)

flow regimes are schematically represented in Fig. 4: the main "core" flow developing around the axis of symmetry, the shear layer zone, a region of recirculating fluid developing at the leeward side of the sudden expansion and finally the near wall region.

Eddy length scales and time scales for each of the above flow regimes are tabulated in Table 2. Stokes numbers (St) are calculated as the ratio of the particle response time, $\tau_p = \rho_p d_p^2/18\mu_f$, to an appropriate turbulent time scale for each of the flow regimes, assuming that the local particle Reynolds number is less that unity. The Stokes numbers presented in Table 2 provide an indication of the expected particle response

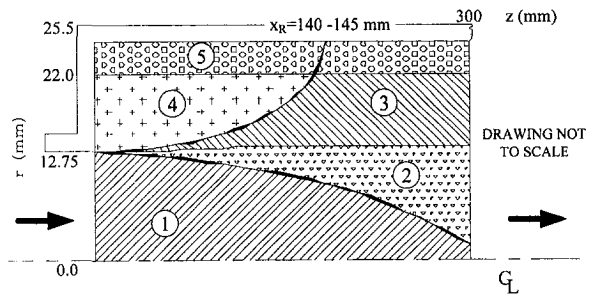

Fig. 4 Flow regimes and mechanisms that affect particle dispersion in the various flow regions.

Symbol	Flow Regime	Mechanism
1	"Core" region	-Particle inertia
2	Shear layer zone	-gravity, transverse shear lift, radial drag force
3	Shear layer zone	-Particle history
4	Recirculation region	-Particle history, gravity
5	Near-wall zone	-Particle-wall collisions, particle-to-particle collisions, shear lift force

Table 2 Characteristic scales and Stokes numbers

Flow region	% vol. particle loading	Eddy length scale (mm) Min	Eddy length scale (mm) Max	Turbulent time scale (ms) Min	Turbulent time scale (ms) Max	Stokes number (St) Max	Stokes number (St) Min	Coupling parameter L/(St+1) Min	Coupling parameter L/(St+1) Max
Main "core"	1	1.27	25.5	1.196	23.92	5.46	0.27	0.005	0.024
	5	"	"	1.180	23.6	5.49	0.27	0.023	0.118
Shear layer	1	-	6	-	28.28	0.23	-	0.024	-
	5	-	-	-	29.88	0.218	-	0.123	-
Recirculation	1	1.27	10.2	1.196	9.62	5.46	0.68	0.005	0.018
	5	"	"	1.180	9.44	5.49	0.69	0.023	0.089

to local turbulent fluctuations. When St $\ll$ 1 the motion of the particles is expected to follow the carrier fluid fluctuations. If St $\gg$ 1, particles do not respond to fluid turbulence and do not follow the fluid. A slip velocity is defined as $U_{slip} = |U_f| - |U_p|$. If a particle moves faster than the fluid by U_{slip}, the time of interaction with the large eddies and consequently particle fluctuations are reduced in the flow areas where the characteristic length scales of the flow are small compared to the flow dimensions, e.g., close to the centerline in the main core region and downstream the reattachment point. Mean slip velocities are expected to become significant in the main-core region and downstream the reattachment zone, where the flow recovers. Also, it can be anticipated that for the particles to enter the recirculation zone by crossing the shear layer, the local Stokes number should be St $<$ 1, which is confirmed by the values in Table 2.

The coupling parameter is defined as $L/(\mathrm{St} + 1)$ where L is the mass loading of the flow in kg/kg. The values tabulated in Table 2 indicate that two-way momentum coupling is not important for all the cases examined. According to Crowe (1981) a flow is characterized as dense if the ratio of the particle relaxation time to the time elapsing between successive collisions is greater than unity. As the particle mass loading increases, the probability of a particle colliding with another also increases, resulting in a reduction of the available mean free path between particles. For 5 percent volumetric loading, average values of the particle relaxation time and of the time elapsing between two successive collisions in the main "core" region of the flow have been calculated to be equal to 2 ms and 1.8 ms, respectively. Thus, the flow can be categorized as nearly dense for the higher volumetric loadings examined here. The consequences of particle-to-particle collisions are expected to be more obvious in the recirculation and near wall regions.

Radial distributions of the fluid and particle axial mean velocities and the corresponding fluid turbulence kinetic energy profiles are plotted in Fig. 5, measured at three axial locations downstream of the inlet plane with 3 percent particle volumetric loading. Local maxima of the fluid turbulence kinetic energy are measured in the shear layer zone. They disappear downstream the mean reattachment point, measured at $z/H = 10.75$.

The experimental data are compared in Fig. 5 with computations. The computational results are used here to help explain the experimental data. A detailed description of the computational approach can be found in Founti and Klipfel (1994, 1998) and it is beyond the scope of this paper. The computations were performed using a Eulerian/Lagrangian approach, considering drag, lift and gravity forces acting on a particle and accounting for particle-dispersion by turbulence and particle-wall collisions. The governing equations of the two phases were coupled by momentum interchange due to the relative velocity fluctuations between the continuous and disperse phases and a modified version of the k-ϵ model has been used to account for the radius of curvature of the flow. The effect of the Magnus lift force due to particle rotation, the influence of the virtual mass force and Basset history force have been neglected because their magnitudes were calculated to be much smaller than the magnitude of the shear lift force.

A typical expression of the transverse lift force acting on a particle due to shear is (Sommerfeld, 1989)

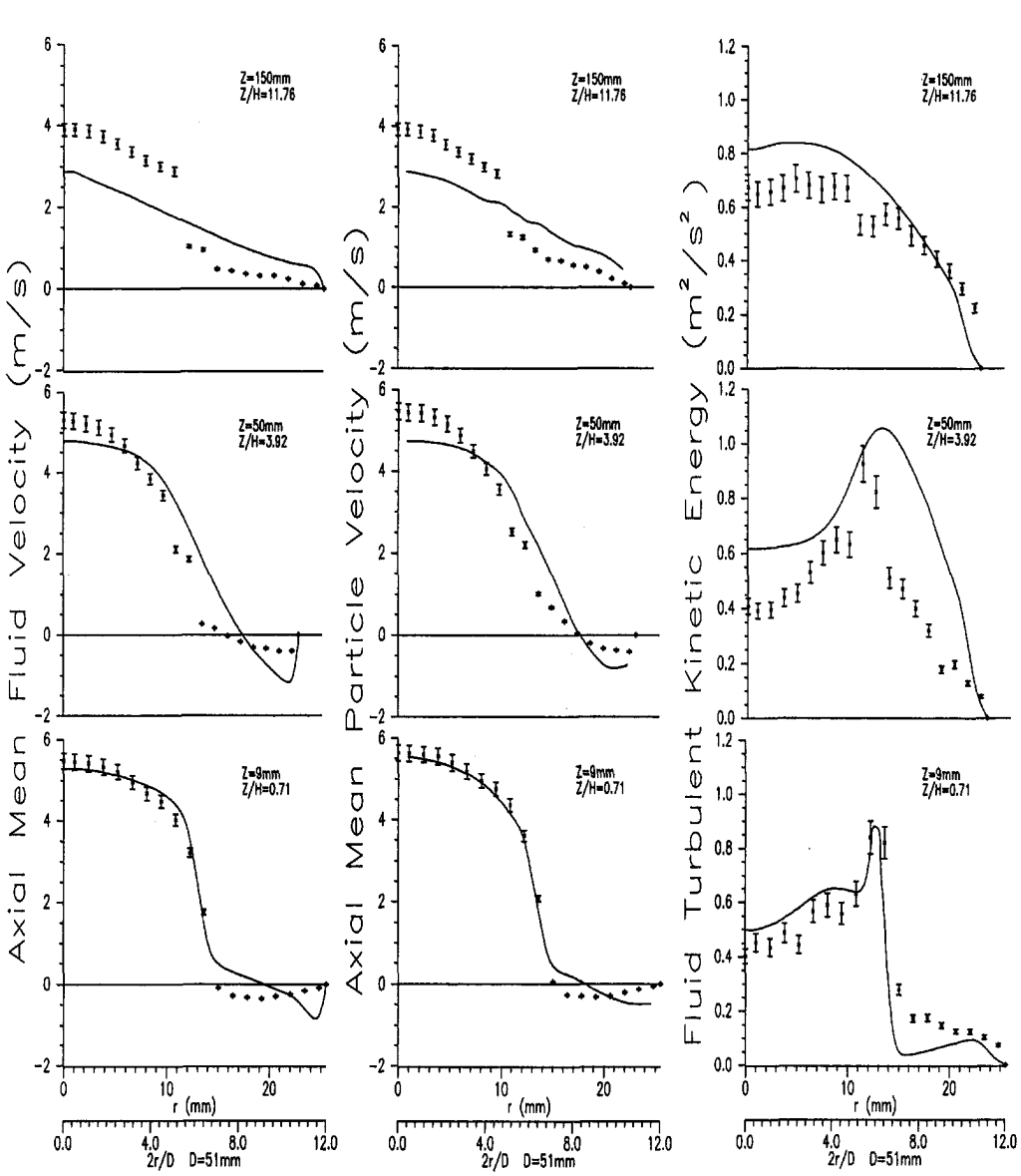

Fig. 5 Measured and computed fluid and particle axial mean velocities and corresponding fluid turbulence kinetic energy profiles in three axial locations downstream the inlet plane (3 percent particle volumetric loading, H = 12.75 mm)

$$F_{SL} = 3.0844 \frac{\sqrt{\rho\mu}}{\rho_p D_p} \sqrt{\left|\frac{du}{dr}\right|} (u - u_P)$$

where u, u_P are, respectively, the axial fluid and particle instantaneous velocities, ρ and μ are the fluid density and dynamic viscosity, ρ_P and D_P are the particle density and diameter.

The expression indicates that the transverse shear lift depends mainly on the slip velocity $(u - u_P)$ and on the shear gradient (du/dr). Hence, values of the local slip velocities can assist the understanding of the mechanisms that affect particle dispersion in the various flow regimes.

The significance of the magnitude of the transverse shear lift force is demonstrated in Fig. 6, where the ratio of calculated values of the shear lift to the transverse drag force are presented. Using the developed computational approach and results of Fig. 5, the transverse component of the drag force was calculated using:

$$F_{\text{DRAG}} = \tfrac{1}{2} \rho_f A_p C_D |\vec{V}_f - \vec{V}_p| (v_f - v_p) \quad \text{where}$$

$$|\vec{V}_f - \vec{V}_p| = \sqrt{(u_f - u_p)^2 + (v_f - v_p)^2 + (w_f - w_p)^2}$$

Figure 6 demonstrates that there exist regions in the flow where the shear lift force is larger than the drag force, for example in the vicinity of the flow reattachment zone and downstream the sudden expansion step in the spreading shear layer zone. In these regions gravity is significant because it influences the

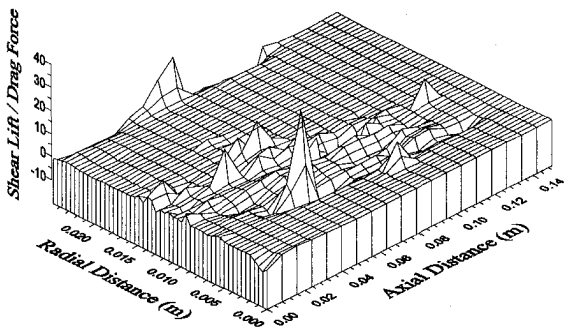

Fig. 6 Computed ratio of the shear lift to the transverse drag force

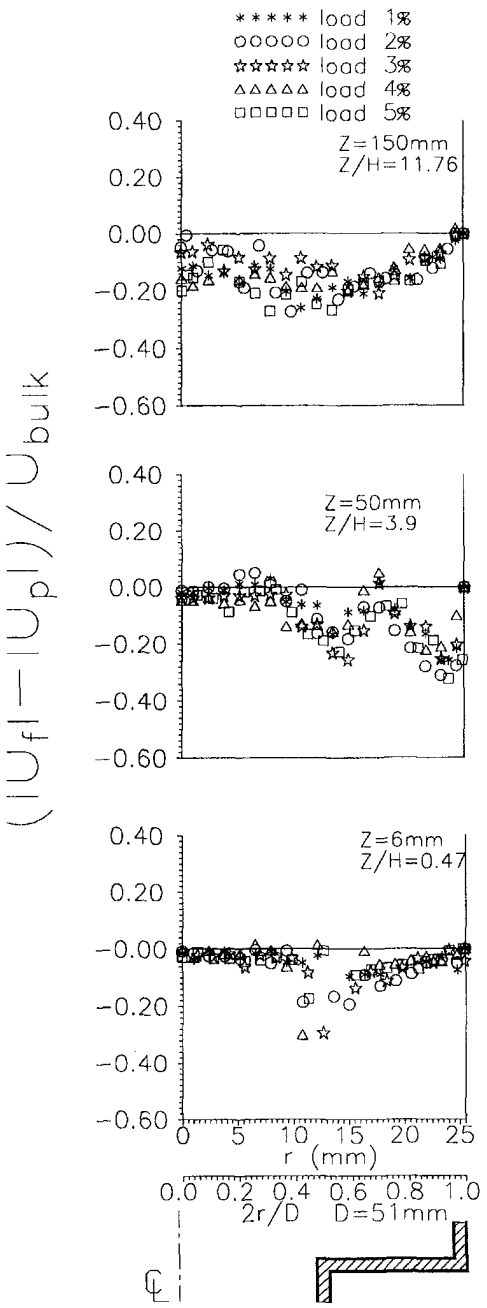

Fig. 7 Variation of axial particle mean slip velocities with particle loading

axial slip velocity which subsequently modifies the magnitude of the shear lift force.

Visual observations and calculations of particle trajectories (not shown here) indicated that particles injected close to the centerline have high axial velocities and they tend to remain in the main core flow region. Particles with relatively lower axial velocities manage to penetrate the shear layer. A number of particles enters the recirculation zone, remains within the vicinity of the wall and after the first collision slides along it. Some particles escape outside the recirculation zone and afterwards follow the main flow. When the particles reach the pipe walls, they collide several times and thereafter remain in the vicinity of the wall.

The radial variation of the axial mean slip velocities for the five volumetric loadings examined are plotted in Fig. 7. Similarly, Fig. 8 presents the radial variation of $(u_f - u_p)$, i.e., the difference between the local axial rms fluid and particle velocities. The difference between the local mean axial fluid velocity measured in the single phase and that in the two phase flow cases, denoted as $(U_f^{1f} - U_f^{2f})$, is shown in Fig. 9. The corresponding difference in the rms values is presented in Fig. 10. In each case, three radial profiles are presented, measured at $z/H = 0.47$ i.e., close to the sudden expansion inlet plane, at $z/H = 3.9$ namely approximately half way the length of the recirculation zone where maximum streamline curvature is expected and at $z/H = 11.76$ immediately downstream the mean reattachment point. The results of Figs. 7, 8, 9, and 10 show some scatter and make it difficult to decide what the effect of gradually increasing the loading is on the profiles at a given section. Nevertheless, they can show the general trends in the particle motion and particle response to turbulent fluctuations in the above named four flow regimes.

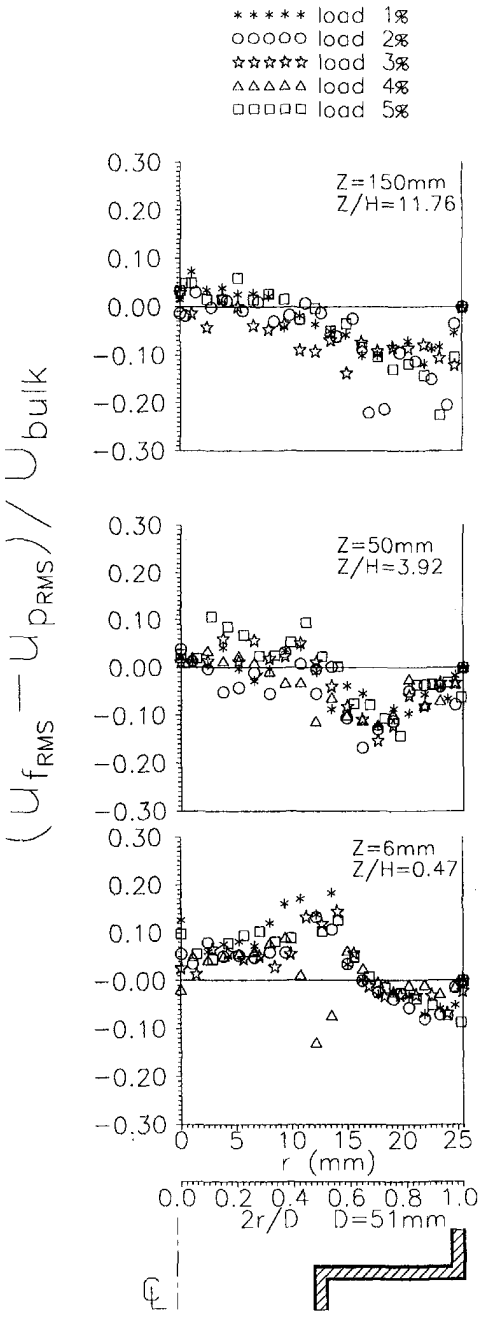

Fig. 8 Variation of particle rms velocities w.r. to the local fluid rms values for various particle loading

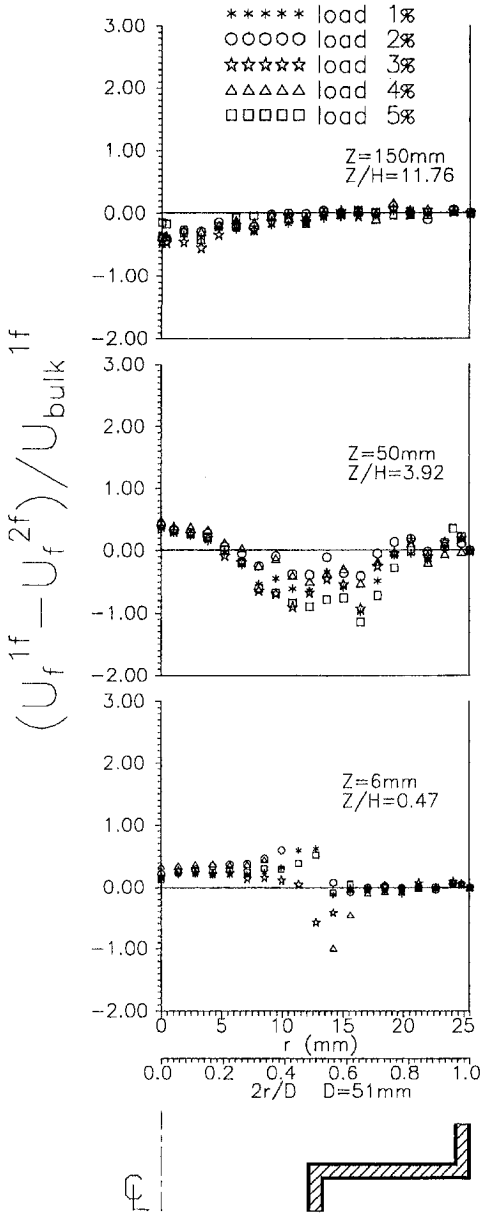

Fig. 9 Modification of the carrier phase mean axial velocities due to particle dispersion

Main "Core" Flow. For all the loadings examined, particles move faster than the carrier fluid in the main "core" region, Fig. 7, extending in the radial direction from the axis of symmetry up to approximately $2r/D = 4$. Local calculated Stokes numbers, Table 2, are larger than unity meaning that the particle response time is longer than the time of interaction of each particle with the large eddies. As a result, particle turbulence characteristics are expected to be different from the carrier fluid. This is confirmed by the $u_f - u_p$ profiles (Fig. 8) that demonstrate positive values everywhere in the main flow region. Particle turbulent fluctuations are lower than the carrier fluid fluctuations, suggesting that particle inertia locally governs the instantaneous particle motion. The locally measured carrier fluid axial mean and rms velocities are lower than in the single phase flow, Figs. 9 and 10, indicating that the presence of the particles affects the carrier fluid mean and turbulence characteristics.

Figure 7 shows that in the main core flow (e.g., at $z/H = 0.47$) the measured particle slip velocities remain nearly independent of the particle loading, suggesting that particle-to-particle collisions are not important in this area of the flow. Further downstream, at $z/H = 11.76$ particle slip velocities increase with increasing loading but still remain negative, i.e., particles always move faster than the fluid in this flow regime. This observation suggests that the particle motion downstream the mean reattachment plane can be locally affected by forces, other than inertia, acting on the particles. Such forces can be (Sommerfeld and Zivkovic, 1992), gravity, the transverse shear lift force, the Magnus force, the Basset force or the added mass force. Computations (Founti and Klipfel, 1994) have shown that the Magnus force, Basset history force, and virtual mass force are smaller in magnitude than the shear lift force.

Shear Layer Zone. Table 2 indicates that local Stokes number are less than unity, implying that the particle response time is less than the local turbulent time scale. Particles are able to follow the variations of fluid turbulence (and can enter the recirculation zone by crossing the shear layer. This is demonstrated by the nearly zero slip velocities (Figs. 7 and 8) measured at $2r/D = 0.4$ at $z/H = 3.9$.

Initially particles enter the flow with trajectories nearly parallel to the flow main axis, following the fluid vectors. When the

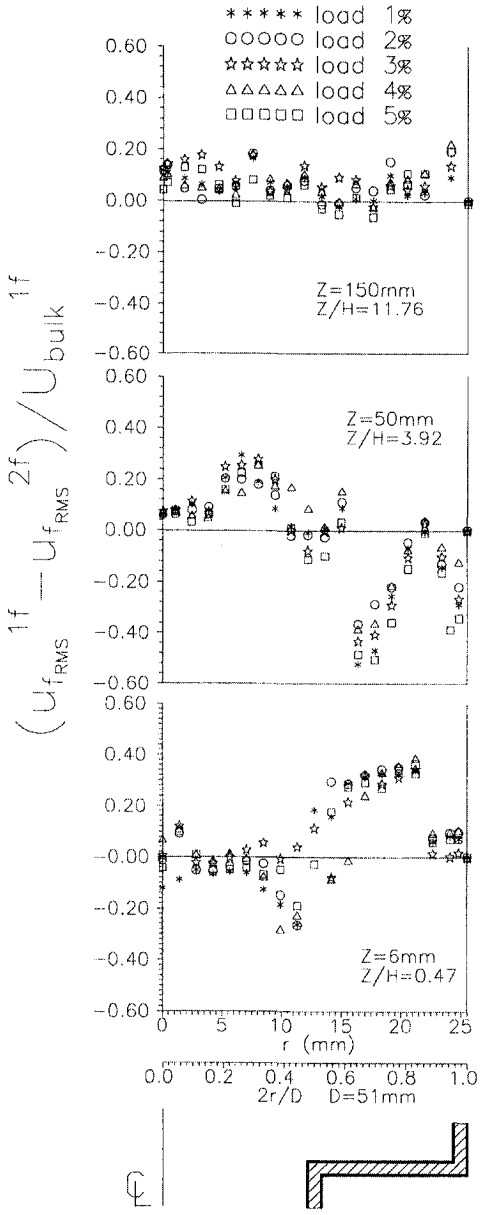

Fig. 10 Effects of particle dispersion on the fluctuating axial velocities of the carrier fluid

magnitude of the transverse shear lift becomes more significant than the drag force, Fig. 6, the particles are driven away from the main core flow toward the shear layer and as explained above they can enter the recirculation zone.

Within the shear layer region ($0.4 < 2r/D < 0.6$, Fig. 7 at $z/H = 0.47$ and $z/H = 3.9$) particle slip velocities become negative. Slip velocities increase with increasing particle loading, suggesting that particle-to-particle collisions are important.

In the same region the values of $(u_f - u_p)$ shown in Fig. 8 are highly positive, whereas the corresponding values of $(u_f^{1f} - u_f^{2f})$, shown in Fig. 10, are negative. Particles move faster but with fluctuations which are smaller than the local fluctuations of the carrier fluid, probably due to successive inter-particle collisions.

Recirculation Zone. Particles, due to their history, can enter the recirculation zone with higher local mean velocities than the carrier fluid (Fig. 7) depending on the size of the energy carrying eddy that drives the particle into the recirculation zone.

In the recirculation zone and in particular close to the pipe wall the carrier fluid axial rms values are relatively small. The history of the particles allows them to approach the wall from a neighboring eddy either with acceleration or with deceleration. Since the carrier fluid locally exhibits low rms values, the particles appear to move with high rms slip velocities, negative values in Fig. 8 ($0.6 < 2r/D < 1$, $z/H = 0.47$ and $z/H = 3.92$), thus transferring momentum to the carrier fluid and increasing its local fluctuations, as shown in Fig. 10. No consistent trends are observed when particle loading is increased.

Near-Wall Zone. Figure 11 presents measured values of U_{slip}, of $(u_f - u_p)$ and of the difference between the single phase (u_{fRMS}^{1f}) and two phase (u_{fRMS}^{2f}) fluid velocities measured

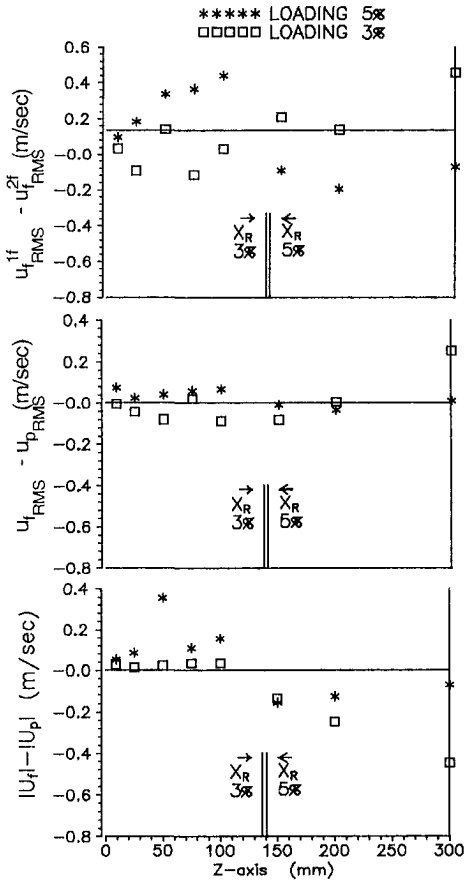

Fig. 11 Effects of particles in the mean and turbulent flow quantities, measured at 3 mm from the pipe wall and along the axial direction

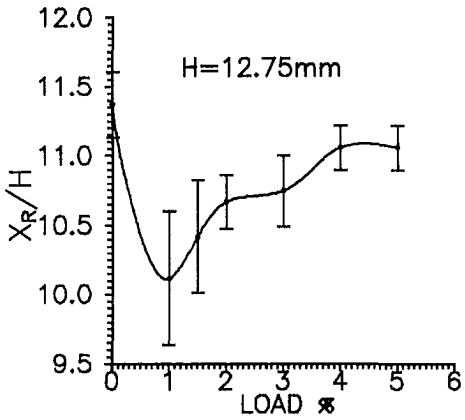

Fig. 12 Effect of particle loading on the measured reattachment lengths for the single and two-phase flows

at 3 mm from the pipe wall and along the z-axis. The general observation of positive local particle mean slip velocities upstream the mean reattachment point for the 3 and 5 percent particle loading is confirmed. The local reduction of the particle fluctuations with increasing loading implies a longer mean reattachment point shown in Fig. 12.

The mean reattachment lengths (Fig. 12) are shorter for the two phase flows than the corresponding single phase flow. Error bars indicate the possible experimental errors in the measurement of reattachment lengths due to positioning errors and due to the instability of the reattachment point. The shortest reattachment length was measured for the 1 percent particle loading. At this loading the flow is not yet affected by particle-to-particle collisions and the measured low value of the reattachment length can only be due to the increased values of the turbulent quantities in the two-phase flow case (Fig. 10) associated with the particle-wall collisions. Close to the pipe wall, particle-wall collisions can induce a spinning of the particles and thus give rise to significant values of the Magnus force. This may lead to the higher rms values measured for the particles in Fig. 8 very close to the pipe walls.

As the concentration was increased the reattachment length recovered, approaching at 5 percent loading the single phase flow value. Smaller eddies are generated with the higher particle loading. The mean free path between particle collisions is reduced inducing a reduction in the local particle fluctuations, as shown in Fig. 11. Particles tend to remain within the region of high particle concentration, due to the successive particle-to-particle collisions. The local reduction of the particle fluctuations with increasing loading implies a longer mean reattachment point, as shown in Fig. 12.

The above analysis allowed the grouping of the forces and mechanisms that affect the particle fluctuations in the four flow regimes of the examined two phase liquid-solid sudden expansion flow, as it is shown in Fig. 4.

5 Summary

The effects of increasing the particle loading have been examined with respect to the reattachment length and the characteristics of particle fluctuations. Measured reattachment lengths for a 1:2 sudden expansion two-phase flow with particle loadings varying between 1 and 5 percent per volume, were always shorter than the reattachment lengths measured in the corresponding single phase flows.

The experimental results demonstrated that particles move faster than the carrier fluid nearly everywhere in the flow, apart when crossing the shear layer zone in order to enter the recirculation zone. Particles exhibited lower axial rms values than the

carrier fluid in the main core zone, but dispersed faster than the carrier fluid inside the recirculation zone.

Particle dispersion is not affected by increases in the particle loading in the main "core" flow. Increasing loading reduces particle fluctuations in the near wall zone, where turbulent quantities tend to attain their single phase values.

Acknowledgments

The authors would like to acknowledge the financial support of the European Commission (Human Capital & Mobility Contract No. ERBCHRXCT930389).

Data Bank Contribution

The velocity measurements obtained with LDA in the investigated vertically flowing axisymmetric liquid-solid sudden expansion flow are contributed to the ASME databank, in the form of radial profiles of the measured axial, radial and azimuthal mean and rms velocities of diesel oil and particles with 3% volumetric loading. The geometrical characteristics of the flow and the physical properties of the fluid and particles are also provided.

References

Achimastos, Th. J., Dimopoulos, D. A., Klipfel, A. S., and Founti, M. A., 1993, "Investigations on Particle Dispersion in an Axisymmetric Vertical Two-Phase Sudden Expansion Flow," *Proceedings of the 5th International Symposium on Refined Flow Modeling and Turbulence Measurements,* Press de l'Ecole National des Ponts et Chaussées, Paris, pp. 465–475.

Berlemont, A., Benoist, F., and Gouesbet, G., 1994, "Influence of Collisions on Particle Fluctuating Velocities Using a Lagrangian Approach," ASME, *Numerical Methods in Multiphase Flows,* Fluids Engineering Division Summer Meeting, Nevada, FED-Vol. 185, pp. 23–28.

Crowe, C. T., 1981, "On The Relative Importance Of Particle-Particle Collision In Gas-Particle Flows," *Proceedings of Conference on Gas Borne Particles,* Institute of Mechanical Engineers, C 78/81, pp. 135–137.

Fessler, J., and Eaton, K., 1994, "Particle-Turbulence Interaction In A Backward-Facing Step Flow," Report No. MD-70, Thermosciences Division, Department of Mechanical Engineering, Stanford University, Stanford, CA.

Fleckhaus, D., Hishida, K., and Maeda, M., 1987, "Effect of Laden Solid Particles on the Turbulent Flow Structure of a Round Free Jet," *Experiments in Fluids,* Vol. 5, pp. 323–333.

Founti, M. A., and Papaioannides, G., 1992, "Influence of Expansion Ratio on the Size of Recirculation Zone in Two-Phase Sudden Expansion Flows," *Proceedings 6th Intern. Symposium on Applications of Laser Techniques to Fluid Mechanics,* Lisbon, Portugal, pp. 33.1.1–33.1.6.

Founti, M., and Klipfel, A., 1994, "The Shear Lift Effects on the Particle Motion in Two-Phase Sudden Expansion Flows," ASME, *Numerical Methods in Multiphase Flows,* Fluids Engineering Division Summer Meeting, Nevada, FED-Vol. 185, pp. 81–92.

Founti, M., and Klipfel, A., 1998, "Experimental and Computational Investigations of Nearly Dense Two-Phase Sudden Expansion Flows," *Experimental Thermal and Fluid Science,* Vol. 17, Issue 1–2, pp. 27–36.

Hardalupas, Y., Taylor, A. M. K. P., and Whitelaw, J. H., 1992, "Particle Dispersion in a Vertical Round Sudden Expansion Flow," *Phil. Transactions of the Royal Society,* London A, Vol. 341, pp. 411–442.

Hishida, K., Nakano, H., and Maeda, M., 1989, "Turbulent Flow Characteristics of Liquid-Solid Particle Confined Jet," International Conference on Mechanics of Two-Phase Flow, National Taiwan Univ., Taiwan, pp. 209–214.

Kaftori, D., Hetsroni G., and Banerjee, S., 1995, "The Effects of Particles on the Structure of Wall Turbulence," *Proceedings of the 2nd International Conference on Multiphase Flows,* Kyoto, 2, PT1, pp. 11–16.

Kenning, V., and Crowe, C. T., 1994, "The Effect of Solids Concentration on Self-Induced Turbulence, in Liquid-Solid Flows," ASME Fluids Engineering Division, USA, FED-Vol. 189, pp. 71–74.

Nouri, J. M., Whitelaw, J. H., and Yianneskis, M., 1987, "Particle Motion and Turbulence in Dense Two-Phase Flows," *International Journal of Multiphase flow,* Vol. 13, No. 6, pp. 729–739.

Qiu, H.-H., and Sommerfeld, M., 1992, "A Reliable Method for Determining the Measurement Volume Size and Particle Mass Fluxes Using Phase-Doppler Anemometry," *Experiments in Fluids,* Vol. 13, pp. 393–404.

Saffman, M., 1987, "Automatic Calibration of LDA Measurement Volume Size," *Applied Optics,* Vol. 26, pp. 2592–2597.

Sommerfeld, M., 1989, "Numerical Simulation of the Particle Motion in Turbulent Flow," 2nd. International Lecture Course on Multiphase Flow, Tokyo, Japan.

Sommerfeld, M., Ando, A., and Wennerberg, D., 1992, "Swirling, Particle-Laden Flows Through a Pipe Expansion," ASME JOURNAL OF FLUIDS ENGINEERING, Vol. 114, pp. 648–656.

Sommerfeld, M. and Qiu, H.-H., 1990, "Detailed Measurements in a Swirling Particulate Two-Phase Flow by a Phase-Doppler Anemometer," *Proceedings of 5th Workshop on Two Phase Flow Predictions,* pp. 15–32, Erlangen.

Sommerfeld, M., and Zivkovic, G., 1992, "Recent Advances in the Numerical Simulation of Pneumatic Conveying Through Pipe Systems," 1st European Computational Fluid Dynamics Conference, Brussels.

Tsuji, Y., Morikawa, Y., Tanaka, T., Karimine, K., and Nishida, S., 1988, "Measurements of an Axisymmetric Jet Laden with Coarse Particles," *International Journal of Multiphase Flow,* Vol. 14, pp. 565–574.

Yanta, W. J., 1973, "Turbulence Measurements with a Laser Doppler Velocimeter," Report NOLTR-73-94, NOL, White Oak, Silver Spring, MD.

Mechanics of Immersed Particle Collisions

Roberto Zenit
Postdoctoral Scholar.

Melany L. Hunt
Associate Professor.

Division of Engineering
and Applied Sciences,
California Institute of Technology,
Pasadena CA 91125

The present work investigates the mechanics of particle collisions submerged in a liquid using a simple pendulum experiment. Particle trajectories for different particles in water are measured using a high-speed digital camera and the magnitude of the collision is recorded using a high-frequency-response pressure transducer at the colliding surface. The particle deceleration occurs at distances less than half a particle diameter from the wall. The measured collision impulse increases with impact velocity and particle mass. Comparisons are drawn between the measured pressures and the predictions of basic impact mechanics assuming a perfectly elastic collision. A control-volume model is proposed that accounts for the fluid inertia and viscosity. When a particle approaches a planar surface or another particle, the fluid is squeezed prior to contact, reducing the initial kinetic energy and decelerating the particle. The pressure profile is integrated over the surface of the particle to obtain a force that is a function of the initial particle Reynolds number, Re_o, and the ratio of the densities of the particle and fluid phases, ρ_p/ρ_f. The model predicts a critical Stokes number at which the particle reaches the wall with zero velocity. Comparisons between the proposed model and the experimental measurements show qualitative agreement.

1 Introduction

Interest in particulate two-phase flows arises from industrial applications and many natural processes such as fluidized beds, pneumatic transport, filtration processes, erosion, dune formation, and land slides. In many cases, the collisions of particles against themselves and against walls may affect the properties of the mixture. Efforts have been made to describe the fundamental mechanics of particle collisions.

Dry collisions have been studied since the beginning of the century (Johnson, 1985) and the rebound and energy losses can be modeled for most simple cases with few exceptions. The mechanics of liquid immersed collisions remain a subject of current research. When a particle approaches a rigid planar surface, or another particle, the fluid film must be expelled for contact, resulting in a pressure increase. In this process some kinetic energy is dissipated or transferred to the fluid. Depending on the magnitude of the dissipation the contact may or may not result in a rebound of the particle.

1.1 The Impact Paradox. As a particle approaches a wall, the gap between the surfaces and the Reynolds number based on the gap decrease. Using the creeping flow approximation, Happel and Brenner (1965) calculated the pressure profile around the particle approaching a wall. The net force exerted by the fluid on the particle grows infinitely as the gap tends to zero. Therefore, direct contact never occurs.

Davis et al. (1985) modified the creeping flow model by allowing elastic deformation of the approaching surfaces due to a hydrodynamic pressure built up. Some of the kinetic energy is stored as elastic deformation. Hence, rebound is possible, but physical contact between the two surfaces does not occur.

If the flow around the particle approaching a wall is inviscid and irrotational, the hydrodynamic force on the sphere can be calculated in the form of added masses and the flow can be resolved in a non-explicit form in terms of an infinite series of doublets (Milne-Thomson, 1950). Landweber and Shahshashan (1992) obtained a simplification that allows the accurate calculation of the hydrodynamic forces when the two surfaces are very close to each other. As in the creeping flow case, the hydrodynamic force grows unbounded when the distance between the two surfaces tends to zero. This effect is due to the discontinuity of the velocities between the moving particle and the stationary plane.

The question remains. What happens when the distance between the two surfaces tends to zero? If the velocity of approach is small, the viscous effects would dominate, and most of the kinetic energy would be dissipated in viscous friction. But in the case when the velocity of approach is large, it has been experimentally observed that particles come into "apparent contact" and rebound freely (McLaughlin, 1968). In the case of particles colliding immersed in a gas, the phenomena have been explored assuming that the continuum mechanics assumptions are no longer valid when the gap distance is comparable with the mean free path of the gas molecules (Sundararajakumar and Koch, 1996; Hocking, 1973). In the case of a liquid, the mean free path is nearly zero and the continuum assumptions are expected to hold up to distances of tens of molecular diameters. Smart and Leighton (1989) argued that contact could take place through the surface roughnesses, viewed as sharp edges in the microscopic scale. Some studies have suggested that under the compression levels generated during a collision, the liquid in the gap solidifies for a brief time period (Gee et al., 1990), and therefore the collision pressure is transmitted between surfaces without physical contact.

Studies with detailed experimental measurements have been rare. Using a thin layer of fluid, Lundberg and Shen (1992) performed measurements of the collisional coefficient of restitution for steel and nylon particles and obtained correlations for the coefficient of restitution as a function of the kinematic viscosity. Their results showed decreasing values of the coefficient of restitution for increasing viscosities, and also concluded that the impact velocity had a negligible effect on the measured coefficient of restitution. Barnocky and Davis (1988) conducted experiments to find the conditions under which a particle would rebound, as opposed to stick, when dropped on a surface with a thin layer of fluid. McLaughlin (1968) dropped steel particles under gravity through a viscous fluid onto a solid surface. Position-time curves were obtained using high-speed photography. For higher impact velocities the viscous effects became smaller. A critical Reynolds number was found at which the particle did not rebound after contact.

Contributed by the Fluids Engineering Division for publication in the JOURNAL OF FLUIDS ENGINEERING. Manuscript received by the Fluids Engineering Division January 21, 1998; revised manuscript received October 6, 1998. Associate Technical Editor: J. K. Eaton.

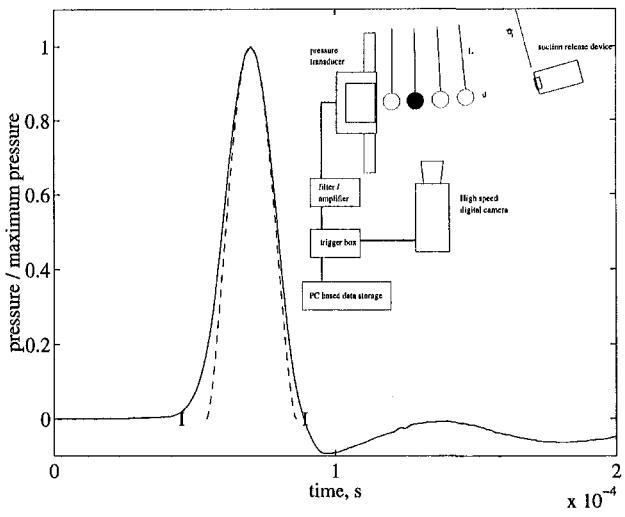

Fig. 1 Experimental setup and typical pressure pulse resulting from a collision of a 6 mm glass particle in water. Maximum pressure = 17.1 × 10^{-4} Pa. The dashed line represents the time-pressure trace produced by a perfectly elastic collision.

The present article provides documentation for particle-wall collisions when the effect of the density and the viscosity of the fluid are not negligible. Using a pendulum, spheres of various diameters and densities submerged in water impact a wall. The trajectory of a particle before and after impact and the strength of the impact are measured. Additionally, a model is proposed to account for the effects of the fluid as the particle approaches a wall prior to collision. The results provide information on individual particle-wall (or particle-particle) collisions needed in theoretical models and computer simulations of particulate liquid-solid flows.

2 Experimental Setup

In Fig. 1, a single pendulum is shown using a fine string attached to a particle that starts from rest at some initial angle, θ_i. On the wall, at $\theta = 0$, a high-frequency response pressure transducer was flush mounted. A suction system positioned the particle and released it from rest without rotation. Once released, the particle accelerated towards the pressure transducer. The motion of the particle was recorded using high speed digital camera, able to record images up to 500 frames per second. When the collision was sensed by the pressure transducer, the trigger system activated the digital camera, storing images before and after the impact. The images were digitally processed to calculate the centroid of the particle for different times. The velocity was calculated from the displacement of the particle centroid between consecutive images. A typical pressure signal is presented in Fig. 1 consisting of a positive spike, followed by a decaying oscillation, which results from the dynamics of the membrane. The liquid used for all the experiments was deionized water.

The manufacturer's calibration of the high-frequency response pressure transducer was corroborated by comparing the results of dry impacts with Hertzian theory predictions (Zenit, 1997).

The uncertainty in the measurement of displacements and velocities was estimated to be ±3.5 percent, arising from the imprecision of the pixel resolution of the imaging system. The pressure and impulse measurements have an uncertainty of ±2 percent, resulting from the performance of the pressure transducer.

2.1 Immersed Pendulum Equation. To verify the experimental technique, measurements were taken for a swinging immersed pendulum with no colliding wall. A particle was released from an initial angle and photographed for part of one oscillation cycle. The measurements were then compared with the prediction of an immersed pendulum. The model used the unsteady drag model proposed by Mei (1994), valid for a sphere at finite Reynolds numbers. The equation of motion of an immersed pendulum in a stagnant fluid is

$$\frac{4}{3}\pi a^3\frac{\partial^2 s}{\partial t^2} = \frac{4}{3}\pi a^3(\rho_p - \rho_f)g\sin(s/L) - \frac{2}{3}\rho_f\pi a^3\frac{\partial^2 s}{\partial t^2} + 6\pi\mu a\phi(t)\frac{\partial s}{\partial t} - 6\pi\mu a^2\int_{-\infty}^{t} H(t-\tau)\frac{\partial}{\partial\tau}\left(\frac{\partial s}{\partial t}\right)d\tau \quad (1)$$

where s is the arc-length position, L is the length of the pendulum string, ρ_p and ρ_f are the densities of the solid particle and the fluid, respectively, $\partial s/\partial t$ is the velocity of the particle, $\phi(t)$ is a drag force function, $H(t)$ is the history force kernel and a is the radius of the particle. This equation was solved numerically. Figure 2 shows a comparison of the predicted phase plot against the experimental results obtained for a glass particle of 6 mm diameter with a pendulum length of 97 mm. Several experimental runs were taken under the same nominal conditions. The experimental measurements are within five percent of the theory. Errors arise, in part, from the determination of the centroid of a particle with a discrete number of pixels. No attempt was made to account for the drag force exerted on the string.

2.2 Measurement of the Collision Impulse. The strength of collision was quantified by its collision impulse. The collision impulse is defined as

$$I = \int_0^{\tau} P(t)dt \quad (2)$$

where $P(t)$ is the pressure signal produced during an individual impact, and τ is the duration of the main pressure pulse. The pressure reverberations were ignored. Assuming a perfect elastic impact, the pressure impulse resulting from a collision based on simple mechanics predictions, I_{MP}, is

$$I_{MP} = 2u_i m_p/A_{tr} \quad (3)$$

where u_i is the impact velocity, m_p is the particle mass and A_{tr}

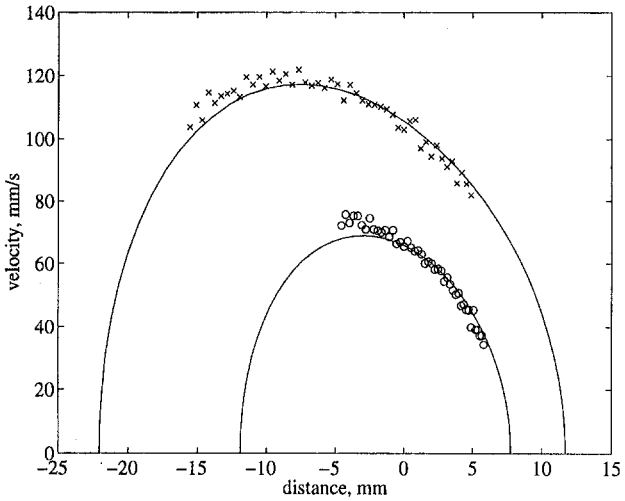

Fig. 2 Phase plot of an immersed pendulum. Model predicted by Mei (1994) (solid lines). Experiments: θ_i = 13° (×); θ_i = 7° (○). (Uncertainty in velocity ±3.5%, in distance ±3.5%)

Table 1 Properties of particles used in experiments

Material	d_p, mm	ρ_p/ρ_w	u_t, mm/s	Re_t
Glass ×	3.00	2.54	318	954
Glass □	4.00	2.54	368	1338
Glass ○	6.00	2.54	474	2583
Steel ◇	4.50	7.78	896	3665
Nylon △	6.35	1.14	136	785

is the active area of the pressure transducer. The properties of the particles used in the experiments are presented in Table 1.

The experimental measurements of the impulse showed scatter, which appear to result from the nature of the experiment and not from the imprecision of the measuring techniques. Other researchers have found similar behavior when studying contact or collision of particles (Campbell, 1997), attributed to the modification of the surface properties resulting from contact itself. To assess the variance of the measurements, histograms were constructed. For a typical set of data, the standard deviation was of 6 percent. The maximum value measured was 11% higher than the mean, and the minimum was 23 percent lower than the mean.

3 Results

3.1 Approach and Rebound. Figure 3 shows a typical position-time and velocity-time plot of the pendulum motion during the approach and rebound of a particle. The case shown corresponds to the motion of a 6 mm glass particle with a pendulum length of 107 mm, and an initial release angle of 12 deg. The pendulum equation (dashed lines) predicted an impact velocity of 117 mm/s. The experimental measurements agree with the pendulum equation prediction for distances at about half a diameter away from the wall. Close to the wall a significant deceleration is observed. Note that after the particle has rebounded from the wall, its velocity continues to increase. In a dry collision the maximum velocity of rebound occurs at the moment when the particle loses contact with the wall. In the case of an immersed collision, the fluid appears to accelerate the particle after it has lost contact with the wall. As the particle moves further from the wall, its velocity decreases. A similar behavior was found for all cases. The distance at which the wall begins to affect the motion of the particle was observed to increase for smaller velocities of approach and for smaller and lighter particles. The measurement of the coefficient of restitution of immersed collisions can be found in Zenit and Hunt (1998).

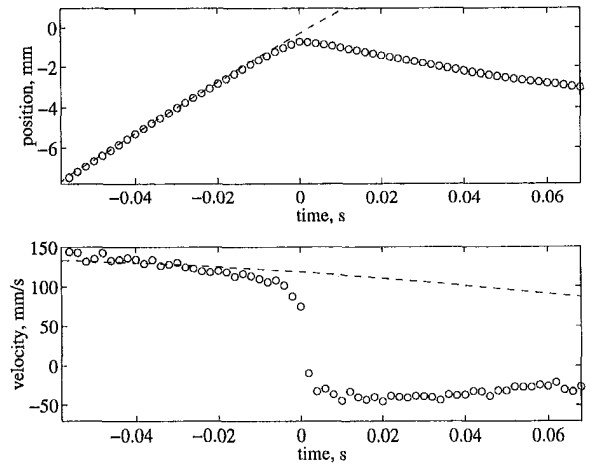

Fig. 3 Position-time and velocity-time plots for a 6 mm glass particle, immersed in water. Comparison between pendulum equation predictions (dashed lines) and experiments (○). $\theta_i \approx 12°$. Predicted impact velocity 117 mm/s. (Uncertainty in velocity ±3.5%, in distance ±3.5%)

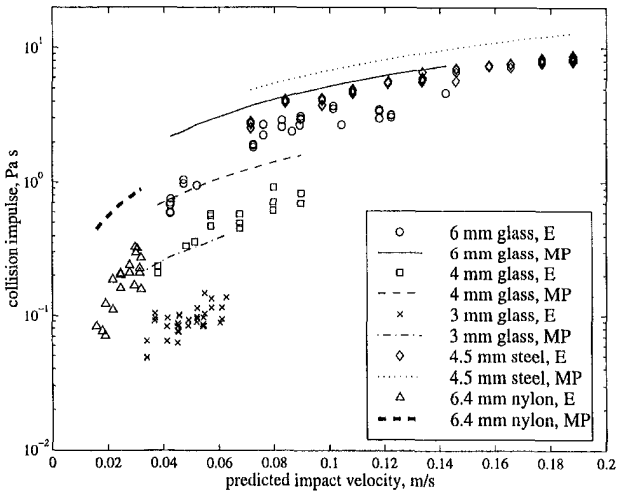

Fig. 4 Measured collision impulse as a function of impact velocity (E, experiment). The lines represent the predictions from collision mechanics (MP, mechanics prediction). (Uncertainty in predicted impact velocity ±4%, in collision impulse ±2%)

3.2 Collision Impulse. Figure 1 compares the pressure pulse generated by the typical collision of a 6 mm glass particle against the prediction from Hertzian theory. The theory of Hertz is appropriate for dry collisions and requires the velocity of the impacting particle. To compare the time-pressure variation an impact velocity is chosen that predicts the same maximum pressure. Tabulated elastic properties of the glass particle are used ($E_{\mathrm{glass}} = 70$ GPa, $\nu_{\mathrm{glass}} = 0.22$). For this case the impact velocity predicted by the pendulum equation is 72 mm/s, and the value used in the Hertzian comparison is 58 mm/s. The Hertzian calculation represents the maximum pressure for an ideal collision in which the fluid has no effect and the surfaces are smooth and perfectly elastic; therefore, it serves as a base to assess the total effect of the fluid during the collision.

While the ideal prediction is symmetric with respect to the point of maximum pressure, the experimental pressure pulse is wider and slightly asymmetric. This asymmetry may be the result from the pressure build up due to the presence of the fluid. Before the solid surfaces contact a considerable hydrodynamic pressure is exerted on the surface of the transducer. Note that, since the internal structure of the pressure transducer is unknown, a correction for the Hertzian theory to account for nonidealities of the colliding surface is not possible.

3.3 Impact Velocities and Collision Impulses. Figure 4 shows the measured collision impulse as a function of the predicted impact velocity for three different glass particle diameters, 4.5 mm steel particles and 6.35 mm nylon particles in water. The velocity of impact, u_i, is assumed to be that predicted by the pendulum equation (Eq. (2)). This velocity is a function of the initial position of the particle and serves as measure of the initial potential energy of the particle. Hence, it does not account for the effect of the wall. The predictions from Eq. (3) are also shown in the plots.

The experimental measurements follow the prediction from Eq. (3) and indicate an increase in collision impulse with particle mass and velocity of impact. As expected, the measured collision impulse is smaller than that predicted by the theory for the same impact velocity. The difference between the ideal prediction and the measurements is the total effect of the interstitial fluid.

Following Eq. (3), the collision impulse results are nondimensionalized using $\hat{I} = I/I_{MP}$, where I is the measured colli-

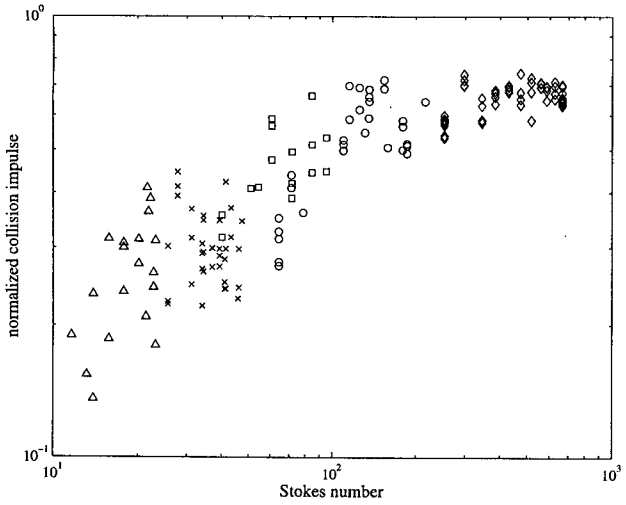

Fig. 5 Normalized collision impulses as a function of the Stokes number. For symbol identification see Table 1. (Uncertainty in normalized collision impulse ±8.5%, in Stokes number ±4.5%)

sion impulse and I_{MP} is the impulse based on the predicted impact velocity. The normalized results are shown in Fig. 5 in terms of the Stokes number. The Stokes number is defined as $\mathrm{St} = (\mathrm{Re}/9)(\rho_p/\rho_f)$, where Re is the Reynolds number, defined as $\mathrm{Re} = (u_i d_p \rho_f)/\mu_f$. The data forms a single band of values. For small Stokes numbers the normalized impulse is small. Clearly, the deviation from the mechanics prediction increases for decreasing values of the Stokes number indicating increasing importance of the viscous effects.

The normalized impulse measurements can be interpreted as the experimental impact velocity (as implied from the measured impulse) divided by the theoretical impact velocity. Clearly, the deviation from $\hat{I} = 1$ is a measure of the retardation caused by the fluid between the sphere and the wall. Therefore, $\hat{I}$ can be used to calculate a reduced impact velocity

$$u_{i\,(\mathrm{red})} = u_i \hat{I}$$

and to calculate a reduced Stokes number, $\mathrm{St}_{\mathrm{red}} = \mathrm{St}(u_{i\,(\mathrm{red})}/u_i)$. Figure 6 shows the reduced Stokes number (based on the reduced value of the impact velocity) as a function of the Stokes

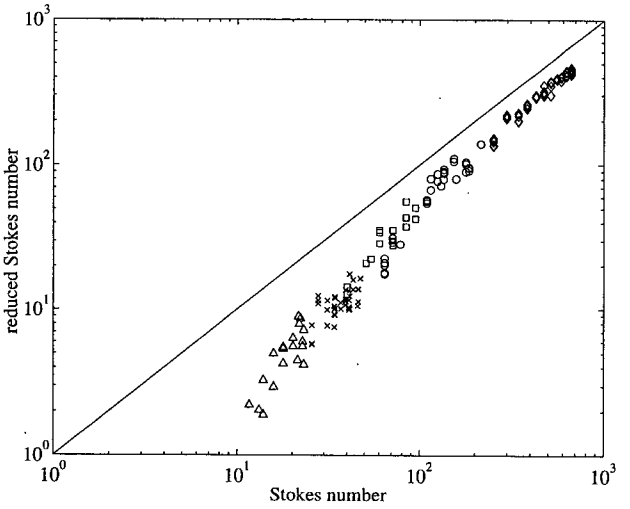

Fig. 6 Reduced Stokes number as a function of Stokes number. For symbol identification see Table 1. (Uncertainty in reduced Stokes number ±13%, in Stokes number ±4.5%)

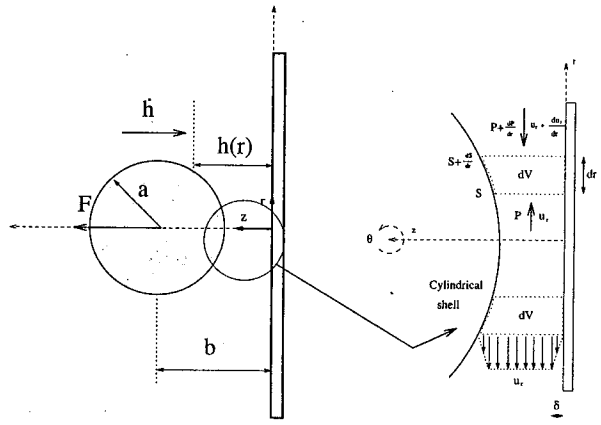

Fig. 7 Schematic of the problem and coordinate system. Control volume: momentum and mass fluxes.

number. If the fluid had a negligible effect on the collision of the sphere then $\mathrm{St}_{\mathrm{red}}$ would be equal to St.

4 Modeling

To predict the effect of the fluid as a spherical particle approaches a flat solid wall, an approximate model based on a control volume is proposed. Consider a spherical particle, as shown in Fig. 7, moving towards a flat wall, which center is positioned at $b(t)$ at some instant t in time, immersed in a viscous and incompressible fluid; $h(r)$ is the distance from the surface of the sphere to the wall. The velocity and acceleration of the sphere moving towards a solid boundary are therefore $\dot{b}$ and $\ddot{b}$ respectively.

The motion of the particle in the z-direction will impose a radial velocity u_r to the fluid in the gap. For contact, the fluid in between the particle and the wall has to be displaced. Therefore, some kinetic energy of the particle will be transferred to the fluid, and some will be dissipated in viscous friction. The control volume, as shown in the right of Fig. 7, is a cylindrical shell of infinitesimal thickness dr (shaded area). Assuming that the flow in the gap is axisymmetric ($\partial/\partial\theta = 0$) and purely radial ($\vec{u} = (u_r, 0, 0)$), and that the pressure field is uniform with respect to the z direction, the mass and momentum balances for the control volume can be obtained. The assumption that the fluid motion is unidirectional is rigorously valid only in the region near $r = 0$; since most of the pressure build up is expected to occur in that region, the assumption is valid as a first approximation.

The mass conservation analysis leads to

$$u_r h = -\frac{r}{2}\dot{h} \tag{4}$$

where u_r is the mean radial velocity of the fluid in the gap, $h(r)$ is particle profile and $\dot{h}$ is the velocity at which the particle is moving. The equation obtained from the momentum balance is

$$r\frac{\partial}{\partial t}(u_r h) + \frac{\partial}{\partial r}(u_r^2 h r) = -\frac{1}{\rho_f}\frac{\partial}{\partial r}(Phr) - \frac{2r}{\rho_f}\tau_w \tag{5}$$

where $P(r)$ is the pressure in the fluid in the gap and τ_w is the wall shear stress.

Combining Eqs. (4) and (5) and integrating over r an explicit expression for the pressure $P(r)$ in the gap is obtained

$$P(r) = \frac{\rho_f}{6}\frac{r^2\ddot{h}}{h} - \frac{\rho_f}{4}\left(\frac{r\dot{h}}{h}\right)^2 - \frac{2}{hr}\int_0^r r'\tau_w dr' \tag{6}$$

To account for the viscous shear stress a simple model is

used, which assumes the effects of viscosity remain in a thin layer of fluid near the surfaces

$$\tau_w = \mu \left.\frac{du}{dz}\right|_w \approx \mu \frac{u_r}{\delta} \tag{7}$$

where δ represents the thickness of the viscous fluid layer. Note that this formulation differs from that suggested by lubrication theory.

The total force exerted by the fluid on the particle is obtained by integrating Eq. (6) over the projected area of the particle, assuming that the pressure outside the gap is a constant P_o (zero for convenience),

$$F(t) = \int_A P(r)dA = 2\pi \int_0^a P(r) r dr$$

$$= 2\pi \frac{\rho_f \ddot{h}}{6} \int_0^a \frac{r'^3}{h} dr' - 2\pi \frac{\rho_f \dot{h}^2}{4} \int_0^a \frac{r'^3}{h^2} dr'$$

$$-2\pi \frac{\mu \dot{h}}{\delta} \int_0^a \frac{1}{h} \left[\int_0^r \frac{r''^2}{h} dr'' \right] dr' \tag{8}$$

To calculate the force, an expression for the for the the particle profile, $h(r)$, is needed. For a spherical particle the exact profile is

$$h(r) = h_0 + a - \sqrt{a^2 - r^2} \tag{9}$$

To make the integrals simpler, an approximation for the profile is used

$$h(r) = h_0 + \frac{r^2}{a} + \ldots = (b - a) + \frac{r^2}{a} + \ldots \tag{10}$$

which makes the expressions tractable, yet preserves the geometric characteristics of the curved surface.

For convenience the expressions are non-dimensionalized, $\hat{r} = r/a$, $\hat{h} = h/a$, $\hat{t} = t/t_c$, with t_c a characteristic time, to be specified. Using these and integrating using the simplified profile (Eq. 10), the expression obtained for the nondimensional force is

$$\hat{F}(\hat{t}) = A(\hat{b})\ddot{\hat{h}} - B(\hat{b})\dot{\hat{h}}^2 - C(\hat{b}) \frac{\mu_f t_c}{\rho_f a^2} \frac{a}{\delta} \dot{\hat{h}} \tag{11}$$

where $\hat{F}(\hat{t})$ is normalized by $\rho_f (a/t_c)^2 a^2$ and $A(\hat{b})$, $B(\hat{b})$ and $C(\hat{b})$ are functions of $\hat{b}$ defined as

$$A(\hat{b}) = \frac{\pi}{6}\left(1 - (\hat{b} - 1)\log\left(\frac{\hat{b}}{\hat{b} - 1}\right)\right)$$

$$B(\hat{b}) = \frac{\pi}{4}\left(\frac{\hat{b} - 1}{\hat{b}} - 1 + \log\left(\frac{\hat{b}}{\hat{b} - 1}\right)\right)$$

$$C(\hat{b}) = \pi\left(\log\left(\frac{\hat{b}}{\hat{b} - 1}\right) - \tan^{-1}\left(\frac{1}{\sqrt{\hat{b} - 1}}\right)^2\right)$$

where $\hat{b} = b/a$.

4.1 Particle Equation of Motion. Once an expression for the force on the particle has been obtained, it can be incorporated in the equation of motion of the particle and solved to obtain the deceleration of the particle prior to collision,

$$-\hat{F} = \hat{m}\ddot{\hat{h}} \tag{12}$$

where $\hat{m}$ is the normalized mass of the particle defined as $\hat{m} = \rho_p/\rho_f$. Grouping terms

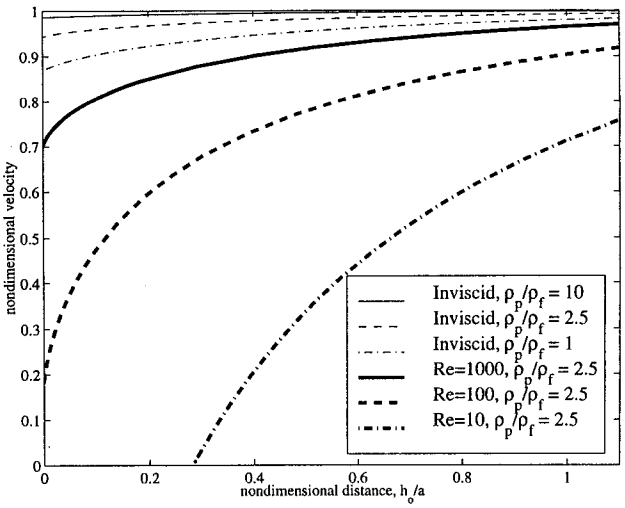

Fig. 8 Phase plot of nondimensional velocity as a function of nondimensional distance for different density ratios and Reynolds numbers

$$\ddot{\hat{h}}(\hat{m} + A(\hat{b})) = B(\hat{b})\dot{\hat{h}}^2 + C(\hat{b})K\dot{\hat{h}} \tag{13}$$

where $K = (\mu t_c/\rho_f a^2)(a/\delta)$. Equation (13) is a second order non-linear ODE, which can be solved numerically. The characteristic time t_c can be now specified as $t_c = a/\dot{h}_0$. The set of initial conditions is

$$\dot{\hat{h}}(t = 0) = 1$$

$$\hat{h}(t = 0) = 2.$$

In this case the particle has a velocity $\dot{h}_0$ at a distance $2a$ (a diameter) away from the wall. The coefficient K in Eq. (13) becomes

$$K = \frac{2\mu_f}{\rho_f 2ab_0} \frac{a}{\delta} = \frac{2}{\mathrm{Re}_0} \frac{a}{\delta} \tag{14}$$

where Re_0 is the initial Reynolds number.

Figure 8 shows results obtained from this model in terms of the nondimensional approach velocity ($\dot{b}/\dot{b}_0$) and the dimensionless distance from the wall, $\hat{h}_0$. The first three lines show the effect of the density ratio for an inviscid collision. The particle impact velocity, e.g., the velocity at $\hat{h}_0 = 0$, is larger for a larger density ratio.

Also shown are results at a fixed density ratio ($\rho_p/\rho_f = 2.5$) and for Reynolds numbers from 10 to 1000. The value of the parameter K was calculated assuming that

$$\frac{\delta}{a} \propto \frac{1}{\sqrt{\mathrm{Re}_0}} \tag{15}$$

therefore

$$K = \frac{C_0}{\sqrt{\mathrm{Re}_0}} \tag{16}$$

where C_0 is a proportionality constant ($C_0 = 0.03$ was chosen for these calculations). The figure shows that for decreasing Reynolds number the deceleration of the particle is higher. The prediction of a finite impact velocity results from the assumed scaling law to account for viscous effects. In the proposed model the viscous force scales with the particle radius, a, and not with the particle-wall gap, h, as suggested by the lubrication theory.

A critical Stokes number can be found for each density ratio at which the particle reaches the wall with zero velocity. Below that critical value, the particle stops completely before reaching

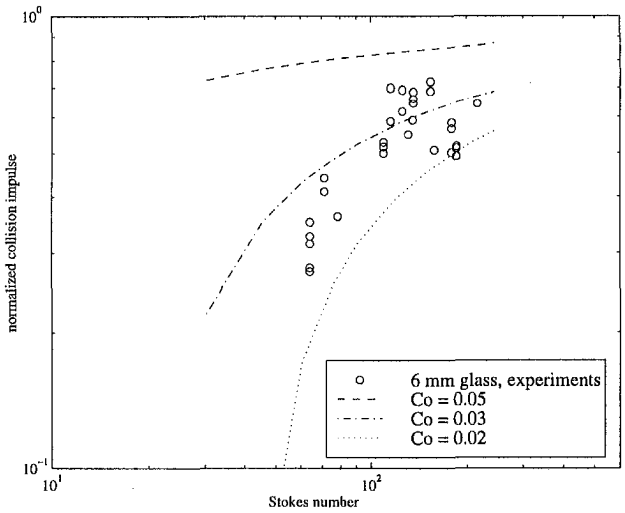

Fig. 9 Normalized collisional impulse as a function of impact Stokes number. Comparison between the 6 mm glass particle experimental measurements and the predictions from the model for different values of the proportionality constant C_o. (Uncertainty in normalized collision impulse ±8.5%, in Stokes number ±4.5%)

the wall. The calculated value of the critical Stokes number can be curve fitted and is approximated by

$$St_{cr} = \frac{e^{-\pi}}{C_0^2}\frac{\rho_f}{\rho_p}. \tag{17}$$

The existence of this critical value of the Stokes number is in agreement with experiments performed by McLaughlin (1968). As the density ratio decreases, the critical Stokes number decreases. Hence, as the particles become lighter the viscous forces become more dominant and therefore the stoppage Stokes number increases.

5 Comparisons With Experiments

To validate the predictions from the model, a comparison with the experimental measurements is presented. Using the velocity of the particle at a distance of one particle diameter from the wall as an initial condition, the model can be used to predict the velocity of the particle prior to collision. Once the corrected value of the impact velocity is known, a new estimate of the collision pressure can be calculated using Eq. (3).

Figure 9 shows a typical comparison of the normalized measured collision impulse as a function of the Stokes number, based on the predicted impact velocity. The different dashed lines show the predicted impulse when the impact velocity is corrected using the model, for different values of the proportionality constant C_0.

6 Conclusions

Immersed collisions of particles were studied experimentally using a simple pendulum, with a high-frequency response pressure transducer to record the collision impulse and a high-speed digital camera to observe the trajectory. For the current experiments, the effects of the wall were not significant for distances greater than a diameter away from the wall. The dynamics of the rebound were found to be more complex than in the dry case, and indicated that the particle accelerated after rebound due to the fluid motion. The measured collision impulse was found to increase with the particle mass and impact velocity, following the trends suggested by simple mechanics. When the impulse measurements were normalized by the particle mass and the predicted impact velocity, the data collapsed into a single band of values. By comparing with the prediction from simple mechanics, it was observed that the effect of the interstitial fluid increased for decreasing particle Stokes number.

An approximate control-volume model was proposed to account for the effects of the liquid as the particle approaches a wall. The model predicts the hydrodynamics force produced by the drainage of the fluid in the gap between the particle and the wall. The model assumes that the flow is the gap is nearly unidirectional and that the viscous effects scale with the particle radius. The deceleration prior to contact can be obtained as a function of the particle Reynolds number and the density ratio. The model predicts a critical Stokes number when the particle reaches the wall with zero velocity. The collision impulse was predicted using the corrected impact velocities. The predicted impulses appeared to agree well with the experimental measurements.

Acknowledgments

The National Council for Science and Technology of Mexico (CONACYT) is acknowledged for partially supporting R. Zenit during his graduate sojourn at the California Institute of Technology. The help of M. Noble is acknowledged during the construction of the experimental setup.

References

Barnocky, G., and Davis, R. H., 1988, "Elastohydrodynamic Collision and Rebound of Spheres: Experimental Verification," *Physics of Fluids,* Vol. 31, No. 6, pp. 1324–1329.

Campbell, C. S., 1997, "Computer Simulations of Powder Flows," *Powder Technology Handbook,* K. Gotoh, H. Masuda and K. Higashitani, eds., Marcel Dekker, New York.

Davis, R. H., Serayssol, J. M., and Hinch, E. J., 1986, "The Elastohydrodynamic Collision of Two Spheres," *Journal of Fluid Mechanics,* Vol. 163, pp. 479–497.

Gee, M. L., Mcguiggan, P. M., Israelachvili, J. N., and Homola, A. M., 1990, "Liquid to Solid-Like Transitions of Molecularly Thin-Films Under Shear," *Journal of Chemistry Physics,* Vol. 93, pp. 1895–1906.

Happel, J., and Brenner, H., 1965, *Low Reynolds Number Hydrodynamics,* Prentice-Hall, New York.

Hocking, L. M., 1973, "The Effect of Slip on a Motion of a Sphere Close to a Wall and of Two Adjacent Spheres," *Journal of Engineering Mathematics,* Vol. 7, pp. 207–221.

Johnson, J. K., 1987, *Contact Mechanics,* Cambridge University Press, Cambridge, U.K.

Landweber, L., and Shahshahan, A., 1992, "Added Masses and Forces on Two Bodies Approaching Central Impact in an Inviscid Fluid," *Journal of Ship Research,* Vol. 36, 99–122.

Lundberg, J., and Shen, H. H., 1992, "Collisional Restitution Dependence on Viscosity," *Journal of Engineering Mechanics,* Vol. 118, 979–989.

McLaughlin, M. H., 1968, "An Experimental Study of Particle-Wall Collision Relating of Flow of Solid Particles in a Fluid," Engineer Degree Thesis, California Institute of Technology, Pasadena CA.

Mei, R., 1994, "Flow Due to an Oscillating Sphere and an Expression for the Unsteady Drag on the Sphere at Finite Reynolds Number," *Journal of Fluid Mechanics,* Vol. 270.

Milne-Thompson, L. M., 1950, *Theoretical Hydrodynamics,* Macmillan, New York.

Smart, J. R., and Leighton, D. T., 1989, "Measurements of the Hydrodynamic Surface Roughness of Non-Colloidal Spheres," *Physics of Fluids A,* Vol. 1 (52).

Sundararajakumar, R. R., and Koch, D. L., 1996, "Non-Continuum Lubrication Flows Between Particles Colliding in a Gas," *Journal of Fluid Mechanics,* Vol. 313, 283–308.

Zenit, R., 1997, "Collisional Mechanics in Liquid-Solid Flows," Ph.D. thesis, California Institute of Technology, Pasadena CA.

Zenit, R., and M. L. Hunt, 1998, "Restitution Coefficient Measurements for Immersed Collision of Particles," in preparation.

Analysis on Liquid-Vapor Bubbly-Flow Systems in Reciprocating Motion

Claudia O. Iyer[1]
Graduate Research Assistant.

Wen-Jei Yang
Professor of Mechanical Engineering.

Department of Mechanical Engineering
and Applied Mechanics,
University of Michigan, Ann Arbor, MI
48109-2125

An analytical study is performed on the dynamics and hydrodynamic stability of liquid-vapor mixtures in the bubbly-flow range in reciprocating motion through a horizontal channel. The perturbation technique is applied on the one-dimensional conservation equations for laminar flow and on the thermodynamic equation of state. The Laplace transform is operated on the linearized equations from which a transfer function is derived, relating the flow rate change due to a change in pressure drop along the channel. The resulting characteristic equation is analyzed to determine the dynamic behavior of the two-phase flow in reciprocating motion and the conditions for neutral stability under which self-induced oscillations occur. The natural frequency of the physical system is derived, which can be used to predict the resonance that will occur in forced vibrations. Results can be applied to systems such as car suspensions (shock absorbers) in which oil is susceptible to cavitation, resulting in bubbly flow due to vibrations. Conditions under which resonance occurs in the two-phase system are determined. Resonance leads to severe oscillations and noise generation, as experienced in shock absorbers in car suspensions.

Introduction

The vapor pressure of mineral oils used in hydraulic machinery is extremely low, while its air content is considerably high, relative to common liquids such as water. Hydraulic machinery is commonly equipped with flow constrictors, such as valves and orifices. Backe and Riedel (1972) and Riedel (1972) studied the origin and effects of cavitation and the variables affecting its development. They disclosed the phenomena of cavitation hysteresis in oil flows subjected to timewisely sinusoidal variations in pressure drop or flow rate. Ishihara et al. (1975) investigated the unsteady characteristics of oil flow through flow constrictors in hydraulic equipment. Later, Ishihara et al. (1979) used scattered laser beams to detect cavitation phenomena in the unsteady flow of oil through sharp-edged orifices. In research on oil flow through a rotating flow passage, Backe (1973) employed an electric circuit (i.e., analogy between fluid and electrical flow) in his hydraulic analysis. Kojima et al. (1991) simulated an automatic transmission for front-wheel drive vehicles using a rotating main shaft with multiple (eleven) oil exit holes. Cheng and Yang (1996a and b) used oil flow through a rotating shaft with twin branches to simulate an automatic transmission line in automobiles. Air from the atmosphere was sucked in from the upstream branch, encountered oil flow in the main rotating shaft, and exited from the downstream branch. Different air-oil flow patterns such as bubbly, plug, and annular flow patterns, were observed, varying with the rotating speed.

In contrast to two-phase flow through a rotating tube, this paper investigates vapor-oil mixtures in reciprocating flow through a channel, which simulates flow through valves in shock absorbers. The dynamic behavior of the one-dimensional, unsteady, two-phase system is analyzed in the bubbly-flow regime. The damping factor, natural frequency, and neutral stability condition (to induce self-excited oscillations) are determined together with resonance.

Shock absorbers are designed and manufactured for virtually any motion damping application. Their functions include:

(i) reducing road effects transmitted to the vehicle and its passengers by controlling tire bounce and excessive spring movement, in automotive applications;
(ii) reducing impact and rebound of equipment designed with mechanical pivot action;
(iii) aiding in controlling the motion of a mechanical impact lever to drive a part and improve performance;
(iv) cushioning parts that move in and out at high frequencies, in industrial applications.

All shock absorbers have two things in common: they are both suspension system components and motion damping devices. A shock absorber is designed to function in parallel with a spring force that is exerted by the suspension system components. It does not support a static load by itself, but rather helps reduce or absorb the motion between two points that move in relation to one another, such as up-and-down movement on a vehicle. This is why, it is called a "motion damping device." A shock absorber is a velocity-sensitive device, with the speed and resulting control force being directly proportional.

Figure 1 shows a schematic diagram of a shock absorber in vertical position during the compression cycle, or stroke. The shock absorbers consist of two concentric tubes sealed at both ends, a piston connected to a piston rod, two valves, and a working fluid (oil). The inner and outer tubes are called pressure and reserve tubes, respectively. The piston is fitted with the inner tube forming a space, chamber A, on the piston rod side and another space, chamber B, between the piston head and the base valve at the lower end. The annular space between the two concentric tubes forms chamber C with the compression valve. The chambers B and C are connected through the base and the compression valves. Chambers A and B contain a working fluid under pressure, namely oil.

The principle of fluid displacement works in both shock absorber cycles—compression and extension. The extension cycle controls the motions of the vehicle body sprung weight, while the compression cycle controls the same motions of the lighter axle and tire unsprung weight. A car shock absorber will have

[1] née Gavrilescu.

Contributed by the Fluids Engineering Division for publication in the JOURNAL OF FLUIDS ENGINEERING. Manuscript received by the Fluids Engineering Division September 15, 1997; revised manuscript received October 13, 1998. Associate Technical Editor: M. Sommerfeld.

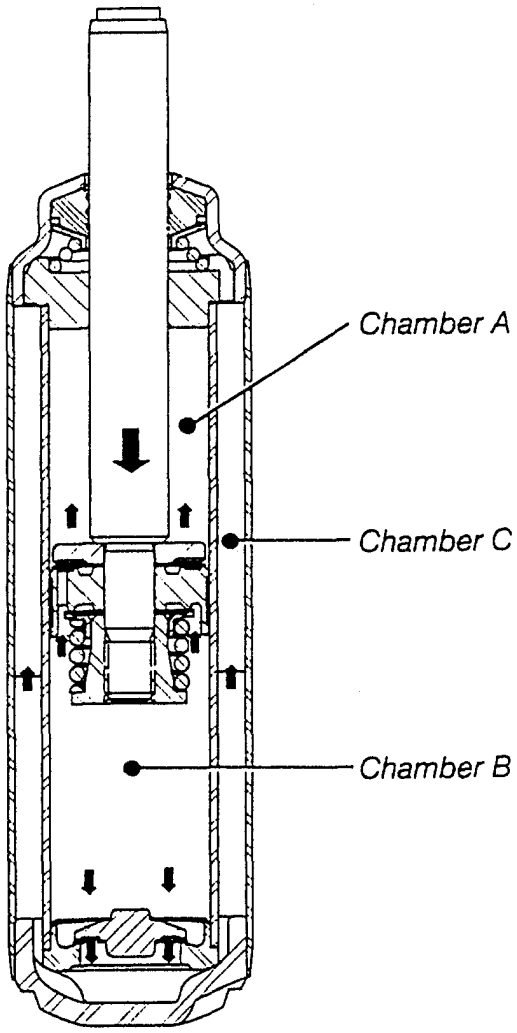

Fig. 1 A schematic of a shock absorber under the compression cycle

more resistance during its extension cycle than during its compression cycle.

Compression Cycle. During the compression cycle, the fluid flows through the piston from chamber B to chamber A, and some flows through the compression valve into the reservoir, chamber C, as illustrated in Fig. 1. To control this flow, there are three valving stages in the piston and in the compression valves. Oil flows through the oil ports of the piston.

(i) At slow piston speeds, the first stage opens allowing fluid to flow from chamber B to chamber A.
(ii) At faster piston speeds, the increase in fluid pressure below the piston in chamber B causes the second stage piston valve to open.
(iii) At high speeds, the limits of the second stage phase into the third stage orifice restrictions.

At the bottom of chamber B, oil which is displaced by the piston rod passes through the three-stage compression valve into chamber C.

(i) At low speeds, the oil flows through an orifice in the compression valve.
(ii) As piston speed increases, the fluid pressure increases, causing the disc to open up away from the valve seat.
(iii) At high speeds, the orifice restriction becomes effective.

Compression control then, is the force which results from the higher pressure present in chamber B that acts on the bottom of the piston and the piston rod area.

Extension Cycle. All arrow signs in Fig. 1 are reversed during the extension cycle. As the piston and rod are moved upward toward the top of the pressure tube, the volume of chamber A is reduced causing its pressure to become higher than that of chamber B. Because of this higher pressure, the fluid flows down through the piston's three-stage extension valve into chamber B, whose volume increases greatly because of the withdrawing of the piston rod. This implies that the volume of fluid from chamber A is insufficient to fill chamber B. As a result, the pressure in chamber C exceeds that in chamber B, forcing the compression intake valve to unseat. This causes fluid flows from chamber C into chamber B, keeping the pressure tube full. Therefore, extension control is the force present as a result of higher pressure in chamber A acting on the top side of the piston area.

The hydraulic damping requirements of any shock absorber application are controlled by several factors, including:

(i) mass (weight) of the suspended system, m;
(ii) relative velocity between the two mounting points, in other words, the damping factor, c;
(iii) mounting compliances;
(iv) suspension geometry, namely the spring constant, k;
(v) system natural frequency, ω_n.

Hence, shock absorbers are similar to a mass-damper spring system whose dynamic behavior can be described as:

$$m\ddot{x} + c\dot{x} + kx = F(t) \tag{1}$$

where x denotes the displacement, $\dot{x}$ its time derivative, $\ddot{x}$ its second time derivative, and F force. Then, the natural frequency of the system is:

$$\omega_n = \left(\frac{k}{m}\right)^{1/2} \tag{2}$$

Figure 2 depicts a force versus displacement graph of a shock absorber for three different speeds, low at 30 CPM (0.5 Hz), medium at 85 CPM (1.416 Hz), and high at 170 CPM (2.833 Hz).

The reduction of tire and suspension motion in a vehicle, for example, is achieved by the controlled movement of fluid under pressure, called "hydraulic damping." It is the motion of the piston inside the shock absorber that pressurizes the fluid. The resistance to this motion (kinetic energy) produces heat (thermal energy), which is then dissipated into the atmosphere through the shock housing. The amount of resistance is governed by moving fluid from one chamber to another through various orifices, springs, and discs. The disks are held in place

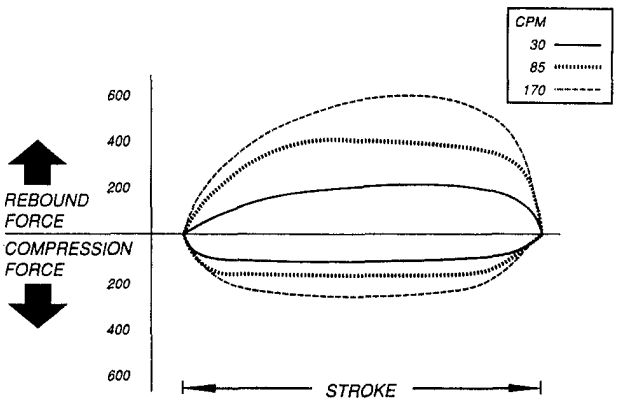

Fig. 2 Force versus piston displacement graph

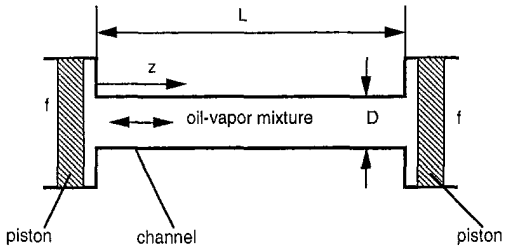

Fig. 3 A model of reciprocating flow of oil through an orifice in a shock absorber, during the compression and extension strokes

by springs. When the relative velocity is low, fluid passes from one chamber to another through an orifice. When pressure builds up to a specific preset level, the force causes the spring to retract. Then, the disks blow off, allowing movement of fluid through orifices, and release of pressure.

Analysis

The physical system to be studied is schematically depicted in Fig. 3. It consists of a rectangular channel with each end connected to a cylinder with piston. The channel is filled with an oil-vapor mixture. The two pistons perform reciprocating motions synchronously to induce a reciprocating flow of the two-phase mixture through the channel at a frequency of Ω. D and L denote the channel diameter and length, respectively; z denotes the coordinate measured from the left of the channel and t denotes the time. There are two types of cavitation, namely, gaseous and vaporous cavitation. In the present analytical study the effect of non-condensable gases is neglected because the device we are dealing with is sealed and because we tried to avoid dealing with two components in the vapor phase which would complicate the analysis considerably. Therefore, we treat the two-component vapor phase as a single component of density ρ_v and void fraction α. The subscripts l and v stand for the liquid and vapor phases, respectively.

The basic conservation equations for unsteady one-dimensional slip flow in a horizontal channel can be written as:
Continuity equation:

$$\frac{\partial}{\partial t}[\rho_l(1-\alpha)+\rho_v\alpha]+\frac{\partial}{\partial z}[\rho_l u_l(1-\alpha)+\rho_v u_v\alpha]=0 \quad (3)$$

Momentum equation:

$$\frac{\partial}{\partial t}[\rho_l u_l(1-\alpha)+\rho_v u_v\alpha]+\frac{\partial}{\partial z}[\rho_l u_l^2(1-\alpha)+\rho_v u_v^2\alpha]+\frac{dp}{dz}+F=0 \quad (4)$$

where F is the frictional force per unit volume of fluid, $F = fG^2/2D\rho$, ρ the density, and f the friction coefficient.

Defining the local mass velocity as:

$$G=\rho_l u_l(1-\alpha)+\rho_v u_v\alpha \quad (5)$$

and the local volume weighted mean density as:

$$\rho=\rho_l(1-\alpha)+\rho_v\alpha \quad (6)$$

the basic Eqs. (3) and (4) are simplified as:

$$\frac{\partial\rho}{\partial t}+\frac{\partial G}{\partial z}=0 \quad (7)$$

and

$$\frac{\partial G}{\partial t}+\frac{\partial}{\partial z}(v'G^2)+\frac{dp}{dz}+F=0 \quad (8)$$

respectively.

The "effective specific volume for spatial acceleration" defined by:

$$v'=\frac{1}{G^2}[\rho_l u_l^2(1-\alpha)+\rho_v u_v^2\alpha] \quad (9)$$

reduces to $v' = 1/\rho$ for a non-slip flow.

A simplified formulation of these basic equations may be obtained from the exact formulation by linearization of the equations to provide approximate analytical solutions (Quandt, 1961). By utilizing the technique of small perturbations, the variables in the basic equations can be written as:

$$G(z,t)=G(z,0)+\Delta G(z,t) \quad (10)$$

$$\rho(z,t)=\rho(z,0)+\Delta\rho(z,t) \quad (11)$$

$$h(z,t)=h(z,0)+\Delta h(z,t) \quad (12)$$

where h stands for enthalpy.

By using the forms of the variables as given in Eqs. (10)–(12), that is, a steady-state component plus a transient component, Eqs. (7) and (8) may be reduced to a set of linear partial differential equations with variable coefficients. One of the assumptions of our study is that the transient components of the variables are small.
Continuity:

$$\frac{\partial\Delta\rho}{\partial t}+\frac{\partial\Delta G}{\partial z}=0 \quad (13)$$

Momentum:

$$\frac{\partial\Delta G}{\partial t}+\frac{\partial}{\partial z}\left(\frac{2G}{\rho}\Delta G-\frac{G^2}{\rho^2}\Delta\rho\right)+\frac{\partial\Delta p}{\partial z}+\frac{fG}{D\rho}\Delta G-\frac{fG^2}{2D\rho^2}\Delta\rho=0 \quad (14)$$

Thermodynamic equation of state:

$$\Delta\rho=\frac{\partial\rho}{\partial h}\Delta h \quad (15)$$

By applying the Laplace transformation to these linearized equations we get:
Continuity:

$$\frac{\partial}{\partial z}\Delta G(z,s)=-s\Delta\rho(z,s) \quad (16)$$

Momentum:

$$s\Delta G+\frac{\partial}{\partial z}\left(\frac{2G}{\rho}\Delta G\right)-\frac{\partial}{\partial z}\left(\frac{G^2}{\rho^2}\Delta\rho\right)+\frac{\partial\Delta p}{\partial z}+\frac{fG}{D\rho}\Delta G-\frac{fG^2}{2D\rho^2}\Delta\rho=0 \quad (17)$$

where s is the Laplace variable.

Integrating Eq. (17) along the channel length, L, we get:

$$s\int_0^L\Delta G dz+2G\left(\frac{\Delta G_e}{\rho_e}-\frac{\Delta G_i}{\rho_i}\right)-G^2\left(\frac{\Delta\rho_e}{\rho_e^2}-\frac{\Delta\rho_i}{\rho_i^2}\right)-\Delta(\Delta p_{ch})+\frac{G}{D}\int_0^L\frac{f}{\rho}\Delta G dz-\frac{G^2}{2D}\int_0^L\frac{f}{\rho^2}\Delta\rho dz=0 \quad (18)$$

where Δp_{ch} is the pressure loss from the inlet to the exit of the flow passage.

In the following, assumptions are made regarding the spatial form of the flow and enthalpy perturbations. Let ΔG be expressed in series form as:

$$\Delta G = a + b\frac{z}{L} = \Delta G_i + (\Delta G_e - \Delta G_i)\frac{z}{L} \tag{19}$$

where a and b are constants. Integrating we get:

$$\int_0^L \Delta G dz = \Delta G_i \frac{L}{2} + \Delta G_e \frac{L}{2} \tag{20}$$

Introducing Eq. (20) in (18) yields:

$$\Delta(\Delta p_{ch}) = \left(\frac{sL}{2} - \frac{2G}{\rho_i}\right)\Delta G_i + \left(\frac{sL}{2} + \frac{2G}{\rho_e}\right)\Delta G_e$$

$$- G^2\left(\frac{\Delta\rho_e}{\rho_e^2} - \frac{\Delta\rho_i}{\rho_i^2}\right) + \int_0^L \left[\frac{Gf}{D\rho}\Delta G - \frac{G^2 f}{2D\rho^2}\Delta\rho\right]dz \tag{21}$$

Similarly, Δh is expanded in series form with a' and b' as constants:

$$\Delta h = a' + b'\frac{z}{L} = \Delta h_e \frac{z}{L} \tag{22}$$

It is then substituted into Eq. (15) to yield:

$$\Delta\rho = \frac{\partial\rho}{\partial h}\frac{z}{L}\Delta h_e \tag{23}$$

Eqs. (23) and (13) are combined to give:

$$\frac{\partial\Delta G}{\partial z} = -\frac{\partial\rho}{\partial h}\frac{z}{L}\frac{\partial\Delta h_e}{\partial t} \tag{24}$$

which is integrated over the length L to yield:

$$\Delta G_e - \Delta G_i = -\frac{\partial\Delta h_e}{\partial t}\int_0^L \frac{\partial\rho}{\partial h}\frac{z}{L}dz \tag{25}$$

With the definition of:

$$\Psi = -\int_0^L \frac{\partial\rho}{\partial h}\frac{z}{L}dz \tag{26}$$

where Ψ is a constant for any given initial condition, Eq. (25) becomes:

$$\Delta G_e - \Delta G_i = \Psi\frac{\partial\Delta h_e}{\partial t} \tag{27}$$

The Laplace transform of Eq. (27) yields:

$$\Delta G_e - \Delta G_i = \Psi s\Delta h_e \text{ or } \Delta h_e = \frac{\Delta G_e - \Delta G_i}{\Psi s} \tag{28}$$

The substitution of Eq. (28) into (23) gives:

$$\Delta\rho = \frac{\partial\rho}{\partial h}\frac{z}{L}\frac{\Delta G_e - \Delta G_i}{\Psi s} \tag{29}$$

which takes a value of:

$$\Delta\rho_e = \frac{\partial\rho}{\partial h}(e)\frac{\Delta G_e - \Delta G_i}{\Psi s} \quad \text{at } z = L \tag{30}$$

and:

$$\Delta\rho_i = 0 \quad \text{at } z = 0 \tag{31}$$

A combination of Eqs. (19) and (29)–(31) with Eq. (21) gives:

$$\Delta(\Delta p_{ch}) = \left(\frac{sL}{2} - \frac{2G}{\rho_i}\right)\Delta G_i + \left(\frac{sL}{2} + \frac{2G}{\rho_e}\right)\Delta G_e$$

$$- \frac{G^2}{\rho_e^2}\frac{\partial\rho}{\partial h}(e)\frac{\Delta G_e - \Delta G_i}{\Psi s}$$

$$+ \int_0^L \left[\frac{Gf}{D\rho}\left(\Delta G_i + (\Delta G_e - \Delta G_i)\frac{z}{L}\right)\right.$$

$$\left. - \frac{G^2 f}{2D\rho^2}\frac{\partial\rho}{\partial h}\frac{z}{L}\frac{\Delta G_e - \Delta G_i}{\Psi s}\right]dz \tag{32}$$

Multiplying Eq. (32) by the Laplace variable, s, and then rearranging yields:

$$s\Delta(\Delta p_{ch}) = \Delta G_i\left\{\frac{s^2 L}{2} + s\left[-\frac{2G}{\rho_i} + \int_0^L \frac{Gf}{D\rho}\left(1 - \frac{z}{L}\right)dz\right]\right.$$

$$\left. + \frac{1}{\Psi}\left[\frac{G^2}{\rho_e^2}\frac{\partial\rho}{\partial h}(e) + \int_0^L \frac{G^2 f}{2D\rho^2}\frac{\partial\rho}{\partial h}\frac{z}{L}dz\right]\right\}$$

$$+ \Delta G_e\left\{\frac{s^2 L}{2} + s\left[\frac{2G}{\rho_e} + \int_0^L \frac{Gf}{D\rho}\frac{z}{L}dz\right]\right.$$

$$\left. + \frac{1}{\Psi}\left[-\frac{G^2}{\rho_e^2}\frac{\partial\rho}{\partial h}(e) - \int_0^L \frac{G^2 f}{2D\rho^2}\frac{\partial\rho}{\partial h}\frac{z}{L}dz\right]\right\} \tag{33}$$

Equation (33) can be written as:

$$s\Delta(\Delta p_{ch}) = \Delta G_i(ms^2 + cs + k) + \Delta G_e(ms^2 + As - k) \tag{34}$$

where

$$m = \frac{L}{2} \tag{35}$$

$$c = -\frac{2G}{\rho_i} + \int_0^L \frac{Gf}{D\rho}\left(1 - \frac{z}{L}\right)dz \tag{36}$$

$$k = \frac{1}{\Psi}\left[\frac{G^2}{\rho_e^2}\frac{\partial\rho}{\partial h}(e) + \int_0^L \frac{G^2 f}{2D\rho^2}\frac{\partial\rho}{\partial h}\frac{z}{L}dz\right] \tag{37}$$

$$A = \frac{2G}{\rho_e} + \int_0^L \frac{Gf}{D\rho}\frac{z}{L}dz \tag{38}$$

For a zero perturbed exit mass velocity, $\Delta G_e = 0$, one obtains from Eq. (34) the transfer function of the inlet mass velocity with respect to a variation of the pressure drop across the channel as:

$$\frac{\Delta G_i}{\Delta(\Delta p_{ch})} = \frac{s}{ms^2 + cs + k} \tag{39}$$

This represents the hydrodynamic behavior of the two-phase flow system. The characteristic equation is obtained by setting the denominator of Eq. (39) to zero, which gives:

$$ms^2 + cs + k = 0 \tag{40}$$

The above equation resembles the characteristic equation of a mass-damper-spring system with mass m, coefficient of damping c, and spring constant k, given in Eq. (1). It has the roots:

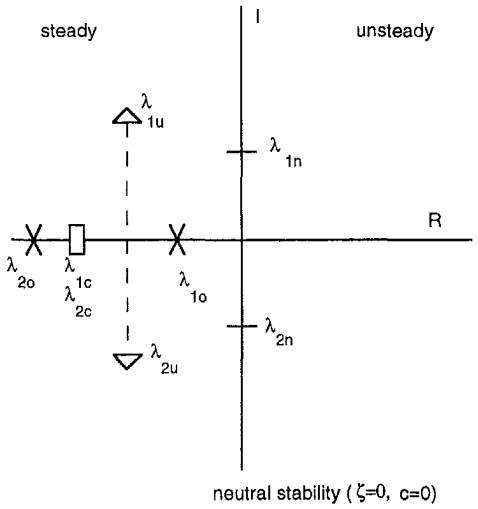

Fig. 4 Representation in complex domain for the roots of dynamic equation (40)

$$\lambda_{1,2} = \frac{-c \pm \sqrt{c^2 - 4mk}}{2m} \tag{41}$$

Let us define the damping ratio as:

$$\zeta = \frac{c}{2(mk)^{1/2}} \tag{42}$$

and the natural circular frequency as:

$$\omega_n = \left(\frac{k}{m}\right)^{1/2} \tag{43}$$

Now, the roots can be rewritten in terms of the more convenient variables ζ and ω_n as:

$$\lambda_{1,2} = -\zeta\omega_n \pm \omega_n(\zeta^2 - 1)^{1/2} \tag{44}$$

The dynamic behavior of the system depends on whether the quantity under the radical in Eq. (44) is positive, zero, or negative. The value of c that makes the radical zero is called the critical damping coefficient, c_{cr}. Therefore,

$$c_{cr} = 2m\omega_n = 2(mk)^{1/2} \tag{45}$$

There are three totally distinct types of dynamic behavior depending on whether the actual system damping c is greater than, equal to, or less than c_{cr}. The overdamped system for $c > c_{cr}$ and the critically damped system for $c = c_{cr}$ are nonvibratory, while only the underdamped system for $c < c_{cr}$ is vibratory. The roots for these three types are plotted on the complex plane of the imaginary (I) axis against the real (R) axis in Fig. 4. Here, the double subscripts o, c, u, and n denote overdamped, critically damped, underdamped, and neutral stability systems, respectively.

In the underdamped system ($c < c_{cr}$), the damping ratio ζ is less than unity, the radical in Eq. (44) is imaginary, and the two roots λ_{1u} and λ_{2u} are complex conjugates:

$$\lambda_{1u,2u} = -\zeta\omega_n \pm i\omega_n(1 - \zeta^2)^{1/2} = -\zeta\omega_n \pm i\omega_d \tag{46}$$

where

$$\omega_d = \omega_n(1 - \zeta^2)^{1/2} \tag{47}$$

is the damped natural circular frequency and $i = (-1)^{1/2}$.

For $\zeta = 0$, the system is under the neutral stability condition and undergoes self-induced vibrations with:

$$\lambda_{1n,2n} = \pm i\omega_n \tag{48}$$

Consider a forced vibration of the liquid-vapor system produced and maintained by the two pistons in a synchronized reciprocating motion. Let the force F be a harmonic function of time as:

$$F = F_0 \sin \Omega t \tag{49}$$

where the constants F_0 and Ω are the amplitude and the frequency of the driving force.

When the force is applied at a frequency close to the natural frequency of the system ($\Omega \approx \omega_n$) and the damping is light ($\zeta \approx 0$), the amplitude of the vibration is magnified substantially. This condition is called resonance.

By using average values for the velocity, the coefficients c and k in Eqs. (36) and (37), respectively, can be written as:

$$c = -\frac{2G}{\rho_i} + \int_0^L \frac{\rho u f}{D\rho}\left(1 - \frac{z}{L}\right)dz$$

$$= -\frac{2G}{\rho_i} + \int_0^L \frac{uf}{D}\left(1 - \frac{z}{L}\right)dz \tag{50}$$

$$k = \frac{1}{\Psi}\left[\frac{\rho^2u^2}{\rho_e^2}\frac{\partial\rho}{\partial h}(e) + \int_0^L \frac{\rho^2u^2f}{2D\rho^2}\frac{\partial\rho}{\partial h}\frac{z}{L}\,dz\right]$$

$$= \frac{1}{\Psi}\left[\frac{\rho^2u^2}{\rho_e^2c_p}\frac{\partial\rho}{\partial T}(e) + \int_0^L \frac{u^2f}{2Dc_p}\frac{\partial\rho}{\partial T}\frac{z}{L}\,dz\right] \tag{51}$$

where

$$\Psi = -\int_0^L \frac{1}{c_p}\frac{\partial\rho}{\partial T}\frac{z}{L}\,dz \tag{52}$$

Both self-excited oscillation and resonance require $\zeta = 0$, i.e., $c = 0$, which gives:

$$G = \frac{\rho_i}{2}\int_0^L \frac{uf}{D}\left(1 - \frac{z}{L}\right)dz \tag{53}$$

In addition, resonance needs $\Omega = \omega_n$, namely:

$$\Omega = \left\{\frac{2}{L\Psi}\left[\frac{G^2}{\rho_e^2}\frac{\partial\rho}{\partial h}(e) + \int_0^L \frac{G^2f}{2D\rho^2}\frac{\partial\rho}{\partial h}\frac{z}{L}\,dz\right]\right\}^{1/2} \tag{54}$$

Under these conditions, given by Eqs. (53) and (54), the liquid-vapor system, like that in a shock absorber in car suspensions, will produce severe vibrations accompanied by noise.

Results and Discussion

Consider a channel of length $L = 50$ mm and diameter $D = 3$ mm with an oil-vapor mixture of $\alpha = 0.5$ at the exit; $\rho_v = 1.2$ kg/m^3 and $\rho_l = 886$ kg/m^3. It gives an exit density of $\rho_e = 443.6$ kg/m^3 and an average density along the channel of $\rho_{ave} = 664.8$ kg/m^3. The inlet and outlet mass velocities for an average velocity, u, of 2 m/s are found to be $G_i = 1772$ kg/m^2 s and $G_e = 887.2$ kg/m^2 s, respectively. Then the average mass velocity along the channel is $G_{ave} = 1329.6$ kg/m^2 s and the Reynolds number is:

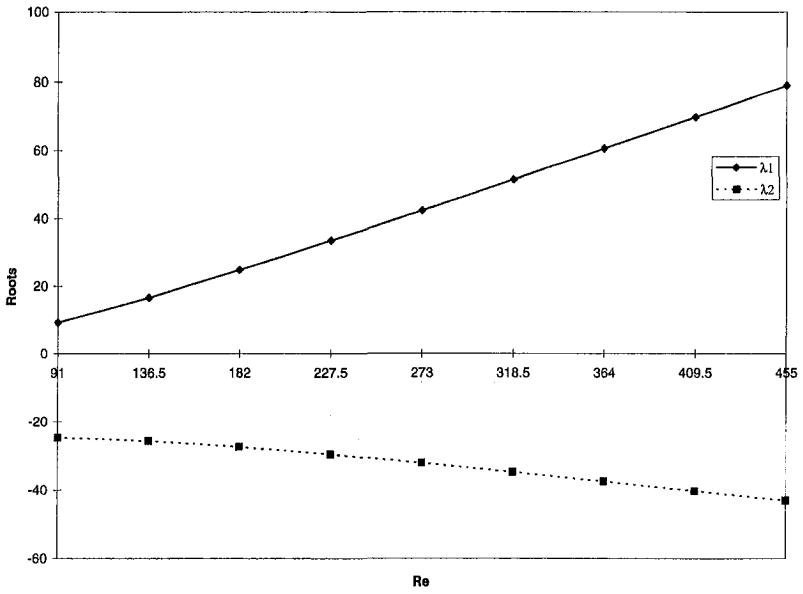

Fig. 5 Variations of the roots λ_1 and λ_2 of the dynamic equation (40) with Reynolds number

$$\mathrm{Re} = \frac{uD}{\upsilon} = \frac{2(3 \times 10^{-3})}{10.99 \times 10^{-6}}$$

$$= 545.9 \text{ For laminar flow, the friction factor is } f$$

$$= \frac{64}{\mathrm{Re}} = 0.1172.$$

With the specific heat, c_p, of 1980 J/kg K:

$$\frac{\partial \rho}{\partial h} = \frac{1}{c_p}\frac{\partial \rho}{\partial T} = -0.00172 \text{ kg}^2/\text{Jm}^3 < 0$$

and

$$\Psi = -\int_0^L \frac{1}{c_p}\frac{\partial \rho}{\partial T}\frac{z}{L}\,dz = 0.000043$$

Subsequently, the values of c and k are determine to be $c = -1.048$ and $k = -437.495$, respectively, which lead to the roots $\lambda_1 = 154.89$ and $\lambda_2 = -112.98$. Hence, the system is unstable since λ_1 is positive.

Using the average values from the above example we get:

$$G = \frac{\rho_i}{2}\int_0^L \frac{uf}{D}\left(1 - \frac{z}{L}\right)dz$$

$$= \frac{886}{2}\int_0^L \frac{2(0.1172)}{3 \times 10^{-3}}\left(1 - \frac{z}{L}\right)dz = 865.33 \text{ kg/m}^2 \text{ s}$$

for resonance to occur.

Figure 5 shows the variations of the roots λ_1 and λ_2 of the dynamic equation (40) with Reynolds number, for the specific case when the exit void fraction is 0.3. It can be observed that as Reynolds number increases the system becomes more unstable.

Conclusions

The present paper presents the results of an analytical investigation of flow instabilities occurring in liquid-vapor bubbly-flow systems in reciprocating motion. The analysis starts from the basic transient equations for two-phase flows: continuity, momentum, and state. The effect of noncondensable gases has been neglected. Small perturbations are applied to each variable and assumptions are made regarding the spatial form of the flow and enthalpy perturbations. The perturbed equations are integrated along the channel and then Laplace transformed. A transfer function relating the flow rate change due to a change in the pressure drop along the channel has been derived and shown to represent a second-order system. Our perturbation-type analysis is able to predict the flow conditions under which resonance occurs. The results of this study can be applied to systems such as shock absorbers in which oil cavitates.

References

Backe, W., 1973, "Ein Neues Konzept fuer Hydraulische Widerstandssteurungen" (A New Concept for Hydraulic Resistance Controls), *Industrie-Anzeiger,* Vol. 95, No. 53, pp. 1137–1141 for Part 1 and No. 62, pp. 1431–1434 for Part 2.

Backe, W., and Riedel, H.-P., 1972, "Kavitation in Oelhydraulischen Systemen" (Cavitation in Oil-Hydraulic Systems), *Industrie-Anzeiger,* Vol. 94, No. 8, pp. 153–158.

Cheng, S.-W., and Yang, W.-J., 1996a, "Onset of Cavitation in Oil Flow through a Rotating Shaft with Twin Branches," *Rotating Machinery 1996,* D. C. Han, S. T. Ro, and J. H. Kim, eds., Vol. II (Transport Phenomena), pp. 57–66.

Cheng, S.-W., and Yang, W.-J., 1996b, "Visualization of Oil-Cavitation Flow in a Rotating Horizontal Tube with Twin Exit Branches," *Proceedings of ASME FED Summer Meeting,* Vol. 4, FED-Vol. 239, *Experimental and Numerical Visualization and Laser Anemometry,* B. Khalighi, D. H. Fruman, W.-J. Yang, M. J. Braun, M. V. Otugen, C. J. Freitas, and F. Bahan eds., pp. 17–21.

Ishihara, T., Ouchi, M., Kobayashi, T., and Tamura, N., 1979, "An Experimental Study on Cavitation in Unsteady Oil Flow," *Bulletin of JSME,* Vol. 22, No. 170, pp. 1099–1106.

Ishihara, T., Tanaka, H., and Kojima, E., 1975, "Dynamic Characteristics of Oil-Hydraulic Pressure Control Valves," *Bulletin of JSME,* Vol. 18, No. 122, pp. 858–865.

Kojima, M., Fukumura, K., and Yasue, H., 1991, "A Study on the Lubricating Oil Flow in the Automatic Transmission," SAE paper 910801.

Quandt, E. R., 1961, "Analysis and Measurement of Flow Oscillations," *Chem. Eng. Progr. Symp. Ser.,* Vol. 57, No. 32, pp. 111–126.

Riedel, H.-P., 1972, "Kavitationsverhaltung von Verschiedenen Druckfluessigkeiten" (Cavitation Behavior of Various Pressure Fluids), *Industrie-Anzeiger,* Vol. 94, No. 71, pp. 1724–1727.

A. Tokuhiro
PNC International Fellow,
Power Reactor and Nuclear Fuel
Development Corporation,
4002 Narita, Oarai, Ibaraki 311-1393, Japan

A. Fujiwara
Current M. S. Student.

K. Hishida
Professor.

M. Maeda
Professor.

Department of System Design Engineering,
Keio University,
3-14-1 Hiyoshi, Kohoku-ku, Yokohama,
223-8522 Japan

Measurement in the Wake Region of Two Bubbles in Close Proximity by Combined Shadow-Image and PIV Techniques

An experimental study on flow around two similarly-sized, adjacent air bubbles confined in a 1000 mm vertical, square channel (100 × 100 mm²) with downward flow of water was conducted. The bubbles were D = 11.7 mm in major diameter, ellipsoidal in shape (0.4 ml volume) and 12 mm apart. The Reynolds and Eötvös numbers were 1950 < Re_D < 2250, 11 < Eo < 11.5 such that the bubbles oscillated. Velocity measurements were taken using Digital Particle Image Velocimetry, complemented by Laser Induced Fluorescence. Simultaneously, a second CCD camera recorded the shadow image of the bubble pair's motions. Visualization revealed that the bubbles move out of phase and do not collide nor coalesce. The velocity data revealed the dynamic interaction of two wake-flow velocity fields with a jet-like flow in-between. From the DPIV data, estimates of the vorticity, Reynolds-stress and turbulent kinetic energy (TKE) distributions confirmed the spatio-temporal nature of the flow. Details will be presented.

Introduction

The study of flow around a solid body such as a hemisphere or that around a single rising gas bubble in a volume of liquid are two classic examples of problems in fluid mechanics of multi-phase flows. It goes without saying that our understanding of such rudimentary systems can be and is often extrapolated and applied to larger scale systems such as fluidized-beds, bio-reactor bubble columns and other equipment involving solid-liquid, gas-liquid and solid-gas-liquid flows. Our accumulated knowledge on the fundamental aspects of these types of flows over many years is contained, for example in texts such as those by Levich (1962) and Clift et al. (1978). There are additionally many, many works on specific flows such as bubbly-flow, for which progress made on the analytical side (modeling and theory) is sometimes lacking experimental verification and data.

In the present work we applied Digital Particle Image Velocimetry (DPIV) along with Laser Induced Fluorescence (LIF) and an Infrared Shadow Technique (IST) in unison to the fundamental problem of flow around two adjacent bubbles. Our objectives were two-fold: 1) to explore the applicability of DPIV, LIF and a specifically developed IST to this problem and 2) to evaluate the information content produced by our measurement system; that is, to investigate the turbulent wake flow of two adjacent and nearly identical air bubbles suspended in downward flow of water in a vertical channel.

Measurement Method

In order to detect the interaction between the bubble motion and the turbulent flow field around it we implemented a DPIV system previously described by Sakakibara et al. (1993a, 1993b). The hardware components consisted of the following: 1) a 4W INNOVA Model 70 Ar-ion laser, 2) a Sony XC-77RR, NTSC 768 × 493 pixel, Charge-Coupled Device (CCD) camera and 3) a timing counter to synchronize the laser and camera (built in-house). An acoustic optical modulator (AOM) cell chops the laser beam (Hoya Model A-160) and is synchronized to the vertical signal of the CCD camera. The video signal was recorded on a Panasonic AG-700, S-VHS, NTSC videotape recorder with each frame encoded by an unique 24 bits, 8 × 8 pixels black or white bar-code. Our original approach was to simultaneously capture both the bubble and tracer particle motions with only DPIV. However, it became clear that the intensity of light reflected from the bubble's surface not only saturated the CCD camera, but also overwhelmed the intensity of light from the tracer particles in its vicinity. We thus used DPIV in conjunction with LIF using fluorescent tracer particles. Previously, Hassan et al. (1993) used this method in order to investigate a condensing steam bubble in water. In our application, the fluorescent particles were Rhodamine-B impregnated, nominally 1–10 μm (specific density 1.02) and illuminated in a light-sheet of approximately 1 mm thickness. The fluorescence was recorded through a color filter (to cut reflections) by our CCD camera. We found that with this set-up we could detect the motion of tracer particles in the vicinity of the bubble-liquid interface. The test media were air for the bubbles and water.

In order to measure the bubble's shape we supplemented the DPIV-LIF system with IST specifically prepared for this experiment. Figure 1 depicts our arrangement consisting of two CCD cameras; the rear camera for DPIV-LIF and the front for IST. A shadow was produced from infrared LEDs outlining a square and located behind the bubbles. The emitted light was filtered through a translucent sheet and produced a shadow of the bubbles, then captured by the CCD camera. A color filter that passed only infrared light was attached to the CCD. In order to capture both the bubble shape and the flow field around it, we synchronized the triggering of the laser, the 2 CCD cameras and the LEDs. The laser sheet is shown to enter the test section from the right side.

As for the experimental apparatus it consisted of two rectangular tanks, a lower and upper, connected in-between by a vertical, square channel (100 × 100 mm²) 1000 mm in length. At the top of the channel there is a honeycomb entrance section in order to rectify the flow. Water thus flowed downward through the channel to the lower tank where it was pumped

Contributed by the Fluids Engineering Division for publication in the JOURNAL OF FLUIDS ENGINEERING. Manuscript received by the Fluids Engineering Division May 11, 1998; revised manuscript received October 19, 1998. Associate Technical Editor: D. R. Williams.

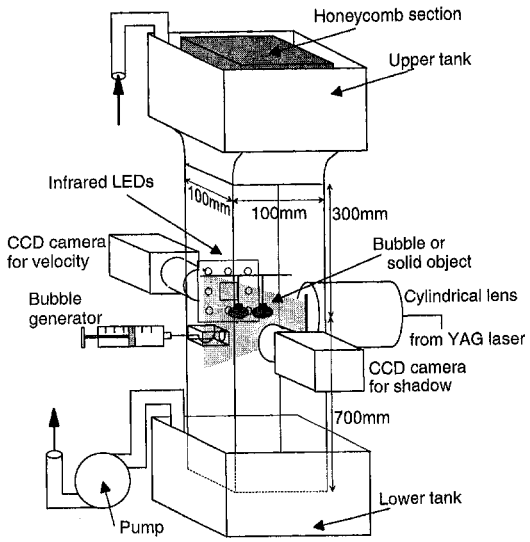

Fig. 1 Schematic of experimental setup

back up to upper tank. The mid-region of the channel was our measurement section and consisted of a port from where the bubbles could be introduced. Two bubbles of approximately 0.4 ml volume (estimated error ±0.05 ml) were attached to two small disks ($D_{disk} < 2$ mm) located at the end of two needles, suspended across the channel by piano-wire. The equivalent bubble diameter was $d_e \sim 9.1$ mm (major diameter, $D \sim 11.7$ mm). The separation distance between the disks in the present experiment was 12 mm. We note that surface tension kept the bubbles attached to the disks, even as water flowed downward. The bubbles did not detach themselves nor float momentarily during the measurement. Otherwise without the disks, it was difficult to keep a bubble suspended at the axial location of measurement, because any slight flow fluctuation moved the bubbles. Earlier studies by Davidson and Kirk (1969), Moo-Young et al. (1971) and Kojima et al. (1975) on single-bubble systems used flow tailoring or contoured entrance sections not only to fix an entrance flow profile, but by doing so kept a single bubble quasi-stationary. We did not want this for lack of generality of the entrance flow conditions. So, the small disks provided a surface onto which the bubble could attach itself. We note that the terminal rise velocity of a free bubble in our channel was measured to be on average, 24.5 cm/s. The downward flow velocity specified in Moo-Young et al., corresponding to the equivalent diameter of our bubble is within 10 percent of that specified in the present experiment. So the operational flowrate was held constant at $U_o = 0.245$ m/s while the corresponding turbulent intensity level due solely to grid-generated turbulence was ~3 percent in the channel. This level was measured separately by LDV. The calculated Re and Eo (Eötvös) numbers for a temperature range, 15°–20°C, in our experiment were: $1950 < \mathrm{Re}_D < 2250$ and $11 < \mathrm{Eo} < 11.5$. To the best of our ability, we attached bubbles of equal volume to the stationary disks. Finally we assumed that the influence of the disk on the shedding and oscillating tail mechanisms are minor and differences (with and without), if they can even be detected, are small. For a disk and bubble equivalent diameter range, $1 \le D_{disk} \le 2$ mm, $9 \le d_e \le 12$ mm, the cross-sectional area ratio can be as little as 2.8 percent or as much as 19.8 percent of the area of the bubble. In the former case the potential influence is within experimental error, while in the latter the surface tension at the disk-bubble-water interface constrains movement along its periphery and any propagating surface deformations (waves and instabilities) that may cross the central region. Nevertheless, we observed both vortex shedding and oscillatory motions. The experimental conditions are summarized in Fig. 2(*a*).

Regarding the methodology of our DPIV system, for lack of space we refer the reader to Sakakibara et al. and additionally, Adrian (1986). We performed cross-correlation analysis of two consecutive digitized images of particles moving with the flow. The point-to-point (particle pixel) correlation with the highest, and next two highest coefficients were noted, with the initial vector drawn based on the highest coefficient. Subsequently, the calculated vectors were checked for directional consistency with the "average" vector of its neighbors. Any inconsistent vectors were replaced with the vector corresponding to the second or third highest correlation coefficient. Any remaining inconsistent vectors were recalculated with an enlarged reference matrix. With the so-described analysis method, the calculated error in magnitude (of velocity) with respect to $U_o = 24.5$ cm/s as reference was ± 3.4 percent. In other words, the error in magnitude corresponds to ±8.3 mm/s. In terms of the total number of vectors, typically 245 in the figures shown, there were 27 "inconsistent" vectors (directional inconsistency) which upon recalculation were reduced to 15 possible error vectors (6.1 percent).

Results

Figure 2 also shows typical images of, (*b*) the tracer particles for DPIV/LIF and (*c*) the IST images (negative) of the bubble pair in 3 representative positions. We note that in (*b*), the tracer particles in the wake and a partial outline of the bubble boundaries are visible. Note that even with LIF, there are "white-out" regions (intensity saturation), and also the laser-sheet entering from the left cannot illuminate the regions in-between the bubbles and to the far right. In (*c*) each bubble gyrates such that the bubble pair can be oriented in opposite

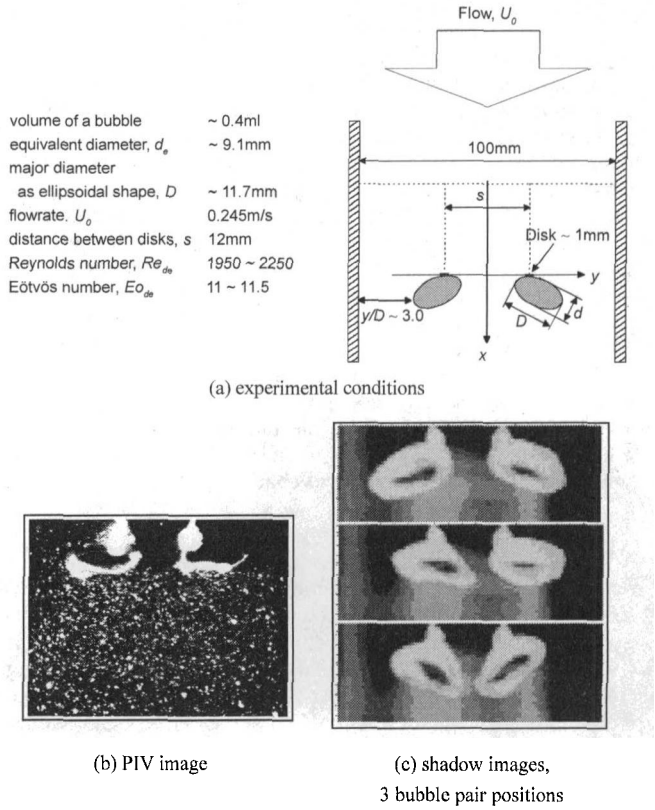

Fig. 2 (*a*) Schematic of experimental conditions and ranges. (*b*) Typical shadow image of the bubble pair. (*c*) Typical PIV snapshot around the bubble pair.

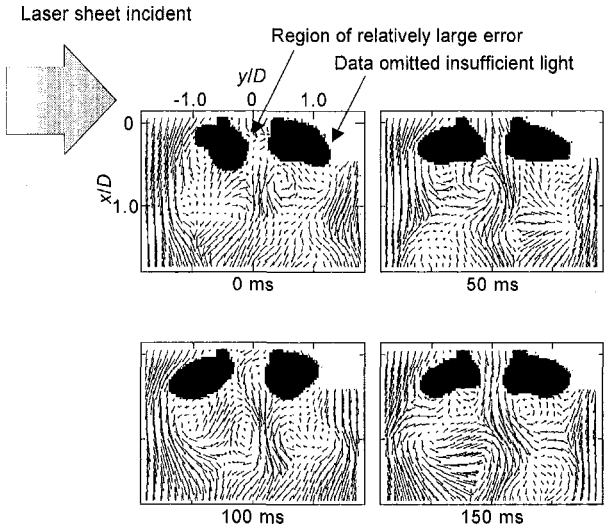

Fig. 3 Sequence in time of measured vector flow field

directions (top) as depicted, in the same direction (bottom) and anywhere in-between (middle). The black region in the background represents part of the square array of LED elements. The square frame represents an area of approximately 30×20 mm^2. In the wake however, there were sufficient number of points from which we could calculate the velocity vectors. Based on these and similar images, 1000 images in total, we extracted our velocity information. Other velocity-related information were subsequently calculated.

Thus in Fig. 3 we show a representative time sequence of four DPIV/LIF-derived vector field plots with the shadow-image superimposed. The size of the vectors have been enlarged for clarity. Note that behind the bubbles, there are identifiable vortices that are shed. Equally, there is a "jet-like" flow in-between the bubbles. It is evident, even for this sequence that the vortex shedding interacts with the "jet-like" flow. Because the illumination in-between the bubbles ($x/D \sim 0$) and at the far right differ from the rest of the field, these regions have "relatively large error" or no vectors are shown, respectively.

Next in Figs. 4 and 5 we show the average velocity profiles U/U_0 and V/U_0 at selected downstream locations, x/D, where U_0 is the average velocity at the entrance. One can see that U/U_0 is essentially a composite of a velocity defect behind each bubble, with a "jet-like" region in between. For V/U_0, due in part to the vortices in its near-wake, the profile is not as prominent as U/U_0 until $x/D > 0.68$, which in fact approximately defines the axial extent of the near-wake. Note the difference in velocity scales shown. Beyond $x/D = 0.68$, the V/U_0 profile is symmetric about the centerline, but inverted (anti-symmetric). This correctly indicates that "on-average" a pair of oppositely circulating vortices is located behind each bubble. In Fig. 4 (to Fig. 10) the error bars at representative axial (x/D) and spanwise (y/D) locations represent the 95 percent confidence estimation consisting of the precision and bias limits. The precision limits has been estimated based on a student t-distribution method. The bias limit consists of a pixel resolution limit of our video image and estimate of the overall error resulting from a cross-correlation analysis of DPIV as mentioned above.

Analogously in Figs. 6 and 7 we plot u_{rms}/U_0 and v_{rms}/U_0 (rms = root-mean-square) versus y/D with x/D as parameter. We note that for $x/D < 0.89$, u_{rms}/U_0 depicts yet again the jet-like flow in-between the bubbles and that characteristically of the near-wake, which beyond (by $x/D \sim 1.5$) becomes quasi-constant. Equally, v_{rms}/U_0 profiles show symmetric near-wake flows, which tend toward uniformity except for the central region, beyond $x/D > 0.68$.

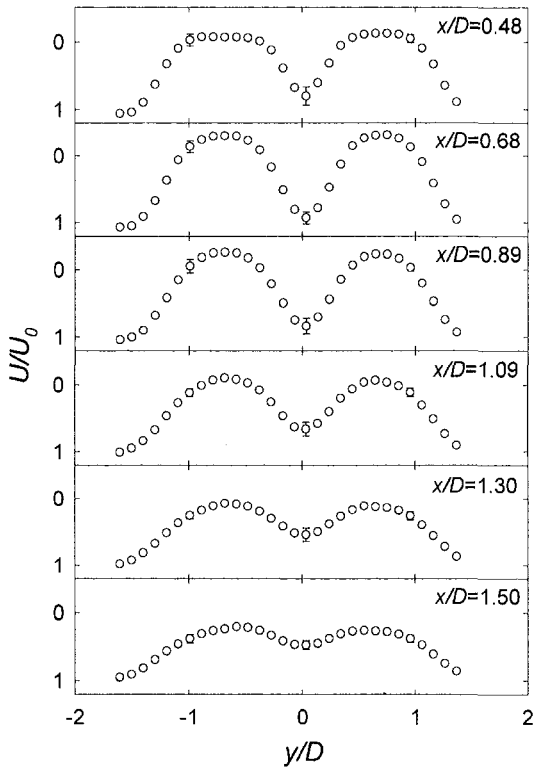

Fig. 4 Average vector, U/U_0, with downstream distance as parameter

In order to substantiate our characterization of the jet-like flow, we present in Fig. 8 a plot of two typical jet parameters versus axial distance, x/D, first the centerline decay velocity, $(U_0/U_{max} - U_{min})$ and the "jet" half-radius, $r_{1/2}$. In our case,

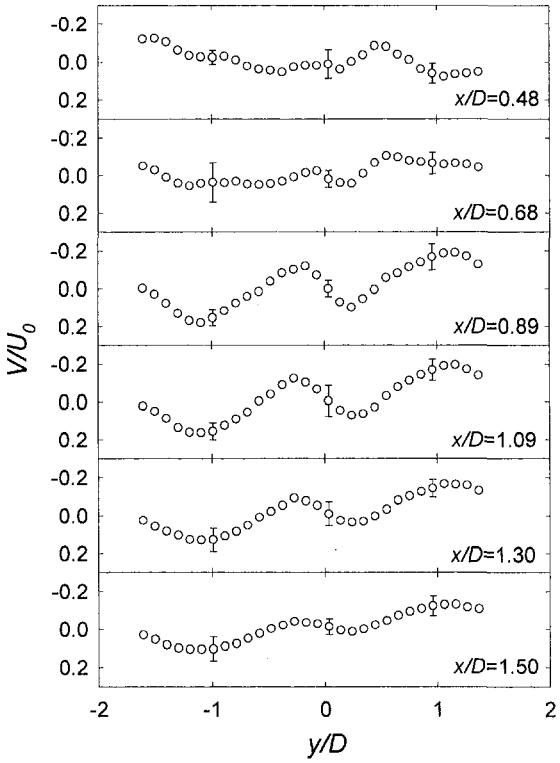

Fig. 5 Average velocity profile, V/U_0, with downstream distance as parameter

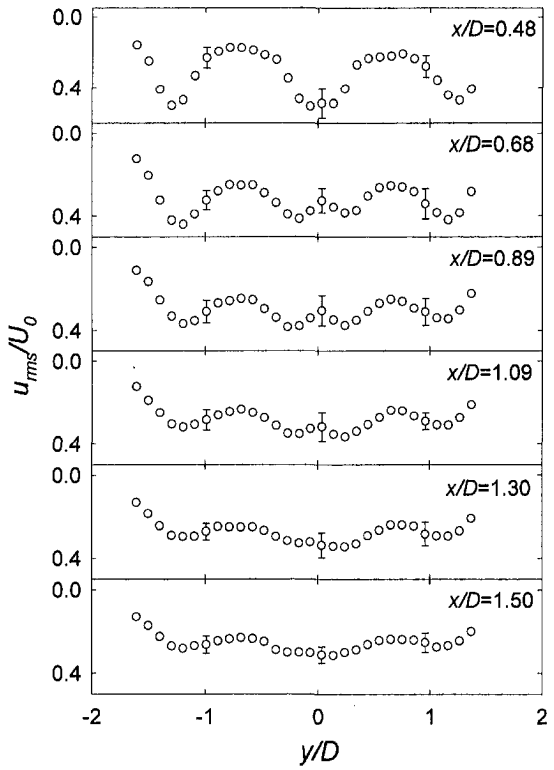

Fig. 6 Average root-mean-square velocity profile, u_{rms}/U_0, with downstream distance as parameter

we derived $(U_0/U_{max} - U_{min})$ by taking the maximum/minimum values of the velocity profile in the central region of Fig. 4.

Next in Figs. 9 and 10 we plot the normalized Reynolds-stress and turbulent kinetic energy (TKE) distributions respectively. We note that both quantities have been calculated from the velocity data. The TKE is here defined as $k = \frac{1}{2}(u^2 + 2v^2)/U_0^2$, such that v and w are assumed to be equivalent Note that the Reynolds-stress profile beyond $x/D > 0.48$ is approximately anti-symmetric. In each wake region, a gradient of similar magnitude appears, while a positive gradient of axially decreasing value appears in-between the bubbles. The TKE profile is similar to u_{rms}/U_0, which suggests a strong correlation between them; that is, energy in the near-wake is generated along the far edge of each bubble ($y/D \geq \pm 1$), and in the center region. The energy of the jet-like flow is however, redistributed uniformly by $x/D \sim 1.5$ (for $y/D \leq |1|$).

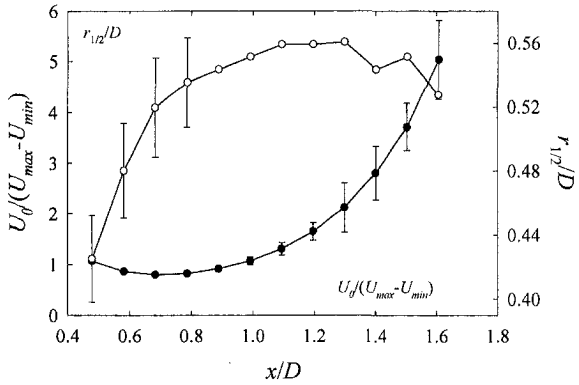

Fig. 8 Change in the centerline velocity (left) and half-radius (right) versus axial distance, x/D, of flow in the central region

Finally in Fig. 11 we show the average of the following quantities, that is: (a) the velocity vector field, (b) the vorticity isocontours, (c) the Reynolds-stress isocontours, (d) the TKE isocontours and lastly, (e) the production term isocontours of TKE. In (a) we have encircled, in solid line, the approximate extent of the vortical flow region behind each bubble. We then

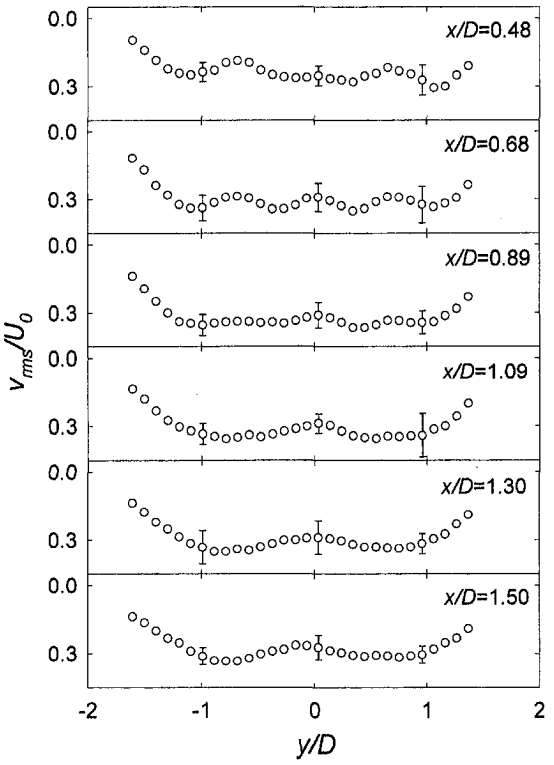

Fig. 7 Average root-mean-square velocity profile, v_{rms}/U_0, with downstream distance as parameter

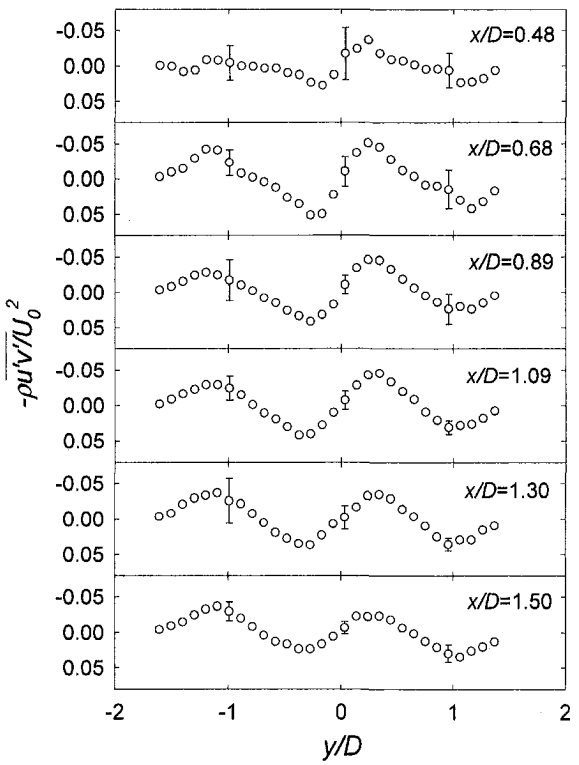

Fig. 9 Normalized Reynolds stress distribution for selected downstream locations

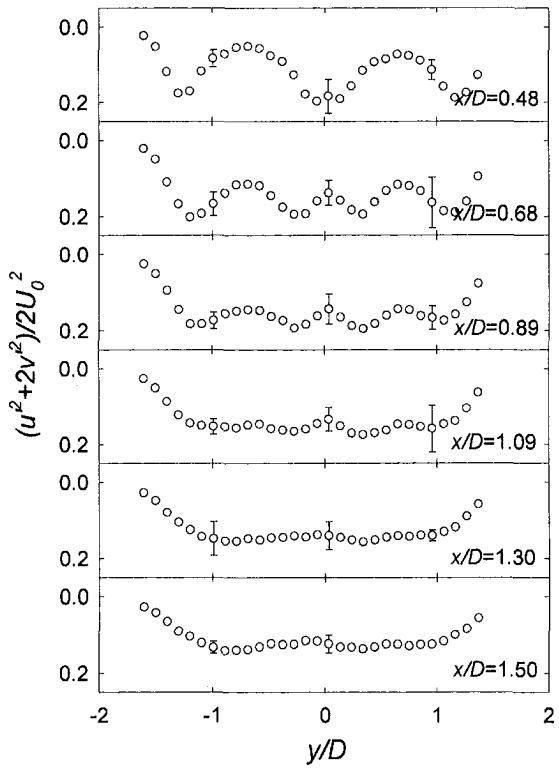

Fig. 10 Normalized turbulent kinetic energy (TKE) distribution for selected downstream locations

reproduce this in (*b*) so we semi-quantitatively note that besides the far left, right and center, vorticity gradients exist in the identified vortical flow regions. In addition, as expected, vorticity is generated along the flow separation points (to either side) of the bubble-liquid interface. When we then superimpose the relative maximum and minimum isocontours of vorticity onto the Re-stress isocontours, we see that beside the separation point, the peak isocontours of Re-stress and vorticity coincide. Otherwise, Re-stress isocontours are located axially downstream to either edge of each bubble. Note that the isocontours to either side of the vertical centerline are larger in magnitude. In (*d*) we again reproduce the vorticity isocontours, and in addition in (*e*) note in dotted line the vortical flow regions. The spatial congruence of the peak TKE and vorticity isocontours is evident in (*d*) and in particular in the central region of (*d*). There is a substantial production of TKE due to the interaction of the jet-like flow and vortex shedding mechanism.

Discussion

Our experimental results appear to fulfill much of our first objective; that is, the combined use of DPIV, LIF and IST enables one to identify both the moving shadow image of the bubble pair and to measure the flow field around it. The DPIV/LIF/IST technique does have its limitations and associated errors. First of all the gyrating bubble motion and the flow field are three-dimensional. However, the measured velocity field and shadow images are two-dimensional. These are limitations of our (2D) DPIV system and that in general of projected images, respectively. In fact, we cannot deny that the image of the bubble as taken from the front, and velocity field taken from the rear, may correspond to slightly different measurement planes, inspite of attention to center both the laser sheet and LED light source. This is an unavoidable physical limitation. As for the error associated with the velocity and shadow image, the DPIV error is 3.4 percent as stated, while the imaging error with respect to a known reference (measured cross-sectional area) was estimated at 4–5 percent. Further regarding the velocity vector data, the error in-between the bubbles and to the right of the right bubble, are regions of relatively larger error because the intensity of light is lacking (and different) in these regions,

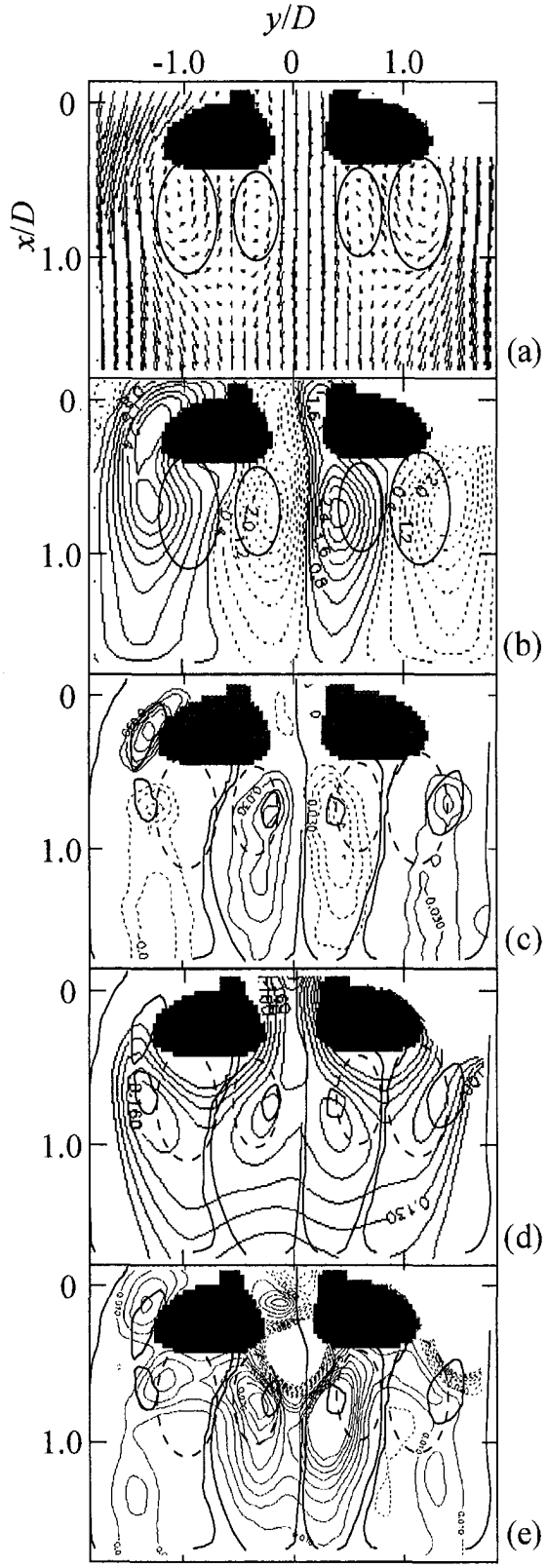

Fig. 11 (*a*) Average vector field, (*b*) vorticity contour, (*c*) Reynolds stress contour, (*d*) turbulent kinetic energy (TKE) contour, (*e*) TKE production

compared to the rest of the field. In Fig. 3 where the laser sheet enters from the left, the vectors in-between the bubbles are included, but those at the far right are excluded due to a lack of light, which led to a poor correlation of the few points in this region.

We next discuss aspects of the bubble motion and the flow field with which it interacts in order to familiarize the readers. The bubble pair under the configuration and flow conditions noted in Fig. 2(*a*) oscillate slightly out of phase with each other while attached to their small disks. The individual motions are similar to a single-bubble arrangement as previously reported by Tokuhiro et al. (1996). Thus the shadow images reveal instances (see Fig. 3) wherein the bubbles "faced" opposite directions (at 50, 150 ms), while at other instances approaching each other (at 0 ms), but never colliding nor coalescing. We estimated from images that the left and right bubbles oscillate individually in the range 4–6 Hz, while the frequency of joint motion was 4.5–5 Hz. Since the bubbles oscillate out of phase, the frequency of joint motion is here defined as the inverse of the period between recognizably similar bubble pair positions as viewed from video taken at 120 fps. In contrast, a single-bubble centered in the same channel oscillated at ~4.5 Hz. The observed oscillatory motion of the bubbles, considered singly, is consistent with flow regime maps based on the Reynolds and Eötvös numbers. Here the bubble Reynolds is based on the rise velocity (downward velocity U_0 in our case) and equivalent diameter of the bubble, d_e. The Eötvös number is based on d_e and thermophysical properties of water taken at 15° and 20°C. We estimate the Re- and Eo-numbers to be, $1800 < \mathrm{Re}_D < 2250$ and $11 < \mathrm{Eo} < 11.5$. Thus, according to Clift et al. (1978) the bubble is in the "wobbling" regime as we confirmed; that is, of relevance to the discussions to follow, the tail of the bubble(s) wobble/oscillate as the bubble rises. In addition, consistent with Fan and Tsuchiya (1990), the wake behind the bubble is turbulent. We also confirmed the validity of our observation regarding the bubbles' oscillation frequency and quoted Re-number by estimating the Strouhal (Sr) number. Using Re_D, we see from a plot of past experimental data (Fan and Tsuchiya, 1990), that our corresponding Sr-number for vortex shedding should be 0.15–0.20, in a plot of Sr versus Re-number (for an oscillating single bubble). An equally separate calculation based on an estimate of the bubble's oscillation frequency, from video taken at 120 fps, yields $0.16 < \mathrm{Sr} < 0.245$. Thus the ranges approximately agree.

Having described the out-of-phase oscillatory motion of the bubble pair, we describe at this point, the apparent limitation and scope of the data, with respect to investigating the turbulent wake flow. The DPIV-based vector data such as that shown in Fig. 3, was collected at a normal video framing rate of 27 fps (frames-per-second) and does not contain the time resolution necessary to elucidate the step-by-step, spatio-temporal nature of the vortex shedding mechanism itself. For this reason we mainly present data averaged over 1000 images and equally vector field plots. In this respect, we also assume for brevity some familiarity of the reader with the vortex shedding mechanism of an oscillating bubble, which we summarize as: 1) generation of vorticity near the flow separation points, along the edge of the gas-liquid interface, 2) the conveyance of this vorticity along the nearby free shear layer, 3) the formation of circular vortices (two-dimensionally) or vortex ring (three-dimensionally) in the wake, and 4) eventual shedding of vortices by an entrained cross-flow. Additional details are given in Fan and Tsuchiya. The extension of this much investigated wake flow behind a single bubble to two, side-by-side is on the whole as one expects; that is, there are two wake flows (vortices), slightly out-of-phase as described. Additionally, there is along the central region a spatio-temporal "jet-like" flow, in-between and dividing the wake of the bubbles. Both these features can be seen vectorally in Fig. 3 and via profiles in Fig. 4–7. In particular, the axial change in the profile of the central region, when expressed in terms of traditional jet parameters such as the decay of the centerline velocity and half-width radius is as shown in Fig. 8. In plotting $(U_0/U_{\max} - U_{\min})$ and $r_{1/2}$ versus x/D in Fig. 8, we see that due to the jet's interaction with the vortex shedding to either sides, both these parameters increase faster than a simple jet. Recall that in a simple jet (Cheremisinoff, 1986), beyond the jet's potential core length, both the centerline decay velocity $(U_0/U_{\mathrm{center,max}})$ and half-radius $(r_{1/2}/D)$ increase linearly over, typically 10–15 diameters. The relevant length scale in our case however, is sensibly the 1 to 2 diameters in the wake as shown in the figure. We also note that the half-radius, in contrast to a jet, increases rapidly to a quasi-constant value. Thus the jet-like flow originating from in-between the bubbles is shortly changed, within 1–1.5 diameters into the bubbles' wakes, by the shedding mechanism to either side.

So Figs. 4–7 reflect our sense derived from Fig. 3, that the velocity information in a two bubble system essentially observes the axi- and anti-symmetry measured by the authors of a single-bubble arrangement (Tokuhiro et al. 1996), but side-by-side. The derived quantities, Reynolds stress and turbulent kinetic energy (TKE) are of equal interest, since their relevance to multi-bubble systems is self-evident. We thus note that while Fig. 9 is anti-symmetric, the maxima in Fig. 10 are located in the center and along the far edge of each bubble ($y/D \sim \pm 1.25$). That is, the flow in-between the bubbles as seen from the distribution and gradient of the Re-stress clearly generates and transports vorticity, at $x/D \lesssim 0.68$, while the contribution outward to $y/D \sim \pm 1.25$ develops over $1.5D$. This is equally the case for TKE; that is, flow in-between the bubbles immediately generates TKE at $x/D \sim 0.48$, but contributes to uniformity in its distribution beyond $x/D \gtrsim 0.48$ or what can be described as the "near-wake". In contrast, along the outer regions of the bubbles, the contribution of TKE though evident at $x/D \sim 0.48$, redistributes itself over $x/D \sim 1.5$. These observations are further substantiated by Fig. 11(*a*)–(*e*), where we first encircle the vortical flow regions in (*a*) and subsequently reproduce this in (*b*)–(*e*). We also include in (*c*)–(*e*) the maximum and minimum isocontours of vorticity so that the correlation between vorticity, Re-stress, TKE and TKE production are semi-quantitatively established. In using this approach we consulted Cantwell and Coles (1983), who studied the flow in the turbulent wake of a (stationary) circular cylinder in air. Their data, taken with a rotating X-array hot-wire probe on a traversing mechanism, is roughly equivalent to the present work in terms of vector field plots, Re-stress and TKE contour plots. Cantwell and Coles argued that turbulence production is by vortex stretching near the saddle points in the flow field; that is, by stretching of small-scale vorticity oriented along the diverging separatices. A diverging separatix is a small region into which flow enters from opposite ends and exits out, normally (ideally) in two opposite directions. Fortunately in their work, the saddle points of the vector field are easily identified as there are only 4 saddle points located over 8 diameters of the wake. Of relevance here is the fact that TKE production has a maximum near these points.

Thus to begin we see in (*b*) that vorticity is generated at the separation points (at $x/D \sim 0.25$, $y/D \sim -1.25$) and at right and left, along the outer edge of each vortical region, behind each bubble. In (*c*) we see the congruence of the peak value of both vorticity and Re-stress values, within or on the outskirts of the vortical flow regions. Note that the spatial variation of the vortex shedding location in the wake, likely influenced by the jet-like flow in-between the bubbles, elongates the Re-stress distribution in the wake, and preferentially in terms of peak values along the central region. That is, as qualitatively supported by Fig. 3 and 11(*b*), vortex shedding and vorticity stretching/transport tends to occur in the central region. Consequently, we see in (*d*) from a congruence of the peak vorticity (thus Re-stress) and TKE isocontours that the vortex shedding

mechanism of each bubble, as characterized by the respective oscillatory motion of each bubble and its interaction with the jet-like flow in-between, localizes the peaks of the latter (TKE) symmetrically in the near-wake ($x/D \sim 0.75$, $y/D \sim |0.25|$ and $y/D \sim |1.25|$) of each bubble. In terms of the flow vectors, much of the energy is generated along the outer edges of each vortical region. As for production of TKE, the production of energy is mainly located about the central region as shown in (e), symmetrically distributed, located beyond $x/D > 0.5$ and bounded by $y/D < |0.5|$. In addition, there is TKE production along the separation points as expected, and a smaller source in the near-wake (far left and right), in the vicinity of the outer edge of the oscillating tail of each bubble. Additionally, in contrasting (d) and (e), we develop a sense of the contributions from advection (of energy by the mean flow), transport (of turbulence motion) and dissipation to the overall energy distribution. In particular, it appears that advection and transport contributes TKE along the right/left periphery ($y/D \sim |1.25|$), where TKE production is relatively smaller in magnitude. Interestingly enough, the relative lack of TKE production in a circular region, in-between the bubbles ($0.50 < x/D < 0.75$, $y/D < |0.25|$), indicates the strong influence of advection, transport and dissipation here.

Conclusions

Using DPIV/LIF/IST, an experimental investigation on the turbulent wake flow field of two adjacent and similarly-shaped air bubbles, suspended in downward flow of water, in a vertical channel was conducted. We discovered that first, the implemented measurement system could produce velocity data of "quality" equivalent to that previously used to study a single air bubble using the same DPIV/LIF/IST arrangement. We additionally confirmed that the oscillatory or gyrating motion of the each bubble was consistent with the Reynolds, Eötvös and Strouhals numbers, under the given experimental conditions. The bubbles did not oscillate in-phase, but slightly out of phase which produced a number of interesting velocity-derived quantities such as distributions of average velocity, rms-velocity, vorticity, Reynolds stress, turbulent kinetic energy (TKE) and production of TKE. The flow in the wake can be described as an interaction of a vortex shedding mechanism from each bubble, a turbulence generating oscillatory motion and a "jet-like" flow in-between the bubble pair influential in the near-wake ($x/D < 0.5$). The jet-like trends, expressed in terms of the decay velocity and half-radius, were found to change over 1–2 diameters in the wake. As for the TKE distribution, energy is generated from flow along the separation points of each bubble and along the outer edge of the vortical flow regions, in the central region. In particular, most of the production of TKE originates in this central region, while advection and transport of TKE are stronger along the outer edge of the vortical flow regions of each bubble.

Acknowledgments

The first author expresses his sincere appreciation to Professors Maeda and Hishida for providing the opportunity to conduct this experiment and to Professor P. S. Lykoudis for his ideas on the experimental techniques of relevance to this experiment. The first author also expresses his gratitude to Mr. Maekawa and Ms. Fujiwara for conducting the experiment and assisting in the data analysis.

References

Adrian, R. J., 1986, "Multi-Point Optical Measurements of Simultaneous Vectors in Unsteady Flow—A Review," *International Journal of Heat & Fluid Flow,* Vol. 7, pp. 127–145.

Cantwell, B. and Coles, D., 1983 "An Experimental Study of Entrainment and Transport in the Turbulent Near Wake of a Circular Cylinder," *Journal of Fluid Mechanics,* Vol. 136, pp. 321–374.

Cheremisinoff, N. P., Ed., 1986, *Encyclopedia of Fluid Mechanics, Vol. 2,* Gulf Publishing Houston, Texas.

Clift, R., Grace, J. R. and Weber, M. E., 1978, *Bubbles, Drops, and Particles,* Academic Press, New York.

Davidson, J. F., and Kirk, F. A., 1969 "Holding a Bubble Fixed by Downward Flow," *Chemical Engineering Science,* Vol. 24, pp. 1529–1530.

Fan, L.-S. and Tsuchiya, K., 1990, *Bubble Wake Dynamics in Liquids and Liquid-Solid Suspensions,* Butterworth-Heinemann Series in Chemical Engineering, Boston (USA)

Hassan, Y. A., Philip, O. G., and Schmidl, W. D., 1993, "Bubble Collapse Velocity Measurements Using a Particle Image Velocimetry Technique with Fluorescent Tracers," *Experimental Numerical Flow Visualization,* ASME, FED-Vol. 172, pp. 85–92.

Kojima, E., Akehata, T., and Shirai, T., 1975, "Behavior of Single Air Bubbles Held Stationary in Down-Ward Flow," *Journal of Chemical Engineering of Japan,* Vol. 8, No. 2, pp. 108–113.

Levich, V. G., 1962, *Physicochemical Hydrodynamics,* Prentice-Hall, Englewood Cliffs, New Jersey (USA)

Moo-Young, M., Fulford, G., and Cheyne, I., 1971, "Bubble Motion Studies in a Countercurrent Flow Apparatus," *Industrial and Engineering Chemistry Fundamentals,* Vol. 10, No. 1, pp. 157–160.

Sakakibara, J., Hishida, K., and Maeda, M., 1993a, "Quantitative Visualization of Convective Heat Transfer Near the Stagnation Region of an Impinging Jet," *Experimental Numerical Flow Visualization,* ASME, FED-Vol. 172, pp. 93–99.

Sakakibara, J., Hishida, K. and Maeda, M., 1993b, "Measurement of Thermally Stratified Pipe Flow Using Image-Processing Techniques," *Experiments in Fluids,* Vol. 16, pp. 82–96.

A. Tokuhiro, M. Maekawa, K., Iizuka, K. Hishida, and M. Maeda, 1996, "The Effect of a Single Bubble on Turbulence Structure in Grid Turbulence Flow by Combined Shadow-Image and PIV Technique," *8th International Symposium on Applications of Laser Techniques to Fluid Mechanics,* Lisbon, Portugal, 8–11. July.

Study of Tip Vortex Cavitation Inception Using Navier-Stokes Computation and Bubble Dynamics Model

Chao-Tsung Hsiao[1]
Research Assistant.

Laura L. Pauley
Associate Professor.

Mechanical Engineering Department,
The Pennsylvania State University,
University Park, PA 16802-1412

The Rayleigh-Plesset bubble dynamics equation coupled with the bubble motion equation developed by Johnson and Hsieh was applied to study the real flow effects on the prediction of cavitation inception in tip vortex flows. A three-dimensional steady-state tip vortex flow obtained from a Reynolds-Averaged Navier-Stokes computation was used as a prescribed flow field through which the bubble was passively convected. A "window of opportunity" through which a candidate bubble must pass in order to be drawn into the tip-vortex core and cavitate was determined for different initial bubble sizes. It was found that bubbles with larger initial size can be entrained into the tip-vortex core from a larger window size and also had a higher cavitation inception number.

1 Introduction

The type of cavitation known as hydrodynamic cavitation can take many physical forms, or geometric shapes, at inception. There are two primary groups, traveling cavitation (traveling bubble; bubble ring; travelling patch) and attached cavitation (sheet; band; fixed-patch; spot). For such devices as propellers, several forms of cavitation may appear simultaneously due to the different flow characteristics on the pressure and suction sides of the blades and the quite different flow over the tip. The three-dimensional flow around the blade tips of propellers produces an additional form named *tip vortex cavitation,* which is related to the travelling bubble form of cavitation (Billet and Holl, 1979). Of particular interest is cavitation in the trailing vortex system since the tip vortex cavitation is associated with inboard noise generation and induced hull vibrations and in some cases is the first type of cavitation to appear. It may also be responsible for erosion problems in certain propulsive configurations such as ducted propellers.

In general, flows with cavitation are characterized by the cavitation number σ which is defined as

$$\sigma = \frac{p_\infty - p_v}{1/2\rho U_\infty^2}, \tag{1}$$

with p_∞ and U_∞ being the freestream pressure and velocity, respectively, ρ the liquid density, and p_v the vapor pressure at the bulk temperature. The cavitation inception number, σ_i, describes the conditions at the onset of cavitation when approached from noncavitating flow at higher p_∞. Engineering predictions of cavitation inception for a single phase flow are often made by equating the cavitation inception number to the negative of local minimum pressure coefficient. The onset of the cavitation, however, has been observed to occur at pressures above and below the vapor pressure. The deviation from the ideal cavitation number is caused by some real fluid effects such as the random pressure fluctuation, bubble/flow interaction, bubble deformation, nucleus size spectra, and distribution. These real flow effects always complicate the inception process and the phenomenon is governed by intractable mathematics rich in nonlinear behavior. The complexity of the problem has led various studies to neglect one or more of the factors in play, and therefore to only investigate the influence of a limited set of parameters.

Two different approaches have been used to study the dynamics of traveling bubble cavitation inception in vortex flows. In one approach (Bovis, 1980; Chahine et al., 1995; Sarkar et al., 1995) the underlying flow is described by inviscid potential flow but important phenomena such as the modification of the vortex flow by the presence of the bubble and the shape deformation of the bubble are considered. The second approach (Johnson and Hsieh, 1966; Latorre, 1982; Ligneul and Latorre, 1989) considers real fluid effects to determine the bubble motion equation, but neglects the bubble shape deformation and modification of the flow caused by the bubble. Since the bubble/vortex interaction is significant only when the ratio of bubble size to vortex-core size is large, the second approach can offer good approximation for small ratio of bubble size to vortex core size. For tip vortex cavitation inception, the traveling bubble is usually small relative to the vortex core. The second approach is, therefore, adopted in the present study.

In the second approach, the gas nucleus is assumed to remain spherical during volume variation so that a relatively simple bubble dynamics model known as the Rayleigh-Plesset equation (Plesset, 1948) can be applied to determine the bubble volume variation with time. Since tip vortex cavitation inception is related to the traveling bubble form of cavitation, further assumption of discrete and noninteracting nuclei can be made for computing bubble motion. This assumption allows the adoption of the nucleus motion equation of Johnson and Hsieh (1966) coupled with the Rayleigh-Plesset equation to determine the bubble trajectory in the tip vortex flow and the influence of the nucleus size and distribution on cavitation inception. Latorre (1982) successfully applied these two equations to deduce noise emission in the tip-vortex cavitation. However, the tip vortex flow field was given by using a simple Rankine vortex model. To realistically simulate the bubble moving around the tip vortex flow, the tip-vortex flow over a finite-span hydrofoil calculated from the Reynolds-Averaged Navier-Stokes (RANS) equations with a turbulence model is used as the prescribed flow field in the present study. Although the random pressure fluctuations are expected to influence the bubble trajectory, the bubble tra-

[1] Currently at Dynaflow Inc in Fulton, MD.

Contributed by the Fluids Engineering Division for publication in the JOURNAL OF FLUIDS ENGINEERING. Manuscript received by the Fluids Engineering Division May 5, 1997; revised manuscript received September 21, 1998. Associate Technical Editor: M. M. Sindir.

jectory in the mean flow will still be a good approximation of the ensemble-averaged trajectory in the actual time-varying turbulent flow.

2 Numerical Method

2.1 Navier-Stokes Computation. In the present study, the three-dimensional incompressible Navier-Stokes flow solver, INS3D-UP, developed by Rogers et al. (1991) is adopted to solve the tip vortex flow over a finite-span hydrofoil. The INS3D-UP code is based on the artificial-compressibility method in which a time derivative of pressure is added to the continuity equation to couple it with the momentum equations. As a consequence, a hyperbolic system of equations is formed and can be solved using a time-marching scheme. The spatial differencing of the convective terms uses a fifth-order accurate flux-difference splitting based on Roe's method (1981). A second-order central differencing is used for the viscous terms. The resulting system of algebraic equations is solved by a Gauss-Seidel line-relaxation method in which several line-relaxation sweeps through the computational domain are performed before the solution is updated at the new pseudo-time step. This method can be marched in pseudo-time to reach a steady-state solution where a divergence-free velocity field is obtained. In the present study, the steady-state solution is acquired when the maximum divergence of velocity is less than 10^{-3}.

The INS3D-UP code is also accompanied by the Baldwin-Barth one-equation turbulence model (Baldwin and Barth, 1990) which is derived from a simplified form of the standard $k - \epsilon$ equation. This model is not only simpler than the two-equation model, but also eliminates the need to define the turbulent mixing length which is required in the Baldwin-Lomax algebraic model.

Since the multiblock scheme (one block for suction side and one block for pressure side) is used in the present study, there are two types of boundaries where conditions have to be specified: 1) the physical boundaries, such as inflow, outflow, far field, and solid surfaces; and 2) the block-interface boundaries across which all flow quantities must be continuous. For the physical boundaries, freestream velocity and pressure are specified at the far-field boundary and the inflow boundary while the first-order extrapolation for all variables is used at the outflow boundary. On the solid hydrofoil surface, no-slip flow and zero normal pressure gradient conditions are used. At the root section a symmetric boundary condition is applied. For the block-interface boundaries, a semi-implicit method of passing the boundary conditions between blocks can be easily accomplished by updating the velocities and pressure at the block-interface after each Gauss-Seidel line-relaxation sweep of a block. The next sweep through the other block would utilize the updated values at the common block interface.

2.2 Bubble Dynamics Model. By considering all forces acting on a spherical particle with radius R, the dimensional vector form of the motion equation (Maxey and Riley, 1983) is written as

$$\rho_b V_b \frac{d\vec{U}_b}{dt} = V_b(\rho_b - \rho)\vec{g} - V_b \nabla p + \frac{1}{2}\rho C_D A_b(\vec{U} - \vec{U}_b)|\vec{U} - \vec{U}_b| + \frac{1}{2}\rho V_b\left(\frac{D\vec{U}}{Dt} - \frac{d\vec{U}_b}{dt}\right) + 6A_b\sqrt{\frac{\rho\mu}{\pi}}\int_0^t \frac{\left(\frac{D\vec{U}}{D\tau} - \frac{d\vec{U}_b}{d\tau}\right)}{\sqrt{t-\tau}}\,d\tau \quad (2)$$

where parameters with the subscript b are related to the bubble/particle and those without the subscript b are related to the carrying fluid. V_b and A_b are the bubble volume and projected area, which are equal to $4/3\pi R^3$ and πR^2, respectively. The bubble drag coefficient C_D in Eq. (2) can be determined by using the empirical equation of Haberman and Morton (1953):

$$C_D = \frac{24}{\mathrm{Re}_b}(1 + 0.197\,\mathrm{Re}_b^{0.63} + 2.6 \times 10^{-4}\,\mathrm{Re}_b^{1.38}) \quad (3)$$

where the bubble Reynolds number is defined as

$$\mathrm{Re}_b = \frac{2R|\vec{U} - \vec{U}_b|}{\nu} \quad (4)$$

The first term on the right-hand side of Eq. (2) is the buoyant force. The second term is due to the pressure gradient in the fluid surrounding the particle. The third term is the drag force. The fourth term is the force to accelerate the virtual "added mass" of the particle relative to the ambient fluid. The last term, called the Basset term, takes into account the effect of the deviation in flow pattern from steady state. Equation (2), however, does not include the lift force which is caused by the particle spin.

Since Eq. (2) is developed to describe the motion of a solid particle in the flow, one may need to adapt the equation for a gas bubble. For a gas bubble the mass of the gas inside the bubble can be neglected since it is small compared to the added mass of the fluid. To describe the motion of a gas bubble, however, one may need to take into account the force due to the bubble volume variation. Johnson and Hsieh (1966) added an additional term to consider the bubble volume variation but the Basset term was neglected. An analysis by Morrison and Stewart (1976) shows that the Basset term depends on the time rate of change of the relative velocity. For flows in which the frequency of the oscillatory motion of the carrier fluid is small the Basset term can be neglected. Since the prescribed flow field for carrying the bubble was computed from the RANS equations, random turbulent fluctuation has been eliminated. Although the bubble will still experience unsteady velocities when the bubble travels through the steady flow field in time, the rate of change of the relative velocity is small. Furthermore, Maxey and Riley (1983) have presented order of magnitude estimates for various forces acting on the bubble. They concluded that once the motion is established, the Basset history term was only of secondary order when compared to other forces. Since the bubble will be released at the local water velocity, the Basset term is neglected in the present study.

By adding an additional term to consider the bubble volume variation, neglecting the Basset term, and using the Euler equation for relating the local pressure gradient to the acceleration of the fluid elements, Eq. (2) can be rearranged as

$$\frac{d\vec{U}_b}{dt} = -2\vec{g} - \frac{3}{\rho}\nabla p + \frac{3}{4}\frac{C_D}{R}(\vec{U} - \vec{U}_b)|\vec{U} - \vec{U}_b| + \frac{3}{R}(\vec{U} - \vec{U}_b)\frac{dR}{dt} \quad (5)$$

Equation (5) is the equation given by Johnson and Hsieh (1966) except that they omitted the buoyant term. The last term of the right-hand side in Eq. (5) is the additional term related to the bubble volume variation.

To determine the bubble volume variation with time, the Rayleigh-Plesset equation given by Plesset (1948) is used:

$$R\frac{d^2R}{dt^2} + \frac{3}{2}\left(\frac{dR}{dt}\right)^2 = \frac{1}{\rho}\left[p_v + p_{go}\left(\frac{R_0}{R}\right)^{3k} - p - \frac{2S}{R} - \frac{4\mu}{R}\frac{dR}{dt}\right] \quad (6)$$

where p_{go} is the initial gas pressure inside the bubble with k the polytropic gas constant ($k = 1$ for isothermal behavior), p is the ambient pressure local to the bubble, and S is the surface tension. The Rayleigh-Plesset equation is derived with the assumptions of liquid incompressibility and spherical bubble variation. The bubble size grows principally in response to gaseous expansion and to an increase in the vaporous mass within the bubble. The pressure within the bubble is considered to be the sum of gas and vapor pressure with the assumptions of polytropic gas and equilibrium vaporization process.

To determine the bubble motion and its volume variation, the Runge-Kutta fourth-order scheme is applied to integrate Eqs. (5) and (6) through time. The effect of the underlying flow is to produce a prescribed pressure field through which the bubble is passively convected. The flow field computed from the RANS equations is applied to provide the ambient pressure and velocities local to the bubble. The numerical solution of the RANS equations, however, can only offer the result at grid points. To obtain the values of pressure and velocities at an any specified point (x, y, z) in the computational domain, one needs to interpolate the values from the solution at the grid points. The three-dimensional linear interpolation scheme as described by Thompson et al. (1985) is applied in the present study. Computations of the bubble trajectory were conducted using the RANS solution on the primary grid (1.2 million grid points) and a higher resolution grid (2.2 million grid points). Since only slight differences were found for the bubble trajectories produced by the two grids, the primary grid was used for all results presented here.

3 Results and Discussion

3.1 3D Steady-State Tip Vortex Flow. In the present study, a rectangular hydrofoil having a NACA 0015 cross section with a chord length $c = 0.52$ m and an aspect ratio (based on semi-span) $Ar = 3$ is considered. For the Navier-Stokes computation, the present study uses an H-H type grid which contains $135 \times 91 \times 61$ for suction side and $135 \times 91 \times 41$ for pressure side in the streamwise, spanwise and normal direction respectively. In this grid, the tip-vortex core includes at least 17 grid points in the crosswise direction and 28 grid points in the spanwise direction. An extensive grid-independence study and validation of numerical solution with experimental data were conducted by Hsiao and Pauley (1998). It was shown that the tip vortex flow was well predicted in the near-field region, where cavitation inception occurs although over-diffusive and dissipative errors were found far downstream. The comparison of the tangential and axial velocity components across the tip-vortex core between the numerical solution and experimental data (McAlister and Takahashi, 1991) at $x/c = 1.1$ for $\mathrm{Re} = 1.5 \times 10^6$ and $\alpha = 12°$ is shown in Fig. 1. The tip vortex can be visualized by creating particle traces near the tip region as shown in Fig. 2.

3.2 Bubble Trajectory. For computation of bubble dynamics and motion equations, all water properties, the density ($\rho = 998$ kg/m^3), viscosity ($\mu = 0.001$ kg/ms), surface tension ($S = 0.0728$ N/m), and the vapor pressure ($p_v = 2337$ Pa), are defined at 20°C. According to previous experimental data collected by Billet (1984), the nucleus size measured in different water tunnels and in the ocean ranges from several microns to 200 μm. The initial bubble size used in the present study will therefore be within this range. Since the size of the tip-vortex core in the near-field region is about 30 mm for the current case (measured from peak to peak in Fig. 1.a), the ratio of bubble size to vortex-core size is very small and neglecting bubble/vortex interaction is justified.

In a practical situation, various bubble sizes can be located at any position in the free stream. When determining the conditions for incipient cavitation, however, we are interested only in the initial positions which will lead the bubble along its trajectory to the minimum pressure region.

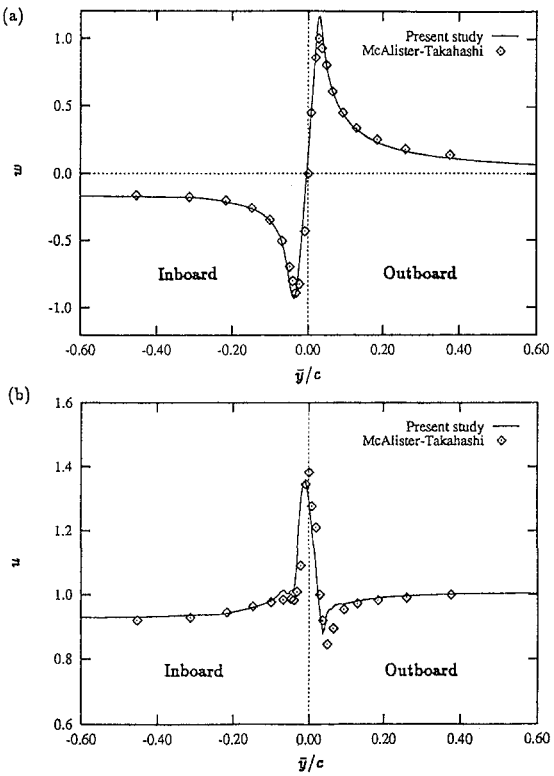

Fig. 1 Comparison of the vertical and axial velocity components across the tip-vortex core at $x/c = 1.1$ for $\alpha = 12°$ and $\mathrm{Re} = 1.5 \times 10^6$ (Hsiao and Pauley, 1998)

In studying the influence of initial bubble size on its trajectory for a two-dimensional half body, Johnson and Hsieh (1966) found a "screening" process in which the pressure gradient field ahead of the leading edge expelled larger sized bubbles and only allowed smaller sized bubbles to approach the body surface. Since the minimum pressure was located on the body surface, only bubbles smaller than a certain size can encounter the minimum pressure in the flow field. Such a screening process, however, may not occur in the three-dimensional tip-vortex flow. Maines and Arndt (1993) suggested that there was a "window" through which a candidate bubble must pass in order to be drawn into the tip-vortex core and cavitate but they did not measure enough data to have a reliable statistical mean. Furthermore, it is expected that the "window of opportunity" will be different sizes for different initial bubble sizes.

To better understand the window of opportunity, bubbles with different initial sizes are released ahead of the hydrofoil. In the present study, a streamwise location ahead of the hydrofoil leading edge is specified for releasing bubbles (see Fig. 3). Ideally, this streamwise location should be located at infinity ahead of the hydrofoil. Far upstream of the hydrofoil, however, the pressure gradient produced by the hydrofoil has negligible effect on the bubble trajectory and bubble size. The bubble will remain its original size and virtually follow the streamline if no external force (such as the buoyant force) is present. To save computational time, the initial streamwise location is chosen at a place where the pressure gradient can be neglected. To determine this streamwise location a bubble ($R_0 = 100$ μm) is released along a known streamline far upstream of the hydrofoil leading edge. It was found that for $x/c \leq -0.1$ the bubble retains its original size and virtually follows the streamline. It should be noted that the buoyant force is not included in this calculation.

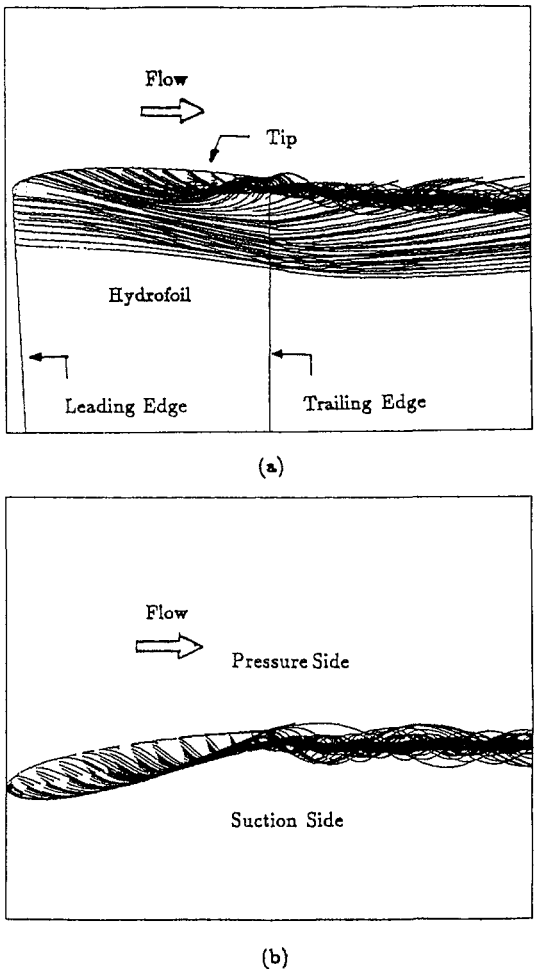

Fig. 2 The tip vortex flow over a finite-span hydrofoil *a*) view in $x - y$ plane, *b*) in $x - z$ plane for $\alpha = 12°$ and Re = 1.5×10^6 (Hsiao and Pauley, 1998)

For a specified initial bubble size, the window of opportunity is determined by releasing bubbles at prescribed matrix points on the $y - z$ plane at $x/c = -0.1$. Two different initial bubble sizes, $R_0 = 50$ and 100 μm, are applied to investigate the influence of the initial bubble size on the window of opportunity. Usually, these prescribed matrix points are established based on trial and error. Inversely integrating the streamline from the minimum pressure location in the tip-vortex core back to the bubble release plane can offer approximate matrix points. Once a release point is found to lead the bubble to the tip-vortex core, other matrix points can be established by arranging them adjacent to that release point. More than 100 points are used to release bubbles in each case. All computations are made with a cavitation number $\sigma = 3.2$ at which no bubble will grow unstably through its trajectory. Each released bubble is tracked and the minimum pressure which the bubble experiences along its trajectory is recorded at the release point. It should be pointed out that if the bubble is entrained into the tip vortex, the bubble will encounter the minimum pressure along its trajectory in the tip vortex. Otherwise, the bubble may encounter its minimum pressure on the hydrofoil surface. Only release points which cause the bubble to be entrained to the tip vortex will therefore be considered here. Another consideration is that some release points will lead bubbles to collide with the hydrofoil due to the local pressure gradient. It is assumed that after collision the bubble trajectory will remain tangent to the hydrofoil surface as it moves past the hydrofoil. After collision, however, most bubbles will stop moving when they encounter a local minimum pressure on the hydrofoil surface because the fluid velocity is very small near the surface.

To produce the window of opportunity, matrix points which lead the bubble to encounter a negative minimum pressure coefficient along its trajectory larger than 3.0 are plotted as a contour with the encountered minimum pressure coefficient. Figures 4 and 5 show the contours on the release plane for two different initial bubble sizes. Matrix points whose streamlines pass

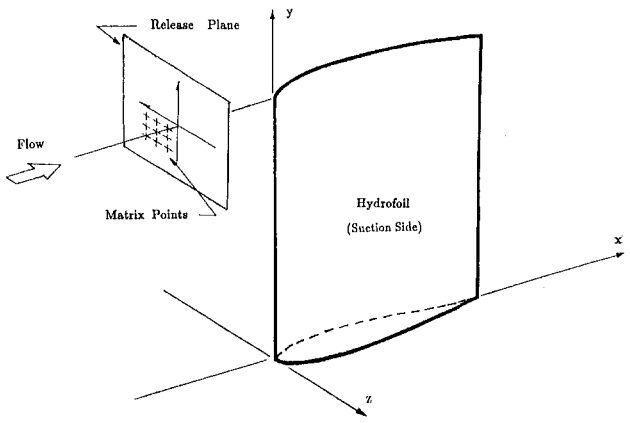

Fig. 3 Illustration of the bubble release plane and matrix points

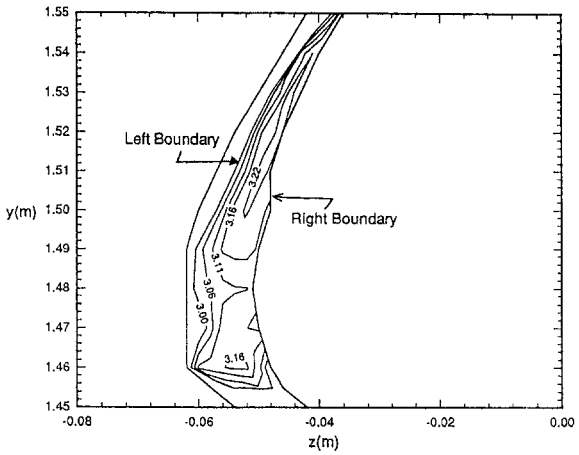

Fig. 4 The contour of the encountered negative minimum pressure coefficient larger than 3.0 for $R_o = 100$ μm at the release plane, $x/c = -0.1$

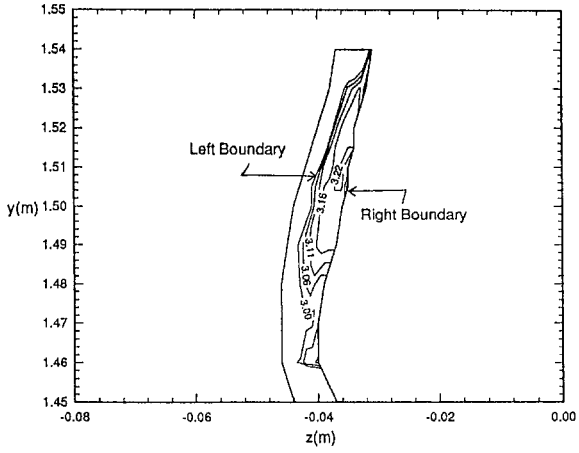

Fig. 5 The contour of the encountered negative minimum pressure coefficient larger than 3.0 for $R_o = 50$ μm at the release plane, $x/c = -0.1$

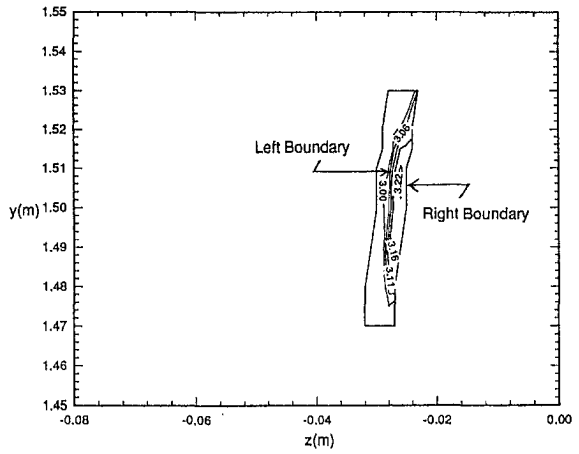

Fig. 6 The contour of the encountered negative minimum pressure coefficient larger than 3.0 for streamlines at the release plane, $x/c = -0.1$

through the negative pressure coefficient larger than 3.0 are also plotted as contours shown in Fig. 6. In each figure the right boundary of the contour is formed by those release points which cause the bubble to collide with the hydrofoil surface. It is seen that the shape of the window is strip-like. The window is always located below the tip leading edge, $(y, z) = (1.56, 0.0)$ m, and on the pressure side. As the initial bubble size is decreased, the window location and size will approach that of the streamline in which the bubble size can be assumed infinitely small. Comparison of Figs. 4–6 shows that larger bubbles are entrained into the tip-vortex core from a larger initial area. In other words, bubbles with larger initial size have more opportunities to enter the tip-vortex core and cavitate. This result is in contrast to the "screen" process found for two-dimensional flows by Johnson and Hsieh (1966). In their study larger sized bubbles were expelled by the adverse pressure gradient field ahead of the leading edge and consequently were prevented from approaching the body surface. In the current three-dimensional study, the adverse pressure gradient field ahead of the leading edge did not prevent larger sized bubbles from entering the tip vortex. The entrainment of large bubbles into the tip vortex was also observed by Maines and Arndt (1993).

For infinitesimal bubble size, the nucleus concentration within the tip-vortex core is the same as the incoming flow condition since the bubble actually follows the streamline. By comparison of Figs. 4–6, it can be seen that the window of opportunity increases with increasing bubble size. Since the region of the tip-vortex core with the negative pressure coefficient larger than 3.0 is the same for each case, it is concluded that for a finite bubble size the nucleus concentration within the tip vortex core is higher than the upstream conditions. The ratio of nucleus concentration in the tip-vortex core to the upstream incoming flow conditions increases with increasing bubble size.

3.3 Cavitation Inception. Before the cavitation inception number can be determined from the present bubble dynamics model, a consistent and adequate definition of the cavitation inception event is needed. Although many different definitions of cavitation inception have been suggested and applied by researchers, there are practical complications in determining the actual cavitation event. Using a scientific definition, cavitation inception can be defined as gaseous or vaporous cavitation. Rapid growth of a microbubble that remains stable is called gaseous cavitation while unstable growth is referred to as vaporous cavitation. From an engineering definition, cavitation inception is determined indirectly through visual or acoustic techniques, in which case a notion of events per unit time is often required. Cavitation inception is defined to occur when the measurement detects events above a predefined threshold. Another definition given in many laboratory studies (Ling et al., 1982) is actually directed towards gaseous traveling bubble dynamics. The cavitation inception event is usually defined by bubble growth to a threshold size.

Based on the different definitions described above, three different criteria will be used in the present study to determine the cavitation inception number. The first criterion given by Shen and Gowing (1986) assumes that the cavitation inception occurs when the bubble has grown to 10 times its original size. The cavitation inception number determined by this criterion is designated as σ_i^1. Instead of growing to 10 times its original size, the second criterion defines a certain size which can be detected through visual techniques in the experiment. In the present study, this size is set to 1 mm to determine σ_i^2. The third criterion corresponds to the stability of the numerical solution. For unstable bubble growth in the present numerical solution, the bubble size will become negative when the bubble reduces its size after passing the minimum pressure location. By decreasing the cavitation number in a series of simulations, the first cavitation number which causes the bubble to grow unstably is identified as σ_i^3.

It is known from experimental studies that the nucleus size spectrum is a determinant of the cavitation inception number. To numerically study the effect of nucleus size, cavitation inception is predicted for three different initial bubble sizes (R_0 = 50, 100, 200 μm). From the previous section, we know that different initial bubble sizes will influence the bubble trajectory. Bubbles with different initial sizes are therefore released at different positions so that they all pass through the minimum

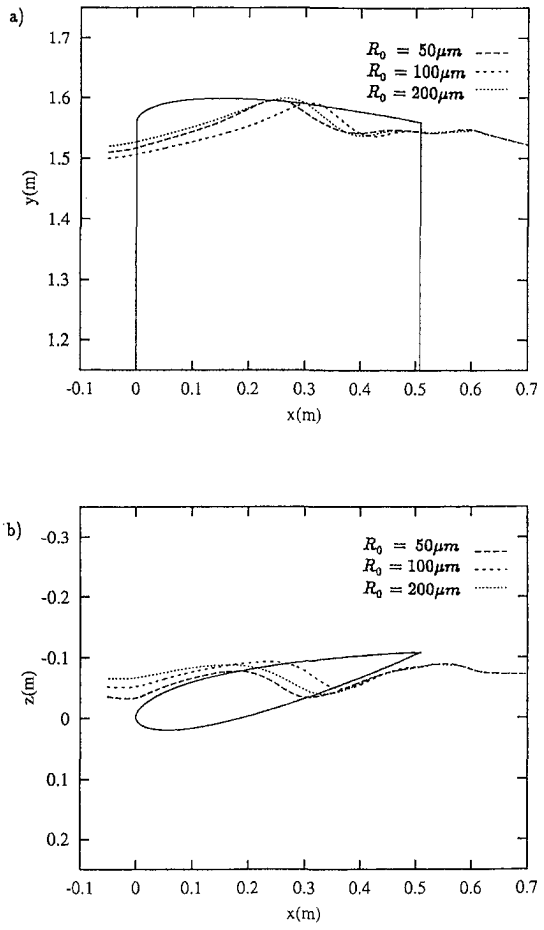

Fig. 7 Comparison of the bubble trajectories for different R_o a) $x - y$ plane, b) $x - z$ plane

Table 1 Cavitation inception number for R_0 = 50, 100, 200 μm

R_0	50 μm	100 μm	200 μm
σ_i^1	3.11	3.15	3.16
σ_i^2	3.10	3.15	3.22
σ_i^3	3.11	3.18	3.22

pressure location in the tip-vortex core. The bubble trajectories for different R_0 are shown in Fig. 7. It can be seen that bubbles with different initial sizes released at different positions are all entrained into the tip vortex and downstream have almost the same trajectory. For each case, the cavitation inception number is determined using the three different cavitation inception criteria. Although each definition of cavitation inception results in a different cavitation number, the effect on the bubble trajectory is negligible as long as the variation in σ is not very large. The cavitation inception numbers determined by applying the three different criteria are summarized in Table 1 for different sized nuclei.

It is seen that different definitions of the cavitation inception event lead to slightly different cavitation inception numbers. No matter which definition is applied, however, the cavitation inception number always increases with increasing initial bubble size. The cavitation inception numbers for the three different R_0 studied in the present study are all smaller than the negative minimum pressure coefficient ($-C_{p_{\min}} = 3.23$) in the tip-vortex core. Due to the bubble response time and brief passage of the bubble through the minimum pressure region, the minimum pressure is below the vapor pressure when cavitation inception occurs. The pressure field which bubbles experience along their trajectories for different R_0 is plotted in Fig. 8. It is seen that bubbles experience almost the same pressure field after crossing over the tip. In each case the bubble experiences two pressure peaks along its trajectory. The first peak is smaller and is encountered when the bubble crosses over the hydrofoil tip. The second peak is the minimum pressure in the tip-vortex core. It is also observed that delayed response of the bubble causes the location of the maximum bubble size (x = 0.517 m) to occur downstream of the minimum pressure location (x = 0.503 m).

To demonstrate the influence of the initial bubble size on the bubble growth rate near the cavitation location, the bubble size variations of each R_0 along their trajectories for different cavitation numbers are plotted in Figs. 9a–c. In each figure three different cavitation numbers are applied to produce an increase in bubble size of approximately 4, 11, and 23 times its original size. Although the bubble returns to its original size at lower cavitation numbers, the numerical solution is terminated due to the unstable recovery rate which causes the bubble size to be negative. A reasonable explanation for this result is that the bubble collapses after passing the minimum pressure location. Oscillation of the bubble size is observed when the bubble recovers from its maximum size at higher cavitation numbers. A stable and damping variation of the bubble size, however, is found after the bubble passes the minimum pressure location. Comparison of Figs. 9(a–c) also shows that as the initial bubble size is decreased, the bubble growth rate near the cavitation location becomes more sensitive to the cavitation number, i.e., for smaller initial bubble size a slight change in the cavitation number may cause a stable bubble growth to become unstable when the cavitation number is close to σ_i. It is also found that the bubble response time for adjusting its size to the pressure field is shorter for smaller R_0.

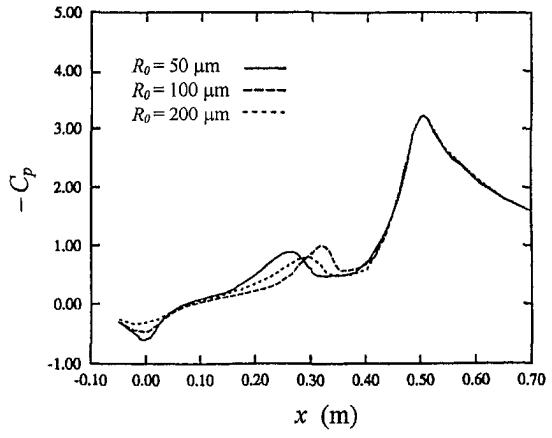

Fig. 8 The pressure field which bubbles experience along their trajectory for different R_0

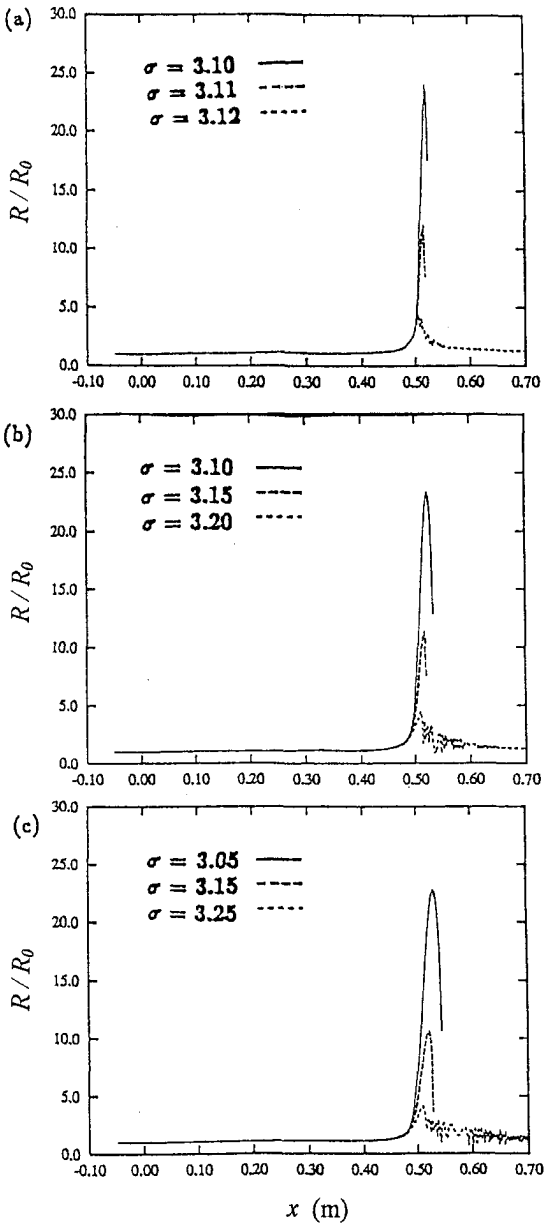

Fig. 9 The bubble size variation along the bubble trajectory at different cavitation numbers for a) R_o = 50 μm, b) R_o = 100 μm c) R_o = 200 μm

4 Conclusions

A window of opportunity through which a candidate bubble must pass in order to be drawn into the tip-vortex core and

cavitate was determined for different initial bubble sizes. Bubbles with larger initial size can be entrained into the tip-vortex core from a larger window size. This implies that the cavitation inception event will be easier to observe for a flow with larger nuclei.

Three different criteria were applied to determine the cavitation inception number in the present study. It was found that different definitions of the cavitation inception event lead to different cavitation inception numbers. No matter which definition was applied, however, the cavitation inception number was smaller than the negative minimum pressure coefficient in the tip-vortex core and increased with increasing initial bubble size.

The bubble growth rate near the cavitation location became more sensitive to the cavitation number as the initial bubble size was decreased, i.e., for smaller initial bubble size a slight change in the cavitation number may cause stable bubble growth to become unstable when the cavitation number is close to σ_i. It was also found that the size of initially smaller bubbles responded more quickly to pressure changes.

Acknowledgments

This research has been supported by the Office of Naval Research under contract N00014-90-J-1169 monitored by Dr. Edwin P. Rood. Computational facilities were provided by the NAVOCEANO Supercomputer Center and the CEWES High Performance Computing Center. These contributions are gratefully acknowledged.

References

Baldwin, B. S., and Barth, T. J., 1990, "A One-Equation Turbulence Transport Model for High Reynolds Number Wall-Bounded Flows," NASA TM 102847.

Billet, M. L., 1984, "Cavitation Nuclei Measurements," *International Symposium on Cavitation Inception,* ASME Winter Annual Meeting Dec. 9–14, FED-Vol. 16, pp. 33–42.

Billet, M. L., Holl, J. W., 1979, "Scale Effects on Viscous Types of Limited Cavitation," *International Symposium on Cavitation Inception,* New York, ASME Winter Annual Meeting Dec. 2–7, pp. 11–23.

Chahine, G. L., 1995, "Bubble Interaction with Vortices," *Vortex Flow* S. Green, ed., Kluwer Academic.

Haberman, W. L., and Morton, R. K., 1953, "An Experimental Investigation of the Drag and Shape of Air Bubbles Rising in Various Liquids," DTMB Report 802.

Hsiao, C.-T., and Pauley, L. L., 1998, "Numerical Study of the Steady-State Tip Vortex Flow Over a Finite-Span Hydrofoil," ASME JOURNAL OF FLUIDS ENGINEERING, Vol. 120, pp. 345–353.

Johnson, V. E., and Hsieh, T., 1966, "The Influence of the Trajectories of Gas Nuclei on Cavitation Inception," *Sixth Symposium on Naval Hydrodynamics,* pp. 163–179.

Latorre, R., 1982, "TVC Noise Envelope—An Approach to Tip Vortex Cavitation Noise Scaling," *Journal of Ship Research,* Vol. 26, No. 1, pp. 65–75.

Ling, S. C., Gowing, S., and Shen, Y. T., 1982, "The Role of Microbubbles on Cavitation Inception on Head Form," *Fourteenth Symposium on Naval Hydrodynamics,* Ann Arbor, MI.

Maines, B. H., and Arndt, R. E., 1993, "Bubble Dynamics of Cavitation Inception in a Wing Tip Vortex," *ASME Cavitation and Multiphase Flow Forum,* FED-Vol. 153, pp. 93–97.

Maxey, M. R., and Riley, J. J., 1983, "Equation of Motion for a Small Rigid Sphere in a Nonuniform Flow," *Physics of Fluids,* Vol. 26, No. 4, pp. 883–889.

McAlister, K. W., and Takahashi, R. K., 1991, "NACA0015 Wing Pressure and Trailing Vortex Measurements," NASA Technical Paper 3151.

Morrison, F. A., and Stewart, M. B., 1976, "Small Bubble Motion in an Accelerating Liquid," ASME *Journal of Applied Mechanics,* Vol. 43, pp. 399–403.

Plesset, M. S., 1948, "Dynamics of Cavitation Bubbles," ASME *Journal of Applied Mechanics,* Vol. 16, pp. 228–231.

Roe, P. L., 1981, "Approximate Riemann Solvers, Parameter Vectors, and Difference Schemes," *Journal of Computational Physics,* Vol. 43, pp. 357–372.

Sarkar, K., Duraiswami, R., and Chahine, G. L., 1995, "Three-Dimensional Numerical Simulation of Bubble-Vortical Flow Interaction," ASME *Cavitation and Multiphase Flow Forum,* FED-Vol. 210, pp. 135–143.

Shen, Y. T., and Gowing, S., 1986, "Cavitation Susceptibility of Ocean and Laboratory Water," Twenty First Meeting of American Towing Tank Conference, Washington, D.C.

Thompson, J. F., Warsi, Z. U. A., and Mastin, C. W., 1985, *Numerical Grid Generation,* North-Holland, New York, pp. 310–326.

Journal of Fluids Engineering

Technical Briefs

Finite Element Modeling of the Acoustic Wave Propagation From a Cavity Near a Free-Surface

M. Lee[1]

Introduction

The problem of the radiation and propagation of an acoustic pressure wave from a spherical cavity located near free-surface is solved exactly within the scope of the linear acoustic theory and the limit of series solution (Gorshkov et al., 1991). The effect of the free-surface reflection is taken into account using the image source method. However, it was difficult to get accurate results by retaining four terms of the infinite series in Legendre polynomials in the calculation. Due to the complexity of the solutions which involve combinations of modified Bessel functions and infinite system of algebraic equations, the use of numerical methods of higher accuracy and flexibility is needed to obtain the correct results. Herein, both solutions to full nonlinear Euler equations and to a scalar acoustic wave equation are obtained using finite element method for the case of an uniformly distributed Heaviside pressure function over the spherical cavity. After establishing the credibility of the present finite element modeling, the propagation of an acoustic pressure wave from a cylindrical cavity located near free-surface is also presented.

Finite Element Method

Suppose a spherical or cylindrical cavity of radius R is located at a distance h below the free-surface. Figure 1 shows the geometry including the image source located at a distance h above the free-surface. A constant pressure is applied to the inside surface of the cavity. For the full nonlinear Euler solutions, we solve the compressible, time-dependent, inviscid conservation equations for mass density, momentum, and energy. An equation of state (EOS) for water is assumed to follow a bulk modulus equation of state,

$$P(\rho) = \rho_o c^2 \left(\frac{\rho}{\rho_o} - 1 \right) \tag{1}$$

here, P and ρ are the total pressure and current fluid density, respectively, in the acoustic fluid medium. c is the acoustic velocity and ρ_o is the hydrostatic density.

For the acoustic wave solutions, we use an acoustic pressure element formulation which solves a scalar wave equation, $\Psi_{tt} = c^2 \nabla^2 \Psi$. Ψ is the scalar displacement potential (Newton, 1978, 1981). Although this element formulation is discussed in detail by Felippa and DeRuntz (1984), it is given here to make this paper self-contained. For the small and irrotational motions of a compressible fluid, the dynamic equilibrium vector equation is,

$$\rho \hat{\ddot{d}} = \hat{\nabla} p + \hat{f} \tag{2}$$

where $\hat{d}$ is the fluid particle displacement relative to a reference hydrostatic displacement, $\hat{f}$ is the body force, and superposed dots denote temporal differentiation. The field $\hat{d}$ is derivable from the scalar displacement potential, $\hat{\nabla}\psi = -\rho \hat{d}$. The displacement potential is then related to pressure by,

$$\hat{\nabla} \ddot{\psi} = \hat{\nabla}(p - p^H) \tag{3}$$

here the static equilibrium vector equation, $\hat{\nabla} p^H + \hat{f} = 0$, is used and p^H is the hydrostatic pressure in the acoustic fluid medium. Equation (3) is spatially integrated to yield the equation of motion,

$$\ddot{\psi} = p - p^H \tag{4}$$

The finite element matrix equations are derived by using the displacement-potential formulation of Newton (1978, 1891). The primary variables are ψ and the condensation, $s = -\rho \hat{\nabla} \hat{d} = \nabla^2 \psi$. And the Galerkin equation is $\int_V N(s - \nabla^2 \psi) dV = 0$, here N is a column vector of trilinear shape functions associated with nodes and V is the volume occupied by the fluid. Following the isoparametric finite element technique, the two primary variables are interpolated with the geometry shape functions, $\psi = N^t \tilde{\psi}$ and $s = N^t \tilde{s}$. Superscript t denotes transposition. Application of the divergence theorem to this equation and finite element interpolation equation yields the Galerkin matrix equation,

$$Q\tilde{s} + H\tilde{\psi} = b \tag{5}$$

where the capacitance $Q = \int_V NN^t dV$, reactance $H = \int_V (\nabla N)(\nabla N)^t dV$, and the column vector $b = \int_B N(\partial \psi / \partial n) dB$. n denotes the outward normal to the boundary B of V. These entries are determined by standard numerical integration technique using Gauss-Legendre quadrature rules. The space discrete field equation of motion is $\ddot{\tilde{\psi}} = \tilde{p} - \tilde{p}^H$. In the time-integration scheme, Eq. (5) and the space discrete field equation of motion are used. Explicit central difference scheme is used for the integration of the two equations. It is important to note that this model is appropriate for tracking low pressure waves in an acoustic media. Pressure is the only unknown variable such that it is a very cost effective element. A comparison of these results with the analytical one may confirm a high degree

[1] Assistant Professor, Department of Mechanical Engineering, Naval Postgraduate School, Monterey, CA 93943. Current Address: Assistant Professor, School of Mech. & Aero. Engineering, Sejong University, Seoul, Korea.

Contributed by the Fluids Engineering Division of THE AMERICAN SOCIETY OF MECHANICAL ENGINEERS. Manuscript received by the Fluids Engineering Division October 20, 1997; revised manuscript received September 21, 1998. Associate Technical Editor: M. M. Sindir.

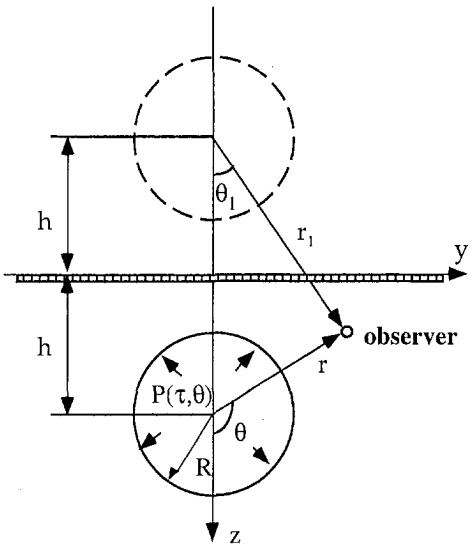

Fig. 1 Acoustic wave radiation from a cavity located near free-surface

of credibility of the present numerical method. This set of equations is solved using a Lagrangian scheme in the finite element program, LS-DYNA (John, 1995).

The surrounding medium is taken to be an isotropic and homogeneous water with the acoustic speed of 1480 m/s and density of 1000 kg/m^3. However, the problem was nondimensionalized using the radius of the cavity (R) as the characteristic length, the time for an acoustic wave to transit one radius of the cavity as the characteristic time (τ), and the bulk modulus of water (ρc^2) as the characteristic pressure. Since the geometry is axially symmetric, with the symmetry axis being the z axis, only two-dimensional axisymmetry half plane is considered in the analysis. The computation mesh is displayed in Fig. 2. It is necessary to include a fairly large number of elements near the cavity in order to get a converged solution. Because only a finite volume of water can be modeled, it was decided to construct a model for which the solution would be unaffected by reflections

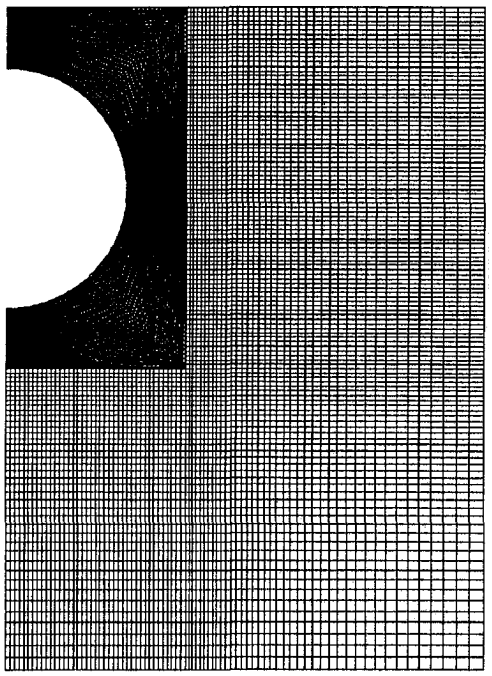

Fig. 2 Computational mesh

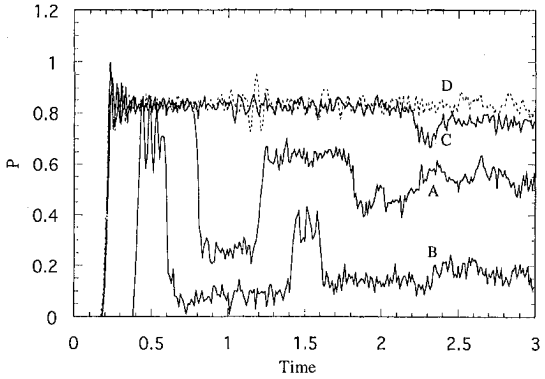

Fig. 3 Simulated results for pressures using full non-linear Euler equation, for h = 1.5: r = 1.2 and $\theta = \pi$ (curve A), r = 1.4 and $\theta = \pi$ (curve B), r = 1.2 and $\theta = \pi/2$ (curve C), r = 1.2 and θ = 0 (curve D), spherical cavity

from the boundaries, except free-surface, of the fluid volume for times less than 6 radius transit times. The block of fluid is thus a rectangular shaped volume bounded by the planes $z = 0$ and $z = h + 4$, and $y = 0$ $y = 4$, where the point $(h, 0, 0)$ represents the center of the cavity and again units are in terms of the radius of the cavity.

Results and Discussions

A small pressure magnitude of 1×10^{-3} bulk modulus is applied to the surface of a cavity, and the time histories of pressure waves are calculated for $h = 1.5$ and at four locations: $r = 1.2$ and $\theta = \pi$ (A), $r = 1.4$ and $\theta = \pi$ (B), $r = 1.2$ and $\theta = \pi/2$ (C), $r = 1.2$ and $\theta = 0$ (D). The results obtained from three methods are compared in this section. First, the finite element solution to the full Euler equations and the corresponding analytical solution of Gorshkov et al. (1991) are presented in Fig. 3 and Fig. 4, respectively. The pressures shown in the figures are normalized by the magnitude of pressure at the surface of the cavity. The total number of brick elements used in this calculation is 17600 which provides better nodal results for the propagation of spherical waves of rectangular profile (step waves) and less high frequency oscillations and sharper wave front compared to the solution of 9600 element, although not shown. Figure 5 shows the finite element solutions to the acoustic element formulation using total number of element of 17600 and 9600. For the solution of 9600 elements, the transition between one pulse to another is not perfectly clear and more oscillations are observed.

The overall agreement between three solutions are quite good, showing the correct wave propagation and reflections from the free-surface. It is of interest to analyze the characteristics of

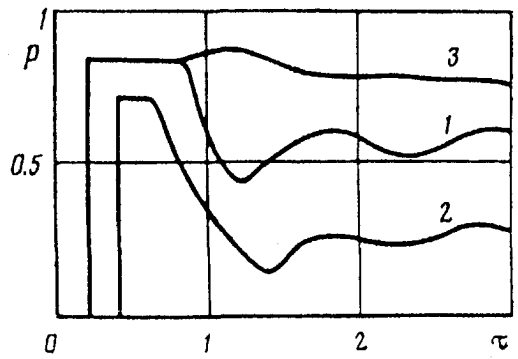

Fig. 4 Analytical solutions from Gorshkov et al. (1991), for h = 1.5: r = 1.2 and $\theta = \pi$ (curve 1), r = 1.4 and $\theta = \pi$ (curve 2), r = 1.2 and $\theta = \pi/2$ (curve 3), spherical cavity

solutions for A and B locations which are bounded by free-surface and cavity wall. The solutions can be derived by successive addition of solutions for an infinite array of cavities located above and below the free-surface. As time continues, the number of reflected waves will increase. As shown in the solutions, the pressure waves are begin to be seen after a time lag ($\tau = r - 1$) for the incidence wave to arrive at the calculation locations. The pressure remains unchanged until arrival of the first image wave at time, $\tau = r_1 - 1$. After this wave, it should drop quickly due to the superposition of the incidence and reflected waves. According to the spherical spreading loss, the magnitude of normalized pressure at location A, when the first incidence wave arrives, is $1/1.2 = 0.833$. At $\tau = 0.8$, the pressure must drop to $1/1.2 + (-1/1.8) = 0.278$. These values match well with the finite element solutions, although some numerical dispersion effects are observed. On the other hand, slowly decaying curves are predicted by the analytical solution. Even the prediction at location C shows somewhat overshoot around $\tau = 1$. This phenomenon which is present at all calculation locations is attributed to the limited number of terms of the infinite series in Legendre polynomials.

Another issue is the high frequency oscillations perceptible in the finite element (FE) solution to the full Euler equations. Since this phenomenon disappears in the FE solution to the linear acoustic pressure element formulation, it seems to be caused by the nonlinearities in the governing equations. Hence, the use of the acoustic element formulation is desirable for modeling low intensity waves in acoustic medium.

Since the finite element solutions for the acoustic wave propagation from a spherical cavity located near the free-surface are quite good, and by taking advantage of the plane-symmetry, the acoustic wave propagation from a cylindrical cavity can be solved rather easily. Figures 6 and 7 show the FE solutions (total number of element, 17600) to the full Euler equations and to the acoustic element formulation, respectively. The calculation locations are the same as the previous case. Apparently, the solutions correspond to cylindrical waves with the amplitude decaying proportional to $r^{1/2}$ in range.

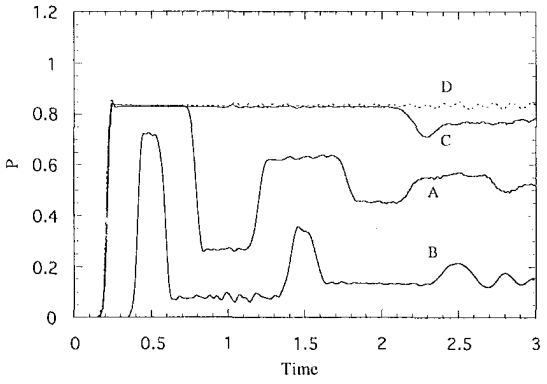

Fig. 5(*a*)

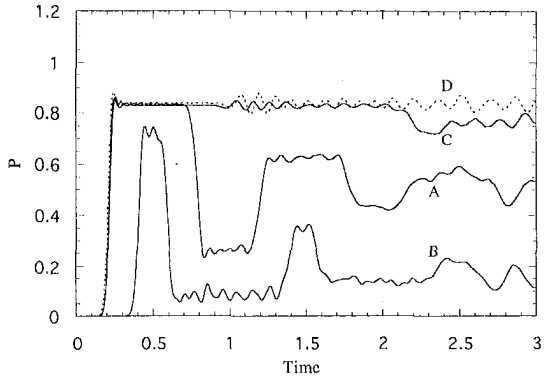

Fig. 5(*b*)

Fig. 5 Simulated results for pressures using linear acoustic element formulation, spherical cavity, total number of elements 17600 (*a*), 9600 (*b*)

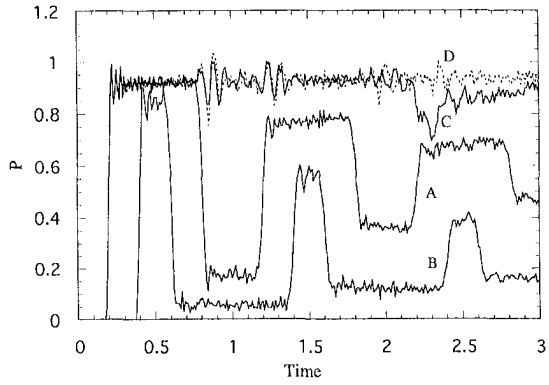

Fig. 6 Simulated results for pressures using full nonlinear Euler equation, cylindrical cavity

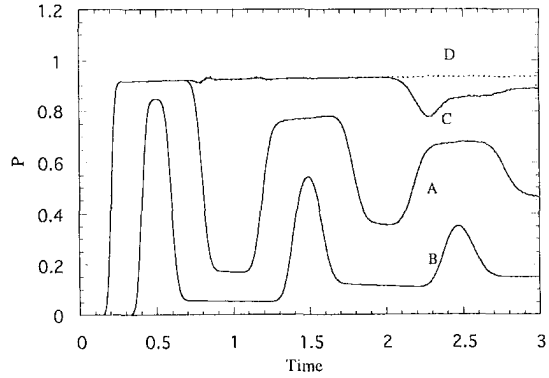

Fig. 7 Simulated results for pressures using linear acoustic element formulation, cylindrical cavity

It can be noted that in the finite element solutions the compressive waves brode as they propagate. This is due to the dispersion effects since the methods rely on the space discretization of the computational domain (Serico and Priolo, 1994; Dauksher and Emery, 1997; Cohen et al., 1994), and use artificial viscosities to solve the discontinuities such as shock waves (Neumann and Richtmyer, 1950).

Concluding Remarks

The finite element method for the analysis of acoustic wave propagation from a cavity located near free-surface has been tested against the corresponding analytical solution which retains insufficient terms of the infinite series in Legendre polynomials. The accuracy and adequacy of the present numerical modeling are demonstrated. Due to the flexibility in describing problems with complex geometry, such as three dimensional cavity, the current approach can be extended to much complex geometry. However, numerical solutions of the wave equation yield some dispersion errors such that the wave front is smeared.

References

Gorshkov, A. G., Tarlakovskii, D. V., and Shukurov, A. M., 1991, "The Propagation of Waves From a Spherical Cavity in an Acoustic Half-Space," *Journal of Applied Mathematics and Mechanics,* Vol. 55, pp. 142–144.

Cohen, G., Joly, P., and Tordjman, N., 1994, "Higher-Order Finite Elements with Mass-Lumped for the 1D Wave Equation," *Finite Elements in Analysis and Design,* Vol. 16, pp. 329–336.

Seriani, G., and Priolo, E., 1994, "Spectral Element Method for Acoustic Wave Simulation in Heterogeneous Media," *Finite Elements in Analysis and Design,* Vol. 16, pp. 337–348.

Dauksher, W., and Emery, A. F., 1997, "Accuracy in Modeling the Acoustic Wave Equation with Chebyshev Spectral Finite Elements," *Finite Elements in Analysis and Design,* Vol. 26, pp. 115–128.

Hallquist, John et al., 1997, "LS-DYNA User's Manual," Livermore Software Technology Corporation Report 1082, Livermore CA. USA.

Felippa, C. A., and DeRuntz, J. A., 1984, "Finite Element Analysis of Shock-Induced Hull Cavitation," *Computer Methods in Applied Mechanics and Engineering,* Vol. 44, pp. 297–337.

Neumann J. von, and Richtmyer, R. D., 1950, "A Method for the Numerical Calculation of Hydrodynamic Shocks," *Journal of Applied Physics,* Vol. 21, pp 232.

Newton, R. E., 1978, "Effects of Cavitations on Underwater Shock Loading—Part I," Report. NPS69-78-013, Naval Postgraduate School, Monterey, CA.

Newton, R. E., 1981, "Effects of Cavitations on Underwater Shock Loading-Plane Problem," Final Report. NPS69-81-001, Naval Postgraduate School, Monterey, CA.

Modified Formula for the Flow Velocity Profile in a Vortex

A. Szumowski,[1] J. Piechna,[1] W. Selerowicz,[1] and G. Sobieraj[1]

Introduction

A tip vortex shed from the helicopter rotor blade can interact with the following blade. This phenomenon (Blade Vortex Interaction) is responsible for unsteady airfoil loading and impulsive noise radiation. The effect of interaction depends on the vortex itself, its trajectory, flow Mach number at infinity, and the airfoil contour.

The present paper proposes for the BVI numerical simulation how to determine the flow velocity distribution through the vortex approaching the airfoil when the pressure distribution in it is known, e.g., from an experiment. The flow velocity field induced by the vortex when superimposed on a uniform velocity field at infinity gives the initial condition used during numerical calculations of the BVI process.

A distribution of tangential velocity in the vortex proposed by Sculley (1975) has been used in BVI analysis by investigators like Lee and Bershader (1994) and Lin and Chin (1995):

$$v_\theta = \frac{\Gamma_o}{2\pi r}\frac{2r^2}{r^2 + r_o^2} \tag{1}$$

In the above formula r_o is the radius for maximum tangential flow velocity (approximate vortex core radius) and r the distance from the center of the vortex, Γ_o is the circulation around the circle of radius r_o. For the assumed $v_\theta(r)$, pressure distribution $p(r)$ can be calculated from the momentum equation

$$\frac{dp}{dr} = \frac{\rho v_\theta^2}{r}, \tag{2}$$

where the gas density ρ is obtained from the energy equation for adiabatic flow

$$\frac{\gamma}{\gamma - 1}\frac{p}{\rho} + \frac{v_\theta^2}{2} = \frac{\gamma}{\gamma - 1}\frac{p_\infty}{\rho_\infty}. \tag{3}$$

In the above equations the air viscosity is not accounted because the BVI process is usually calculated for the inviscid gas.

Equation (2) in conjunction with Eqs. (1) and (3) where solved numerically by previous authors mentioned above. The integration was carried out from a large value of r, where pressure and density were prescribed, to the center of the vortex. Unfortunately, the integration must be repeated many times with different assumed values of Γ_o and r_o in order to match the calculated and measured pressure distribution in the vortex. This matching is required if the numerical computation of the BVI is to predict the behavior of a real phenomenon.

Results

The above numerical procedure which requires to deal with two parameters Γ_o and r_o can be avoided. Equation (2) in conjunction with Eqs. (3) can be transformed as follows

$$\frac{d\bar{p}}{\bar{p}} = \gamma\frac{d\bar{r}}{\bar{r}}\Big/\left(\frac{1}{\bar{v}_\theta^2} - \frac{\gamma - 1}{2}\right), \tag{4}$$

where

$$\bar{r} = r/r_o, \quad \bar{v}_\theta = v_\theta/a_\infty, \quad \bar{p} = p/p_\infty,$$

$a_\infty = \sqrt{\gamma\, p_\infty/\rho_\infty}$ is a speed of sound in the infinity.

In the present case, $\bar{v}_\theta = \bar{\Gamma}_o\bar{r}/(1 + \bar{r}^2)$ where $\bar{\Gamma}_o = \Gamma_o/\pi r_o a_\infty$.

The pressure gradient $d\bar{p}/d\bar{r}$ is positive throughout the vortex. This means that the denominator in the right-hand side of Eq. (4) should be positive for every $\bar{r}$

$$\left(\frac{1 + \bar{r}^2}{\bar{\Gamma}_o}\right)^2 - \frac{\gamma - 1}{2}\bar{r}^2 > 0. \tag{5}$$

This condition is satisfied if

$$\bar{\Gamma}_o < \sqrt{8/(\gamma - 1)}. \tag{6}$$

This corresponds to the requirement that the pressure in the vortex center cannot be lower then zero. Under the condition (6), Eq. (4) has the a following analytical integral.

$$\bar{p} = \mathrm{Exp}\left[\bar{\Gamma}_o^2\frac{\gamma}{2\sin\beta}\left(\mathrm{arc\ tg}\,\frac{\bar{r}^2 - \cos\beta}{\sin\beta} - \frac{\pi}{2}\right)\right] \tag{7}$$

where $\cos\beta = 0.25(\gamma - 1)\bar{\Gamma}_o^2 - 1$.

Equation (7) has a minimum for $\bar{r} = 0$

$$\bar{p}_{\min} = \mathrm{Exp}\left\{\bar{\Gamma}_o^2\frac{\gamma}{2\sin\beta}\left[\mathrm{arc\ tg}\left(-\frac{1}{tg\beta}\right) - \frac{\pi}{2}\right]\right\}. \tag{8}$$

For a measured pressure distribution $p(r)$ the following data can be easily obtained:

(i) The pressure in the center of the vortex ($p_{\min}$) and (ii) the radius (r_1) of the maximum pressure gradient $(dp/dr)_{\max}$. The former can be directly used to calculate Γ_o (Eq. 8) whereas the latter to obtain r_o. To this end Eq. (4) is differentiated and the derivative is set to zero. The result is

$$r_o = r_1\sqrt{6/[\sqrt{(2 - A)^2 + 12} - (2 - A)]} \tag{9}$$

where $A = \bar{\Gamma}_o^2(3\gamma - 1)/2$. For the experimental data of Lee and Bershader (1994) one can obtain $\bar{\Gamma}_o = 1.234$ and $r_o = 1.24$ mm.

The results of analogous experiments performed by the present authors are employed here. In our experiments the vortex was generated over a NACA 0012 airfoil (120 mm chord length,

[1] Professor, Researcher, Researcher, Researcher, respectively, Warsaw University of Technology, 00-665 Warsaw, ul.Nowowiejska 24, Poland.

Contributed by the Fluids Engineering Division of THE AMERICAN SOCIETY OF MECHANICAL ENGINEERS. Manuscript received by the Fluids Engineering Division February 12, 1998; revised manuscript received December 2, 1998. Associate Technical Editor: D. P. Telionis.

Seriani, G., and Priolo, E., 1994, "Spectral Element Method for Acoustic Wave Simulation in Heterogeneous Media," *Finite Elements in Analysis and Design,* Vol. 16, pp. 337–348.

Dauksher, W., and Emery, A. F., 1997, "Accuracy in Modeling the Acoustic Wave Equation with Chebyshev Spectral Finite Elements," *Finite Elements in Analysis and Design,* Vol. 26, pp. 115–128.

Hallquist, John et al., 1997, "LS-DYNA User's Manual," Livermore Software Technology Corporation Report 1082, Livermore CA. USA.

Felippa, C. A., and DeRuntz, J. A., 1984, "Finite Element Analysis of Shock-Induced Hull Cavitation," *Computer Methods in Applied Mechanics and Engineering,* Vol. 44, pp. 297–337.

Neumann J. von, and Richtmyer, R. D., 1950, "A Method for the Numerical Calculation of Hydrodynamic Shocks," *Journal of Applied Physics,* Vol. 21, pp 232.

Newton, R. E., 1978, "Effects of Cavitations on Underwater Shock Loading—Part I," Report. NPS69-78-013, Naval Postgraduate School, Monterey, CA.

Newton, R. E., 1981, "Effects of Cavitations on Underwater Shock Loading-Plane Problem," Final Report. NPS69-81-001, Naval Postgraduate School, Monterey, CA.

Modified Formula for the Flow Velocity Profile in a Vortex

A. Szumowski,[1] J. Piechna,[1] W. Selerowicz,[1] and G. Sobieraj[1]

Introduction

A tip vortex shed from the helicopter rotor blade can interact with the following blade. This phenomenon (Blade Vortex Interaction) is responsible for unsteady airfoil loading and impulsive noise radiation. The effect of interaction depends on the vortex itself, its trajectory, flow Mach number at infinity, and the airfoil contour.

The present paper proposes for the BVI numerical simulation how to determine the flow velocity distribution through the vortex approaching the airfoil when the pressure distribution in it is known, e.g., from an experiment. The flow velocity field induced by the vortex when superimposed on a uniform velocity field at infinity gives the initial condition used during numerical calculations of the BVI process.

A distribution of tangential velocity in the vortex proposed by Sculley (1975) has been used in BVI analysis by investigators like Lee and Bershader (1994) and Lin and Chin (1995):

$$v_\theta = \frac{\Gamma_o}{2\pi r}\frac{2r^2}{r^2 + r_o^2} \tag{1}$$

In the above formula r_o is the radius for maximum tangential flow velocity (approximate vortex core radius) and r the distance from the center of the vortex, Γ_o is the circulation around the circle of radius r_o. For the assumed $v_\theta(r)$, pressure distribution $p(r)$ can be calculated from the momentum equation

$$\frac{dp}{dr} = \frac{\rho v_\theta^2}{r}, \tag{2}$$

where the gas density ρ is obtained from the energy equation for adiabatic flow

$$\frac{\gamma}{\gamma - 1}\frac{p}{\rho} + \frac{v_\theta^2}{2} = \frac{\gamma}{\gamma - 1}\frac{p_\infty}{\rho_\infty}. \tag{3}$$

In the above equations the air viscosity is not accounted because the BVI process is usually calculated for the inviscid gas.

Equation (2) in conjunction with Eqs. (1) and (3) where solved numerically by previous authors mentioned above. The integration was carried out from a large value of r, where pressure and density were prescribed, to the center of the vortex. Unfortunately, the integration must be repeated many times with different assumed values of Γ_o and r_o in order to match the calculated and measured pressure distribution in the vortex. This matching is required if the numerical computation of the BVI is to predict the behavior of a real phenomenon.

Results

The above numerical procedure which requires to deal with two parameters Γ_o and r_o can be avoided. Equation (2) in conjunction with Eqs. (3) can be transformed as follows

$$\frac{d\bar{p}}{\bar{p}} = \gamma\frac{d\bar{r}}{\bar{r}}\Big/\left(\frac{1}{\bar{v}_\theta^2} - \frac{\gamma - 1}{2}\right), \tag{4}$$

where

$$\bar{r} = r/r_o, \quad \bar{v}_\theta = v_\theta/a_\infty, \quad \bar{p} = p/p_\infty,$$

$a_\infty = \sqrt{\gamma\, p_\infty/\rho_\infty}$ is a speed of sound in the infinity.

In the present case, $\bar{v}_\theta = \bar{\Gamma}_o\bar{r}/(1 + \bar{r}^2)$ where $\bar{\Gamma}_o = \Gamma_o/\pi r_o a_\infty$.

The pressure gradient $d\bar{p}/d\bar{r}$ is positive throughout the vortex. This means that the denominator in the right-hand side of Eq. (4) should be positive for every $\bar{r}$

$$\left(\frac{1 + \bar{r}^2}{\bar{\Gamma}_o}\right)^2 - \frac{\gamma - 1}{2}\bar{r}^2 > 0. \tag{5}$$

This condition is satisfied if

$$\bar{\Gamma}_o < \sqrt{8/(\gamma - 1)}. \tag{6}$$

This corresponds to the requirement that the pressure in the vortex center cannot be lower then zero. Under the condition (6), Eq. (4) has the a following analytical integral.

$$\bar{p} = \mathrm{Exp}\left[\bar{\Gamma}_o^2\frac{\gamma}{2\sin\beta}\left(\mathrm{arc\ tg}\,\frac{\bar{r}^2 - \cos\beta}{\sin\beta} - \frac{\pi}{2}\right)\right] \tag{7}$$

where $\cos\beta = 0.25(\gamma - 1)\bar{\Gamma}_o^2 - 1$.

Equation (7) has a minimum for $\bar{r} = 0$

$$\bar{p}_{\min} = \mathrm{Exp}\left\{\bar{\Gamma}_o^2\frac{\gamma}{2\sin\beta}\left[\mathrm{arc\ tg}\left(-\frac{1}{tg\beta}\right) - \frac{\pi}{2}\right]\right\}. \tag{8}$$

For a measured pressure distribution $p(r)$ the following data can be easily obtained:

(i) The pressure in the center of the vortex ($p_{\min}$) and (ii) the radius (r_1) of the maximum pressure gradient $(dp/dr)_{\max}$. The former can be directly used to calculate Γ_o (Eq. 8) whereas the latter to obtain r_o. To this end Eq. (4) is differentiated and the derivative is set to zero. The result is

$$r_o = r_1\sqrt{6/[\sqrt{(2 - A)^2 + 12} - (2 - A)]} \tag{9}$$

where $A = \bar{\Gamma}_o^2(3\gamma - 1)/2$. For the experimental data of Lee and Bershader (1994) one can obtain $\bar{\Gamma}_o = 1.234$ and $r_o = 1.24$ mm.

The results of analogous experiments performed by the present authors are employed here. In our experiments the vortex was generated over a NACA 0012 airfoil (120 mm chord length,

[1] Professor, Researcher, Researcher, Researcher, respectively, Warsaw University of Technology, 00-665 Warsaw, ul.Nowowiejska 24, Poland.

Contributed by the Fluids Engineering Division of THE AMERICAN SOCIETY OF MECHANICAL ENGINEERS. Manuscript received by the Fluids Engineering Division February 12, 1998; revised manuscript received December 2, 1998. Associate Technical Editor: D. P. Telionis.

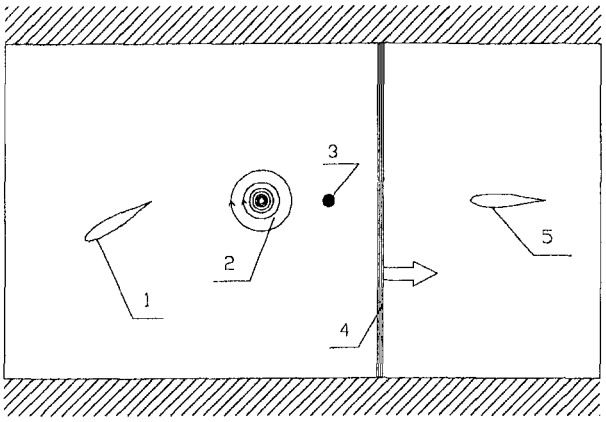

Fig. 1 Test section of the shock tube. 1 - vortex generator, 2 - starting vortex induced by moving shock wave, 3 - pressure transducer, 4 - moving shock wave, 5 - test airfoil

15 deg angle of attack) placed in a shock tube with rectangular cross-section 100 × 500 mm (Fig. 1). A test airfoil of the same tipe and of the same cord length was located four cord length downstream the vortex generator. The pressure, the flow velocity, and the speed of sound behind the shock wave induced by the break-up of a diaphragm in the shock tube were $p_\infty = 0.225$ bar, $u_\infty = 279$ m/s and $a_\infty = 404$ m/s. The curve fits for p and dp/dr corresponding to Eq. (1) are marked by dashed lines in Fig. 2. For these curves $\bar{\Gamma}_o$ and r_o obtained from Eqs. (8) and (9) are 0.9037 and 5.8 mm, respectively. It can be noticed that the curve fit for dp/dr shows a maximum $(dp/dr)_{\max}$ (proportional to $v^2_{\theta\,\max}$) which is about 20 percent lower then the corresponding experimental value. This discrepancy can be easily avoided by modifying formula (1) for the velocity distribution in the vortex. The proposed new formula is

$$v_\theta = \frac{\Gamma_o}{2\pi r}\,\frac{r^2(1+c)}{r^2\,\mathrm{Exp}[\alpha(r-r_o)/r_o] + cr_o^2} \qquad (10)$$

where:

$$c = \alpha + 1 \quad \text{and} \quad \alpha \geq 0.$$

From Eq. (10) it follows that the maximum velocity $v_{\theta\,\max}$ (at $r = r_o$) does not depend on α. Moreover, for $\alpha = 0$, Eq. (10) simplifies to Eq. (1). The normalized flow velocities $v_\theta/v_{\theta\,\max}$, as a function of r/r_o for certain values of α, are shown in Fig. 3. It can be noticed, that due to the proposed improvement, the predicted distribution of flow velocity in the vortex strongly depends on α in the region outside of the vortex core and weakly inside the core. It seems that by changing α the velocity distribution can by effectively adjusted to match the experimental data. The three coefficients Γ_o, r_o, and α in Eq. (10) can be obtained from the measured pressure distribution $p(r)$ using the following values: $p_{\min}$, $(dp/dr)_{\max}$ and $r = r_1$ where dp/dr is maximum.

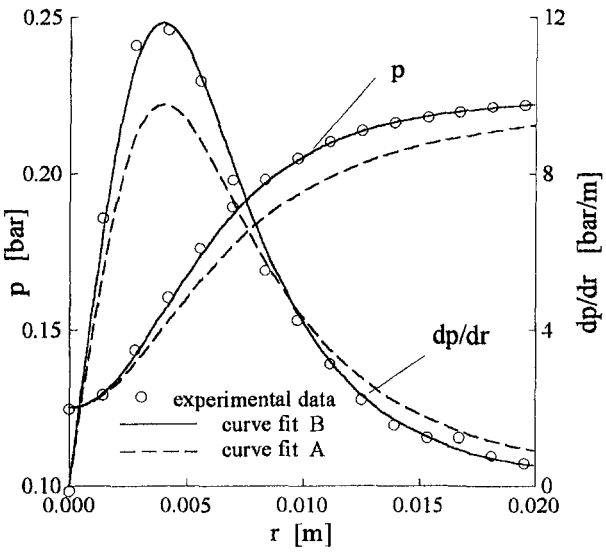

Fig. 2 Profiles of pressure and pressure gradient measured at four chord length of the NACA 0012 airfoil downstream of its trailing edge and their curve fits obtained by use of Eq. (1) - curve A, and Eq. (10) - curve B

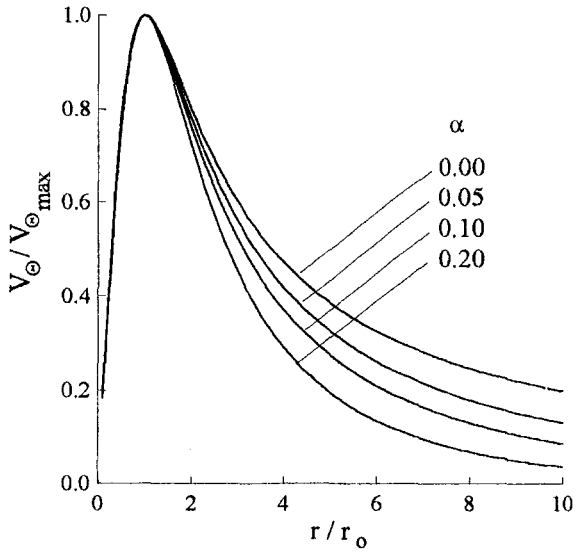

Fig. 3 Tangential velocity profiles

To this end the following relationships can been derived from Eq. (4) where v_θ is determined by Eq. (10).

$$\bar{p}_{\min} = \mathrm{Exp}\left(-\gamma \int_o^\infty f(\bar{r})\,d\bar{r}\right) \qquad (11)$$

where

$$f(\bar{r}) = \frac{\bar{r}}{\left(\dfrac{2}{\bar{\Gamma}_o(1+c)}\right)^2 (\bar{r}^2\varphi + c)^2 - \dfrac{\gamma-1}{2}\,\bar{r}^2}$$

$$\text{and} \quad \varphi = \mathrm{Exp}\,[\alpha(\bar{r}-1)]$$

$$\left(\frac{d\bar{p}}{d\bar{r}}\right)_{\max} = \gamma f(\bar{r}_1)\bar{p}_{\min}\,\mathrm{Exp}\left(\gamma \int_o^{\bar{r}_1} f(\bar{r})\,d\bar{r}\right) \qquad (12)$$

where $\bar{r}_1$ is a rood of equation

$$(r^2\varphi + c)[2\bar{r}^2\varphi(2+\alpha\bar{r}) - (\bar{r}^2\varphi + c)] - \left[\frac{\bar{\Gamma}_o}{2}(1+c)\right]^2 \frac{3\gamma-1}{2}\,\bar{r}^2 = 0 \qquad (13)$$

which corresponds to the condition $d^2\bar{p}/d\bar{r}^2 = 0$.

For the measured distribution of p and dp/dr shown in Fig. 2 the following coefficients have been obtained from Eqs. (11 ÷ 13) for $\gamma = 1.4$.

$$\bar{\Gamma}_o = 0.958,\ \bar{r}_1 = 0.746,\ r_o = 5.36 \text{ mm and } \alpha = 0.14.$$

These values have been used to draw the curves presented by continuous lines in Fig. 2. These curves approximate very well both the pressure and the derivative of the pressure. A correct

approximation of dp/dr is required to obtain actual distribution of the flow velocity in the vortex (dp/dr is proportional to v_θ^2 – Eq. (2)).

References

Lee, S., and Bershader D., 1994, "Head-On Parallel Blade-Vortex Interaction," *AIAA Journal,* Vol. 32, No. 1, pp. 16–22.

Lin, S. Y., and Chin, Y. S., 1995, "Numerical Study of Transonic Blade-Vortex Interaction," *AIAA Journal,* Vol. 33, No. 8, pp. 1377–1382.

Sculley, M. P., 1975, "Computation of Helicopter Rotor Wake Geometry and its Influence on Rotor Harmonic Loads," Massachusetts Inst. of Technology, Cambridge, ASRL TR-178-1, Mar.

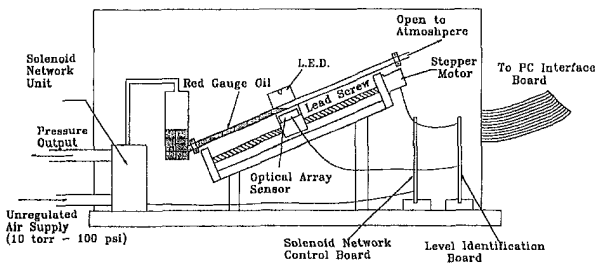

Fig. 1 Schematic of the ACCUPRES

A Computer-Controlled Pressure Standard

Othon K. Rediniotis[1]

The operating principles, as well as the technical aspects of the implementation of a new computer-controlled pressure standard are presented. The instrument can have dual use: either as a pressure source or as a pressure sensor. The device is intended mostly for use in problems where small differential pressures are of interest, i.e., 0–2.5 KPa and high accuracy is desired. Such a pressure range encompasses, for example, most of the pressure measurement applications in subsonic wind-tunnel testing. The device interfaces to a PC and is ideal for fully-automated pressure transducer calibration applications. The accuracy of the pressures produced or measured by the device is 0.08 percent F.S. (Full Scale).

Introduction

Many differential pressure transducers, especially silicon-based ones, used today in basic research facilities require often calibration since their response tends to change with time and temperature. For example, a series of electronically scanned pressure transducers, the ESP series from PSI Inc., have to be calibrated once every hour if an accuracy of 0.1 percent F.S. should be expected. Such an accuracy, although seemingly high, might be the bare minimum required in several applications such as low-speed aerodynamic research, when for example, a +/−10 in H_2O (+/−2.5 KPa) F.S. pressure transducer is used. An automated calibration process requires a known, constant and accurate value of pressure, a pressure standard. The key words "automated," "known" and "accurate" are the focus of attention in the present work.

With rather simple hardware, one could generate, with relative ease, a constant value of pressure. The challenge is in whether this pressure value is known and to what degree of accuracy, as well as whether the pressure standard could be interfaced to an automatic calibration process. Moreover, in a calibration process, both positive and negative differential pressures have to be generated if a +/− range of calibration is desired. A compact, versatile, and accurate device, the ACCUPRES, that meets the above requirements, is described in the present work. Its operation is based on simple pneumatic and optical principles, a fact that results in the following important features of the device: (a) pressure ranges as low as +/− 270 Pa F.S.; (b) pressure resolution as high as 0.15 Pa; (c) pressure accuracy as high as 0.08 percent F.S. which translates to about 0.25 Pa for the smallest range; and (d) low cost—in the low four digits.

The pressure standards currently existing in the market offer lowest pressure ranges that are significantly higher than 0 to 270 Pa, most of them do not provide positive and negative pressures, can not operate both as pressure standard and pressure sensor, and their cost is significantly higher than that of the ACCUPRES. For example, the Model 300 Pressure Standard from Mensor has a minimum available pressure range of 0 to 2500 Pa and its cost starts in the five digits. However its accuracy is very good, 0.01 percent F.S. which translates to 0.25 Pa for the smallest range. Deadweight pressure standards from DH Instruments provide a minimum pressure range of 0 to 10 KPa and cost in the five digits.

Principle of Operation

A summary of the principle of operation is given first. In the continuation, each physical principle as well as the technical aspects of the implementation are discussed in more detail. A schematic of the unit is presented in Fig. 1. As shown there, an elevation difference is generated between the levels of the liquid in the two members of an inclined manometer, through a network of solenoid valves. The main element of the unit, a 64-pixel CCD sensor, is mounted on a computer-controlled traversing mechanism. This assembly optically searches for the location of the liquid-air interface in the inclined member of the manometer. Once the interface has been identified, basic manometry principles along with the knowledge of the unit's geometry, accurately yield the generated differential pressure value.

Device Description

Optical Sensor. The unit's main element is a cost-efficient linear CCD optical sensor from Texas Instruments (Texas Instruments, 1992). Its optically sensitive surface has an overall length of 8 mm and consists of 64 discrete photosensing areas which will be called pixels. The distance between consecutive pixel centers is 125 μm. Each pixel's dimensions are 120 μm long by 70 μm wide. Light energy striking a pixel generates electron-hole pairs in the region under the pixel. The electrons are collected at the pixel element while the holes are swept in the substrate. The amount of charge accumulated in the element is directly proportional to the intensity of the incident light and the integration time, i.e., the time between consecutive interrogations of the pixel by the sensor-driving circuit. Every time a pixel is addressed and interrogated, its accumulated charge is translated, through internal circuitry, to voltage which appears at the sensor's output pin. From the sensor's data sheets it is obvious that for fixed light irradiance (light energy incident on a unit surface per unit of time), each pixel's output voltage is proportional to the integration time. Also, if the integration

[1] Assistant Professor, Mem. ASME. Aerospace Engineering Department, Texas A&M University, College Station, TX 77843-3141.

Contributed by the Fluids Engineering Division of THE AMERICAN SOCIETY OF MECHANICAL ENGINEERS. Manuscript received by the Fluids Engineering Division December 8, 1997; revised manuscript received November 2, 1998. Associate Technical Editor: M. Sommerfeld.

approximation of dp/dr is required to obtain actual distribution of the flow velocity in the vortex (dp/dr is proportional to v_θ^2 – Eq. (2)).

References

Lee, S., and Bershader D., 1994, "Head-On Parallel Blade-Vortex Interaction," *AIAA Journal,* Vol. 32, No. 1, pp. 16–22.

Lin, S. Y., and Chin, Y. S., 1995, "Numerical Study of Transonic Blade-Vortex Interaction," *AIAA Journal,* Vol. 33, No. 8, pp. 1377–1382.

Sculley, M. P., 1975, "Computation of Helicopter Rotor Wake Geometry and its Influence on Rotor Harmonic Loads," Massachusetts Inst. of Technology, Cambridge, ASRL TR-178-1, Mar.

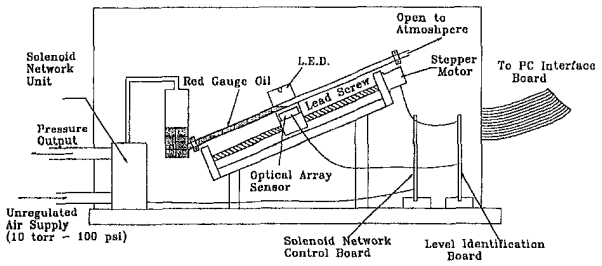

Fig. 1 Schematic of the ACCUPRES

A Computer-Controlled Pressure Standard

Othon K. Rediniotis[1]

The operating principles, as well as the technical aspects of the implementation of a new computer-controlled pressure standard are presented. The instrument can have dual use: either as a pressure source or as a pressure sensor. The device is intended mostly for use in problems where small differential pressures are of interest, i.e., 0–2.5 KPa and high accuracy is desired. Such a pressure range encompasses, for example, most of the pressure measurement applications in subsonic wind-tunnel testing. The device interfaces to a PC and is ideal for fully-automated pressure transducer calibration applications. The accuracy of the pressures produced or measured by the device is 0.08 percent F.S. (Full Scale).

Introduction

Many differential pressure transducers, especially silicon-based ones, used today in basic research facilities require often calibration since their response tends to change with time and temperature. For example, a series of electronically scanned pressure transducers, the ESP series from PSI Inc., have to be calibrated once every hour if an accuracy of 0.1 percent F.S. should be expected. Such an accuracy, although seemingly high, might be the bare minimum required in several applications such as low-speed aerodynamic research, when for example, a +/−10 in H_2O (+/−2.5 KPa) F.S. pressure transducer is used. An automated calibration process requires a known, constant and accurate value of pressure, a pressure standard. The key words "automated," "known" and "accurate" are the focus of attention in the present work.

With rather simple hardware, one could generate, with relative ease, a constant value of pressure. The challenge is in whether this pressure value is known and to what degree of accuracy, as well as whether the pressure standard could be interfaced to an automatic calibration process. Moreover, in a calibration process, both positive and negative differential pressures have to be generated if a +/− range of calibration is desired. A compact, versatile, and accurate device, the ACCUPRES, that meets the above requirements, is described in the present work. Its operation is based on simple pneumatic and optical principles, a fact that results in the following important features of the device: (a) pressure ranges as low as +/− 270 Pa F.S.; (b) pressure resolution as high as 0.15 Pa; (c) pressure accuracy as high as 0.08 percent F.S. which translates to about 0.25 Pa for the smallest range; and (d) low cost—in the low four digits.

The pressure standards currently existing in the market offer lowest pressure ranges that are significantly higher than 0 to 270 Pa, most of them do not provide positive and negative pressures, can not operate both as pressure standard and pressure sensor, and their cost is significantly higher than that of the ACCUPRES. For example, the Model 300 Pressure Standard from Mensor has a minimum available pressure range of 0 to 2500 Pa and its cost starts in the five digits. However its accuracy is very good, 0.01 percent F.S. which translates to 0.25 Pa for the smallest range. Deadweight pressure standards from DH Instruments provide a minimum pressure range of 0 to 10 KPa and cost in the five digits.

Principle of Operation

A summary of the principle of operation is given first. In the continuation, each physical principle as well as the technical aspects of the implementation are discussed in more detail. A schematic of the unit is presented in Fig. 1. As shown there, an elevation difference is generated between the levels of the liquid in the two members of an inclined manometer, through a network of solenoid valves. The main element of the unit, a 64-pixel CCD sensor, is mounted on a computer-controlled traversing mechanism. This assembly optically searches for the location of the liquid-air interface in the inclined member of the manometer. Once the interface has been identified, basic manometry principles along with the knowledge of the unit's geometry, accurately yield the generated differential pressure value.

Device Description

Optical Sensor. The unit's main element is a cost-efficient linear CCD optical sensor from Texas Instruments (Texas Instruments, 1992). Its optically sensitive surface has an overall length of 8 mm and consists of 64 discrete photosensing areas which will be called pixels. The distance between consecutive pixel centers is 125 μm. Each pixel's dimensions are 120 μm long by 70 μm wide. Light energy striking a pixel generates electron-hole pairs in the region under the pixel. The electrons are collected at the pixel element while the holes are swept in the substrate. The amount of charge accumulated in the element is directly proportional to the intensity of the incident light and the integration time, i.e., the time between consecutive interrogations of the pixel by the sensor-driving circuit. Every time a pixel is addressed and interrogated, its accumulated charge is translated, through internal circuitry, to voltage which appears at the sensor's output pin. From the sensor's data sheets it is obvious that for fixed light irradiance (light energy incident on a unit surface per unit of time), each pixel's output voltage is proportional to the integration time. Also, if the integration

[1] Assistant Professor, Mem. ASME. Aerospace Engineering Department, Texas A&M University, College Station, TX 77843-3141.

Contributed by the Fluids Engineering Division of THE AMERICAN SOCIETY OF MECHANICAL ENGINEERS. Manuscript received by the Fluids Engineering Division December 8, 1997; revised manuscript received November 2, 1998. Associate Technical Editor: M. Sommerfeld.

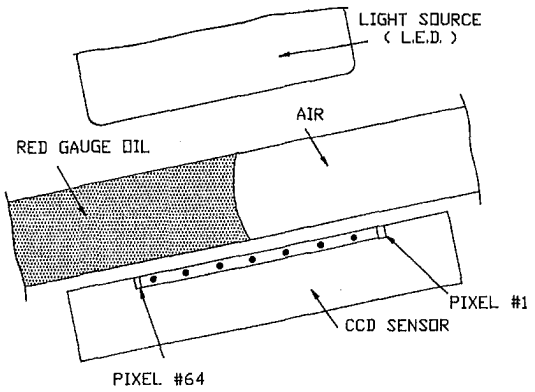

Fig. 2 Structural and functional details in the sensor's neighborhood

time is kept constant, the pixel's voltage output is almost proportional to the light irradiance. The sensor has its highest sensitivity to light wavelengths (λ) in the neighborhood of red ($\lambda = 632$ nm).

Glass Manometer and Liquid-Air Interface Detection. The liquid used in the inclined manometer is red gauge oil. The inside diameter of the inclined manometer member was selected small enough (3 mm) so that the mean liquid-air interface is almost perpendicular to the manometer axis (Fig. 2). As shown in Fig. 2, the light source used is a red L.E.D. with diameter almost equal to the length of the sensor pixel array. The L.E.D. is fixed with respect to the sensor and they are both traversed in unison. This insures that the light irradiance incident on the sensor is constant, regardless of the sensor's position along the manometer.

The pixels right underneath the liquid-filled part of the manometer collect more light compared to those underneath the air part because the liquid with the glass tube act as a focusing lens to concentrate the L.E.D. light onto the pixels. Figure 3 presents the sensor's voltage output as it appears on the screen of a HP 3562A Dynamic Signal Analyzer. This figure presents several consecutive scans of the sensor. The last half of the pixels receives significantly more light than the first third of the pixels. This light intensity causes their voltage output to saturate to approximately 3.7 volts. The intermediate section of steeply rising voltages corresponds to the pixels right underneath the liquid-air interface. This rising part of the curve is further processed to detect the location of the interface. In that rising part, the first pixel whose voltage exceeds a set threshold voltage V_{trig} (set between 2.5 and 3.5 Volts), is considered to be the pixel that corresponds to the location of the liquid-air interface.

Device Operation

The inclination of the unit's manometer, i.e., the angle that the inclined section of the manometer forms with the horizontal,

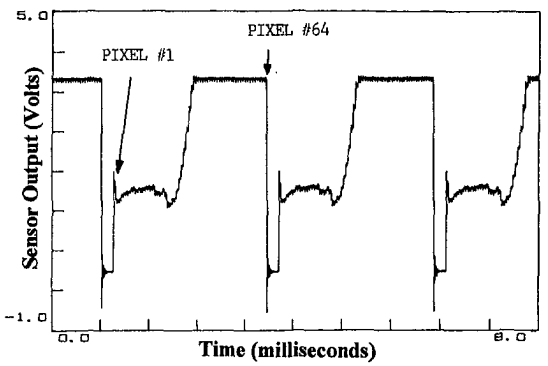

Fig. 3 Sensor's voltage output for several consecutive pixel scans

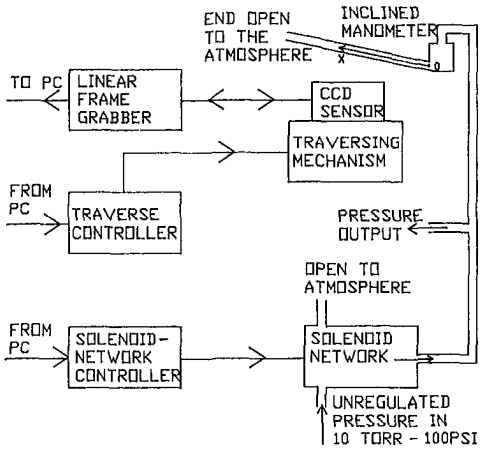

Fig. 4 Device's functional block diagram

can be adjusted. Each inclination setting of the unit's manometer is characterized by two parameters. The first is the ratio $\Delta P/\Delta x$ which indicates how much the pressure output will rise or fall if the liquid level is displaced along the inclined manometer member by a length Δx upwards or downwards, respectively. For each fixed unit geometry, the corresponding ratio $\Delta P/\Delta x$ was determined by calibrating the unit against a high-accuracy, high-resolution Air Neotronics digital manometer with an accuracy of 0.1 Pa. It was found that for a fixed unit geometry, the value of this ratio stays constant for a temperature range 10°–30°C which covers a wide range of working environments. If a user desires to employ a unit in temperature conditions beyond this range, temperature functions can be generated by calibrating the unit at such conditions. These functions are then incorporated into the unit's software. The correct value of the ratio $\Delta P/\Delta x$ is automatically selected by the software upon the user's selection of the working temperature.

The second characteristic of the unit is the location of the liquid level along the inclined manometer that corresponds to zero pressure output (the unit's output is differential pressure, with respect to atmospheric pressure). The liquid used is red gauge oil with a specific gravity of 0.826. Experiments conducted with it show that its evaporation rate is negligible. However, the unit automatically performs a self-detection of the zero-pressure level at user-specified time intervals.

For the following discussion, the reader is referred to Fig. 4. Let us define a one-dimensional coordinate system $0x$ with its axis aligned with the inclined member of the manometer as shown in Fig. 4. The location of the origin 0 is not important. Here, we take it to be located at the junction of the two manometer members. In the analysis below, all liquid levels will be specified by their coordinate x_i with respect to system $0x$. Let us assume that the user desires to generate a differential pressure value P_1 (with respect to atmospheric pressure). The unit's hardware and software achieve that through the following process. If x_0 is the zero-pressure level location, the traversing mechanism moves the CCD sensor such that its pixel #30 (for pixel numbering refer to Fig. 2) is located at coordinate x_1, such that

$$\frac{P_1}{x_1 - x_0} = \frac{\Delta P}{\Delta x} \qquad \text{(A)}$$

This means that if the liquid level were located at the 30th pixel the pressure output would be equal to P_1. Then, the solenoid network allows the unregulated pressure input to slowly increase the pressure at the output through an adjustable pressure regulator and an adjustable needle valve. Both pressure regulator and needle valve adjustments are set once, upon unit assembly, depending on the pressure range the unit is designed for.

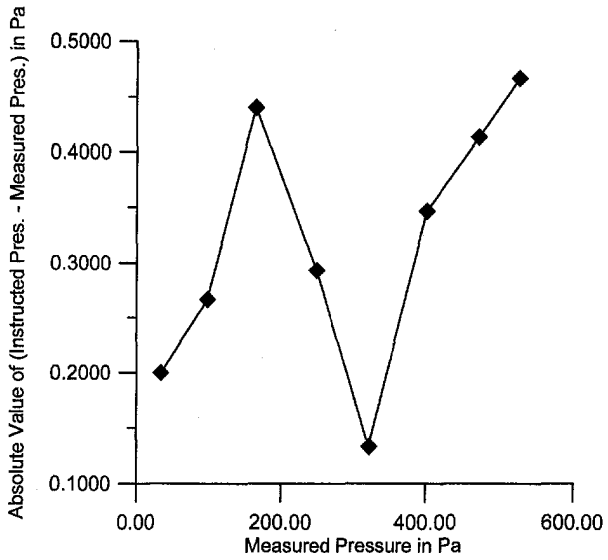

Fig. 5 ACCUPRES accuracy documentation plot

The rest of the solenoid network consists of typical two-way and three-way solenoid valves. They perform either of the following tasks: (a) route the pressure from the regulator-valve assembly to the manometer; (b) trap the generated pressure in the manometer when the desired pressure value has been achieved; and (c) vent the trapped pressure to the atmosphere for pressure resetting purposes. The pressure output is assumed to be connected to the instrument that accepts that pressure as input, for example a pressure transducer. The increase in pressure in turn causes the liquid level in the inclined manometer to rise. At the same time the sensor is checking for the existence of liquid-air interface above it. When the rising liquid level reaches the 50th sensor pixel, the solenoid network traps the generated pressure. It should be noted here that the solenoid valves of the network have a response time of about 20 ms. As a result, although the solenoid network receives the signal to trap the pressure when the level is at the 50th pixel, the valves actually engage to do so by the time the liquid level, which has continued to rise, has reached the neighborhood of the 30th pixel. However, if for any reason the level significantly overshoots the 20th pixel, the solenoid network releases some of the trapped pressure in increments of approximately 10 pixels, until the level reaches the neighborhood of the 30th pixel. This neighborhood is defined as the pixels between #20 and #40. Let us assume that the final location of the level is at pixel i, with $20 < i < 40$. The final output pressure will therefore be:

$$P = P_1 + (30 - i) \cdot w \cdot \left(\frac{\Delta P}{\Delta x}\right) \qquad \text{(B)}$$

where $w = 0.125$ mm is the distance between consecutive pixel centers.

Validation of Device Operation and Accuracy

Many tests were repeatedly conducted to validate the trouble-free operation of the device and document its accuracy. To ensure proper operation, independent of the host-computer processor type and speed, the device was tested in conjunction with different PC types from '286s to Pentium PCs. The typical test setup and sample test results are presented below.

The ACCUPRES output was connected to port P1 of a 590 Integral Barocel Pressure Transducer. The 590 Barocel in conjunction with a 1450 Electronic Manometer provided the capability for accurate differential pressure measurements over a range of 0–13.3 KPa with an accuracy of +/− 0.05 percent of the reading plus 0.001 percent of the full scale (F.S.). Port P2 of the Barocel was left open to the atmosphere so the measured pressure was with respect to atmospheric pressure. The Barocel's analog output was first amplified (×10 or ×100, depending on the pressure full scale that was being tested) by an instrumentation amplifier. The amplifier's output was then sampled by a DAS-08 A/D data-acquisition board installed in the ACCUPRES-host PC.

Through the control software, the ACCUPRES was instructed to generate a series of user-defined values of differential pressures (with respect to atmospheric pressure). Each generated pressure value was sensed by the Barocel and its output was sampled by the PC. Figure 5 presents the absolute value of the difference between the instructed and the measured (actually generated) pressure versus the measured pressure, for an ACCUPRES with full scale pressure output of +/− 533 Pa. It can be inferred from the figure that the accuracy is actually better than 0.08 percent F.S. (the accuracy here is defined as the standard deviation of the errors, following the work of Moffat, 1982).

The ACCUPRES as a Pressure Sensor

In a second mode of operation, the ACCUPRES can be used as a very accurate pressure measuring device. Its frequency response is low, therefore it is not suitable for fast varying pressure signals. However, it can accurately measure static pressures. In this mode of operation, the pressure to be measured should be connected to the unit's output (Fig. 4). The software takes care of the rest. The unregulated pressure input is no longer required. The accuracy is maintained at 0.08 percent F.S.

Conclusions

The operation and use of a new computer-controlled pressure-calibration/pressure-measurement device was presented. The unit can generate or measure low differential pressures (up to +/− 2.7 KPa) with an accuracy of 0.08 percent F.S. It is ideal for the automated calibration of pressure transducers employed in low-speed wind-tunnel testing as well as for static pressure measurements. The simplicity of its principle of operation is the source of its affordability and accuracy.

References

Moffat, R. J., 1982, "Contributions to the Theory of Single-Sample Uncertainty Analysis," ASME JOURNAL OF FLUIDS ENGINEERING, Vol. 104, pp. 250–258, June.

Rediniotis, O. K., and Chrysanthakopoulos, G., 1998, "A Wide-Range, High-Accuracy Neural/Fuzzy Calibration Technique for Flow-Diagnostics Instrumentation," ASME JOURNAL OF FLUIDS ENGINEERING, Vol. 120, No. 1, pp. 95–101, Mar.

Rediniotis, O. K., Hoang, N. T., and Telionis, D. P., 1993, "The Seven-Hole Probe: Its Calibration and Use," (invited) *Forum on Instructional Fluid Dynamics Experiments,* Vol. 152, pp. 21–26, June.

Texas Instruments, 1992, "TSL214, 64 1 Integrated Opto Sensor," May.